MODELLING AND CONTROL OF SERIES-CONNECTED FIVE-PHASE AND SIX-PHASE TWO-MOTOR DRIVES

Atif Iqbal

A thesis submitted in partial fulfilment of the requirements of Liverpool John Moores University for the degree of Doctor of Philosophy

August 2005

CONTENT

LIST OF PRINCIPAL SYMBOLS

v :	Voltage
i :	Current
ψ :	Flux linkage
R :	Resistance
L :	Inductance
M :	Magnetising inductance (per phase)
P :	Number of pole pairs
T_e :	Torque developed by the machine
T_L :	Load torque
J :	Inertia
p :	Differential operator
T_r :	Rotor time constant
ω :	Rotational speed of the rotor with respect to the stator
ω_a :	Rotational speed of the d-axis of the arbitrary common reference frame
ω_r :	Rotational speed of the rotor flux space vector with respect to the stator
ω_{sl} :	Slip speed
θ :	Instantaneous position of the magnetic axis of the rotor phase 'a' with respect to the stationary magnetic axis of the stator phase 'a'
θ_s :	Instantaneous angular position of the d-axis of the common reference frame with respect to the phase 'a' magnetic axis of the stator
θ_r :	Instantaneous angular position of the d-axis of the common reference frame with respect to the phase 'a' magnetic axis of the rotor
ϕ_r :	Instantaneous angular position of the rotor flux with respect to the phase "a" magnetic axis of the stator
$\underline{A}_s$:	Transformation matrix applied to stator quantities
$\underline{A}_r$	Transformation matrix applied to rotor quantities
$\underline{C}$:	Decoupling (Clark's) transformation matrix

$\underline{D}$: Rotational transformation matrix

α : 2π/*n* (where *n* = number of phases)

K_P : Proportional gain

K_i : Integral gain

T_i : Integral time constant

v_A, v_B, v_C.... : Inverter leg voltages

v_a, v_b, v_c.... : Phase to neutral voltages

v_{nN} : Voltage between star point of load and negative rail of dc bus

V_{DC} : DC link voltage

S_a, S_b, S_c.... : Switching functions

t_a, t_b : Time of application of neighbouring space vectors

t_s : Sampling time or switching time

t_o : Time of application of zero space vectors

γ : Proportion of time of application of medium space vectors

δ : Proportion of time of application of large space vectors

t_l : Time of application of large space vectors

t_m : Time of application of medium space vectors

t_{sh} : Time of application of short space vectors

<u>Superscripts</u>

* : Reference (commanded value)

INV : Inverter

I : Associated with first system of line voltages in six-phase VSI

II : Associated with second system of line voltages in six-phase VSI

III : Associated with third system of line voltages in six-phase VSI

<u>Subscripts</u>

n : Rated value

s : Associated with stator winding

r : Associated with rotor winding

l : Associated with leakage

α, β : Relates to variables after application of the decoupling transformation

d,q : Relates to variables after application of the decoupling and rotational transformations

$x-y$: Relates to non flux/torque producing variables

$abc...$: Associated with phase domain

$1,2$: Relates to machine number

ll : Line quantities

$0+$: Positive zero sequence quantities

$0-$: Negative zero sequence quantities

General

$\underline{\ }$: Underlined symbols are matrices except in sections 3.2.2, 3.3, 4.6, 5.2.2, 5.3 and 6.5 where underlining identifies space vectors

ABSTRACT

Numerous industrial applications, such as textile industry, paper mills, robotics and railway traction, require more than one electric drive. Currently, the multi-machine drive system is available in two different configurations. The first one comprises *n* three-phase VSIs feeding *n* three-phase motors individually while the second one is a system with *n* parallel-connected three-phase motors fed from a single three-phase VSI. The former drive system requires *n* three-phase VSIs while the latter system requires the motors to run under identical speed and torque conditions and hence it lacks means for independent control of motors. Thus in the present configurations it is not possible to independently control more than one machine with the supply coming from only one inverter.

This thesis considers means for independent control within multi-motor drive systems based on multi-phase machines and multi-phase VSIs. The objective is to accomplish independent control of all multi-phase machines in the group while using a single VSI. Such an independent control is enabled by using an appropriate series connection of stator windings of multi-phase motors and vector control principles. The fundamentals of the concept emerge from the fact that the multi-phase machines, regardless of the number of phases, require only two currents for flux and torque control. Hence there are extra currents, which can be utilised to control the second and subsequent multi-phase motors in a multi-motor drive system. An appropriate series connection of the stator windings converts the flux/torque producing currents of one machine into the non-flux/torque producing currents for the other machines, allowing independent control of each multi-phase motor using a vector control scheme.

Two multi-phase two-motor series-connected drive configurations are considered in detail in this thesis. These are the five-phase drive, consisting of two five-phase machines and a five-phase VSI, and the six-phase drive, comprising a symmetrical six-phase machine, a three-phase machine and a six-phase VSI. Detailed mathematical modelling of both drive systems is performed. It is proved in this way mathematically that independent vector control is indeed possible due to the specific stator winding connection. Detailed modelling of both five-phase and six-phase VSIs is further reported and a number of space vector PWM schemes are developed. Numerous simulation studies are performed for both five-phase and six-phase two-motor drives using indirect vector control principles and current control in the stationary reference frame (hysteresis and ramp-comparison), thus proving by simulation the possibility of independent control under realistic supply conditions.

Finally, a laboratory rig is described, which utilises a five-phase inverter. Five-phase two-motor drive systems, comprising two five-phase induction motors and a five-phase induction motor and a five-phase synchronous reluctance motor, respectively, are investigated experimentally. An analysis of the motor’s performance within the five-phase two-motor drive is presented and it is compared with performance of a single five-phase motor drive. The experimental results fully verify the existence of decoupled dynamic control of two machines in the series-connected five-phase drive.

Chapter 2

LITERATURE REVIEW

2.1 PRELIMINARY REMARKS

Literature review of some of the relevant research in the areas of multi-phase machines and multi-motor drives has been detailed in Jones (2002) and Jones (2005). The various aspects covered have included advantages of multi-phase machines over their three-phase counterparts, modelling and control of multi-phase machines, three-phase multi-motor drives, etc. This chapter reviews the latest progress made in the area of multi-phase machine drives, highlighting several other relevant aspects and addressing the features of the drives not covered in Jones (2002) and Jones (2005). Although the references are available for drive phase numbers equal to five, six, seven, nine and even fifteen, the literature review focuses on five-phase and six-phase drives. The reasons for concentrating on these two particular numbers of phases are twofold. Firstly, the project examines these two specific phase numbers only. Secondly, these are the two most frequently discussed phase numbers in literature.

The chapter gives an overview of the following aspects relevant for the project: application areas of multi-phase machines, the techniques for reduction of the switch power rating and count in three-phase motor drives supplied from three-phase inverters, and the modelling and control of multi-phase and three-phase inverters. It additionally includes a review of the newest developments in five-phase and six-phase motor drives, with an emphasis on papers published from 2002 onwards and not covered by Jones (2002) and Jones (2005).

2.2 SHIP PROPULSION, MORE ELECTRIC AIRCRAFT AND ELECTRIC VEHICLE APPLICATIONS OF MULTI-PHASE MACHINES

Ship propulsion, more-electric aircraft, hybrid electric vehicles and battery-powered electric vehicles have rapidly emerged during the last couple of years as the main potential application areas for multi-phase motor drives. The reasons behind this are primarily twofold. In high power applications (such as ship propulsion) use of multi-phase drives enables reduction of the required power rating per inverter leg (phase). In safety-critical applications (such as more-electric aircraft) use of multi-phase drives enables greater fault tolerance, which is of paramount importance. Finally, in electric vehicle and hybrid electric vehicle applications, utilisation of multi-phase drives for propulsion enables reduction of the required semiconductor switch current rating (although these drives are not characterised with high power, low voltage available in vehicles makes current high).

One particular interesting potential application of multi-phase motor drives is for an integrated starter/alternator in hybrid electric vehicles and ordinary vehicles with combustion engines. This idea enables replacement of two electric machines with a single machine. Due to its numerous good features, an induction machine is a candidate for this role. A single induction machine was proposed as the integrated starter-generator set in Miller et al (2001a, 2001b) and Miller and Stefanovic (2002). A special method of control, termed pole-phase-modulation (PPM) speed control, was developed for use in passenger hybrid electric car. An integrated starter-generator must suffice the very differing needs of both the starter (high starting torque at low speed) and the generator (wide speed constant-power range with fast voltage control). For this purpose, a nine-phase inverter was utilised and a nine-phase twelve-pole induction motor with toroidal winding was reconfigured into three-phase four-pole machine under vector control conditions by using PPM. By using a multi-phase machine in conjunction with this discrete speed control method it became possible to meet the requirements for an integrated starter-generator.

A six-phase permanent magnet (PM) synchronous motor with a specially designed stator and an outside rotor was investigated by Rattei (2001) for use in parallel hybrid electric vehicle drive for propulsion purposes in conjunction with internal combustion engine. The proposed motor nominal power was 8 kW at 2000 rpm and the maximum speed was 6000 rpm. The stator and rotor structures were designed with two poles and ten poles, respectively. The proposed structure offers several advantages over conventional surface mounted permanent magnet synchronous machine. Another example of an electric vehicle related proposal for utilisation of a six-phase machine is the work of Jiang et al (2003), where a novel PWM technique has been proposed. The method was aimed at six-phase induction motor drives, with the stator winding consisting of two sets of three-phase windings which were used to form dual-star six-phase winding with separate neutral points. The idea behind the concept was to extend the constant-power speed range. The proposed sinusoidal PWM reduces the phase current and dc link current harmonics and thus can increase the battery life which forms a considerable fraction of the operating cost of an electric vehicle.

Simoes and Vieira (2002) have proposed a five-phase high-torque low-speed PM brushless machine, which can be used as an in-wheel motor arrangement for electric vehicles. Very much the same proposal is contained in Simoes et al (2001) as well. The machine is in this case of the so-called brushless dc motor design, meaning that the spatial distribution of the MMF in the air-gap is trapezoidal and the machine therefore requires square-wave currents for normal operation.

As already noted, there is considerable ongoing research interest in the utilisation of multi-phase machine in safety-critical applications, such as more-electric aircraft fuel pump drives and flight control surface actuators. The conventional technology is to run the aircraft fuel pump from the engine gearbox. The fuel pumps are typically designed for maximum-output fuel flow rate at low engine speed, which is the take-off condition. At high altitude the engine runs at very high speed but requires less fuel. Consequently, a fuel by-pass system is used to return the excess fuel into the tank. Thus a need is felt to have an independent variable speed electric drive for the fuel pump. One of the most important aspects of such drives is the fault tolerant property to meet the crucial high reliability requirement. A four-phase six-pole, 16 kW, 15000 rpm PM machine was proposed by Mecrow et al (2003) to be used in more-electric aircraft fuel pump drive. The four phases of the machine are supplied independently by four single-phase inverters. The four phases are essentially isolated physically, magnetically and thermally, leading to a fault tolerant high reliability motor structure. Only alternate stator teeth carry a winding in this type of PM machine. A comprehensive design of such modular multi-phase PM brushless machines for use in more-electric aircraft fuel pumps and flight control surface actuators was presented by Ede et al (2002). The design is based on higher value of reactance so as to limit the short circuit current. It was pointed out that the machines have to be overrated if they are to be used as fault tolerant structures. The overrating factors for four, five and six-phase machines are found to be 1.33, 1.25 and 1.2, respectively. Thus a six-phase machine is suggested to be the optimum choice. Green et al (2003) have highlighted the problem of using the position sensor in more-electric aircraft fuel pump fault tolerant drive. The drive utilises a 16 kW, 13000 rpm six-phase permanent magnet motor with six independent single-phase inverters supplying each of the six phases. The authors proposed an alternative sensor-less drive scheme. The proposed technique makes use of flux linkage-current-angle model to estimate the rotor position.

A comprehensive description of possible three-phase fault tolerant motor drive structures was given by Ertugrul et al (2002) for use in safety-critical applications such as aerospace, nuclear power plants, military and medical services. The proposed modular motor drive (two-motor system with separate controllers and inverters for each machine) system configuration for three-phase permanent magnet ac motor increases the reliability through redundancy. Another proposed scheme is to feed the three windings of the three-phase motor from three single-phase inverters rather than a standard three-phase inverter.

The use of multi-phase electric generator sets for providing power to electric drives in ship propulsion is being investigated as well. Calfo et al (2002) have presented the comparative study regarding the use of conventional turbo synchronous generator and specially designed synchronous generators for such an application. It was shown that by using multi-phase (fifteen-phase) generator system, there is no need for special phase shifting transformers, which reduces the weight of the overall generating system. Further, by using high frequency generators, high pole number construction can be used, which leads to the reduction in the volume of the generator and associated transformer (if required), and vibration (resulting in more robust solution, resistant to mechanical shock). In aircrafts and ships the dc power is normally supplied by ac/dc converters. This requires special filters to eliminate the current ripple. Weiming et al (2002) have proposed an integrated multi-phase generator (with three-phase and twelve-phase windings) design to provide simultaneous ac and dc power generation. The twelve-phase winding has embedded rectifier to generate dc power and three-phase winding provides ac power. Use of multi-phase generator reduces the rectified dc voltage ripple as the ripple frequency is proportional to the number of pulses in the rectifier output, which is twice the number of phases.

2.3 THE NEWEST DEVELOPMENTS IN THE AREAS OF DUAL THREE-PHASE (QUASI SIX-PHASE) AND FIVE-PHASE SINGLE-MOTOR DRIVES

2.3.1 Dual three-phase (quasi six-phase) motor drives

Among different multi-phase drive solutions, so-called quasi six-phase machines (having dual three-phase windings with 30° spatial phase displacement) are probably considered most often in the literature. This is so since such a machine can be supplied from two three-phase inverters, thus eliminating the need for a design of a customised power electronic supply.

The major drawback of a true six-phase machine (with 60 degrees spatial displacement between any two consecutive phases) is the production of large stator current harmonics, if the machine is fed by two six-step VSIs. These generate additional losses resulting in increase in the size and cost of the machine and the inverter. These negative effects reduce significantly if quasi six-phase machine is used instead of a true six-phase machine [Klingshirn (1983)]. This, together with the easiness of obtaining a quasi six-phase machine from an existing three-phase machine, are the main reasons why quasi six-phase machines are predominantly dealt within literature.

The process of dynamic modelling of a quasi-six phase induction machine decomposes the original six-dimensional phase space into three two-dimensional orthogonal subspaces (d-q, x-y and 0+-0-). The neutral points of the two three-phase windings are in vast majority of cases isolated. In such a case the 0+-0- sequence components are eliminated since they cannot appear in any of the two star-connected three-phase windings. The d-q current components are flux and torque producing currents, while x-y stator current components appear due to stator current harmonics and are non flux/torque producing current components. Modelling procedures for quasi six-phase induction and synchronous machines have been discussed in detail in Bojoi et al (2002a), Hadiouche et al (2000), Lyra and Lipo (2002) and Benkhoris et al (2002). The dynamic decoupled model of a double-star synchronous machine with general spatial displacement between two three-phase windings, including decoupling algorithm, was presented by Benkhoris et al (2002). Two decoupling algorithms (called 'complete diagonalisation' and 'partial diagonalisation') were developed, based on the coupling due to mutual inductance between windings and due to rotational terms, respectively. The model contains two pairs of stator d-q axis currents (one pair for d-axis and another pair for q-axis) for use in a vector control scheme. The developed model was verified by simulation studies and by experimental investigation. A novel d-q-0 synchronous reference frame model of a quasi six-phase induction machine, which includes the third harmonic current injection effect, was presented by Lyra and Lipo (2002). Third harmonic current injection makes the stator current waveform and resulting air gap flux almost rectangular leading to an improvement in the flux density and an increase in the output torque of the machine. The model was validated by simulation and by experiments.

A complete model of a dual-stator induction motor, which consists of a single rotor winding and two identical stator windings, was presented by Pienkowski (2002). Two stator windings have in this case no magnetic coupling between them but they are magnetically coupled with the rotor winding and are supplied from the same or independent three-phase supply of the same frequency.

The major advantages of using a quasi six-phase machine, in contrast to a true six-phase machine, are once again shown by Singh et al (2003). The model developed in an arbitrary reference frame takes into account the common mutual inductances between two three-phase winding sets. The detailed comparison of performance of quasi six-phase and true six-phase induction machine has been presented. The simulation results are given for acceleration transients and steady state behaviour under six-step and PWM inverter supplies. The results show a significant reduction in torque and rotor current pulsation in quasi six-phase configuration. The frequency of torque pulsation in quasi six-phase machine is found to be doubled compared to true six-phase machine case. The reason for the reduction in the torque pulsation is due to the complete elimination of $6k\pm1$ (k = 1,3,5….) harmonics from the air-gap mmf. Further investigation under loaded conditions reveals that the torque pulsation is minimum in quasi six-phase machine. However, very little difference in the behaviour of the two configurations is found under PWM supply condition.

Two solutions are in general available as a mean of improving a six-phase motor drive performance. These include modified machine design and application of an appropriate PWM technique. Attempts have been made to exploit both possible solutions, with more effort being put into the second one. Hadiouche et al (2002) have proposed a new winding configuration for dual three-phase (i.e. dual-stator, as the machine is often referred to) induction machine aiming to maximise the stator slot leakage inductance to limit the harmonic current. The basic principle of the winding design consists in the placement of the conductors of stator 1 (the first three-phase winding) and stator 2 (the second three-phase winding) in two alternating slots with 8/9 pole pitch. This winding arrangement increases the x-y leakage inductance and thus limits the stator harmonic current.

A digital PWM technique called double zero-sequence injection modulation technique was proposed by Bojoi et al (2002a) to act on x-y components of voltage to limit the harmonic current in vector controlled quasi six-phase induction motor drive with isolated neutral points. Here one six-phase inverter is considered as combination of two identical three-phase inverters sharing a common dc link. Two sets of three-phase reference voltages are obtained from two reference voltage vectors, shifted in phase by 30° (electrical). This method was shown to produce satisfactory results with easy implementation on a low cost DSP platform. A double d-q synchronous reference frame current control, which uses four simple PI regulators instead of six, is proposed for inverter current control. The two sets of stator currents are independently controlled to compensate the inherent asymmetries in the two three-phase windings.

A comprehensive comparison of performance of quasi six-phase induction machine drive for six types of digital PWM techniques (space vector, multi-level space vector, vector space decomposition, multi-level vector space decomposition, vector classification and double zero-sequence injection) based on simulation and experimental study was given by Bojoi et al

(2002b). The study reveals that the vector classification and double zero sequence injection PWM techniques offer good results by minimizing the stator harmonic currents and simultaneously reduce the implementation complexity in a low-cost fixed-point DSP controller.

A number of papers, discussed further on, deal with some more specific issues related to six-phase motor drives. These include speed controller design, parameter estimation, dc link current calculation and operation under fault conditions.

A fuzzy logic based speed controller for quasi six-phase induction machine drive was proposed by Kalantari et al (2002). The flexible nature of the fuzzy logic speed controller gives good results for high precision speed control in wide speed range. With simple modification in fuzzy rules the same controller can be used under fault conditions as well.

On-line stator resistance estimation technique was proposed by Jacobina et al (2002) for quasi six-phase induction machine with connected neutral points. In the proposed technique non-torque producing homopolar voltage component (zero-sequence component) is injected along with the symmetrical six-phase voltages in the machine. This distorted voltage is used as the modulating signal for the six-phase pulse width modulator. Three line voltages and currents are measured and the non-torque producing voltage and current are calculated using the developed model. These non-torque producing current components are filtered by low pass filter and their derivatives are calculated. By processing the filtered data through the developed least square algorithm the values of resistances and leakage inductances are determined.

An analytical technique of formulating the dc link RMS current in PWM VSI fed quasi six-phase induction motor drive with isolated neutral points has been presented by Bojoi et al (2002c). Two PWM techniques were considered, sinusoidal PWM and sinusoidal PWM with 16.6% third harmonic addition. Both techniques were found to give similar results.

A double-star synchronous machine with an arbitrary spatial displacement between two three-phase windings with isolated neutral points, fed by two three-phase PWM inverters, was considered by Merabtene and Benkhoris (2002). A model was developed and it was further used to study the machine behaviour under open-circuit fault condition.

2.3.2 Five-phase single-motor drives

Direct torque control (DTC) is one of the powerful methods for high performance control of motor drives, which has become an industrially accepted standard for three-phase induction machines. The basic operating principle of DTC is based on instantaneous space vector theory and relies on utilisation of the non-ideal inverter nature to achieve good dynamic control. Toliyat and Xu (2000) have recently extended the DTC concept to a five-phase induction motor control and they presented a comparison between the three-phase and five-phase DTC drives. The implementation of the control system was done using 32 bit floating point TMS320C32 DSP. The three-phase inverter has only eight voltage space vectors that can be applied to a motor, while a five-phase inverter has 32 possible voltage space vectors. There is therefore a greater flexibility in controlling a five-phase drive system. The authors achieved high performance in terms of precise and fast flux and torque control and a smaller torque and flux ripple for five-phase induction machine as compared to three-phase induction machine.

Vector control and direct torque control of a five-phase induction motor with concentrated full-pitch winding was also developed and implemented again using 32 bit floating point DSP TMS320C32 in Xu et al (2002a). The proposed vector controller uses fundamental current in conjunction with 15% third harmonic stator current injection to provide quasi-rectangular current, which yields rectangular air gap flux in the concentrated-winding induction motor. It was shown that this approach enhances torque output by 11.2% under dynamic condition and by 10% during steady state operation, compared to the case when only fundamental current is fed to the machine. The DTC provides high performance in terms of smaller current, flux and torque ripples due to large number of space vectors for controlling the machine. Further, zero switching vectors are not needed to implement space vector modulation for five-phase PWM inverter for DTC and thus the wear and tear of motor bearing can be avoided. Shi and Toliyat (2002) have developed the vector control scheme based on space vector PMW for a five-phase synchronous reluctance motor drive. The control system for the proposed drive was again implemented using 32 bit floating point DSP TMS320C32.

A special current control scheme has been developed for a five-phase induction motor drive by Xu et al (2002b), which enables operation under open-circuit fault condition with loss of one or two phases. Concentrated winding induction motor was considered for the study and thus third harmonic current was used in conjunction with the fundamental component to obtain rectangular air–gap flux profile. The amplitudes of the fundamental and the third harmonic current need proper adjustment under fault condition. The speed and load have to be lowered under loss of two phases in order to prevent the stator current from exceeding the rated value. The whole system was implemented to validate the theoretical findings.

A detailed performance analysis of concentrated winding multi-phase induction motors encompassing multiple of three and non-multiple of three numbers of phases was carried out by Toliyat and Qahtany (2002) using finite element analysis (FEA) method. The study reveals the fact that the torque pulsation decreases with an increase in the number of phases due to smaller step changes in MMF, except in seven-phase case where ripple was high due to cogging phenomena. The efficiency was seen to improve with increasing number of phases because of the reduction in ripple in rotor current. Further the five-phase machine was seen to provide the highest torque to current ratio due to an increase in the amplitude of fundamental MMF. The FEA results also showed a decrease in the stator back iron flux and an increase in stator tooth flux if third harmonic current is injected along with the fundamental in the five-phase induction motor. This suggests a new geometry (pancake shape) for a five-phase machine stator supplied by the third harmonic along with the fundamental. A comparison of performance was also given for different multi-phase machines with respect to the conventional three-phase distributed winding induction motor.

A general modelling approach encompassing dynamic and control issues for a five-phase permanent magnet brushless dc machine was presented by Franceschetti and Simoes (2001). The simulation was done for a five-phase, twelve-pole machine with rated torque of 30 Nm, with concentrated stator winding. The same machine type, which requires square-wave current for its normal operation, has been considered in Simoes et al (2001) as well, where experimental implementation was based on Motorola 56824 DSP. The switching frequency of the inverter was set to 10 kHz. Five-phase trapezoidal back-emf permanent magnet synchronous machine was elaborated by McCleer et al (1991) as well. The motor was supplied from a five-phase VSI in 144º conduction mode with square wave currents. The five-phase machine was shown to have higher torque capacity compared to similar sized three-phase machine and lower peak VA requirement of the switching devices.

The modelling and analysis of a five-phase permanent magnet synchronous machine supplied from a five-phase PWM inverter under normal and fault conditions (one phase open-circuited) was examined by Robert-Dehault et al (2002). The linear permanent magnet machine model was developed in phase variable form for fault condition and also its d-q form was given for normal operating conditions. The machine leakage reactance was considered as 5% with PWM inverter commutating at 2 kHz. The proposed control strategy allows the machine to produce the same torque under fault condition as under normal condition, with very small torque ripple (6% torque ripple was observed because of the current controller type). Pereira and Canalli (2002) have presented the design, modelling and performance analysis of a five-phase permanent magnet synchronous machine operating as a generator feeding a resistive load through five-phase bridge rectifier. The parameters of the machine were determined using FEA. The performance in terms of load voltage versus current, output power, rectified voltage waveform, phase to neutral and phase to phase voltages and phase currents of the machine was assessed and examined using simulation and actual measurements.

2.4 METHODS FOR REDUCTION OF THE INVERTER SWITCH RATING AND INVERTER SWITCH COUNT

The primary focus in large power drive applications is on the reduction of the power switch rating, due to the limited voltage/current ratings of the available power semiconductor switches. This is, as already noted, one of the main driving forces behind the recent increase in the interest in multi-phase drives. The additional benefit of the reduction in the switch power rating is the possibility of the converter operation at a higher switching frequency.

In large power drive applications six-step inverters are sometimes used, with series and/or parallel connection of devices, depending on the voltage and current ratings. With such an arrangement some amount of motor derating is essential and there is the difficulty of dynamic voltage and/or current sharing during switching. A possible solution is the use of two (or more) parallel connected six-step inverters through a centre-tapped reactor at the output. This effectively increases the number of steps at the output from six to twelve, if two inverters are paralleled (or eighteen if three inverters are paralleled). The use of higher number of steps eliminates the lower order harmonics (the fifth and seventh if two inverters are paralleled), but at the cost of a large number of devices with complex power and control circuit. It is for this reason that, whenever possible, pulse width modulated inverter is used in industrial applications. This inverter control method is characterised with control flexibility and an acceptable harmonic spectrum. In general, higher the PWM inverter switching frequency is, better the harmonic content will be, since the output voltage harmonics appear in the linear PWM mode around multiples of the switching frequency. However, high switching frequency leads to high switching losses and its application is nowadays restricted to low and medium power drives. High power drives, when operated in the PWM mode, have a rather low switching frequency of the order of a couple of hundreds of Hertz.

An interesting potential solution to the problem of the switch rating reduction in three-phase induction motor drives is to bring to the machine’s terminal box all six terminals of the stator three-phase winding. Instead of forming a neutral point and supplying the winding from one three-phase inverter, the winding is now supplied from two three-phase inverters. The first one is connected to the input terminals of the winding, while the second three-phase inverter is connected to the output terminals of the same winding. An open-ended stator winding is formed in this way. This concept actually enables creation of an overall voltage at the winding, which corresponds to a multilevel inverter output, although both three-phase inverters are actually two-level. In particular, Shivakumar et al (2001, 2002) have shown that the three-level voltage waveform can be obtained by feeding both ends of the open-end three-phase induction motor by two two-level inverters. The open-ended three-phase induction motor is supplied from two inverters, whose input dc voltage is one half of the normal dc link voltage which would have been required had only one two-level inverter been used. Using such scheme sixty four voltage vectors (compared to twenty seven vectors for a conventional three-level inverter) are produced, whose vertices form twenty four equilateral triangles. This large number of space vectors are utilised by a space vector PWM algorithm to generate high resolution output voltage. The triplen harmonic currents, which are generated because of the open-end winding configuration of the motor, are suppressed by using two separate isolated transformers to feed the two inverters. This technique reduces the individual inverter switching frequency to half the motor phase voltage switching frequency and lowers the switch rating to half that of the conventional two-level inverter. The switch rating halves as well. The concept was further extended by Somasekhar et al (2002a) by using two two-level inverters with asymmetrical dc link voltage (2/3 V_{DC} and 1/3 V_{DC}, where V_{DC} is the dc link voltage of a conventional two-level inverter) in conjunction with space vector PWM. By using asymmetrical dc link voltages for two inverters a total of thirty seven voltage space vectors are generated. The proposed scheme enables operation of the two-inverter set as two-level (the lowest speeds), three-level (medium speeds) and four-level (high speeds) inverter, by properly choosing the space vectors from the available set forming a total of fifty four equilateral triangle sectors. The main benefit of the proposed configuration is that the lower voltage inverter is switched more often than the high voltage inverter, thus making it an ideal choice for high power drives. A reduction in switching losses and a lower switch rating are achieved, however at the expense of a complex control strategy and the requirement for two isolated transformers. A special space vector based PWM scheme is proposed by Somasekhar et al (2002b) for an open-end three-phase induction motor drive fed by two two-level inverters, with the idea of eliminating the fluctuating neutral phenomena by allowing only ripple current to flow through the dc link capacitor. The proposed PWM switching strategy also suppresses the zero sequence component of the current by using auxiliary switch-assisted neutral generation without the need for isolated transformers for supplying the two inverters. Mohapatra et al (2002) have used different dc link voltage ratio (1:0.366) for controlling the open-end three-phase induction motor drive. The proposed triangular PWM scheme is used to eliminate lower order harmonics ($6n\pm1$, n=1,3,5….) from motor phase voltages. Two different modulating signals (square and square with symmetrical notches) are used for controlling the two two-level inverters. The next higher order harmonics (11^{th}, 13^{th}, 23^{rd}, etc) can be suppressed by increasing the frequency modulation ratio. The inverter switching frequency is controlled within 500 Hz by properly selecting the frequency modulation ratio.

The same technique is applied in a six-phase induction motor drive (two sets of three-phase groups with 30 degrees spatial displacement, termed here quasi six-phase and originally called by Gopakumar et al (1993) split-phase) by Mohapatra et al (2002a). Each three-phase winding is fed from both sides by two two-level inverters, having isolated asymmetrical (1:0.366) dc link supply. The inverter switching frequency is controlled within 600 Hz by properly selecting the frequency modulation ratio.

Another inverter configuration was proposed by Baiju et al (2003) to generate space vector equivalent to a five-level inverter (sixty one space vector locations with ninety six triangular sectors) for an open-end winding three-phase induction motor drive in order to reduce the switching losses and the switch rating. The five-level inverter equivalent was obtained by using two three-level inverters, where the three-level inverter equivalents are realised by cascading two two-level inverters. A modified sinusoidal PWM with addition of discrete dc bias depending upon the speed range of the motor was proposed. This technique reduces the switching frequency at low speeds by operating the inverter as a two-level and the number of levels increases with an increase in the speed. There is no need for neutral clamping diodes and the fluctuating neutral is absent in the proposed scheme.

The schemes reviewed so far in this section were aimed at reduction of the switch power rating, at the expense of an increase in the number of switches required. Such schemes are predominantly being developed for high power applications. Another possibility, which is very attractive in low and medium power applications, is the reduction of the switch count, which can be achieved at the expense of an increase in the switch rating. One such solution is a multi-motor three-phase drive system fed by a single three-phase inverter. The use of multi-motor drives is common in many industries (textile, paper mills, traction and steel mills etc). For a two-motor drive, the approach halves the number of required switches, compared to the system with two individual inverters. However, if two motors are paralleled to the same inverter output, voltage and frequency applied to the two motors are always identical and independent control of the two motors is not possible. The idea is therefore applicable only in multi-motor drives that have identical motors and the motors are required to operate with an identical speed under the same loading conditions. Vector control method can then be employed to control such a two-motor system, where two paralleled motors are treated as a single motor. Any unbalance in loading of the motors will lead to the instability of the whole drive system. This technique was discussed by Kawai et al (2002) and was applied to two three-phase induction motors with same ratings (2.2 kW, 180 V). Kuono et al (2001a, 2001b) and Matsuse et al (2002) have proposed sensor-less vector control method based on average and differential current to control two parallel connected three-phase induction motors fed by a single inverter. They have attempted to extend the control method to two motors of different ratings (3.7 kW, 160 V & 2.2 kW, 180 V) which nevertheless have to operate under identical conditions.

Several schemes have been developed with the idea of reducing the number of switches in three-phase induction motor drives. Reduction of the switch count leads to a reduction in the count of auxiliary electronic components, volume and weight of the inverter. One such scheme was proposed by Francois and Bouscayrol (1999). They reduced the power switch count by using a five-phase VSI to feed two three-phase induction motors. The power circuit topology is such to feed the four phases of the motors (two phases of each) by four legs of the inverter, while the fifth leg is common to both motors. The inverter control technique based on Pulse Position and Width Modulation (PPWM) was developed to independently control the two three-phase induction motors. The number of power switches has been reduced from twelve (for two three phase inverters) to ten, but the dc link voltage is doubled in order to maintain the same performance of the drive.

2.5 CONTROL OF THREE-PHASE AND MULTI-PHASE VOLTAGE SOURCE INVERTERS

2.5.1 Control of three-phase voltage source inverters

Control of three-phase VSIs is nowadays, except in the highest power range, always based on PWM schemes. PWM is the basic energy processing technique, used to obtain the converter output power of required properties. Semiconductors are switched at a high frequency, ranging from a few kilohertz (motor control) to several megahertz (resonant converters for power supply) [Kazmierkowski et al (2002)]. A broad classification of PWM techniques groups the methods into two classes: open-loop PWM and closed-loop PWM.

Among the best known open-loop PWM techniques is the carrier-based sinusoidal PWM, which is also called ramp-comparison or sine-triangle or sub-oscillation method. In this technique triangular carrier signals are compared with sinusoidal modulating waves to generate the switching signals for power switches [Bose (1996)]. With the advent of high speed and cheap digital signal processors, space vector pulse width modulation (SVPWM) has become a standard for power inverters as it gives superior performance compared to the ramp-comparison technique. The reference voltage space vector is generated on average by imposing two neighbouring active vectors and a zero space vector in the three-phase VSI. The basic theory and implementation of SVPWM are discussed at length by Neascu (2001). The major advantages of SVPWM include wide linear modulation range for output line-to-line voltages and easiness of digital implementation. The digital implementation can be done using memory look-up table for sinusoidal function within a 60º interval. The alternative solution is based on interpolation of a minimized look-up table, which can be implemented by a fuzzy logic controller as well. A detailed comparison of carrier-based PWM methods, including those with additional zero sequence signal injection, with SVPWM was presented by Zhou and Wang (2002). The comparison looked at the relationship between modulation signals and space vectors, modulation signals and space vector sectors, switching pattern of space vectors and the type of the carrier, distribution of zero vectors and different zero-sequence signals. It was observed that the methods are closely related and can be derived from each other.

Multi-level (especially three-level) inverters are nowadays normally employed in high power applications. There have been many three-level modulation techniques reported in literature. Similar to two-level inverters, the popular choices are again carrier-based PWM and SVPWM. In carrier-based PWM, each phase reference voltage is compared to two identically shaped (but with different offset content) triangular waveforms in order to generate the switching pattern. In the case of SVPWM a higher number of space vectors (sixty four) are available for precise and flexible control of the three-level inverters. A comparative analysis of ramp-comparison PWM and SVPWM for three-level inverters was reported by Wang (2002). The three-level SVPWM equivalent can be realised by ramp-comparison PWM using a proper third harmonic injection, while three-level sine-triangle PWM can be realised through SVPWM by selecting proper dwell times (times spent in a given switching state).

The second group of methods encompasses closed-loop PWM techniques. In this case the inverter PWM pattern is determined by closed-loop current control of inverter output currents. The basic reason of introducing current control is the elimination of stator dynamics

[Novotony and Lipo (2000)]. The main task of a current controlled PWM inverter is to force the load current to follow the desired reference current. By comparing the actual and reference phase currents, the current controller generates the switching signals for power devices in order to reduce the current error. The current controller therefore performs two functions, current error compensation and PWM. Various current control techniques have been developed over the years. The examples include hysteresis, ramp-comparison and predictive current control. Application of these methods to three-phase drives were examined by Andriux and Lajoie-Mazenc (1985), Brod and Novotony (1985), and Gio et al (1988). Among these techniques, hysteresis current control is the simplest to implement, it gives fast dynamic response, is insensitive to load parameter variations and it offers inherent current limitation. The major disadvantage of the hysteresis current control is that it gives a varying switching frequency over one cycle of the inverter output. Several other techniques are available, including already mentioned ramp-comparison current control, which give constant switching frequency of inverter. These include adaptive hysteresis controller proposed by Bose (1990), in which the hysteresis band is modulated with load and supply parameters, and dual-band hysteresis current control. In dual-band hysteresis current control also known as space-vector based hysteresis current control, the switching states and thus the inverter output voltage vectors are chosen such as to minimize the derivative of the current error vector. A fully digital implementation of this scheme, using field programmable gate array (FPGA), was done by Brabandere et al (2002) in three-phase induction motor drive. The ramp-comparison current control is however still the most popular choice because of its simplicity and inherent advantages. Almost all the motor DSP controllers available today have hardware peripherals for implementation of digital modulation based on the ramp-comparison technique.

The main objective in a high performance drive is to control the torque and flux of the machine, which are governed by the fundamental current. A fast current control scheme must be incorporated to achieve the set goal. All the current control methods, utilised in vector controlled drives, essentially belong to one of the two categories: current control in stationary reference frame or current control in rotational reference frame. A comparative study of the methods belonging to these two categories was presented by Sokola et al (1992) in conjunction with a permanent magnet synchronous motor drive. Current control by means of hysteresis controllers and ramp-comparison controllers (in the stationary reference frame) and current control in the rotational reference frame (in conjunction with voltage generation by ramp-comparison method and by space vector modulator) was examined. The current control in the rotational reference frame was found to be superior to the current control in the stationary reference frame.

A space vector approach has been proposed by Bolognani and Zigliotto (2002) for analysis and design of stationary and rotating reference frame current controllers which allows deeper understanding of the behaviour of the controllers. An adaptive high-bandwidth current control algorithm was introduced by Telford et al (2003) for an indirect rotor flux oriented induction motor drive. A comparison between the conventional rotating reference frame PI controller, a conventional dead-beat controller and the proposed adaptive high-bandwidth controller has been conducted by simulation and experimentation. The proposed controller gives similar dynamic performance as the dead-beat controller, with no overshoot. However, it is immune to machine parameter variations, errors in flux estimates and dc bus voltage level fluctuations. Further, it was found to be superior to synchronous rotating reference frame PI controller since it was capable of producing faster dynamic response. However, its steady state error was higher.

2.5.2 Control of multi-phase voltage source inverters

The use of multi-phase inverter was first reported by Ward and Härer (1969) in a variable speed five-phase induction motor drive application. It utilised a forced commutated thyristor based inverter in ten-step operating mode. The torque ripple was decreased to one third compared to the equivalent three-phase case and was at an increased frequency. However, the machine current contained strong third harmonic component, which generated additional losses. To avoid these losses and to obtain fast current control, several PWM techniques for multi-phase VSIs have been developed, such as those reported in Pavitharan et al (1988), Toliyat (1998) and Toliyat et al (2000).

A complete mathematical model of a five-phase VSI, based on space vector representation, was developed by Toliyat et al (1993). The inverter operation in ten-step mode and PWM mode was discussed. The hysteresis type PWM current regulation was used for the drive under rotor flux oriented indirect vector control conditions. A SVPWM was proposed by Gataric (2000) for a five-phase VSI control in conjunction with induction motor drives. The same strategy was employed by Shi and Toliyat (2002) and Toliyat et al (2000) in a five-phase synchronous reluctance motor drive. Gopakumar et al (1993) employed SVPWM technique in split-phase induction motor drive fed by six-phase VSI.

Takami and Matsumoto (1993) have proposed optimum pulse pattern PWM for large capacity nine-phase VSI feeding a nine-phase induction motor (with three sets of three-phase windings on the stator with isolated neutral points and a single three-phase winding on the rotor). The current control loop was eliminated from the inverter control system. A new configuration, which includes nine low-rating (20% of the motor capacity) single-phase reactors, was introduced. The reactor turns ratio was selected equal to 1:2sin(π/18):1 so as to eliminate the lower order harmonics (5^{th}, 7^{th}, 11^{th} and 13^{th}) from the inverter/motor phase voltages and currents and also to balance the fundamental currents in the event of unbalancing. To eliminate even harmonics from the current/voltage waveform the optimal pulse pattern was developed based on Lagrangian multiplier method. The proposed optimal pulse pattern PWM technique was compared with the ramp-comparison PWM and it was shown to reduce the harmonic amplitudes to a significantly lower value. The proposed configuration also reduces the electromagnetic noise of the motor to a great extent.

Kelly et al (2001) have examined general *n*-phase (leg) inverter control techniques taking nine-phase inverter as a specific example. An *n*-phase inverter has (*n*-1)/2 possible load equivalent circuits and each operates in *n*-step mode to produce a unique step voltage waveform with different fundamental and harmonic contents. The nine-phase inverter was examined for four different load equivalent configurations in eighteen-step mode and 4-5 configuration was found to be the optimum choice because of the highest switching efficiency (only one switch changes state between conduction intervals), maximum phase current delivery and maximum fundamental content. Four different SVPWM techniques have been developed for the general *n*-phase inverter. The first technique is a natural extension of the conventional three-phase SVPWM and it resulted in lower dc bus utilisation. The second technique asks for injection of $\sqrt{n}$ order harmonic, resulting in higher dc bus utilisation (maximum attainable fundamental component increases). However, $\sqrt{n}$ separate neutrals have to be used. The third proposed technique utilises smaller number of space vectors (74 instead of 512) but the switching efficiency was found to be poor in this case (in the case of nine-phase inverter, eighteen switches change state between conduction intervals). To improve the switching efficiency the fourth technique was proposed, which does not use zero space vectors (in the case of a nine-phase inverter, only six switches change state between conduction intervals). The first proposed technique (SVPWM) in the above referenced work was compared analytically and by experimentation to the ramp-comparison PWM by Kelly et al (2003) in conjunction with a nine-phase inverter fed nine-phase induction motor drive. The SVPWM was shown to enhance the fundamental by 1.55% compared to the sine-triangle PWM and thus enables better utilisation of the dc bus.

From various publications related to current control of inverter fed multi-phase machines it is evident that the same current control strategies as for a three-phase machine are in principal applicable regardless of the number of phases. Hysteresis current control scheme for a five-phase induction motor drive was reported by Toliyat (1998). In the vector control of a five-phase synchronous reluctance motor, hysteresis current controllers were used by Shi et al (2001). A global current control method for a five phase H-bridge VSI (i.e. an inverter system consisting of five single-phase inverters) was presented by Martin et al (2002). It was based on space vector control method and was aimed at control of a five-phase permanent magnet synchronous machine (PMSM). The independent current control of each phase leads to high current ripple as the dynamics of one phase depend on the states of the other inverter legs and because of the magnetic coupling between the phases. The basic principle consists in the representation of a machine by fictitious machines consisting of two groups, named the main machine and the secondary machines. For an odd number of phases equal to n, the equivalent number of fictitious machines are $(n+1)/2$ without mutual magnetic coupling. Out of this number there are $(n-1)/2$ two-phase machines and one single-phase machine. The torque-producing machine is only the first two-phase machine and the remaining machines just add to the losses. The current dynamics of non-torque producing machines are limited by only small leakage inductance, which leads to high current ripple. Thus the duration of excitation to these non-torque producing fictitious machines are reduced by means of global current control strategy. The current controller produces the voltage reference vector, which is reconstituted over each sampling period by an optimal combination of the voltage vectors. It should be noted that the concept of space vector decomposition was applied in this paper, similar to Gataric (2000). This thesis will use both the concept of matrix transformations [White and Woodson (1959)] and space vector decomposition.

Ramp-comparison current controller was used by Bojoi (2002a) for a six-phase PWM inverter. Several types of current control schemes were proposed by Figueroa et al (2002) for controlling a seven-phase VSI for a brushless dc motor drive. These include the sinusoidal reference current control, synchronous reference frame current control, sampled sinusoidal current control, dc bus current control, square voltage and sampled sinusoidal voltage control. The comparative performance analysis was conducted using simulation and experimentation and it was observed that the last strategy provides an optimum result. It yielded high efficiency, low torque ripple, good torque-speed characteristic and simple control with low cost Hall position sensors.

2.6 SUMMARY

A comprehensive literature review, related to the relevant aspects of the research in this project, is presented in this chapter. The potential application areas for multi-phase motor drives, such as more-electric aircraft, ship propulsion and electric and hybrid vehicles are surveyed at first. It is concluded that multi-phase machine drives in such applications offer many advantages when compared to their three-phase counterparts, primarily due to the increased reliability, flexible control features and potential for reduction of the switch power rating. The latest developments in the area of multi-phase motor drives are examined next, with an emphasis on five-phase and six-phase (true and quasi) drives.

In high power three-phase drive applications the power switches have to be connected in series and/or parallel resulting in static and dynamic voltage sharing problem. Any multi-phase drive is a way of reducing the switch rating, when compared to the three-phase drive of the same power. The relevant literature for reduction of the inverter per-phase (i.e. switch) rating using an open-end three-phase motor drive is reviewed further in this chapter. The same applies to the six-phase (split-winding) open-end induction motor drive. Another aspect, important in low and medium power range, is the reduction of the switch count. This can be achieved by paralleling three-phase motors and supplying them from a single three-phase inverter. Such schemes are available in the literature and are reviewed in the chapter. Several limitations of this approach are addressed as well.

The papers related to the modelling and control of three-phase and multi-phase inverters, encompassing both the open-loop and closed-loop PWM schemes, are finally studied and a review is presented. Some newly developed inverter control methods, such as for example adaptive high-bandwidth current control algorithm, are also examined. The choice of an appropriate PWM technique for a multi-phase inverter is an important issue, as the use of multi-phase machines introduces severe distortion of stator current, leading to large winding losses and increased stress on inverter. It is concluded that, in principle, the already available current control methods for three-phase inverters are applicable to multi-phase inverters as well.

Chapter 3

MODELLING AND CONTROL OF A FIVE-PHASE INDUCTION MOTOR DRIVE

3.1 INTRODUCTION

This chapter details at first the modelling and control of a five-phase VSI. The modelling of five-phase VSI is done for ten-step (section 3.2) and PWM operation (section 3.3) modes based on space vector theory, and Fourier analysis is given for ten-step mode as well. The five-phase machine model is developed next in phase domain and then it is transformed into a system of decoupled equations in orthogonal reference frames (section 3.4). The d-q axis reference frame currents contribute towards torque and flux production, whereas the remaining x-y components plus the zero-sequence components do not. This allows a simple extension of the rotor flux oriented control (RFOC) principle to a five-phase machine, as elaborated in section 3.5.

The inverter current control techniques, used in vector control, are further reviewed in section 3.6. Current control in stationary reference frame is elaborated using hysteresis method and ramp-comparison method. Tuning of the speed controller and the current controller is performed for the given drive parameters and the procedure is described in detail. A simulation study is finally performed for speed mode of operation, for a number of transients, and the results are presented in section 3.7. In this section, a steady state analysis is carried out using Fast Fourier Transform (FFT) of voltage and current waveforms for hysteresis current control method and the resulting plots and values are given.

The analysis of the five-phase voltage source inverter operation, reported in sections 3.2–3.3, is in full agreement with findings reported in Shi and Toliyat (2002), Xu et al (2002a), Toliyat et al (2000), Toliyat (1998), Toliyat et al (1993), and Ward and Härer (1969). Five-phase induction motor modelling and vector control principles, reviewed in sections 3.4–3.5, are elaborated in more detail in Jones (2002) and Jones (2005). Some original research results, obtained during the work on this project, are contained in section 3.7 and have been published in Iqbal et al (2003).

3.2 TEN-STEP OPERATION OF A FIVE-PHASE VOLTAGE SOURCE INVERTER

Formatted: Bullets and Numbering

3.2.1 Power circuit and switch control signals

Power circuit topology of a five-phase VSI, which was used probably for the first time by Ward and Härer (1969), is shown in Fig. 3.1. Each switch in the circuit consists of two power semiconductor devices, connected in anti-parallel. One of these is a fully controllable semiconductor, such as a bipolar transistor or IGBT, while the second one is a diode. The input of the inverter is a dc voltage, which is regarded further on as being constant. The inverter outputs are denoted in Fig. 3.1 with lower case symbols (a,b,c,d,e), while the points of connection of the outputs to inverter legs have symbols in capital letters (A,B,C,D,E). The basic operating principles of the five-phase VSI are developed in what follows assuming the ideal commutation and zero forward voltage drop.

Deleted: voltage source inverter (

Deleted:)

Each switch is assumed to conduct for 180°, leading to the operation in the ten-step mode. Phase delay between firing of two switches in any subsequent two phases is equal to 360°/5 = 72°. The driving control gate/base signals for the ten switches of the inverter in Fig. 3.1 are illustrated in Fig. 3.2. One complete cycle of operation of the inverter can be divided into ten distinct modes indicated in Fig. 3.2 and summarised in Table 3.1. It follows from Fig. 3.2 and Table 3.1 that at any instant in time there are five switches that are ‘on’ and five switches that are ‘off’. In the ten-step mode of operation there are two conducting switches from the upper five and three from the lower five, or vice versa.

3.2.2 Space vector representation of a five-phase voltage source inverter

In order to introduce space vector representation of the five-phase inverter output voltages, an ideal sinusoidal five-phase supply source is considered first. Let the phase voltages of a five-phase pure balanced sinusoidal supply be given with

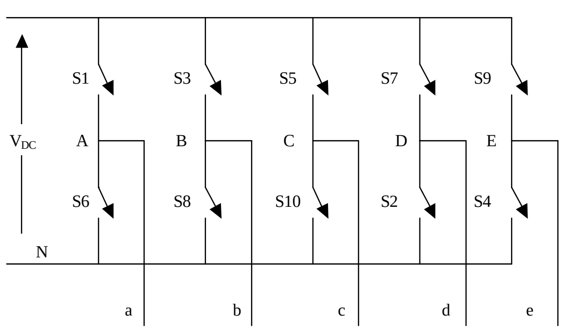

Fig. 3.1. Five-phase voltage source inverter power circuit.

Deleted:

Table 3.1. Modes of operation of the five-phase voltage source inverter (ten-step operation).

Mode	**Switches ON**	**Terminal polarity**
9	1,7,8,9,10	$A^+B^-C^-D^+E^-$
10	8,9,10,1,2	$A^+B^-C^-D^-E^+$
1	9,10,1,2,3	$A^+B^+C^-D^-E^+$
2	10,1,2,3,4	$A^+B^+C^-D^-E^-$
3	1,2,3,4,5	$A^+B^+C^+D^-E^-$
4	2,3,4,5,6	$A^-B^+C^+D^-E^-$
5	3,4,5,6,7	$A^-B^+C^+D^+E^-$
6	4,5,6,7,8	$A^-B^-C^+D^+E^-$
7	5,6,7,8,9	$A^-B^-C^+D^+E^+$
8	6,7,8,9,10	$A^-B^-C^-D^+E^+$

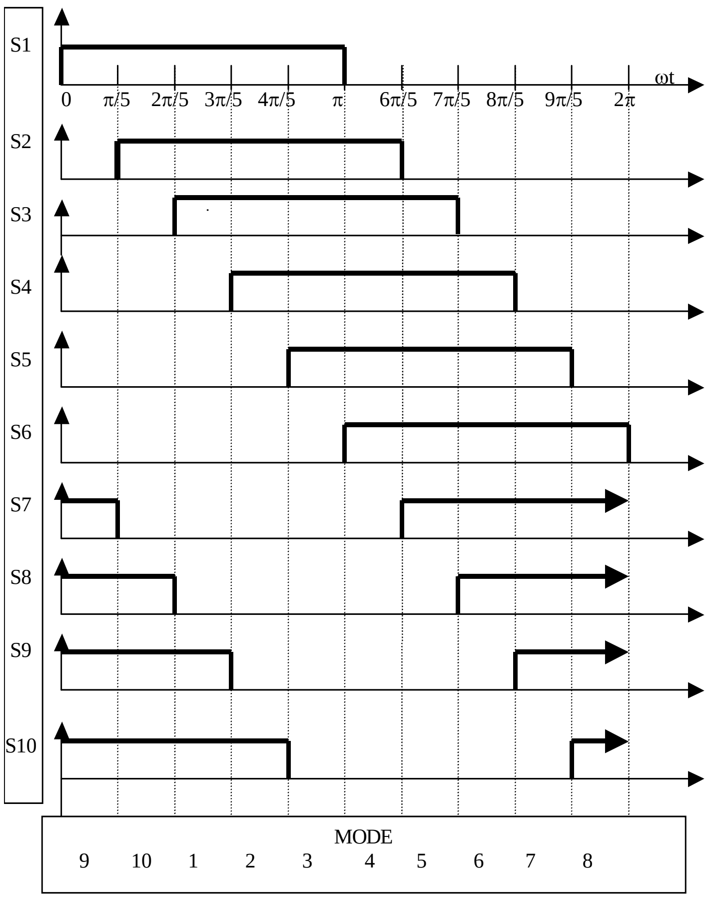

Fig. 3.2. Driving switch signals of a five-phase voltage source inverter in the ten-step mode.

Deleted:

$$
\begin{aligned}
v_a &= \sqrt{2}V\cos(\omega t) \\
v_b &= \sqrt{2}V\cos(\omega t - 2\pi/5) \\
v_c &= \sqrt{2}V\cos(\omega t - 4\pi/5) \qquad\qquad (3.1) \\
v_d &= \sqrt{2}V\cos(\omega t + 4\pi/5) \\
v_e &= \sqrt{2}V\cos(\omega t + 2\pi/5)
\end{aligned}
$$

Space vector of phase voltages is defined, using power invariant transformation, as:

$$\underline{v} = \sqrt{2/5}(v_a + \underline{a}v_b + \underline{a}^2 v_b + \underline{a}^{*2} v_d + \underline{a}^* v_e) \qquad (3.2)$$

where $\underline{a}$ = exp(j2π/5), $\underline{a}^2$ = exp(j4π/5), $\underline{a}^*$ = exp(-j2π/5), $\underline{a}^{*2}$ = exp(-j4π/5) and * stands for a complex conjugate. The space vector is a complex quantity, which represents the five-phase balanced supply with a single complex variable. Substitution of (3.1) into (3.2) yields for an ideal sinusoidal source the space vector

$$\underline{v} = \sqrt{5}V \exp(j\omega t) \qquad (3.3)$$

However, the voltages are not sinusoidal any more with the inverter supply. They are in general of quasi-square waveform. Leg voltages (i.e. voltages between points A,B,C,D,E and the negative rail of the dc bus N in Fig. 3.1) are considered first. Table 3.2 summarises the values of leg voltages in the ten 36 degrees intervals and includes the numbers of the switches that are conducting.

Table 3.2. Leg voltages of the five-phase VSI.

Deleted:

Deleted: V

Switching state (mode)	Switches ON	Space vector	Leg voltage v_A	Leg voltage v_B	Leg voltage v_C	Leg voltage v_D	Leg voltage v_E
1	9,10,1,2,3	$\underline{v}_1$	V_{DC}	V_{DC}	0	0	V_{DC}
2	10,1,2,3,4	$\underline{v}_2$	V_{DC}	V_{DC}	0	0	0
3	1,2,3,4,5	$\underline{v}_3$	V_{DC}	V_{DC}	V_{DC}	0	0
4	2,3,4,5,6	$\underline{v}_4$	0	V_{DC}	V_{DC}	0	0
5	3,4,5,6,7	$\underline{v}_5$	0	V_{DC}	V_{DC}	V_{DC}	0
6	4,5,6,7,8	$\underline{v}_6$	0	0	V_{DC}	V_{DC}	0
7	5,6,7,8,9	$\underline{v}_7$	0	0	V_{DC}	V_{DC}	V_{DC}
8	6,7,8,9,10	$\underline{v}_8$	0	0	0	V_{DC}	V_{DC}
9	7,8,9,10,1	$\underline{v}_9$	V_{DC}	0	0	V_{DC}	V_{DC}
10	8,9,10,1,2	$\underline{v}_{10}$	V_{DC}	0	0	0	V_{DC}

For calculation of leg voltage space vectors, individual leg voltage values from Table 3.2 are inserted in the equation (3.2) which defines the voltage space vector. The results are tabulated in Table 3.3 and an illustration of leg voltage space vectors is shown in Fig. 3.3.

Line-to-line voltages are elaborated next. The adjacent line-to-line voltages at the output of the five-phase inverter are defined in Fig. 3.4, for a fictitious load. Table 3.4 summarises the values of the adjacent line-to-line voltages in the ten 36 degrees intervals. Since each line-to-line voltage is a difference of corresponding two leg voltages, the values of line-to-line voltages in Table 3.4 are obtained using leg voltage values in Table 3.2.

The adjacent line-to-line voltage space vectors are calculated by substituting the values from Table 3.4 into the defining expression (3.2) and the results are tabulated in Table

3.5. The adjacent line-to-line voltage space vectors are illustrated in Fig. 3.5. Corresponding time-domain waveforms are displayed in Fig. 3.6.

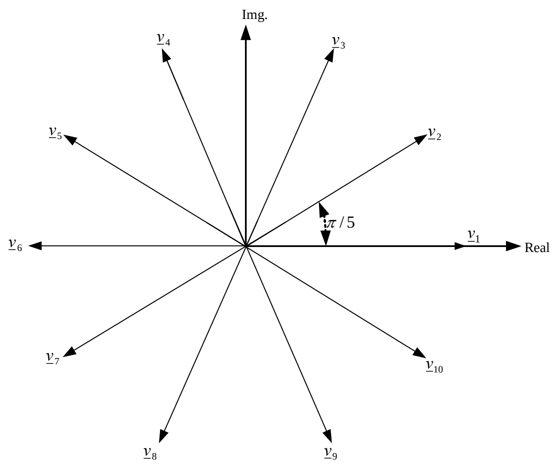

Fig. 3.3. Leg voltage space vectors in the complex plane.

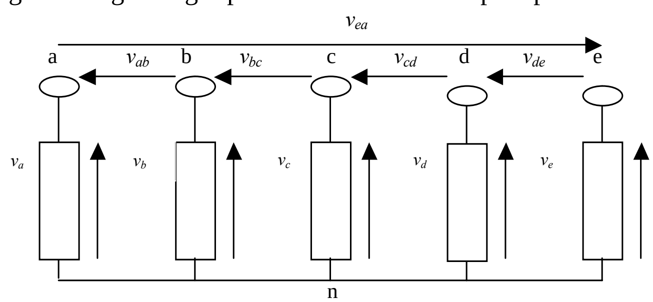

Fig. 3.4. Adjacent line-to-line voltages of a five-phase star-connected load.

Table 3.3. Leg voltage space vectors of the five-phase VSI.

Leg voltage space vectors	
$\underline{v}_1$	$\sqrt{2/5}V_{DC}\,2\cos(\pi/5)\exp(j0)$
$\underline{v}_2$	$\sqrt{2/5}V_{DC}\,2\cos(\pi/5)\exp(j\pi/5)$
$\underline{v}_3$	$\sqrt{2/5}V_{DC}\,2\cos(\pi/5)\exp(j2\pi/5)$
$\underline{v}_4$	$\sqrt{2/5}V_{DC}\,2\cos(\pi/5)\exp(j3\pi/5)$
$\underline{v}_5$	$\sqrt{2/5}V_{DC}\,2\cos(\pi/5)\exp(j4\pi/5)$
$\underline{v}_6$	$\sqrt{2/5}V_{DC}\,2\cos(\pi/5)\exp(j\pi)$
$\underline{v}_7$	$\sqrt{2/5}V_{DC}\,2\cos(\pi/5)\exp(j6\pi/5)$
$\underline{v}_8$	$\sqrt{2/5}V_{DC}\,2\cos(\pi/5)\exp(j7\pi/5)$
$\underline{v}_9$	$\sqrt{2/5}V_{DC}\,2\cos(\pi/5)\exp(j8\pi/5)$
$\underline{v}_{10}$	$\sqrt{2/5}V_{DC}\,2\cos(\pi/5)\exp(j9\pi/5)$

Formatted

Deleted: ¶

Table 3.4. Adjacent line-to-line voltages of the five-phase VSI.

Switching state	Switches ON	Space Vector	v_{ab}	v_{bc}	v_{cd}	v_{de}	v_{ea}
1	9,10,1,2,3	$\underline{v}_{1l}$	0	V_{DC}	0	$-V_{DC}$	0
2	10,1,2,3,4	$\underline{v}_{2l}$	0	V_{DC}	0	0	$-V_{DC}$
3	1,2,3,4,5	$\underline{v}_{3l}$	0	0	V_{DC}	0	$-V_{DC}$
4	2,3,4,5,6	$\underline{v}_{4l}$	$-V_{DC}$	0	V_{DC}	0	0
5	3,4,5,6,7	$\underline{v}_{5l}$	$-V_{DC}$	0	0	V_{DC}	0
6	4,5,6,7,8	$\underline{v}_{6l}$	0	$-V_{DC}$	0	V_{DC}	0
7	5,6,7,8,9	$\underline{v}_{7l}$	0	$-V_{DC}$	0	0	V_{DC}
8	6,7,8,9,10	$\underline{v}_{8l}$	0	0	$-V_{DC}$	0	V_{DC}
9	7,8,9,10,1	$\underline{v}_{9l}$	V_{DC}	0	$-V_{DC}$	0	0
10	8,9,10,1,2	$\underline{v}_{10l}$	V_{DC}	0	0	$-V_{DC}$	0

Table 3.5. Adjacent line-to-line voltage space vectors.

Adjacent line voltage space vectors	
$\underline{v}_{1l}$	$\sqrt{1.382} * \sqrt{2/5} V_{DC}\, 2\cos(\pi/5)\exp(j3\pi/10)$
$\underline{v}_{2l}$	$\sqrt{1.382} * \sqrt{2/5} V_{DC}\, 2\cos(\pi/5)\exp(j\pi/2)$
$\underline{v}_{3l}$	$\sqrt{1.382} * \sqrt{2/5} V_{DC}\, 2\cos(\pi/5)\exp(j7\pi/10)$
$\underline{v}_{4l}$	$\sqrt{1.382} * \sqrt{2/5} V_{DC}\, 2\cos(\pi/5)\exp(j9\pi/10)$
$\underline{v}_{5l}$	$\sqrt{1.382} * \sqrt{2/5} V_{DC}\, 2\cos(\pi/5)\exp(j11\pi/10)$
$\underline{v}_{6l}$	$\sqrt{1.382} * \sqrt{2/5} V_{DC}\, 2\cos(\pi/5)\exp(j13\pi/10)$
$\underline{v}_{7l}$	$\sqrt{1.382} * \sqrt{2/5} V_{DC}\, 2\cos(\pi/5)\exp(j15\pi/10)$
$\underline{v}_{8l}$	$\sqrt{1.382} * \sqrt{2/5} V_{DC}\, 2\cos(\pi/5)\exp(j17\pi/10)$
$\underline{v}_{9l}$	$\sqrt{1.382} * \sqrt{2/5} V_{DC}\, 2\cos(\pi/5)\exp(j19\pi/10)$
$\underline{v}_{10l}$	$\sqrt{1.382} * \sqrt{2/5} V_{DC}\, 2\cos(\pi/5)\exp(j21\pi/10)$

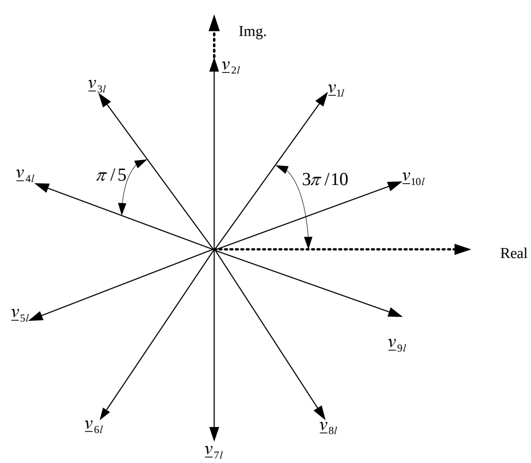

Fig. 3.5. Adjacent line-to-line voltage space vectors of the five-phase VSI.

Apart from the adjacent line-to-line voltages, there are two sets of non-adjacent line-to-line voltages. Due to symmetry, these two sets lead to the same values of the line-to-line voltage space vectors, with a different phase order. Only the set $v_{ac}, v_{bd}, v_{ce}, v_{da}, v_{eb}$ is analysed for this reason. Table 3.6 lists the states and the values for these line-to-line voltages.

Table 3.6. Non-adjacent line-to-line voltages of the five-phase VSI.

Switching state	Switches ON	Space Vector	v_{ac}	v_{bd}	v_{ce}	v_{da}	v_{eb}
1	9,10,1,2,3	$\underline{v}_{1ll}$	V_{DC}	V_{DC}	$-V_{DC}$	$-V_{DC}$	0
2	10,1,2,3,4	$\underline{v}_{2ll}$	V_{DC}	V_{DC}	0	$-V_{DC}$	$-V_{DC}$
3	1,2,3,4,5	$\underline{v}_{3ll}$	0	V_{DC}	V_{DC}	$-V_{DC}$	$-V_{DC}$
4	2,3,4,5,6	$\underline{v}_{4ll}$	$-V_{DC}$	V_{DC}	V_{DC}	0	$-V_{DC}$
5	3,4,5,6,7	$\underline{v}_{5ll}$	$-V_{DC}$	0	V_{DC}	V_{DC}	$-V_{DC}$
6	4,5,6,7,8	$\underline{v}_{6ll}$	$-V_{DC}$	$-V_{DC}$	V_{DC}	V_{DC}	0
7	5,6,7,8,9	$\underline{v}_{7ll}$	$-V_{DC}$	$-V_{DC}$	0	V_{DC}	V_{DC}
8	6,7,8,9,10	$\underline{v}_{8ll}$	0	$-V_{DC}$	$-V_{DC}$	V_{DC}	V_{DC}
9	7,8,9,10,1	$\underline{v}_{9ll}$	V_{DC}	$-V_{DC}$	$-V_{DC}$	0	V_{DC}
10	8,9,10,1,2	$\underline{v}_{10ll}$	V_{DC}	0	$-V_{DC}$	$-V_{DC}$	V_{DC}

Time-domain waveforms of non-adjacent line-to-line voltages are illustrated in Fig. 3.7. Space vectors of non-adjacent line-to-line voltages are determined once more using the defining expression (3.2) and are summarised in Table 3.7. In principle, representation of non-adjacent line-to-line voltage space vectors is the same as for the adjacent (shown in Fig. 3.5) and only the magnitude and the ordering are different. Non-adjacent space vectors are therefore not illustrated separately.

Phase-to-neutral voltages of the star connected load are most easily found by defining a voltage difference between the star point *n* of the load and the negative rail of the dc bus *N*. The following correlation then holds true:

$$\begin{aligned} v_A &= v_a + v_{nN} \\ v_B &= v_b + v_{nN} \\ v_C &= v_c + v_{nN} \\ v_D &= v_d + v_{nN} \\ v_E &= v_e + v_{nN} \end{aligned} \tag{3.4}$$

Since the phase voltages in a star connected load sum to zero, summation of the equations (3.4) yields

$$v_{nN} = (1/5)(v_A + v_B + v_C + v_D + v_E) \tag{3.5}$$

Substitution of (3.5) into (3.4) yields phase-to-neutral voltages of the load in the following form:

$$\begin{aligned} v_a &= (4/5)v_A - (1/5)(v_B + v_C + v_D + v_E) \\ v_b &= (4/5)v_B - (1/5)(v_A + v_C + v_D + v_E) \\ v_c &= (4/5)v_C - (1/5)(v_A + v_B + v_D + v_E) \\ v_d &= (4/5)v_D - (1/5)(v_A + v_B + v_C + v_E) \\ v_e &= (4/5)v_E - (1/5)(v_A + v_B + v_C + v_D) \end{aligned} \tag{3.6}$$

Table 3.7. Non-adjacent line-to-line voltage space vectors.

Non-adjacent line-to-line voltage space vectors	
$\underline{v}_{1ll}$	$3.07768^* \sqrt{2/5} V_{DC} \exp(j\pi/10)$
$\underline{v}_{2ll}$	$3.07768^* \sqrt{2/5} V_{DC} \exp(j3\pi/10)$
$\underline{v}_{3ll}$	$3.07768^* \sqrt{2/5} V_{DC} \exp(j\pi/2)$
$\underline{v}_{4ll}$	$3.07768^* \sqrt{2/5} V_{DC} \exp(j7\pi/10)$
$\underline{v}_{5ll}$	$3.07768^* \sqrt{2/5} V_{DC} \exp(j9\pi/10)$
$\underline{v}_{6ll}$	$3.07768^* \sqrt{2/5} V_{DC} \exp(j11\pi/10)$
$\underline{v}_{7ll}$	$3.07768^* \sqrt{2/5} V_{DC} \exp(j13\pi/10)$
$\underline{v}_{8ll}$	$3.07768^* \sqrt{2/5} V_{DC} \exp(j3\pi/2)$
$\underline{v}_{9ll}$	$3.07768^* \sqrt{2/5} V_{DC} \exp(j17\pi/10)$
$\underline{v}_{10ll}$	$3.07768^* \sqrt{2/5} V_{DC} \exp(j19\pi/10)$

Deleted: ¶

Hence the values of the phase voltages in the ten distinct intervals of 36 degrees duration can be determined using the values of the leg voltages in Table 3.2. Table 3.8 gives the phase voltages for different switching states, obtained using expression (3.6) and Table 3.2.

Time domain waveforms of phase-to-neutral voltages of the star connected load are shown in Fig. 3.8 for the five-phase inverter operation in the ten-step mode. Phase-to-neutral voltages are of non-zero value throughout the period and their value alternates between positive and negative $2/5V_{DC}$ and $3/5V_{DC}$. The waveforms of the phase-to-neutral voltages show ten distinct steps, each of 36 degrees duration, and hence the name of this mode of operation, ten-step mode.

In order to determine the space vectors of phase-to-neutral voltages, the instantaneous values of phase voltages from the Table 3.8 are inserted into (3.2). The phase voltage space vectors for the ten-step mode of operation turn out to be same as those of the leg voltages. Hence the space vectors of phase voltages can be given as in Table 3.9. The space vector representation of phase voltages remains to be as shown in Fig. 3.3 for leg voltages.

The relationship between phase-to-neutral voltages of the inverter and the dc link voltage, given in (3.6) in terms of leg voltages, can be expressed using switching functions for the five individual inverter legs. Each switching function takes the value of one when the upper switch is on and the value of zero when the lower switch is on (alternatively, if leg voltages are referred to the mid-point of the dc supply, the switching functions take the values of 0.5 and –0.5). Hence (*Sa* stands for the switching function of phase *a*, *Sb* stands for the switching function of phase *b* and so on):

Table 3.8. Phase-to-neutral voltages of a star connected load supplied from a five-phase VSI.

State	Switches ON	Space vector	v_a	v_b	v_c	v_d	v_e
1	9,10,1,2,3	$\underline{v}_{1phase}$	2/5 V_{DC}	2/5V_{DC}	-3/5 V_{DC}	-3/5V_{DC}	2/5 V_{DC}
2	10,1,2,3,4	$\underline{v}_{2phase}$	3/5 V_{DC}	3/5V_{DC}	-2/5 V_{DC}	-2/5 V_{DC}	-2/5V_{DC}
3	1,2,3,4,5	$\underline{v}_{3phase}$	2/5 V_{DC}	2/5 V_{DC}	2/5 V_{DC}	-3/5 V_{DC}	-3/5V_{DC}
4	2,3,4,5,6	$\underline{v}_{4phase}$	-2/5V_{DC}	3/5 V_{DC}	3/5V_{DC}	-2/5 V_{DC}	-2/5 V_{DC}
5	3,4,5,6,7	$\underline{v}_{5phase}$	-3/5V_{DC}	2/5 V_{DC}	2/5 V_{DC}	2/5V_{DC}	-3/5 V_{DC}
6	4,5,6,7,8	$\underline{v}_{6phase}$	-2/5V_{DC}	-2/5V_{DC}	3/5 V_{DC}	3/5V_{DC}	-2/5 V_{DC}
7	5,6,7,8,9	$\underline{v}_{7phase}$	-3/5V_{DC}	-3/5V_{DC}	2/5 V_{DC}	2/5 V_{DC}	2/5V_{DC}
8	6,7,8,9,10	$\underline{v}_{8phase}$	-2/5 V_{DC}	-2/5 V_{DC}	-2/5V_{DC}	3/5 V_{DC}	3/5V_{DC}
9	7,8,9,10,1	$\underline{v}_{9phase}$	2/5V_{DC}	-3/5 V_{DC}	-3/5V_{DC}	2/5 V_{DC}	2/5 V_{DC}
10	8,9,10,1,2	$\underline{v}_{10phase}$	3/5V_{DC}	-2/5 V_{DC}	-2/5 V_{DC}	-2/5V_{DC}	3/5 V_{DC}

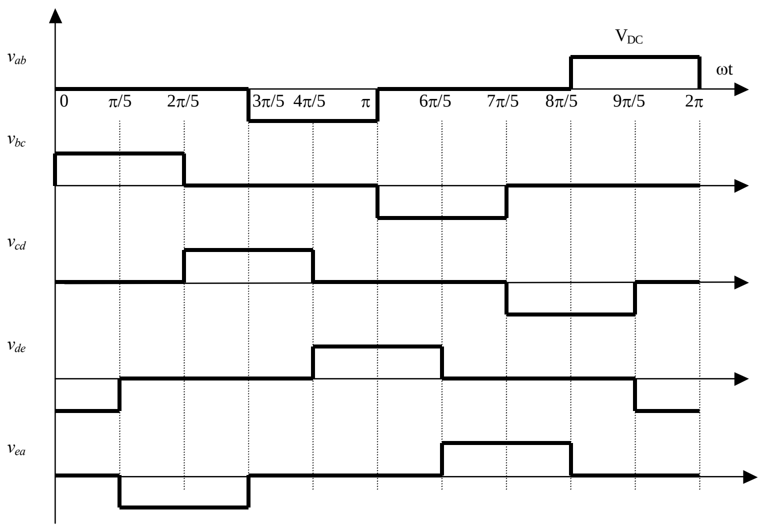

Fig. 3.6. Adjacent line-to-line voltages of the five-phase VSI.

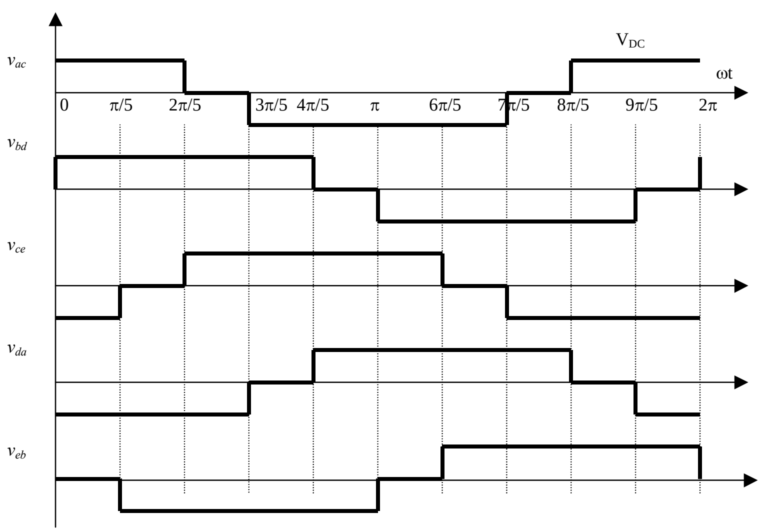

Fig. 3.7. Non-adjacent line-to-line voltages of the five-phase VSI.

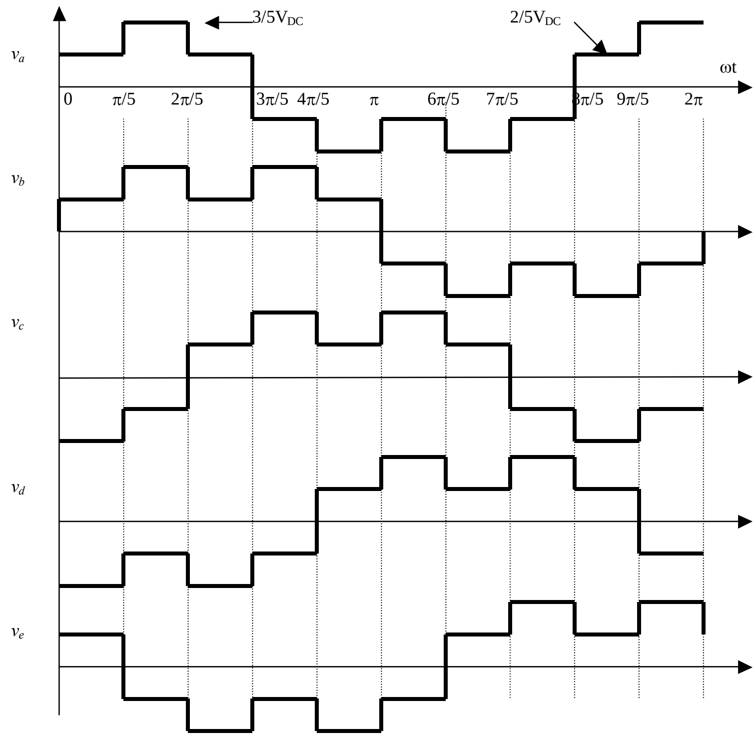

Fig. 3.8. Phase-to-neutral voltages of the five-phase VSI in the ten-step mode of operation.

Table 3.9. Phase-to-neutral voltage space vectors of the five-phase VSI.

Phase voltage space vectors	
$\underline{v}_{1phase}$	$\sqrt{2/5}V_{DC}\,2\cos(\pi/5)\exp(j0)$
$\underline{v}_{2phase}$	$\sqrt{2/5}V_{DC}\,2\cos(\pi/5)\exp(j\pi/5)$
$\underline{v}_{3phase}$	$\sqrt{2/5}V_{DC}\,2\cos(\pi/5)\exp(j2\pi/5)$
$\underline{v}_{4phase}$	$\sqrt{2/5}V_{DC}\,2\cos(\pi/5)\exp(j3\pi/5)$
$\underline{v}_{5phase}$	$\sqrt{2/5}V_{DC}\,2\cos(\pi/5)\exp(j4\pi/5)$
$\underline{v}_{6phase}$	$\sqrt{2/5}V_{DC}\,2\cos(\pi/5)\exp(j\pi)$
$\underline{v}_{7phase}$	$\sqrt{2/5}V_{DC}\,2\cos(\pi/5)\exp(j6\pi/5)$
$\underline{v}_{8phase}$	$\sqrt{2/5}V_{DC}\,2\cos(\pi/5)\exp(j7\pi/5)$
$\underline{v}_{9phase}$	$\sqrt{2/5}V_{DC}\,2\cos(\pi/5)\exp(j8\pi/5)$
$\underline{v}_{10phase}$	$\sqrt{2/5}V_{DC}\,2\cos(\pi/5)\exp(j9\pi/5)$

Formatted

Deleted: Leg

Deleted: ¶

$$
\begin{aligned}
v_a &= (V_{DC}/5)\,[4\,Sa - Sb - Sc - Sd - Se] \\
v_b &= (V_{DC}/5)\,[4\,Sb - Sa - Sc - Sd - Se] \\
v_c &= (V_{DC}/5)\,[4\,Sc - Sb - Sa - Sd - Se] \\
v_d &= (V_{DC}/5)\,[4\,Sd - Sb - Sc - Sa - Se] \\
v_e &= (V_{DC}/5)\,[4\,Se - Sb - Sc - Sd - Sa]
\end{aligned}
\qquad (3.7)
$$

3.2.3 Fourier analysis of the five-phase inverter output voltages

In order to relate the input dc link voltage of the inverter with the output phase-to-neutral and line-to-line voltages, Fourier analysis of the voltage waveforms is undertaken in this section. Out of the two sets of the line-to-line voltages, discussed in the preceding sub-section, only non-adjacent line-to-line voltages are analysed since they have higher fundamental harmonic values than the adjacent line-to-line voltages.

Using definition of the Fourier series for a periodic waveform

$$v(t) = V_o + \sum_{k=1}^{\infty}\left(A_k \cos k\omega t + B_k \sin k\omega t\right) \tag{3.8a}$$

where the coefficients of the Fourier series are given with

$$\begin{aligned} V_o &= \frac{1}{T}\int_0^T v(t)dt = \frac{1}{2\pi}\int_0^{2\pi} v(\theta)d\theta \\ A_k &= \frac{2}{T}\int_0^T v(t)\cos k\omega t dt = \frac{1}{\pi}\int_0^{2\pi} v(\theta)\cos k\theta d\theta \\ B_k &= \frac{2}{T}\int_0^T v(t)\sin k\omega t dt = \frac{1}{\pi}\int_0^{2\pi} v(\theta)\sin k\theta d\theta \end{aligned} \tag{3.8b}$$

and observing that the waveforms possess quarter-wave symmetry and can be conveniently taken as odd functions, one can represent phase-to-neutral voltages and line-to-line voltages with the following expressions:

$$\begin{aligned} v(t) &= \sum_{k=0}^{\infty} B_{2k+1}\sin(2k+1)\omega t) = \sqrt{2}\sum_{k=0}^{\infty} V_{2k+1}\sin(2k+1)\omega t \\ B_{2k+1} &= \sqrt{2}V_{2k+1} = \frac{1}{\pi}4\int_0^{\pi/2} v(\theta)\sin(2k+1)\theta d\theta \end{aligned} \tag{3.9}$$

Deleted:

In the case of the phase-to-neutral voltage v_b, shown in Fig. 3.8, one further has for the coefficients of the Fourier series

$$B_{2k+1} = \frac{1}{\pi}\frac{4}{5}V_{DC}\frac{1}{2k+1}\left[2+\cos(2k+1)\frac{\pi}{5} - \cos(2k+1)\frac{2\pi}{5}\right] \tag{3.10}$$

The expression in brackets in the second equation of (3.10) equals zero for all the harmonics whose order is divisible by five. For all the other harmonics it equals 2.5. Hence one can write the Fourier series of the phase-to-neutral voltage as

$$v(t) = \frac{2}{\pi}V_{DC}\left[\sin\omega t + \frac{1}{3}\sin 3\omega t + \frac{1}{7}\sin 7\omega t + \frac{1}{9}\sin 9\omega t + \frac{1}{11}\sin 11\omega t + \frac{1}{13}\sin 13\omega t + ...\right] \tag{3.11}$$

From (3.11) it follows that the fundamental component of the output phase-to-neutral voltage has an RMS value equal to

$$V_1 = \frac{\sqrt{2}}{\pi}V_{DC} = 0.45V_{DC} \tag{3.12}$$

Fourier analysis of the non-adjacent line-to-line voltages is performed in the same manner. Fourier series remains to be given with (3.9). Taking the second voltage in Fig. 3.7 and shifting the zero time instant by π/10 degrees leftwards, one has the following Fourier series coefficients:

$$B_{2k+1} = \frac{1}{\pi} 4 \int_{\pi/10}^{\pi/2} V_{DC} \sin(2k+1)\theta d\theta = \frac{1}{\pi} 4V_{DC} \frac{1}{2k+1} \cos(2k+1)\frac{\pi}{10} \tag{3.13}$$

Hence the Fourier series of the non-adjacent line-to-line voltage is

$$v(t) = \frac{4}{\pi} V_{DC} \left[0.95 \sin \omega t + \frac{0.59}{3} \sin 3\omega t - \frac{0.59}{7} \sin 7\omega t - \frac{0.95}{9} \sin 9\omega t - \frac{0.95}{11} \sin 11\omega t - .... \right] \tag{3.14}$$

and the fundamental harmonic RMS value of the non-adjacent line-to-line voltage is

$$V_{1L} = \frac{2\sqrt{2}}{\pi} V_{DC} \cos \frac{\pi}{10} = 0.856 V_{DC} = 1.902 V_1 \tag{3.15}$$

It is important to note at this stage that the space vectors described by (3.2) provides mapping of inverter voltages into a two-dimensional space. However, since five-phase inverter essentially requires description in a five-dimensional space not all the harmonics contained in (3.11) and (3.14) will be encompassed by the space vector of (3.2). In particular, space vectors calculated using (3.2) will only represent harmonics of the order $10k \pm 1,\ k = 0,1,2,3.....$, that is, the first, the ninth, the eleventh, and so on. Harmonics of the order $5k,\ k = 1,2,3.....$ cannot appear due to the isolated neutral point. However, harmonics of the order $5k \pm 2,\ k = 1,3,5.....$ are present in (3.11) and (3.14) but are not encompassed by the space vector definition of (3.2). These harmonics in essence appear in the second two-dimensional space, which requires introduction of the second space vector for the five-phase system. This issue will be addressed in detail in Chapter 7, where space vector modulation schemes for a five-phase VSI are elaborated.

Deleted: c

3.3 OPERATION OF THE FIVE-PHASE VOLTAGE SOURCE INVERTER IN PULSE WIDTH MODULATION MODE

If a five-phase VSI is operated in PWM mode, apart from the already described ten states there will be additional 22 switching states. This is so since there are five inverter legs and each of them can be in two states. The number of possible switching states is in general equal to 2^n, where n is the number of inverter legs (i.e. output phases). This correlation is valid for any two-level VSI.

Deleted: pulse width modulated (

Deleted:)

Deleted: voltage source inverter

Table 3.10 summarises the additional switching states which are associated with PWM mode of operation and which are absent in the ten-step mode of operation. Switches that are ‘on’ and the corresponding terminal polarity are included in the Table 3.10. As can be seen from Table 3.10, the remaining twenty two switching states encompass three possible situations: all the states when four switches from upper (or lower) half and one from the lower (or upper) half of the inverter are on (states 11-20); two states when either all the five upper (or lower) switches are ‘on’ (states 31 and 32); and the remaining states with three switches from the upper (lower) half and two switches from the lower (upper) half in conduction mode (states 21-30). Table 3.11 summarises the values of leg voltages for the ten switching states denoted with numbers 11-20 and lists the switches that are in the conduction mode.

Space vectors of leg voltages are found for states 11-20 using the same procedure as outlined in conjunction with the ten-step mode. Leg voltage space vectors for states 11-20 are given in Table 3.12. Table 3.13 summarises the values of phase-to-neutral voltages in the ten switching states 11-20. Corresponding space vectors are displayed in Table 3.14.

Table 3.10. Additional switching states of the five-phase VSI in PWM mode.

Switching state	Switches ON	Terminal Polarity
11	1,2,4,8,10	$A^+B^-C^-D^-E^-$
12	1,2,3,5,9	$A^+B^+C^+D^-E^+$
13	2,3,4,6,10	$A^-B^+C^-D^-E^-$
14	1,3,4,5,7	$A^+B^+C^+D^+E^-$
15	2,4,5,6,8	$A^-B^-C^+D^-E^-$
16	3,5,6,7,9	$A^-B^+C^+D^+E^+$
17	4,6,7,8,10	$A^-B^-C^-D^+E^-$
18	1,5,7,8,9	$A^+B^-C^+D^+E^+$
19	2,6,8,9,10	$A^-B^-C^-D^-E^+$
20	1,3,7,9,10	$A^+B^+C^-D^+E^+$
21	2,3,6,9,10	$A^-B^+C^-D^-E^+$
22	1,3,4,7,10	$A^+B^+C^-D^+E^-$
23	1,2,4,5,8	$A^+B^-C^+D^-E^-$
24	2,3,5,6,9	$A^-B^+C^+D^-E^+$
25	3,4,6,7,10	$A^-B^+C^-D^+E^-$
26	1,4,5,7,8	$A^+B^-C^+D^+E^-$
27	2,5,6,8,9	$A^-B^-C^+D^-E^+$
28	3,6,7,9,10	$A^-B^+C^-D^+E^+$
29	1,2,4,7,8	$A^+B^-C^-D^+E^-$
30	1,2,5,8,9	$A^+B^-C^+D^-E^+$
31	1,3,5,7,9	$A^+B^+C^+D^+E^+$
32	2,4,6,8,10	$A^-B^-C^-D^-E^-$

Table 3.11. Leg voltages for states 11-20.

Switching state	Switches ON	Space vector	Leg voltage v_A	Leg voltage v_B	Leg voltage v_C	Leg voltage v_D	Leg voltage v_E
11	1,2,4,8,10	$\underline{v}_{11}$	V_{DC}	0	0	0	0
12	1,2,3,5,9	$\underline{v}_{12}$	V_{DC}	V_{DC}	V_{DC}	0	V_{DC}
13	2,3,4,6,10	$\underline{v}_{13}$	0	V_{DC}	0	0	0
14	1,3,4,5,7	$\underline{v}_{14}$	V_{DC}	V_{DC}	V_{DC}	V_{DC}	0
15	2,4,5,6,8	$\underline{v}_{15}$	0	0	V_{DC}	0	0
16	3,5,6,7,9	$\underline{v}_{16}$	0	V_{DC}	V_{DC}	V_{DC}	V_{DC}
17	4,6,7,8,10	$\underline{v}_{17}$	0	0	0	V_{DC}	0
18	1,5,7,8,9	$\underline{v}_{18}$	V_{DC}	0	V_{DC}	V_{DC}	V_{DC}
19	2,6,8,9,10	$\underline{v}_{19}$	0	0	0	0	V_{DC}
20	1,3,7,9,10	$\underline{v}_{20}$	V_{DC}	V_{DC}	0	V_{DC}	V_{DC}

Switching states 21-30 are considered next. Table 3.15 summarises the values of leg voltages in these ten switching states and lists switches that are 'on'. Corresponding leg voltage space vectors are given in Table 3.16. Table 3.17 summarises the values of phase voltages for switching states 21-30 and lists switches that are 'on'. The same procedure is adopted once more to calculate the space vectors of phase voltages for states 21-30 and the results are given in Table 3.18.

Table 3.12. Leg voltage space vectors for states 11-20.

Leg voltage space vectors	
$\underline{v}_{11}$	$\sqrt{2/5}V_{DC}2\exp(j0)$
$\underline{v}_{12}$	$\sqrt{2/5}V_{DC}2\exp(j\pi/5)$
$\underline{v}_{13}$	$\sqrt{2/5}V_{DC}2\exp(j2\pi/5)$
$\underline{v}_{14}$	$\sqrt{2/5}V_{DC}2\exp(j3\pi/5)$
$\underline{v}_{15}$	$\sqrt{2/5}V_{DC}2\exp(j4\pi/5)$
$\underline{v}_{16}$	$\sqrt{2/5}V_{DC}2\exp(j\pi)$
$\underline{v}_{17}$	$\sqrt{2/5}V_{DC}2\exp(j6\pi/5)$
$\underline{v}_{18}$	$\sqrt{2/5}V_{DC}2\exp(j7\pi/5)$
$\underline{v}_{19}$	$\sqrt{2/5}V_{DC}2\exp(j8\pi/5)$
$\underline{v}_{20}$	$\sqrt{2/5}V_{DC}2\exp(j9\pi/5)$

Table 3.13. Phase-to-neutral voltages for states 11-20.

State	Switches ON	Space Vector	v_a	v_b	v_c	v_d	v_e
11	1,2,4,8,10	$\underline{v}_{11phase}$	4/5 V_{DC}	-1/5V_{DC}	-1/5 V_{DC}	-1/5V_{DC}	-1/5 V_{DC}
12	1,2,3,5,9	$\underline{v}_{12phase}$	1/5 V_{DC}	1/5V_{DC}	1/5 V_{DC}	-4/5 V_{DC}	1/5V_{DC}
13	2,3,4,6,10	$\underline{v}_{13phase}$	-1/5 V_{DC}	4/5 V_{DC}	-1/5 V_{DC}	-1/5 V_{DC}	-1/5V_{DC}
14	1,3,4,5,7	$\underline{v}_{14phase}$	1/5V_{DC}	1/5 V_{DC}	1/5V_{DC}	1/5 V_{DC}	-4/5 V_{DC}
15	2,4,5,6,8	$\underline{v}_{15phase}$	-1/5V_{DC}	-1/5 V_{DC}	4/5 V_{DC}	-1/5V_{DC}	-1/5 V_{DC}
16	3,5,6,7,9	$\underline{v}_{16phase}$	-4/5V_{DC}	1/5V_{DC}	1/5 V_{DC}	1/5V_{DC}	1/5 V_{DC}
17	4,6,7,8,10	$\underline{v}_{17phase}$	-1/5V_{DC}	-1/5V_{DC}	-1/5 V_{DC}	4/5 V_{DC}	-1/5V_{DC}
18	1,5,7,8,9	$\underline{v}_{18phase}$	1/5 V_{DC}	-4/5 V_{DC}	1/5V_{DC}	1/5 V_{DC}	1/5V_{DC}
19	2,6,8,9,10	$\underline{v}_{19phase}$	-1/5V_{DC}	-1/5 V_{DC}	-1/5V_{DC}	-1/5 V_{DC}	4/5 V_{DC}
20	1,3,7,9,10	$\underline{v}_{20phase}$	1/5V_{DC}	1/5 V_{DC}	-4/5 V_{DC}	1/5V_{DC}	1/5 V_{DC}

The remaining two switching states 31 and 32 yield zero values of both leg and phase voltage space vectors. The two states represent short-circuiting of the load terminals.

Thus it can be seen that the total of 32 space vectors, available in the PWM operation, fall into four distinct categories regarding the magnitude of the available output phase voltage. The phase voltage space vectors are summarised in Table 3.19 for all 32 switching states. Corresponding leg voltage space vectors are given in Table 3.20.

Table 3.14. Phase-to-neutral voltage space vectors for states 11-20.

Phase voltage space vectors	
$\underline{v}_{11phase}$	$\sqrt{2/5}V_{DC}\exp(j0)$
$\underline{V}_{12phase}$	$\sqrt{2/5}V_{DC}\exp(j\pi/5)$
$\underline{V}_{13phase}$	$\sqrt{2/5}V_{DC}\exp(j2\pi/5)$
$\underline{V}_{14phase}$	$\sqrt{2/5}V_{DC}\exp(j3\pi/5)$
$\underline{V}_{15phase}$	$\sqrt{2/5}V_{DC}\exp(j4\pi/5)$
$\underline{V}_{16phase}$	$\sqrt{2/5}V_{DC}\exp(j\pi)$
$\underline{V}_{17phase}$	$\sqrt{2/5}V_{DC}\exp(j6\pi/5)$
$\underline{V}_{18phase}$	$\sqrt{2/5}V_{DC}\exp(j7\pi/5)$
$\underline{V}_{19phase}$	$\sqrt{2/5}V_{DC}\exp(j8\pi/5)$
$\underline{V}_{20phase}$	$\sqrt{2/5}V_{DC}\exp(j9\pi/5)$

Table 3.15. Leg voltages for states 21-30.

Switching state	Switches ON	Space vector	Leg voltage v_A	Leg voltage v_B	Leg voltage v_C	Leg voltage v_D	Leg voltage v_E
21	2,3,6,9,10	$\underline{v}_{21}$	0	V_{DC}	0	0	V_{DC}
22	1,3,4,7,10	$\underline{v}_{22}$	V_{DC}	V_{DC}	0	V_{DC}	0
23	1,2,4,5,8	$\underline{v}_{23}$	V_{DC}	0	V_{DC}	0	0
24	2,3,5,6,9	$\underline{v}_{24}$	0	V_{DC}	V_{DC}	0	V_{DC}
25	3,4,6,7,10	$\underline{v}_{25}$	0	V_{DC}	0	V_{DC}	0
26	1,4,5,7,8	$\underline{v}_{26}$	V_{DC}	0	V_{DC}	V_{DC}	0
27	2,5,6,8,9	$\underline{v}_{27}$	0	0	V_{DC}	0	V_{DC}
28	3,6,7,9,10	$\underline{v}_{28}$	0	V_{DC}	0	V_{DC}	V_{DC}
29	1,2,4,7,8	$\underline{v}_{29}$	V_{DC}	0	0	V_{DC}	0
30	1,2,5,8,9	$\underline{v}_{30}$	V_{DC}	0	V_{DC}	0	V_{DC}

Table 3.16. Leg voltage space vectors for states 21-30.

Leg voltage space vectors	
$\underline{v}_{21}$	$\sqrt{2/5}V_{DC}4\cos(2\pi/5)\exp(0)$
$\underline{v}_{22}$	$\sqrt{2/5}V_{DC}4\cos(2\pi/5)\exp(j\pi/5)$
$\underline{v}_{23}$	$\sqrt{2/5}V_{DC}4\cos(2\pi/5)\exp(j2\pi/5)$
$\underline{v}_{24}$	$\sqrt{2/5}V_{DC}4\cos(2\pi/5)\exp(j3\pi/5)$
$\underline{v}_{25}$	$\sqrt{2/5}V_{DC}4\cos(2\pi/5)\exp(j4\pi/5)$
$\underline{v}_{26}$	$\sqrt{2/5}V_{DC}4\cos(2\pi/5)\exp(j\pi)$
$\underline{v}_{27}$	$\sqrt{2/5}V_{DC}4\cos(2\pi/5)\exp(j6\pi/5)$
$\underline{v}_{28}$	$\sqrt{2/5}V_{DC}4\cos(2\pi/5)\exp(j7\pi/5)$
$\underline{v}_{29}$	$\sqrt{2/5}V_{DC}4\cos(2\pi/5)\exp(j8\pi/5)$
$\underline{v}_{30}$	$\sqrt{2/5}V_{DC}4\cos(2\pi/5)\exp(j9\pi/5)$

Table 3.17. Phase-to-neutral voltages for states 21-30.

Switching state	Switches ON	Space vector	v_a	v_b	v_c	v_d	v_e
21	2,3,6,9,10	$\underline{v}_{21phase}$	-2/5 V_{DC}	3/5V_{DC}	-2/5 V_{DC}	-2/5V_{DC}	3/5 V_{DC}
22	1,3,4,7,10	$\underline{v}_{22phase}$	2/5 V_{DC}	2/5V_{DC}	-3/5 V_{DC}	2/5 V_{DC}	-3/5V_{DC}
23	1,2,4,5,8	$\underline{v}_{23phase}$	3/5 V_{DC}	-2/5 V_{DC}	3/5 V_{DC}	-2/5 V_{DC}	-2/5V_{DC}
24	2,3,5,6,9	$\underline{v}_{24phase}$	-3/5V_{DC}	2/5 V_{DC}	2/5V_{DC}	-3/5 V_{DC}	2/5 V_{DC}
25	3,4,6,7,10	$\underline{v}_{25phase}$	-2/5V_{DC}	3/5 V_{DC}	-2/5 V_{DC}	3/5V_{DC}	-2/5 V_{DC}
26	1,4,5,7,8	$\underline{v}_{26phase}$	3/5V_{DC}	-2/5V_{DC}	3/5 V_{DC}	3/5V_{DC}	-2/5 V_{DC}
27	2,5,6,8,9	$\underline{v}_{27phase}$	-2/5V_{DC}	-2/5V_{DC}	3/5 V_{DC}	-2/5 V_{DC}	3/5V_{DC}
28	3,6,7,9,10	$\underline{v}_{28phase}$	-3/5 V_{DC}	2/5 V_{DC}	-3/5V_{DC}	2/5 V_{DC}	2/5V_{DC}
29	1,2,4,7,8	$\underline{v}_{29phase}$	3/5V_{DC}	-2/5 V_{DC}	-2/5V_{DC}	3/5 V_{DC}	-2/5 V_{DC}
30	1,2,5,8,9	$\underline{v}_{30phase}$	2/5V_{DC}	-3/5 V_{DC}	2/5 V_{DC}	-3/5V_{DC}	2/5 V_{DC}

Table 3.18. Phase-to-neutral voltage space vectors for states 21-30.

Phase voltage space vectors	
$\underline{v}_{21\,phase}$	$\sqrt{2/5}V_{DC}\,2\cos(2\pi/5)\exp(0)$
$\underline{v}_{22\,phase}$	$\sqrt{2/5}V_{DC}\,2\cos(2\pi/5)\exp(j\pi/5)$
$\underline{v}_{23\,phase}$	$\sqrt{2/5}V_{DC}\,2\cos(2\pi/5)\exp(j2\pi/5)$
$\underline{v}_{24\,phase}$	$\sqrt{2/5}V_{DC}\,2\cos(2\pi/5)\exp(j3\pi/5)$
$\underline{v}_{25\,phase}$	$\sqrt{2/5}V_{DC}\,2\cos(2\pi/5)\exp(j4\pi/5)$
$\underline{v}_{26\,phase}$	$\sqrt{2/5}V_{DC}\,2\cos(2\pi/5)\exp(j\pi)$
$\underline{v}_{27\,phase}$	$\sqrt{2/5}V_{DC}\,2\cos(2\pi/5)\exp(j6\pi/5)$
$\underline{v}_{28\,phase}$	$\sqrt{2/5}V_{DC}\,2\cos(2\pi/5)\exp(j7\pi/5)$
$\underline{v}_{29\,phase}$	$\sqrt{2/5}V_{DC}\,2\cos(2\pi/5)\exp(j8\pi/5)$
$\underline{v}_{30\,phase}$	$\sqrt{2/5}V_{DC}\,2\cos(2\pi/5)\exp(j9\pi/5)$

Table 3.19. Phase-to-neutral voltage space vectors for states 1-32.

Space vectors	Value of the space vectors
$\underline{v}_{1phase}$ to $\underline{v}_{10phase}$	$\sqrt{2/5}V_{DC}\,2\cos(\pi/5)\exp(jk\pi/5)$ for k = 0,1,2 ….9
$\underline{v}_{11phase}$ to $\underline{v}_{20phase}$	$\sqrt{2/5}V_{DC}\,\exp(jk\pi/5)$ for k = 0,1,2 ….9
$\underline{v}_{21phase}$ to $\underline{v}_{30phase}$	$\sqrt{2/5}V_{DC}\,2\cos(2\pi/5)\exp(jk\pi/5)$ for k = 0,1,2 ….9
$\underline{v}_{31phase}$ to $\underline{v}_{32phase}$	0

Table 3.20. Leg voltage space vectors for states 1-32.

Space vectors	Value of the space vectors
$\underline{v}_{1}$ to $\underline{v}_{10}$	$\sqrt{2/5}V_{DC}\,2\cos(\pi/5)\exp(jk\pi/5)$ for k = 0,1,2 ….9
$\underline{v}_{11}$ to $\underline{v}_{20}$	$\sqrt{2/5}V_{DC}\,2\exp(jk\pi/5)$ for k =0,1,2,…..9
$\underline{v}_{21}$ to $\underline{v}_{30}$	$\sqrt{2/5}V_{DC}\,4\cos(2\pi/5)\exp(jk\pi/5)$ for k = 0,1,2 ….9
$\underline{v}_{31}$ to $\underline{v}_{32}$	0

The phase voltage space vectors are shown in Fig. 3.9. All the three sets of non-zero phase voltage space vectors have the same angular positions and are located as the vertices on

Deleted: 2

Deleted: ¶ Thus it can be seen that the total of 32 space vectors, available in the PWM operation, fall into four distinct categories regarding the magnitude of the available output phase voltage. The phase voltage space vectors are summarised in Table 3.19 for all 32 switching states. Corresponding leg voltage space vectors are given in Table 3.20.

Deleted: ¶

Deleted:

Deleted: ¶

Deleted: vertexes

the three decagons. The only difference among the three sets is the length of their sides. The ratio of phase voltage space vector magnitudes is $1{:}1.618{:}(1.618)^2$, from the smallest one to the largest one, respectively.

3.4 MODELLING OF A FIVE-PHASE INDUCTION MOTOR

A model of a five-phase induction motor is developed initially in phase variable form. In order to simplify the model by removing the time variation of inductance terms, a transformation is applied and so-called d-q-x-y-0 model of the machine is constructed. It is assumed that the spatial distribution of all the magneto-motive forces (fields) in the machine is sinusoidal, since only torque production due to the first harmonic of the filed is of relevance in this project. All the other standard assumptions of the general theory of electrical machines apply. The model derivation is summarised in the following sub-sections. A more detailed discussion of the modelling procedure is available in Jones (2002) and Jones (2005).

Deleted: o

Deleted: 4

Deleted:)

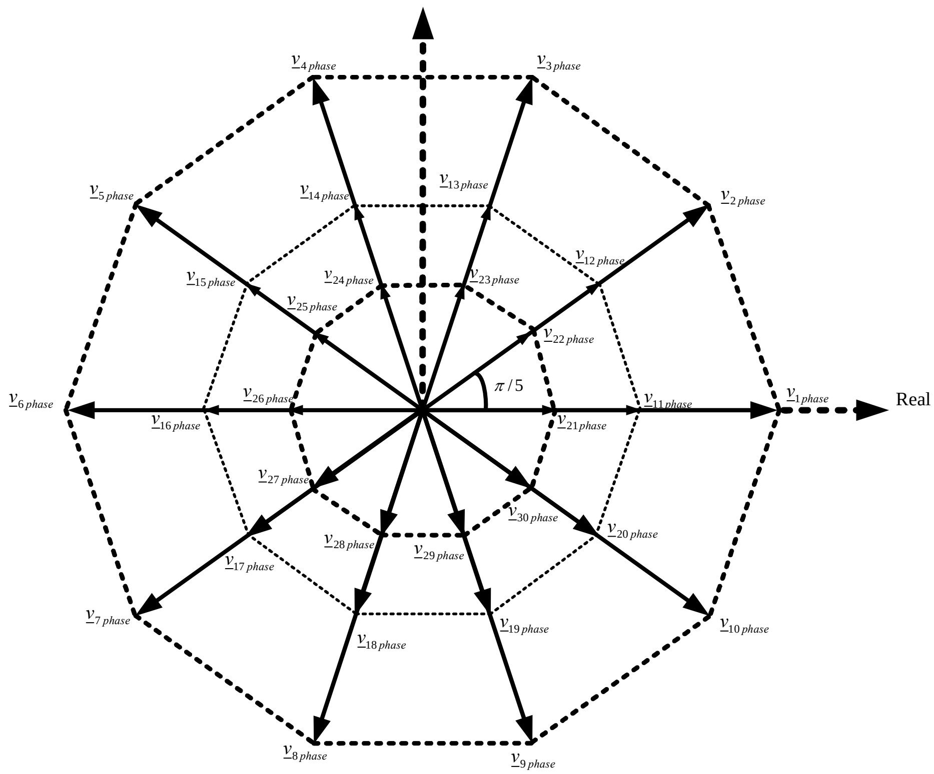

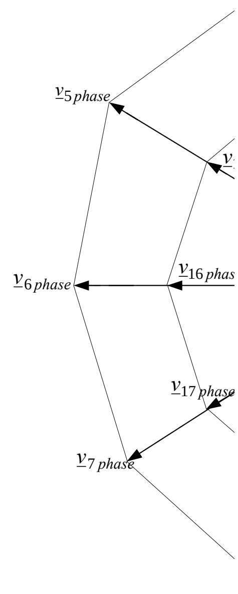

Deleted:

Deleted:

Fig. 3.9. Phase-to-neutral voltage space vectors.

3.4.1 Phase variable model

Deleted: ¶

A five-phase induction machine is constructed using ten phase belts, each of 36 degrees, along the circumference of the stator. The spatial displacement between phases is therefore 72 degrees. The rotor winding is treated as an equivalent five-phase winding, of the same properties as the stator winding. It is assumed that the rotor winding has already been referred to stator winding, using winding transformation ratio. A five-phase induction machine can then be described with the following voltage equilibrium and flux linkage equations in matrix form (underlined symbols):

Deleted:

Deleted: ,

Deleted: so that the maximum value of the mutual stator to rotor inductance terms equals in value mutual inductance within the five-phase stator winding and mutual inductance within the five-phase rotor winding (*M*).

$$\underline{v}^s_{abcde} = \underline{R}_s \underline{i}^s_{abcde} + \frac{d\underline{\psi}^s_{abcde}}{dt} \qquad \underline{\psi}^s_{abcde} = \underline{L}_s \underline{i}^s_{abcde} + \underline{L}_{sr} \underline{i}^r_{abcde} \tag{3.16}$$

$$\underline{v}^r_{abcde} = \underline{R}_r \underline{i}^r_{abcde} + \frac{d\underline{\psi}^r_{abcde}}{dt} \qquad \underline{\psi}^r_{abcde} = \underline{L}_r \underline{i}^r_{abcde} + \underline{L}_{rs} \underline{i}^s_{abcde} \tag{3.17}$$

The following definition of phase voltages, currents and flux linkages applies to (3.16)-(3.17):

$$\underline{v}^s_{abcde} = [v_{as} \quad v_{bs} \quad v_{cs} \quad v_{ds} \quad v_{es}]^T \qquad \underline{i}^s_{abcde} = [i_{as} \quad i_{bs} \quad i_{cs} \quad i_{ds} \quad i_{es}]^T \qquad \underline{\psi}^s_{abcde} = [\psi_{as} \quad \psi_{bs} \quad \psi_{cs} \quad \psi_{ds} \quad \psi_{es}]^T \tag{3.18}$$

$$\underline{v}^r_{abcde} = [v_{ar} \quad v_{br} \quad v_{cr} \quad v_{dr} \quad v_{er}]^T \qquad \underline{i}^r_{abcde} = [i_{ar} \quad i_{br} \quad i_{cr} \quad i_{dr} \quad i_{er}]^T \qquad \underline{\psi}^r_{abcde} = [\psi_{ar} \quad \psi_{br} \quad \psi_{cr} \quad \psi_{dr} \quad \psi_{er}]^T \tag{3.19}$$

The matrices of stator and rotor inductances are given with ($\alpha = 2\pi/5$):

$$\underline{L}_s = \begin{bmatrix} L_{aas} & L_{abs} & L_{acs} & L_{ads} & L_{aes} \\ L_{abs} & L_{bbs} & L_{bcs} & L_{bds} & L_{bes} \\ L_{acs} & L_{bcs} & L_{ccs} & L_{cds} & L_{ces} \\ L_{ads} & L_{bds} & L_{cds} & L_{dds} & L_{des} \\ L_{aes} & L_{bes} & L_{ces} & L_{des} & L_{ees} \end{bmatrix}$$

$$\underline{L}_s = \begin{bmatrix} L_{ls}+M & M\cos\alpha & M\cos 2\alpha & M\cos 2\alpha & M\cos\alpha \\ M\cos\alpha & L_{ls}+M & M\cos\alpha & M\cos 2\alpha & M\cos 2\alpha \\ M\cos 2\alpha & M\cos\alpha & L_{ls}+M & M\cos\alpha & M\cos 2\alpha \\ M\cos 2\alpha & M\cos 2\alpha & M\cos\alpha & L_{ls}+M & M\cos\alpha \\ M\cos\alpha & M\cos 2\alpha & M\cos 2\alpha & M\cos\alpha & L_{ls}+M \end{bmatrix} \tag{3.20}$$

$$\underline{L}_r = \begin{bmatrix} L_{aar} & L_{abr} & L_{acr} & L_{adr} & L_{aer} \\ L_{abr} & L_{bbr} & L_{bcr} & L_{bdr} & L_{ber} \\ L_{acr} & L_{bcr} & L_{ccr} & L_{cdr} & L_{cer} \\ L_{adr} & L_{bdr} & L_{cdr} & L_{ddr} & L_{der} \\ L_{aer} & L_{ber} & L_{cer} & L_{der} & L_{eer} \end{bmatrix}$$

$$\underline{L}_r = \begin{bmatrix} L_{lr}+M & M\cos\alpha & M\cos 2\alpha & M\cos 2\alpha & M\cos\alpha \\ M\cos\alpha & L_{lr}+M & M\cos\alpha & M\cos 2\alpha & M\cos 2\alpha \\ M\cos 2\alpha & M\cos\alpha & L_{lr}+M & M\cos\alpha & M\cos 2\alpha \\ M\cos 2\alpha & M\cos 2\alpha & M\cos\alpha & L_{lr}+M & M\cos\alpha \\ M\cos\alpha & M\cos 2\alpha & M\cos 2\alpha & M\cos\alpha & L_{lr}+M \end{bmatrix} \tag{3.21}$$

Formatted

Mutual inductances between stator and rotor windings are given with:

$$\underline{L}_{sr} = M\begin{bmatrix} \cos\theta & \cos(\theta+\alpha) & \cos(\theta+2\alpha) & \cos(\theta-2\alpha) & \cos(\theta-\alpha) \\ \cos(\theta-\alpha) & \cos\theta & \cos(\theta+\alpha) & \cos(\theta+2\alpha) & \cos(\theta-2\alpha) \\ \cos(\theta-2\alpha) & \cos(\theta-\alpha) & \cos\theta & \cos(\theta+\alpha) & \cos(\theta+2\alpha) \\ \cos(\theta+2\alpha) & \cos(\theta-2\alpha) & \cos(\theta-\alpha) & \cos\theta & \cos(\theta+\alpha) \\ \cos(\theta+\alpha) & \cos(\theta+2\alpha) & \cos(\theta-2\alpha) & \cos(\theta-\alpha) & \cos\theta \end{bmatrix} \tag{3.22}$$

$$\underline{L}_{rs} = \underline{L}_{sr}^T$$

The angle θ denotes the instantaneous position of the magnetic axis of the rotor phase 'a' with respect to the stationary stator phase 'a' magnetic axis (i.e. the instantaneous position of the rotor with respect to stator). Stator and rotor resistance matrices are 5x5 diagonal matrices,

Deleted:

Deleted: s

Deleted: "

Deleted: "

Deleted: magnetic axis of the

Deleted: "

Deleted: "

Deleted: diagonal

$$\begin{aligned} \underline{R}_s &= diag(R_s \quad R_s \quad R_s \quad R_s \quad R_s) \\ \underline{R}_r &= diag(R_r \quad R_r \quad R_r \quad R_r \quad R_r) \end{aligned} \tag{3.23}$$

Motor torque can be expressed in terms of phase variables as

$$T_e = \frac{P}{2}\underline{i}^T \frac{d\underline{L}_{abcde}}{d\theta}\underline{i} = \frac{P}{2}\begin{bmatrix} \underline{i}^{sT}_{abcde} & \underline{i}^{rT}_{abcde} \end{bmatrix} \frac{d\underline{L}_{abcde}}{d\theta}\begin{bmatrix} \underline{i}^s_{abcde} \\ \underline{i}^r_{abcde} \end{bmatrix} \tag{3.24a}$$

$$T_e = P\underline{i}^{sT}_{abcde}\frac{d\underline{L}_{sr}}{d\theta}\underline{i}^r_{abcde} \tag{3.24b}$$

Substitution of stator and rotor currents from (3.18)-(3.19) and (3.22) into (3.24b) yields the torque equation in developed form:

$$T_e = -PM\left\{\begin{matrix} (i_{as}i_{ar}+i_{bs}i_{br}+i_{cs}i_{cr}+i_{ds}i_{dr}+i_{es}i_{er})\sin\theta + (i_{es}i_{ar}+i_{as}i_{br}+i_{bs}i_{cr}+i_{cs}i_{dr}+i_{ds}i_{er})\sin(\theta+\alpha)+ \\ (i_{ds}i_{ar}+i_{es}i_{br}+i_{as}i_{cr}+i_{bs}i_{dr}+i_{cs}i_{er})\sin(\theta+2\alpha)+(i_{cs}i_{ar}+i_{ds}i_{br}+i_{es}i_{cr}+i_{as}i_{dr}+i_{bs}i_{er}) \\ \sin(\theta-2\alpha)+(i_{bs}i_{ar}+i_{cs}i_{br}+i_{ds}i_{cr}+i_{es}i_{dr}+i_{as}i_{er})\sin(\theta-\alpha) \end{matrix}\right\} \tag{3.25}$$

3.4.2 Model transformation

In order to simplify the model, it is necessary to apply a co-ordinate transformation, that will remove the time varying inductances. The co-ordinate transformation is utilised in the power invariant form. The following transformation matrix is therefore applied to the stator five-phase winding:

$$\underline{A}_s = \sqrt{\frac{2}{5}} \begin{bmatrix} \cos\theta_s & \cos(\theta_s - \alpha) & \cos(\theta_s - 2\alpha) & \cos(\theta_s + 2\alpha) & \cos(\theta_s + \alpha) \\ -\sin\theta_s & -\sin(\theta_s - \alpha) & -\sin(\theta_s - 2\alpha) & -\sin(\theta_s + 2\alpha) & -\sin(\theta_s + \alpha) \\ 1 & \cos(2\alpha) & \cos(4\alpha) & \cos(4\alpha) & \cos(2\alpha) \\ 0 & \sin(2\alpha) & \sin(4\alpha) & -\sin(4\alpha) & -\sin(2\alpha) \\ \frac{1}{\sqrt{2}} & \frac{1}{\sqrt{2}} & \frac{1}{\sqrt{2}} & \frac{1}{\sqrt{2}} & \frac{1}{\sqrt{2}} \end{bmatrix} \tag{3.26}$$

Transformation of the rotor variables is performed using the same transformation expression, except that θ_s is replaced with β, where $\beta = \theta_s - \theta$. Here θ_s is the instantaneous angular position of the d-axis of the common reference frame with respect to the phase 'a' magnetic axis of the stator, while β is the instantaneous angular position of the d-axis of the common reference frame with respect to the phase 'a' magnetic axis of the rotor. Hence the transformation matrix for rotor is:

Deleted: "
Deleted: "
Deleted:
Deleted:
Deleted: and
Deleted: "
Deleted: "

$$\underline{A}_r = \sqrt{\frac{2}{5}} \begin{bmatrix} \cos\beta & \cos(\beta - \alpha) & \cos(\beta - 2\alpha) & \cos(\beta + 2\alpha) & \cos(\beta + \alpha) \\ -\sin\beta & -\sin(\beta - \alpha) & -\sin(\beta - 2\alpha) & -\sin(\beta + 2\alpha) & -\sin(\beta + \alpha) \\ 1 & \cos(2\alpha) & \cos(4\alpha) & \cos(4\alpha) & \cos(2\alpha) \\ 0 & \sin(2\alpha) & \sin(4\alpha) & -\sin(4\alpha) & -\sin(2\alpha) \\ \frac{1}{\sqrt{2}} & \frac{1}{\sqrt{2}} & \frac{1}{\sqrt{2}} & \frac{1}{\sqrt{2}} & \frac{1}{\sqrt{2}} \end{bmatrix} \tag{3.27}$$

The angles of transformation for stator quantities and for rotor quantities are related to the arbitrary speed of the selected common reference frame through:

$$\begin{aligned} \theta_s &= \int \omega_a dt \\ \beta &= \theta_s - \theta = \int (\omega_a - \omega) dt \end{aligned} \tag{3.28}$$

where ω is the instantaneous electrical angular speed of rotation of the rotor.

3.4.3 Machine model in an arbitrary common reference frame

Correlation between original phase variables and new variables in the transformed domain is governed with the following transformation expressions:

$$\begin{aligned} &\underline{v}^s_{dq} = \underline{A}_s \underline{v}^s_{abcde} \qquad \underline{i}^s_{dq} = \underline{A}_s \underline{i}^s_{abcde} \qquad \underline{\psi}^s_{dq} = \underline{A}_s \underline{\psi}^s_{abcde} \\ &\underline{v}^r_{dq} = \underline{A}_r \underline{v}^r_{abcde} \qquad \underline{i}^r_{dq} = \underline{A}_r \underline{i}^r_{abcde} \qquad \underline{\psi}^r_{dq} = \underline{A}_r \underline{\psi}^r_{abcde} \end{aligned} \tag{3.29}$$

Substitution of (3.16)-(3.17) into (3.29) and application of (3.26)-(3.27) yields the machine's voltage equations in the common reference frame:

Deleted: e
Deleted: i
Deleted: s
Deleted:

$$\begin{aligned} v_{ds} &= R_s i_{ds} - \omega_a \psi_{qs} + p\psi_{ds} & v_{dr} &= R_r i_{dr} - (\omega_a - \omega)\psi_{qr} + p\psi_{dr} \\ v_{qs} &= R_s i_{qs} + \omega_a \psi_{ds} + p\psi_{qs} & v_{qr} &= R_r i_{qr} + (\omega_a - \omega)\psi_{dr} + p\psi_{qr} \\ v_{xs} &= R_s i_{xs} + p\psi_{xs} & v_{xr} &= R_r i_{xr} + p\psi_{xr} \\ v_{ys} &= R_s i_{ys} + p\psi_{ys} & v_{yr} &= R_r i_{yr} + p\psi_{yr} \\ v_{0s} &= R_s i_{0s} + p\psi_{0s} & v_{0r} &= R_r i_{0r} + p\psi_{0r} \end{aligned} \tag{3.30}$$

Transformation of flux linkage equations of (3.16)-(3.17) results in:

Deleted:

$$
\begin{aligned}
&\psi_{ds} = (L_{ls} + 2.5M)i_{ds} + 2.5Mi_{dr} && \psi_{dr} = (L_{lr} + 2.5M)i_{dr} + 2.5Mi_{ds} \\
&\psi_{qs} = (L_{ls} + 2.5M)i_{qs} + 2.5Mi_{qr} && \psi_{qr} = (L_{lr} + 2.5M)i_{qr} + 2.5Mi_{qs} \\
&\psi_{xs} = L_{ls}i_{xs} && \psi_{xr} = L_{lr}i_{xr} \\
&\psi_{ys} = L_{ls}i_{ys} && \psi_{yr} = L_{lr}i_{yr} \\
&\psi_{0s} = L_{ls}i_{0s} && \psi_{0r} = L_{lr}i_{0r}
\end{aligned}
\tag{3.31}
$$

Introduction of the magnetising inductance $L_m = 2.5M$ enables writing of (3.31) in the following form:

Deleted:

$$
\begin{aligned}
&\psi_{ds} = (L_{ls} + L_m)i_{ds} + L_m i_{dr} && \psi_{dr} = (L_{lr} + L_m)i_{dr} + L_m i_{ds} \\
&\psi_{qs} = (L_{ls} + L_m)i_{qs} + L_m i_{qr} && \psi_{qr} = (L_{lr} + L_m)i_{qr} + L_m i_{qs} \\
&\psi_{xs} = L_{ls}i_{xs} && \psi_{xr} = L_{lr}i_{xr} \\
&\psi_{ys} = L_{ls}i_{ys} && \psi_{yr} = L_{lr}i_{yr} \\
&\psi_{0s} = L_{ls}i_{0s} && \psi_{0r} = L_{lr}i_{0r}
\end{aligned}
\tag{3.32}
$$

Finally, transformation of the original torque equation (3.24b) yields

$$
\begin{aligned}
T_e &= \frac{5P}{2} M\left[i_{dr}i_{qs} - i_{ds}i_{qr}\right] \\
T_e &= PL_m\left[i_{dr}i_{qs} - i_{ds}i_{qr}\right]
\end{aligned}
\tag{3.33}
$$

Mechanical equation of rotor motion is invariant under the transformation and is

$$
T_e - T_L = \frac{J}{P}\frac{d\omega}{dt} \tag{3.34}
$$

3.5 ROTOR FLUX ORIENTED CONTROL OF A FIVE-PHASE INDUCTION MOTOR

Deleted: ¶

3.5.1 Indirect vector controller

The basis of vector control is the selection of the speed of the common reference frame. In rotor flux oriented control scheme the speed of the reference frame is selected as equal to the speed of the rotor flux space vector. The rotor flux space vector is kept aligned at all times with the real axis (d-axis) of the common reference frame, while q-axis is perpendicular to it. As the rotor flux space vector is aligned with the real axis its imaginary component always remains equal to zero.

Rotor flux oriented reference frame is defined with

$$
\begin{aligned}
&\theta_s = \phi_r && \theta_r = \phi_r - \theta \\
&\omega_a = \omega_r && \omega_r = \frac{d\phi_r}{dt}
\end{aligned}
\tag{3.35}
$$

where angle ϕ_r denotes instantaneous rotor flux space vector position. Rotor flux space vector becomes a pure real variable in this special frame of reference,

$$\underline{\psi}_r = \psi_{dr} + j\psi_{qr} = \psi_r \tag{3.36a}$$

i.e., it follows that

$$\psi_{dr} = \psi_r \qquad \psi_{qr} = 0 \qquad \mathrm{d}\psi_{qr}/dt = 0 \tag{3.36b}$$

Machine model obtained by transforming only d-q windings with the rotational transformation is considered further on. Assuming that the machine is current fed, one can omit the stator voltage equations from further consideration. From the model of the machine in an arbitrary reference frame (3.30), (3.32), (3.33), with stator equations omitted,

$$\begin{aligned}
0 &= R_r i_{dr} - (\omega_a - \omega)\psi_{qr} + p\psi_{dr} \\
0 &= R_r i_{qr} + (\omega_a - \omega)\psi_{dr} + p\psi_{qr} \\
0 &= R_r i_{xr} + p\psi_{xr} \\
0 &= R_r i_{yr} + p\psi_{yr} \\
0 &= R_r i_{0r} + p\psi_{0r}
\end{aligned} \tag{3.37}$$

$$\begin{aligned}
\psi_{dr} &= (L_{lr} + L_m)i_{dr} + L_m i_{ds} \\
\psi_{qr} &= (L_{lr} + L_m)i_{qr} + L_m i_{qs} \\
\psi_{xr} &= L_{lr} i_{xr} \\
\psi_{yr} &= L_{lr} i_{yr} \\
\psi_{0r} &= L_{lr} i_{0r}
\end{aligned} \tag{3.38}$$

$$T_e = PL_m\left(i_{dr} i_{qs} - i_{ds} i_{qr}\right) \tag{3.39}$$

and observing that x-y-0 rotor current and flux components are identically equal to zero, one further obtains by substitution of (3.36) into (3.37)-(3.39)

$$\psi_r + T_r \frac{d\psi_r}{dt} = L_m i_{ds} \tag{3.40}$$

$$\begin{aligned}
(\omega_r - \omega)\psi_r T_r &= L_m i_{qs} \\
\omega_{sl} &= \frac{L_m i_{qs}}{T_r \psi_r}
\end{aligned} \tag{3.41}$$

$$T_e = P\frac{L_m}{L_r}\psi_r i_{qs} \tag{3.42}$$

where $T_r = L_r / R_r$. It can be seen from (3.40)-(3.42) that the flux and torque producing currents in five-phase machines are only d-q components, thus the vector control scheme for a current fed five-phase machine is identical to the scheme for a current fed three-phase machine. The only difference is that the co-ordinate transformation now generates five phase current references instead of three. The configuration of the indirect vector controller for operation in the base speed region is illustrated in Fig. 3.10 for the five-phase induction machine. Constants in Fig. 3.10 are determined with the following expressions (which are in

Deleted: Consider an indirect vector control scheme for a three-phase machine, aimed at operation in the constant flux region only (i.e. base speed region).

essence identical to those for a three-phase induction machine with indirect rotor flux oriented control):

$$
\begin{aligned}
i_{qs}^{*} &= K_1 T_e^{*} \Rightarrow K_1 = i_{qs}^{*} / T_e^{*} = \frac{1}{P}\frac{L_r}{L_m}\frac{1}{\psi_r^{*}} = \frac{1}{P}\frac{L_r}{L_m^2}\frac{1}{i_{ds}^{*}} \\
\omega_{sl}^{*} &= K_2 i_{qs}^{*} \Rightarrow K_2 = \omega_{sl}^{*} / i_{qs}^{*} = \frac{L_m}{T_r \psi_r^{*}} = \frac{1}{T_r i_{ds}^{*}}
\end{aligned}
\tag{3.43}
$$

Determination of these constants is discussed next, in the following subsection. The same applies to the design of the PI speed controller that will be needed in simulations related to the speed mode of operation of the drive. Induction motor data are given in the Appendix A.

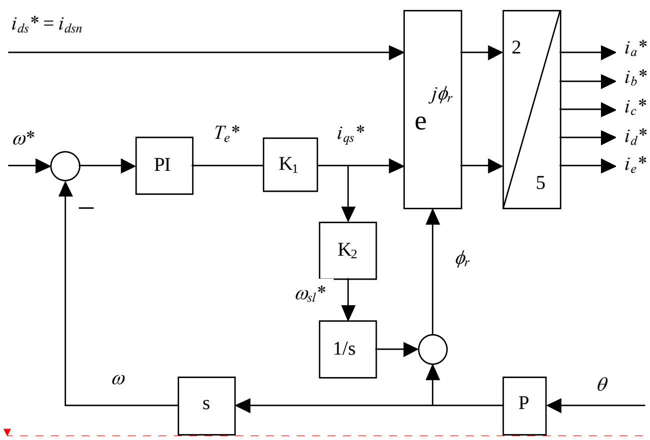

Deleted: ¶

Fig. 3.10. Indirect vector control of a five-phase induction machine in the base speed region.

3.5.2 Design of the indirect vector controller

In order to design an indirect vector controller one needs to determine constants K_1 and K_2 in Fig. 3.10 and speed PI controller parameters.

Deleted: the following parameters have to be de

Deleted: d:

Deleted: rated rotor flux value, rated stator d- and q-axis current values

Deleted: ,

In steady state operation under rated operating conditions (index n stands for rated values) one has

$$
T_{en} = P\frac{L_m}{L_r}\psi_r i_{qs} \qquad \psi_{rn} = L_m i_{dsn} \qquad \omega_{sln} = \frac{L_m i_{qsn}}{T_r \psi_{rn}} \tag{3.44}
$$

$$
\psi_r^{*} = \psi_{rn} \qquad T_L = T_{en} \qquad \omega_{sl} = \omega_{sln} \tag{3.45}
$$

The stator current RMS value will equal the rated value. Since power invariant transformation is used, this means that the magnitude of the stator current space vector will be √5 greater than the RMS value (which is 2.1 A). Hence

$$
\begin{aligned}
i_{sn} &= \sqrt{5} I_{sn} = 4.6957 \text{ A} \\
i_{sn} &= \sqrt{i_{dsn}^2 + i_{qsn}^2}
\end{aligned}
\tag{3.46}
$$

Taking into account that the rated RMS rotor flux is 0.5683 Wb and the rated per-phase torque is 1.667 Nm, one has

$$\psi_{rn} = 0.5683 \times \sqrt{5} = 1.2705 \text{ Wb}$$
$$T_{en} = 5 \times \frac{5}{3} = 8.33 \text{ Nm} \qquad (3.47)$$

The rated torque is determined with (3.44) where the pole pair number equals two and the magnetising and the rotor inductance are 0.42 H and 0.46 H, respectively. By solving (3.46) and the torque equation of (3.44) one gets the rated stator d-q axis current components

$$i_{dsn} = 3.025 \text{ A} \qquad\qquad i_{qsn} = 3.5904 \text{ A} \qquad (3.48)$$

The two constants defined in (3.43) and required in the indirect vector control scheme of Fig. 3.10 are finally

$$K_1 = \frac{1}{P}\frac{L_r}{L_m}\frac{1}{\psi_r^*} = \frac{1}{P}\frac{L_r}{L_m^2}\frac{1}{i_{ds}^*} = 0.431 \qquad K_2 = \omega_{sl}^* \big/ i_{qs}^* = \frac{L_m}{T_r \psi_r^*} = \frac{1}{T_r i_{ds}^*} = 4.527 \qquad (3.49)$$

3.6 CURRENT CONTROL TECHNIQUES AND SPEED CONTROLLER DESIGN

3.6.1 General considerations

Current controlled PWM inverter is the most frequent choice in high performance ac drives as decoupled flux and torque control by instantaneous stator current space vector amplitude and position control is achieved relatively easily.

All the current control techniques for VSIs essentially belong to one of the two major groups. The first group encompasses all the current control methods that operate in the stationary reference frame while the second group includes current control techniques with current controllers operating in the rotational frame of reference. If the current control of an induction machine is performed in rotational reference frame, decoupling of stator voltage equations substitutes local current feedback loops in stationary reference frame, which suppress influence of stator voltage equations.

Deleted: voltage source inverter

Current control in stationary reference frame is usually implemented in an analogue fashion. Three types of current control techniques are met in the literature:

1. Hysteresis control
2. Ramp-comparison control
3. Predictive or adaptive control

Deleted: current

Deleted: .

Hysteresis controllers utilise a hysteresis band in comparing the actual current with the reference current. The ramp-comparison controllers compare the current error to a triangular carrier waveform to generate the switching signals for the inverter. In predictive control schemes the inverter voltage is calculated to force the current to follow the reference current.

The most pronounced shortcoming of the hysteresis current control is the variable inverter switching frequency over a period of output voltage. Current control by ramp-comparison controllers overcomes this problem. Here current error serves as modulating signal, which is compared to the triangular carrier wave. Deviation of amplitude and phase of phase currents with respect to commanded values unfortunately takes place and some compensation has to be introduced. Another difficulty arises from a possibility that multiple crossing of the carrier may occur if the frequency of the current error becomes greater than the carrier frequency. This can be overcome by adding hysteresis to the controller. The advantage of the ramp-comparison current control with respect to hysteresis current control is the fixed and constant inverter switching frequency. The predictive control is characterised by a fixed switching frequency as well. However, time required for the calculations is significant. Moreover, an efficient prediction requires the load knowledge as well.

Ramp-comparison current control in stationary reference frame requires that current PI controllers process alternating signals, that can be of a large frequency range. Furthermore, controller characteristics in steady state depend on the operating frequency and the machine impedance. These shortcomings can be partially but not completely eliminated by different modifications of the basic current control principles. At low operating speeds the induced rotational electromotive force in the machine is small and current control enables very good tracking between reference and actual currents, with respect to both amplitude and phase. However at higher speeds, due to limited voltage capability of the inverter and finite inverter switching frequency, tracking worsens and an error is met in both amplitude and phase of actual currents compared to reference currents. This feature becomes very pronounced in the field-weakening region where the inverter operates very close to the voltage limit. The problem may be solved by moving current controllers from the stationary to the rotating reference frame. The outputs of the current controllers then become voltage references in rotational reference frame. If the inverter switching frequency is high enough, decoupling circuit for stator dynamics is usually omitted.

Current control in rotational reference frame is well suited to fully digital realisation. The main advantage of this method of current control is that current controllers (most frequently of PI type) process dc signals. As the current control is performed in rotational reference frame, measured currents have to be transformed from stationary to rotational reference frame. When current control in rotational reference frame is applied, different

Deleted: ,

Deleted: the common choice being a PI compensator.

Deleted: e

Deleted:

Deleted:

Deleted: introduces a large delay

Deleted: C

Deleted:

Deleted:

Deleted: and the machine is still treated as being current fed. In the field-weakening region the machine is usually fed with square-wave voltages and here the concept of current feeding has to be abandoned. Decoupling circuit is included in the control system and the machine is treated as being fed from a voltage source. The same concept of voltage feeding has to be applied in the base speed range as well if the switching frequency of the inverter is low, this being the case with thyristor inverters utilised in conjunction with vector controlled high power induction motors.

PWM methods may be utilised for creation of the desired voltages at machine terminals. For example, sinusoidal PWM may be selected or voltage space vector modulation may be chosen.

3.6.2 Current control in stationary reference frame - hysteresis controllers

The structure of an induction motor drive with current control in the stationary reference frame is depicted in Fig. 3.11. Five independent controllers in five phases *a,b,c,d,e* reference frame are used. The current controllers in Fig. 3.11 can be of either hysteresis type or ramp-comparison type.

The idea of hysteresis current control is in essence very simple and well suited for analogue realisation. Actual currents are allowed to deviate from their reference values for a fixed value termed as hysteresis band (Fig. 3.12). The discrepancy between actual and reference currents will vary in time and will be either positive or negative. The values of the hysteresis band are the same for both positive and negative variation. The state of the appropriate leg of the inverter bridge changes once when the difference between actual and reference current exceeds hysteresis band. For example, suppose that the upper switch in phase 'a' leg is closed, while the lower switch is open. This state will be preserved as long as the current error in phase 'a' is within hysteresis band. However, when the actual current in phase 'a' becomes greater than the reference value plus hysteresis band, the upper switch will be opened and the lower switch will be closed. Thus the actual current will be forced to reduce and fall once more within the hysteresis band. As the actual current change in time is function of the drive dynamics and operating state, the instants of inverter semiconductor switching cannot be predicted and will vary. Furthermore the switching frequency of the inverter varies and is not constant even over one cycle of the output frequency. The principle of hysteresis current control is illustrated in Fig. 3.13, where the inverter leg voltage is shown as well. One clearly observes in Fig. 3.13 how the switching frequency of the inverter varies from one cycle of operation to the other cycle. Periods of inverter switching are denoted as T1, T2, T3 and T4 and one easily observes that T1 is the largest out of the four, while T4 is the smallest.

In the system shown in Fig. 3.11 only speed controller is present (its input is the speed error, not shown in Fig. 3.11), whose output becomes after appropriate scaling q-axis current command. The d-axis reference current is obtained by dividing the reference rotor flux by magnetising inductance.

Hysteresis band for hysteresis current control is selected in all simulations (for both a single-motor drive in this chapter and multi-motor drives in subsequent chapter) as ±2.5% of the motor rated (peak) current value, i.e. as equal to ±0.07425 A (motor rated RMS current is 2.1 A). Speed controller parameter setting is discussed in detail in section 3.6.4.

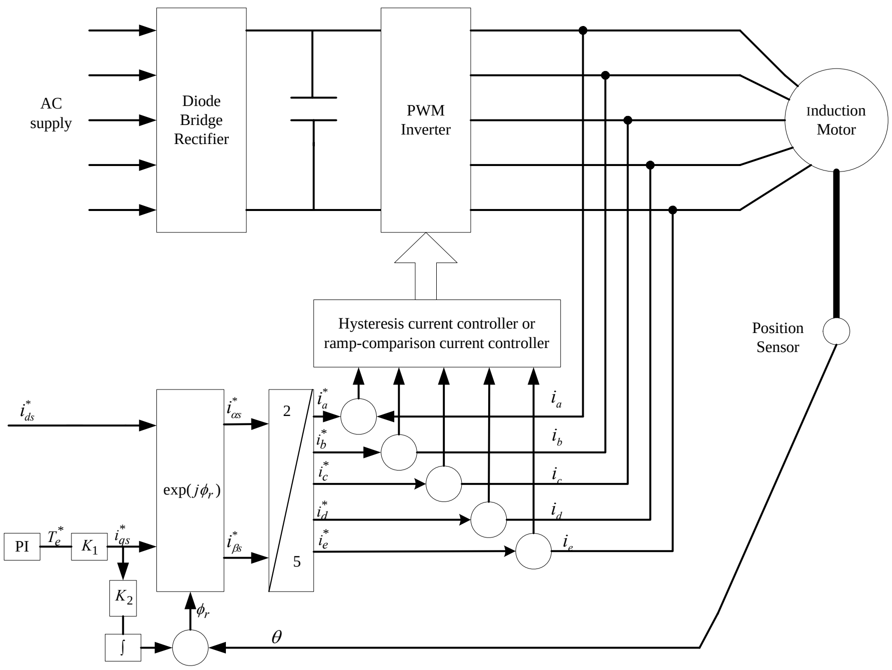

Fig. 3.11. Induction motor drive structure with current control in the stationary reference frame.

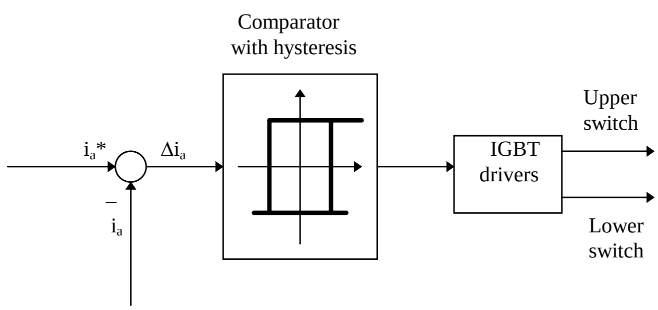

Fig. 3.12. Hysteresis current controller.

3.6.3 Current control in stationary reference frame - ramp-comparison control

The structure of the drive system with ramp-comparison controller is again the one shown in Fig. 3.11. Current error is formed in the stationary reference frame and is further passed through PI current controllers. The outputs of the current controllers are phase voltage references which are compared to the triangular carrier wave of the fixed frequency. As the triangular carrier wave is of fixed frequency, while frequency of the current error varies, the ratio of these two frequencies is not an integer and so-called asynchronous PWM results. Asynchronous PWM in general leads to generation of unwanted sub-harmonics in the output voltage waveform. However, if the triangular carrier wave frequency is high enough this effect can be neglected as it will not have any serious impact on the drive behaviour. In general, five carrier waves are needed, one per phase. However, if the triangular carrier frequency is high enough, one carrier wave may be used for all the five phases. Generation of the inverter voltages using ramp-comparison control is illustrated in Fig. 3.14.

Deleted: of output voltages results in this way.

Deleted:

Deleted:

Deleted:

Deleted:

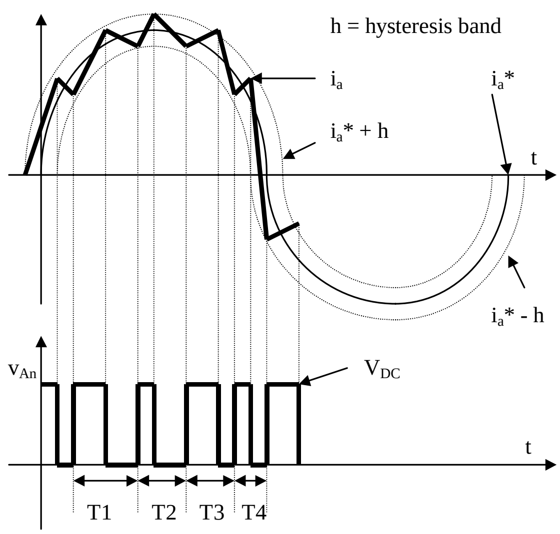

Fig. 3.13. Principle of hysteresis current control (currents and a leg voltage).

Deleted: Hysteresis current controller and

Deleted: p

The tuning of PI current controller is discussed next. The frequency of the triangular carrier wave for ramp-comparison control is fixed at all times to 5 kHz and its amplitude is ±1. The outputs of the PI current controllers, which are implemented as discrete PI controllers, are limited to ±1 in order to ensure operation in the full PWM mode at all times. Tuning of the current controller parameters is performed first, with speed control loop kept open. Phase current references are generated through the co-ordinate transformation, from imposed d-q axis current references. Stator d-q axis current references are given as pulsed current waveforms, with a period of 0.01 s and the pulse duration of 0.005 s. The amplitude of the pulse in d-q axis current references is set to 2.5 A. The integral gain is kept at a sufficiently low value and the proportional gain is gradually increased in order to achieve good tracking between the pulsed phase current reference and the actual current response. Once the current response becomes of acceptable nature, the proportional gain is fixed and the integral gain is gradually altered to obtain an acceptable overshoot in the current response. The procedure is illustrated in Fig. 3.15, where the reference pulsed phase 'a' current and the actual current response are shown for four different pairs of proportional and integral gains. The current response obtained with the proportional gain equal to 0.6 and the integral gain equal to 0.8 was deemed to be acceptable and is selected for further work. It should be noted that, due to the discrete form of the PI controller, what is called here integral gain is, strictly speaking, not the integral gain. The value of 0.8 mentioned above is in essence a product of the sampling time (19 μs) and the integral gain of the continuous PI controller equivalent.

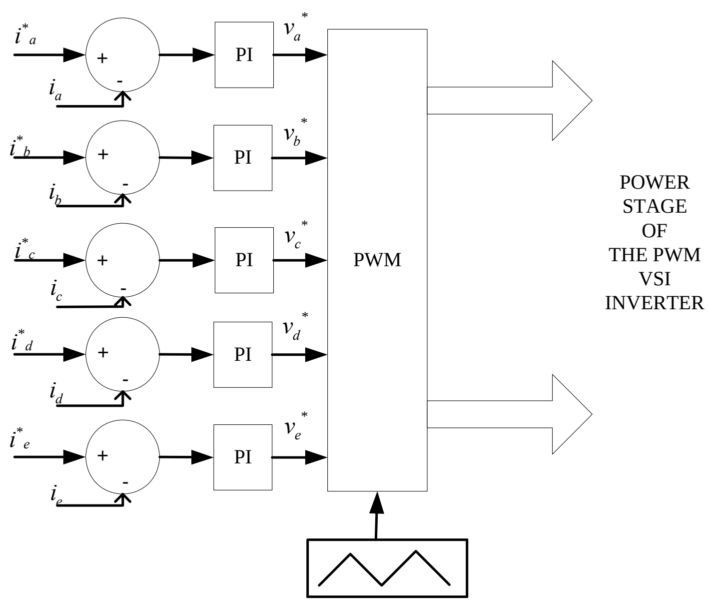

Fig. 3.14. Ramp-comparison current control.

Deleted:

The same tuning procedure was repeated for the two two-motor drive systems (five-phase and six-phase). The impedance, seen by current controllers, changes due to the series connection of two machines. Figures 3.16 and 3.17 illustrate the phase 'a' current reference (which is the same as for one five-phase machine case) and the actual current response for the five-phase two-motor drive and the six-phase two-motor drive system, respectively. As can be seen from these two figures, the current response obtained with the proportional gain of 0.6 and the integral gain of 0.8 is very similar as for the single-motor five-phase drive. These

Deleted: (five-phase and six-phase) which will be considered in detail in subsequent two Chapters.

current controller parameters are therefore used in all simulations related to ramp-comparison current control, reported in this and the subsequent chapter.

Deleted: C

Deleted: s

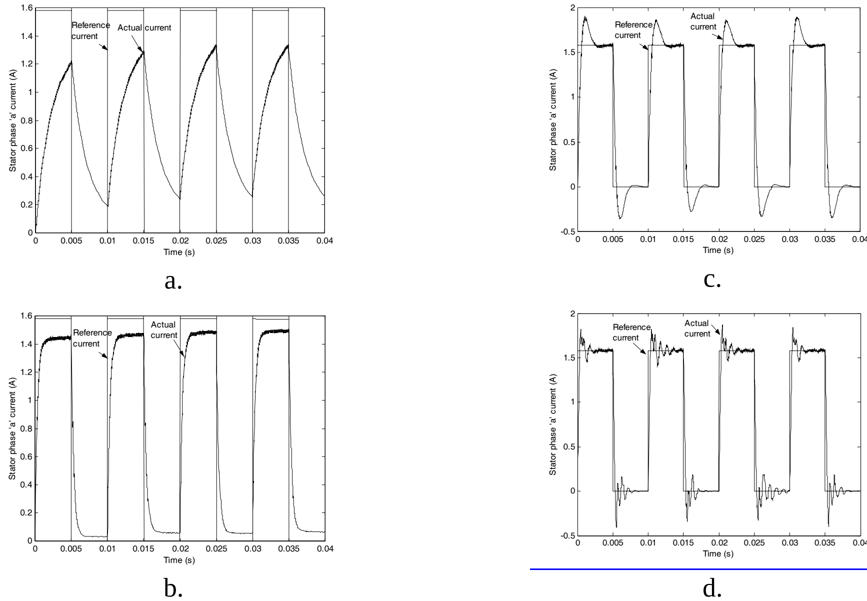

Deleted:

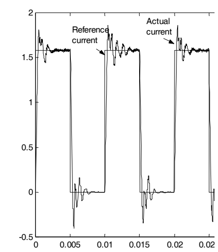

Fig. 3.15. Tuning of the current PI controller for a single-motor five-phase drive, using a pulsed current reference. The values of K_p and K_i are, respectively: a. 0.1 and 0.001; b. 0.6 and 0.001; c. 0.6 and 0.1; d. 0.6 and 0.8.

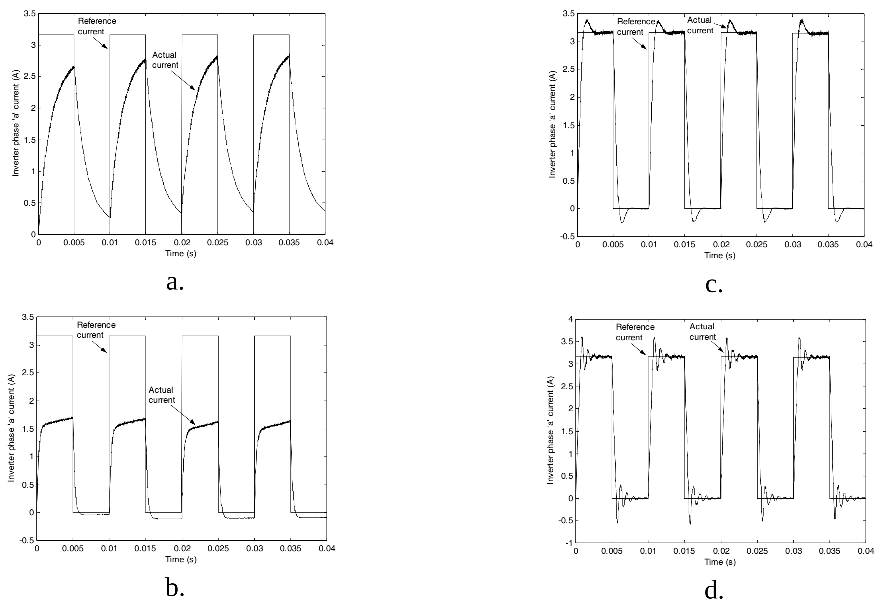

Fig. 3.16. Tuning of the current PI controller for a two-motor five-phase drive. The values of K_p and K_i are, respectively: a. 0.1 and 0.001; b. 0.6 and 0.001; c. 0.6 and 0.1; d. 0.6 and 0.8.

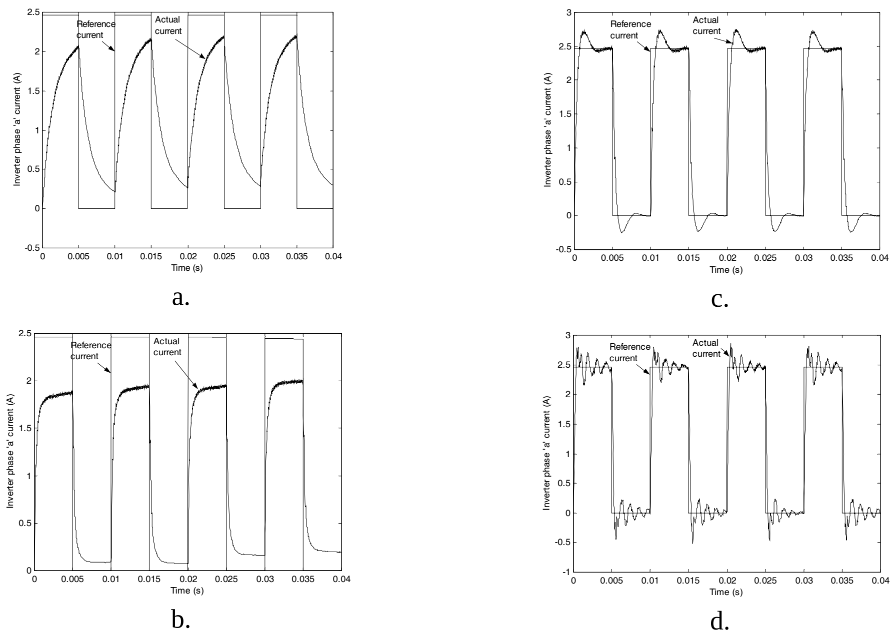

Fig. 3.17. Tuning of the current PI controller for a two-motor six-phase drive. The values of K_p and K_i are, respectively: a. 0.1 and 0.001; b. 0.6 and 0.001; c. 0.6 and 0.1; d. 0.6 and 0.8.

3.6.4 Speed controller design

PI speed controller is considered next. Two different speed controllers are designed, a continuous one and a discrete one. Both speed controllers are used in simulations further on. The type of the speed controller used in conjunction with any specific simulation will be indicated in the corresponding section with simulation results. The design of continuous speed controller is presented first. For this purpose, and having in mind that the inverter current control will be performed in the stationary reference frame using hysteresis or ramp-comparison technique, the whole current control loop is approximated with unity gain and zero time delay. The structure of the speed control loop is then as shown in Fig. 3.18.

Deleted:

The transfer function of the PI speed controller is

$$G_{PI}(s) = K_P(1+\frac{1}{sT_i}) = K_p + K_i\frac{1}{s} \tag{3.50}$$

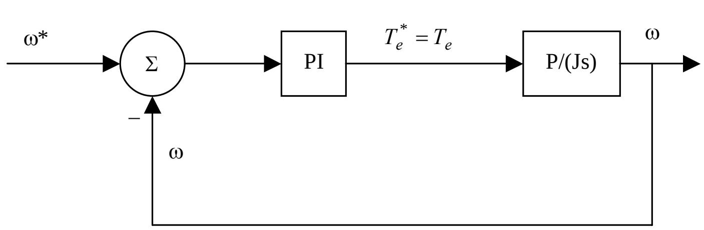

Fig. 3.18. Structure of the speed control loop.

The characteristic equation of the above speed control loop is solved for $1+G_{PI}(s)H(s)=0$, where according to Fig. 3.18 $H(s)=1/(sJ/P)$. The parameters are $J=0.03\,\text{kgm}^2$, $\text{P}=2$. Hence the characteristic equation is

Deleted: ¶ $G_{PI}(s)=K_P(1+\frac{1}{sT_i})=K_p+K_i$ (3.50)¶

$$s^2+66.67K_P s+66.67K_i=0 \qquad (3.51)$$

The coefficients in the above equation are equated with those in the following equation, which defines the desired closed loop dynamics in terms of the damping ratio ξ and natural frequency ω_0:

$$s^2+2\xi\omega_0 s+\omega_0^2=0 \qquad (3.52)$$

Damping ratio is selected as 0.707. The natural frequency for the speed control loop is dependent on the bandwidth of the inner current control loop. Maximum practical value of the current control loop bandwidth in the case of ramp-comparison control with 5 kHz switching frequency is 1 kHz. For the purpose of the speed controller design, current loop bandwidth is taken as one tenth of the maximum value (i.e. as 100 Hz). Taking the speed control bandwidth as one tenth of this value (10 Hz) and approximating the natural frequency with the bandwidth, one has $\omega_0=2\pi 10=62.8318$ rad/s. Substitution of the damping ratio and natural frequency values into (3.52) and comparison with (3.51) yields the following values for the speed controller parameters:

Deleted:

$$K_p=1.332 \qquad K_i=59.214 \qquad T_i=0.0225\text{ s} \qquad (3.53)$$

In the design of a discrete PI speed controller the same procedure is adopted as the one used for the PI current controller tuning. A pulsed speed reference (of 200 rad/s amplitude) is applied as the input of the PI speed controller and the speed of the machine is observed. The reference speed pulsed waveform is applied at 0.2 s. The period of the reference speed pulse is equal to 0.6 s, and the pulse duration is 0.3 s. Tuning is again performed using the single-machine five-phase drive system. The responses obtained with four different pairs of proportional and integral gain values are shown in Fig. 3.19. The speed response obtained with the proportional gain equal to 2 and the integral gain equal to 0.1184 is deemed as being satisfactory. The integral gain is rounded to 0.12 (the same remark as the one given in section 3.6.3, regarding the meaning of the term integral gain in relation to a discrete PI controller, applies here as well).

Deleted: ec

These discrete speed controller parameters ($K_p=2,\ K_i=0.12$) are used further on in simulations of a single five-phase induction machine described in this chapter, in conjunction with both hysteresis current control and ramp-comparison current control. For the speed controller there is no need to perform additional tuning trials for the two-motor drive systems,

Deleted: C

since addition of the second machine in series with the first one affects only the current control loop, while the speed control loop remains unaffected.

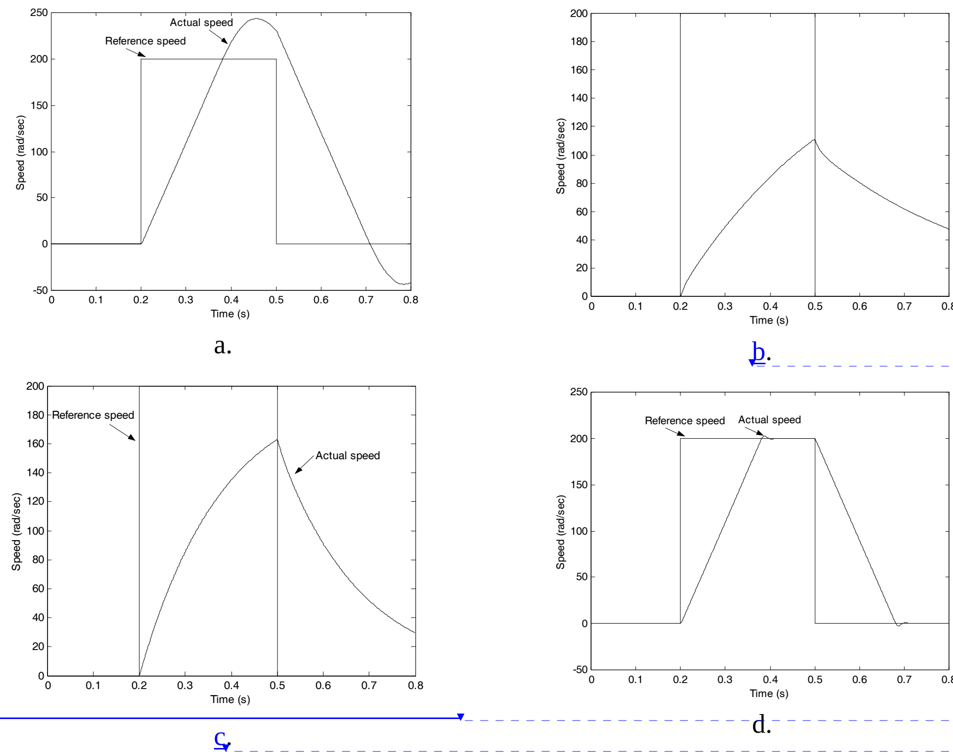

Deleted: c

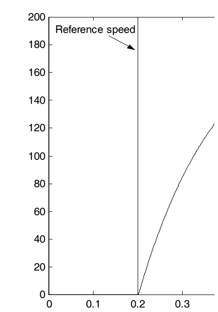

Deleted:

Deleted: b

Fig. 3.19. Tuning of the speed PI controller for a single five-phase induction motor drive, using a pulsed speed reference. The values of the proportional and the integral gain are, respectively: a. 0.1 and 0.001; b. 2 and 0.001; c. 1 and 0.001; d. 2 and 0.1184.

3.7 SIMULATION OF A SINGLE FIVE-PHASE INDUCTION MOTOR DRIVE

Formatted: Bullets and Numbering

3.7.1 Hysteresis current control

A simulation program is written using MATLAB/SIMULINK software for an indirect rotor flux oriented five-phase induction motor drive. The motor is simulated using developed d-q model in the stationary reference frame. The machine is fed by a PWM voltage source inverter and hysteresis current control is exercised upon motor phase currents. The drive is operated in closed loop speed control mode with discrete anti-windup PI speed controller. The anti-windup feature restricts the saturation of the integral part of the controller while working in the limiting region. The torque is limited to twice the rated value (16.67 Nm). The drive is simulated for acceleration, disturbance rejection and speed reversal transients, at two different operating speeds, 1200 and 1500 rpm.

Deleted: voltage source inverter

Deleted: phase

Deleted: load

Forced excitation is initiated first. Rotor flux reference (i.e. stator d-axis current reference) is ramped from t = 0 to t = 0.01 s to twice the rated value. It is further reduced from twice the rated value to the rated value in a linear fashion from t = 0.05 to t = 0.06 s. and it is then kept constant for the rest of the simulation period. Once the rotor flux has reached steady state, a speed command of 1200 rpm (or 1500 rpm) is applied at t = 0.3 s in ramp wise manner from t = 0.3 to t = 0.35 s. The inverter dc link voltage is set to 415x$\sqrt{2}$ = 586.9 V. A step load torque, equal to the motor rated torque (8.33 Nm), is applied at t = 1 s and the machine is allowed to run for sufficient time so as to reach the steady state condition. A speed reversal is then initiated in the ramp-wise manner (ramp duration from t = 1.2 to t = 1.25 s).

Deleted: (rated RMS = 0.5683 Wb).

Deleted: se

Deleted: c.

Deleted: sec

Deleted: The hysteresis current controller band is kept at ±2.5% (±0.07425 A, motor rated RMS current is 2.1 A).

Simulation results for the 1200 rpm speed command are shown in Figs. 3.20-3.22. In particular, Fig. 3.20 illustrates rotor flux and rotor flux reference for the complete duration of the transient, as well as motor speed response, torque response and reference and actual current during the acceleration transient. Rotor flux settles to the reference value after initial transient and then it remains constant throughout the simulation period (2 seconds), indicating that full decoupling between rotor flux and torque control has been achieved. During acceleration motor torque and speed follow the commanded value. Acceleration takes place with the maximum allowed value of the motor torque. Actual motor phase current tracks the reference very well. Consequently, torque response closely follows torque reference. There is sufficient voltage reserve to enable the complete acceleration transient to take place in the torque limit.

Disturbance rejection properties of the drive are studied by applying rated load torque to the machine and the resulting responses are shown in Fig. 3.21. Application of the load torque causes an inevitable speed dip. Motor torque quickly follows the torque reference and enables rapid compensation of the speed dip. The motor torque settles at the value equal to the load torque in less than 100 ms and the motor current becomes rated at the end of the transient. Fig. 3.21 also depicts the stator phase voltage, which is typical for a PWM inverter fed motor drive.

Deleted: The

Deleted: ure

Speed reversal transient study is also simulated and the resulting responses are shown in Fig. 3.22. Once more it is observed that the actual torque closely follows the reference, leading to the rapid speed reversal, with torque in the limit, in the shortest possible time interval (approximately 350 ms). The change of phase sequence in stator current because of the change in the rotational direction is clearly observed from the plot of the stator current.

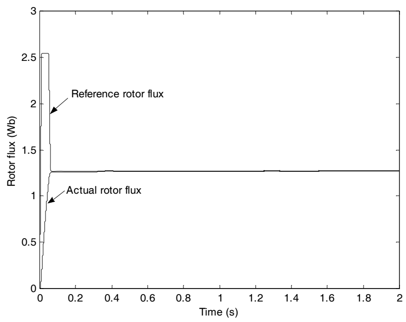

a.

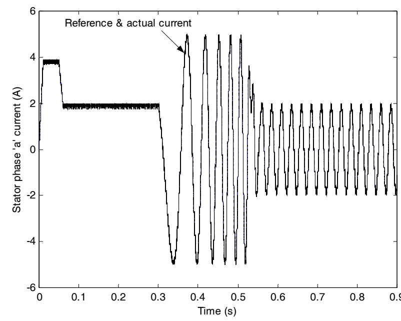

c.

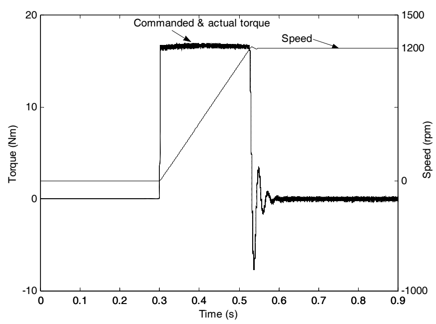

b.

Fig. 3.20. Excitation and acceleration transients (1200 rpm speed command) using hysteresis current control: a. actual and reference rotor flux, b. actual and reference torque, and speed, c. actual and reference stator phase 'a' currents.

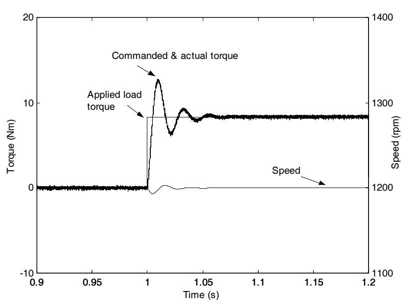

a.

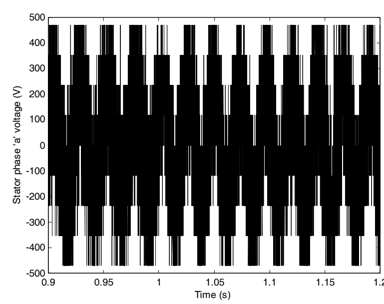

c.

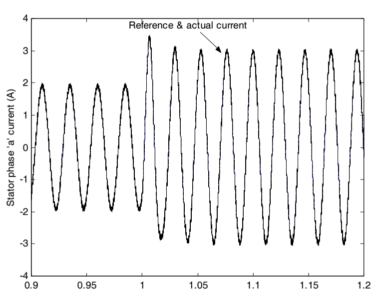

b.

Fig. 3.21. Disturbance rejection transient at 1200 rpm using hysteresis current control: a. actual and reference torque, and speed, b. actual and reference stator phase 'a' currents, c. stator phase 'a' voltage.

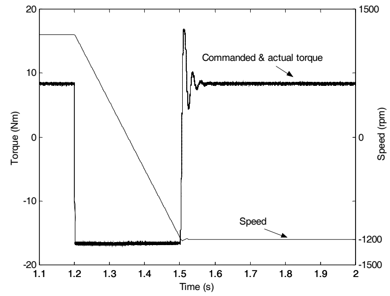

a.

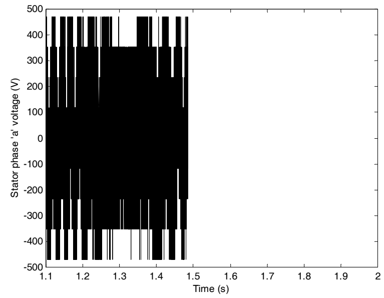

c.

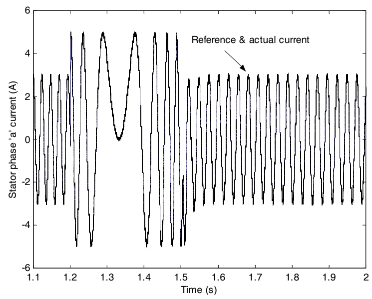

b.

Fig. 3.22. Reversing transient (1200 rpm) using hysteresis current control: a. actual and reference torque, and speed, b. actual and reference stator phase ‘a’ currents, c. stator phase ‘a’ voltage.

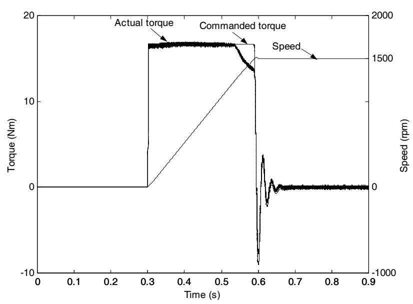

a.

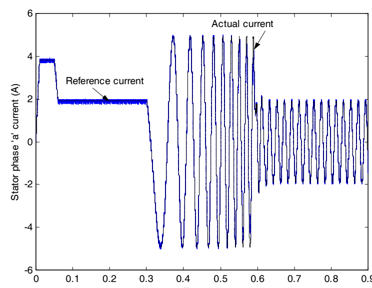

c.

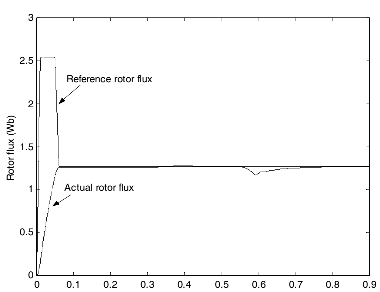

b.

Fig. 3.23. Excitation and acceleration transients (1500 rpm speed command) using hysteresis current control: a. actual and reference torque, and speed, b. actual and reference rotor flux, c. actual and reference stator phase ‘a’ currents.

The same transients have been studied for 1500 rpm speed command and the resulting plots are shown in Fig. 3.23, 3.24 and 3.25. The important difference between the results of

Figs. 3.20-3.22 and results of Figs. 3.23-3.25 is that now the problem of insufficient voltage reserve in the PWM voltage source inverter can be clearly observed in all transients. The insufficient voltage reserve leads to the deterioration in the torque response, which is unable to track the reference torque at high speeds, due to the high value of the back-emf. The difference between the maximum available inverter output voltage and the back-emf is insufficient to push the required reference current through the stator windings. The decoupling of the torque and rotor flux control is lost, as is evident from the rotor flux trace in Figs. 3.23-3.25. The problem can be alleviated by reducing the torque limit value within the controller.

Deleted: voltage source

Deleted: inverter

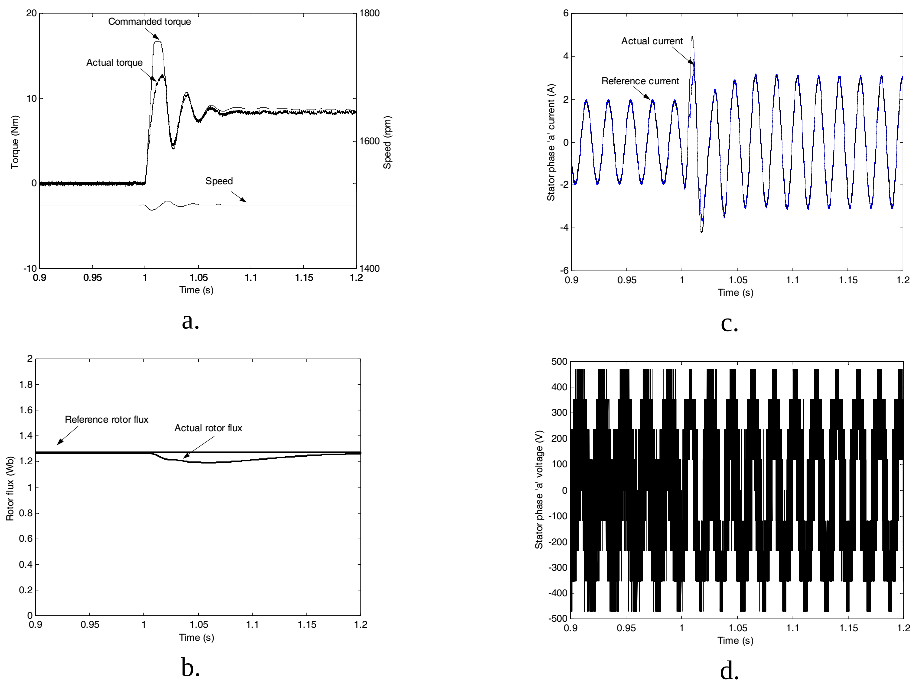

Fig. 3.24. Disturbance rejection transient (1500 rpm) using hysteresis current control: a. actual and reference torque, and speed, b. actual and reference rotor flux, c. actual and reference stator phase 'a' currents, d. stator phase 'a' voltage.

3.7.2 Ramp-comparison current control

Exactly the same set of transients is examined again, this time using ramp-comparison current control. The resulting plots are given in Figs. 3.26-3.28 for 1200 rpm setting of the speed command, and in Figs. 3.29-3.31 for the speed command of 1500 rpm. The switching frequency of the inverter is fixed to 5 kHz and the discrete PI current controller used is the one designed in section 3.6.3. The drive is again operated in the closed loop speed

Deleted: with

Deleted: mode and the same discrete speed PI controller is used as the one for the hysteresis current control. ¶
¶
The results obtained using the ramp-comparison current control show that the dynamics of the drive are essentially the same as those obtained with the hysteresis current control method. The actual torque follows the reference torque very well, provided there is sufficient voltage reserve (at 1200 rpm), and rotor flux and torque control are fully decoupled. ¶

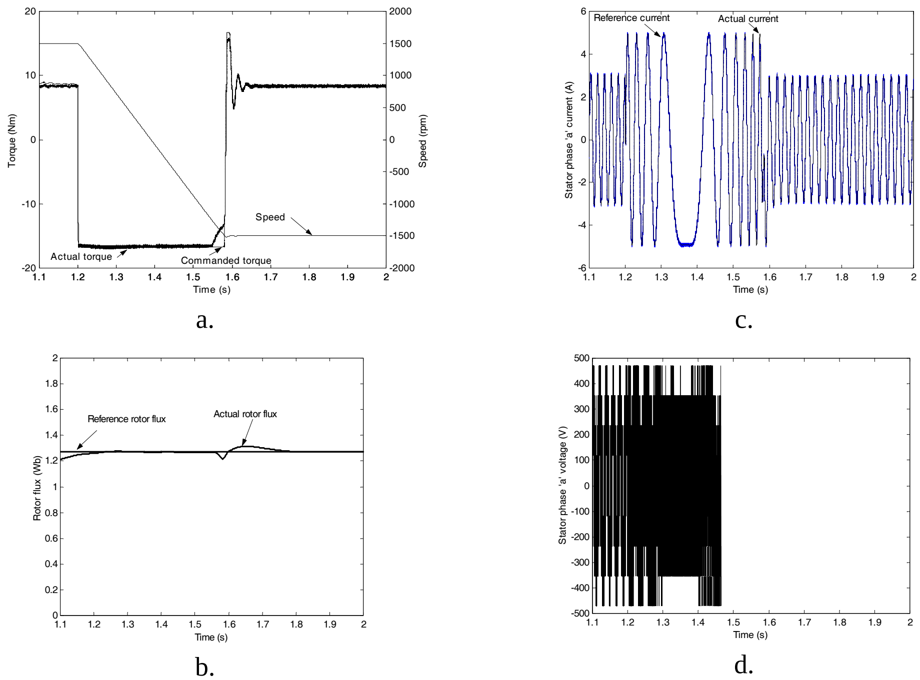

Fig. 3.25. Reversing transient (1500 rpm) using hysteresis current control: a. actual and reference torque, and speed, b. actual and reference rotor flux, c. actual and reference stator phase ‘a’ currents, d. stator phase ‘a’ voltage.

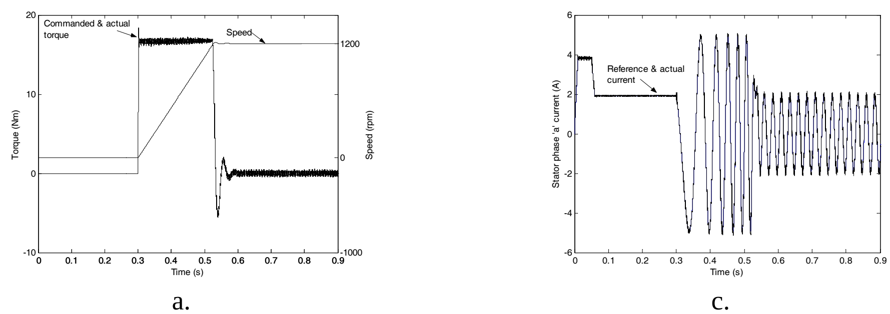

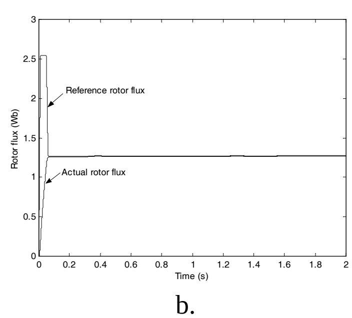

Fig. 3.26. Excitation and acceleration transients (1200 rpm) using ramp-comparison current control: a. actual and reference torque, and speed, b. actual and reference rotor flux, c. actual and reference stator phase ‘a’ currents.

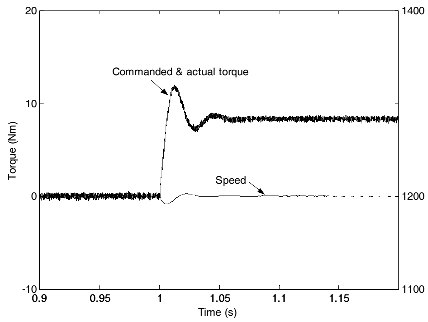

a.

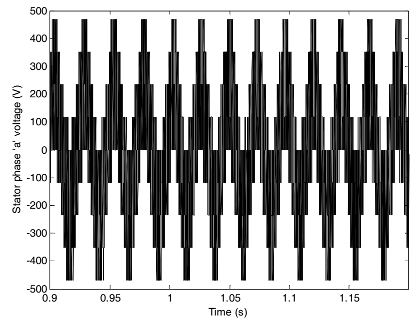

c.

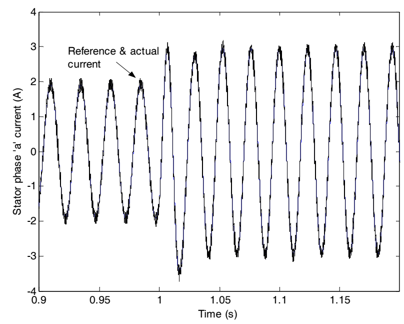

b.

Fig. 3.27. Disturbance rejection transient (1200 rpm) using ramp-comparison current control: a. actual and reference torque, and speed, b. actual and reference stator phase ‘a’ currents, c. stator phase ‘a’ voltage.

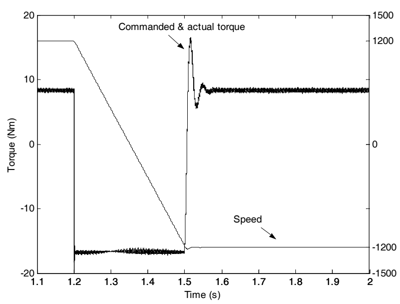

a.

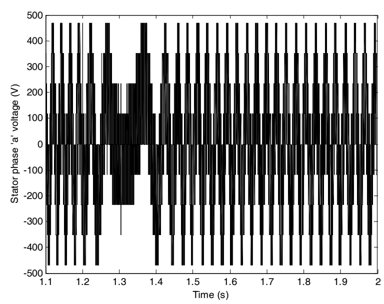

c.

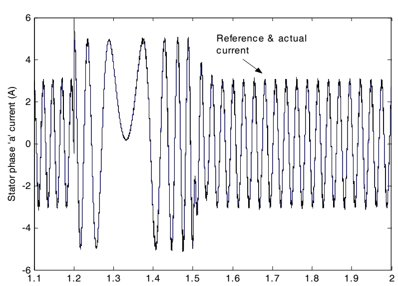

b.

Fig. 3.28. Reversing transient (1200 rpm) using ramp-comparison current control: a. actual and reference torque, and speed, b. actual and reference stator phase ‘a’ currents, c. stator phase ‘a’ voltage.

Deleted: ¶
¶

Deleted: The deterioration in the torque response is again observed in Figs. 3.29-3.31 as the result of the insufficient voltage reserve at high operating speeds (1500 rpm).

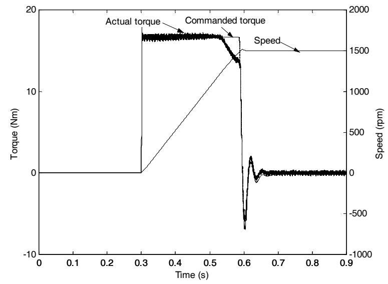

a.

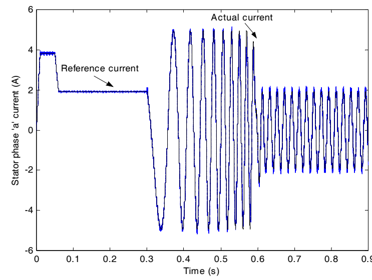

c.

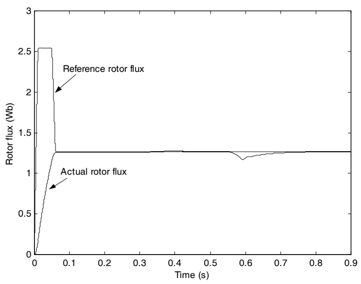

b.

Fig. 3.29. Excitation and acceleration transients (1500 rpm) using ramp-comparison current control: a. actual and reference torque, and speed, b. actual and reference rotor flux, c. actual and reference stator phase ‘a’ currents.

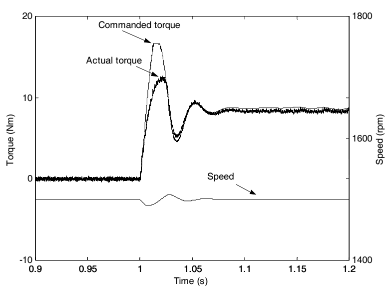

a.

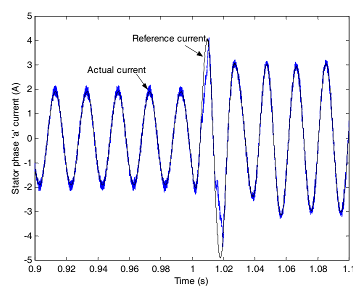

c.

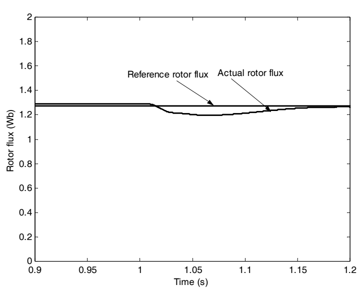

b.

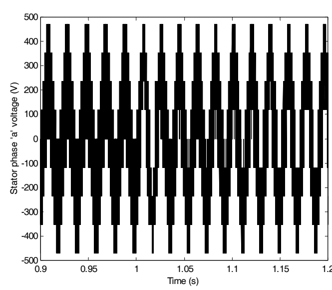

d.

Deleted: .

Fig. 3.30. Disturbance rejection transient (1500 rpm) using ramp-comparison current control: a. actual and reference torque, and speed, b. actual and reference rotor flux, c. actual and reference stator phase ‘a’ currents, d. stator phase ’a’ voltage.

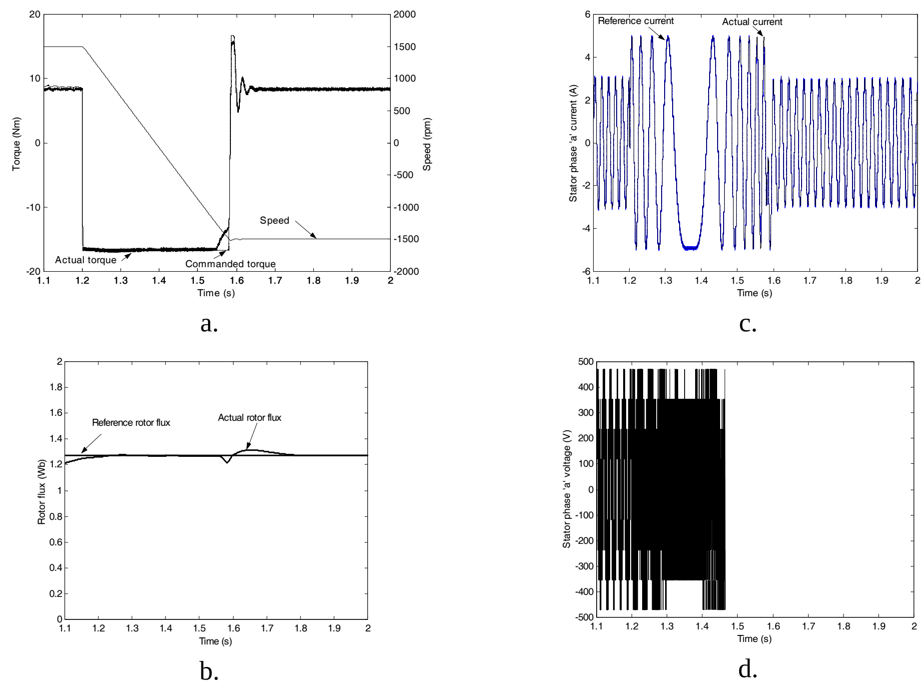

Fig. 3.31. Reversing transient (1500 rpm) using ramp-comparison current control: a. actual and reference torque, and speed, b. actual and reference rotor flux, c. actual and reference stator phase 'a' currents, d. stator phase 'a' voltage.

control mode and the same discrete speed PI controller is used as the one for the hysteresis current control.

The results obtained using the ramp-comparison current control show that the dynamics of the drive are essentially the same as those obtained with the hysteresis current control method. The actual torque follows the reference torque very well, provided there is sufficient voltage reserve (at 1200 rpm), and rotor flux and torque control are fully decoupled. The deterioration in the torque response is again observed in Figs. 3.29-3.31 as a result of the insufficient voltage reserve at high operating speed (1500 rpm).

Deleted: ¶

3.7.3 Harmonic analysis

This section presents results of the harmonic analysis of stator voltage and current of the indirect rotor field oriented controlled induction machine with hysteresis current control method. Harmonic properties of both hysteresis and ramp-comparison current control are well known and the fact that a five-phase inverter is used here instead of a three-phase inverter changes nothing in this respect. However, results of the harmonic analysis, presented in this

Deleted: ramp comparison

Deleted:

section, will be of importance in subsequent chapter, where two-motor drive system will be analysed.

Deleted: C

The reason for presenting results for hysteresis current control only is that the low frequency part of the spectra are essentially identical, regardless of the employed current control method. As the high frequency section of the spectra are of no interest (and these are those that differ depending on the selected current control method), it suffices to analyse only one current control method. In all the figures that follow a time-domain steady state waveform is shown, together with the associated spectrum. All the spectra are given in terms of voltage (current) RMS values. The spectrum is determined for phase ‘a’ voltage, α and x components of the phase voltages, phase ‘a’ current, and α and x components of phase currents under steady state no-load conditions at three different speeds (symbol α stands for stator d-axis components when stationary reference frame is utilised). Figs. 3.32-3.33 show results for operation at 25 Hz (750 rpm) obtained using Fast Fourier transform (FFT).

As is evident from Figs. 3.32-3.33, phase voltage and current spectra show the fundamental component at 25 Hz, which is, as expected, of the same value in both phase and α-component quantities. On the other hand, voltage x-component contains essentially only high frequency harmonics, leading to virtually non-existent x-component current harmonics (note that this scale is in mA). Phase (and α-component) voltage spectrum is continuous, containing voltage harmonics at high frequencies of relatively small values, so that the phase (and α-component) current spectrum is with negligible higher harmonic content. Hysteresis current control gives continuous spectra due to a variable switching frequency. The average switching frequency is estimated as being around 10.5 kHz and the current ripple is 0.15 A.

As already noted, of importance for further work is only the low frequency part of the spectra. It is for this reason that all the subsequent figures show results of the spectral analysis up to 500 Hz only.

Steady state time domain waveforms and associated spectra for 40 Hz (1200 rpm) operation are shown in Figs. 3.34-3.35, while Figs. 3.36-3.37 show the same results for 50 Hz (1500 rpm) operation.

The values of fundamental voltage and current harmonics, obtained from Figs. 3.32-3.37, are tabulated in Table 3.21. Since x-axis voltage components at any of the three fundamental frequencies are negligibly small (and their non-zero values can be assigned to the limited accuracy of the simulations and the FFT analysis), they are not included.

Deleted: As the machine operates in steady state, expected fundamental components of the voltage and current can be calculated on the basis of the per-phase phasor equivalent circuit of ¶

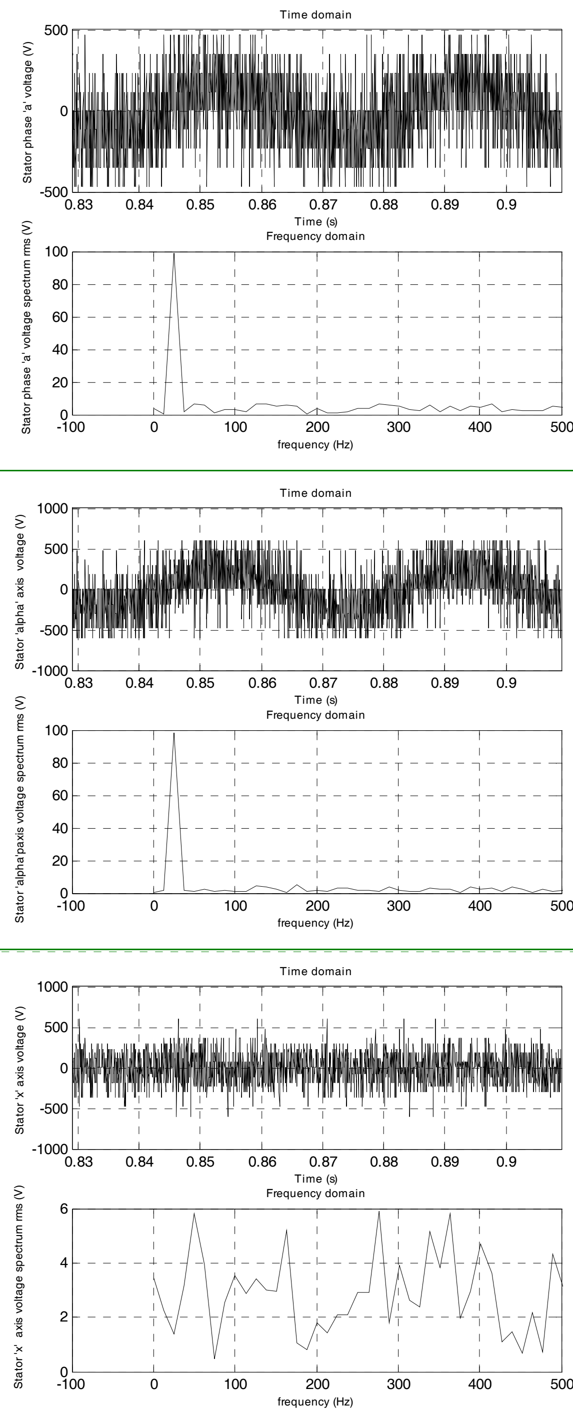

Fig. 3.32. Time-domain waveforms and spectra for 25 Hz operation: phase ‘a’ voltage, α-axis voltage component and x-axis voltage component.

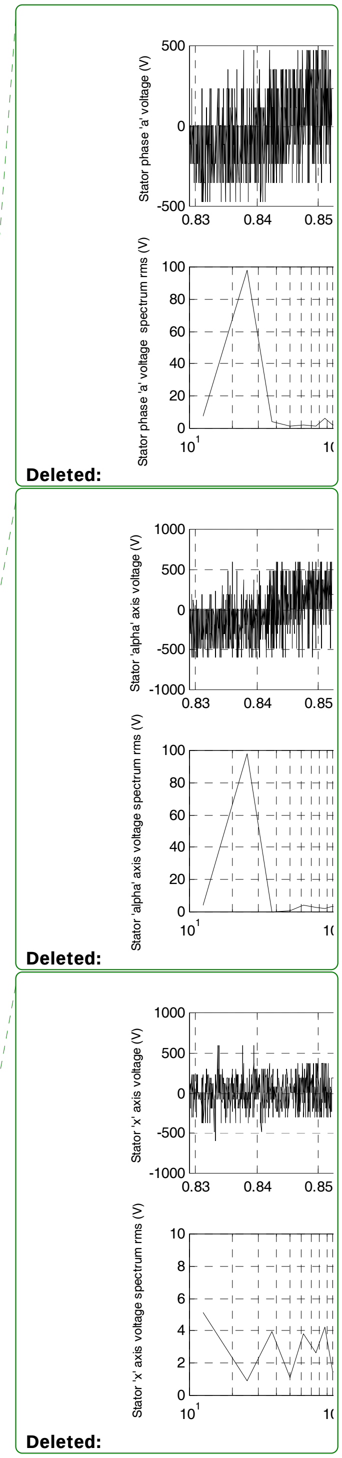

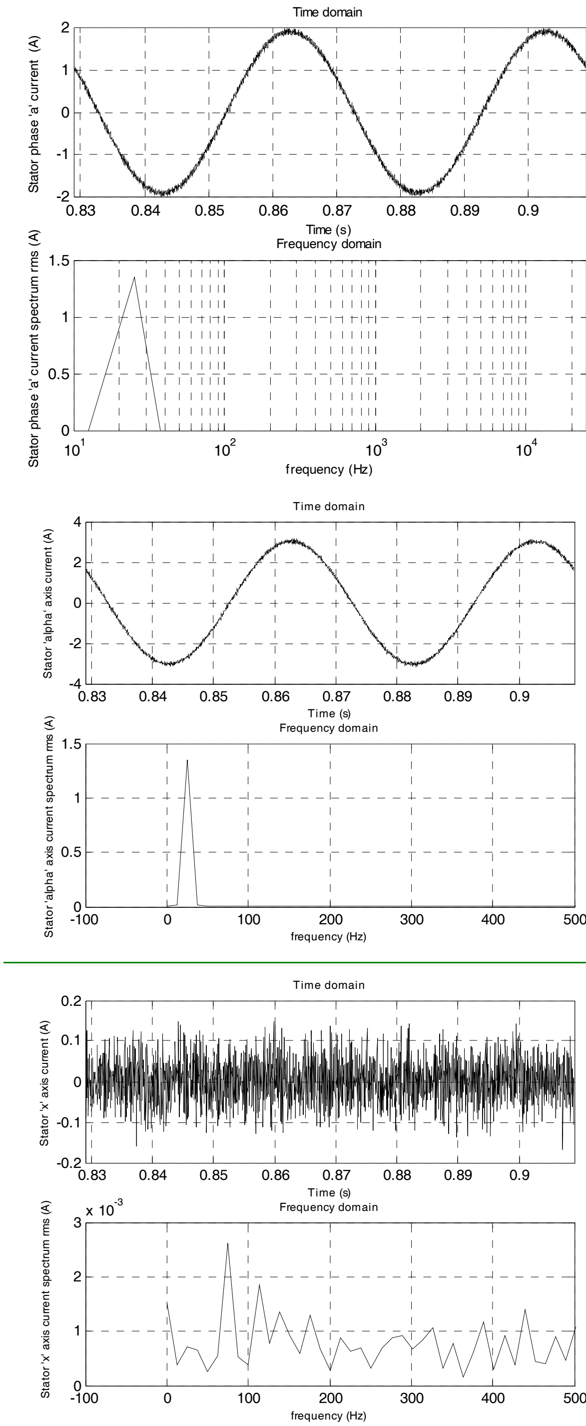

Fig. 3.33. Time-domain waveforms and spectra for 25 Hz operation: phase ‘a’ current, α-axis current component and x-axis current component.

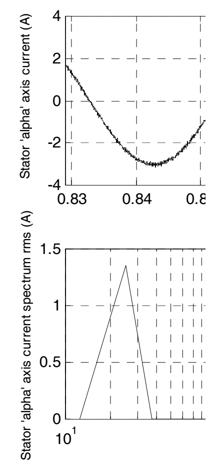

Deleted:

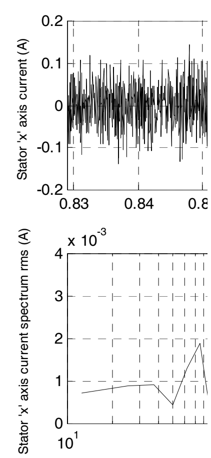

Deleted:

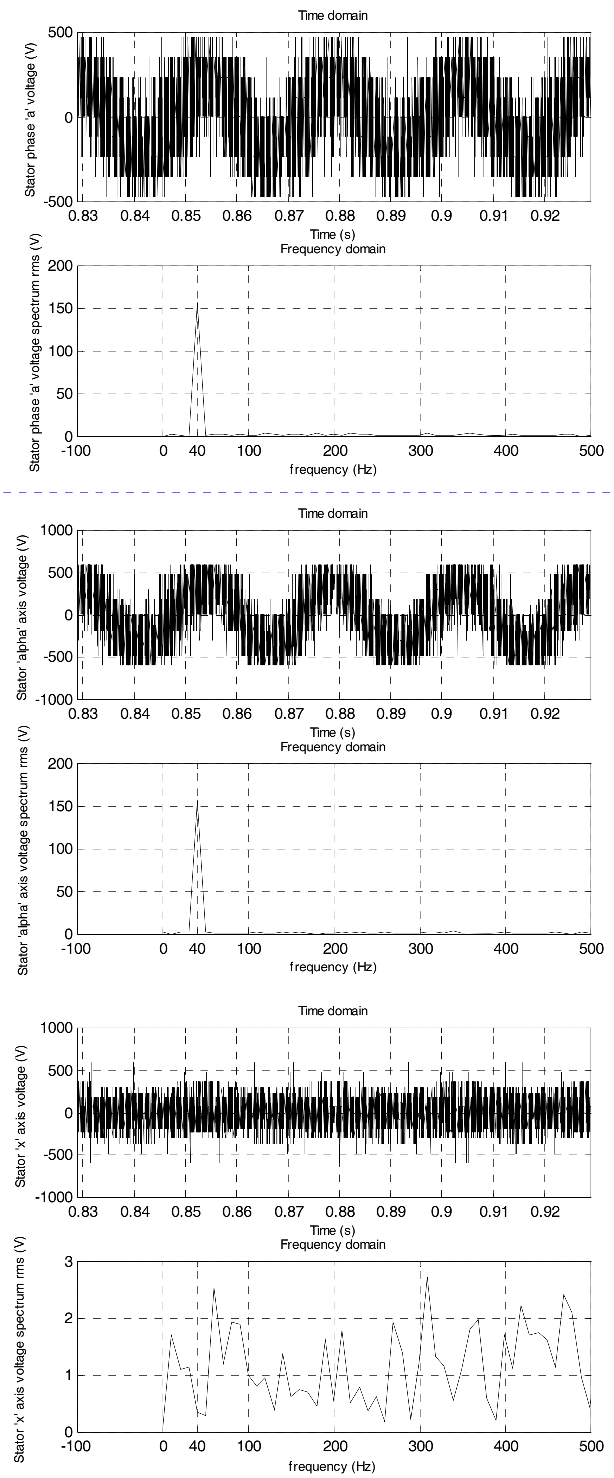

Fig. 3.34. Time-domain waveforms and spectra for 40 Hz operation: phase ‘a’ voltage, α-axis voltage component and x-axis voltage component.

Deleted: section, will be of great importance in subsequent Chapters, where two-motor drive systems will be analysed. ¶

The reason for presenting results for hysteresis current control only is that the low frequency part of the spectra are essentially identical, regardless of the employed current control method. As the high frequency section of the spectra are of no interest (and these are those that differ depending on the selected current control method), it suffices to analyse only one current control method. In all the figures that follow a time-domain steady state waveform is shown, together with the associated spectrum. All the spectra are given in terms of voltage (current) RMS values. The spectrum is determined for phase ‘a’ voltage, α and x components of the phase ‘a’ voltage, phase ‘a’ current, and α and x components of phase ’a’ current under steady state no-load conditions at three speeds. Figs. 3.32-3.33 show results for operation at 25 Hz (750 rpm) obtained using Fast Fourier transform (FFT). As is evident from Figs. 3.32-3.33, phase voltage and current spectra show the fundamental component at 25 Hz, which is, as expected, of the same value in both phase and α-component quantities. On the other hand, voltage x-component contains essentially only high frequency harmonics, leading to virtually non-existent x-component current harmonics (note that this scale is in mA). Phase (and α-component) voltage spectrum is continuous, containing voltage harmonics at high frequencies of relatively small values, so that the phase (and α-component) current spectrum is with negligible higher harmonic content. Hysteresis current control gives continuous spectra due to a variable switching frequency. The average switching frequency is estimated as being around 10.5 kHz and the current ripple is 0.15 A. ¶

As already noted, of importance for further work is only the low frequency part of the spectra. It is for this reason that all the subsequent figures show results of the spectral analysis up to 500 Hz only.¶

Steady state time domain waveforms and associated spectra for 40 Hz (1200 rpm) operation are shown in Figs. 3.34-3.35, while Figs. 3.36-3.37 show the same results for 50 Hz (1500 rpm) operation.¶

The values of fundamental voltage and current harmonics, obtained from Figs. 3.32-3.37, are tabulated in Table 3.21. Since x-axis voltage components at any of the three fundamental frequencies are negligibly small (and their non-zero values can be assigned to the limited accuracy of the simulations and the FFT analysis), they are not included.¶

As the machine operates in steady state, expected fundamental components of the voltage and current can be calculated on the basis of the per-phase phasor equivalent circuit of ¶

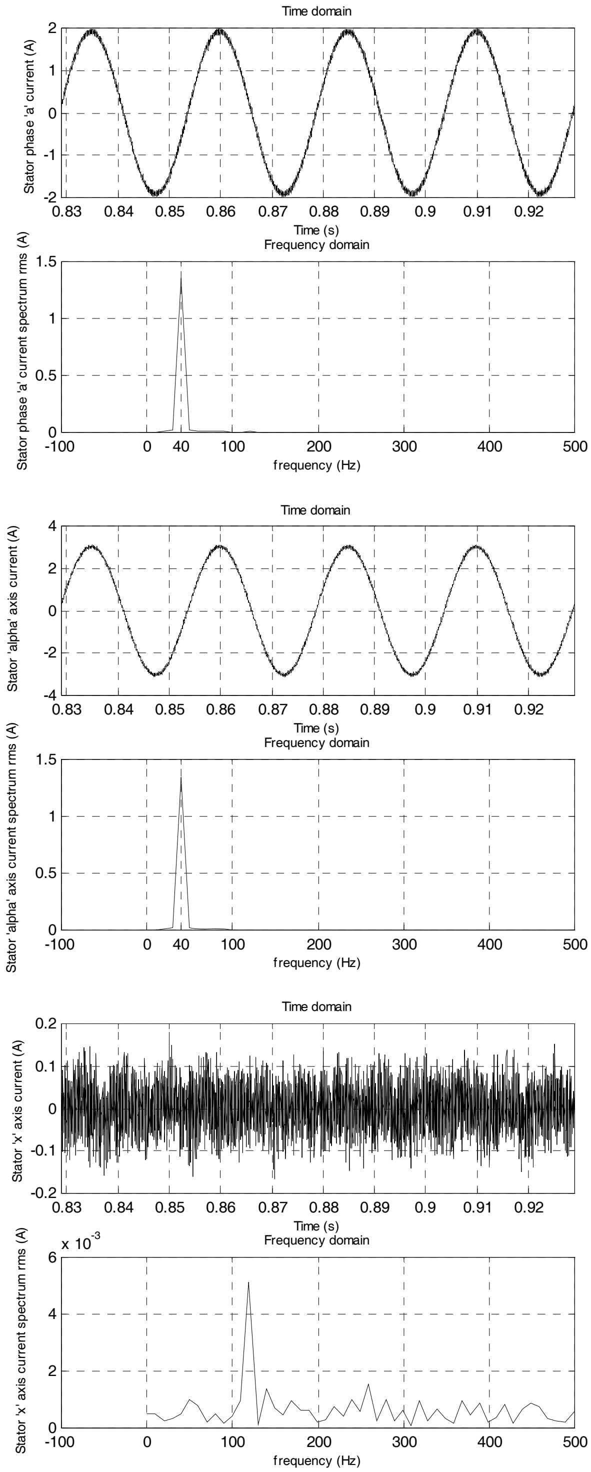

Fig. 3.35. Time-domain waveforms and spectra for 40 Hz operation: phase ‘a’ current, α-axis current component and x-axis current component.

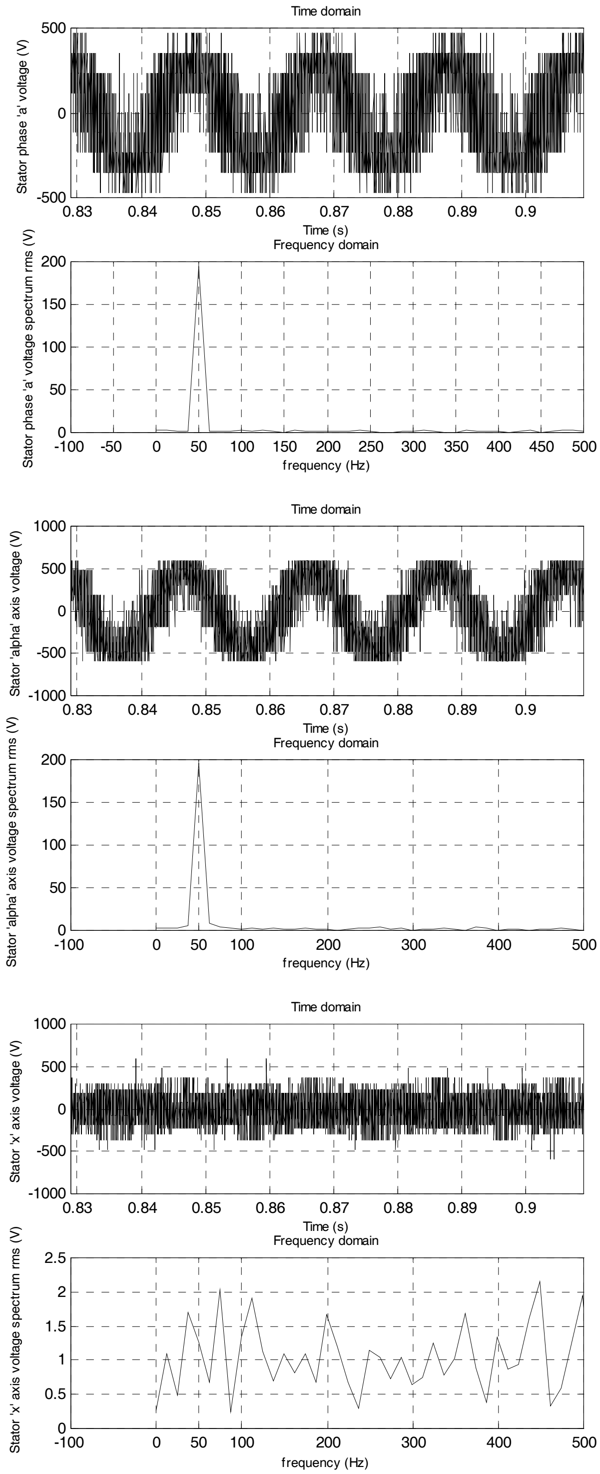

Fig. 3.36. Time-domain waveforms and spectra for 50 Hz operation: phase ‘a’ voltage, α-axis voltage component and x-axis voltage component.

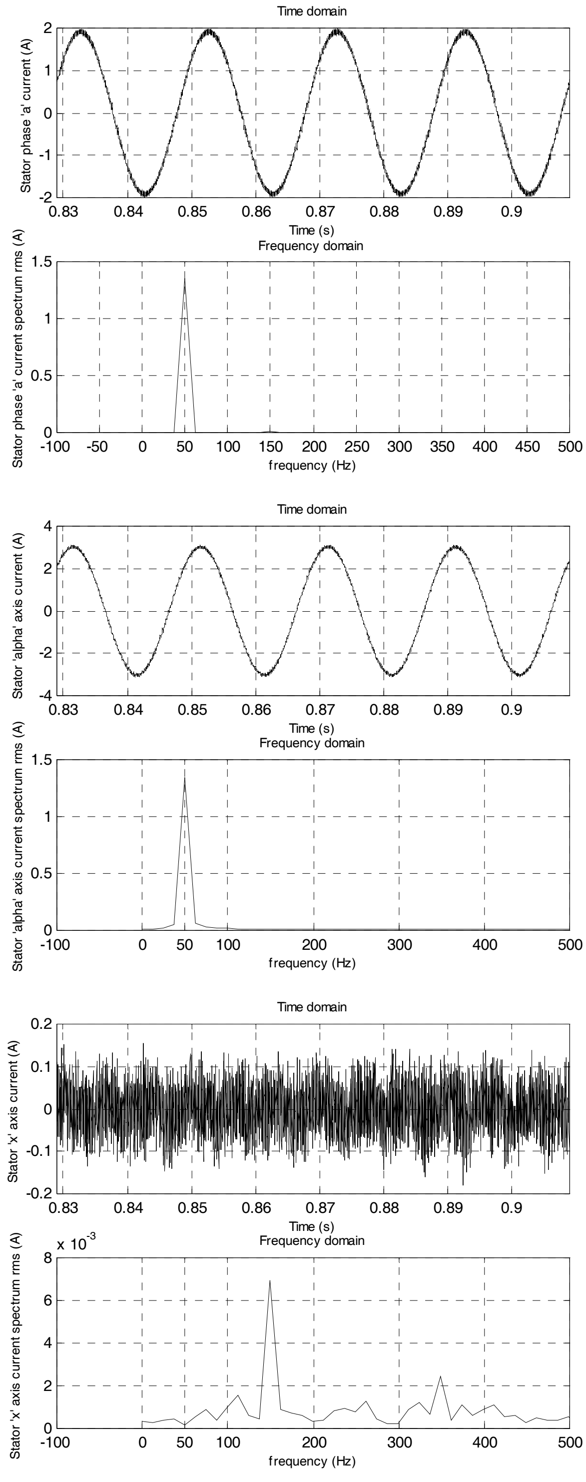

Fig. 3.37. Time-domain waveforms and spectra for 50 Hz operation: phase ‘a’ current, α-axis current component and x-axis current component.

As the machine operates in steady state, expected fundamental components of the voltage and current can be calculated on the basis of the per-phase phasor equivalent circuit of a five-phase induction machine, shown in Fig. 3.38 for no-load operating conditions. The expected fundamental component of the motor current at all frequencies is the same and equals the stator d-axis current reference (with appropriate transformation-related scaling), set by the vector controller (stator q-axis current reference is zero due to no-load operation and neglected mechanical and iron losses). The value of the no-load current set by the vector controller is I_0 = I_{dsn} = 1.3528 A (RMS).

The total no-load equivalent impedance offered by the induction machine is from Fig. 3.38 equal to

Table 3.21. Fundamental components of voltages and currents (from Figs. 3.32-3.37).

Frequency (Hz)	$V_a^{(1)}$ (V)	$V_\alpha^{(1)}$ (V)	$V_x^{(1)}$ (V)	$I_a^{(1)}$ (A)	$I_\alpha^{(1)}$ (A)	$I_x^{(1)}$ (mA)
25	97.7	98	0.4	1.352	1.352	0.8
40	157.4	157.4	0.3	1.35	1.352	0.5
50	196.2	195.8	1.25	1.352	1.344	0.15

Deleted: x 10^{-3}
Deleted: 000
Deleted: 000

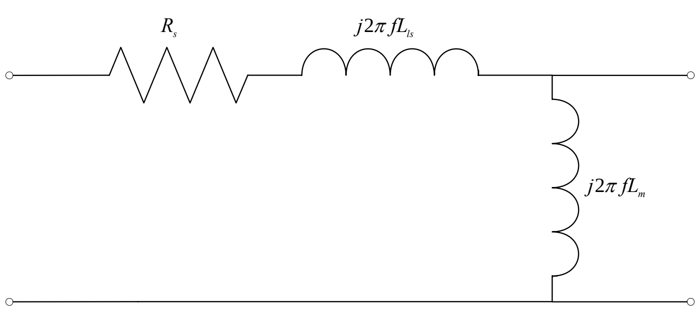

Fig. 3.38. Per-phase phasor equivalent circuit of a five-phase induction machine under no-load conditions.

Deleted:

$$Z_o = R_s + j\left(2\pi fL_{ls} + 2\pi fL_m\right) \tag{3.54}$$

Deleted: ¶

where L_{ls} is the leakage inductance and L_m is the magnetising inductance. Since the no-load impedance changes with the change in the operating frequency of the machine, the fundamental component of the voltage changes as well.

The fundamental voltage harmonic can be calculated as $V_a^{(1)} = I_0 Z_0$ where current I_0 is found as the ratio of the rotor reference flux RMS value (0.5683 Wb) to the magnetizing inductance (0.42 H). The calculated values of fundamental phase voltages for different operating speeds are given in Table 3.22.

Deleted: ¶

Table 3.22. Calculated fundamental components of voltages and currents.

Deleted: results of

Frequency	25 Hz	40 Hz	50 Hz
Fundamental voltage	98.6 V	156.8 V	196 V

By comparing the results in Tables 3.21 and 3.22 one observes that the results obtained by FFT are in very good agreement with theoretical predictions. The difference in the fundamental current component is negligibly small, while the error in fundamental voltage components does not exceed one volt for any of the values.

Deleted: ¶

3.8 SUMMARY

This chapter was devoted to modelling of the components of a single five-phase vector controlled induction motor drive. Principles of operation of a five-phase VSI in ten-step and PWM mode were discussed, together with the d-q modelling of a five-phase induction machine and principles of rotor flux oriented control. Current control in stationary reference frame was further reviewed and current and speed controllers were designed for the given machine and inverter data.

Deleted: ¶

Deleted: C

Deleted: voltage source inverter

Performance of a vector controlled single five-phase induction machine drive, obtainable with hysteresis current control and ramp-comparison control methods, was further evaluated and illustrated for a number of operating conditions on the basis of simulation results. Full decoupling of rotor flux control and torque control was realised by both current control techniques under the condition of a sufficient voltage reserve. Dynamics, achievable with a five-phase vector controlled induction machine, are shown to be essentially identical to those obtainable with a three-phase induction machine. Steady state analysis of stator voltages and currents was finally performed, using harmonic spectrum analysis.

Chapter 5

MODELLING AND CONTROL OF A SIX-PHASE INDUCTION MOTOR DRIVE

5.1 INTRODUCTION

This chapter discusses at first modelling and control of a six-phase voltage source inverter. The modelling is done for 180° conduction mode leading to square wave output (section 5.2) and PWM operation mode (section 5.3) based on space vector theory. Due to 60° phase displacement between subsequent phases a six-phase system consisting of two three-phase systems in phase opposition results. The six-phase machine model is developed next in phase variable domain and it is further transformed into a system of decoupled equations in orthogonal common reference frame (section 5.4). It is shown that d-q axis current components contribute towards torque and flux production, whereas the remaining x-y axis components and the zero-sequence components do not. This again allows a simple extension of the rotor flux oriented control (RFOC) principle to a six-phase machine, section 5.5. Six-phase induction motor modelling and vector control principles, reviewed in sections 5.4–5.5, are elaborated in more detail in Jones (2002) and Jones (2005).

The vector control principle is further applied to control single six-phase and three-phase motor drives using PWM voltage source inverter. Current control in stationary reference frame is utilised again (hysteresis method and ramp-comparison method). A simulation study is performed for speed mode of operation, for a number of transients, and the results are presented in section 5.6. A steady state analysis is carried out as well using Fast Fourier Transform (FFT) of voltage and current waveforms for hysteresis current control method and the resulting plots and values are given.

5.2 OPERATION OF A SIX-PHASE VOLTAGE SOURCE INVERTER IN 180° CONDUCTION MODE

5.2.1 Power circuit and switch control signals

Power circuit topology of a six-phase VSI is shown in Fig. 5.1. The inverter input dc voltage is regarded further on as being constant. Each switch is assumed to conduct for 180°.

Phase delay between firing of two switches in any subsequent two phases is equal to 360°/6 = 60°. One complete cycle of operation of the inverter can be divided into six distinct intervals indicated in the time domain waveforms of leg voltages shown in Fig. 5.2 and summarised in Table 5.1. The second interval of Fig. 5.2 is listed as the first one in Table 5.1. It follows from Fig. 5.2 and Table 5.1 that at any instant in time there are six switches that are 'on' and six switches that are 'off'. In this mode of operation there are three conducting switches from the upper six and three from the lower six, or vice versa. This mode of operation leads to, as shown shortly, a square wave phase-to-neutral output voltage waveform, the reason being the spatial displacement between the six-phases of 60°.

Table 5.1. Leg voltages of the six-phase VSI.

Switching state (mode)	Switches ON	Space vector	Leg voltage v_A	Leg voltage v_B	Leg voltage v_C	Leg voltage v_D	Leg voltage v_E	Leg voltage v_F
1	1,3,6,8,10,11	$\underline{v}_1$	V_{DC}	V_{DC}	0	0	0	V_{DC}
2	1,3,5,8,10,12	$\underline{v}_2$	V_{DC}	V_{DC}	V_{DC}	0	0	0
3	2,3,5,7,10,12	$\underline{v}_3$	0	V_{DC}	V_{DC}	V_{DC}	0	0
4	2,4,5,7,9,12	$\underline{v}_4$	0	0	V_{DC}	V_{DC}	V_{DC}	0
5	2,4,6,7,9,11	$\underline{v}_5$	0	0	0	V_{DC}	V_{DC}	V_{DC}
6	1,4,6,8,9,11	$\underline{v}_6$	V_{DC}	0	0	0	V_{DC}	V_{DC}

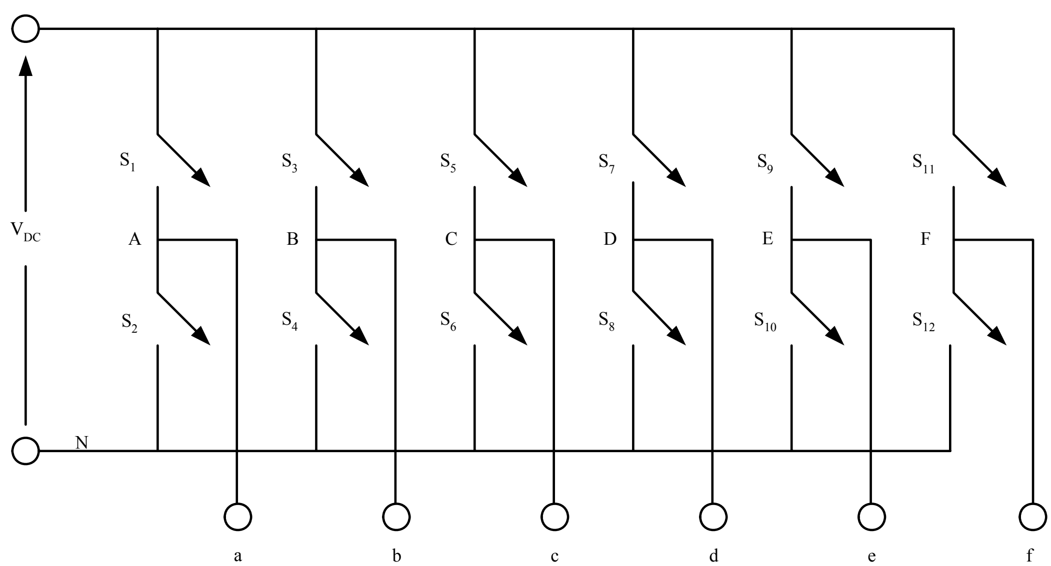

Fig. 5.1. Six-phase voltage source inverter power circuit.

5.2.2 Space vector representation of a six-phase voltage source inverter

If an ideal sinusoidal six-phase supply is considered, similar to (3.1) for the five-phase system, space vector, defined as ($\underline{a} = \exp\left(j\pi/3\right)$)

$$\underline{v} = \sqrt{\frac{2}{6}}(v_a + \underline{a}v_b + \underline{a}^2 v_c + \underline{a}^3 v_d + \underline{a}^4 v_e + \underline{a}^5 v_f) \tag{5.1}$$

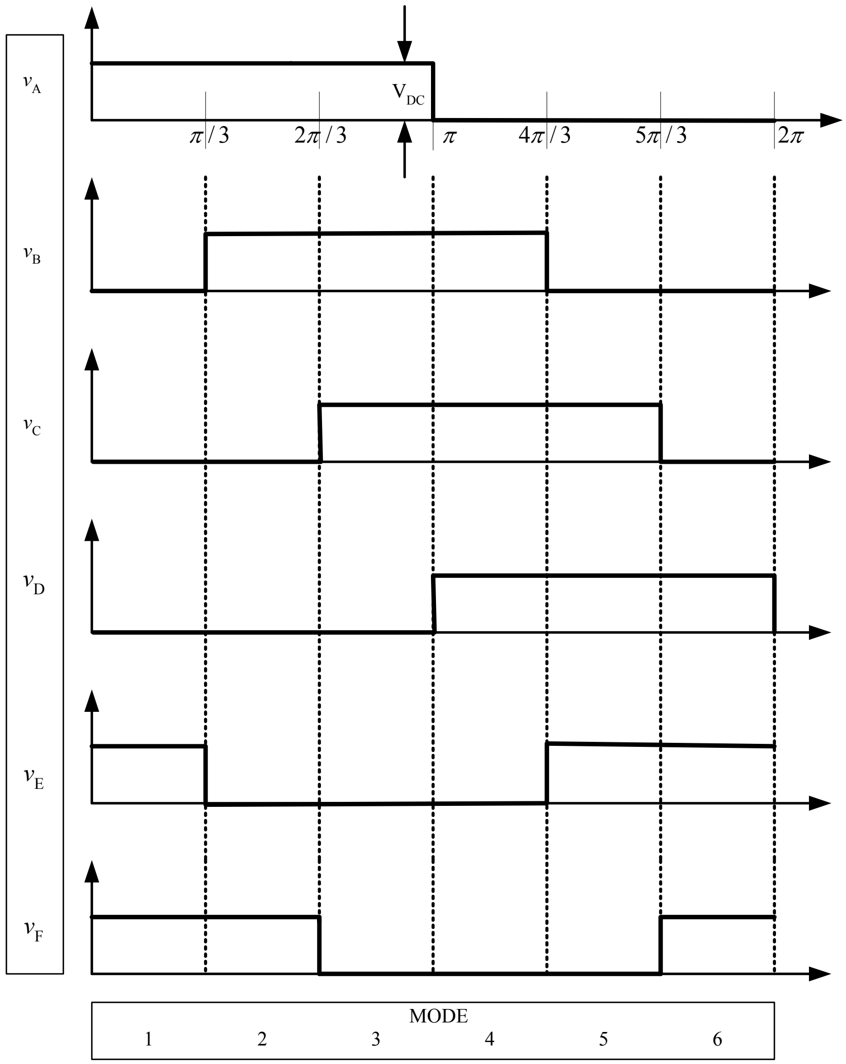

Fig. 5.2. Leg voltages of a six-phase voltage source inverter in 180° conduction mode.

is determined with (V is RMS value)

$$\underline{v} = \sqrt{6}V \exp(j\omega t) \tag{5.2}$$

However, the voltages are not sinusoidal with the inverter supply and are given in Table 5.1 for leg voltages. To determine the phase-to-neutral voltages of a star connected load again a voltage difference between the star point *n* of the load and the negative rail of the dc bus *N* is defined similar to section 3.2. Then the following correlation, similar to (3.4) holds true:

$$\begin{aligned}
v_A &= v_a + v_{nN} \\
v_B &= v_b + v_{nN} \\
v_C &= v_c + v_{nN} \\
v_D &= v_d + v_{nN} \\
v_E &= v_e + v_{nN} \\
v_F &= v_f + v_{nN}
\end{aligned} \tag{5.3}$$

Since phase voltages must sum to zero, v_{nN} is found to be:

$$v_{nN} = (1/6)(v_A + v_B + v_C + v_D + v_E + v_F) \tag{5.4}$$

Phase-to-neutral voltages are obtained in a form similar to (3.6):

$$\begin{aligned}
v_a &= (5/6)v_A - (1/6)(v_B + v_C + v_D + v_E + v_F) \\
v_b &= (5/6)v_B - (1/6)(v_A + v_C + v_D + v_E + v_F) \\
v_c &= (5/6)v_C - (1/6)(v_A + v_B + v_D + v_E + v_F) \\
v_d &= (5/6)v_D - (1/6)(v_A + v_B + v_C + v_E + v_F) \\
v_e &= (5/6)v_E - (1/6)(v_A + v_B + v_C + v_D + v_F) \\
v_f &= (5/6)v_F - (1/6)(v_A + v_B + v_C + v_D + v_E)
\end{aligned} \tag{5.5}$$

Hence the values of the phase-to-neutral voltages in the six distinct intervals of 60 degrees duration can be determined using the values of the leg voltages in Table 5.1. Table 5.2 summarises the phase-to-neutral voltages for different switching states, obtained using (5.5) and Table 5.1.

Table 5.2. Phase voltages of a star connected load supplied from a six-phase VSI.

Switching state (mode)	Switches ON	Space vector	Phase voltage v_a	Phase voltage v_b	Phase voltage v_c	Phase voltage v_d	Phase voltage v_e	Phase voltage v_f
1	1,3,6,8,10,11	$\underline{v}_{1phase}$	$V_{DC}/2$	$V_{DC}/2$	$-V_{DC}/2$	$-V_{DC}/2$	$-V_{DC}/2$	$V_{DC}/2$
2	1,3,5,8,10,12	$\underline{v}_{2phase}$	$V_{DC}/2$	$V_{DC}/2$	$V_{DC}/2$	$-V_{DC}/2$	$-V_{DC}/2$	$-V_{DC}/2$
3	2,3,5,7,10,12	$\underline{v}_{3phase}$	$-V_{DC}/2$	$V_{DC}/2$	$V_{DC}/2$	$V_{DC}/2$	$-V_{DC}/2$	$-V_{DC}/2$
4	2,4,5,7,9,12	$\underline{v}_{4phase}$	$-V_{DC}/2$	$-V_{DC}/2$	$V_{DC}/2$	$V_{DC}/2$	$V_{DC}/2$	$-V_{DC}/2$
5	2,4,6,7,9,11	$\underline{v}_{5phase}$	$-V_{DC}/2$	$-V_{DC}/2$	$-V_{DC}/2$	$V_{DC}/2$	$V_{DC}/2$	$V_{DC}/2$
6	1,4,6,8,9,11	$\underline{v}_{6phase}$	$V_{DC}/2$	$-V_{DC}/2$	$-V_{DC}/2$	$-V_{DC}/2$	$V_{DC}/2$	$V_{DC}/2$

Time domain waveforms of phase-to-neutral voltages are shown in Fig. 5.3. Phase-to-neutral voltages are of non-zero value throughout the period and their value alternates between positive and negative $V_{DC}/2$ and $-V_{DC}/2$. Moreover it is seen that the phase-to-neutral voltages are identically equal to the leg voltages referred to mid-point of the DC supply. Voltage v_{nN} of (5.4) is equal to zero for the whole cycle of the inverter operation and thus the triplen harmonics will appear in the phase-to-neutral voltages.

In order to determine the space vectors of phase-to-neutral voltages, the instantaneous values from Table 5.2 are inserted into (5.1). The phase-to-neutral voltage space vectors are given in Table 5.3 and illustrated in Fig. 5.4. The phase-to-neutral voltage space vectors in the

$\alpha-\beta$ plane are given as (a similar remark regarding other components in the six-dimensional space applies here as in section 3.2.3 for the five-phase VSI. Analysis of the inverter output voltages using six-dimensional space and its subdivision into three orthogonal two-dimensional sub-space will be done in Chapter 8):

$$\underline{v}_{kphase} = \sqrt{\frac{2}{6}} V_{DC} 2\exp\left(j\left(k-1\right)\frac{\pi}{3}\right) \quad k = 1,2,......,6 \tag{5.6}$$

There are six non-zero voltage vectors, as in a three-phase system. This is so since there are three pairs of phases in direct opposition to each other. There are 8 switching states which include six non-zero and two zero states, when all the upper or lower switches are 'on'. The relationship between phase-to-neutral voltages of the inverter and the dc link voltage, given in expression (5.5) in terms of leg voltages, can be expressed using switching functions for the

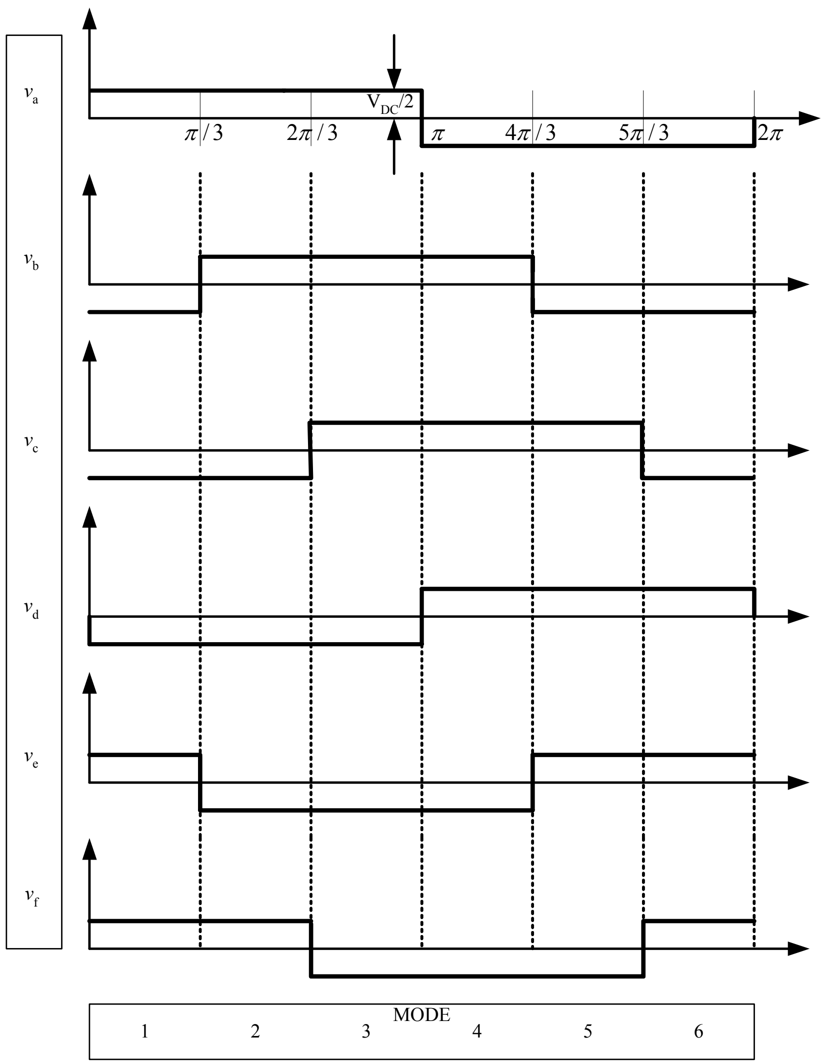

Fig. 5.3. Phase-to-neutral voltages of star connected load fed using the six-phase VSI.

six inverter legs, as has been done for the five-phase inverter (3.7). Each switching function takes the value of one when the upper switch is 'on' and the value of zero when the lower switch is 'on' (alternatively, if leg voltages are referred to the midpoint of the dc supply, the switching functions take the values of 0.5 and –0.5). Hence (*Sa* stands for the switching function of phase *a*, *Sb* stands for the switching function of phase *b* and so on):

$$
\begin{aligned}
v_a &= (V_{DC}/6)\,[5\,Sa - Sb - Sc - Sd - Se - Sf] \\
v_b &= (V_{DC}/6)\,[5\,Sb - Sa - Sc - Sd - Se - Sf] \\
v_c &= (V_{DC}/6)\,[5\,Sc - Sb - Sa - Sd - Se - Sf] \\
v_d &= (V_{DC}/6)\,[5\,Sd - Sb - Sc - Sa - Se - Sf] \\
v_e &= (V_{DC}/6)\,[5\,Se - Sb - Sc - Sd - Sa - Sf] \\
v_f &= (V_{DC}/6)\,[5\,Sf - Sa - Sb - Sc - Sd - Se]
\end{aligned}
\qquad (5.7)
$$

Table 5.3. Phase-to-neutral voltage space vectors of the six-phase VSI.

Phase voltage space vectors	
$\underline{v}_{1phase}$	$\sqrt{2/6}V_{DC}\,2\exp(j0)$
$\underline{v}_{2phase}$	$\sqrt{2/6}V_{DC}\,2\exp(j\pi/3)$
$\underline{v}_{3phase}$	$\sqrt{2/6}V_{DC}\,2\exp(j2\pi/3)$
$\underline{v}_{4phase}$	$\sqrt{2/6}V_{DC}\,2\exp(j\pi)$
$\underline{v}_{5phase}$	$\sqrt{2/6}V_{DC}\,2\exp(j4\pi/3)$
$\underline{v}_{6phase}$	$\sqrt{2/6}V_{DC}\,2\exp(j5\pi/3)$

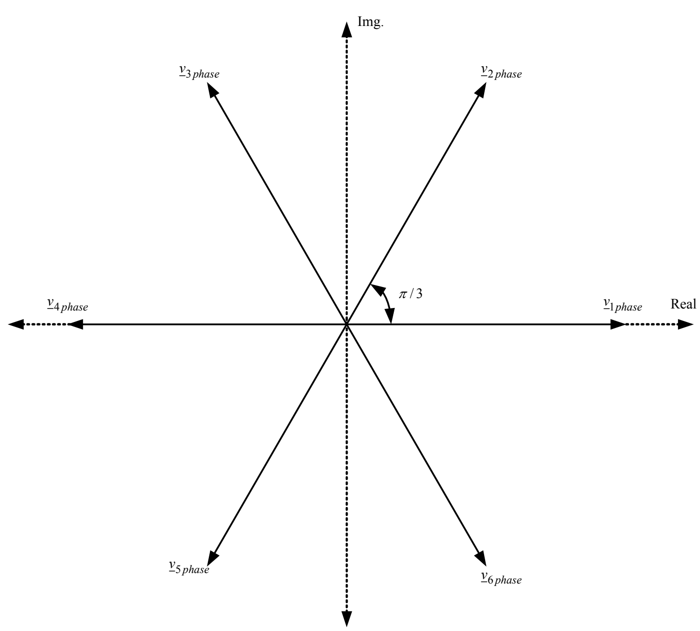

Fig. 5.4. Phase-to-neutral voltage space vectors in the complex plane.

The line-to-line voltages are considered next. There are five systems of line-to-line voltages. The first system includes adjacent line-to-line voltages, $v_{i,i+1}$ (i = A, B,……F). The second system of line-to-line voltages is composed of $v_{i,i+2}$ (i = A, B,……F) while the third system encompasses $v_{i,i+3}$ (i = A, B,……F) voltages. The fourth and the fifth systems are essentially the same as the first and the second, with opposite phases. Table 5.4 summarises the values of the adjacent line-to-line voltages in the six 60 degrees intervals. The values of line-to-line voltages in Table 5.4 are obtained using leg voltage values in Table 5.1.

The adjacent line-to-line voltage space vectors are calculated by substituting the values from Table 5.4 into the defining expression (5.1) and the results are given in Table 5.5. The adjacent line-to-line voltage space vectors are illustrated in Fig. 5.5. Corresponding time-domain waveforms are displayed in Fig. 5.6.

Table 5.4. Adjacent line-to-line voltages (first system) of the six-phase VSI.

Switching state	Switches ON	Space vector	v_{ab}	v_{bc}	v_{cd}	v_{de}	v_{ef}	v_{fa}
1	1,3,6,8,10,11	$\underline{v}_{1l}$	0	V_{DC}	0	0	$-V_{DC}$	0
2	1,3,5,8,10,12	$\underline{v}_{2l}$	0	0	V_{DC}	0	0	$-V_{DC}$
3	2,3,5,7,10,12	$\underline{v}_{3l}$	$-V_{DC}$	0	0	V_{DC}	0	0
4	2,4,5,7,9,12	$\underline{v}_{4l}$	0	$-V_{DC}$	0	0	V_{DC}	0
5	2,4,6,7,9,11	$\underline{v}_{5l}$	0	0	$-V_{DC}$	0	0	V_{DC}
6	1,4,6,8,9,11	$\underline{v}_{6l}$	V_{DC}	0	0	$-V_{DC}$	0	0

Table 5.5 Adjacent line-to-line voltage (first system) space vectors.

Adjacent line-to-line voltage space vectors	
$\underline{v}_{1l}^{I}$	$\sqrt{2/6}V_{DC}2\exp(j\pi/3)$
$\underline{v}_{2l}^{I}$	$\sqrt{2/6}V_{DC}2\exp(j2\pi/3)$
$\underline{v}_{3l}^{I}$	$\sqrt{2/6}V_{DC}2\exp(j\pi)$
$\underline{v}_{4l}^{I}$	$\sqrt{2/6}V_{DC}2\exp(j4\pi/3)$
$\underline{v}_{5l}^{I}$	$\sqrt{2/6}V_{DC}2\exp(j5\pi/3)$
$\underline{v}_{6l}^{I}$	$\sqrt{2/6}V_{DC}2\exp(j2\pi)$

The general form of space vectors of adjacent line-to-line voltages is given with:

$$\underline{v}_{kl}^{I} = \sqrt{\frac{2}{6}}V_{DC}2\exp\left(jk\frac{\pi}{3}\right) \quad k = 1,2,.....,6 \tag{5.8}$$

The non-adjacent systems of line-to-line voltages are examined next. The second system consists of $v_{ac}, v_{bd}, v_{ce}, v_{df}, v_{ea}, v_{fb}$ set while the third system consists of $v_{ad}, v_{be}, v_{cf}, v_{da}, v_{eb}, v_{fc}$. The fourth and the fifth systems are in phase opposition to the first and the second systems and are omitted from discussion. Table 5.6 lists the states and the values for the second system of line-to-line voltages and Fig. 5.7 illustrates time-domain waveforms. The space vectors are found in the same fashion as in the previous case and are tabulated in Table 5.7 and shown in Fig. 5.8.

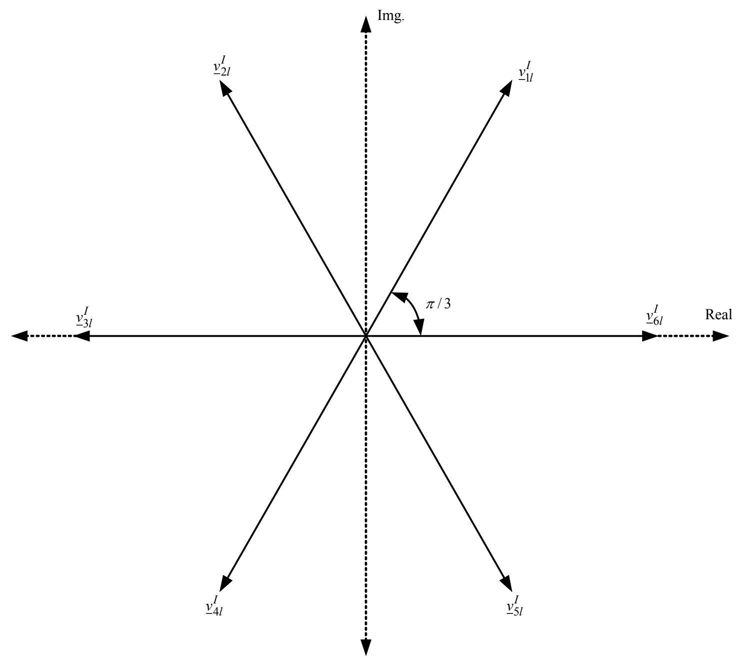

Fig. 5.5. Adjacent line-to-line voltage (first system) space vectors of the six-phase VSI.

Table 5.6. Non-adjacent line-to-line voltages (second system) of the six-phase VSI.

Switching state	Switches ON	Space vector	v_{ac}	v_{bd}	v_{ce}	v_{df}	v_{ea}	v_{fb}
1	1,3,6,8,10,11	$\underline{v}_{1l}^{II}$	V_{DC}	V_{DC}	0	$-V_{DC}$	$-V_{DC}$	0
2	1,3,5,8,10,12	$\underline{v}_{2l}^{II}$	0	V_{DC}	V_{DC}	0	$-V_{DC}$	$-V_{DC}$
3	2,3,5,7,10,12	$\underline{v}_{3l}^{II}$	$-V_{DC}$	0	V_{DC}	V_{DC}	0	$-V_{DC}$
4	2,4,5,7,9,12	$\underline{v}_{4l}^{II}$	$-V_{DC}$	$-V_{DC}$	0	V_{DC}	V_{DC}	0
5	2,4,6,7,9,11	$\underline{v}_{5l}^{II}$	0	$-V_{DC}$	$-V_{DC}$	0	V_{DC}	V_{DC}
6	1,4,6,8,9,11	$\underline{v}_{6l}^{II}$	V_{DC}	0	$-V_{DC}$	$-V_{DC}$	0	V_{DC}

Table 5.7. Non-adjacent line-to-line voltage (second system) space vectors.

Non-adjacent line-to-line voltage (second system) space vectors	
$\underline{v}_{1l}^{II}$	$\sqrt{2/6}V_{DC}\,2\sqrt{3}\exp(j\pi/6)$
$\underline{v}_{2l}^{II}$	$\sqrt{2/6}V_{DC}\,2\sqrt{3}\exp(j3\pi/6)$
$\underline{v}_{3l}^{II}$	$\sqrt{2/6}V_{DC}\,2\sqrt{3}\exp(j5\pi/6)$
$\underline{v}_{4l}^{II}$	$\sqrt{2/6}V_{DC}\,2\sqrt{3}\exp(j7\pi/6)$
$\underline{v}_{5l}^{II}$	$\sqrt{2/6}V_{DC}\,2\sqrt{3}\exp(j9\pi/6)$
$\underline{v}_{6l}^{II}$	$\sqrt{2/6}V_{DC}\,2\sqrt{3}\exp(j11\pi/6)$

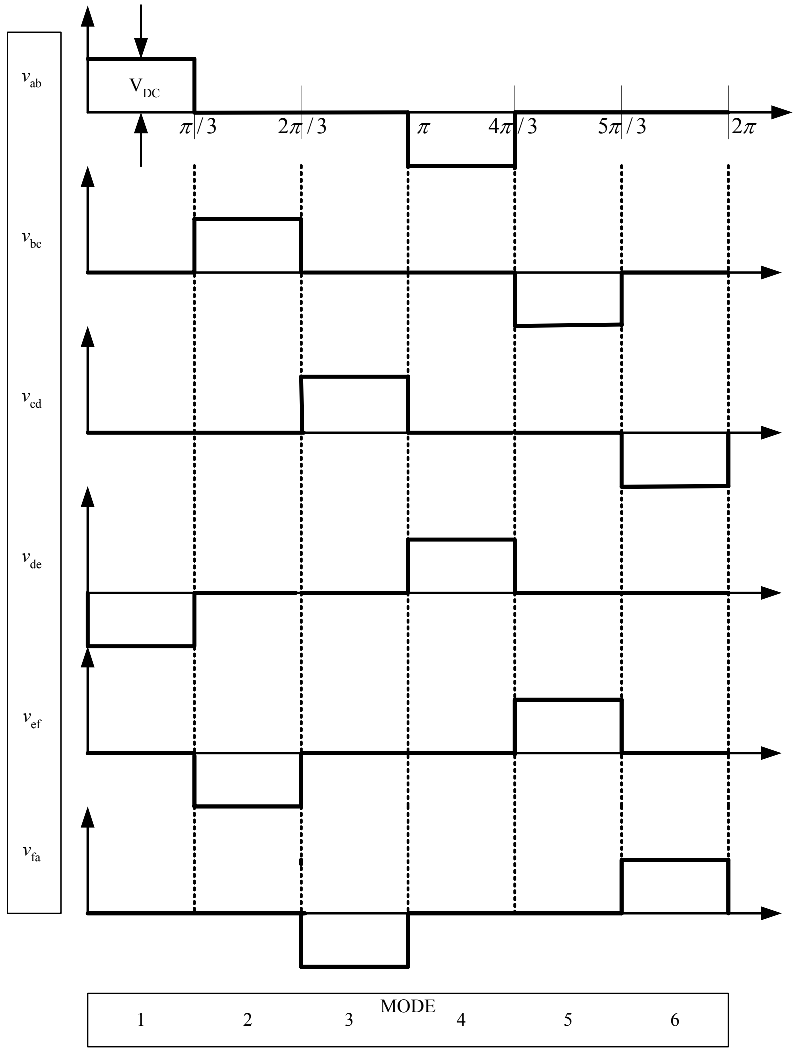

Fig. 5.6. Adjacent line-to-line voltages (first system) of the six-phase VSI.

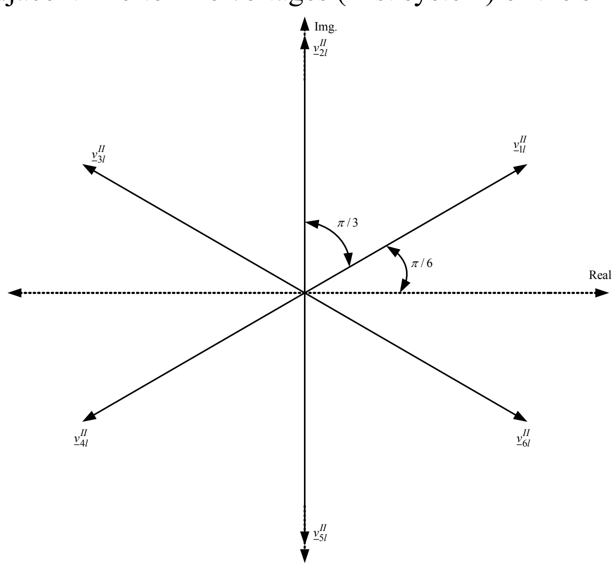

Fig. 5.7. Non adjacent line-to-line voltage (second system) space vectors of the six-phase VSI.

The general form of the space vectors for the second system of line-to-line voltages is given as:

$$\underline{v}_{kl}^{II} = \sqrt{\frac{2}{6}} V_{DC} 2\sqrt{3} \exp\left(j\left(2k-1\right)\frac{\pi}{6} \right) \quad k = 1, 2, \ldots\ldots, 6 \tag{5.9}$$

The third or opposing line-to-line voltage system is represented next. The states and values of the line-to-line voltages are tabulated in Table 5.8 and Fig. 5.9 shows time-domain waveforms. The space vectors are given in Table 5.9 and Fig. 5.10.

Table 5.8. Non-adjacent line-to-line voltage (third system) space vectors.

Non-adjacent line-to-line voltage (third system) space vectors	
$\underline{v}_{1l}^{III}$	$\sqrt{2/6}V_{DC}4\exp(j0)$
$\underline{v}_{2l}^{III}$	$\sqrt{2/6}V_{DC}4\exp(j\pi/3)$
$\underline{v}_{3l}^{III}$	$\sqrt{2/6}V_{DC}4\exp(j2\pi/3)$
$\underline{v}_{4l}^{III}$	$\sqrt{2/6}V_{DC}4\exp(j\pi)$
$\underline{v}_{5l}^{III}$	$\sqrt{2/6}V_{DC}4\exp(j4\pi/3)$
$\underline{v}_{6l}^{III}$	$\sqrt{2/6}V_{DC}4\exp(j5\pi/3)$

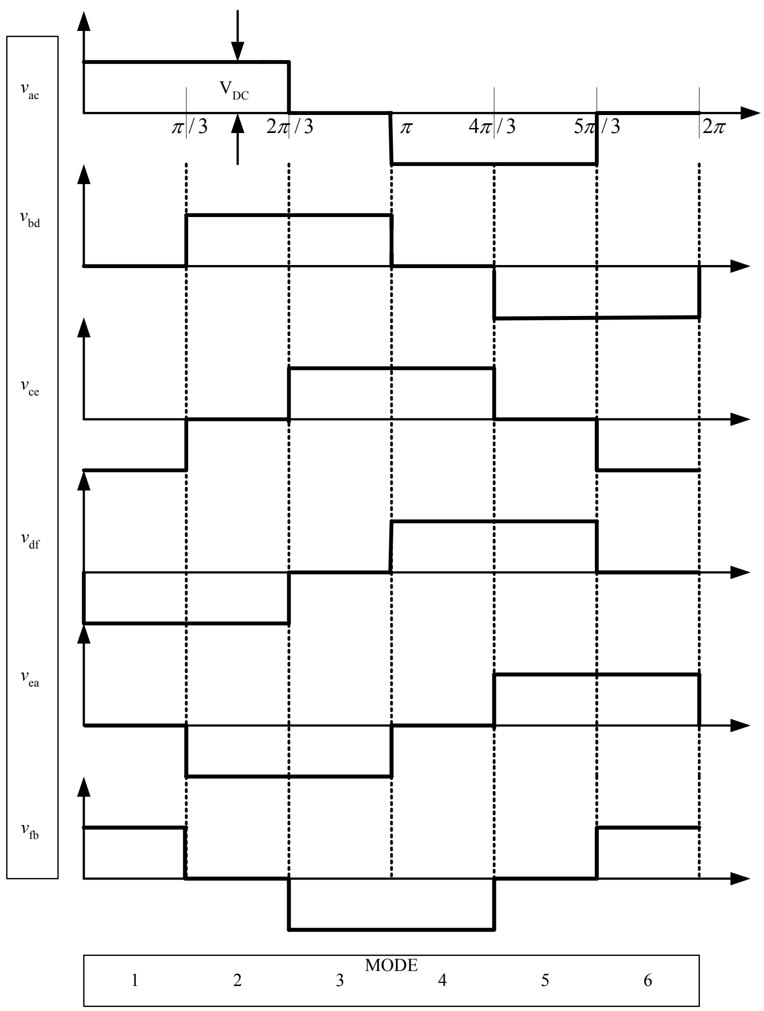

Fig. 5.8. Non-adjacent line-to-line voltages (second system) of the six-phase VSI.

Table 5.9. Non-adjacent line-to-line voltages (third system) of the six-phase VSI.

Switching state	Switches ON	Space vector	v_{ad}	v_{be}	v_{cf}	v_{da}	v_{eb}	v_{fc}
1	1,3,6,8,10,11	$\underline{v}_{1l}^{III}$	V_{DC}	V_{DC}	$-V_{DC}$	$-V_{DC}$	$-V_{DC}$	V_{DC}
2	1,3,5,8,10,12	$\underline{v}_{2l}^{III}$	V_{DC}	V_{DC}	V_{DC}	$-V_{DC}$	$-V_{DC}$	$-V_{DC}$
3	2,3,5,7,10,12	$\underline{v}_{3l}^{III}$	$-V_{DC}$	V_{DC}	V_{DC}	V_{DC}	$-V_{DC}$	$-V_{DC}$
4	2,4,5,7,9,12	$\underline{v}_{4l}^{III}$	$-V_{DC}$	$-V_{DC}$	V_{DC}	V_{DC}	V_{DC}	$-V_{DC}$
5	2,4,6,7,9,11	$\underline{v}_{5l}^{III}$	$-V_{DC}$	$-V_{DC}$	$-V_{DC}$	V_{DC}	V_{DC}	V_{DC}
6	1,4,6,8,9,11	$\underline{v}_{6l}^{III}$	V_{DC}	$-V_{DC}$	$-V_{DC}$	$-V_{DC}$	V_{DC}	V_{DC}

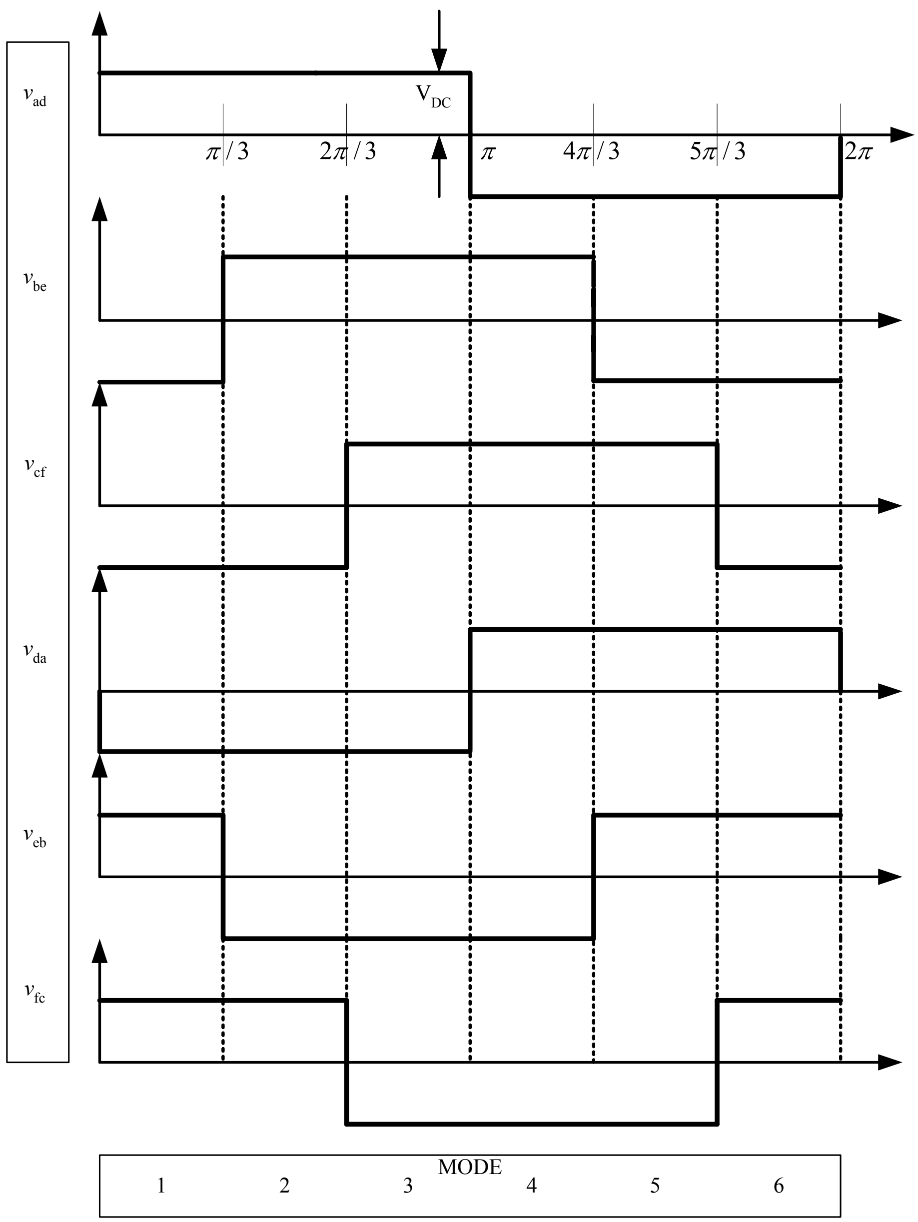

Fig. 5.9. Non-adjacent line-to-line voltages (third system) of the six-phase VSI.

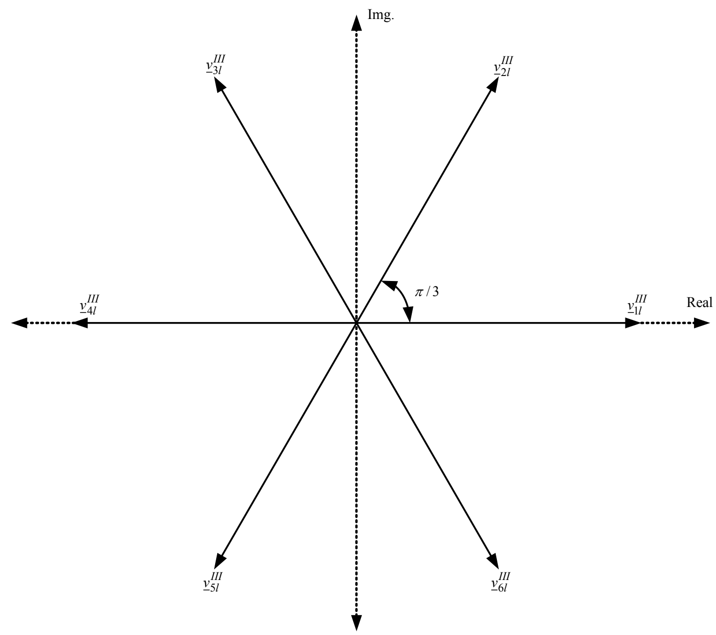

Fig. 5.10. Non-adjacent line-to-line voltage (third system) space vectors of the six-phase VSI.

The general form of representation of the third system of line-to-line voltages is:

$$\underline{v}_{kl}^{III} = \sqrt{\frac{2}{6}} V_{DC}\, 4 \exp\left(j\left(k-1\right)\frac{\pi}{3}\right) \quad k = 1,2,.....,6 \tag{5.10}$$

5.3 OPERATION OF THE SIX-PHASE VOLTAGE SOURCE INVERTER IN PULSE WIDTH MODULATION MODE

If a six-phase VSI is operated in PWM mode, apart from the already described eight states there will be additional fifty six switching states, since the number of possible switching states is in general equal to 2^n, where n is the number of inverter legs (i.e. output phases).

Table 5.10 summarises the additional switching states which are associated with PWM mode of operation and which are absent in the 180° mode of operation. Switches that are 'on' and the corresponding terminal polarity are included in the Table 5.10. As can be seen from Table 5.10, the remaining fifty six switching states encompass three possible situations: fourteen states when three switches from upper (or lower) half and three from the lower (or upper) half of the inverter are on (states 9-22); twelve states when five from upper (or lower) half and one from lower (or upper) half of the inverter are on (states 23-34) and remaining thirty states when four from upper (lower) half and two switches from the lower (upper) half are in conduction mode (states 35-64). There are two and six additional zero states in the first and the third group, respectively. Thus, in total, there are ten zero space vectors in contrast to two zero space vectors in three-phase and five-phase VSI. The three possible sets of space vectors are analysed separately.

Consider first the situation where three switches from upper (lower) half and three switches from lower (upper) half are in conduction. Table 5.11 summarises the values of leg voltages for this situation leading to fourteen states denoted with numbers 9-22 and lists the switches that are in the conduction mode. The values of the phase-to-neutral voltages for states 9-22 are listed in Table 5.12. Space vectors of phase-to–neutral voltages are found for states 9-22 using the same procedure as outlined in conjunction with the 180° mode. Phase-to-neutral voltage space vectors for these states are given in Table 5.13. It is seen from the Table 5.13 that there are two zero space vectors (15 and 22) and twelve non-zero space vectors. These are all with $\sqrt{2/6}V_{DC}$ amplitude and phase difference of 60° and they form twice the same set of six space vectors (i.e. 9-14 and 16-21).

Consider next the situation where five switches from upper (lower) half and one switch from lower (upper) half are in conduction. Table 5.14 summarises the values of leg voltages for twelve states denoted with numbers 23-34 and lists the switches that are in the conduction mode. The values of the phase-to-neutral voltages for these states are listed in Table 5.15. Space vectors of phase-to–neutral voltages are found for states 23-34 using the same procedure as outlined in previous cases. Phase-to-neutral voltage space vectors for these states are given in Table 5.16. It is seen from the Table 5.16 that all twelve non-zero space vectors are with $\sqrt{2/6}V_{DC}$ amplitude and phase difference of 60° and they form twice the same set of six space vectors (i.e. 23-28 and 29-34).

Finally consider the situation where four switches from upper (lower) half and two switches from lower (upper) half are in conduction. Table 5.17 summarises the values of leg voltages for thirty states denoted with numbers 35-64 and lists the switches that are in the conduction mode. The values of the phase-to-neutral voltages for these states are tabulated in Table 5.18. Phase-to-neutral voltage space vectors for these states are given in Table 5.19. It is seen from Table 5.19 that the thirty space vectors form six sets. Four sets consists of six non-zero space vectors and two sets include three zero space vectors. Two sets of zero space vectors (41-43 and 56-58) are discussed further in the subsequent paragraph. Out of four sets of non-zero space vectors, two (35-40 and 50-55) have amplitude of $\sqrt{2/6}V_{DC}$ while remaining two sets (44-49 and 59-64) have amplitude of $\sqrt{2/6}V_{DC}\sqrt{3}$.

Table 5.10. Additional switching states of the six-phase VSI in PWM mode.

Switching state	Switches ON	Terminal Polarity
9	1,3,6,8,9,12	$A^+B^+C^-D^-E^+F^-$
10	1,3,6,7,10,12	$A^+B^+C^-D^+E^-F^-$
11	1,4,5,7,10,12	$A^+B^-C^+D^+E^-F^-$
12	2,4,5,7,10,11	$A^-B^-C^+D^+E^-F^+$
13	2,4,5,8,9,11	$A^-B^-C^+D^-E^+F^+$
14	1,4,6,7,10,11	$A^+B^-C^-D^+E^-F^+$
15	1,4,5,8,9,12	$A^+B^-C^+D^-E^+F^-$
16	1,4,5,8,10,11	$A^+B^-C^+D^-E^-F^+$
17	2,3,5,8,10,11	$A^-B^+C^+D^-E^-F^+$
18	2,3,5,8,9,12	$A^-B^+C^+D^-E^+F^-$
19	2,3,6,7,9,12	$A^-B^+C^-D^+E^+F^-$
20	1,4,6,7,9,12	$A^+B^-C^-D^+E^+F^-$
21	2,3,6,8,9,11	$A^-B^+C^-D^-E^+F^+$
22	2,3,6,7,10,11	$A^-B^+C^-D^+E^-F^+$
23	1,3,5,8,9,11	$A^+B^+C^+D^-E^+F^+$
24	1,3,5,7,10,11	$A^+B^+C^+D^+E^-F^+$
25	1,3,5,7,9,12	$A^+B^+C^+D^+E^+F^-$
26	2,3,5,7,9,11	$A^-B^+C^+D^+E^+F^+$
27	1,4,5,7,9,11	$A^+B^-C^+D^+E^+F^+$
28	1,3,6,7,9,11	$A^+B^+C^-D^+E^+F^+$
29	1,4,6,8,10,12	$A^+B^-C^-D^-E^-F^-$
30	2,3,6,8,10,12	$A^-B^+C^-D^-E^-F^-$
31	2,4,5,8,10,12	$A^-B^-C^+D^-E^-F^-$
32	2,4,6,7,10,12	$A^-B^-C^-D^+E^-F^-$
33	2,4,6,8,9,12	$A^-B^-C^-D^-E^+F^-$
34	2,4,6,8,10,11	$A^-B^-C^-D^-E^-F^+$
35	1,3,6,7,10,11	$A^+B^+C^-D^+E^-F^+$
36	1,3,5,8,9,12	$A^+B^+C^+D^-E^+F^-$
37	2,3,5,7,10,11	$A^-B^+C^+D^+E^-F^+$
38	1,4,5,7,9,12	$A^+B^-C^+D^+E^+F^-$
39	2,3,6,7,9,11	$A^-B^+C^-D^+E^+F^+$
40	1,4,5,8,9,11	$A^+B^-C^+D^-E^+F^+$
41	1,3,6,7,9,12	$A^+B^+C^-D^+E^+F^-$
42	1,4,5,7,10,11	$A^+B^-C^+D^+E^-F^+$
43	2,3,5,8,9,11	$A^-B^+C^+D^-E^+F^+$
44	1,3,5,8,10,11	$A^+B^+C^+D^-E^-F^+$
45	1,3,5,7,10,12	$A^+B^+C^+D^+E^-F^-$
46	2,3,5,7,9,12	$A^-B^+C^+D^+E^+F^-$
47	2,4,5,7,9,11	$A^-B^-C^+ D^+E^+F^+$
48	1,4,6,7,9,11	$A^+B^-C^-D^+E^+F^+$
49	1,3,6,8,9,11	$A^+B^+C^-D^-E^+F^+$
50	2,3,6,8,10,11	$A^-B^+C^-D^-E^-F^+$
51	1,4,5,8,10,12	$A^+B^-C^+D^-E^-F^-$
52	2,3,6,7,10,12	$A^-B^+C^-D^+E^-F^-$
53	2,4,5,8,9,12	$A^-B^-C^+D^-E^+F^-$
54	2,4,6,7,10,11	$A^-B^-C^-D^+E^-F^+$
55	1,4,6,8,9,12	$A^+B^-C^-D^-E^+F^-$
56	2,4,5,8,10,11	$A^-B^-C^+D^-E^-F^+$
57	2,3,6,8,9,12	$A^-B^+C^-D^-E^+F^-$
58	1,4,6,7,10,12	$A^+B^-C^-D^+E^-F^-$
59	1,3,6,8,10,12	$A^+B^+C^-D^-E^-F^-$
60	2,3,5,8,10,12	$A^-B^+C^+D^-E^-F^-$
61	2,4,5,7,10,12	$A^-B^-C^+D^+E^-F^-$
62	2,4,6,7,9,12	$A^-B^-C^-D^+E^+F^-$
63	2,4,6,8,9,11	$A^-B^-C^-D^-E^+F^+$
64	1,4,6,8,10,11	$A^+B^-C^-D^-E^-F^+$

Let us consider the two sets of zero space vectors 41-43 and 56-58. Each of these states converts the six-phase inverter into three single-phase H-bridge inverters for each pair of consecutive phases. However, in contrast to zero states 15 and 22, here one single-phase inverter is short-circuited. For example, states 41-43 short-circuit single-phase inverters A-B, C-D and E-F, respectively. The same applies to states 56-58, except that the inverters are short-circuited at the negative bus-bar of the dc link, rather than at the positive bus-bar.

Thus it can be seen that the total of 64 space vectors, available in the PWM operation, fall into four distinct categories regarding the magnitude of the available output phase-to-neutral voltage. The phase-to-neutral voltage space vectors are summarised in Table 5.20 for all 64 switching states and are shown in Fig. 5.11. It is seen from Fig. 5.11 that the ratio of phase-to-neutral voltage space vector magnitudes is 1:√3:2 starting with the smallest.

The findings of this section are in full compliance with the findings of Correa et al (2003a) and (2003b).

Table 5.11. Leg voltages for states 9-22.

Switching state	Switches ON	Space vector	Leg voltage v_A	Leg voltage v_B	Leg voltage v_C	Leg voltage v_D	Leg voltage v_E	Leg voltage v_F
9	1,3,6,8,9,12	$\underline{v}_9$	V_{DC}	V_{DC}	0	0	V_{DC}	0
10	1,3,6,7,10,12	$\underline{v}_{10}$	V_{DC}	V_{DC}	0	V_{DC}	0	0
11	1,4,5,7,10,12	$\underline{v}_{11}$	V_{DC}	0	V_{DC}	V_{DC}	0	0
12	2,4,5,7,10,11	$\underline{v}_{12}$	0	0	V_{DC}	V_{DC}	0	V_{DC}
13	2,4,5,8,9,11	$\underline{v}_{13}$	0	0	V_{DC}	0	V_{DC}	V_{DC}
14	1,4,6,7,10,11	$\underline{v}_{14}$	V_{DC}	0	0	V_{DC}	0	V_{DC}
15	1,4,5,8,9,12	$\underline{v}_{15}$	V_{DC}	0	V_{DC}	0	V_{DC}	0
16	1,4,5,8,10,11	$\underline{v}_{16}$	V_{DC}	0	V_{DC}	0	0	V_{DC}
17	2,3,5,8,10,11	$\underline{v}_{17}$	0	V_{DC}	V_{DC}	0	0	V_{DC}
18	2,3,5,8,9,12	$\underline{v}_{18}$	0	V_{DC}	V_{DC}	0	V_{DC}	0
19	2,3,6,7,9,12	$\underline{v}_{19}$	0	V_{DC}	0	V_{DC}	V_{DC}	0
20	1,4,6,7,9,12	$\underline{v}_{20}$	V_{DC}	0	0	V_{DC}	V_{DC}	0
21	2,3,6,8,9,11	$\underline{v}_{21}$	0	V_{DC}	0	0	V_{DC}	V_{DC}
22	2,3,6,7,10,11	$\underline{v}_{22}$	0	V_{DC}	0	V_{DC}	0	V_{DC}

Table 5.12. Phase-to-neutral voltages for states 9-22.

State	Switches ON	Space vector	v_a	v_b	v_c	v_d	v_e	v_f
9	1,3,6,8,9,12	$\underline{v}_{9phase}$	1/2 V_{DC}	1/2 V_{DC}	-1/2 V_{DC}	-1/2 V_{DC}	1/2 V_{DC}	-1/2 V_{DC}
10	1,3,6,7,10,12	$\underline{v}_{10phase}$	1/2 V_{DC}	1/2 V_{DC}	-1/2 V_{DC}	1/2 V_{DC}	-1/2 V_{DC}	-1/2 V_{DC}
11	1,4,5,7,10,12	$\underline{v}_{11phase}$	1/2 V_{DC}	-1/2 V_{DC}	1/2 V_{DC}	1/2 V_{DC}	-1/2 V_{DC}	-1/2 V_{DC}
12	2,4,5,7,10,11	$\underline{v}_{12phase}$	-1/2 V_{DC}	-1/2 V_{DC}	1/2 V_{DC}	1/2 V_{DC}	-1/2 V_{DC}	1/2 V_{DC}
13	2,4,5,8,9,11	$\underline{v}_{13phase}$	-1/2 V_{DC}	-1/2 V_{DC}	1/2 V_{DC}	-1/2 V_{DC}	1/2 V_{DC}	1/2 V_{DC}
14	1,4,6,7,10,11	$\underline{v}_{14phase}$	1/2 V_{DC}	-1/2 V_{DC}	-1/2 V_{DC}	1/2 V_{DC}	-1/2 V_{DC}	1/2 V_{DC}
15	1,4,5,8,9,12	$\underline{v}_{15phase}$	1/2 V_{DC}	-1/2 V_{DC}	1/2 V_{DC}	-1/2 V_{DC}	1/2 V_{DC}	-1/2 V_{DC}
16	1,4,5,8,10,11	$\underline{v}_{16phase}$	1/2 V_{DC}	-1/2 V_{DC}	1/2 V_{DC}	-1/2 V_{DC}	-1/2 V_{DC}	1/2 V_{DC}
17	2,3,5,8,10,11	$\underline{v}_{17phase}$	-1/2 V_{DC}	1/2 V_{DC}	1/2 V_{DC}	-1/2 V_{DC}	-1/2 V_{DC}	1/2 V_{DC}
18	2,3,5,8,9,12	$\underline{v}_{18phase}$	-1/2 V_{DC}	1/2 V_{DC}	1/2 V_{DC}	-1/2 V_{DC}	1/2 V_{DC}	-1/2 V_{DC}
19	2,3,6,7,9,12	$\underline{v}_{19phase}$	-1/2 V_{DC}	1/2 V_{DC}	-1/2 V_{DC}	1/2 V_{DC}	1/2 V_{DC}	-1/2 V_{DC}
20	1,4,6,7,9,12	$\underline{v}_{20phase}$	1/2 V_{DC}	-1/2 V_{DC}	-1/2 V_{DC}	1/2 V_{DC}	1/2 V_{DC}	-1/2 V_{DC}
21	2,3,6,8,9,11	$\underline{v}_{21phase}$	-1/2 V_{DC}	1/2 V_{DC}	-1/2 V_{DC}	-1/2 V_{DC}	1/2 V_{DC}	1/2 V_{DC}
22	2,3,6,7,10,11	$\underline{v}_{22phase}$	-1/2 V_{DC}	1/2 V_{DC}	-1/2 V_{DC}	1/2 V_{DC}	-1/2 V_{DC}	1/2 V_{DC}

Table 5.13. Phase-to-neutral voltage space vectors for states 9-22.

Phase-to-neutral voltage space vectors	
$\underline{v}_{9phase}$	$\sqrt{2/6}V_{DC}\exp(j0)$
$\underline{v}_{10phase}$	$\sqrt{2/6}V_{DC}\exp(j\pi/3)$
$\underline{v}_{11phase}$	$\sqrt{2/6}V_{DC}\exp(j2\pi/3)$
$\underline{v}_{12phase}$	$\sqrt{2/6}V_{DC}\exp(j\pi)$
$\underline{v}_{13phase}$	$\sqrt{2/6}V_{DC}\exp(j4\pi/3)$
$\underline{v}_{14phase}$	$\sqrt{2/6}V_{DC}\exp(j5\pi/3)$
$\underline{v}_{15phase}$	0
$\underline{v}_{16phase}$	$\sqrt{2/6}V_{DC}\exp(j0)$
$\underline{v}_{17phase}$	$\sqrt{2/6}V_{DC}\exp(j\pi/3)$
$\underline{v}_{18phase}$	$\sqrt{2/6}V_{DC}\exp(j2\pi/3)$
$\underline{v}_{19phase}$	$\sqrt{2/6}V_{DC}\exp(j\pi)$
$\underline{v}_{20phase}$	$\sqrt{2/6}V_{DC}\exp(j4\pi/3)$
$\underline{v}_{21phase}$	$\sqrt{2/6}V_{DC}\exp(j5\pi/3)$
$\underline{v}_{22phase}$	0

Table 5.14. Leg voltages for states 23-34.

Switching state	Switches ON	Space vector	Leg voltage v_A	Leg voltage v_B	Leg voltage v_C	Leg voltage v_D	Leg voltage v_E	Leg voltage v_F
23	1,3,5,8,9,11	$\underline{v}_{23}$	V_{DC}	V_{DC}	V_{DC}	0	V_{DC}	V_{DC}
24	1,3,5,7,10,11	$\underline{v}_{24}$	V_{DC}	V_{DC}	V_{DC}	V_{DC}	0	V_{DC}
25	1,3,5,7,9,12	$\underline{v}_{25}$	V_{DC}	V_{DC}	V_{DC}	V_{DC}	V_{DC}	0
26	2,3,5,7,9,11	$\underline{v}_{26}$	0	V_{DC}	V_{DC}	V_{DC}	V_{DC}	V_{DC}
27	1,4,5,7,9,11	$\underline{v}_{27}$	V_{DC}	0	V_{DC}	V_{DC}	V_{DC}	V_{DC}
28	1,3,6,7,9,11	$\underline{v}_{28}$	V_{DC}	V_{DC}	0	V_{DC}	V_{DC}	V_{DC}
29	1,4,6,8,10,12	$\underline{v}_{29}$	V_{DC}	0	0	0	0	0
30	2,3,6,8,10,12	$\underline{v}_{30}$	0	V_{DC}	0	0	0	0
31	2,4,5,8,10,12	$\underline{v}_{31}$	0	0	V_{DC}	0	0	0
32	2,4,6,7,10,12	$\underline{v}_{32}$	0	0	0	V_{DC}	0	0
33	2,4,6,8,9,12	$\underline{v}_{33}$	0	0	0	0	V_{DC}	0
34	2,4,6,8,10,11	$\underline{v}_{34}$	0	0	0	0	0	V_{DC}

Table 5.15. Phase-to-neutral voltages for states 23-34.

State	Switches ON	Space vector	v_a	v_b	v_c	v_d	v_e	v_f
23	1,3,5,8,9,11	$\underline{v}_{23phase}$	1/6 V_{DC}	1/6 V_{DC}	1/6 V_{DC}	-5/6 V_{DC}	1/6 V_{DC}	1/6 V_{DC}
24	1,3,5,7,10,11	$\underline{v}_{24phase}$	1/6 V_{DC}	1/6 V_{DC}	1/6 V_{DC}	1/6 V_{DC}	-5/6 V_{DC}	1/6 V_{DC}
25	1,3,5,7,9,12	$\underline{v}_{25phase}$	1/6 V_{DC}	1/6 V_{DC}	1/6 V_{DC}	1/6 V_{DC}	1/6 V_{DC}	-5/6 V_{DC}
26	2,3,5,7,9,11	$\underline{v}_{26phase}$	-5/6 V_{DC}	1/6 V_{DC}	1/6 V_{DC}	1/6 V_{DC}	1/6 V_{DC}	1/6 V_{DC}
27	1,4,5,7,9,11	$\underline{v}_{27phase}$	1/6 V_{DC}	-5/6 V_{DC}	1/6 V_{DC}	1/6 V_{DC}	1/6 V_{DC}	1/6 V_{DC}
28	1,3,6,7,9,11	$\underline{v}_{28phase}$	1/6 V_{DC}	1/6 V_{DC}	-5/6 V_{DC}	1/6 V_{DC}	1/6 V_{DC}	1/6 V_{DC}
29	1,4,6,8,10,12	$\underline{v}_{29phase}$	5/6 V_{DC}	-1/6 V_{DC}	-1/6 V_{DC}	-1/6 V_{DC}	-1/6 V_{DC}	-1/6 V_{DC}
30	2,3,6,8,10,12	$\underline{v}_{30phase}$	-1/6 V_{DC}	5/6 V_{DC}	-1/6 V_{DC}	-1/6 V_{DC}	-1/6 V_{DC}	-1/6 V_{DC}
31	2,4,5,8,10,12	$\underline{v}_{31phase}$	-1/6 V_{DC}	-1/6 V_{DC}	5/6 V_{DC}	-1/6 V_{DC}	-1/6 V_{DC}	-1/6 V_{DC}
32	2,4,6,7,10,12	$\underline{v}_{32phase}$	-1/6 V_{DC}	-1/6 V_{DC}	-1/6 V_{DC}	5/6 V_{DC}	-1/6 V_{DC}	-1/6 V_{DC}
33	2,4,6,8,9,12	$\underline{v}_{33phase}$	-1/6 V_{DC}	-1/6 V_{DC}	-1/6 V_{DC}	-1/6 V_{DC}	5/6 V_{DC}	-1/6 V_{DC}
34	2,4,6,8,10,11	$\underline{v}_{34phase}$	-1/6 V_{DC}	-1/6 V_{DC}	-1/6 V_{DC}	-1/6 V_{DC}	-1/6 V_{DC}	5/6 V_{DC}

Table 5.16. Phase-to-neutral voltage space vectors for states 23-34.

Phase-to-neutral voltage space vectors	
$\underline{v}_{23phase}$	$\sqrt{2/6}V_{DC}\exp(j0)$
$\underline{v}_{24phase}$	$\sqrt{2/6}V_{DC}\exp(j\pi/3)$
$\underline{v}_{25phase}$	$\sqrt{2/6}V_{DC}\exp(j2\pi/3)$
$\underline{v}_{26phase}$	$\sqrt{2/6}V_{DC}\exp(j\pi)$
$\underline{v}_{27phase}$	$\sqrt{2/6}V_{DC}\exp(j4\pi/3)$
$\underline{v}_{28phase}$	$\sqrt{2/6}V_{DC}\exp(j5\pi/3)$
$\underline{v}_{29phase}$	$\sqrt{2/6}V_{DC}\exp(j0)$
$\underline{v}_{30phase}$	$\sqrt{2/6}V_{DC}\exp(j\pi/3)$
$\underline{v}_{31phase}$	$\sqrt{2/6}V_{DC}\exp(j2\pi/3)$
$\underline{v}_{32phase}$	$\sqrt{2/6}V_{DC}\exp(j\pi)$
$\underline{v}_{33phase}$	$\sqrt{2/6}V_{DC}\exp(j4\pi/3)$
$\underline{v}_{34phase}$	$\sqrt{2/6}V_{DC}\exp(j5\pi/3)$

Table 5.17. Leg voltages for states 35-64.

Switching state	Switches ON	Space vector	Leg voltage v_A	Leg voltage v_B	Leg voltage v_C	Leg voltage v_D	Leg voltage v_E	Leg voltage v_F
35	1,3,6,7,10,11	$\underline{v}_{35}$	V_{DC}	V_{DC}	0	V_{DC}	0	V_{DC}
36	1,3,5,8,9,12	$\underline{v}_{36}$	V_{DC}	V_{DC}	V_{DC}	0	V_{DC}	0
37	2,3,5,7,10,11	$\underline{v}_{37}$	0	V_{DC}	V_{DC}	V_{DC}	0	V_{DC}
38	1,4,5,7,9,12	$\underline{v}_{38}$	V_{DC}	0	V_{DC}	V_{DC}	V_{DC}	0
39	2,3,6,7,9,11	$\underline{v}_{39}$	0	V_{DC}	0	V_{DC}	V_{DC}	V_{DC}
40	1,4,5,8,9,11	$\underline{v}_{40}$	V_{DC}	0	V_{DC}	0	V_{DC}	V_{DC}
41	1,3,6,7,9,12	$\underline{v}_{41}$	V_{DC}	V_{DC}	0	V_{DC}	V_{DC}	0
42	1,4,5,7,10,11	$\underline{v}_{42}$	V_{DC}	0	V_{DC}	V_{DC}	0	V_{DC}
43	2,3,5,8,9,11	$\underline{v}_{43}$	0	V_{DC}	V_{DC}	0	V_{DC}	V_{DC}
44	1,3,5,8,10,11	$\underline{v}_{44}$	V_{DC}	V_{DC}	V_{DC}	0	0	V_{DC}
45	1,3,5,7,10,12	$\underline{v}_{45}$	V_{DC}	V_{DC}	V_{DC}	V_{DC}	0	0
46	2,3,5,7,9,12	$\underline{v}_{46}$	0	V_{DC}	V_{DC}	V_{DC}	V_{DC}	0
47	2,4,5,7,9,11	$\underline{v}_{47}$	0	0	V_{DC}	V_{DC}	V_{DC}	V_{DC}
48	1,4,6,7,9,11	$\underline{v}_{48}$	V_{DC}	0	0	V_{DC}	V_{DC}	V_{DC}
49	1,3,6,8,9,11	$\underline{v}_{49}$	V_{DC}	V_{DC}	0	0	V_{DC}	V_{DC}
50	2,3,6,8,10,11	$\underline{v}_{50}$	0	V_{DC}	0	0	0	V_{DC}
51	1,4,5,8,10,12	$\underline{v}_{51}$	V_{DC}	0	V_{DC}	0	0	0
52	2,3,6,7,10,12	$\underline{v}_{52}$	0	V_{DC}	0	V_{DC}	0	0
53	2,4,5,8,9,12	$\underline{v}_{53}$	0	0	V_{DC}	0	V_{DC}	0
54	2,4,6,7,10,11	$\underline{v}_{54}$	0	0	0	V_{DC}	0	V_{DC}
55	1,4,6,8,9,12	$\underline{v}_{55}$	V_{DC}	0	0	0	V_{DC}	0
56	2,4,5,8,10,11	$\underline{v}_{56}$	0	0	V_{DC}	0	0	V_{DC}
57	2,3,6,8,9,12	$\underline{v}_{57}$	0	V_{DC}	0	0	V_{DC}	0
58	1,4,6,7,10,12	$\underline{v}_{58}$	V_{DC}	0	0	V_{DC}	0	0
59	1,3,6,8,10,12	$\underline{v}_{59}$	V_{DC}	V_{DC}	0	0	0	0
60	2,3,5,8,10,12	$\underline{v}_{60}$	0	V_{DC}	V_{DC}	0	0	0
61	2,4,5,7,10,12	$\underline{v}_{61}$	0	0	V_{DC}	V_{DC}	0	0
62	2,4,6,7,9,12	$\underline{v}_{62}$	0	0	0	V_{DC}	V_{DC}	0
63	2,4,6,8,9,11	$\underline{v}_{63}$	0	0	0	0	V_{DC}	V_{DC}
64	1,4,6,8,10,11	$\underline{v}_{64}$	V_{DC}	0	0	0	0	V_{DC}

Table 5.18. Phase-to-neutral voltages for states 35-64.

State	Switches ON	Space vector	v_a	v_b	v_c	v_d	v_e	v_f
35	1,3,6,7,10,11	$\underline{v}_{35phase}$	1/3 V_{DC}	1/3 V_{DC}	-2/3 V_{DC}	1/3 V_{DC}	-2/3 V_{DC}	1/3 V_{DC}
36	1,3,5,8,9,12	$\underline{v}_{36phase}$	1/3 V_{DC}	1/3 V_{DC}	1/3 V_{DC}	-2/3 V_{DC}	1/3 V_{DC}	-2/3 V_{DC}
37	2,3,5,7,10,11	$\underline{v}_{37phase}$	-2/3 V_{DC}	1/3 V_{DC}	1/3 V_{DC}	1/3 V_{DC}	-2/3 V_{DC}	1/3 V_{DC}
38	1,4,5,7,9,12	$\underline{v}_{38phase}$	1/3 V_{DC}	-2/3 V_{DC}	1/3 V_{DC}	1/3 V_{DC}	1/3 V_{DC}	-2/3 V_{DC}
39	2,3,6,7,9,11	$\underline{v}_{39phase}$	-2/3 V_{DC}	1/3 V_{DC}	-2/3 V_{DC}	1/3 V_{DC}	1/3 V_{DC}	1/3 V_{DC}
40	1,4,5,8,9,11	$\underline{v}_{40phase}$	1/3 V_{DC}	-2/3 V_{DC}	1/3 V_{DC}	-2/3 V_{DC}	1/3 V_{DC}	1/3 V_{DC}
41	1,3,6,7,9,12	$\underline{v}_{41phase}$	1/3 V_{DC}	1/3 V_{DC}	-2/3 V_{DC}	1/3 V_{DC}	1/3 V_{DC}	-2/3 V_{DC}
42	1,4,5,7,10,11	$\underline{v}_{42phase}$	1/3 V_{DC}	-2/3 V_{DC}	1/3 V_{DC}	1/3 V_{DC}	-2/3 V_{DC}	1/3 V_{DC}
43	2,3,5,8,9,11	$\underline{v}_{43phase}$	-2/3 V_{DC}	1/3 V_{DC}	1/3 V_{DC}	-2/3 V_{DC}	1/3 V_{DC}	1/3 V_{DC}
44	1,3,5,8,10,11	$\underline{v}_{44phase}$	1/3 V_{DC}	1/3 V_{DC}	1/3 V_{DC}	-2/3 V_{DC}	-2/3 V_{DC}	1/3 V_{DC}
45	1,3,5,7,10,12	$\underline{v}_{45phase}$	1/3 V_{DC}	1/3 V_{DC}	1/3 V_{DC}	1/3 V_{DC}	-2/3 V_{DC}	-2/3 V_{DC}
46	2,3,5,7,9,12	$\underline{v}_{46phase}$	-2/3 V_{DC}	1/3 V_{DC}	1/3 V_{DC}	1/3 V_{DC}	1/3 V_{DC}	-2/3 V_{DC}
47	2,4,5,7,9,11	$\underline{v}_{47phase}$	-2/3 V_{DC}	-2/3 V_{DC}	1/3 V_{DC}	1/3 V_{DC}	1/3 V_{DC}	1/3 V_{DC}
48	1,4,6,7,9,11	$\underline{v}_{48phase}$	1/3 V_{DC}	-2/3 V_{DC}	-2/3 V_{DC}	1/3 V_{DC}	1/3 V_{DC}	1/3 V_{DC}
49	1,3,6,8,9,11	$\underline{v}_{49phase}$	1/3 V_{DC}	1/3 V_{DC}	-2/3 V_{DC}	-2/3 V_{DC}	1/3 V_{DC}	1/3 V_{DC}
50	2,3,6,8,10,11	$\underline{v}_{50phase}$	-1/3 V_{DC}	2/3 V_{DC}	-1/3 V_{DC}	-1/3 V_{DC}	-1/3 V_{DC}	2/3 V_{DC}
51	1,4,5,8,10,12	$\underline{v}_{51phase}$	2/3 V_{DC}	-1/3 V_{DC}	2/3 V_{DC}	-1/3 V_{DC}	-1/3 V_{DC}	-1/3 V_{DC}
52	2,3,6,7,10,12	$\underline{v}_{52phase}$	-1/3 V_{DC}	2/3 V_{DC}	-1/3 V_{DC}	2/3 V_{DC}	-1/3 V_{DC}	-1/3 V_{DC}
53	2,4,5,8,9,12	$\underline{v}_{53phase}$	-1/3 V_{DC}	-1/3 V_{DC}	2/3 V_{DC}	-1/3 V_{DC}	2/3 V_{DC}	-1/3 V_{DC}
54	2,4,6,7,10,11	$\underline{v}_{54phase}$	-1/3 V_{DC}	-1/3 V_{DC}	-1/3 V_{DC}	2/3 V_{DC}	-1/3 V_{DC}	2/3 V_{DC}
55	1,4,6,8,9,12	$\underline{v}_{55phase}$	2/3 V_{DC}	-1/3 V_{DC}	-1/3 V_{DC}	-1/3 V_{DC}	2/3 V_{DC}	-1/3 V_{DC}
56	2,4,5,8,10,11	$\underline{v}_{56phase}$	-1/3 V_{DC}	-1/3 V_{DC}	2/3 V_{DC}	-1/3 V_{DC}	-1/3 V_{DC}	2/3 V_{DC}
57	2,3,6,8,9,12	$\underline{v}_{57phase}$	-1/3 V_{DC}	2/3 V_{DC}	-1/3 V_{DC}	-1/3 V_{DC}	2/3 V_{DC}	-1/3 V_{DC}
58	1,4,6,7,10,12	$\underline{v}_{58phase}$	2/3 V_{DC}	-1/3 V_{DC}	-1/3 V_{DC}	2/3 V_{DC}	-1/3 V_{DC}	-1/3 V_{DC}
59	1,3,6,8,10,12	$\underline{v}_{59phase}$	2/3 V_{DC}	2/3 V_{DC}	-1/3 V_{DC}	-1/3 V_{DC}	-1/3 V_{DC}	-1/3 V_{DC}
60	2,3,5,8,10,12	$\underline{v}_{60phase}$	-1/3 V_{DC}	2/3 V_{DC}	2/3 V_{DC}	-1/3 V_{DC}	-1/3 V_{DC}	-1/3 V_{DC}
61	2,4,5,7,10,12	$\underline{v}_{61phase}$	-1/3 V_{DC}	-1/3 V_{DC}	2/3 V_{DC}	2/3 V_{DC}	-1/3 V_{DC}	-1/3 V_{DC}
62	2,4,6,7,9,12	$\underline{v}_{62phase}$	-1/3 V_{DC}	-1/3 V_{DC}	-1/3 V_{DC}	2/3 V_{DC}	2/3 V_{DC}	-1/3 V_{DC}
63	2,4,6,8,9,11	$\underline{v}_{63phase}$	-1/3 V_{DC}	-1/3 V_{DC}	-1/3 V_{DC}	-1/3 V_{DC}	2/3 V_{DC}	2/3 V_{DC}
64	1,4,6,8,10,11	$\underline{v}_{64phase}$	2/3 V_{DC}	-1/3 V_{DC}	-1/3 V_{DC}	-1/3 V_{DC}	-1/3 V_{DC}	2/3 V_{DC}

5.4 MODELLING OF A SIX-PHASE INDUCTION MOTOR

A mathematical model of a six-phase induction machine is formulated first in phase variable form. It is further transformed to obtain the model in an arbitrary common reference frame in the similar fashion as it has been done for the five-phase induction machine (section 3.4). The six-phase machine considered here is a true six-phase machine with 60° spatial and phase displacement between any two consecutive phases. In order to develop the machine model, the same assumptions are considered as that of five-phase machine.

5.4.1 Phase variable model

A six-phase induction machine has six stator phases with 60 degrees spatial displacement between two consecutive phases. The rotor winding is treated as an equivalent six-phase winding for the sake of generality. A six-phase induction machine can be described with the following voltage equilibrium and flux linkage equations:

Table 5.19. Phase-to-neutral voltage space vectors for states 35-64.

Phase-to-neutral voltage space vectors	
$\underline{v}_{35phase}$	$\sqrt{2/6}V_{DC}\exp(j0)$
$\underline{v}_{36phase}$	$\sqrt{2/6}V_{DC}\exp(j\pi/3)$
$\underline{v}_{37phase}$	$\sqrt{2/6}V_{DC}\exp(j2\pi/3)$
$\underline{v}_{38phase}$	$\sqrt{2/6}V_{DC}\exp(j\pi)$
$\underline{v}_{39phase}$	$\sqrt{2/6}V_{DC}\exp(j4\pi/3)$
$\underline{v}_{40phase}$	$\sqrt{2/6}V_{DC}\exp(j5\pi/3)$
$\underline{v}_{41phase}$	0
$\underline{v}_{42phase}$	0
$\underline{v}_{43phase}$	0
$\underline{v}_{44phase}$	$\sqrt{2/6}V_{DC}\sqrt{3}\exp(j\pi/6)$
$\underline{v}_{45phase}$	$\sqrt{2/6}V_{DC}\sqrt{3}\exp(j3\pi/6)$
$\underline{v}_{46phase}$	$\sqrt{2/6}V_{DC}\sqrt{3}\exp(j5\pi/6)$
$\underline{v}_{47phase}$	$\sqrt{2/6}V_{DC}\sqrt{3}\exp(j7\pi/6)$
$\underline{v}_{48phase}$	$\sqrt{2/6}V_{DC}\sqrt{3}\exp(j9\pi/6)$
$\underline{v}_{49phase}$	$\sqrt{2/6}V_{DC}\sqrt{3}\exp(j11\pi/6)$
$\underline{v}_{50phase}$	$\sqrt{2/6}V_{DC}\exp(j0)$
$\underline{v}_{51phase}$	$\sqrt{2/6}V_{DC}\exp(j\pi/3)$
$\underline{v}_{52phase}$	$\sqrt{2/6}V_{DC}\exp(j2\pi/3)$
$\underline{v}_{53phase}$	$\sqrt{2/6}V_{DC}\exp(j\pi)$
$\underline{v}_{54phase}$	$\sqrt{2/6}V_{DC}\exp(j4\pi/3)$
$\underline{v}_{55phase}$	$\sqrt{2/6}V_{DC}\exp(j5\pi/3)$
$\underline{v}_{56phase}$	0
$\underline{v}_{57phase}$	0
$\underline{v}_{58phase}$	0
$\underline{v}_{59phase}$	$\sqrt{2/6}V_{DC}\sqrt{3}\exp(j\pi/6)$
$\underline{v}_{60phase}$	$\sqrt{2/6}V_{DC}\sqrt{3}\exp(j3\pi/6)$
$\underline{v}_{61phase}$	$\sqrt{2/6}V_{DC}\sqrt{3}\exp(j5\pi/6)$
$\underline{v}_{62phase}$	$\sqrt{2/6}V_{DC}\sqrt{3}\exp(j7\pi/6)$
$\underline{v}_{63phase}$	$\sqrt{2/6}V_{DC}\sqrt{3}\exp(j9\pi/6)$
$\underline{v}_{64phase}$	$\sqrt{2/6}V_{DC}\sqrt{3}\exp(j11\pi/6)$

$$\begin{aligned} \underline{v}^s_{abcdef} &= \underline{R}_s \underline{i}^s_{abcdef} + \frac{d\underline{\psi}^s_{abcdef}}{dt} \\ \underline{\psi}^s_{abcdef} &= \underline{L}_s \underline{i}^s_{abcdef} + \underline{L}_{sr} \underline{i}^r_{abcdef} \end{aligned} \tag{5.11}$$

Table 5.20. Phase-to-neutral voltage space vectors for states 1-64.

Space vectors	Value of the space vectors
$\underline{v}_{1phase}$ to $\underline{v}_{6phase}$	$\sqrt{2/6}V_{DC}\,2\exp(j(k-1)\frac{\pi}{3})$ for k = 1,2,….,6
$\underline{v}_{7phase} = \underline{v}_{8phase}$	0
$\underline{v}_{9phase}$ to $\underline{v}_{14phase}$ and $\underline{v}_{16phase}$ to $\underline{v}_{21phase}$	$\sqrt{2/6}V_{DC}\exp(j(k-1)\frac{\pi}{3})$ for k = 1,2,….,6
$\underline{v}_{15phase} = \underline{v}_{22phase}$	0
$\underline{v}_{23phase}$ to $\underline{v}_{28phase}$ and $\underline{v}_{29phase}$ to $\underline{v}_{34phase}$	$\sqrt{2/6}V_{DC}\exp(j(k-1)\frac{\pi}{3})$ for k = 1,2,….,6
$\underline{v}_{35phase}$ to $\underline{v}_{40phase}$ and $\underline{v}_{50phase}$ to $\underline{v}_{55phase}$	$\sqrt{2/6}V_{DC}\exp(j(k-1)\frac{\pi}{3})$ for k = 1,2,….,6
$\underline{v}_{41phase}$ to $\underline{v}_{43phase}$ and $\underline{v}_{56phase}$ to $\underline{v}_{58phase}$	0
$\underline{v}_{44phase}$ to $\underline{v}_{49phase}$ and $\underline{v}_{59phase}$ to $\underline{v}_{64phase}$	$\sqrt{2/6}V_{DC}\sqrt{3}\exp(j(2k-1)\frac{\pi}{6})$ for k = 1,2,….,6

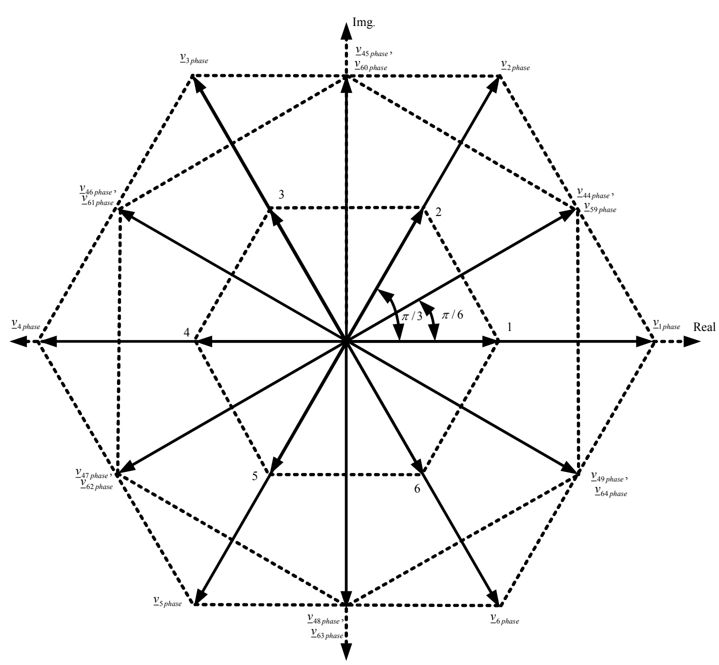

Fig. 5.11. Phase-to-neutral voltage space vectors where zero vectors (not shown) are 7,8,15,22,41,42,43,56,57,58; 1 = vectors 9,16,23,29,35,50; 2 = vectors 10,17,24,30,36,51; 3 = vectors 11,18,25,31,37,52; 4 = vectors 12,19,26,32,38,53; 5 = vectors 13,20,27,33,39,54; 6 = vectors 14,21,28,34,40,55.

$$\begin{aligned}
\underline{v}^r_{abcdef} &= \underline{R}_r \underline{i}^r_{abcdef} + \frac{d\underline{\psi}^r_{abcdef}}{dt} \\
\underline{\psi}^r_{abcdef} &= \underline{L}_r \underline{i}^r_{abcdef} + \underline{L}_{rs} \underline{i}^s_{abcdef}
\end{aligned} \tag{5.12}$$

where, similar to (3.18)-(3.19):

$$\begin{aligned}
\underline{v}^s_{abcdef} &= \begin{bmatrix} v_{as} & v_{bs} & v_{cs} & v_{ds} & v_{es} & v_{fs} \end{bmatrix}^T \\
\underline{i}^s_{abcdef} &= \begin{bmatrix} i_{as} & i_{bs} & i_{cs} & i_{ds} & i_{es} & i_{fs} \end{bmatrix}^T \\
\underline{\psi}^s_{abcdef} &= \begin{bmatrix} \psi_{as} & \psi_{bs} & \psi_{cs} & \psi_{ds} & \psi_{es} & \psi_{fs} \end{bmatrix}^T
\end{aligned} \tag{5.13}$$

$$\begin{aligned}
\underline{v}^r_{abcdef} &= \begin{bmatrix} v_{ar} & v_{br} & v_{cr} & v_{dr} & v_{er} & v_{fr} \end{bmatrix}^T \\
\underline{i}^r_{abcdef} &= \begin{bmatrix} i_{ar} & i_{br} & i_{cr} & i_{dr} & i_{er} & i_{fr} \end{bmatrix}^T \\
\underline{\psi}^r_{abcdef} &= \begin{bmatrix} \psi_{ar} & \psi_{br} & \psi_{cr} & \psi_{dr} & \psi_{er} & \psi_{fr} \end{bmatrix}^T
\end{aligned} \tag{5.14}$$

The matrices of inductances are ($\alpha = 2\pi/6$):

$$\underline{L}_s = \begin{bmatrix}
L_{ls}+M & M\cos\alpha & M\cos 2\alpha & M\cos 3\alpha & M\cos 4\alpha & M\cos 5\alpha \\
M\cos 5\alpha & L_{ls}+M & M\cos\alpha & M\cos 2\alpha & M\cos 3\alpha & M\cos 4\alpha \\
M\cos 4\alpha & M\cos 5\alpha & L_{ls}+M & M\cos\alpha & M\cos 2\alpha & M\cos 3\alpha \\
M\cos 3\alpha & M\cos 4\alpha & M\cos 5\alpha & L_{ls}+M & M\cos\alpha & M\cos 2\alpha \\
M\cos 2\alpha & M\cos 3\alpha & M\cos 4\alpha & M\cos 5\alpha & L_{ls}+M & M\cos\alpha \\
M\cos\alpha & M\cos 2\alpha & M\cos 3\alpha & M\cos 4\alpha & M\cos 5\alpha & L_{ls}+M
\end{bmatrix} \tag{5.15}$$

$$\underline{L}_r = \begin{bmatrix}
L_{lr}+M & M\cos\alpha & M\cos 2\alpha & M\cos 3\alpha & M\cos 4\alpha & M\cos 5\alpha \\
M\cos 5\alpha & L_{lr}+M & M\cos\alpha & M\cos 2\alpha & M\cos 3\alpha & M\cos 4\alpha \\
M\cos 4\alpha & M\cos 5\alpha & L_{lr}+M & M\cos\alpha & M\cos 2\alpha & M\cos 3\alpha \\
M\cos 3\alpha & M\cos 4\alpha & M\cos 5\alpha & L_{lr}+M & M\cos\alpha & M\cos 2\alpha \\
M\cos 2\alpha & M\cos 3\alpha & M\cos 4\alpha & M\cos 5\alpha & L_{lr}+M & M\cos\alpha \\
M\cos\alpha & M\cos 2\alpha & M\cos 3\alpha & M\cos 4\alpha & M\cos 5\alpha & L_{lr}+M
\end{bmatrix} \tag{5.16}$$

$$\begin{aligned}
\underline{L}_{sr} &= M\begin{bmatrix}
\cos\theta & \cos(\theta-5\alpha) & \cos(\theta-4\alpha) & \cos(\theta-3\alpha) & \cos(\theta-2\alpha) & \cos(\theta-\alpha) \\
\cos(\theta-\alpha) & \cos\theta & \cos(\theta-5\alpha) & \cos(\theta-4\alpha) & \cos(\theta-3\alpha) & \cos(\theta-2\alpha) \\
\cos(\theta-2\alpha) & \cos(\theta-\alpha) & \cos\theta & \cos(\theta-5\alpha) & \cos(\theta-4\alpha) & \cos(\theta-3\alpha) \\
\cos(\theta-3\alpha) & \cos(\theta-2\alpha) & \cos(\theta-\alpha) & \cos\theta & \cos(\theta-5\alpha) & \cos(\theta-4\alpha) \\
\cos(\theta-4\alpha) & \cos(\theta-3\alpha) & \cos(\theta-2\alpha) & \cos(\theta-\alpha) & \cos\theta & \cos(\theta-5\alpha) \\
\cos(\theta-5\alpha) & \cos(\theta-4\alpha) & \cos(\theta-3\alpha) & \cos(\theta-2\alpha) & \cos(\theta-\alpha) & \cos\theta
\end{bmatrix} \\
\underline{L}_{rs} &= \underline{L}^T_{sr}
\end{aligned} \tag{5.17}$$

Stator and rotor resistance matrices are six by six diagonal matrices,

$$\begin{aligned}
\underline{R}_s &= diag(R_s \quad R_s \quad R_s \quad R_s \quad R_s \quad R_s) \\
\underline{R}_r &= diag(R_r \quad R_r \quad R_r \quad R_r \quad R_r \quad R_r)
\end{aligned} \tag{5.18}$$

Motor torque can be expressed in terms of phase currents as:

$$T_e = -PM\left\{\begin{array}{l}(i_{as}i_{ar} + i_{bs}i_{br} + i_{cs}i_{cr} + i_{ds}i_{dr} + i_{es}i_{er} + i_{fs}i_{fr})\sin\theta + \\ (i_{fs}i_{ar} + i_{as}i_{br} + i_{bs}i_{cr} + i_{cs}i_{dr} + i_{ds}i_{er} + i_{es}i_{fr})\sin(\theta - 5\alpha) + \\ (i_{es}i_{ar} + i_{fs}i_{br} + i_{as}i_{cr} + i_{bs}i_{dr} + i_{cs}i_{er} + i_{ds}i_{fr})\sin(\theta - 4\alpha) + \\ (i_{ds}i_{ar} + i_{es}i_{br} + i_{fs}i_{cr} + i_{as}i_{dr} + i_{bs}i_{er} + i_{cs}i_{fr})\sin(\theta - 3\alpha) + \\ (i_{cs}i_{ar} + i_{ds}i_{br} + i_{es}i_{cr} + i_{fs}i_{dr} + i_{as}i_{er} + i_{bs}i_{fr})\sin(\theta - 2\alpha) + \\ (i_{bs}i_{ar} + i_{cs}i_{br} + i_{ds}i_{cr} + i_{es}i_{dr} + i_{fs}i_{er} + i_{as}i_{fr})\sin(\theta - \alpha)\end{array}\right\} \tag{5.19}$$

5.4.2 Model transformation

The transformation matrix in power invariant form is applied to stator six-phase windings [White and Woodson (1959)]:

$$\underline{A}_s = \sqrt{\frac{2}{6}}\begin{bmatrix} \cos\theta_s & \cos(\theta_s-\alpha) & \cos(\theta_s-2\alpha) & \cos(\theta_s-3\alpha) & \cos(\theta_s-4\alpha) & \cos(\theta_s-5\alpha) \\ -\sin\theta_s & -\sin(\theta_s-\alpha) & -\sin(\theta_s-2\alpha) & -\sin(\theta_s-3\alpha) & -\sin(\theta_s-4\alpha) & \sin(\theta_s-5\alpha) \\ 1 & \cos(2\alpha) & \cos(4\alpha) & \cos(6\alpha) & \cos(8\alpha) & \cos(10\alpha) \\ 0 & \sin(2\alpha) & \sin(4\alpha) & \sin(6\alpha) & \sin(8\alpha) & \sin(10\alpha) \\ \frac{1}{\sqrt{2}} & \frac{1}{\sqrt{2}} & \frac{1}{\sqrt{2}} & \frac{1}{\sqrt{2}} & \frac{1}{\sqrt{2}} & \frac{1}{\sqrt{2}} \\ \frac{1}{\sqrt{2}} & -\frac{1}{\sqrt{2}} & \frac{1}{\sqrt{2}} & -\frac{1}{\sqrt{2}} & \frac{1}{\sqrt{2}} & -\frac{1}{\sqrt{2}} \end{bmatrix} \tag{5.20}$$

$\underline{A}_s^{-1} = \underline{A}_s^T$

Transformation of the rotor variables is performed using the same transformation matrix, except that θ_s is replaced with β, where $\beta = \theta_s - \theta$. Hence for rotor:

$$\underline{A}_r = \sqrt{\frac{2}{6}}\begin{bmatrix} \cos\beta & \cos(\beta-\alpha) & \cos(\beta-2\alpha) & \cos(\beta-3\alpha) & \cos(\beta-4\alpha) & \cos(\beta-5\alpha) \\ -\sin\beta & -\sin(\beta-\alpha) & -\sin(\beta-2\alpha) & -\sin(\beta-3\alpha) & -\sin(\beta-4\alpha) & \sin(\beta-5\alpha) \\ 1 & \cos(2\alpha) & \cos(4\alpha) & \cos(6\alpha) & \cos(8\alpha) & \cos(10\alpha) \\ 0 & \sin(2\alpha) & \sin(4\alpha) & \sin(6\alpha) & \sin(8\alpha) & \sin(10\alpha) \\ \frac{1}{\sqrt{2}} & \frac{1}{\sqrt{2}} & \frac{1}{\sqrt{2}} & \frac{1}{\sqrt{2}} & \frac{1}{\sqrt{2}} & \frac{1}{\sqrt{2}} \\ \frac{1}{\sqrt{2}} & -\frac{1}{\sqrt{2}} & \frac{1}{\sqrt{2}} & -\frac{1}{\sqrt{2}} & \frac{1}{\sqrt{2}} & -\frac{1}{\sqrt{2}} \end{bmatrix} \tag{5.21}$$

$\underline{A}_r^{-1} = \underline{A}_r^T$

The angles of transformation remain to be given with (3.28)

5.4.3 Machine model in an arbitrary common reference frame

Correlation between original phase variables and new variables in the transformed domain is still governed with (3.29) where transformation matrices are now those of (5.20)-(5.21). Upon completion of the transformation the equations in terms of d-q variables become

$$
\begin{aligned}
v_{ds} &= R_s i_{ds} - \omega_a \psi_{qs} + p\psi_{ds} & v_{dr} &= R_r i_{dr} - (\omega_a - \omega)\psi_{qr} + p\psi_{dr} \\
v_{qs} &= R_s i_{qs} + \omega_a \psi_{ds} + p\psi_{qs} & v_{qr} &= R_r i_{qr} + (\omega_a - \omega)\psi_{dr} + p\psi_{qr} \\
v_{xs} &= R_s i_{xs} + p\psi_{xs} & v_{xr} &= R_r i_{xr} + p\psi_{xr} \\
v_{ys} &= R_s i_{ys} + p\psi_{ys} & v_{yr} &= R_r i_{yr} + p\psi_{yr} \\
v_{0+s} &= R_s i_{0+s} + p\psi_{0+s} & v_{0+r} &= R_r i_{0+r} + p\psi_{0+r} \\
v_{0-s} &= R_s i_{0-s} + p\psi_{0-s} & v_{0-r} &= R_r i_{0-r} + p\psi_{0-r}
\end{aligned}
\tag{5.22}
$$

while flux linkage equations are:

$$
\begin{aligned}
\psi_{ds} &= (L_{ls} + L_m) i_{ds} + L_m i_{dr} & \psi_{dr} &= (L_{lr} + L_m) i_{dr} + L_m i_{ds} \\
\psi_{qs} &= (L_{ls} + L_m) i_{qs} + L_m i_{qr} & \psi_{qr} &= (L_{lr} + L_m) i_{qr} + L_m i_{qs} \\
\psi_{xs} &= L_{ls} i_{xs} & \psi_{xr} &= L_{lr} i_{xr} \\
\psi_{ys} &= L_{ls} i_{ys} & \psi_{yr} &= L_{lr} i_{yr} \\
\psi_{0+s} &= L_{ls} i_{0+s} & \psi_{0+r} &= L_{lr} i_{0+r} \\
\psi_{0-s} &= L_{ls} i_{0-s} & \psi_{0-r} &= L_{lr} i_{0-r}
\end{aligned}
\tag{5.23}
$$

Magnetising inductance $L_m = 3M = (6/2)M$ is introduced in (5.23).

Torque equation in transformed domain becomes:

$$T_e = PL_m \left[i_{dr} i_{qs} - i_{ds} i_{qr} \right] \tag{5.24}$$

Mechanical equation of motion (3.34) is still valid.

Comparison of model (5.22)-(5.24) with the corresponding five-phase machine model (3.30)-(3.33) shows that the only difference is in the number of zero-sequence equations. Since six is an even number, there are two zero-sequence equations for both stator and rotor rather than just one as for the five-phase machines.

5.5 ROTOR FLUX ORIENTED CONTROL OF A SIX-PHASE INDUCTION MOTOR

Due to the analogy between five-phase and six-phase machine models, equations (3.35)-(3.36), (3.40)-(3.42) remain to be valid in the identical form. Hence vector control scheme for a six-phase machine is identical to the scheme for a three-phase and a five-phase machine, except that the transformation block creates now six-phase currents. The configuration of the indirect vector controller for operation in the base speed region is illustrated in Fig. 5.12. Expressions for constants in the Fig. 5.12 are the same as in Fig. 3.10 and are given with (3.43). It should be however, noted that, due to the applied power invariant transformation, all d-q axis quantities have a magnitude of √6 times the RMS value for the six-phase machine. Machine data given in Appendix A apply once more. Hence in the case of a six-phase machine one has, $\psi_r^* = \sqrt{6}\psi_{rn} = 1.392$ Wb and $T_{en} = 6(5/3) = 10$ Nm. Thus the constants K_1 and K_2 of (3.49) are found as 0.3934 and 4.1332 respectively.

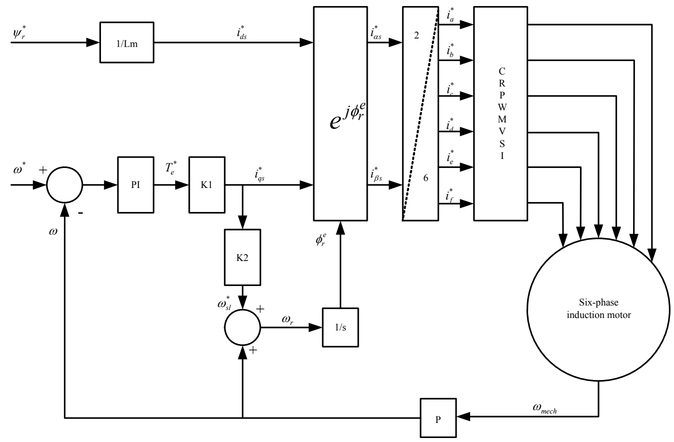

Fig. 5.12. Indirect vector control of a six-phase induction machine in the base speed region.

5.6 SIMULATION RESULTS

5.6.1 Six-phase induction motor

An indirect rotor field oriented six-phase induction motor drive is investigated. The motor is simulated using both model in the stationary reference frame and the phase variable model. The results obtained from two models are identical and thus only one set of results is presented here. The machine model in the stationary reference frame, used in the simulation, also incorporates the two (positive and negative) zero-sequence components of stator voltages. The machine is fed by a PWM voltage source inverter and hysteresis current control and ramp-comparison current control are exercised upon motor phase currents. The drive is operated in closed loop speed control mode with discrete anti-windup PI speed controller. The speed and current controllers are the same as those used in five-phase single-motor drive (section 3.7) and five-phase two-motor drive (section 4.8). The torque is limited to 150% of the rated value (15 Nm). The drive is simulated for acceleration, disturbance rejection and speed reversal transients, at operating speed of 1500 rpm corresponding to 50 Hz operation.

Forced excitation is initiated first. Rotor flux reference (i.e. stator d-axis current reference) is ramped from t = 0 to t = 0.01 s to twice the rated value. It is further reduced from twice the rated value to the rated value in a linear fashion from t = 0.05 to t = 0.06 s and it is then kept constant for the rest of the simulation period. Once the rotor flux has reached steady state a speed command of 1500 rpm is applied at t = 0.3 s in ramp wise manner from t = 0.3 to t = 0.35 s. The hysteresis current controller band is kept at ±2.5%. The inverter dc link voltage is set to 415x√2 = 586.9 V. A step load torque, equal to the motor rated torque (10 Nm), is applied at t = 1 s and the machine is allowed to run for sufficient time so as to reach the steady state condition. A speed reversal is then initiated in the ramp-wise manner (ramp duration from t = 1.25 to t = 1.3 s).

Simulation results are shown in Figs. 5.13-5.16 for hysteresis and Figs. 5.17-5.20 for ramp-comparison current control, respectively. Results in Figs. 5.13, 5.15 and 5.16 for the three transients are in principle very much the same as for a five-phase induction machine, Figs. 3.23-3.25. The commanded and actual torque responses are not identical in Figs. 5.15 and 5.19 due to lack of voltage reserve capability of VSI. The same observation was made in Figs. 3.24 and 3.30. The most interesting results are however those of Fig. 5.14, where the two zero-sequence component voltages and currents are shown. It can be observed from Fig. 5.14 that positive sequence stator voltage and current component do not exist. However, negative zero-sequence components do exist and they include triplen stator current harmonics, which can freely flow in this true six-phase winding arrangement. Harmonic analysis for negative zero-sequence components will be performed in section 5.6.3.

Very much the same conclusions apply to the results obtained with ramp-comparison control, Figs. 5.17, 5.19 and 5.20. All the transient responses are very much the same as in the case of five-phase induction machine, Figs. 3.29-3.31. The existence of negative zero-sequence current and the non-existence of positive zero-sequence current component is again verified in Fig. 5.18.

5.6.2 Three-phase induction motor

Since vector control of a two motor drive system, consisting of a six-phase and a three-phase machine, will be studied in the next chapter, simulation of vector controlled three-phase machine is performed as well. The excitation and acceleration (to 750 rpm), disturbance rejection and reversing transients (from 750 rpm to -750 rpm) are studied again and hysteresis and ramp-comparison current control techniques are used once more to control the three-phase PWM voltage source inverter feeding the three-phase induction machine. Torque limit is set to twice the rated torque value (10 Nm). The resulting plots are shown in Figs. 5.21 to 5.26. These results will be of use in the next chapter, where it will be shown that the same quality of control results in series-connected two-motor drive system.

5.6.3 Harmonic analysis

This section presents results of the harmonic analysis of stator voltage and current of six-phase and three-phase induction motors with hysteresis current control method. The

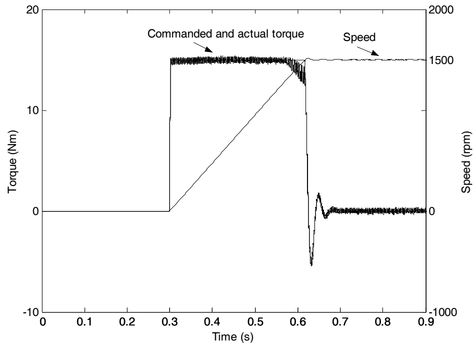

a.

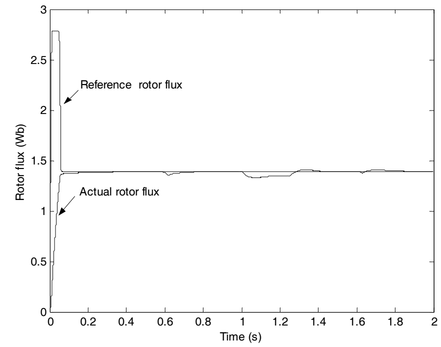

b.

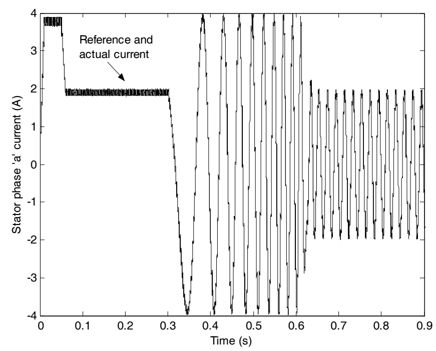

c.

Fig. 5.13. Excitation and acceleration transients using hysteresis current control: a. actual and reference torque, and speed, b. actual and reference rotor flux, c. actual and reference stator phase ‘a’ current.

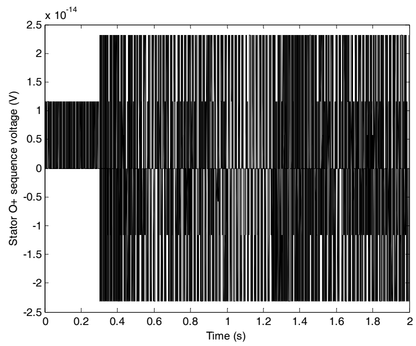

a.

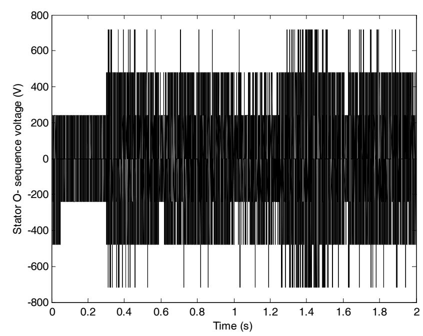

b.

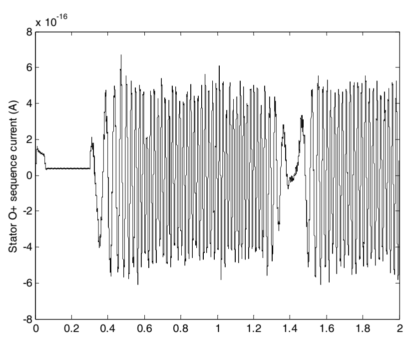

c.

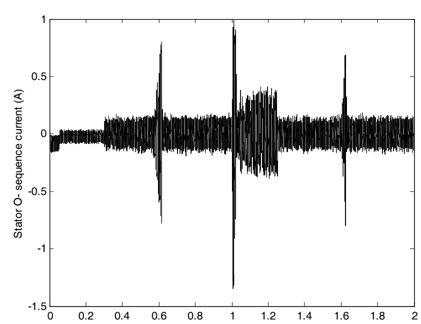

d.

Fig. 5.14 a. Stator 0+ sequence voltage, b. Stator 0- sequence voltage, c. Stator 0+ sequence current, d. Stator 0- sequence current.

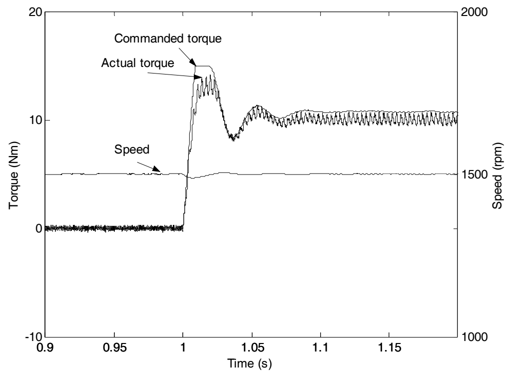

a.

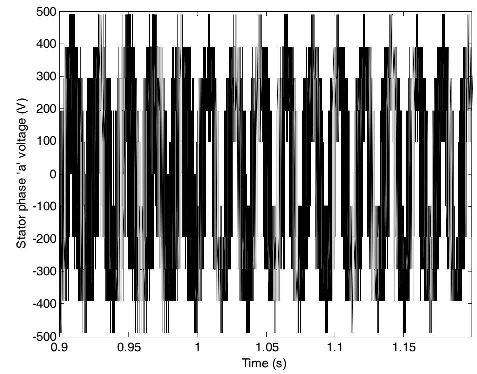

c.

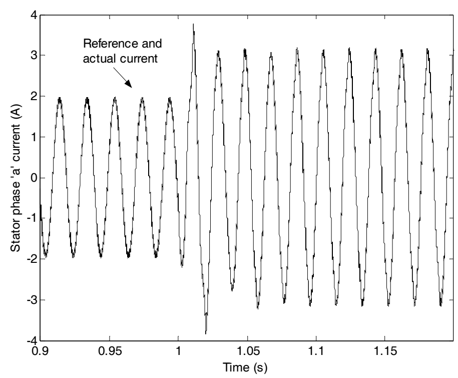

b.

Fig. 5.15. Disturbance rejection transient using hysteresis current control: a. actual and reference torque, and speed, b. actual and reference stator phase ‘a’ current, c. stator phase ‘a’ voltage.

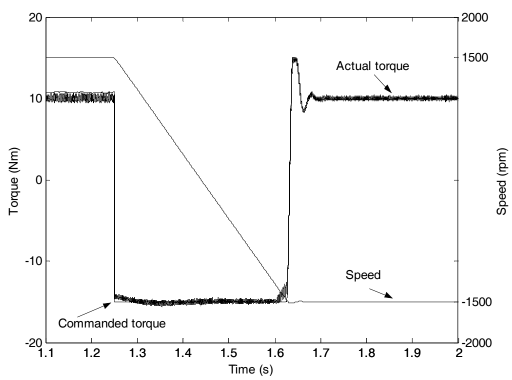

a.

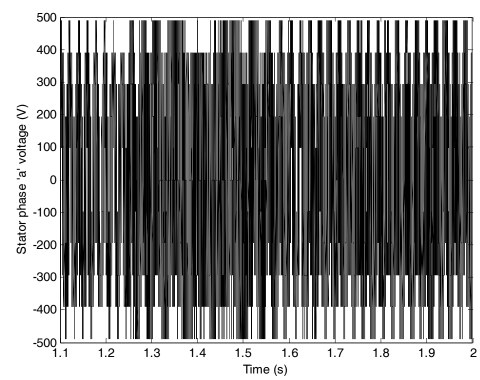

c.

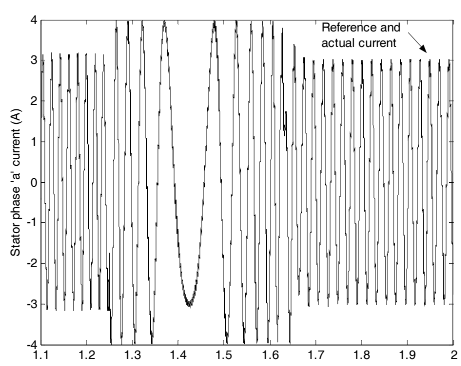

b.

Fig. 5.16. Reversing transient using hysteresis current control: a. actual and reference torque, and speed, b. actual and reference stator phase ‘a’ current, c. stator phase ‘a’ voltage.

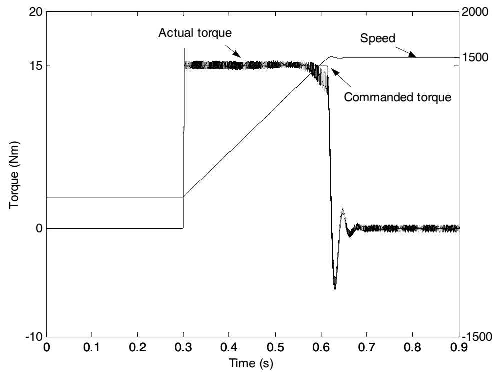

a.

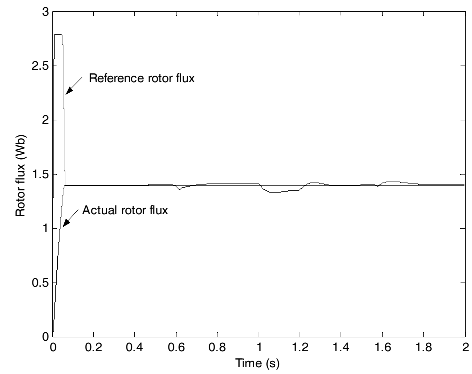

b.

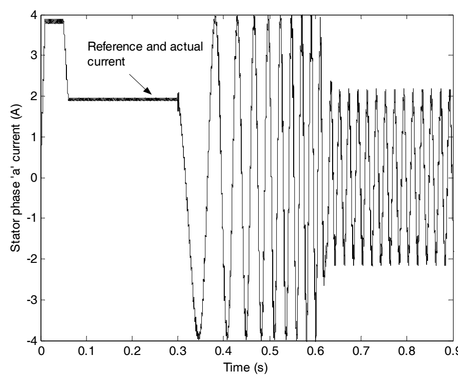

c.

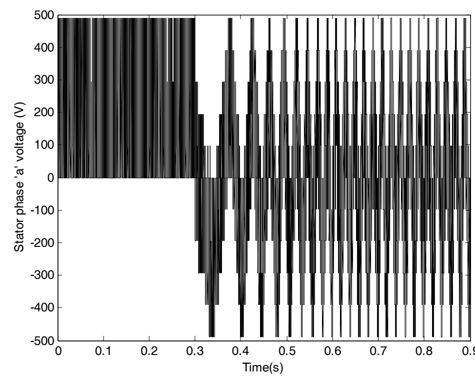

d.

Fig. 5.17. Excitation and acceleration transients using ramp-comparison current control: a. actual and reference torque, and speed, b. actual and reference rotor flux, c. actual and reference stator phase ‘a’ current, d. stator phase ‘a’ voltage.

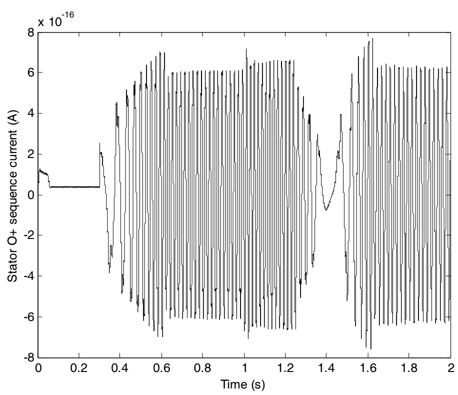

a.

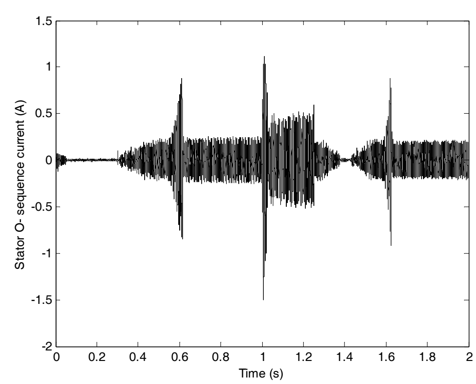

b.

Fig. 5.18 a. Stator 0+ sequence current, b. Stator 0- sequence current.

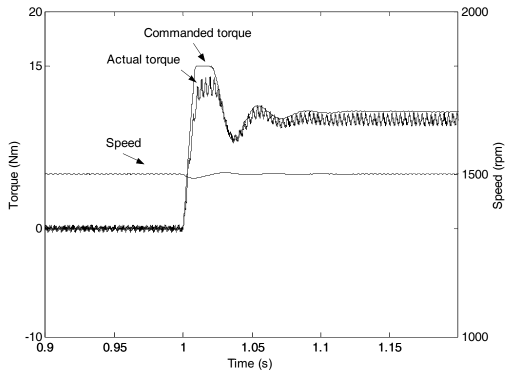

a.

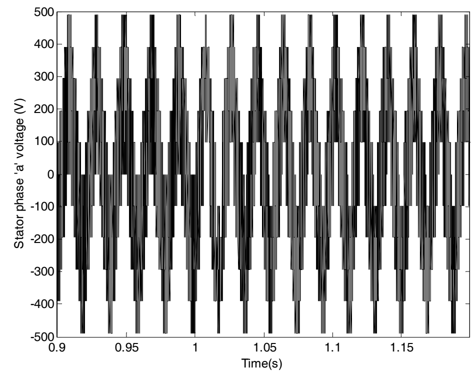

c.

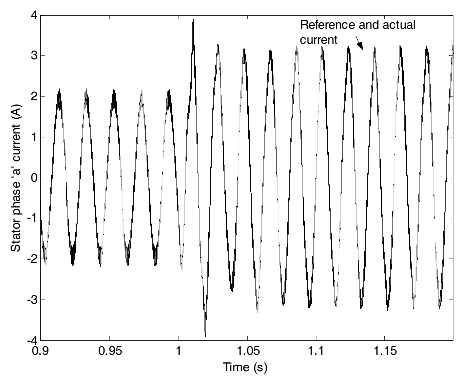

b.

Fig. 5.19. Disturbance rejection transient using ramp-comparison current control: a. actual and reference torque, and speed, b. actual and reference stator phase ‘a’ current, c. stator phase ‘a’ voltage.

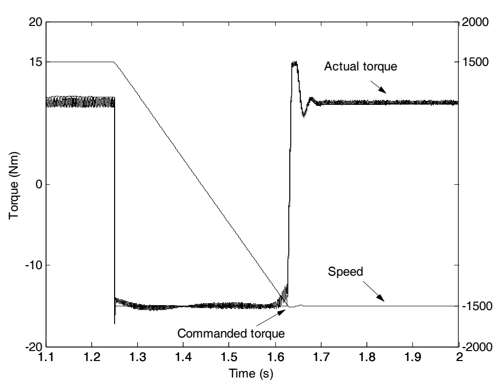

a.

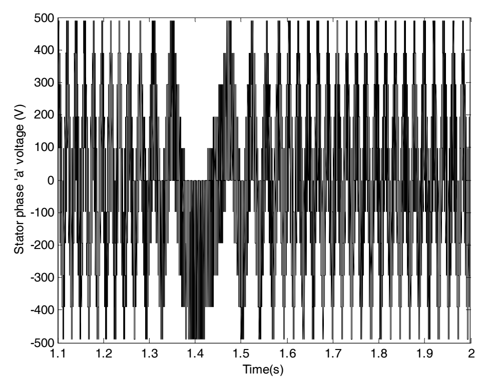

c.

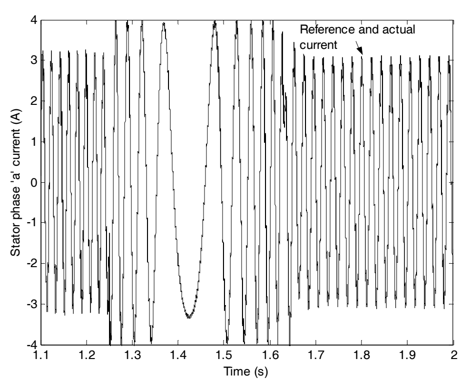

c.

Fig. 5.20. Reversing transient using ramp-comparison current control: a. actual and reference torque, and speed, b. actual and reference stator phase ‘a’ current, c. stator phase ‘a’ voltage.

harmonic analysis is done for steady state no-load operating condition. All the spectra are given in terms of RMS values. The spectrum is determined for phase ‘a’ voltage and current for six-phase and three-phase machines. Additionally α-axis, x-axis and negative zero-sequence axis components of stator voltage and current for six-phase machine are analysed and spectra are determined. The resulting plots are given in Fig. 5.27-5.28 for six-phase machine and Fig. 5.29 for three-phase machine.

As is evident from Figs. 5.27-5.28, phase voltage and current spectra show the fundamental component at 50 Hz, which is, as expected, of the same value in both phase and α-axis components. On the other hand, voltage x-axis component contains essentially only high frequency harmonics, leading to virtually non-existent x-axis component current harmonics. Further, the negative zero-sequence current component is seen to exist at third harmonic frequency (150 Hz). The magnitude is very small though (note that the scale is in mA).

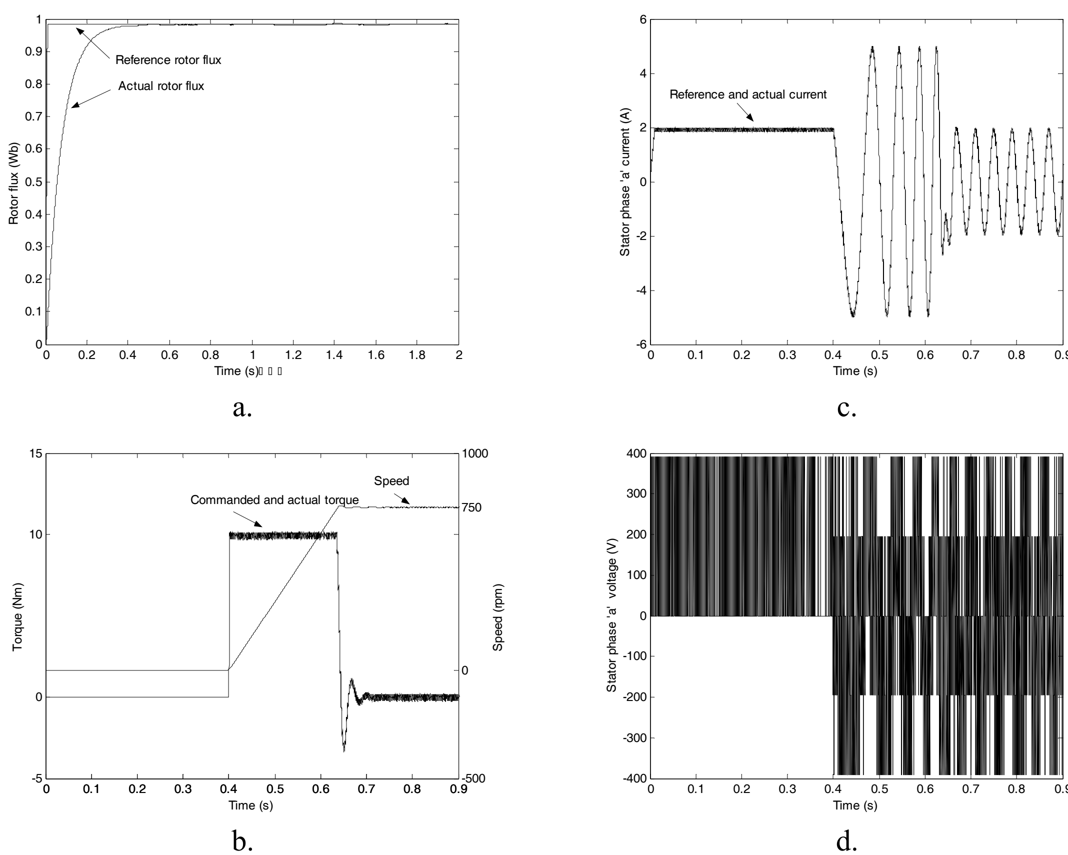

Fig. 5.21. Excitation and acceleration transients using hysteresis current control: a. actual and reference rotor flux, b. actual and reference torque, and speed, c. actual and reference stator phase ‘a’ currents, d. stator phase ‘a’ voltage.

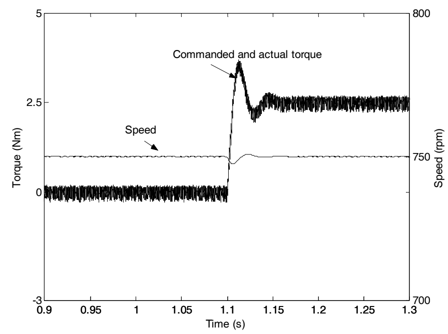

a.

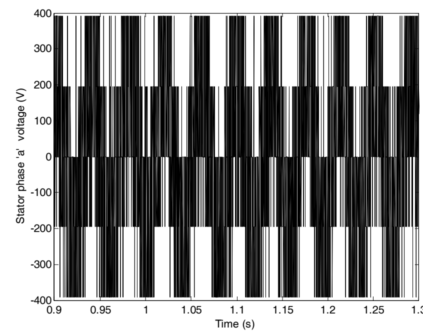

c.

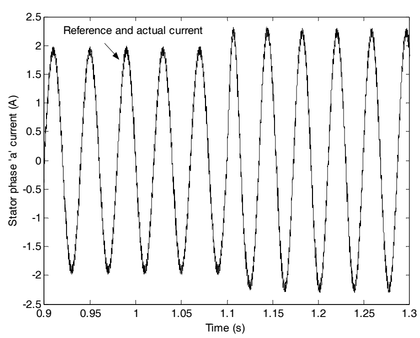

b.

Fig. 5.22. Disturbance rejection transient using hysteresis current control: a. actual and reference torque, and speed, b. actual and reference stator phase ‘a’ currents, c. stator phase ‘a’ voltage.

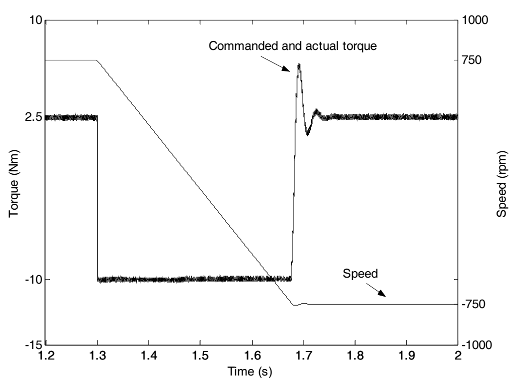

a.

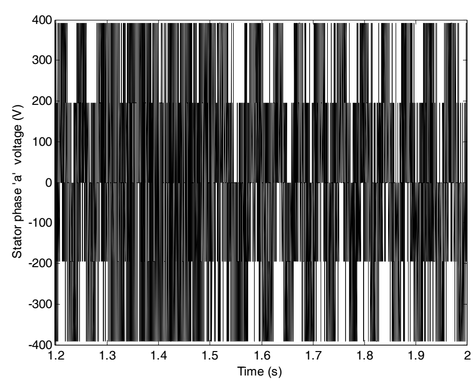

c.

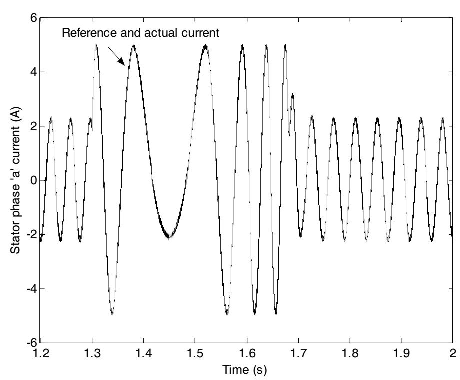

b.

Fig. 5.23. Reversing transient using hysteresis current control: a. actual and reference torque, and speed, b. actual and reference stator phase ‘a’ currents, c. stator phase ‘a’ voltage.

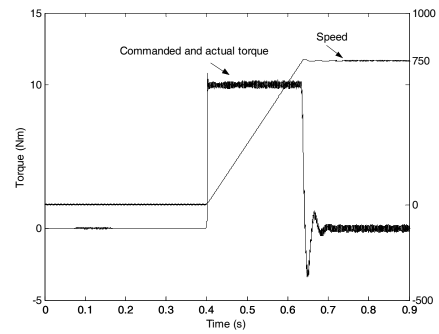

a.

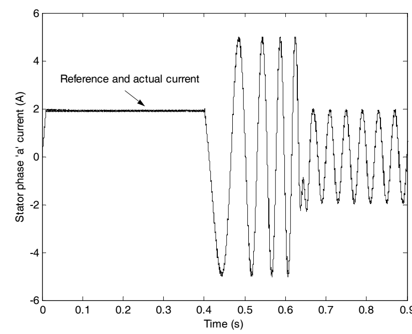

c.

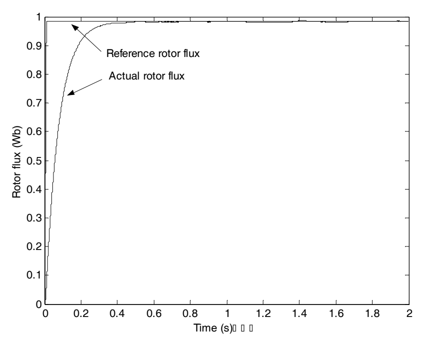

b.

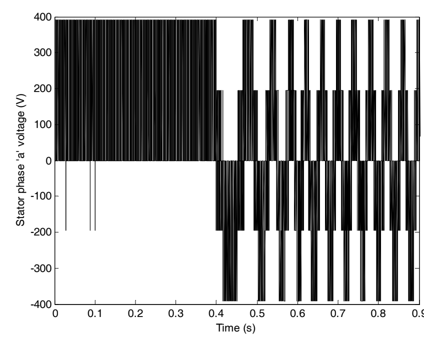

d.

Fig. 5.24. Excitation and acceleration transients using ramp-comparison current control: a. actual and reference rotor flux, b. actual and reference torque, and speed, c. actual and reference stator phase ‘a’ currents, d. stator phase ‘a’ voltage.

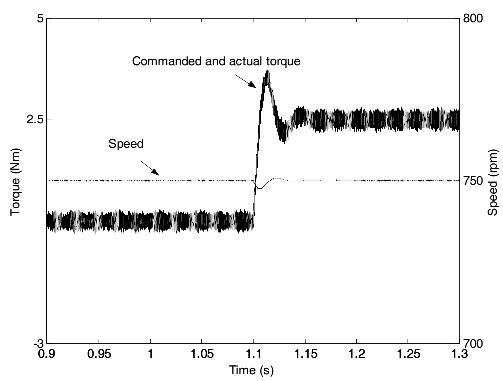

a.

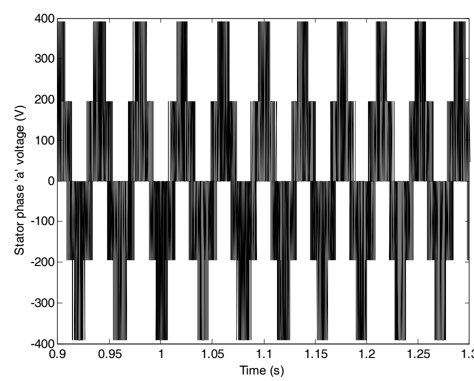

c.

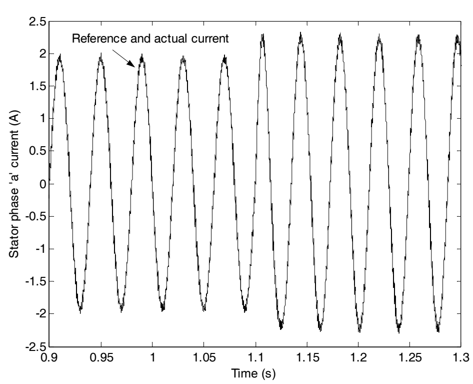

b.

Fig. 5.25. Disturbance rejection transient using ramp-comparison current control: a. actual and reference torque, and speed, b. actual and reference stator phase ‘a’ currents, c. stator phase ‘a’ voltage.

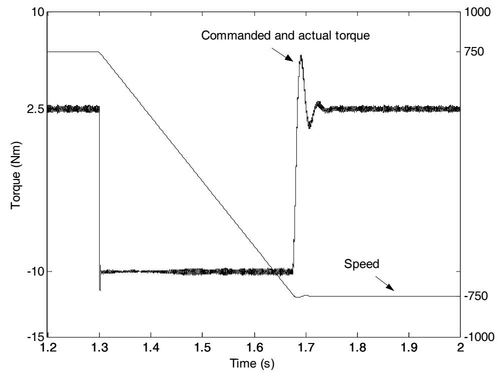

a.

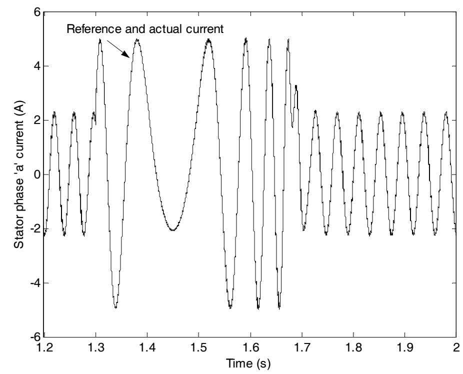

b.

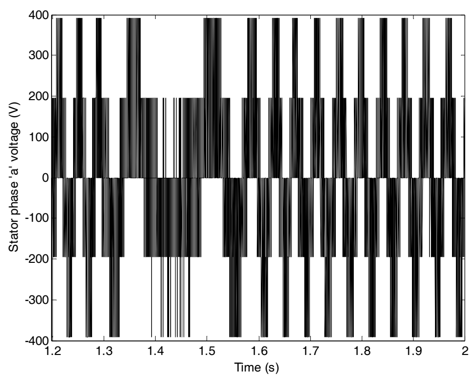

c.

Fig. 5.26. Reversing transient using ramp-comparison current control: a. actual and commanded torque and speed, b. stator phase ‘a’ reference and actual current, c. stator phase ‘a’ voltage.

In case of the three-phase machine only phase ‘a’ voltage and current harmonic spectra are shown at 25 Hz fundamental frequency. The values obtained from the graphs are tabulated in Table 5.21a and Table 5.21b for the six-phase and the three-phase machine, respectively. The values obtained here are in good agreement with the theoretical values given in Table 3.22.

Table 5.21. Harmonic content for six-phase and three-phase machines

a. Fundamental (50 Hz) and third harmonic (150 Hz) components of voltages and currents (from Figs. 5.27-5.28).

$V_a^{(1)}$ (V)	$V_\alpha^{(1)}$ (V)	$V_x^{(1)}$ (V)	$I_a^{(1)}$ (A)	$I_\alpha^{(1)}$ (A)	$I_x^{(1)}$ (mA)
196.5	195.8	2.2	1.35	1.35	0.6

b. Fundamental (25 Hz) component of voltage and current (from Fig. 5.29).

99.6	N/A	N/A	1.35	N/A	N/A

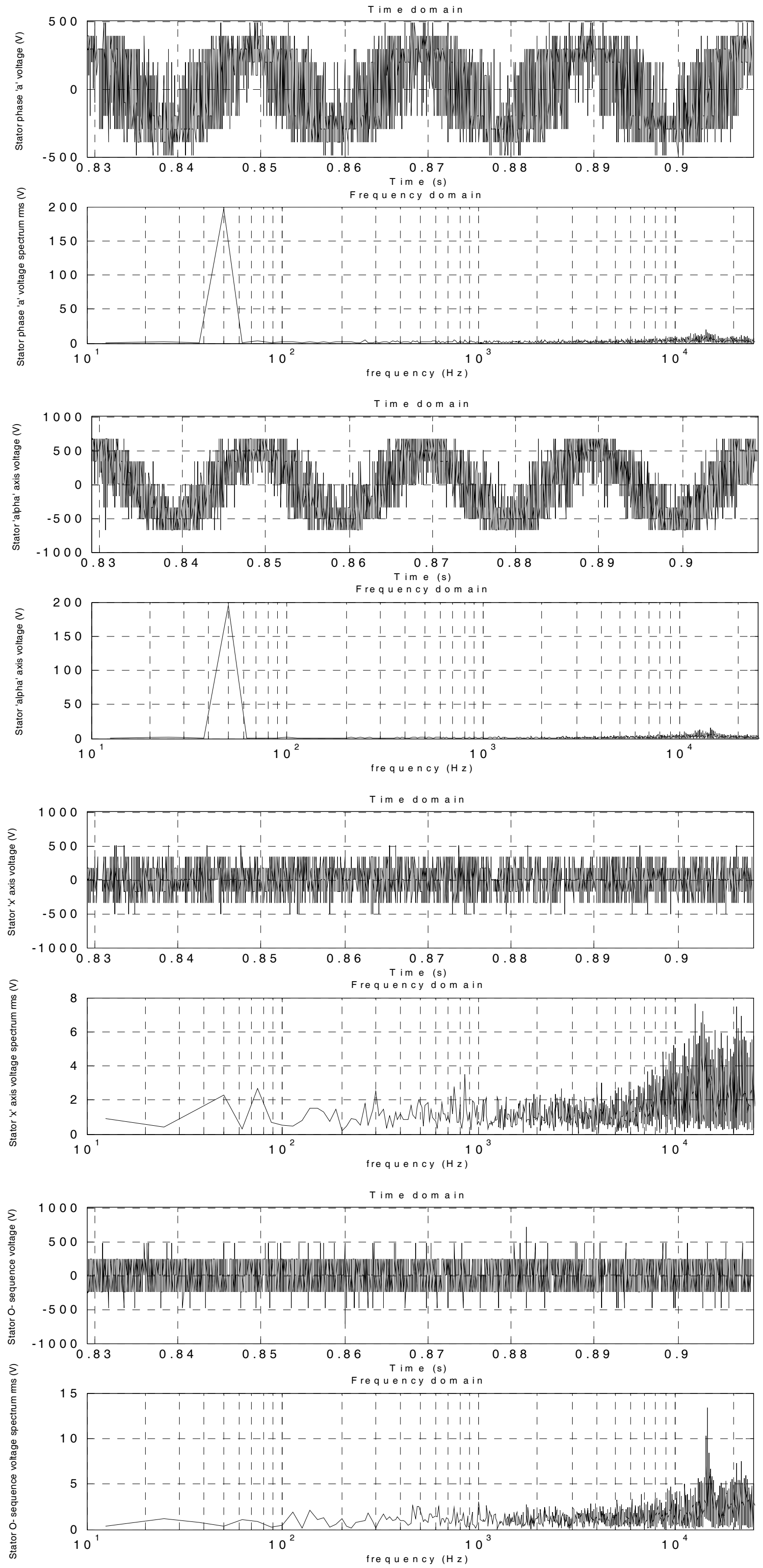

Fig. 5.27. Time domain waveforms and spectra for 50 Hz operation of six-phase machine: phase ‘a’ voltage, α-axis voltage component, x-axis voltage component, and negative zero-sequence voltage component.

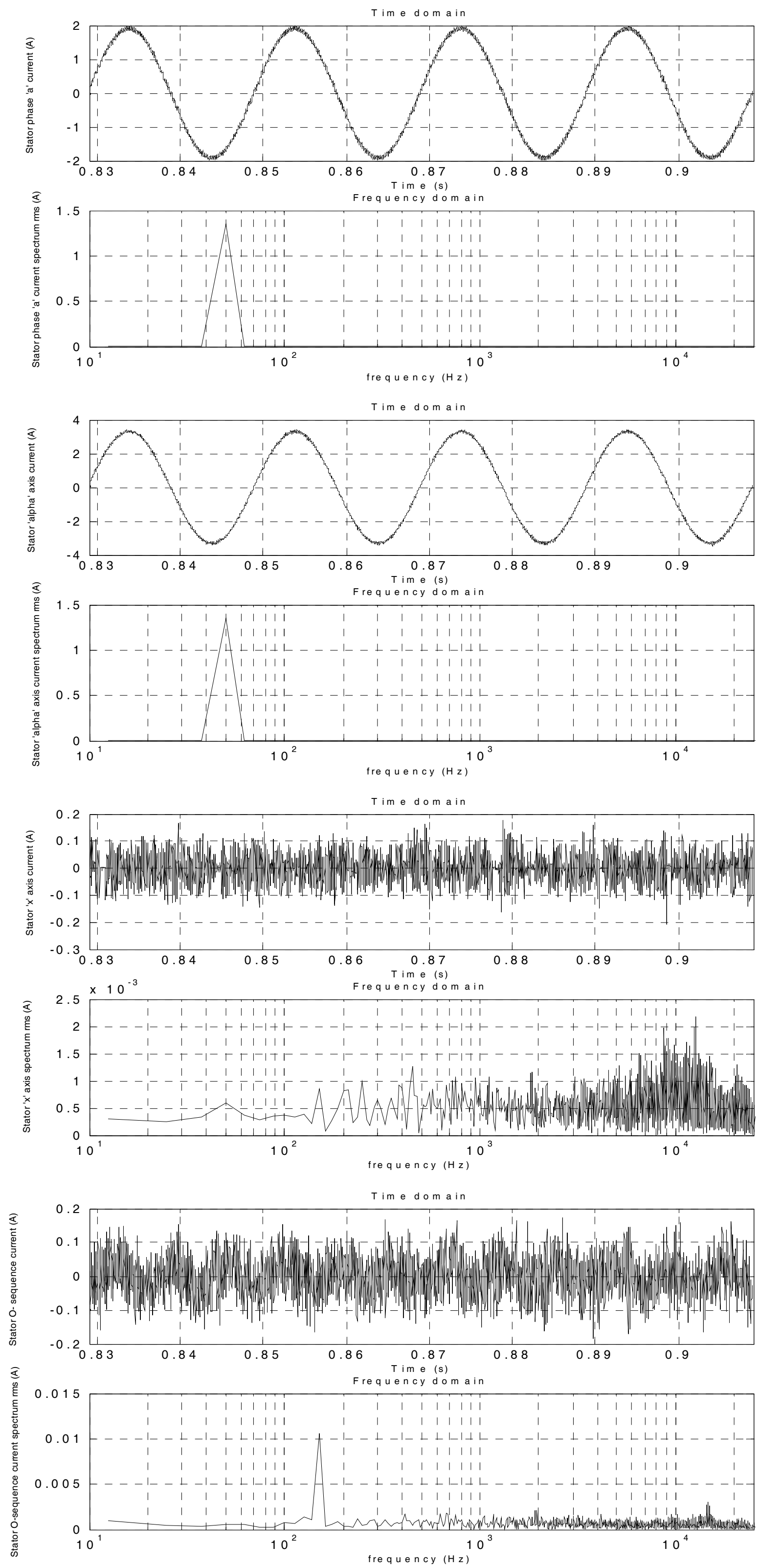

Fig. 5.28. Time domain waveforms and spectra for 50 Hz operation of the six-phase machine: phase ‘a’ current, α-axis current component, x-axis current component, and negative zero-sequence current.

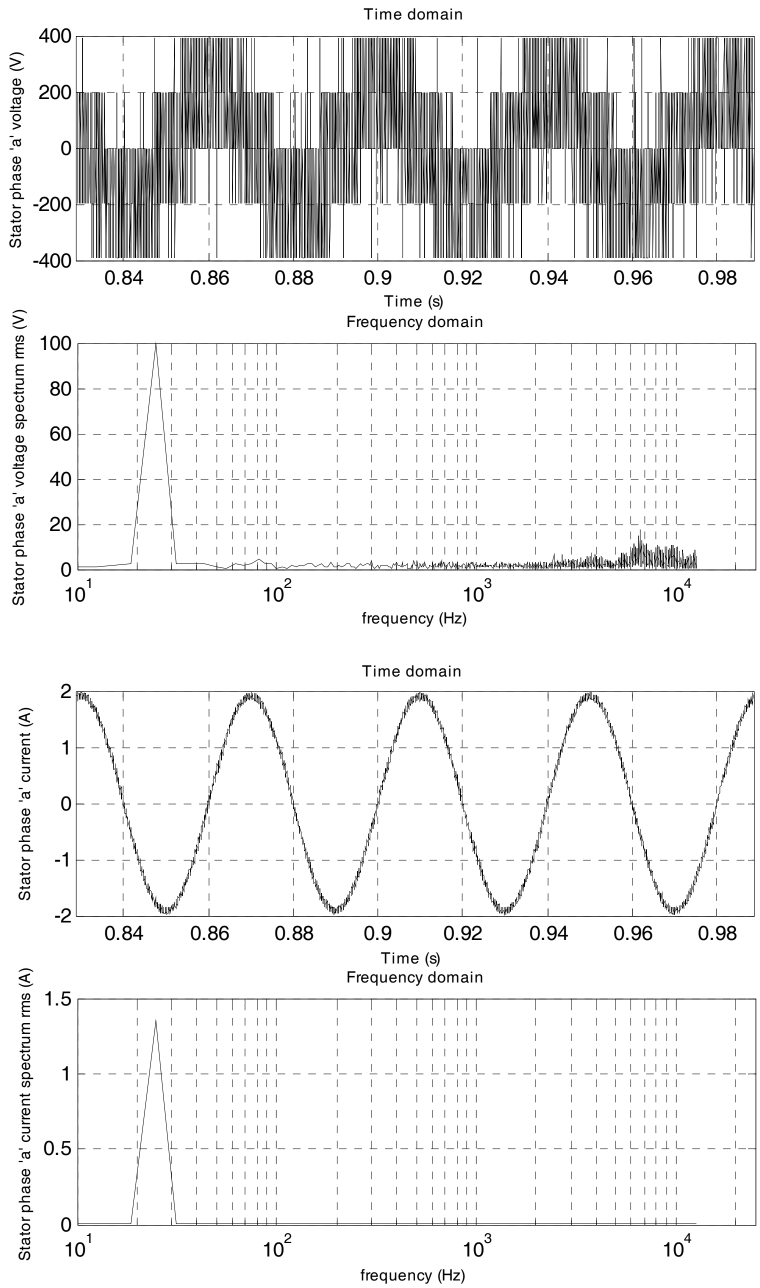

Fig. 5.29. Time domain waveform and spectra for 25 Hz operation of the three-phase machine: phase ‘a’ voltage and phase ‘a’ current.

5.7 SUMMARY

This chapter has elaborated the modelling of the components of a single six-phase vector controlled induction motor drive. The principles of operation of a six-phase VSI in 180° conduction mode and PWM mode were discussed, together with the modelling of a six-phase induction machine and principles of rotor flux oriented control. The analysis of six-phase inverter revealed ten zero and fifty four non-zero space vectors.

Performance of a vector controlled single six-phase induction machine drive and single three-phase machine drive, obtainable with hysteresis current control and ramp-comparison control methods, was further evaluated and illustrated for a number of operating conditions on the basis of simulation results. Full decoupling of rotor flux control and torque control was realised by both current control techniques under the condition of a sufficient voltage reserve. Dynamics, achievable with a six-phase vector controlled induction machine, are shown to be essentially identical to those obtainable with a three-phase induction machine. Steady state analysis of stator voltages and currents was finally performed, using harmonic spectrum analysis.

Chapter 6

MODELLING AND CONTROL OF A TWO-MOTOR SERIES-CONNECTED SIX-PHASE INDUCTION MOTOR DRIVE SYSTEM

6.1 INTRODUCTION

This chapter is devoted to the series-connected two-motor six-phase drive system consisting of a six-phase and a three-phase induction machine. Appropriate phase transposition in the series connection of the two machines leads to complete decoupling of the flux/torque producing currents of one machine from the flux/torque producing currents of the other machine. The complete independent control of the two machines is shown to be possible by feeding them from a single six-phase PWM voltage source inverter and using field oriented control principle. Phase-domain model is developed in section 6.2 by considering three-phase machine as a virtual six-phase machine and then by representing three-phase machine as a standard three-phase machine. Decoupled equations are obtained in orthogonal reference frame and is presented in section 6.3. The model is further transformed into the stationary common reference frame in section 6.4. Finally, in section 6.5, the models in an arbitrary common reference frame and in field oriented reference frames are developed. Section 6.6 describes vector control for the six-phase two-motor drive. The behavior of the drive system is investigated for various transients, the results of which are reported in section 6.7. Hysteresis current control and ramp-comparison current control methods are utilized to control the inverter. Harmonic analysis is done to study the behavior of the six-phase two-motor drive under no-load steady state conditions in section 6.8. The original findings of this chapter are reported in Iqbal and Levi (2004) and Jones et al (2004).

6.2 PHASE-DOMAIN MODELING OF THE SERIES-CONNECTED SIX-PHASE TWO-MOTOR DRIVE

6.2.1 Representation of the three-phase machine as a virtual six-phase machine

Phase domain model of the series-connected six-phase two-motor drive system is developed using two methods. Three-phase machine is at first represented as a virtual six-phase machine and then as a true three-phase machine.

Connection diagram for series connection of stator windings of a six-phase and a three-phase machine is shown in Fig. 6.1 [Jones (2002) and Jones (2005)].

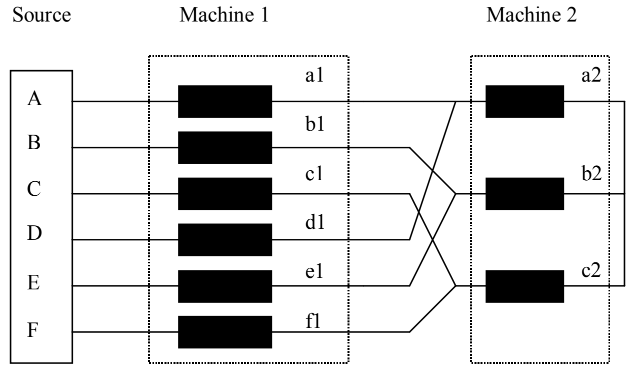

Fig. 6.1. Connection diagram for series connection of a six-phase and a three-phase machine.

This section develops the model of the complete six-phase two-motor drive system by considering the three-phase machine as a virtual six-phase machine. Let the parameters and variables of the six-phase machine be identified with index 1, while index 2 applies to the three-phase machine. Phase domain model of the six-phase machine is given with the equations (5.11)-(5.19) of Chapter 5. Since the system of Fig. 6.1 is six-phase, it is convenient to represent the three-phase machine as a 'virtual' six-phase machine, meaning that the spatial displacement α stays at 60 degrees and the phases *a2, b2, c2* of the three-phase machine are actually phases *a2, c2, e2* of the virtual six-phase machine with spatial displacements of 120 degrees. Hence the three-phase machine can be represented as a virtual six-phase machine with the following set of equations:

$$\begin{aligned} \underline{v}_{s2} &= \underline{R}_{s2}\underline{i}_{s2} + \frac{d\underline{\psi}_{s2}}{dt} \\ \underline{\psi}_{s2} &= \underline{L}_{s2}\underline{i}_{s2} + \underline{L}_{sr2}\underline{i}_{r2} \end{aligned} \tag{6.1}$$

$$\begin{aligned} \underline{v}_{r2} &= \underline{R}_{r2}\underline{i}_{r2} + \frac{d\underline{\psi}_{r2}}{dt} \\ \underline{\psi}_{r2} &= \underline{L}_{r2}\underline{i}_{r2} + \underline{L}_{rs2}\underline{i}_{s2} \end{aligned} \tag{6.2}$$

where

$$\begin{aligned} \underline{v}_{s2} &= \begin{bmatrix} v_{as2} & 0 & v_{cs2} & 0 & v_{es2} & 0 \end{bmatrix}^T \\ \underline{i}_{s2} &= \begin{bmatrix} i_{as2} & 0 & i_{cs2} & 0 & i_{es2} & 0 \end{bmatrix}^T \\ \underline{\psi}_{s2} &= \begin{bmatrix} \psi_{as2} & 0 & \psi_{cs2} & 0 & \psi_{es2} & 0 \end{bmatrix}^T \end{aligned} \tag{6.3}$$

$$\begin{aligned} \underline{v}_{r2} &= \begin{bmatrix} v_{ar2} & 0 & v_{cr2} & 0 & v_{er2} & 0 \end{bmatrix}^T \\ \underline{i}_{r2} &= \begin{bmatrix} i_{ar2} & 0 & i_{cr2} & 0 & i_{er2} & 0 \end{bmatrix}^T \\ \underline{\psi}_{r2} &= \begin{bmatrix} \psi_{ar2} & 0 & \psi_{cr2} & 0 & \psi_{er2} & 0 \end{bmatrix}^T \end{aligned} \tag{6.4}$$

The matrices of stator and rotor inductances are given with ($\alpha = 2\pi/6$):

$$\underline{L}_{s2} = \begin{bmatrix} L_{ls2} + M_2 & 0 & M_2 \cos 2\alpha & 0 & M_2 \cos 4\alpha & 0 \\ 0 & 0 & 0 & 0 & 0 & 0 \\ M_2 \cos 4\alpha & 0 & L_{ls2} + M_2 & 0 & M_2 \cos 2\alpha & 0 \\ 0 & 0 & 0 & 0 & 0 & 0 \\ M_2 \cos 2\alpha & 0 & M_2 \cos 4\alpha & 0 & L_{ls2} + M_2 & 0 \\ 0 & 0 & 0 & 0 & 0 & 0 \end{bmatrix} \tag{6.5}$$

$$\underline{L}_{r2} = \begin{bmatrix} L_{lr2} + M_2 & 0 & M_2 \cos 2\alpha & 0 & M_2 \cos 4\alpha & 0 \\ 0 & 0 & 0 & 0 & 0 & 0 \\ M_2 \cos 4\alpha & 0 & L_{lr2} + M_2 & 0 & M_2 \cos 2\alpha & 0 \\ 0 & 0 & 0 & 0 & 0 & 0 \\ M_2 \cos 2\alpha & 0 & M_2 \cos 4\alpha & 0 & L_{lr2} + M_2 & 0 \\ 0 & 0 & 0 & 0 & 0 & 0 \end{bmatrix} \tag{6.6}$$

while mutual inductance matrices between stator and rotor windings are:

$$\underline{L}_{sr2} = M_2 \begin{bmatrix} \cos(\theta_2) & 0 & \cos(\theta_2 - 4\alpha) & 0 & \cos(\theta_2 - 2\alpha) & 0 \\ 0 & 0 & 0 & 0 & 0 & 0 \\ \cos(\theta_2 - 2\alpha) & 0 & \cos(\theta_2) & 0 & \cos(\theta_2 - 4\alpha) & 0 \\ 0 & 0 & 0 & 0 & 0 & 0 \\ \cos(\theta_2 - 4\alpha) & 0 & \cos(\theta_2 - 2\alpha) & 0 & \cos(\theta_2) & 0 \\ 0 & 0 & 0 & 0 & 0 & 0 \end{bmatrix} \tag{6.7}$$

$$\underline{L}_{rs2} = \underline{L}_{sr2}^T$$

Resistance matrices are:

$$\begin{aligned} \underline{R}_{s2} &= diag(R_{s2} \quad 0 \quad R_{s2} \quad 0 \quad R_{s2} \quad 0) \\ \underline{R}_{r2} &= diag(R_{r2} \quad 0 \quad R_{r2} \quad 0 \quad R_{r2} \quad 0) \end{aligned} \tag{6.8}$$

and the machine torque is:

$$T_{e2} = -P_2 M_2 \left\{ \begin{aligned} &\left(i_{as2} i_{ar2} + i_{cs2} i_{cr2} + i_{es2} i_{er2}\right) \sin\theta_2 + \left(i_{es2} i_{ar2} + i_{as2} i_{cr2} + i_{cs2} i_{er2}\right) \sin(\theta_2 - 4\alpha) + \\ &+ \left(i_{cs2} i_{ar2} + i_{es2} i_{cr2} + i_{as2} i_{er2}\right) \sin(\theta_2 - 2\alpha) \end{aligned} \right\} \tag{6.9}$$

Correlation between machine voltages and inverter voltages is given with Fig. 6.1, where the phases of the three-phase machine are now labelled as *a2*, *c2*, *e2*. Hence

$$\begin{aligned} v_A &= v_{a1} + v_{a2} \qquad & v_B &= v_{b1} + v_{c2} \qquad & v_C &= v_{c1} + v_{e2} \\ v_D &= v_{d1} + v_{a2} \qquad & v_E &= v_{e1} + v_{c2} \qquad & v_F &= v_{f1} + v_{e2} \end{aligned} \tag{6.10}$$

or in matrix form

$$\underline{v}^{INV} = \begin{bmatrix} v_A \\ v_B \\ v_C \\ v_D \\ v_E \\ v_F \end{bmatrix} = \begin{bmatrix} v_{as1} + v_{as2} \\ v_{bs1} + v_{cs2} \\ v_{cs1} + v_{es2} \\ v_{ds1} + v_{as2} \\ v_{es1} + v_{cs2} \\ v_{fs1} + v_{es2} \end{bmatrix} \tag{6.10a}$$

Correlation between machine currents and inverter currents is the following:

$$\underline{i}_{s1} = \begin{bmatrix} i_{as1} \\ i_{bs1} \\ i_{cs1} \\ i_{ds1} \\ i_{es1} \\ i_{fs1} \end{bmatrix} = \begin{bmatrix} i_A \\ i_B \\ i_C \\ i_D \\ i_E \\ i_F \end{bmatrix} = \underline{i}^{INV} \qquad \underline{i}_{s2} = \begin{bmatrix} i_{as2} \\ i_{bs2} \\ i_{cs2} \\ i_{ds2} \\ i_{es2} \\ i_{fs2} \end{bmatrix} = \begin{bmatrix} i_A + i_D \\ 0 \\ i_B + i_E \\ 0 \\ i_C + i_F \\ 0 \end{bmatrix} \tag{6.11}$$

Voltage equations of the complete two-motor system are formulated in terms of inverter currents and voltages. The system is of the 18th order, since the three-phase phase machine is represented as a virtual six-phase machine. However, three rotor equations will be redundant (equations for rotor phases *b,d,f*). The complete set of voltage equations can be written as

$$\begin{bmatrix} \underline{v}^{INV} \\ \underline{0} \\ \underline{0} \end{bmatrix} = \begin{bmatrix} \underline{R}_{s1} + \underline{R}_{s2}' & \underline{0} & \underline{0} \\ \underline{0} & \underline{R}_{r1} & \underline{0} \\ \underline{0} & \underline{0} & \underline{R}_{r2} \end{bmatrix} \begin{bmatrix} \underline{i}^{INV} \\ \underline{i}_{r1} \\ \underline{i}_{r2} \end{bmatrix} + \frac{d}{dt} \left\{ \begin{bmatrix} \underline{L}_{s1} + \underline{L}_{s2}' & \underline{L}_{sr1} & \underline{L}_{sr2}' \\ \underline{L}_{rs1} & \underline{L}_{r1} & \underline{0} \\ \underline{L}_{rs2}' & \underline{0} & \underline{L}_{r2} \end{bmatrix} \begin{bmatrix} \underline{i}^{INV} \\ \underline{i}_{r1} \\ \underline{i}_{r2} \end{bmatrix} \right\} \tag{6.12}$$

All the inductance, resistance and null sub-matrices are of six by six order. Primed sub-matrices are those that have been modified, with respect to their original form given above, in the process of series connection of two machines through the phase transposition operation. These sub-matrices are equal to:

$$\underline{R}_{s2}' = \begin{bmatrix} R_{s2} & 0 & 0 & R_{s2} & 0 & 0 \\ 0 & R_{s2} & 0 & 0 & R_{s2} & 0 \\ 0 & 0 & R_{s2} & 0 & 0 & R_{s2} \\ R_{s2} & 0 & 0 & R_{s2} & 0 & 0 \\ 0 & R_{s2} & 0 & 0 & R_{s2} & 0 \\ 0 & 0 & R_{s2} & 0 & 0 & R_{s2} \end{bmatrix} \tag{6.13}$$

$$\underline{L}_{s2}' = \begin{bmatrix} L_{ls2} + M_2 & M_2\cos 2\alpha & M_2\cos 4\alpha & L_{ls2} + M_2 & M_2\cos 2\alpha & M_2\cos 4\alpha \\ M_2\cos 4\alpha & L_{ls2} + M_2 & M_2\cos 2\alpha & M_2\cos 4\alpha & L_{ls2} + M_2 & M_2\cos 2\alpha \\ M_2\cos 2\alpha & M_2\cos 4\alpha & L_{ls2} + M_2 & M_2\cos 2\alpha & M_2\cos 4\alpha & L_{ls2} + M_2 \\ L_{ls2} + M_2 & M_2\cos 2\alpha & M_2\cos 4\alpha & L_{ls2} + M_2 & M_2\cos 2\alpha & M_2\cos 4\alpha \\ M_2\cos 4\alpha & L_{ls2} + M_2 & M_2\cos 2\alpha & M_2\cos 4\alpha & L_{ls2} + M_2 & M_2\cos 2\alpha \\ M_2\cos 2\alpha & M_2\cos 4\alpha & L_{ls2} + M_2 & M_2\cos 2\alpha & M_2\cos 4\alpha & L_{ls2} + M_2 \end{bmatrix} \tag{6.14}$$

$$\underline{L}_{sr2}' = M_2 \begin{bmatrix} \cos\theta_2 & 0 & \cos(\theta_2 - 4\alpha) & 0 & \cos(\theta_2 - 2\alpha) & 0 \\ \cos(\theta_2 - 2\alpha) & 0 & \cos\theta_2 & 0 & \cos(\theta_2 - 4\alpha) & 0 \\ \cos(\theta_2 - 4\alpha) & 0 & \cos(\theta_2 - 2\alpha) & 0 & \cos\theta_2 & 0 \\ \cos\theta_2 & 0 & \cos(\theta_2 - 4\alpha) & 0 & \cos(\theta_2 - 2\alpha) & 0 \\ \cos(\theta_2 - 2\alpha) & 0 & \cos\theta_2 & 0 & \cos(\theta_2 - 4\alpha) & 0 \\ \cos(\theta_2 - 4\alpha) & 0 & \cos(\theta_2 - 2\alpha) & 0 & \cos\theta_2 & 0 \end{bmatrix} \tag{6.15}$$

$$\underline{L}_{rs2}' = \left(\underline{L}_{sr2}'\right)^T$$

Torque equations of the two machines can be given in terms of inverter currents as

$$T_{e2} = -P_2 M_2 \begin{Bmatrix} \left((i_A + i_D)i_{ar2} + (i_B + i_E)i_{cr2} + (i_C + i_F)i_{er2}\right)\sin\theta_2 + \\ +\left((i_C + i_F)i_{ar2} + (i_A + i_D)i_{cr2} + (i_B + i_E)i_{er2}\right)\sin(\theta_2 - 4\alpha) + \\ +\left((i_B + i_E)i_{ar2} + (i_C + i_F)i_{cr2} + (i_A + i_D)i_{er2}\right)\sin(\theta_2 - 2\alpha) \end{Bmatrix} \tag{6.16}$$

$$T_{e1} = -P_1 M_1 \begin{Bmatrix} \left(i_A i_{ar1} + i_B i_{br1} + i_C i_{cr1} + i_D i_{dr1} + i_E i_{er1} + i_F i_{fr1}\right)\sin\theta_1 + \\ \left(i_F i_{ar1} + i_A i_{br1} + i_B i_{cr1} + i_C i_{dr1} + i_D i_{er1} + i_E i_{fr1}\right)\sin(\theta_1 - 5\alpha) + \\ \left(i_E i_{ar1} + i_F i_{br1} + i_A i_{cr1} + i_B i_{dr1} + i_C i_{er1} + i_D i_{fr1}\right)\sin(\theta_1 - 4\alpha) + \\ \left(i_D i_{ar1} + i_E i_{br1} + i_F i_{cr1} + i_A i_{dr1} + i_B i_{er1} + i_C i_{fr1}\right)\sin(\theta_1 - 3\alpha) + \\ \left(i_C i_{ar1} + i_D i_{br1} + i_E i_{cr1} + i_F i_{dr1} + i_A i_{er1} + i_B i_{fr1}\right)\sin(\theta_1 - 2\alpha) + \\ \left(i_B i_{ar1} + i_C i_{br1} + i_D i_{cr1} + i_E i_{dr1} + i_F i_{er1} + i_A i_{fr1}\right)\sin(\theta_1 - \alpha) \end{Bmatrix} \tag{6.17}$$

6.2.2 Representation of the three-phase machine as a standard three-phase machine

Another possibility is to develop phase domain model in state space form by representing the three-phase machine as a three-phase machine. Equations of the six-phase machine remain to be given with (5.11)-(5.19). Equations of the three-phase machine (6.1)-(6.2) still hold true. However, (6.3)-(6.8) now become (rotor phases are *a ,c, e)*:

$$\begin{aligned} \underline{v}_{s2} &= \begin{bmatrix} v_{as2} & v_{cs2} & v_{es2} \end{bmatrix}^T \\ \underline{i}_{s2} &= \begin{bmatrix} i_{as2} & i_{cs2} & i_{es2} \end{bmatrix}^T \\ \underline{\psi}_{s2} &= \begin{bmatrix} \psi_{as2} & \psi_{cs2} & \psi_{es2} \end{bmatrix}^T \end{aligned} \tag{6.18}$$

$$\begin{aligned} \underline{v}_{r2} &= \begin{bmatrix} v_{ar2} & v_{cr2} & v_{er2} \end{bmatrix}^T \\ \underline{i}_{r2} &= \begin{bmatrix} i_{ar2} & i_{cr2} & i_{er2} \end{bmatrix}^T \\ \underline{\psi}_{r2} &= \begin{bmatrix} \psi_{ar2} & \psi_{cr2} & \psi_{er2} \end{bmatrix}^T \end{aligned} \tag{6.19}$$

$$\underline{L}_{s2} = \begin{bmatrix} L_{ls2} + M_2 & M_2\cos 2\alpha & M_2\cos 4\alpha \\ M_2\cos 4\alpha & L_{ls2} + M_2 & M_2\cos 2\alpha \\ M_2\cos 2\alpha & M_2\cos 4\alpha & L_{ls2} + M_2 \end{bmatrix} \tag{6.20}$$

$$\underline{L}_{r2} = \begin{bmatrix} L_{lr2} + M_2 & M_2 \cos 2\alpha & M_2 \cos 4\alpha \\ M_2 \cos 4\alpha & L_{lr2} + M_2 & M_2 \cos 2\alpha \\ M_2 \cos 2\alpha & M_2 \cos 4\alpha & L_{lr2} + M_2 \end{bmatrix} \tag{6.21}$$

$$\begin{aligned} \underline{L}_{sr2} &= M_2 \begin{bmatrix} \cos\theta_2 & \cos(\theta_2 - 4\alpha) & \cos(\theta_2 - 2\alpha) \\ \cos(\theta_2 - 2\alpha) & \cos\theta_2 & \cos(\theta_2 - 4\alpha) \\ \cos(\theta_2 - 4\alpha) & \cos(\theta_2 - 2\alpha) & \cos\theta_2 \end{bmatrix} \\ \underline{L}_{rs2} &= \underline{L}_{sr2}^T \end{aligned} \tag{6.22}$$

$$\begin{aligned} \underline{R}_{s2} &= diag\begin{bmatrix} R_{s2} & R_{s2} & R_{s2} \end{bmatrix} \\ \underline{R}_{r2} &= diag\begin{bmatrix} R_{r2} & R_{r2} & R_{r2} \end{bmatrix} \end{aligned} \tag{6.23}$$

Torque equation (6.16) remains unchanged with this representation of the three-phase machine.

The system of equations for the complete two-motor drive is however now of the 15th order due to the three-phase machine representation in standard manner. The complete set of voltage equations remain to be given with (6.12). However, the zero sub-matrix in the second row, third column is of six by three order while the zero sub-matrix in the third row, second column is of three by six order. The primed sub-matrices of (6.12) are now equal to:

$$\underline{R}_{s2}' = \begin{bmatrix} \underline{R}_{s2} & \underline{R}_{s2} \\ \underline{R}_{s2} & \underline{R}_{s2} \end{bmatrix} \tag{6.24}$$

$$\underline{L}_{s2}' = \begin{bmatrix} \underline{L}_{s2} & \underline{L}_{s2} \\ \underline{L}_{s2} & \underline{L}_{s2} \end{bmatrix} \tag{6.25}$$

$$\begin{aligned} \underline{L}_{sr2}' &= \begin{bmatrix} \underline{L}_{sr2} \\ \underline{L}_{sr2} \end{bmatrix} \\ \underline{L}_{rs2}' &= \begin{bmatrix} \underline{L}_{rs2} & \underline{L}_{rs2} \end{bmatrix} = \begin{bmatrix} \underline{L}_{sr2}^T & \underline{L}_{sr2}^T \end{bmatrix} \end{aligned} \tag{6.26}$$

Torque equations for the six-phase two-motor system in terms of inverter currents remain the same as in (6.16) and (6.17). The two-motor model in phase variable form of the 15th order is considered further on.

6.3 APPLICATION OF THE DECOUPLING TRANSFORMATION MATRIX

To obtain orthogonal form of the model, the following Clark's decoupling transformation matrices in power invariant form are applied to the phase variable model:

$$\underline{C}_{(6)} = \sqrt{\frac{2}{6}} \begin{array}{c} \alpha \\ \beta \\ x \\ y \\ 0_+ \\ 0_- \end{array} \begin{bmatrix} 1 & \cos\alpha & \cos 2\alpha & \cos 3\alpha & \cos 4\alpha & \cos 5\alpha \\ 0 & \sin\alpha & \sin 2\alpha & \sin 3\alpha & \sin 4\alpha & \sin 5\alpha \\ 1 & \cos 2\alpha & \cos 4\alpha & \cos 6\alpha & \cos 8\alpha & \cos 10\alpha \\ 0 & \sin 2\alpha & \sin 4\alpha & \sin 6\alpha & \sin 8\alpha & \sin 10\alpha \\ 1/\sqrt{2} & 1/\sqrt{2} & 1/\sqrt{2} & 1/\sqrt{2} & 1/\sqrt{2} & 1/\sqrt{2} \\ 1/\sqrt{2} & -1/\sqrt{2} & 1/\sqrt{2} & -1/\sqrt{2} & 1/\sqrt{2} & -1/\sqrt{2} \end{bmatrix} \tag{6.27a}$$

$$\underline{C}_{(3)} = \sqrt{\frac{2}{3}} \begin{bmatrix} 1 & \cos 2\alpha & \cos 4\alpha \\ 0 & \sin 2\alpha & \sin 4\alpha \\ 1/\sqrt{2} & 1/\sqrt{2} & 1/\sqrt{2} \end{bmatrix} \tag{6.27b}$$

Axis components of inverter output phase voltages are

$$\underline{v}_{\alpha\beta}^{INV} = \begin{bmatrix} v_\alpha^{INV} \\ v_\beta^{INV} \\ v_x^{INV} \\ v_y^{INV} \\ v_{0+}^{INV} \\ v_{0-}^{INV} \end{bmatrix} = \underline{C}_{(6)} \begin{bmatrix} v_A \\ v_B \\ v_C \\ v_D \\ v_E \\ v_F \end{bmatrix} \tag{6.28}$$

Application of (6.27a)-(6.28) in conjunction with (6.10a) yields:

$$\underline{v}_{\alpha\beta}^{INV} = \begin{bmatrix} v_\alpha^{INV} \\ v_\beta^{INV} \\ v_x^{INV} \\ v_y^{INV} \\ v_{0+}^{INV} \\ v_{0-}^{INV} \end{bmatrix} = \underline{C}_{(6)} \begin{bmatrix} v_{a1} + v_{a2} \\ v_{b1} + v_{c2} \\ v_{c1} + v_{e2} \\ v_{d1} + v_{a2} \\ v_{e1} + v_{c2} \\ v_{f1} + v_{e2} \end{bmatrix} = \begin{bmatrix} v_{\alpha s1} \\ v_{\beta s1} \\ v_{xs1} + \sqrt{2} v_{\alpha s2} \\ v_{ys1} + \sqrt{2} v_{\beta s2} \\ v_{0+s1} + \sqrt{2} v_{0s2} \\ v_{0-s1} \end{bmatrix} \tag{6.29}$$

Application of the decoupling transformation changes (6.12) into

$$\begin{aligned} \begin{bmatrix} \underline{v}_{\alpha\beta}^{INV} \\ \underline{0} \\ \underline{0} \end{bmatrix} &= \begin{bmatrix} \underline{C}_{(6)} & \underline{0} & \underline{0} \\ \underline{0} & \underline{C}_{(6)} & \underline{0} \\ \underline{0} & \underline{0} & \underline{C}_{(3)} \end{bmatrix} \begin{bmatrix} \underline{R}_{s1} + \underline{R}_{s2}' & \underline{0} & \underline{0} \\ \underline{0} & \underline{R}_{r1} & \underline{0} \\ \underline{0} & \underline{0} & \underline{R}_{r2} \end{bmatrix} \begin{bmatrix} \underline{C}_{(6)}^T & \underline{0} & \underline{0} \\ \underline{0} & \underline{C}_{(6)}^T & \underline{0} \\ \underline{0} & \underline{0} & \underline{C}_{(3)}^T \end{bmatrix} \begin{bmatrix} \underline{i}_{\alpha\beta}^{INV} \\ \underline{i}_{\alpha\beta}^{r1} \\ \underline{i}_{\alpha\beta}^{r2} \end{bmatrix} + \\ &+ \frac{d}{dt} \left\{ \begin{bmatrix} \underline{C}_{(6)} & \underline{0} & \underline{0} \\ \underline{0} & \underline{C}_{(6)} & \underline{0} \\ \underline{0} & \underline{0} & \underline{C}_{(3)} \end{bmatrix} \begin{bmatrix} \underline{L}_{s1} + \underline{L}_{s2}' & \underline{L}_{sr1} & \underline{L}_{sr2}' \\ \underline{L}_{rs1} & \underline{L}_{r1} & \underline{0} \\ \underline{L}_{rs2}' & \underline{0} & \underline{L}_{r2} \end{bmatrix} \begin{bmatrix} \underline{C}_{(6)}^T & \underline{0} & \underline{0} \\ \underline{0} & \underline{C}_{(6)}^T & \underline{0} \\ \underline{0} & \underline{0} & \underline{C}_{(3)}^T \end{bmatrix} \begin{bmatrix} \underline{i}_{\alpha\beta}^{INV} \\ \underline{i}_{\alpha\beta}^{r1} \\ \underline{i}_{\alpha\beta}^{r2} \end{bmatrix} \right\} \end{aligned} \tag{6.30}$$

Further derivation closely corresponds to the one of section 4.4 and is therefore omitted.

Manipulation of (6.30) yields the complete decoupled model of the six-phase two-motor drive system. Inverter-stator voltage equations are obtained as:

$$
\begin{aligned}
v_\alpha^{INV} &= R_{s1} i_\alpha^{INV} + L_{s1}\frac{di_\alpha^{INV}}{dt} + \frac{d}{dt}L_{m1}\left(\cos\theta_1 i_{\alpha r1} - \sin\theta_1 i_{\beta r1}\right)\\
v_\beta^{INV} &= R_{s1} i_\beta^{INV} + L_{s1}\frac{di_\beta^{INV}}{dt} + \frac{d}{dt}L_{m1}\left(\sin\theta_1 i_{\alpha r1} - \cos\theta_1 i_{\beta r1}\right)\\
v_x^{INV} &= R_{s1} i_x^{INV} + L_{ls1}\frac{di_x^{INV}}{dt} + \sqrt{2}\left(R_{s2}\sqrt{2}i_x^{INV} + L_{s2}\frac{d\sqrt{2}i_x^{INV}}{dt} + L_{m2}\frac{d}{dt}\left(\cos\theta_2 i_{\alpha r2} - \sin\theta_2 i_{\beta r2}\right)\right)\\
v_y^{INV} &= R_{s1} i_y^{INV} + L_{ls1}\frac{di_y^{INV}}{dt} + \sqrt{2}\left(R_{s2}\sqrt{2}i_y^{INV} + L_{s2}\frac{d\sqrt{2}i_y^{INV}}{dt} + L_{m2}\frac{d}{dt}\left(\sin\theta_2 i_{\alpha r2} + \cos\theta_2 i_{\beta r2}\right)\right)\\
v_{0+}^{INV} &= R_{s1} i_{0+}^{INV} + L_{ls1}\frac{di_{0+}^{INV}}{dt} + \sqrt{2}\left(R_{s2}\sqrt{2}i_{0+}^{INV} + L_{ls2}\frac{d\sqrt{2}i_{0+}^{INV}}{dt}\right)\\
v_{0-}^{INV} &= R_{s1} i_{0-}^{INV} + L_{ls1}\frac{di_{0-}^{INV}}{dt}
\end{aligned}
\tag{6.31}
$$

where $L_{m1} = 3M_1$, $L_{m2} = 1.5M_2$. Relationship between inverter current axis components and axis components of stator currents of the two machines is found using (6.11) and (6.27) in the following form:

$$
\begin{aligned}
i_\alpha^{INV} &= i_{\alpha s1}\\
i_\beta^{INV} &= i_{\beta s1}\\
i_x^{INV} &= i_{xs1} = i_{\alpha s2}/\sqrt{2}\\
i_y^{INV} &= i_{ys1} = i_{\beta s2}/\sqrt{2}\\
i_{0+}^{INV} &= i_{0+s1} = i_{0s2}/\sqrt{2}\\
i_{0-}^{INV} &= i_{0-s1}
\end{aligned}
\tag{6.32}
$$

Rotor voltage equations of the six-phase machine result in the form:

$$
\begin{aligned}
0 &= R_{r1} i_{\alpha r1} + L_{r1}\frac{di_{\alpha r1}}{dt} + \frac{d}{dt}L_{m1}\left(\cos\theta_1 i_\alpha^{INV} + \sin\theta_1 i_\beta^{INV}\right)\\
0 &= R_{r1} i_{\beta r1} + L_{r1}\frac{di_{\beta r1}}{dt} + \frac{d}{dt}L_{m1}\left(-\sin\theta_1 i_\alpha^{INV} + \cos\theta_1 i_\beta^{INV}\right)\\
0 &= R_{r1} i_k + L_{lr1}\frac{di_k}{dt} \qquad k = xr1,\ yr1,\ 0+r1,\ 0-r1
\end{aligned}
\tag{6.33}
$$

while rotor voltage equations of the three-phase machine become:

$$
\begin{aligned}
0 &= R_{r2} i_{\alpha r2} + L_{r2}\frac{di_{\alpha r2}}{dt} + \frac{d}{dt}\sqrt{2}L_{m2}\left(\cos\theta_2 i_x^{INV} + \sin\theta_2 i_y^{INV}\right)\\
0 &= R_{r2} i_{\beta r2} + L_{r2}\frac{di_{\beta r2}}{dt} + \frac{d}{dt}\sqrt{2}L_{m2}\left(-\sin\theta_2 i_x^{INV} + \cos\theta_2 i_y^{INV}\right)\\
0 &= R_{r2} i_{0r2} + L_{lr2}\frac{di_{0r2}}{dt}
\end{aligned}
\tag{6.34}
$$

Torque equations of the two machines are

$$
\begin{aligned}
T_{e1} &= P_1 L_{m1}\left[\cos(\theta_1)\left(i_{\alpha r1} i_\beta^{INV} - i_{\beta r1} i_\alpha^{INV}\right) - \sin(\theta_1)\left(i_{\alpha r1} i_\alpha^{INV} + i_{\beta r1} i_\beta^{INV}\right)\right]\\
T_{e2} &= \sqrt{2}P_2 L_{m2}\left[\cos(\theta_2)\left(i_{\alpha r2} i_y^{INV} - i_{\beta r2} i_x^{INV}\right) - \sin(\theta_2)\left(i_{\alpha r2} i_x^{INV} + i_{\beta r2} i_y^{INV}\right)\right]
\end{aligned}
\tag{6.35}
$$

6.4 TRANSFORMATION OF THE MODEL INTO THE STATIONARY COMMON REFERENCE FRAME

Since the model is formulated in stationary common reference frame, axis voltage components of the supply remain to be given with (6.28)-(6.29),

$$\underline{v}_{\alpha\beta}^{INV} = \begin{bmatrix} v_{\alpha}^{INV} \\ v_{\beta}^{INV} \\ v_{x}^{INV} \\ v_{y}^{INV} \\ v_{0+}^{INV} \\ v_{0-}^{INV} \end{bmatrix} \tag{6.36}$$

Rotational transformation is again applied to rotor equations of the two machines. The form of transformation matrices is identical to (4.38)-(4.39), the only difference being in dimensions of the matrices (6x6 and 3x3 here, 5x5 in (4.38)-(4.39)). Once more, only $\alpha - \beta$ equations are transformed for the reasons detailed in section 4.5. The obtained model in the stationary common reference frame is described with (4.42),

$$\underline{v}_{dq} = \underline{R}\,\underline{i}_{dq} + \frac{d\left(\underline{L}_{dq}\,\underline{i}_{dq}\right)}{dt} + \underline{\Omega}\,\underline{G}\,\underline{i}_{dq} \tag{6.37}$$

where the system is of the 15th order and

$$\underline{v}_{dq} = \begin{bmatrix} \underline{v}_{\alpha\beta}^{INV} \\ \underline{0} \\ \underline{0} \end{bmatrix} \qquad \underline{i}_{dq} = \begin{bmatrix} \underline{i}_{\alpha\beta}^{INV} \\ \underline{i}_{dq}^{r1} \\ \underline{i}_{dq}^{r2} \end{bmatrix} \tag{6.38}$$

In (6.38)

$$\begin{aligned} \underline{v}_{\alpha\beta}^{INV} &= \begin{bmatrix} v_{\alpha}^{INV} & v_{\beta}^{INV} & v_{x}^{INV} & v_{y}^{INV} & v_{0+}^{INV} & v_{0-}^{INV} \end{bmatrix}^T \\ \underline{i}_{\alpha\beta}^{INV} &= \begin{bmatrix} i_{\alpha}^{INV} & i_{\beta}^{INV} & i_{x}^{INV} & i_{y}^{INV} & i_{0+}^{INV} & i_{0-}^{INV} \end{bmatrix}^T \end{aligned} \tag{6.39}$$

$$\begin{aligned} \underline{i}_{dq}^{r1} &= \begin{bmatrix} i_{dr1} & i_{qr1} & i_{xr1} & i_{yr1} & i_{0+r1} & i_{0-r1} \end{bmatrix}^T \\ \underline{i}_{dq}^{r2} &= \begin{bmatrix} i_{dr2} & i_{qr2} & i_{0r2} \end{bmatrix}^T \end{aligned} \tag{6.40}$$

The resistance and inductance matrices of (6.37) can be written as

$$\underline{R} = \begin{bmatrix} \underline{R}_{s1} + \underline{R}_{s2}\,' & \underline{0} & \underline{0} \\ \underline{0} & \underline{R}_{r1} & \underline{0} \\ \underline{0} & \underline{0} & \underline{R}_{r2} \end{bmatrix} \tag{6.41}$$

$$\underline{L}_{dq} = \begin{bmatrix} \underline{L}_{dq}^{s1} + \underline{L}_{dq}^{s2}\,' & \underline{L}_{dq}^{sr1} & \underline{L}_{dq}^{sr2}\,' \\ \underline{L}_{dq}^{rs1} & \underline{L}_{dq}^{r1} & \underline{0} \\ \underline{L}_{dq}^{rs2}\,' & \underline{0} & \underline{L}_{dq}^{r2} \end{bmatrix} \tag{6.42}$$

Submatrices of (6.41)-(6.42) are given with:

$$\underline{R}_{s2}\,' = 2diag\left[0 \quad 0 \quad R_{s2} \quad R_{s2} \quad R_{s2} \quad 0\right] \tag{6.43}$$

$$\underline{L}_{dq}^{s2}\,' = 2diag\left[0 \quad 0 \quad L_{ls2}+L_{m2} \quad L_{ls2}+L_{m2} \quad L_{ls2} \quad 0\right] \tag{6.44}$$

$$\underline{L}_{dq}^{s1} = diag\left[L_{ls1}+L_{m1} \quad L_{ls1}+L_{m1} \quad L_{ls1} \quad L_{ls1} \quad L_{ls1} \quad L_{ls1}\right] \tag{6.45}$$

$$\underline{L}_{dq}^{r1} = diag\left[L_{lr1}+L_{m1} \quad L_{lr1}+L_{m1} \quad L_{lr1} \quad L_{lr1} \quad L_{lr1} \quad L_{lr1}\right] \tag{6.46}$$

$$\underline{R}_{s1} = diag\left[R_{s1} \quad R_{s1} \quad R_{s1} \quad R_{s1} \quad R_{s1} \quad R_{s1}\right] \tag{6.47}$$

$$\underline{R}_{r1} = diag\left[R_{r1} \quad R_{r1} \quad R_{r1} \quad R_{r1} \quad R_{r1} \quad R_{r1}\right] \tag{6.48}$$

$$\underline{R}_{r2} = diag\left[R_{r2} \quad R_{r2} \quad R_{r2}\right] \tag{6.49}$$

$$\underline{L}_{dq}^{r2} = diag\left[L_{lr2}+L_{m2} \quad L_{lr2}+L_{m2} \quad L_{lr2}\right] \tag{6.50}$$

$$\underline{L}_{dq}^{sr1} = L_{m1} diag\left[1 \quad 1 \quad 0 \quad 0 \quad 0 \quad 0\right] \tag{6.51}$$

$$\underline{L}_{dq}^{rs1} = L_{m1} diag\left[1 \quad 1 \quad 0 \quad 0 \quad 0 \quad 0\right] \tag{6.52}$$

$$\underline{L}_{dq}^{sr2}\,' = \sqrt{2} L_{m2} \begin{bmatrix} 0 & 0 & 0 \\ 0 & 0 & 0 \\ 1 & 0 & 0 \\ 0 & 1 & 0 \\ 0 & 0 & 0 \\ 0 & 0 & 0 \end{bmatrix} \tag{6.53}$$

$$\underline{L}_{dq}^{rs2}\,' = \left(\underline{L}_{dq}^{sr2}\,'\right)^T = \sqrt{2} L_{m2} \begin{bmatrix} 0 & 0 & 1 & 0 & 0 & 0 \\ 0 & 0 & 0 & 1 & 0 & 0 \\ 0 & 0 & 0 & 0 & 0 & 0 \end{bmatrix} \tag{6.54}$$

$$\underline{\Omega} = \begin{bmatrix} \underline{0} & \underline{0} & \underline{0} \\ \underline{0} & \underline{\Omega}_1 & \underline{0} \\ \underline{0} & \underline{0} & \underline{\Omega}_2 \end{bmatrix}$$
$$\underline{\Omega}_1 = \omega_1 \underline{I} \tag{6.55}$$
$$\underline{\Omega}_2 = \omega_2 \underline{I}$$

The two unity matrices are of dimensions six by six and three by three, respectively, in (6.55). Further

$$
\begin{aligned}
&\underline{G} = \begin{bmatrix} \underline{0} & \underline{0} & \underline{0} \\ \underline{G}_1 & \underline{G}_2 & \underline{0} \\ \underline{G}_3 & \underline{0} & \underline{G}_4 \end{bmatrix} \\
&\underline{G}_1 = \begin{bmatrix} 0 & L_{m1} & \\ -L_{m1} & 0 & \\ & & \underline{0} \end{bmatrix} \qquad \underline{G}_2 = \begin{bmatrix} 0 & L_{lr1}+L_{m1} & \\ -\left(L_{lr1}+L_{m1}\right) & 0 & \\ & & \underline{0} \end{bmatrix} \\
&\underline{G}_3 = \sqrt{2}\begin{bmatrix} 0 & 0 & 0 & L_{m2} & 0 & 0 \\ 0 & 0 & -L_{m2} & 0 & 0 & 0 \\ 0 & 0 & 0 & 0 & 0 & 0 \end{bmatrix} \\
&\underline{G}_4 = \begin{bmatrix} 0 & L_{lr2}+L_{m2} & 0 \\ -\left(L_{lr2}+L_{m2}\right) & 0 & 0 \\ 0 & 0 & 0 \end{bmatrix}
\end{aligned}
\tag{6.56}
$$

Torque equations of the two machines are

$$
\begin{aligned}
T_{e1} &= P_1 L_{m1}\left[i_{dr1} i_q^{INV} - i_d^{INV} i_{qr1} \right] \\
T_{e2} &= \sqrt{2} P_2 L_{m2}\left[i_{dr2} i_y^{INV} - i_x^{INV} i_{qr2} \right]
\end{aligned}
\tag{6.57}
$$

Since the x-y and zero-sequence components of the rotor voltages and currents are zero, the complete model in the stationary reference frame for the six-phase and the three-phase series connected machines consists of ten differential equations. The developed form of inverter voltage equations is:

$$
\begin{aligned}
v_\alpha^{INV} &= R_{s1} i_\alpha^{INV} + (L_{ls1}+L_{m1})\frac{di_\alpha^{INV}}{dt} + L_{m1}\frac{di_{dr1}}{dt} \\
v_\beta^{INV} &= R_{s1} i_\beta^{INV} + (L_{ls1}+L_{m1})\frac{di_\beta^{INV}}{dt} + L_{m1}\frac{di_{qr1}}{dt} \\
v_x^{INV} &= R_{s1} i_x^{INV} + L_{ls1}\frac{di_x^{INV}}{dt} + \sqrt{2}\left\{ R_{s2}\sqrt{2} i_x^{INV} + (L_{ls2}+L_{m2})\frac{d\sqrt{2} i_x^{INV}}{dt} + L_{m2}\frac{di_{dr2}}{dt} \right\} \\
v_y^{INV} &= R_{s1} i_y^{INV} + L_{ls1}\frac{di_y^{INV}}{dt} + \sqrt{2}\left\{ R_{s2}\sqrt{2} i_y^{INV} + (L_{ls2}+L_{m2})\frac{d\sqrt{2} i_y^{INV}}{dt} + L_{m2}\frac{di_{qr2}}{dt} \right\} \\
v_{0+}^{INV} &= R_{s1} i_{0+}^{INV} + L_{ls1}\frac{di_{0+}^{INV}}{dt} + \sqrt{2}\left\{ R_{s2}\sqrt{2} i_{0+}^{INV} + L_{ls2}\frac{d\sqrt{2} i_{0+}^{INV}}{dt} \right\} \\
v_{0-}^{INV} &= R_{s1} i_{0-}^{INV} + L_{ls1}\frac{di_{0-}^{INV}}{dt}
\end{aligned}
\tag{6.58}
$$

Rotor voltage equations of the six-phase machine are:

$$
\begin{aligned}
0 &= R_{r1} i_{dr1} + L_{m1}\frac{di_\alpha^{INV}}{dt} + \left(L_{lr1}+L_{m1}\right)\frac{di_{dr1}}{dt} + \omega_1\left(L_{m1} i_\beta^{INV} + \left(L_{lr1}+L_{m1}\right) i_{qr1} \right) \\
0 &= R_{r1} i_{qr1} + L_{m1}\frac{di_\beta^{INV}}{dt} + \left(L_{lr1}+L_{m1}\right)\frac{di_{qr1}}{dt} - \omega_1\left(L_{m1} i_\alpha^{INV} + \left(L_{lr1}+L_{m1}\right) i_{dr1} \right)
\end{aligned}
\tag{6.59}
$$

and rotor voltage equations of the three-phase machine are:

$$\begin{aligned}
0 &= R_{r2} i_{dr2} + \sqrt{2} L_{m2} \frac{di_x^{INV}}{dt} + \left(L_{lr2} + L_{m2}\right) \frac{di_{dr2}}{dt} + \omega_2 \left(L_{m2} \sqrt{2} i_y^{INV} + \left(L_{lr2} + L_{m2}\right) i_{qr2}\right) \\
0 &= R_{r2} i_{qr2} + \sqrt{2} L_{m2} \frac{di_y^{INV}}{dt} + \left(L_{lr2} + L_{m2}\right) \frac{di_{qr2}}{dt} - \omega_2 \left(L_{m2} \sqrt{2} i_x^{INV} + \left(L_{lr2} + L_{m2}\right) i_{dr2}\right)
\end{aligned} \tag{6.60}$$

Torque equations are given with (6.57).

Inverter voltage axis components are related with stator voltage axis components of the two machines through essentially (6.29),

$$\begin{bmatrix} v_\alpha^{INV} \\ v_\beta^{INV} \\ v_x^{INV} \\ v_y^{INV} \\ v_{0+}^{INV} \\ v_{0-}^{INV} \end{bmatrix} = \begin{bmatrix} v_{\alpha s1} \\ v_{\beta s1} \\ v_{xs1} + \sqrt{2} v_{\alpha s2} \\ v_{ys1} + \sqrt{2} v_{\beta s2} \\ v_{0+s1} + \sqrt{2} v_{0s2} \\ v_{0-s1} \end{bmatrix} \tag{6.61}$$

Corresponding relationship for inverter current components and individual machine axis current components are,

$$\begin{aligned}
i_\alpha^{INV} &= i_{\alpha s1} \\
i_\beta^{INV} &= i_{\beta s1} \\
i_x^{INV} &= i_{xs1} = i_{\alpha s2} / \sqrt{2} \\
i_y^{INV} &= i_{ys1} = i_{\beta s2} / \sqrt{2} \\
i_{0+}^{INV} &= i_{0+s1} = i_{0s2} / \sqrt{2} \\
i_{0-}^{INV} &= i_{0-s1}
\end{aligned} \tag{6.62}$$

Hence, in terms of inverter axis current components, one has the following machine's axis current components:

$$\begin{aligned}
i_{\alpha s1} &= i_\alpha^{INV} & \qquad & \\
i_{\beta s1} &= i_\beta^{INV} & & i_{\alpha s2} = \sqrt{2} i_x^{INV} \\
i_{xs1} &= i_x^{INV} & & i_{\beta s2} = \sqrt{2} i_y^{INV} \\
i_{ys1} &= i_y^{INV} & & i_{0s2} = \sqrt{2} i_{0+}^{INV} \\
i_{0+s1} &= i_{0+}^{INV} & & \\
i_{0-s1} &= i_{0-}^{INV} & &
\end{aligned} \tag{6.63}$$

6.5 EXTENSION OF THE MODEL TO AN ARBITRARY COMMON REFERENCE FRAME AND REFERENCE FRAMES FIXED TO ROTOR FLUX SPACE VECTORS OF THE TWO MACHINES

In principle, the same procedure is followed as for the five-phase case in the section 4.6. The easiest way to proceed further is to take the equations in the stationary reference frame (6.58)-(6.60) and define the following space vectors:

$$\begin{aligned}
\underline{v}_{\alpha\beta}^{INV} &= v_{\alpha}^{INV} + jv_{\beta}^{INV} \\
\underline{i}_{\alpha\beta}^{INV} &= i_{\alpha}^{INV} + ji_{\beta}^{INV} \\
\underline{v}_{xy}^{INV} &= v_{x}^{INV} + jv_{y}^{INV} \\
\underline{i}_{xy}^{INV} &= i_{x}^{INV} + ji_{y}^{INV} \\
\underline{i}_{r1} &= i_{dr1} + ji_{qr1} \\
\underline{i}_{r2} &= i_{dr2} + ji_{qr2}
\end{aligned} \tag{6.64}$$

Then, in the stationary common reference frame, one can write the first four inverter equations of (6.58) in space vector as:

$$\begin{aligned}
\underline{v}_{\alpha\beta}^{INV} &= R_{s1}\underline{i}_{\alpha\beta}^{INV} + (L_{ls1}+L_{m1})\frac{d\underline{i}_{\alpha\beta}^{INV}}{dt} + L_{m1}\frac{d\underline{i}_{r1}}{dt} \\
\underline{v}_{xy}^{INV} &= R_{s1}\underline{i}_{xy}^{INV} + L_{ls1}\frac{d\underline{i}_{xy}^{INV}}{dt} + \sqrt{2}\left\{R_{s2}\sqrt{2}\underline{i}_{xy}^{INV} + (L_{ls2}+L_{m2})\frac{d\sqrt{2}\underline{i}_{xy}^{INV}}{dt} + L_{m2}\frac{d\underline{i}_{r2}}{dt}\right\}
\end{aligned} \tag{6.65}$$

Rotor voltage equations of six-phase machine and three-phase machine are:

$$0 = R_{r1}\underline{i}_{r1} + L_{m1}\frac{d\underline{i}_{\alpha\beta}^{INV}}{dt} + \left(L_{lr1}+L_{m1}\right)\frac{d\underline{i}_{r1}}{dt} + j(-\omega_1)\left(L_{m1}\underline{i}_{dq}^{INV} + \left(L_{lr1}+L_{m1}\right)\underline{i}_{r1}\right) \tag{6.66}$$

$$0 = R_{r2}\underline{i}_{r2} + \sqrt{2}L_{m2}\frac{d\underline{i}_{xy}^{INV}}{dt} + \left(L_{lr2}+L_{m2}\right)\frac{d\underline{i}_{r2}}{dt} + j(-\omega_2)\left(L_{m2}\sqrt{2}\underline{i}_{xy}^{INV} + \left(L_{lr2}+L_{m2}\right)\underline{i}_{r2}\right) \tag{6.67}$$

Transformation is further done into an arbitrary reference frame, so that the angle of transformation and speed of the reference frame are $\theta_s = \int \omega_a dt$ and ω_a. Correlation between current and voltage space vectors in the stationary and in the arbitrary reference frame is determined with (4.66),

$$\begin{aligned}
\underline{f} &= \underline{f}^{a}\exp(j\theta_s) \\
\underline{f}^{a} &= \underline{f}\exp(-j\theta_s)
\end{aligned} \tag{4.66}$$

Substituting the first of (4.66) into (6.65)-(6.67) yields for the inverter

$$\begin{aligned}
\underline{v}_{dq}^{INVa} &= R_{s1}\underline{i}_{dq}^{INVa} + (L_{ls1}+L_{m1})\frac{d\underline{i}_{dq}^{INVa}}{dt} + L_{m1}\frac{d\underline{i}_{r1}^{a}}{dt} + j\omega_a[(L_{ls1}+L_{m1})\underline{i}_{dq}^{INVa} + L_{m1}\underline{i}_{r1}^{a}] \\
\underline{v}_{xy}^{INVa} &= (R_{s1}+2R_{s2})\underline{i}_{xy}^{INVa} + (L_{ls1}+2L_{ls2}+2L_{m2})\frac{d\underline{i}_{xy}^{INVa}}{dt} + L_{m2}\sqrt{2}\frac{d\underline{i}_{r2}^{a}}{dt} + \\
&\quad + j\omega_a[(L_{ls1}+2L_{m2}+2L_{ls2})\underline{i}_{xy}^{INVa} + L_{m2}\sqrt{2}\underline{i}_{r2}^{a}]
\end{aligned} \tag{6.68}$$

and for the rotor of machines 1 and 2

$$0 = R_{r1}\underline{i}_{r1}^{a} + L_{m1}\frac{d\underline{i}_{dq}^{INVa}}{dt} + \left(L_{lr1}+L_{m1}\right)\frac{d\underline{i}_{r1}^{a}}{dt} + j(\omega_a-\omega_1)\left(L_{m1}\underline{i}_{dq}^{INVa} + \left(L_{lr1}+L_{m1}\right)\underline{i}_{r1}^{a}\right) \tag{6.69}$$

$$0 = R_{r2}\underline{i}_{r2}^{a} + \sqrt{2}L_{m2}\frac{d\underline{i}_{xy}^{INVa}}{dt} + \left(L_{lr2}+L_{m2}\right)\frac{d\underline{i}_{r2}^{a}}{dt} + j(\omega_a-\omega_2)\left(L_{m2}\sqrt{2}\underline{i}_{xy}^{INVa} + \left(L_{lr2}+L_{m2}\right)\underline{i}_{r2}^{a}\right) \tag{6.70}$$

For rotor flux oriented control purposes speed of the reference frame for inverter d-q equations and for rotor equations of machine 1 is selected as equal to the angular speed of rotor flux in machine 1, while for the inverter x-y equations and rotor equations of machine 2 the speed is selected as equal to the angular speed of rotor flux in machine 2. Quantities in the reference frame attached to the rotor flux of machine 1 are identified with superscript (1), while those in the reference frame attached to the rotor flux of machine 2 have a superscript (2). These superscripts substitute superscript *a* in (6.68)-(6.70), so that

$$\begin{aligned}
\underline{v}_{dq}^{INV(1)} &= R_{s1}\underline{i}_{dq}^{INV(1)} + (L_{ls1}+L_{m1})\frac{d\underline{i}_{dq}^{INV(1)}}{dt} + L_{m1}\frac{d\underline{i}_{r1}^{(1)}}{dt} + j\omega_{r1}[(L_{ls1}+L_{m1})\underline{i}_{dq}^{INV(1)} + L_{m1}\underline{i}_{r1}^{(1)}] \\
\underline{v}_{xy}^{INV(2)} &= (R_{s1}+2R_{s2})\underline{i}_{xy}^{INV(2)} + (L_{ls1}+2L_{ls2}+2L_{m2})\frac{d\underline{i}_{xy}^{INV(2)}}{dt} + L_{m2}\sqrt{2}\frac{d\underline{i}_{r2}^{(2)}}{dt} + \\
&\quad + j\omega_{r2}[(L_{ls1}+2L_{m2}+2L_{ls2})\underline{i}_{xy}^{INV(2)} + \sqrt{2}L_{m2}\underline{i}_{r2}^{(2)}]
\end{aligned} \tag{6.71}$$

$$0 = R_{r1}\underline{i}_{r1}^{(1)} + L_{m1}\frac{d\underline{i}_{dq}^{INV(1)}}{dt} + \left(L_{lr1}+L_{m1}\right)\frac{d\underline{i}_{r1}^{(1)}}{dt} + j(\omega_{r1}-\omega_1)\left(L_{m1}\underline{i}_{dq}^{INV(1)} + \left(L_{lr1}+L_{m1}\right)\underline{i}_{r1}^{(1)}\right) \tag{6.72}$$

$$0 = R_{r2}\underline{i}_{r2}^{(2)} + \sqrt{2}L_{m2}\frac{d\underline{i}_{xy}^{INV(2)}}{dt} + \left(L_{lr2}+L_{m2}\right)\frac{d\underline{i}_{r2}^{(2)}}{dt} + j(\omega_{r2}-\omega_2)\left(L_{m2}\sqrt{2}\underline{i}_{xy}^{INV(2)} + \left(L_{lr2}+L_{m2}\right)\underline{i}_{r2}^{(2)}\right) \tag{6.73}$$

Equations (6.72)-(6.73) are once more identical as for a three-phase RFO machine, indicating that independent vector control of the two series-connected machines supplied from a single inverter is possible. Inverter d-q axis currents can be used to control flux and torque production in the six-phase machine, while inverter x-y currents can control flux and torque production of the three-phase machine.

6.6 VECTOR CONTROL OF THE TWO-MOTOR SERIES-CONNECTED SIX-PHASE DRIVE USING CURRENT CONTROL IN THE STATIONARY REFERENCE FRAME

The indirect rotor flux oriented vector control scheme is utilised to independently control the series-connected six-phase and three-phase induction machines. The basic vector controller has already been discussed in section 3.5. The same controller structure is utilised here except that the current transformation blocks are 2 to 6 and 2 to 3 for the six-phase and the three-phase induction machine, respectively. The constants of the vector controller for the six-phase machine were calculated in section 5.5. and are obtained for the three-phase machine using (3.43). The vector controller constants are repeated in Table 6.1 for convenience.

The structure of the indirect vector control scheme is illustrated in Fig. 6.2. The stators of the two machines in Fig. 6.2 are connected as per the connection diagram in Fig. 6.1. The

Table 6.1. Vector controller constants.

Six-phase machine	K_1=0.3934	K_2 = 4.1332
Three-phase machine	K_1=0.5562	K_2 = 5.843

actual speeds of both machines are assumed to be sensed and are used as feedback signals for vector controllers. The vector controllers generate appropriate phase current references which are summed up according to the connection diagram of Fig. 6.1 to form the phase current references. These reference currents are then compared with actual inverter phase currents to generate the phase current errors. An appropriate current control algorithm (hysteresis or ramp-comparison) is further used to provide necessary switching signals to the power switches of the VSI to eliminate the phase current error. In this study both the hysteresis and ramp-comparison current control methods are used, in conjunction with phase current control, to control the machines.

The phase current references are formed for two machines separately, as follows (phases of the three-phase machine are now labelled as *a*,*b*,*c* in accordance with Fig. 6.1):

$$
\begin{aligned}
i_{a1}^* &= \sqrt{\frac{2}{6}}\left(i_{ds1}^*\cos\left(\phi_{r1}\right) - i_{qs1}^*\sin\left(\phi_{r1}\right)\right)\\
i_{b1}^* &= \sqrt{\frac{2}{6}}\left(i_{ds1}^*\cos\left(\phi_{r1}-\alpha\right) - i_{qs1}^*\sin\left(\phi_{r1}-\alpha\right)\right)\\
i_{c1}^* &= \sqrt{\frac{2}{6}}\left(i_{ds1}^*\cos\left(\phi_{r1}-2\alpha\right) - i_{qs1}^*\sin\left(\phi_{r1}-2\alpha\right)\right)\\
i_{d1}^* &= \sqrt{\frac{2}{6}}\left(i_{ds1}^*\cos\left(\phi_{r1}-3\alpha\right) - i_{qs1}^*\sin\left(\phi_{r1}-3\alpha\right)\right)\\
i_{e1}^* &= \sqrt{\frac{2}{6}}\left(i_{ds1}^*\cos\left(\phi_{r1}-4\alpha\right) - i_{qs1}^*\sin\left(\phi_{r1}-4\alpha\right)\right)\\
i_{f1}^* &= \sqrt{\frac{2}{6}}\left(i_{ds1}^*\cos\left(\phi_{r1}-5\alpha\right) - i_{qs1}^*\sin\left(\phi_{r1}-5\alpha\right)\right)
\end{aligned}
\tag{6.74a}
$$

$$
\begin{aligned}
i_{a2}^* &= \sqrt{\frac{2}{3}}\left(i_{ds2}^*\cos\left(\phi_{r2}\right) - i_{qs2}^*\sin\left(\phi_{r2}\right)\right)\\
i_{b2}^* &= \sqrt{\frac{2}{3}}\left(i_{ds2}^*\cos\left(\phi_{r2}-2\alpha\right) - i_{qs2}^*\sin\left(\phi_{r2}-2\alpha\right)\right)\\
i_{c2}^* &= \sqrt{\frac{2}{3}}\left(i_{ds2}^*\cos\left(\phi_{r2}-4\alpha\right) - i_{qs2}^*\sin\left(\phi_{r2}-4\alpha\right)\right)
\end{aligned}
\tag{6.74b}
$$

Overall inverter current references are then formed as:

$$
\begin{aligned}
i_A^* &= i_{a1}^* + 0.5 i_{a2}^* \qquad & i_B^* &= i_{b1}^* + 0.5 i_{b2}^*\\
i_C^* &= i_{c1}^* + 0.5 i_{c2}^* \qquad & i_D^* &= i_{d1}^* + 0.5 i_{a2}^*\\
i_E^* &= i_{e1}^* + 0.5 i_{b2}^* \qquad & i_F^* &= i_{f1}^* + 0.5 i_{c2}^*
\end{aligned}
\tag{6.75}
$$

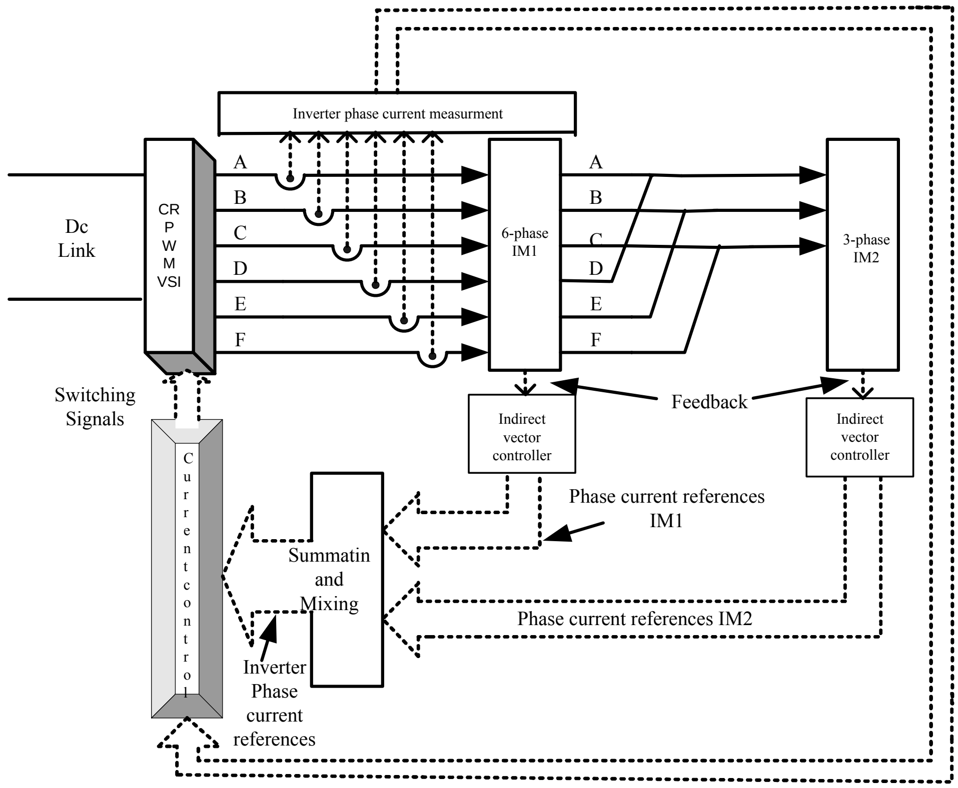

Fig. 6.2. Vector control scheme for six-phase two-motor drive system.

6.7 TRANSIENT BEHAVIOUR OF THE SIX-PHASE TWO-MOTOR VECTOR CONTROLLED DRIVE

6.7.1 Hysteresis current control

An indirect rotor flux oriented controlled six-phase series-connected two-motor drive system is simulated, using both model in phase variable form and model in the stationary common reference frame. Only one set of result is presented here since both models yield identical results. The drive is supplied from a six-phase PWM voltage source inverter with hysteresis current control. The drive is operated in closed-loop speed control mode with anti-windup discrete PI speed controller in the speed loop of each machine. The speed controller used is the one designed in section 3.6.4. Limiters are used to limit the torque of the six-phase machine to 150% (15 Nm) of the rated value and that of the three-phase machine to twice (10 Nm) the rated value. Operation is simulated for excitation and acceleration transients, disturbance rejection and reversing transients. The set speed of the six-phase machine (IM1) is 1500 rpm while it is 750 rpm for the three-phase machine (IM2). Results are shown in Figs. 6.3-6.5.

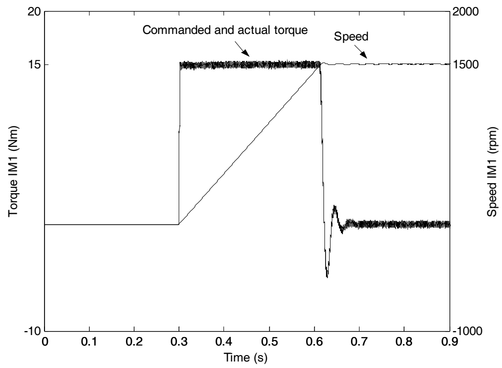

a.

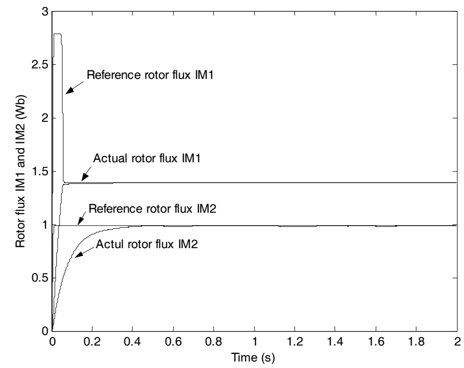

e.

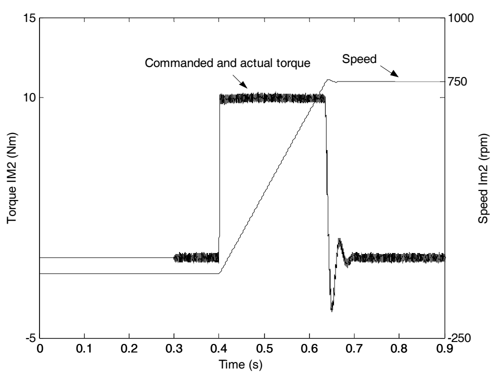

b.

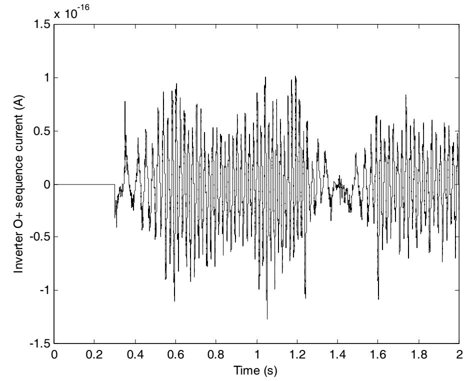

f.

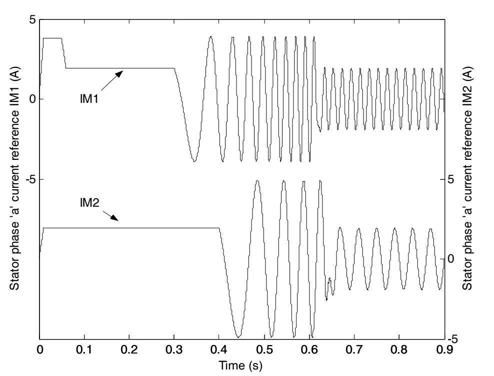

c.

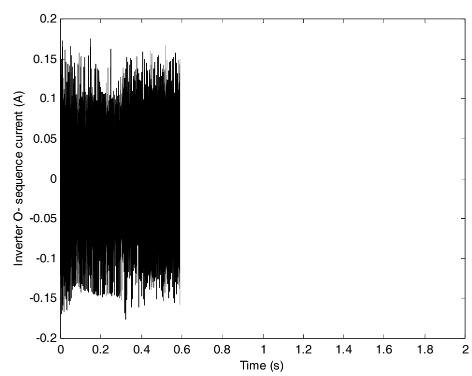

g.

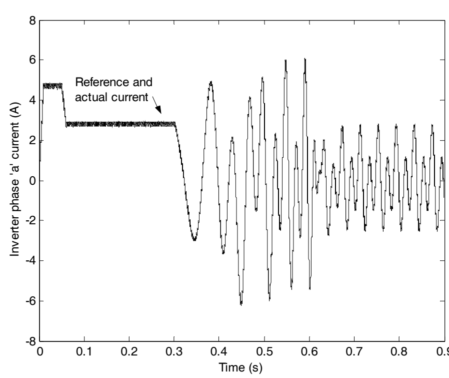

d.

Fig. 6.3. Excitation and acceleration transients using hysteresis current control: a. actual and reference torque, and speed, IM1, b. actual and reference torque, and speed, IM2, c. stator phase 'a' current references IM1 and IM2, d. actual and reference inverter phase 'a' current, e. actual and reference rotor flux IM1 and IM2, f. inverter positive zero-sequence current, g. inverter negative zero-sequence current.

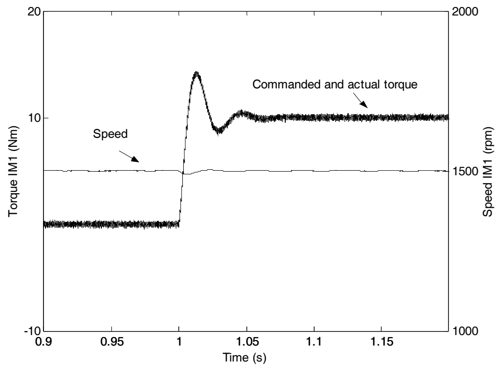

a.

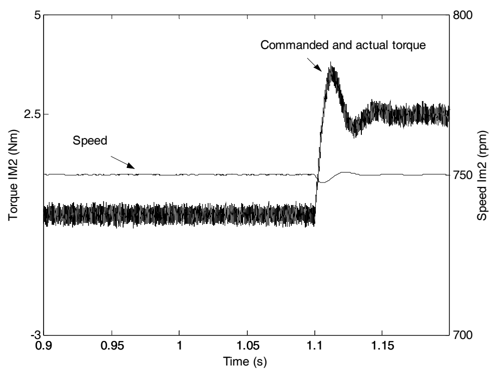

b.

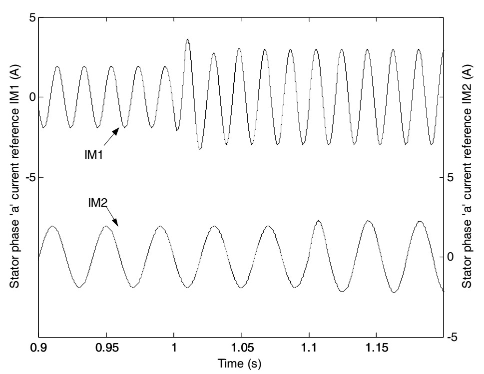

c.

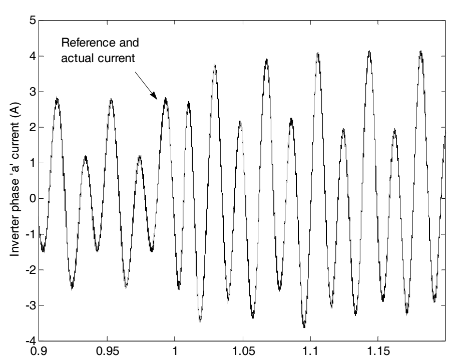

d.

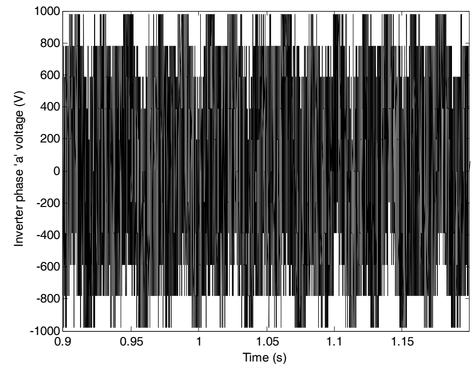

e.

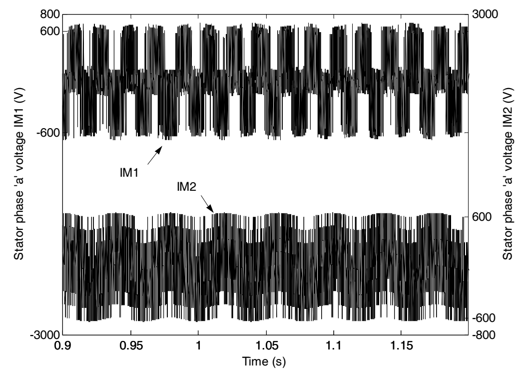

f.

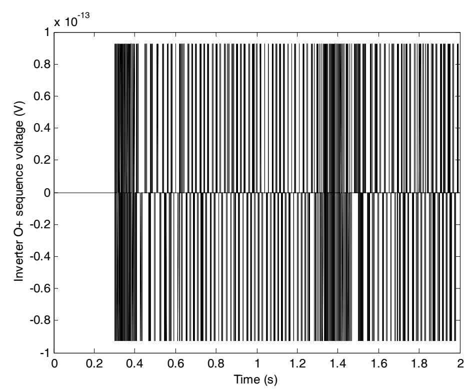

g.

Fig. 6.4. Disturbance rejection transient using hysteresis current control: a. actual and reference torque, and speed, IM1, b. actual and reference torque, and speed, IM2, c. stator phase ‘a’ current references, IM1 and IM2, d. actual and reference inverter phase ‘a’ current, e. inverter phase ‘a’ voltage, f. stator phase ‘a’ voltage IM1 and IM2, g. inverter positive zero-sequence voltage.

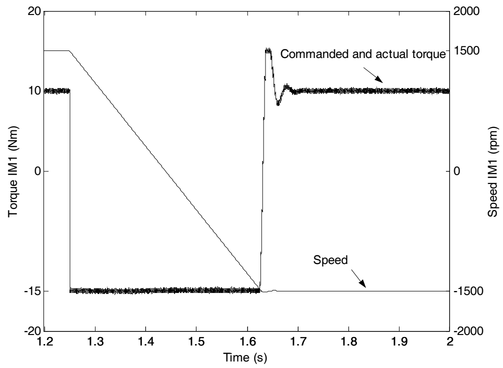

a.

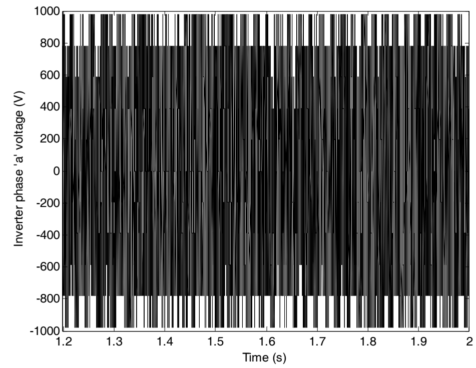

e.

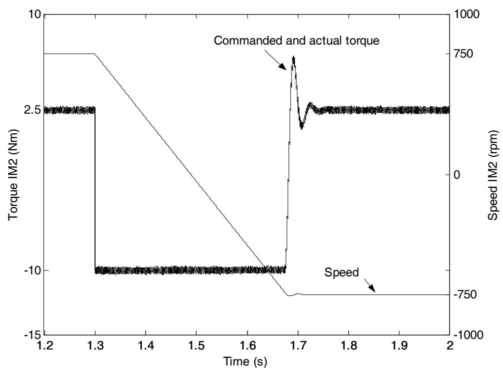

b.

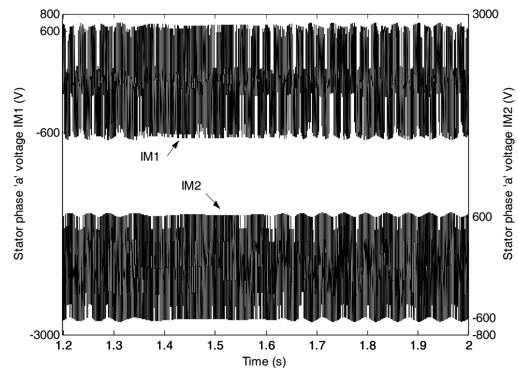

f.

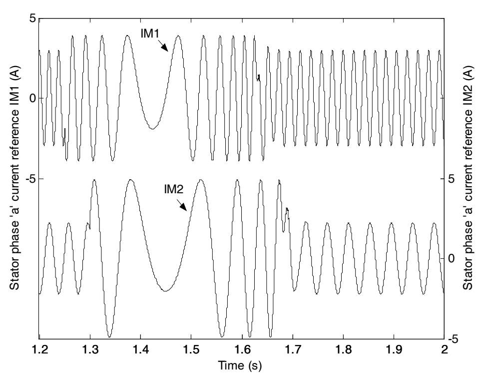

c.

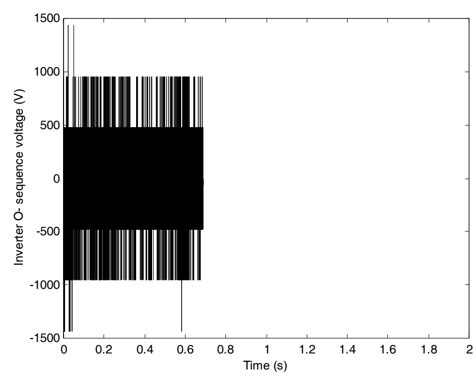

g.

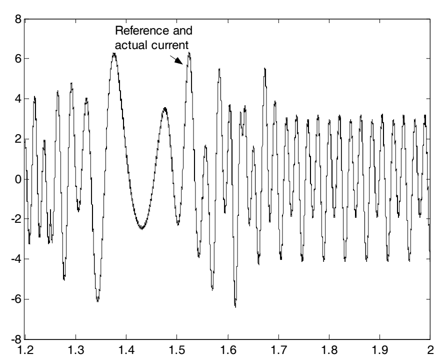

d.

Fig. 6.5. Reversing transients using hysteresis current control: a. actual and reference torque, and speed, IM1, b. actual and reference torque, and speed, IM2, c. stator phase ‘a’ current references, IM1 and IM2, d. actual and reference inverter phase ‘a’ current, e. stator phase ‘a’ voltage IM1 and IM2, f. inverter phase ‘a’ voltage, g. inverter negative zero-sequence voltage.

Forced excitation is initiated first in IM1. Rotor flux reference (i.e. stator d-axis current reference) is ramped from t = 0.0 to t = 0.01 s to twice the rated value. It is further reduced from twice the rated value to the rated value in a linear fashion from t = 0.05 to t = 0.06 s and it is then kept constant for the rest of the simulation. The IM2 rotor flux command is ramped to rated flux from t = 0.0 to t = 0.01 s and is then kept constant. Once the rotor flux has reached steady state a speed command of 1500 rpm is applied at t = 0.3 s in ramp wise manner from t = 0.3 to t = 0.35 s to IM1. The IM2 is accelerated to 750 rpm at t = 0.4 s (ramped speed command from t = 0.4 s to t = 0.45 s). The hysteresis current controller band is kept at ±2.5%. The inverter dc link voltage is set to 1173.8 V, similar to section 4.8. A step load torque, equal to the motor rated torque (10 Nm), is applied to IM1 at t = 1 s and equal to half the rated value (2.5 Nm) to IM2 at t = 1.1 s. Speed reversal is initiated from these steady states (from t = 1.25 s to t = 1.30 s for IM1 and from t = 1.30 s to t = 1.35 s for IM2).

It is seen from Fig. 6.3e that the rotor flux builds up independently in the two machines and, after attaining rated values, remains further on unchanged regardless of what happens to any of the two machines. This indicates that rotor flux control in any of the two machines is completely decoupled from torque control of both machines. Such a situation is confirmed in Fig. 6.3a and Fig. 6.3b, where torque and speed responses of the two machines are shown for the initial accelerations (up to 0.9 s). Toque variation in one machine does not affect torque of the other machine and vice versa, so that both machines accelerate with the torque in the limit. One notices appearance of the torque ripple in IM2 prior to the application of the speed command to it (time interval 0.3 to 0.4 s). This is a consequence of the inverter current higher harmonics and is an expected consequence of the non-ideal nature of the inverter.

Stator phase ‘a’ current references, as well as the inverter phase ‘a’ current reference and actual inverter phase ‘a’ current, are shown in Figs. 6.3c-6.3d for the same time interval. While the individual phase current references are sinusoidal functions in final steady state, the inverter current references (and hence the actual currents as well) are highly distorted due to the summation described with expression (6.75). In final steady state of Fig. 6.3d inverter current references are sums of two sinusoidal functions, of 50 Hz (corresponding to 1500 rpm) and 25 Hz (corresponding to 750 rpm) frequency, respectively.

The positive and negative zero-sequence inverter currents are shown in Figs. 6.3f-6.3g respectively, for the whole simulation period. It is seen that although positive zero-sequence is absent, negative zero-sequence current is present with a small amplitude.

Disturbance rejection properties of the drive are illustrated in Fig. 6.4. Since the rotor flux remains undisturbed (Fig. 6.3e), torque responses are the quickest possible, leading to a rapid compensation of the speed dip, caused by the load torque application. The positive zero-sequence voltage shown in Fig. 6.4g is virtually non existent.

Reversing transient is illustrated in Fig 6.5. Fully decoupled flux and torque control, as well as a fully independent control of the two machines, are again evident from the results for this transient. The change of phase sequence in stator current because of the change in the rotational direction is evident from the current responses. The negative zero-sequence voltage shown in Fig. 6.5g indicates once more presence of negative zero-sequence current.

6.7.2 Ramp-comparison current control

The same set of transients is examined, this time using ramp-comparison current control. The plots are given in Figs. 6.6-6.8. The switching frequency of the inverter is fixed to 5 kHz (the same as in section 3.7.2, section 4.8.2 and section 5.6). The discrete anti-windup PI current controller is used in the current control loop (the one designed in section 3.6.3). The current controller is implemented using zero-order hold with sampling time equal to 20 μs and unit-delay sampling time is chosen as 48 μs. The output of the current controller is limited to ±1 to obtain full PWM in all conditions. The drive is operated in closed-loop speed control mode with discrete anti-windup PI speed controller in both speed loops. The speed controller is the one of section 3.6.4. The speed controller is implemented using zero-order hold with sampling time equal to 48 μs and unit-delay sampling time is chosen as 98 μs.

The response of the drive using ramp-comparison current control is essentially the same as obtained using hysteresis current control in all the three modes. It fully verifies the concept and confirms the feasibility of independent vector control of the six-phase two-motor drive with single inverter supply. It is interesting to note that ramp-comparison control results in higher value of the negative zero-sequence current component, Fig. 6.6g.

Comparison of results, reported in Figs. 6.3-6.8, with corresponding results given in sections 5.6.1 and 5.6.2 for the single motor drives clearly proves that the same quality of decoupled flux and torque control is achievable in this series-connected two-motor drive system as when a single vector controlled machine is used.

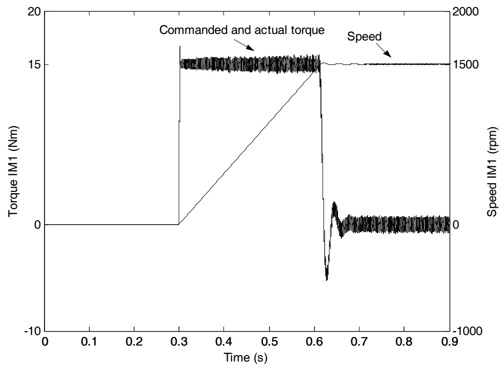

a.

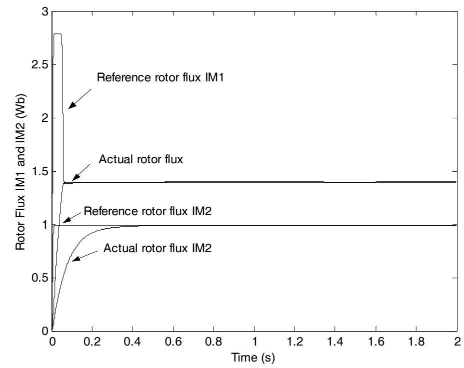

e.

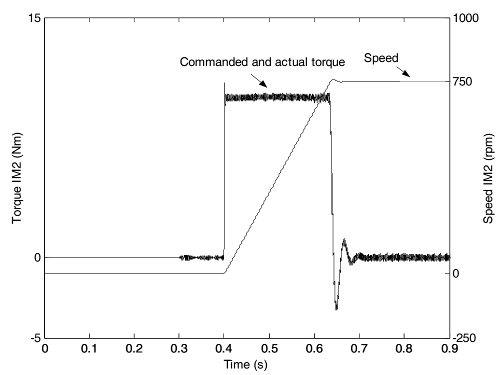

b.

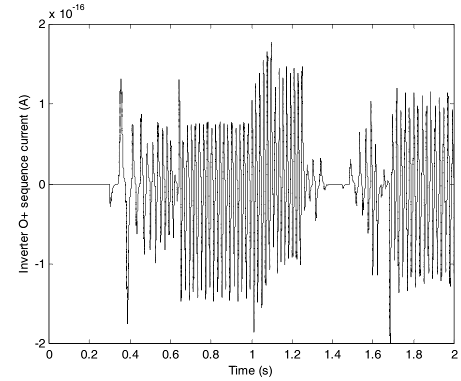

f.

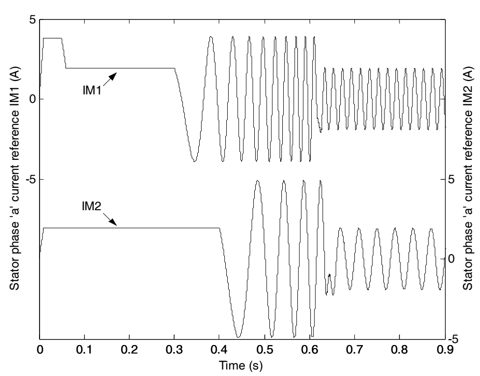

c.

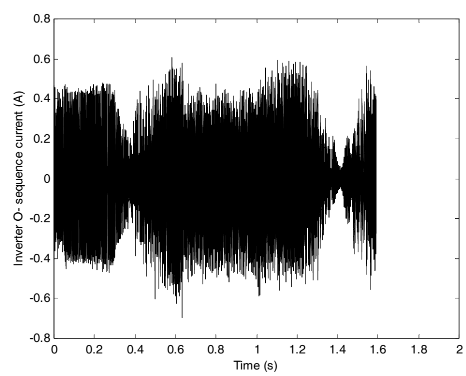

g.

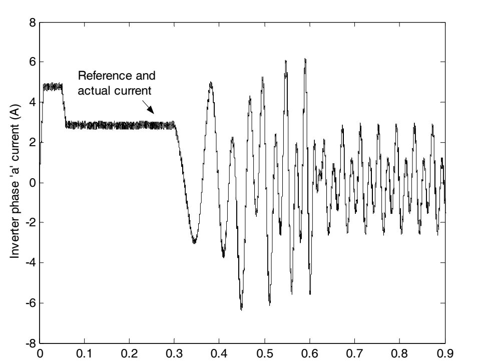

d.

Fig. 6.6. Excitation and acceleration transients using ramp-comparison current control: a. actual and reference torque, and speed, IM1, b. actual and reference torque, and speed, IM2, c. stator phase ‘a’ currents references IM1 and IM2, d. actual and reference inverter phase ‘a’ current, e. actual and reference rotor flux IM1 and IM2, f. inverter positive zero-sequence current, g. inverter negative zero-sequence current.

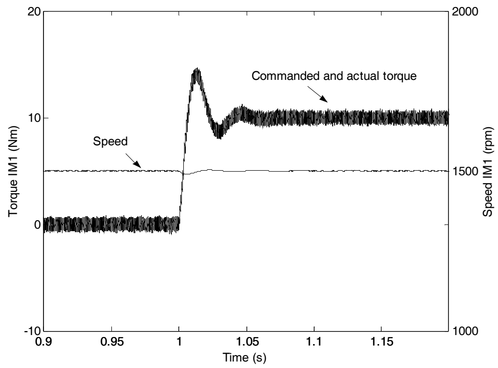

a.

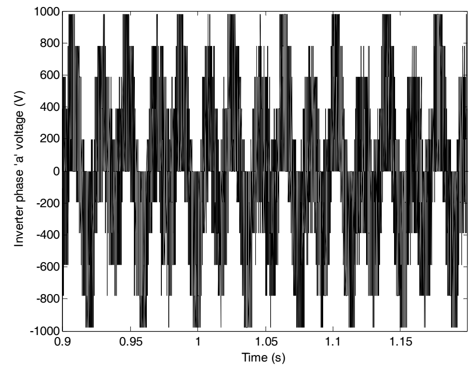

e.

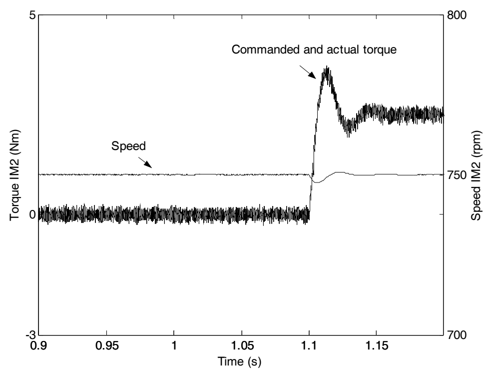

b.

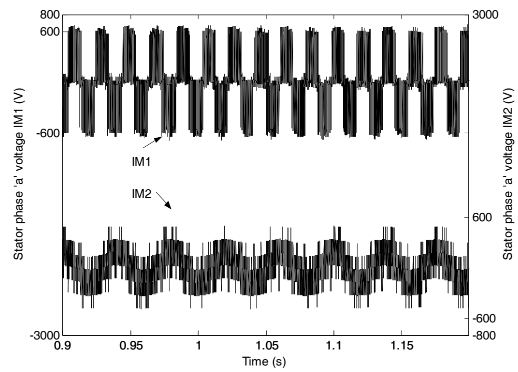

f.

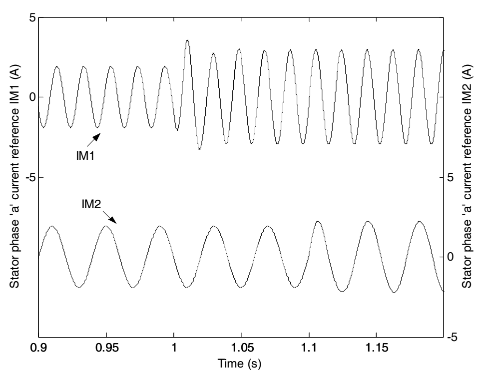

c.

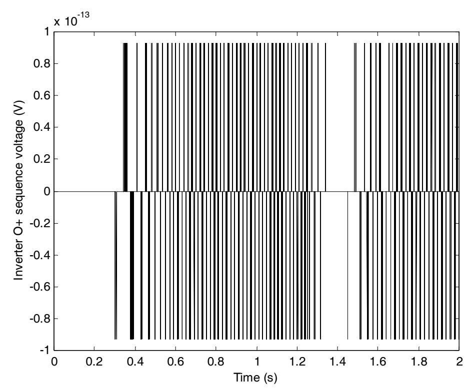

g.

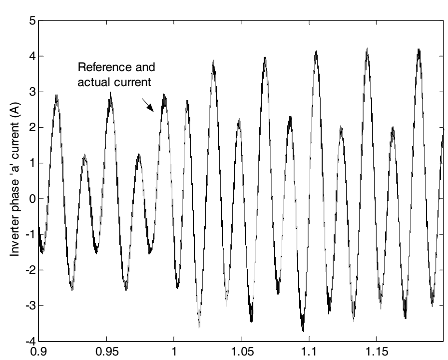

d.

Fig. 6.7. Disturbance rejection transient using ramp-comparison current control: a. actual and reference torque, and speed, IM1, b. actual and reference torque, and speed, IM2, c. stator phase ‘a’ current references, IM1 and IM2, d. actual and reference inverter phase ‘a’ current, e. inverter phase ‘a’ voltage, f. stator phase ‘a’ voltage IM1 and IM2, g. inverter positive zero-sequence voltage.

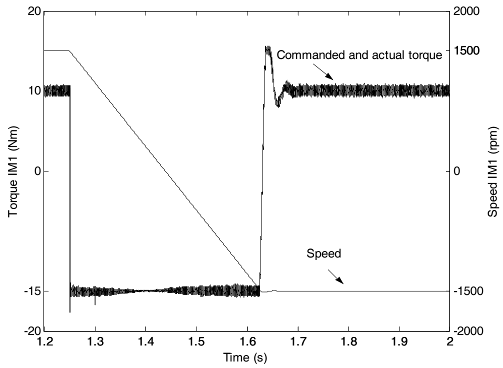

a.

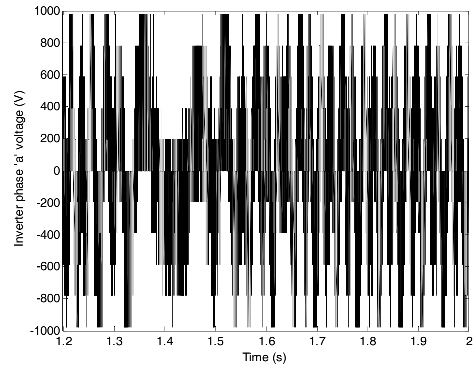

e.

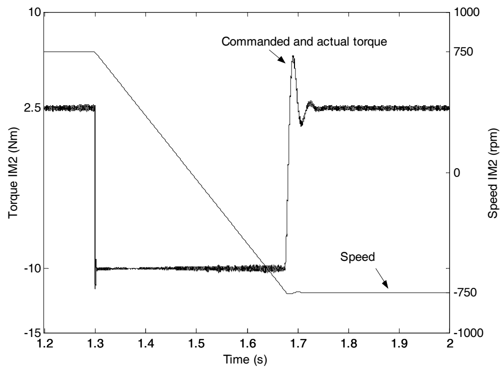

b.

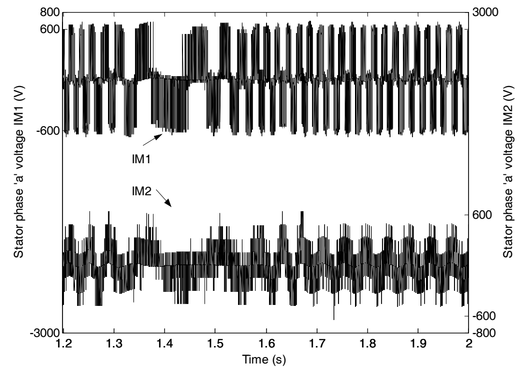

f.

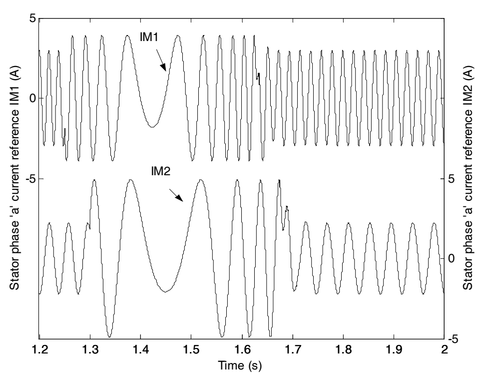

c.

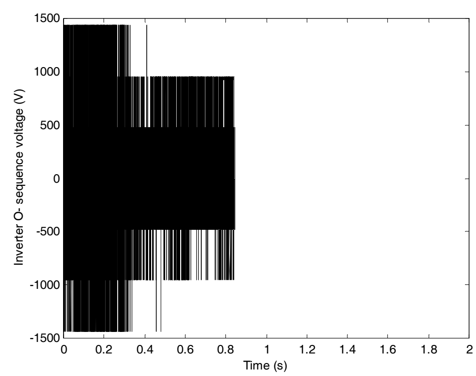

g.

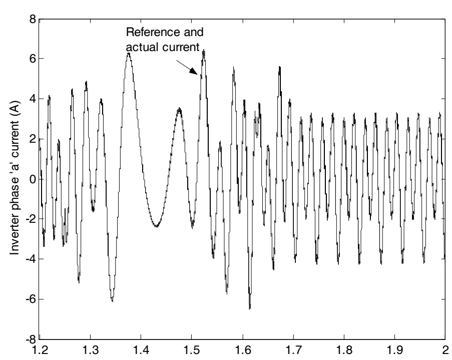

d.

Fig. 6.8. Reversing transient using ramp-comparison current control: a. actual and reference torque, and speed, IM1, b. actual and reference torque, and speed, IM2, c. stator phase ‘a’ current references, IM1 and IM2, d. actual and reference inverter phase ‘a’ current e. inverter phase ‘a’ voltage, f. stator phase ‘a’ voltage IM1 and IM2, g. inverter negative zero-sequence voltage.

6.8 HARMONIC ANALYSIS OF THE DRIVE BEHAVIOUR IN STEADY STATE

To study the behaviour of the six-phase two-motor drive system under no-load steady state operating condition, harmonic analysis is performed for phase ‘a’, α-axis and x-axis voltages and currents of the inverter, and phase ‘a’ voltages of IM1 and IM2. The spectrum is shown for hysteresis current control method and ramp-comparison current control method in Fig. 6.9 and Fig. 6.10, respectively. The values of fundamental components obtained from hysteresis and ramp-comparison current control methods are listed in Table 6.2 and Table 6.3, respectively. All the spectra are given in terms of voltage (current) RMS values. The spectra are determined using Fast Fourier Transform (FFT) in MATLAB.

The inverter phase ‘a’ voltage spectrum obtained from hysteresis current control is shown in Fig. 6.9a. The spectrum shows two fundamental components at 25 Hz and 50 Hz, which correspond to operating frequencies 25 Hz and 50 Hz of IM2 and IM1, respectively. The 50 Hz component appears as main component of stator phase ‘a’ voltage of IM1, while 25 Hz component appears as main component of stator phase ‘a’ voltage of IM2 (Fig. 6.9b). The α-axis inverter voltage component shows one fundamental component at 50 Hz which is equal to the phase ‘a’ inverter voltage component at 50 Hz. No voltage component exists at 25 Hz. The x-axis inverter voltage component shows one fundamental component at 25 Hz, which is equal to the phase ‘a’ inverter voltage component at 25 Hz. No voltage component exists at 50 Hz.

The first trace of Fig. 6.9b shows the phase ‘a’ voltage spectrum of IM1. Two fundamental components are seen at, 25 Hz and 50 Hz. The 50 Hz component is the torque and flux producing component while 25 Hz component is the voltage drop in x-y circuit due to current of IM2. The second set of traces shows the voltage and spectrum of IM2. There is only one component, at 25 Hz, which is the torque and flux producing (α-β circuit). Component at 50 Hz is absent since no x-y circuit exists in the three-phase machine. One observes from Fig. 6.9 and Table 6.2 the following. Inverter voltage component at 50 Hz is approximately 196 V and this is at the same time voltage at 50 Hz across IM1. One the other hand, inverter voltage component at 25 Hz is approximately 104 V and this predominantly appears as voltage across IM2 (approximately 98 V). However, part of the inverter 25 Hz component is dropped on IM1 as well (approximately 9 V) due to the flow of flux/torque producing current of IM2 through windings of IM1.

The inverter phase ‘a’ current spectrum obtained with hysteresis current control is shown in Fig. 6.9c. Two fundamental components at 25 Hz and 50 Hz are evident in the spectrum. The 50 Hz component is the flux/torque producing current of the IM1 while 25 Hz

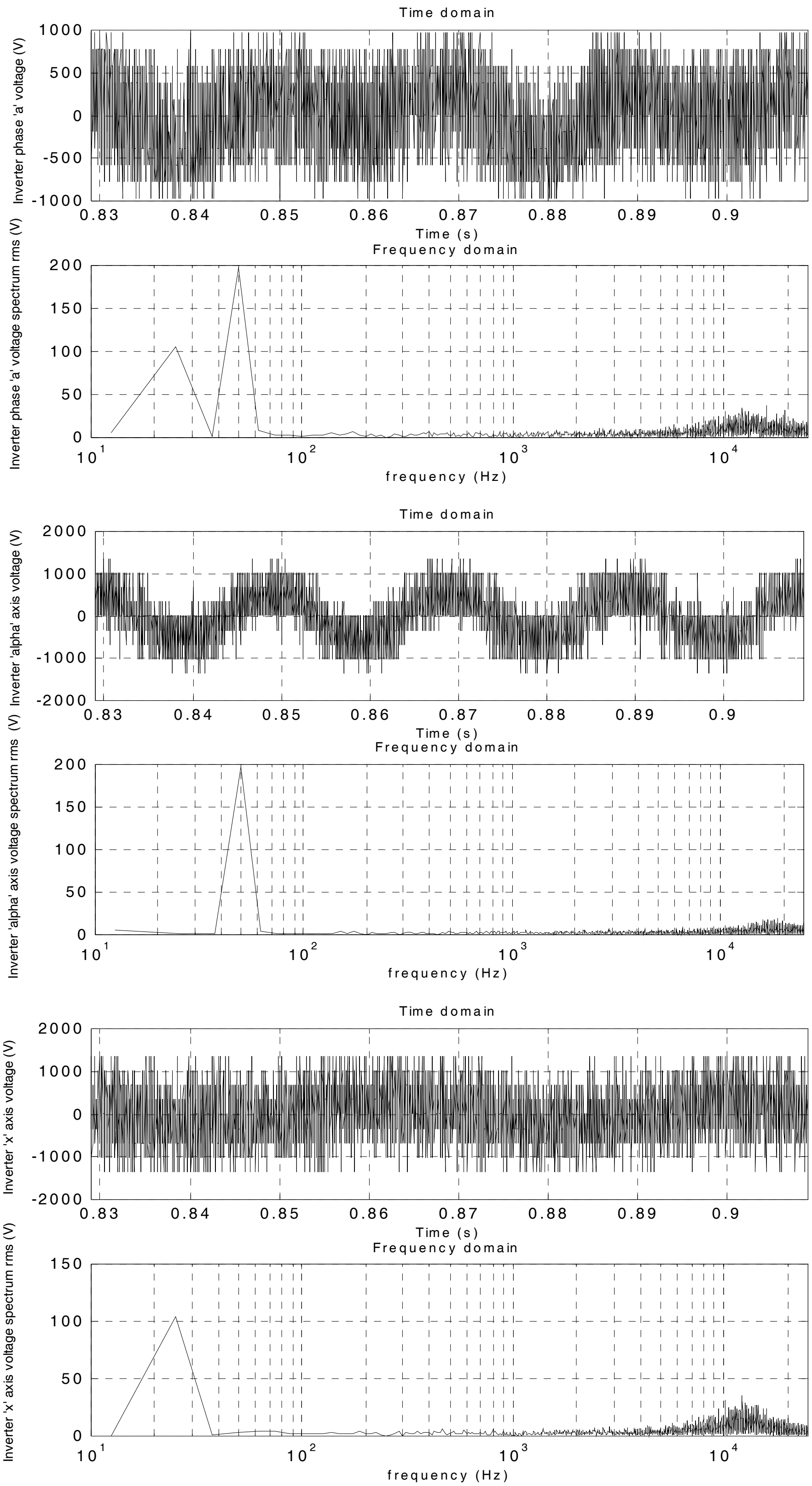

Fig. 6.9a. Time domain waveforms and spectra with hysteresis current control: phase ‘a’ inverter voltage, α-axis inverter voltage and x-axis inverter voltage.

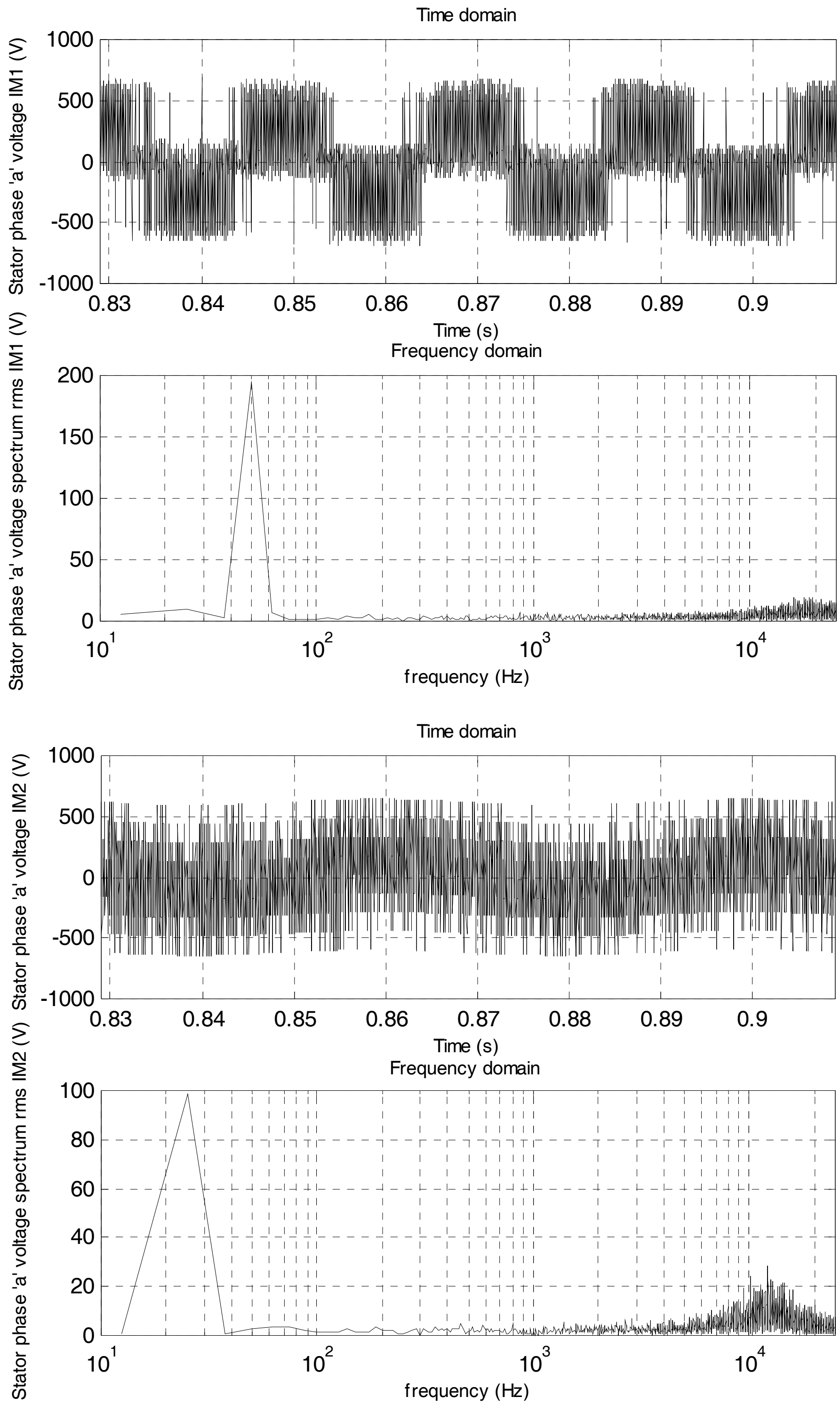

Fig. 6.9b. Time domain waveforms and spectra with hysteresis current control: stator phase ‘a’ voltage of IM1 and stator phase ‘a’ voltage of IM2.

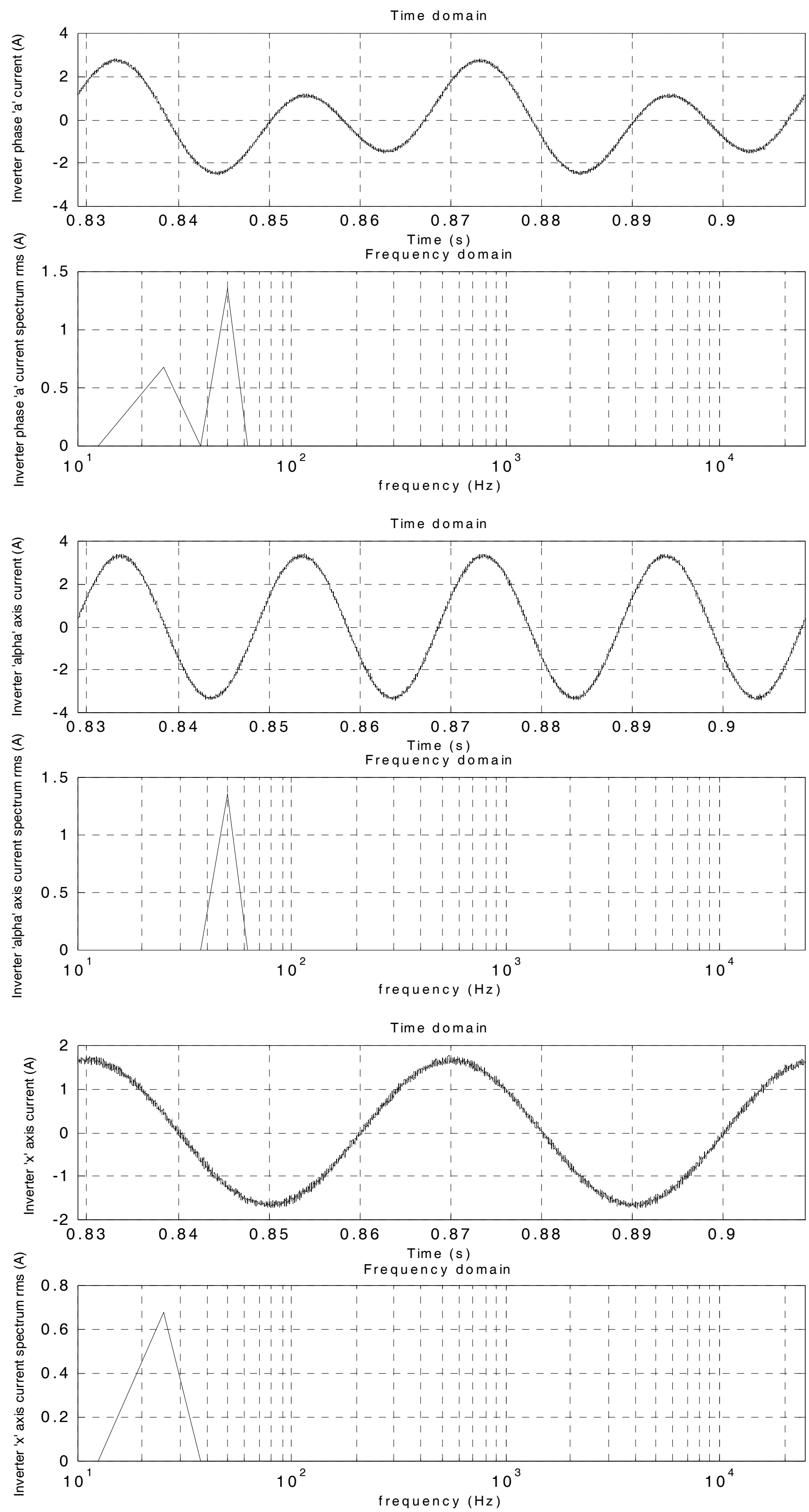

Fig. 6.9c. Time domain waveforms and spectra with hysteresis current control: phase ‘a’ inverter current, α-axis inverter current and x-axis inverter current.

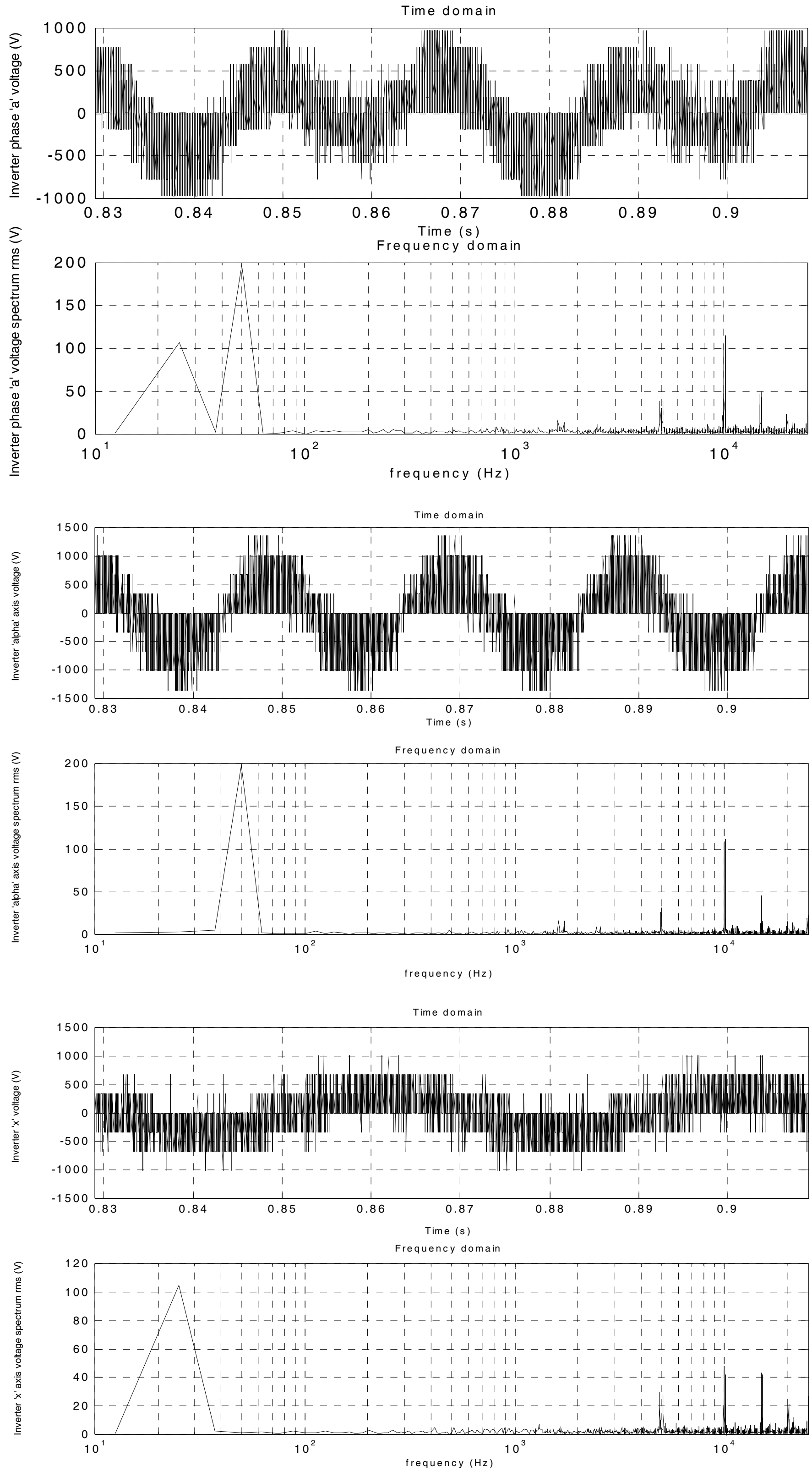

Fig. 6.10a. Time domain waveforms and spectra with ramp-comparison current control: phase 'a' inverter voltage, α-axis inverter voltage and x-axis inverter voltage.

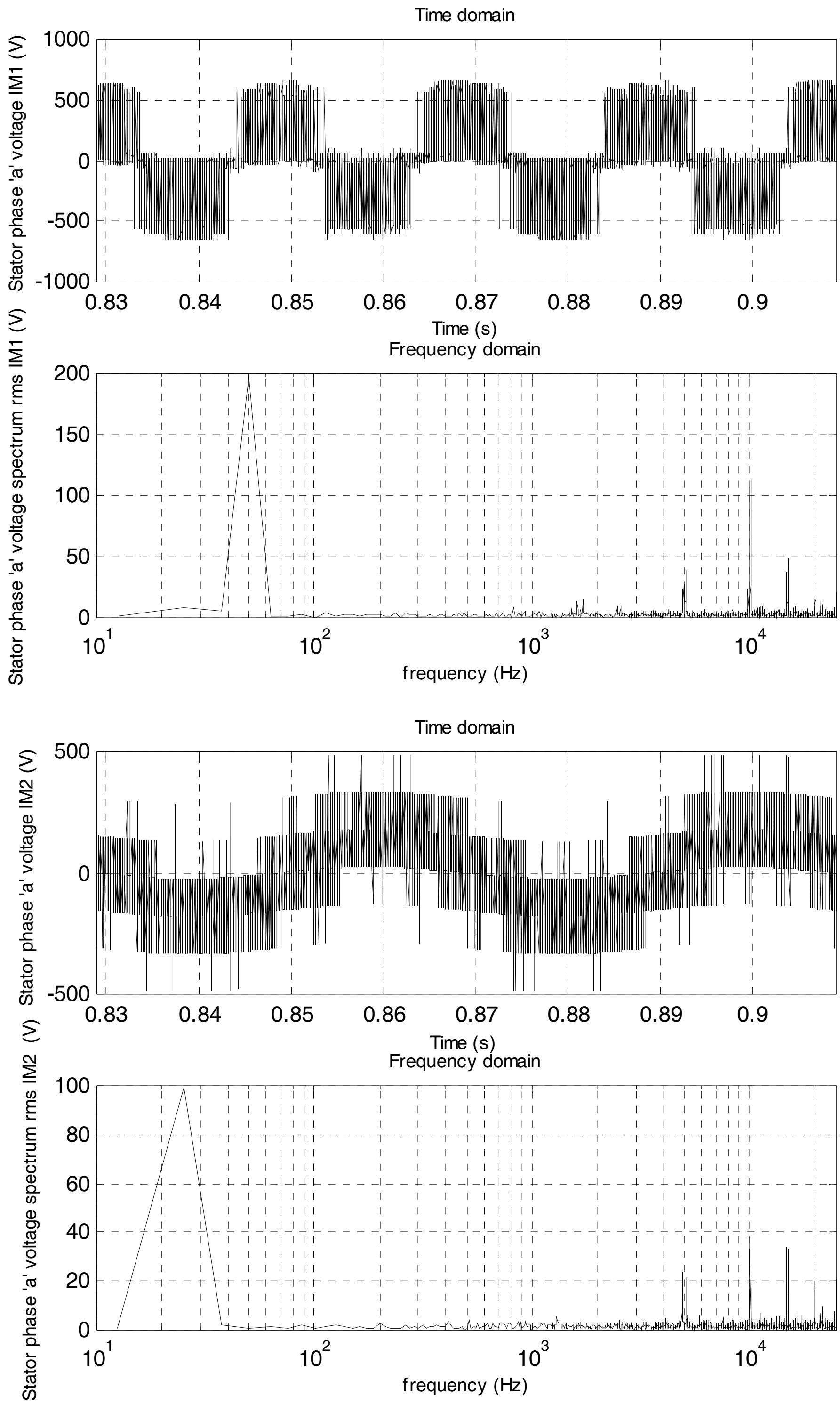

Fig. 6.10b. Time domain waveforms and spectra with ramp-comparison current control: stator phase ‘a’ voltage, IM1, and stator phase ‘a’ voltage, IM2.

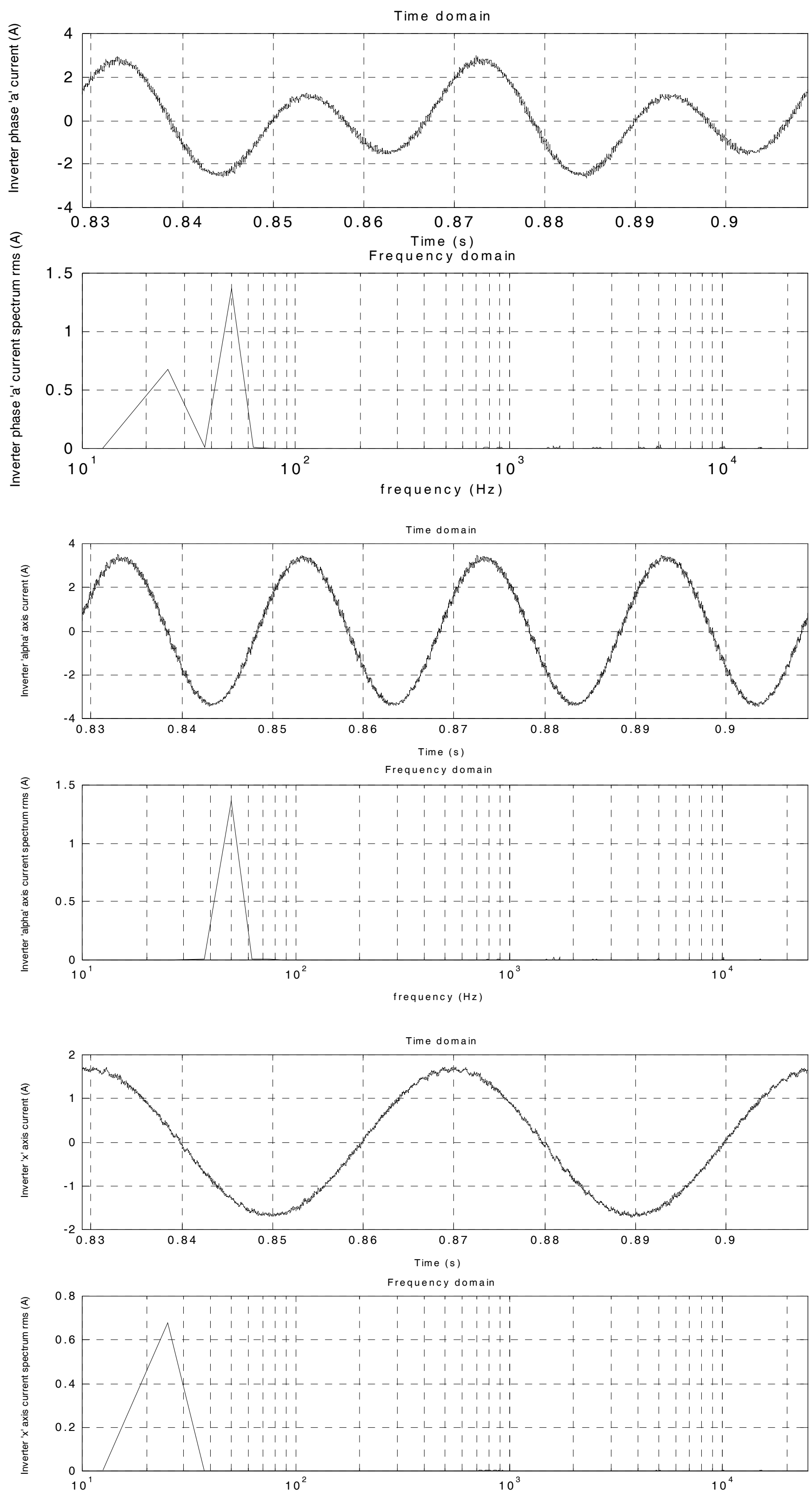

Fig. 6.10c. Time domain waveforms and spectra with ramp-comparison current control: phase ‘a’ inverter current, α-axis inverter current, and x-axis inverter current.

component is the flux/torque producing current of IM2, as is evident from α-axis and x-axis current component spectra, respectively. The current through IM2, of 25 Hz, is twice the inverter current (current through IM1) at 25 Hz and this is in agreement with equation (6.75).

The spectra obtained from ramp-comparison current control method are shown in Fig. 6.10. The harmonics around multiples of 5 kHz can be observed, which is typical for the ramp-comparison current control and is due to constant inverter switching frequency. The values obtained are nearly the same as with hysteresis current control.

Table 6.2. Readings from FFT analysis for hysteresis current control

a. Fundamental voltages and currents of inverter (Figs. 6.9a, 6.9c).

Inverter voltage and current (RMS values)						
Frequency	V_a (V)	V_α (V)	V_x (V)	I_a (A)	I_α (A)	I_x (A)
50	196.8	196.7	4.8	1.35	1.35	0
25	105	0.8	104.4	0.676	0	0.676

b. Fundamental phase ‘a’ voltage of IM1 (Fig. 6.9b).

	Harmonic at 50 Hz		Harmonic at 25 Hz	
	RMS value	Frequency	RMS value	Frequency
Phase ‘a’ voltage	195 V	50 Hz	9.1V	25 Hz

c. Fundamental phase ‘a’ voltage of IM2 (Fig. 6.9b).

	Harmonic at 50 Hz		Harmonic at 25 Hz	
	RMS value	Frequency	RMS value	Frequency
Phase ‘a’ voltage	2 V	50 Hz	98.2 V	25 Hz

Table 6.3. Readings from FFT analysis for ramp-comparison current control

a. Fundamental voltages and currents of inverter (Figs. 6.10a, 6.10c).

Inverter voltage and current (RMS values)						
Frequency	V_a (V)	V_α (V)	V_x (V)	I_a (A)	I_α (A)	I_x (A)
50	196.8	197.8	1.2	1.35	1.35	0
25	107.4	2.7	104.8	0.676	0	0.676

b. Fundamental phase ‘a’ voltage of IM1 (Fig. 6.10b).

	Harmonic at 50 Hz		Harmonic at 25 Hz	
	RMS value	Frequency	RMS value	Frequency
Phase ‘a’ voltage	197 V	50 Hz	8.8 V	25 Hz

c. Fundamental phase ‘a’ voltage of IM2 (Fig. 6.10b).

	Harmonic at 50 Hz		Harmonic at 25 Hz	
	RMS value	Frequency	RMS value	Frequency
Phase ‘a’ voltage	0.9 V	50 Hz	99.5 V	25 Hz

To obtain analytically the inverter and stator voltage components at 50 Hz and 25 Hz under no-load conditions, consider the findings of section 4.9. The α-β impedance of the IM1 at 50 Hz equals $144.86\angle 86°$ Ω, while the α-β impedance of the IM2 at 25 Hz equals $72.945\angle 82.12°$ Ω. The x-y impedance ($Z_{x-y} = \sqrt{R_s^2 + \left(2\pi f L_{ls}\right)^2}$) of the IM1 at 25 Hz is $11.81\angle 32.14°$ Ω, while the x-y impedance of IM2 does not exist. Stator phase 'a' of IM1 carries current of RMS value 1.3528 A at 50 Hz and 0.6764 A at 25 Hz while stator phase 'a' of IM2 carries 1.3528 A at 25 Hz only. Using these values inverter phase 'a' voltage at 50 Hz equals $144.86\angle 86^\circ \times 1.3528 = 196\angle 86^\circ$ V at 50 Hz. Similarly inverter phase 'a' voltage at 25 Hz is calculated as $72.945\angle 82.12^\circ \times 1.3528 + 11.81\angle 32.14^\circ \times 0.6764 = 98.68\angle 82.12^\circ + 7.99\angle 32.14^\circ = 104\angle 78.75^\circ$ V at 25 Hz. Stator phase 'a' voltage of IM1 consists of 50 Hz component, which is essentially the α-β axis voltage drop equal to $196\angle 86^\circ$ V and of x-y axis voltage drop at 25 Hz which is equal to $7.99\angle 32.14^\circ$ V. Stator phase 'a' voltage of IM2 consist of 25 Hz component only, which is essentially the α-β axis voltage drop equal to $98.68\angle 82.12^\circ$ V and no voltage component exists at 50 Hz since there is no x-y circuit in IM2.

The values given in Table 6.3, obtained by simulation and subsequent FFT analysis, are in good agreement with the analytical findings. Further, the values of IM1 voltage harmonics at 50 Hz (phase voltage and α-axis component) and values of IM2 voltage harmonics at 25 Hz (phase voltage and α-axis component) are in full agreement with values reported in Table 5.2 for the single six-phase and single three-phase motor drives.

6.9 SUMMARY

This chapter is devoted to the modelling of six-phase two-motor drive with two induction machines. A six-phase and a three-phase machine are connected in series with appropriate phase transposition and are fed by a single six-phase PWM VSI. Phase variable model of the complete drive system is at first developed in state space form. It is further transformed to obtain orthogonal sets of equations using decoupling transformation. Rotational transformation is then applied to obtain the model in the stationary common reference frame. Finally model is transformed into an arbitrary reference frame and into field oriented reference frames. It is seen from the developed model that the inverter α-β axis voltages are equal to the α-β axis voltages of IM1, while x-y axis inverter voltages are the sum of the x-y axis voltages of IM1 and α-β axis voltages of IM2, with a scaling factor. The inverter α-β axis currents become the α-β axis currents of IM1 and inverter x-y axis currents become the α-β axis currents of IM2 (with a scaling factor). It therefore follows that the two machines can be controlled independently, by controlling inverter α-β and x-y current components, respectively. Vector control principle is further developed for the six-phase two-motor drive system. The concept is verified by simulation for various transients using the hysteresis and ramp-comparison current control. The specific advantage of this scheme is that the second machine does not carry the current of the first machine (because of the cancellation of the currents at the points of series connection). Thus the increase in copper losses affects only the six-phase machine. Performance of the drive system under steady state no-load condition is finally examined by harmonic analysis.

Chapter 7

SPACE VECTOR MODULATION SCHEMES FOR FIVE-PHASE VOLTAGE SOURCE INVERTER

7.1 INTRODUCTION

All the simulations, reported so far in Chapters 3-6, have been based on utilisation of current control techniques in the stationary reference frame (hysteresis and ramp-comparison current control). However, the trend in electric drives nowadays is to utilise current control in the rotating reference frame. This means that, instead of controlling directly inverter phase currents, one controls instead inverter current components in the rotating reference frame, firmly fixed to the rotor flux space vector. Typically, PI current controllers are utilised and the outputs of the current controllers are then voltage references. These voltages are further impressed using a suitable method of PWM for voltage source inverter.

Space vector pulse width modulation has become one of the most popular PWM techniques because of its easier digital implementation and better dc bus utilisation, when compared to the ramp-comparison sinusoidal PWM method. SVPWM for three-phase voltage source inverter has been extensively discussed in the literature and the technology has matured [Holmes and Lipo (2003)]. However, for multi-phase VSIs, there are only application specific SVPWM techniques available in the literature and more research work is needed in this area. There is a lot of flexibility available in choosing the proper space vector combination for an effective control of multi-phase VSIs because of large numbers of space vectors. With reference to five-phase VSI, there are a very few examples found in the literature. Some of them have been mentioned before and are elaborated in detail in this chapter. The existing SVPWM techniques for inverters with an even number of phases will be surveyed in the next chapter.

In the case of a five-phase VSI, there are in total 2^5=32 space vectors available, of which thirty are active state vectors and two are zero state vectors forming three concentric decagons. Toliyat et al (2000), Xu et al (2002) and Shi and Toliyat (2002) have used only ten outer large length vectors to implement the symmetrical SVPWM. Two neighbouring active space vectors and two zero space vectors are utilised in one switching period to synthesise the input reference voltage. In total, twenty switchings take place in one switching period, so that state of each switch is changed twice. The switching is done in such a way that, in the first switching half-period the first zero vector is applied, followed by two active state vectors and then by the second zero state vector. The second switching half-period is the mirror image of the first one. The symmetrical SVPWM is achieved in this way. This method is the simplest extension of space vector modulation of three-phase VSIs.

Kelly et al (2003) proposed generalised *n*-phase SVPWM with a specific example of a nine-phase VSI. The total number of available space vectors is 512, but most of them are redundant vectors. The total of 512 vectors are subdivided into four categories corresponding to four different switching conditions (4 switches ‘on’, 5 ‘off’ or vice-versa; 3 ‘on’, 6 ‘off’ or vice-versa; 2 ‘on’, 7 ‘off’ or vice-versa; 1 ‘on’, 8 ‘off’ or vice-versa). Out of these four sets, only those subsets are chosen that correspond to the maximum length vectors from each of the above defined categories. Thus in each sector eight neighbouring active and two zero space vectors are used to realise the SVPWM. The total time of application of active state vectors is determined with regard to the outer-most set of vectors. In order to obtain three-phase equivalent of a nine-phase machine, the total time of application of active state vector is adjusted by using a proper scaling factor. The times of application of other active state vectors are then obtained by subdividing the total time in the ratio of their lengths.

During the work on research reported in this chapter, a novel SVPWM scheme for five-phase VSI has been proposed in de Silva et al (2004). In contrast to the scheme that utilises only two large adjacent active space vectors, this method makes use of both medium and large space vectors by applying four adjacent active space vectors in each switching period. This scheme will be included in this chapter, for comparison purposes. Another reported work on the same subject is in Ryu et al (2004), where SVPWM scheme is suggested to generate non-sinusoidal output voltage. In this work also four neighbouring space vectors are used to synthesise the reference and both $\alpha - \beta$ and x-y voltages are controlled. The motive behind this scheme is to supply five-phase machines with fundamental and third harmonic voltages in order to boost the torque production in concentrated winding machines.

Based on the observations from literature, different alternative SVPWM schemes for five-phase VSI are formulated and presented in this chapter. Firstly, the existing SVPWM based on the standard technique of using only large space vectors is analysed. Next, another scheme based on using only medium space vectors, is presented. The large and medium region space vectors are further utilised together to formulate the alternative modulation schemes. The limitations of using both large and medium space vectors are highlighted. The scheme of de Silva et al (2004) is included at this stage. Next, a detailed comparison of all the SVPWM schemes is performed (both existing and newly developed schemes are included) and a combined scheme of space vector modulation is suggested. The developed techniques have been simulated to prove the viability of their practical implementation. The analytical expressions of average inverter pole voltages for different schemes have been formulated and are given in this chapter.

An ideal SVPWM of a five-phase inverter should satisfy a number of requirements. First of all, in order to keep the switching frequency constant, each switch can change state only twice in the switching-period (once 'on' to 'off' and once 'off' to 'on', or vice-versa). Secondly, the RMS value of the fundamental phase voltage of the output must equal the RMS of the reference space vector. Thirdly, the scheme must provide full utilisation of the available dc bus voltage. Finally, since the inverter is aimed at supplying the load with sinusoidal voltages, the low-order harmonic content needs to be minimised (this especially applies to the third and seventh harmonic, which are included in the analysis at all times). These criteria are used in assessing the merits and demerits of various SVPWM schemes and in formulating the combined schemes towards the end of the chapter.

A novel SVPWM scheme is developed for five-phase VSI feeding two five-phase machines connected in series and controlled independently. The scheme and the results are presented in this chapter.

Some of the original findings of this chapter are reported in Iqbal and Levi (2005a) and Iqbal and Levi (2006).

7.2 SPACE VECTOR MODULATION SCHEMES

It has been shown in section 3.3 that the total number of space vectors available in a five-phase VSI is 32. Out of these 32 space voltage vectors, thirty are active and two are zero space vectors and they form three concentric decagons in $\alpha-\beta$ plane with zero space vectors at the origin as shown in sections 3.2-3.3. However, since a five-phase system is under consideration, one has to represent the inverter space vectors in a five-dimensional space. Such a space can be decomposed into two two-dimensional sub-spaces ($\alpha-\beta$ and x-y) and one single-dimensional sub-space (zero-sequence). Since the load is assumed to be star-connected with isolated neutral point, zero-sequence cannot be excited and it is therefore sufficient to consider only two two-dimensional sub-spaces, $\alpha-\beta$ and x-y. Inverter voltage space vector in $\alpha-\beta$ sub-space is given with,

$$\underline{v}_{\alpha\beta}^{INV} = 2/5\left(v_a + \underline{a}v_b + \underline{a}^2 v_c + \underline{a}^3 v_d + \underline{a}^4 v_e\right) \tag{7.1a}$$

where $\underline{a} = \exp(j2\pi/5)$. On the basis of the general decoupling transformation matrix for an n-phase system [White and Woodson, (1959)] inverter voltage space vectors in the second two-dimensional sub-space are determined with,

$$\underline{v}_{xy}^{INV} = 2/5\left(v_a + \underline{a}^2 v_b + \underline{a}^4 v_c + \underline{a}\ v_d + \underline{a}^3 v_e\right) \tag{7.1b}$$

The 32 space vectors are transformed into two orthogonal sub-spaces using (7.1) but in power variant form. In other words, power per-phase in original and transformed domain is now kept constant, rather than the total power. The scaling factor in (7.1) is therefore set to 2/5 rather than $\sqrt{2/5}$. This choice is more convenient in discussion of SVPWM, since it makes the magnitude of the reference voltage space vector equal to the peak value of the desired sinusoidal output phase voltage. The zero-sequence component is identically equal to zero because of the assumption of isolated neutral point. The phase voltage space vectors in two orthogonal planes, obtained using (7.1) and Tables 3.8, 3.13 and 3.17, are shown in Fig. 7.1.

It can be seen from Fig. 7.1 that the outer decagon space vectors of the $\alpha-\beta$ plane map into the inner-most decagon of the x-y plane, the inner-most decagon of $\alpha-\beta$ plane forms the outer decagon of x-y plane while the middle decagon space vectors map into the same region. Further, it is observed from the above mapping that the phase sequence *a,b,c,d,e* of $\alpha-\beta$ plane corresponds to *a,c,e,b,d*, which are basically the third harmonic voltages. It has been shown by many authors, including Correa et al (2003), Bojoi et al (2002b), Mohapatra et al (2002), Zhao and Lipo (1995) and Gopakumar et al (1993), that the presence of x-y space vector components introduces waveform distortion resulting in unnecessary harmonic losses in the machine fed using SVPWM modulator based VSI.

There are in total ten distinct sectors with 36° spacing. The outer and inner-most decagon space vectors are the result of three switches being ‘on’ from upper (lower) set and two switches being ‘off’ from upper (lower) set or vice versa (section 3.3). Thus the inner-most space vectors in $\alpha-\beta$ plane are redundant and are therefore omitted from further discussion. This is in full compliance with observation of Kelly et al (2003), where it is stated that only subset with maximum length vectors have to be used for any given combination of the switches that are ‘on’ and ‘off’ (3-2 and 2-3 in this case). The middle region space vectors correspond to four switches being ‘on’ from upper (lower) set and one switch being ‘off’ from upper (lower) set or vice-versa (section 3.3). In what follows, the vectors belonging to the middle region are simply termed medium vectors, while the vectors of the outer-most region are called large vectors.

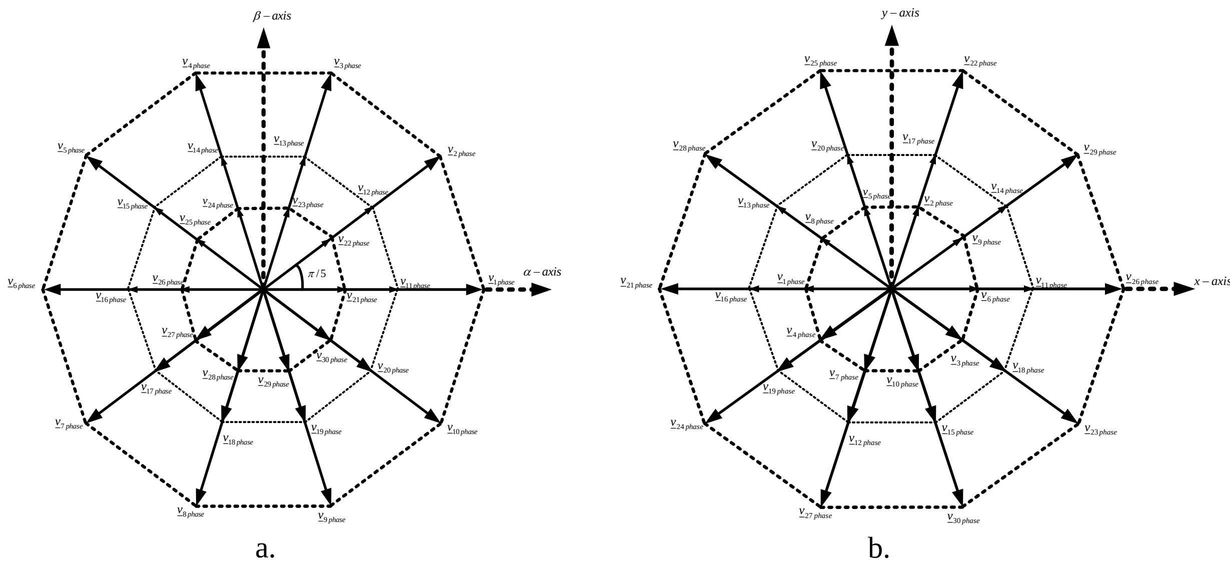

Fig. 7.1. Five-phase VSI phase voltage space vectors in: a. $\alpha-\beta$ plane, and b. x-y plane.

7.2.1 Application of the large space vectors only (three vectors per switching period)

The SVPWM scheme discussed in this section considers the outer-most decagon of space vectors in $\alpha-\beta$ plane. The input reference voltage vector is synthesised from two active neighbouring and zero space vectors. This scheme is used as benchmark to compare the results obtained from the other developed schemes since it is the one commonly used in literature [Toliyat et al (2003), Xu et al (2002), Shi and Toliyat (2002)] for the five-phase VSI.

To calculate the time of application of different vectors, consider Fig. 7.2, depicting the position of different available space vectors and the reference vector in the first sector. The time of application of active space voltage vectors is found from Fig. 7.2 as

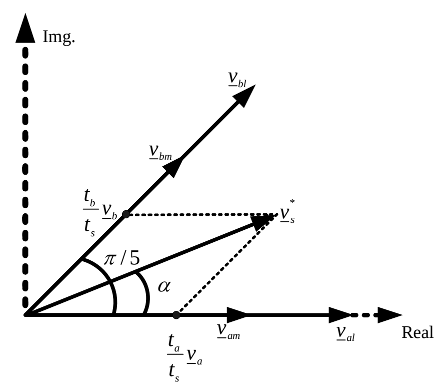

Fig. 7.2. Principle of space vector time calculation for a five-phase VSI.

$$t_a = \frac{|\underline{v}_s^*| \sin(k\pi/5 - \alpha)}{|\underline{v}_l| \sin(\pi/5)} t_s \tag{7.2a}$$

$$t_b = \frac{|\underline{v}_s^*| \sin(\alpha - (k-1)\pi/5)}{|\underline{v}_l| \sin(\pi/5)} t_s \tag{7.2b}$$

$$t_o = t_s - t_a - t_b \tag{7.3}$$

where k is the sector number ($k =$ 1 to 10) and $|\underline{v}_{al}| = |\underline{v}_{bl}| = |\underline{v}_l| = \frac{2}{5} V_{DC}\, 2\cos(\pi/5)$. Also $|\underline{v}_{am}| = |\underline{v}_{bm}| = |\underline{v}_m| = \frac{2}{5} V_{DC}$ (Fig. 7.2), as follows from section 3.3 and (7.1). Symbol $\underline{v}_s^*$ denotes the reference voltage space vector, while $|\underline{x}|$ stands for modulus of a complex number $\underline{x}$. Indices "*l*" and "*m*" stand for large and medium vectors, respectively.

The largest possible fundamental peak voltage magnitude that may be achieved using this scheme corresponds to the radius of the largest circle that can be inscribed within the decagon. The circle is tangential to the mid-point of the lines connecting the ends of the active space vectors. Thus the maximum fundamental peak output voltage $V_{\max}$ is $V_{\max} = (2/5)\, 2\cos(\pi/5)\cos(\pi/10) V_{DC} = 0.61554 V_{DC}$. The maximum peak fundamental output in ten-step mode is, from expression (3.3), given with $V_{\max,10step} = \frac{2}{\pi} V_{DC}$. Thus the ratio of the maximum possible fundamental output voltage with SVPWM and in ten-step mode is $V_{\max} / V_{\max,10step} = 0.96689$.

The sequence of vectors applied in all ten sectors and corresponding switching patterns are shown in Fig. 7.3 where states of five inverter legs take values of -1/2 and 1/2 (referencing to mid-point of the dc supply is applied) and the five traces illustrate, from top to bottom, legs A,B,C,D and E, respectively.

It is seen from the switching pattern (Fig. 7.3) that in the first half of the switching cycle zero space vector is applied, followed by two active space vectors and the second zero space vector. The sequence followed in the second half cycle is the mirror image of the first one. The total number of state changes in one PWM switching period is thus twenty, since each switch changes state twice in one switching period.

The simulation is done for different peak values of the five-phase sinusoidal reference input, ranging from maximum possible magnitude down to 10% of this value in 10% steps. The simulation is also done for 61.8% and 38.2% of the maximum achievable output with large vectors. These two percentage values correspond to the maximum possible output if medium space vectors only and short space vectors only are used alone, respectively. The dc

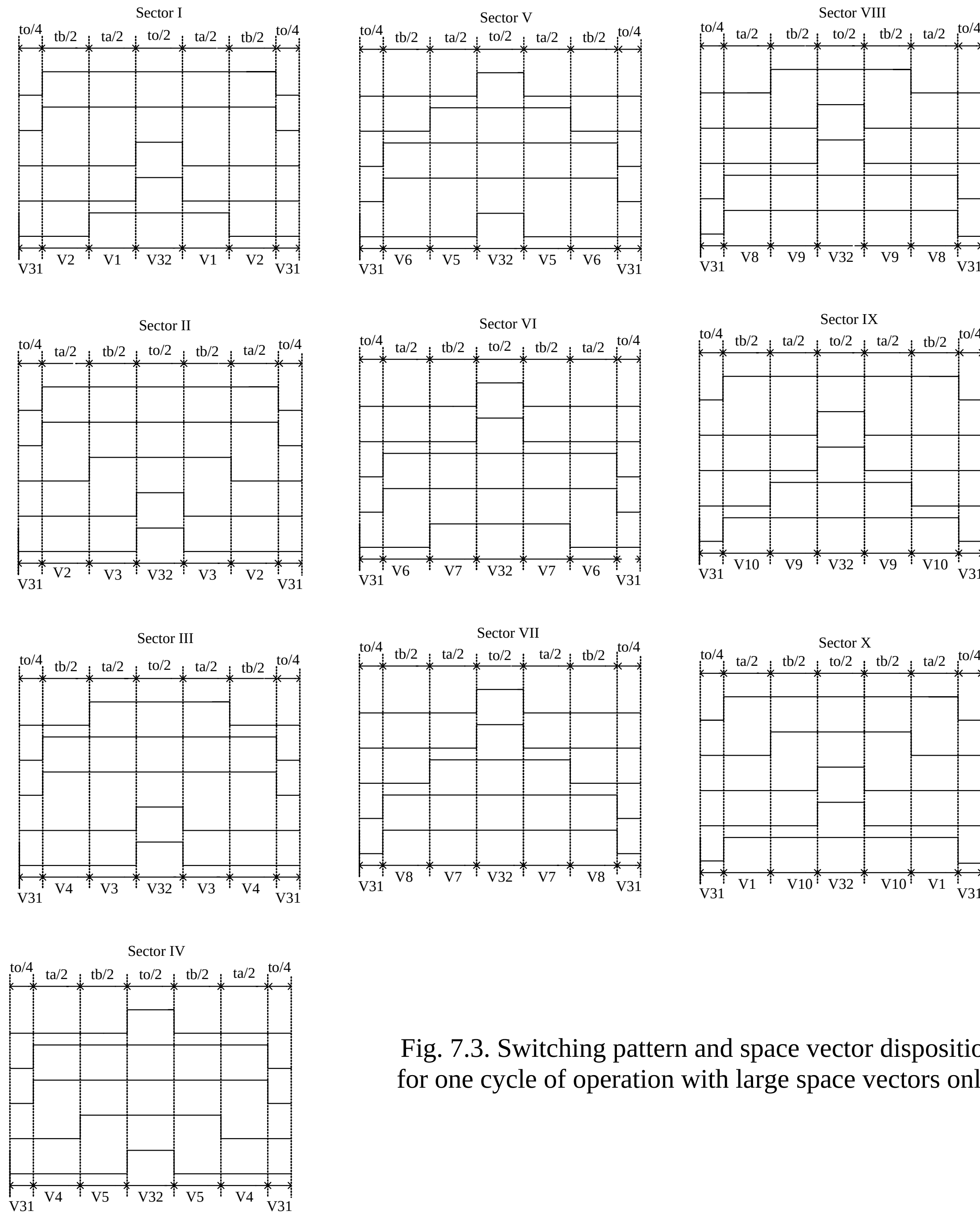

Fig. 7.3. Switching pattern and space vector disposition for one cycle of operation with large space vectors only.

link voltage is set to one per unit and the switching frequency is 5 kHz. An analogue first order filter is used to filter the output voltages and the resulting filtered output phase voltages and leg voltages are shown in Fig. 7.4 for reference equal to the maximum achievable output voltage. The shapes of the phase and the leg voltages are preserved for changes in the input reference voltage, except that there is a corresponding reduction in their amplitude and thus only one case is shown here. The filter time constant used to filter the phase voltages is 0.8 ms and for the leg voltages it is kept equal to 0.4 ms. The frequency of the reference input is kept at 50 Hz. The RMS values of the fundamental output voltages and low-order harmonic components, obtained using FFT, are listed in Table 7.1. Percentage values of higher harmonics are given with respect to the corresponding fundamental harmonic.

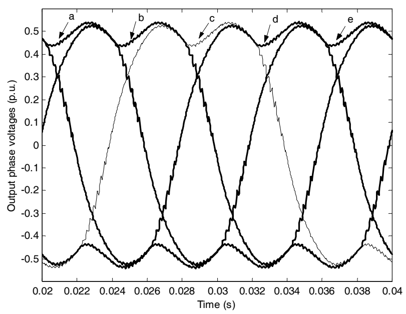

a.

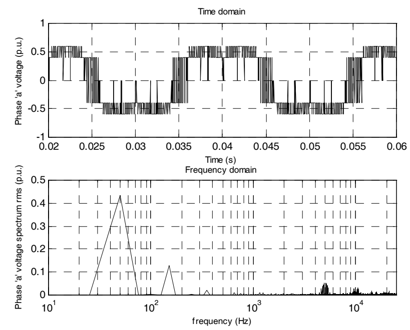

c.

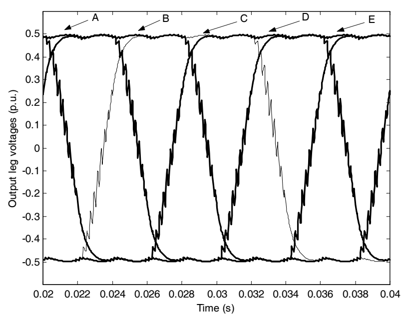

b.

Fig. 7.4. Output of VSI for input reference equal to the maximum achievable (0.6155 p.u.): a. phase voltages, b. leg voltages, c. harmonic spectrum.

Table 7.1. RMS of fundamental and low-order harmonic components of output phase voltages.

$\lvert \underline{v}_s^* \rvert$ (p.u.)	Fundamental (50 Hz)		3rd harmonic (150 Hz, p.u.)	7th harmonic (350 Hz, p.u.)
	Theoretical RMS value (p.u.)	Simulation RMS value (p.u.)		
0.6155 (Max)	0.435	0.435	0.128 (29.42%)	0.022 (5.05%)
90% of Max	0.3917	0.39	0.116 (29.61%)	0.021 (5.36%)
80% of Max	0.348	0.347	0.1 (28.73%)	0.015 (4.31%)
70% of Max	0.304	0.3	0.082 (26.97%)	0.012 (3.94%)
61.8% of Max	0.268	0.267	0.077 (28.73%)	0.0105 (3.91%)
50% of Max	0.217	0.216	0.065 (29.95%)	0.013 (5.99%)
38.2% of Max	0.166	0.166	0.049 (29.52%)	0.008 (4.82%)
30% of Max	0.13	0.129	0.038 (29.23%)	0.008 (6.15%)
20% of Max	0.087	0.086	0.028 (32.18%)	0.0055 (6.32%)
10% of Max	0.0435	0.0435	0.013 (29.88%)	0.0017 (3.9%)

It is observed from Table 7.1 that the output phase voltages contain a considerable amount of the third harmonic. In addition, there is a significant amount of the seventh harmonic component. These harmonic components are the consequence of x-y components of the space vectors. By using only outer decagon set of space vectors, the x-y components are free to cause the production of the third and the seventh harmonic in the output voltages.

The analytical expression for leg voltages averaged over one switching cycle and expressed in terms of the midpoint of the dc bus of the five-phase VSI can be deduced from the switching pattern shown in Fig 7.3. For sector I one has

$$
\begin{aligned}
V_A &= \frac{V_{DC}}{2t_s}\left(-t_o/4+t_b/2+t_a/2+t_o/2+t_a/2+t_b/2-t_o/4\right)\\
V_B &= \frac{V_{DC}}{2t_s}\left(-t_o/4+t_b/2+t_a/2+t_o/2+t_a/2+t_b/2-t_o/4\right)\\
V_C &= \frac{V_{DC}}{2t_s}\left(-t_o/4-t_b/2-t_a/2+t_o/2-t_a/2-t_b/2-t_o/4\right)\\
V_D &= \frac{V_{DC}}{2t_s}\left(-t_o/4-t_b/2-t_a/2+t_o/2-t_a/2-t_b/2-t_o/4\right)\\
V_E &= \frac{V_{DC}}{2t_s}\left(-t_o/4-t_b/2+t_a/2+t_o/2+t_a/2-t_b/2-t_o/4\right)
\end{aligned}
\qquad (7.4)
$$

Substituting the expression for times of applications for different space vectors from (7.1)-(7.3), the average leg voltages are found and are tabulated in Table 7.2. The expressions for average leg voltages in nine other sectors are obtained in a similar fashion.

The analytical expressions of average leg voltages for sectors VI to X are identical to those in sectors I to V in the same order and are thus not shown in Table 7.2.

A calculation of the average leg voltages for maximum achievable reference input voltage is done using expressions of Table 7.2 and the resulting plot for all five legs is shown

Table 7.2. Analytical expression for leg voltages when only large vectors are used.

Sector	Leg a V_A	Leg b V_B	Leg c V_C	Leg d V_D	Leg e V_E
I	$\lvert\underline{v}_s^*\rvert\cos(\pi/5)\bullet\cos(\omega t-\pi/10)$	$\lvert\underline{v}_s^*\rvert\cos(\pi/5)\bullet\cos(\omega t-\pi/10)$	$-\lvert\underline{v}_s^*\rvert\cos(\pi/5)\bullet\cos(\omega t-\pi/10)$	$-\lvert\underline{v}_s^*\rvert\cos(\pi/5)\bullet\cos(\omega t-\pi/10)$	$\frac{5}{2}\lvert\underline{v}_s^*\rvert\bullet\cos(\omega t+2\pi/5)$
II	$\lvert\underline{v}_s^*\rvert\cos(\pi/5)\bullet\sin(\omega t+\pi/5)$	$\lvert\underline{v}_s^*\rvert\cos(\pi/5)\bullet\sin(\omega t+\pi/5)$	$-\frac{5}{2}\lvert\underline{v}_s^*\rvert\bullet\cos(\omega t+\pi/5)$	$-\lvert\underline{v}_s^*\rvert\cos(\pi/5)\bullet\sin(\omega t+\pi/5)$	$-\lvert\underline{v}_s^*\rvert\cos(\pi/5)\bullet\sin(\omega t+\pi/5)$
III	$\frac{5}{2}\lvert\underline{v}_s^*\rvert\cos(\omega t)$	$\lvert\underline{v}_s^*\rvert\cos(\pi/5)\bullet\sin(\omega t)$	$\lvert\underline{v}_s^*\rvert\cos(\pi/5)\bullet\sin(\omega t)$	$-\lvert\underline{v}_s^*\rvert\cos(\pi/5)\bullet\sin(\omega t)$	$-\lvert\underline{v}_s^*\rvert\cos(\pi/5)\bullet\sin(\omega t)$
IV	$\lvert\underline{v}_s^*\rvert\cos(\pi/5)\bullet\cos(\omega t+3\pi/10)$	$-\lvert\underline{v}_s^*\rvert\cos(\pi/5)\bullet\cos(\omega t+3\pi/10)$	$-\lvert\underline{v}_s^*\rvert\cos(\pi/5)\bullet\cos(\omega t+3\pi/10)$	$-\frac{5}{2}\lvert\underline{v}_s^*\rvert\bullet\sin(\omega t+3\pi/10)$	$\lvert\underline{v}_s^*\rvert\cos(\pi/5)\bullet\cos(\omega t+3\pi/10)$
V	$\lvert\underline{v}_s^*\rvert\cos(\pi/5)\bullet\cos(\omega t+\pi/10)$	$\frac{5}{2}\lvert\underline{v}_s^*\rvert\bullet\sin(\omega t+\pi/10)$	$-\lvert\underline{v}_s^*\rvert\cos(\pi/5)\bullet\cos(\omega t+\pi/10)$	$-\lvert\underline{v}_s^*\rvert\cos(\pi/5)\bullet\cos(\omega t+\pi/10)$	$\lvert\underline{v}_s^*\rvert\cos(\pi/5)\bullet\cos(\omega t+\pi/10)$

in Fig. 7.5a. For lower values of input reference voltages, the waveforms of average leg voltages are preserved except for the corresponding reduction in the amplitude. The leg voltages thus obtained are sums of phase voltages and the common-mode voltage, which is the voltage between the neutral point of the load and the dc link midpoint, as indicated by expression (3.4).

Average leg voltages, corresponding to the maximum input reference voltage, obtained using simulation are shown in Fig. 7.5b.

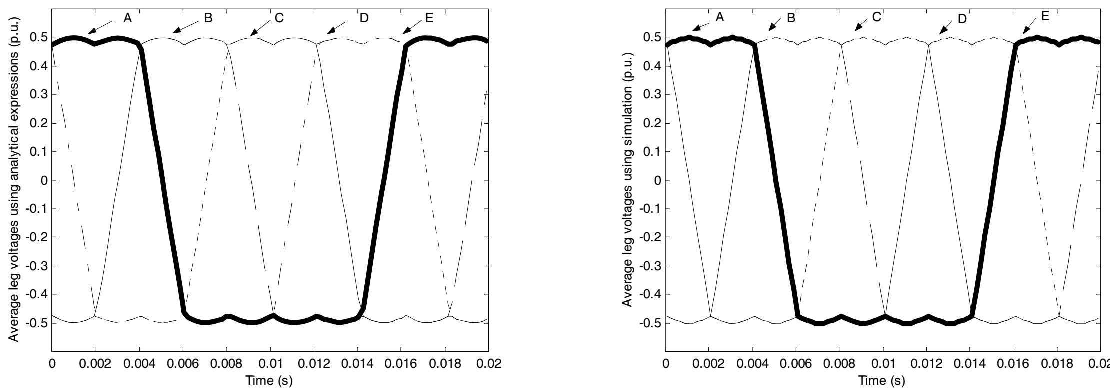

a. b.

Fig. 7.5. Average leg voltages using large space vectors only, obtained using: a. analytical expressions of Table 7.2., b. simulation.

This figure was produced by averaging the PWM leg voltage waveform over each switching period (0.2 ms), for one cycle of the fundamental output voltage (20 ms). By comparing the average leg voltages obtained using analytical expressions (Fig. 7.5a) with those obtained using simulation (Fig. 7.5b), it can be concluded that they are identical and thus this validates the derived analytical expressions of Table 7.2. Furthermore, both figures closely resemble waveforms in Fig. 7.4 (part b) for leg voltages, obtained by low-pass filtering of PWM leg voltages.

7.2.2 Application of the medium space vectors only (three vectors per switching period)

This scheme is based on the medium space vectors only. The method is a simple extension of the standard technique where two active and zero space vector are utilised per switching period to implement the SVPWM. The expressions to calculate the time of application of different space vectors are again given with (7.2)-(7.3), where $\left|\underline{v}_l\right|$ is now replaced with $\left|\underline{v}_m\right|$. The maximum output peak fundamental phase voltage with this set of space vectors is $V_{\max} = (2/5)V_{DC}\cos(\pi/10)$. The switching pattern and space vector disposition for each sector are shown in Fig. 7.6.

It is observed from Fig. 7.6 that only two phases change state in transition from sector to sector, e.g. in transition from sector I to sector II phase 'a' and phase 'b' change states while phases *c, d, e* do not. The total number of switchings is the same as before. However, four switches are 'on' ('off') in upper (lower) part of the inverter for any active state, meaning that in this mode the conduction pattern is 4-1 or 1-4. The distribution of zero space voltage vectors ensures the symmetrical SVPWM pattern.

The simulation conditions are similar to those in section 7.2.1. The input reference voltage vector magnitude is varied from 61.8% of maximum achievable down to 10% and the resulting plots, obtained after filtering, for maximum achievable output voltage are shown in Fig. 7.7. The filter time constant is now 0.25 ms for leg voltages. The filter time constant for the phase voltages is the same as in 7.2.1. The shapes of the phase and the leg voltages are preserved for the changes in the input reference voltages except for a corresponding change in the magnitudes and this is the reason for showing only one case here. The maximum achievable output peak fundamental phase voltage with only medium space vectors is 61.8% of what is available with only large space vectors. The RMS values of the fundamental and the low-order harmonic components are listed in Table 7.3.

Table 7.3. RMS of fundamental and low-order harmonic components of output phase voltages.

$\left\|\underline{v}_s^*\right\|$ (p.u.)	Fundamental (50 Hz)		3rd harmonic (150 Hz, p.u.)	7th harmonic (350 Hz, p.u.)
	Theoretical RMS (p.u.)	Simulation RMS (p.u.)		
61.8% of Max	0.268	0.268	0.204 (76.12%)	0.04 (14.9%)
50% of Max	0.217	0.217	0.165 (76.03%)	0.0275 (12.67%)
38.2 % of Max	0.166	0.166	0.12 (72.28%)	0.02 (12.04%)
30% of Max	0.13	0.125	0.092 (73.6%)	0.0214 (17.12%)
20% of Max	0.087	0.084	0.064 (76.19%)	0.0165 (19.64%)
10% of Max	0.0435	0.044	0.034 (77.27%)	0.0056 (12.72%)

It is observed from Table 7.3 that the third harmonic component percentage value remains more or less fixed for all values of the input reference magnitude. The same applies to the seventh harmonic components. Comparison of the third and the seventh harmonic percentage values in Table 7.1 and Table 7.3 indicates that use of only medium vectors considerably worsens low-frequency part of the spectrum.

The analytical expressions for leg voltages averaged over one switching cycle (expressed with respect to the midpoint of the dc bus of five-phase VSI) can be deduced from the switching pattern shown in Fig 7.6. For sector I one finds

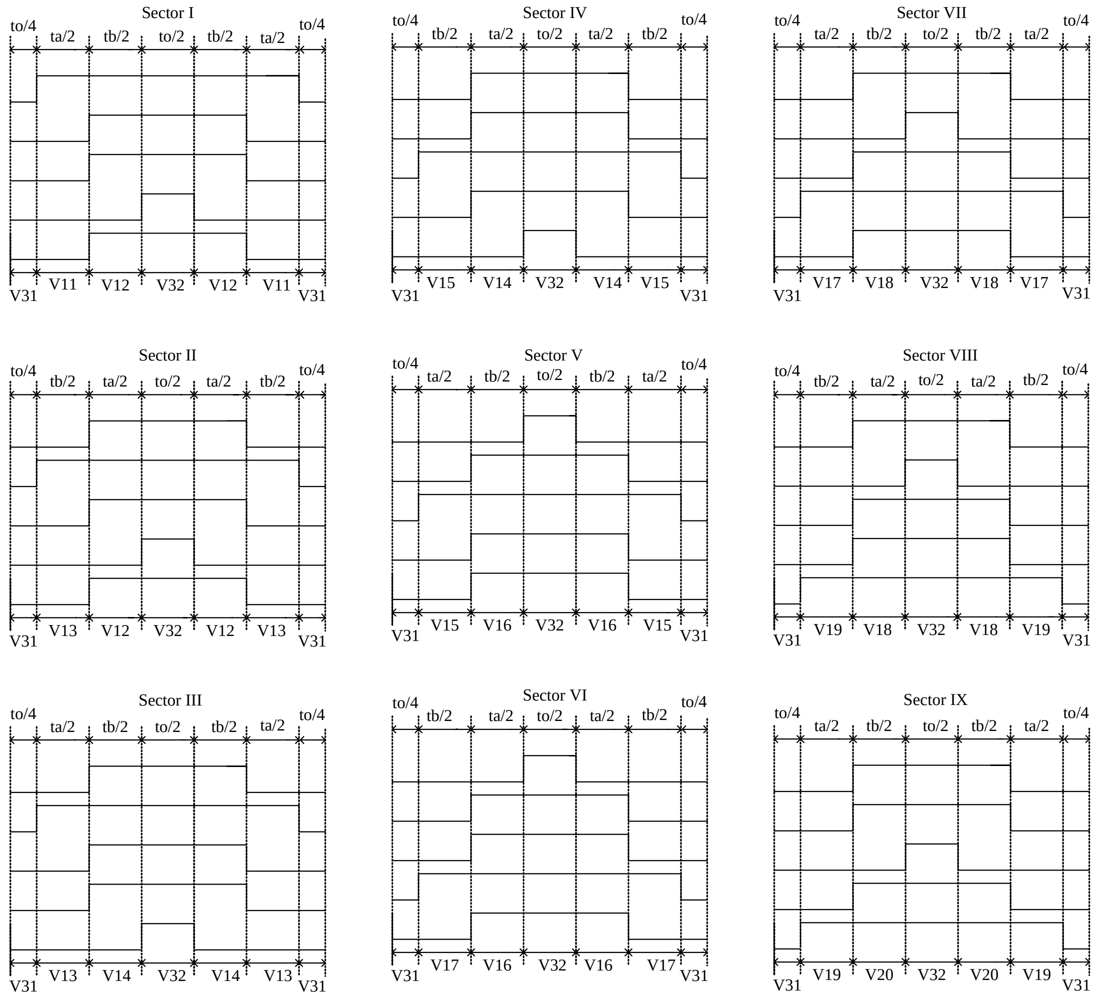

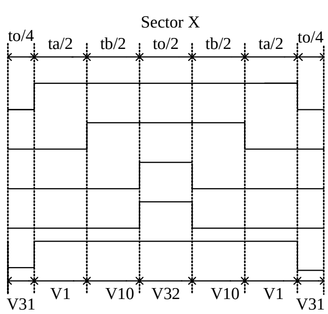

Fig. 7.6. Switching pattern and space vector disposition for one cycle of operation with medium space vectors only.

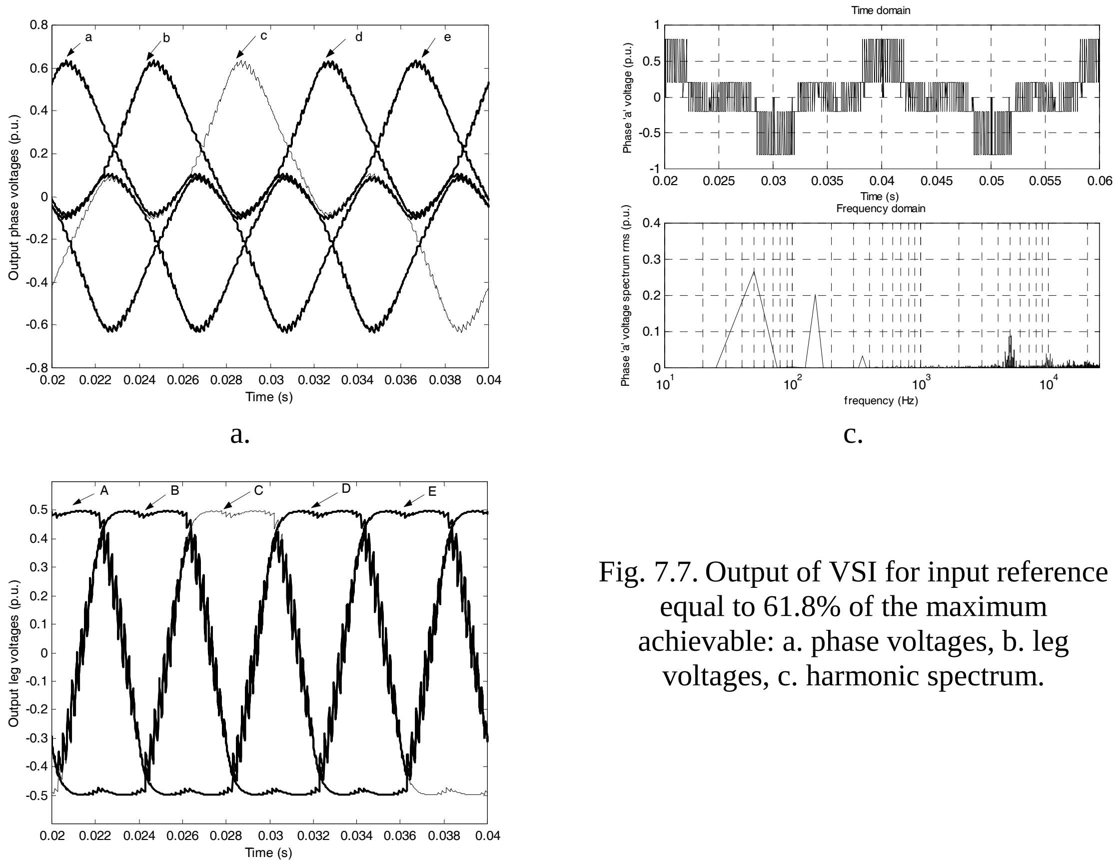

a. c. b.

Fig. 7.7. Output of VSI for input reference equal to 61.8% of the maximum achievable: a. phase voltages, b. leg voltages, c. harmonic spectrum.

$$
\begin{aligned}
V_A &= \frac{V_{DC}}{2t_s}\left(-t_o/4 + t_a/2 + t_b/2 + t_o/2 + t_b/2 + t_a/2 - t_o/4\right) \\
V_B &= \frac{V_{DC}}{2t_s}\left(-t_o/4 - t_a/2 + t_b/2 + t_o/2 + t_b/2 - t_a/2 - t_o/4\right) \\
V_C &= \frac{V_{DC}}{2t_s}\left(-t_o/4 - t_a/2 + t_b/2 + t_o/2 + t_b/2 - t_a/2 - t_o/4\right) \\
V_D &= \frac{V_{DC}}{2t_s}\left(-t_o/4 - t_a/2 - t_b/2 + t_o/2 - t_b/2 - t_a/2 - t_o/4\right) \\
V_E &= \frac{V_{DC}}{2t_s}\left(-t_o/4 - t_a/2 + t_b/2 + t_o/2 + t_b/2 - t_a/2 - t_o/4\right)
\end{aligned}
\tag{7.5}
$$

The resulting expressions for various sectors are listed in Table 7.4. The expressions for sectors VI to X are identical to those for sectors I to V in the same order and are thus not given in Table 7.4.

Calculation is done again to obtain the average leg voltages using analytical expressions, for maximum achievable reference input voltage, and the resulting plot for all five legs is shown in Fig. 7.8a. It is observed from Fig. 7.8a that the leg voltages are highly distorted and are causing highly distorted phase voltage waveforms too.

Table 7.4. Analytical expressions for leg voltages when only medium vectors are used.

Sect.	Leg a V_A	Leg b V_B	Leg c V_C	Leg d V_D	Leg e V_E
I	$\left(\dfrac{\lvert\underline{v}_s^*\rvert\sin(3\pi/10)/}{2\sin(\pi/10)}\right)\bullet\cos(\omega t-\pi/10)$	$-5\lvert\underline{v}_s^*\rvert\sin(3\pi/10)\bullet\cos(\omega t+2\pi/5)$	$-5\lvert\underline{v}_s^*\rvert\sin(3\pi/10)\bullet\cos(\omega t+2\pi/5)$	$-\left(\dfrac{\lvert\underline{v}_s^*\rvert\sin(3\pi/10)/}{2\sin(\pi/10)}\right)\bullet\cos(\omega t-\pi/10)$	$-5\lvert\underline{v}_s^*\rvert\sin(3\pi/10)\bullet\cos(\omega t+2\pi/5)$
II	$5\lvert\underline{v}_s^*\rvert\sin(3\pi/10)\bullet\cos(\omega t+\pi/5)$	$\left(\dfrac{\lvert\underline{v}_s^*\rvert\sin(3\pi/10)/}{2\sin(\pi/10)}\right)\bullet\sin(\omega t+\pi/5)$	$5\lvert\underline{v}_s^*\rvert\sin(3\pi/10)\bullet\cos(\omega t+\pi/5)$	$-\left(\dfrac{\lvert\underline{v}_s^*\rvert\sin(3\pi/10)/}{2\sin(\pi/10)}\right)\bullet\sin(\omega t+\pi/5)$	$5\lvert\underline{v}_s^*\rvert\sin(3\pi/10)\bullet\cos(\omega t+\pi/5)$
III	$-5\lvert\underline{v}_s^*\rvert\sin(3\pi/10)\bullet\cos(\omega t)$	$\left(\dfrac{\lvert\underline{v}_s^*\rvert\sin(3\pi/10)/}{2\sin(\pi/10)}\right)\bullet\sin(\omega t)$	$-5\lvert\underline{v}_s^*\rvert\sin(3\pi/10)\bullet\cos(\omega t)$	$-5\lvert\underline{v}_s^*\rvert\sin(3\pi/10)\bullet\cos(\omega t)$	$-\left(\dfrac{\lvert\underline{v}_s^*\rvert\sin(3\pi/10)/}{2\sin(\pi/10)}\right)\bullet\sin(\omega t)$
IV	$5\lvert\underline{v}_s^*\rvert\sin(3\pi/10)\bullet\sin(\omega t+3\pi/10)$	$5\lvert\underline{v}_s^*\rvert\sin(3\pi/10)\bullet\sin(\omega t+3\pi/10)$	$-\left(\dfrac{\lvert\underline{v}_s^*\rvert\sin(3\pi/10)/}{2\sin(\pi/10)}\right)\bullet\cos(\omega t+3\pi/10)$	$5\lvert\underline{v}_s^*\rvert\sin(3\pi/10)\bullet\sin(\omega t+3\pi/10)$	$\left(\dfrac{\lvert\underline{v}_s^*\rvert\sin(3\pi/10)/}{2\sin(\pi/10)}\right)\bullet\cos(\omega t+3\pi/10)$
V	$\left(\dfrac{\lvert\underline{v}_s^*\rvert\sin(3\pi/10)/}{2\sin(\pi/10)}\right)\bullet\cos(\omega t+\pi/10)$	$-5\lvert\underline{v}_s^*\rvert\sin(3\pi/10)\bullet\sin(\omega t+\pi/10)$	$-\left(\dfrac{\lvert\underline{v}_s^*\rvert\sin(3\pi/10)/}{2\sin(\pi/10)}\right)\bullet\cos(\omega t+\pi/10)$	$-5\lvert\underline{v}_s^*\rvert\sin(3\pi/10)\sin(\omega t+\pi/10)$	$-5\lvert\underline{v}_s^*\rvert\sin(3\pi/10)\sin(\omega t+\pi/10)$

The average leg voltages obtained using analytical expressions (Fig. 7.8a) are further compared with average leg voltages obtained using simulation, Fig. 7.8b. The procedure for obtaining Fig. 7.8b is the same as explained in conjunction with Fig. 7.5b. It is evident from Fig. 7.8a and Fig. 7.8b that these are identical and thus this validates the analytical expressions of Table 7.4. Once more, both figures closely correspond to the one of Fig. 7.7 (part b) obtained by filtering.

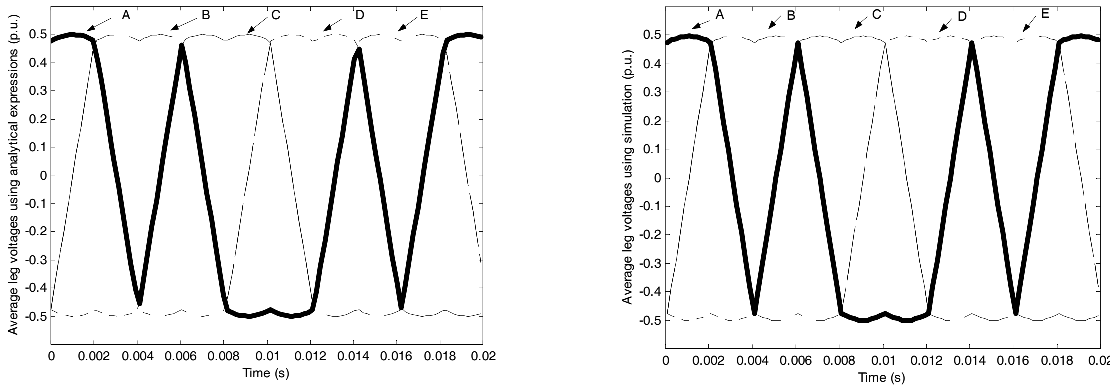

a. b.

Fig. 7.8. Leg voltages using medium space vectors only, obtained using: a. analytical expressions of Table 7.4., b. simulation.

7.2.3 Combined application of medium and large space vectors (five vectors per switching period)

The application of only large space vectors and only medium space vectors, discussed in sections 7.2.1 and 7.2.2, respectively, does not produce satisfactory results in terms of the harmonic content of the output phase voltage. The main reason for this is that only two active voltage vectors are always applied. As emphasised in Kelly et al (2003), the number of applied space vectors for multi-phase VSI with an odd phase number should be equal to the number of inverter phases. This means that one needs to apply four active vectors in each switching period, rather than two. Different schemes are therefore developed in this section by combining the large and medium space vectors. The aim of these schemes is to obtain phase output voltages closer to sinusoidal. Different schemes developed here are based on the sub-division of total time into times for application of large and medium space vectors. The first scheme uses proportional (to their length) sub-division of time of application of large and medium space vectors. The second method, developed here, is a general method, which drives the VSI always to its maximum output. The time of application is variable and depends on the magnitude of the reference voltage. It will be shown that both these methods have a common drawback of not being able to utilise both large and medium space vectors for the complete range of input reference voltage (the scheme of de Silva et al (2004), reviewed in this section as well, suffers from the same drawback). Thus a third scheme is developed, based on pre-defined zero space vector trajectory, in order to utilise both the large and medium space vectors throughout the range. Finally, a comparison of all the schemes is performed and a combined scheme is suggested, based on the properties of various schemes.

The switching pattern and the sequence of the space vectors for the schemes utilising both large and medium space vectors is shown in Fig. 7.9 and this pattern is valid further on for all the discussed cases.

It is observed from the switching pattern of Fig. 7.9 that the switchings in all the phases are staggered. All switches change state at different instants of time. The total number of switchings in each switching period is again twenty, thus preserving the requirement that each switch changes state only twice in a switching period.

7.2.3.1 Proportional sub-division of switching times

This scheme is based on the proportional sub-division of the time of application of each space vector from large and medium space vector sets. The times of application of active space vectors are again calculated using expression (7.2). The times thus obtained are sub-divided in the ratio of medium and large vector lengths,

$$t_{al} = t_a \frac{|\underline{v}_l|}{|\underline{v}_l| + |\underline{v}_m|} \qquad t_{am} = t_a \frac{|\underline{v}_m|}{|\underline{v}_l| + |\underline{v}_m|} \qquad t_{bl} = t_b \frac{|\underline{v}_l|}{|\underline{v}_l| + |\underline{v}_m|} \qquad t_{bm} = t_b \frac{|\underline{v}_m|}{|\underline{v}_l| + |\underline{v}_m|} \tag{7.6}$$

This sub-division of the time of application of different space vectors in essence allocates 61.8% of total active time to the large space vectors and 38.2% to the medium space vectors.

The time of application of zero space vectors is now given as

$$t_o = t_s - t_{al} - t_{am} - t_{bl} - t_{bm} \tag{7.7}$$

To verify the volt-second principle the following expression, valid in the first sector, is considered,

$$\underline{v}_s^* t_s e^{j\alpha} = t_{al}\,\underline{v}_{al} + t_{am}\,\underline{v}_{am} + t_{bl}\,\underline{v}_{bl} e^{j\pi/5} + t_{bm}\,\underline{v}_{bm} e^{j\pi/5} \tag{7.8}$$

After substituting different expressions for application times the following relationship is obtained:

$$\underline{v}_s^* t_s e^{j\alpha} = \frac{|\underline{v}_l|^2 + |\underline{v}_m|^2}{|\underline{v}_l|\left(|\underline{v}_l| + |\underline{v}_m|\right)} \underline{v}_s^* t_s e^{j\alpha} \tag{7.9}$$

The above expression indicates that the output fundamental phase voltages from this type of space vector modulator are only 85.41% of the input reference voltage value. Thus in order to obtain the output fundamental equal to the input reference, the commanded value should be 17.082% larger than the required output.

The simulation is done to obtain the maximum acheivable output value (0.5257 p.u. peak), with the commanded input equal to 0.6155 p.u., thus ensuring the equality of the

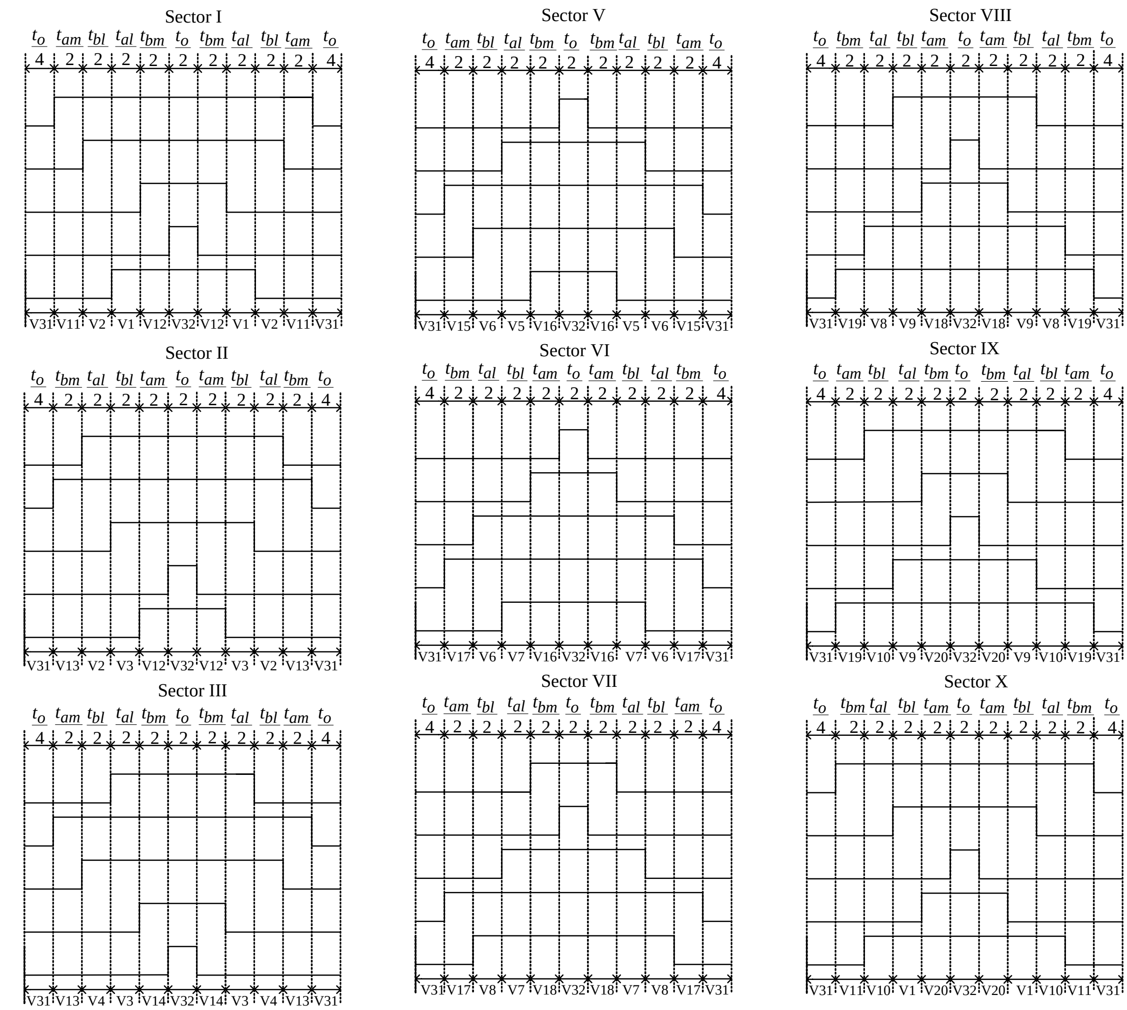

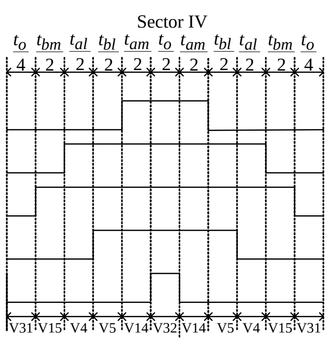

Fig. 7.9. Switching pattern and space vector disposition for one cycle of operation with large and medium space vectors.

fundamental output magnitude and the reference magnitude. The other simulation conditions are identical to those in sections 7.2.1. and 7.2.2. The filter time constant used for leg voltages is 0.4 ms. The filtered phase voltages and leg voltages are shown in Fig. 7.10 along with the harmonic spectrum for maximum achievable fundamental voltage.

It is seen from Fig.7.10 that the spectrum contains only fundamental (0.372 p.u. RMS or 0.5257 p.u. peak, 50 Hz) component and harmonics around multiples of the switching frequency. The low-order harmoics (third and seventh) are absent. The ouptut is almost sinusoidal bacause of the fact that the proportion of time of application of larger and medium space vectors is such that it cancels all the undesirable x-y components (as can be seen from Fig. 7.1). It is to be noted here that for lower values of the input reference phase voltage, the output phase voltages preserve the shape while there will be a correponding reduction in their amplitude.

The analytical expressions for leg voltages averaged over one switching cycle for the scheme utilising both large and medium space vectors with proportional sub-division of application time are derived similar to section 7.2.2. For sector I, the analytical expressions are found from Fig. 7.9 as,

$$
\begin{aligned}
V_A &= \frac{V_{DC}}{2t_s}\left(-t_o/4 + t_{am}/2 + t_{bl}/2 + t_{al}/2 + t_{bm}/2 + t_o/2 + t_{bm}/2 + t_{al}/2 + t_{bl}/2 + t_{am}/2 - t_o/4\right) \\
V_B &= \frac{V_{DC}}{2t_s}\left(-t_o/4 - t_{am}/2 + t_{bl}/2 + t_{al}/2 + t_{bm}/2 + t_o/2 + t_{bm}/2 + t_{al}/2 + t_{bl}/2 - t_{am}/2 - t_o/4\right) \\
V_C &= \frac{V_{DC}}{2t_s}\left(-t_o/4 - t_{am}/2 - t_{bl}/2 - t_{al}/2 + t_{bm}/2 + t_o/2 + t_{bm}/2 - t_{al}/2 - t_{bl}/2 - t_{am}/2 - t_o/4\right) \\
V_D &= \frac{V_{DC}}{2t_s}\left(-t_o/4 - t_{am}/2 - t_{bl}/2 - t_{al}/2 - t_{bm}/2 + t_o/2 - t_{bm}/2 - t_{al}/2 - t_{bl}/2 - t_{am}/2 - t_o/4\right) \\
V_E &= \frac{V_{DC}}{2t_s}\left(-t_o/4 - t_{am}/2 - t_{bl}/2 + t_{al}/2 + t_{bm}/2 + t_o/2 + t_{bm}/2 + t_{al}/2 - t_{bl}/2 - t_{am}/2 - t_o/4\right)
\end{aligned}
\qquad (7.10)
$$

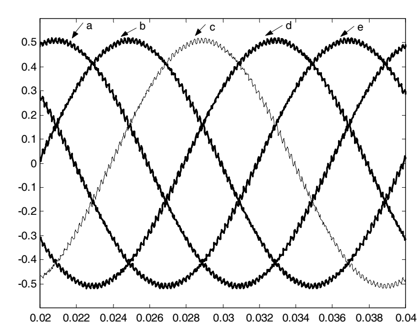

a.

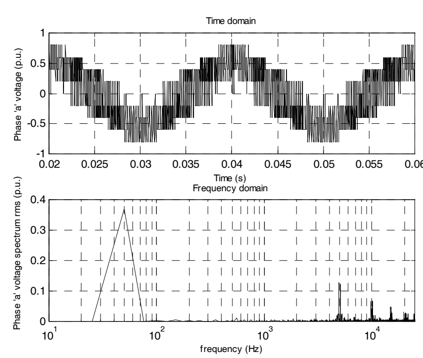

c.

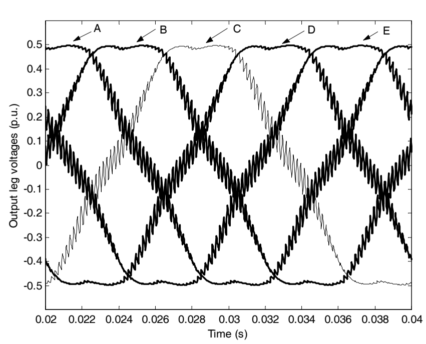

b.

Fig. 7.10. Output of VSI for the maximum achievable output fundamental voltage (85.41% of the one obtainable with large vectors only): a. phase voltages, b. leg voltages, c. harmonic spectrum.

The resulting expressions of the average leg voltages for all sectors are given by (7.11)-(7.15).

Similar to the previous cases, the expressions of average leg voltages for sectors from VI to X are identical to those for sectors I to V, in the same order, and are thus not repeated. A calculation is done using the analytical expressions of leg voltages corresponding to the maximum input reference voltage. The resulting plot is shown in Fig. 7.11a.

Once again, to compare the average leg voltages obtained using analytical expressions and using simulation, the same approach as in sectionss 7.2.1 and 7.2.2 is adopted. The average leg voltages obtained using simulation are shown in Fig. 7.11b. The waveforms in Figs. 7.11a and 7.11b are again in very good agreement.

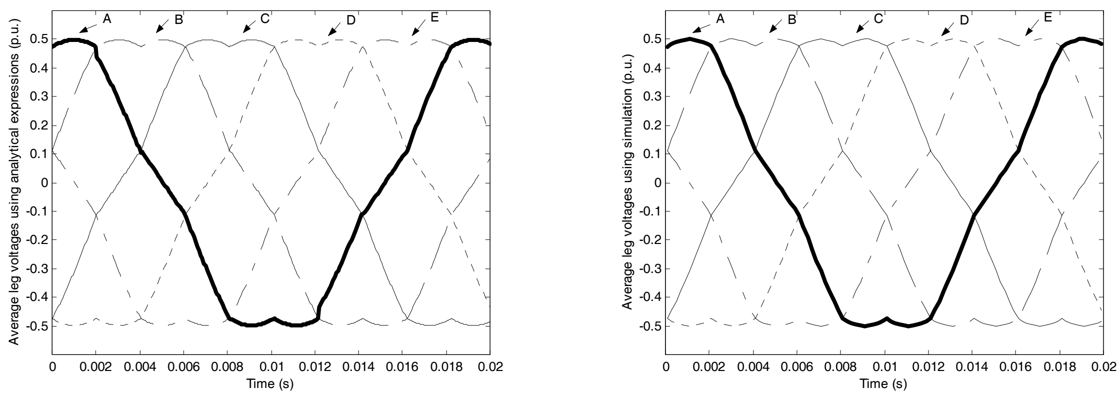

a. b.

Fig. 7.11. Average leg voltages, using both large and medium space vectors with time sub-division in proportion to their length, obtained using: a. analytical expressions, b. simulation.

7.2.3.2 SVPWM to drive the inverter along maximum available output

This scheme also utilises both large and medium space vectors but the principle here is to drive the inverter along the maximum possible output for all input reference voltage magnitudes. This is achived by forcing the zero space vector application time to remain zero for each input reference magnitude in the middle of all sectors. Further, to obtain the maximum possible output from the space vector modulator, ultimately one has to revert to the large space vectors only. This method is applicable when the input reference voltage lies between $0.3804V_{DC} \leq \left|\underline{v}_s^*\right| \leq 0.6155V_{DC}$. Let the proportion of time of application of the medium and large space vectors be γ and δ, respectively. These factors vary with the magnitude of the input reference voltage in such a way that the inverter is always driven to the maximum

SECTOR I:

$$V_A = \left|\underline{v}_s^*\right| \cos(\pi/5)\cos(\omega t - \pi/10)$$
$$V_B = \left|\underline{v}_s^*\right| \begin{pmatrix} \sin(\pi/10)\cos(\omega t + 3\pi/10) + \\ \dfrac{\sin(3\pi/10)}{2\sin(\pi/10)}\sin(\omega t) \end{pmatrix}$$
$$V_C = -\left|\underline{v}_s^*\right| \begin{pmatrix} \dfrac{\sin(3\pi/10)}{2\sin(\pi/10)}\cos(\omega t + 3\pi/10) + \\ \sin(\pi/10)\sin(\omega t) \end{pmatrix}$$
$$V_D = -\left|\underline{v}_s^*\right| \cos(\pi/5)\cos(\omega t - \pi/10)$$
$$V_E = \left|\underline{v}_s^*\right| \sin(\pi/5)\cos(\omega t + 2\pi/5)$$
(7.11)

SECTOR II:

$$V_A = \left|\underline{v}_s^*\right| \begin{pmatrix} \dfrac{\sin(3\pi/10)}{2\sin(\pi/10)}\cos(\omega t + \pi/10) - \\ \sin(\pi/10)\cos(\omega t + 3\pi/10) \end{pmatrix}$$
$$V_B = \left|\underline{v}_s^*\right| \cos(\pi/5)\left(\sin(\omega t + \pi/5)\right)$$
$$V_C = -\left|\underline{v}_s^*\right| \sin(\pi/5)\left(\cos(\omega t + \pi/5)\right)$$
$$V_D = -\left|\underline{v}_s^*\right| \cos(\pi/5)\left(\sin(\omega t + \pi/5)\right)$$
$$V_E = \left|\underline{v}_s^*\right| \begin{pmatrix} -\sin(\pi/10)\cos(\omega t + \pi/10) + \\ \dfrac{\sin(3\pi/10)}{2\sin(\pi/10)}\cos(\omega t + 3\pi/10) \end{pmatrix}$$
(7.12)

SECTOR III:

$$V_A = \left|\underline{v}_s^*\right| \sin(\pi/5)\cos(\omega t)$$
$$V_B = \left|\underline{v}_s^*\right| \cos(\pi/5)\sin(\omega t)$$
$$V_C = \left|\underline{v}_s^*\right| \begin{pmatrix} \sin(\pi/10)\sin(\omega t + 2\pi/5) - \\ \dfrac{\sin(3\pi/10)}{2\sin(\pi/10)}\cos(\omega t + \pi/10) \end{pmatrix}$$
$$V_D = \left|\underline{v}_s^*\right| \begin{pmatrix} -\dfrac{\sin(3\pi/10)}{2\sin(\pi/10)}\sin(\omega t + 2\pi/5) + \\ \sin(\pi/10)\cos(\omega t + \pi/10) \end{pmatrix}$$
$$V_E = -\left|\underline{v}_s^*\right| \cos(\pi/5)\sin(\omega t)$$
(7.13)

SECTOR IV:

$$V_A = \left|\underline{v}_s^*\right| \begin{pmatrix} -\sin(\pi/10)\sin(\omega t + \pi/5) + \\ \dfrac{\sin(3\pi/10)}{2\sin(\pi/10)}\sin(\omega t + 2\pi/5) \end{pmatrix}$$
$$V_B = \left|\underline{v}_s^*\right| \begin{pmatrix} \dfrac{\sin(3\pi/10)}{2\sin(\pi/10)}\sin(\omega t + \pi/5) - \\ \sin(\pi/10)\sin(\omega t + 2\pi/5) \end{pmatrix}$$
$$V_C = -\left|\underline{v}_s^*\right| \cos(\pi/5)\cos(\omega t + 3\pi/10)$$
$$V_D = -\left|\underline{v}_s^*\right| \sin(\pi/5)\sin(\omega t + 3\pi/10)$$
$$V_E = \left|\underline{v}_s^*\right| \cos(\pi/5)\cos(\omega t + 3\pi/10)$$
(7.14)

SECTOR V:

$$V_A = \left|\underline{v}_s^*\right| \cos(\pi/5)\cos(\omega t + \pi/10)$$
$$V_B = \left|\underline{v}_s^*\right| \sin(\pi/5)\sin(\omega t + \pi/10)$$
$$V_C = -\left|\underline{v}_s^*\right| \cos(\pi/5)\cos(\omega t + \pi/10)$$
$$V_D = \left|\underline{v}_s^*\right| \begin{pmatrix} \sin(\pi/10)\sin(\omega t) - \\ \dfrac{\sin(3\pi/10)}{2\sin(\pi/10)}\sin(\omega t + \pi/5) \end{pmatrix}$$
$$V_E = -\left|\underline{v}_s^*\right| \begin{pmatrix} \dfrac{\sin(3\pi/10)}{2\sin(\pi/10)}\sin(\omega t) - \\ \sin(\pi/10)\sin(\omega t + \pi/5) \end{pmatrix}$$
(7.15)

available voltage. Thus the times of application of the two neighbouring vectors in sector I are given as

$$t_a = \frac{\left|\underline{v}_s^*\right| \sin(\pi/5-\alpha)}{\left[\gamma\left|\underline{v}_m\right| + \delta\left|\underline{v}_l\right|\right]\sin(\pi/5)} t_s \tag{7.16}$$

$$t_b = \frac{\left|\underline{v}_s^*\right| \sin(\alpha)}{\left[\gamma\left|\underline{v}_m\right| + \delta\left|\underline{v}_l\right|\right]\sin(\pi/5)} t_s \tag{7.17}$$

The constraints on the expressions for times of application of space vectors are:

if $\left|\underline{v}_s^*\right| \le 0.38042V_{DC}$ then $\gamma = 1$, $\delta = 0$

if $\left|\underline{v}_s^*\right| = 0.6155V_{DC}$ then $\gamma = 0$, $\delta = 1$ (7.18)

if $\alpha = \pi/10$ and $0.38402V_{DC} \le \left|\underline{v}_s^*\right| \le 0.6155V_{DC}$ then $t_a = t_b = 0.5t_s$

Using (7.18) and (7.16) or (7.17) to find the values of γ and δ, one obtains:

$$\gamma\left|\underline{v}_m\right| + \delta\left|\underline{v}_l\right| = 2\frac{\left|\underline{v}_s^*\right| \sin(\pi/10)}{\sin(\pi/5)} \tag{7.19}$$

Substitution of the values of lengths of the medium and large vectors into (7.19) yields

$$\left(\gamma + \delta 2\cos(\pi/5)\right)\frac{2}{5}V_{DC} = 2\frac{\left|\underline{v}_s^*\right| \sin(\pi/10)}{\sin(\pi/5)} \tag{7.20}$$

This condition ensures that the maximum available peak voltage of the inverter equals input reference voltage for every value of the input reference voltage. Factors γ and δ are subject to $0 \le \gamma \le 1$, $0 \le \delta \le 1$ and $\gamma + \delta = 1$. This gives the expressions for γ and δ as:

$$\gamma = \frac{2\cos(\pi/5) - 5\dfrac{\left|\underline{v}_s^*\right| \sin(\pi/10)}{V_{DC}\sin(\pi/5)}}{2\cos(\pi/5)-1} \tag{7.21}$$

$$\delta = \frac{5\dfrac{\left|\underline{v}_s^*\right| \sin(\pi/10)}{V_{DC}\sin(\pi/5)} - 1}{2\cos(\pi/5)-1} \tag{7.22}$$

The switching pattern remains to be given with Fig. 7.9.

A simulation is done to determine the performance of the space vector modulator based on this principle. The filter time constant used here for leg voltages is 0.4 ms except for the reference equal to 61.8% of the maximum, when it is 0.25 ms. It is clearly seen from (7.21) and (7.22) that, for the maximum achievable output voltage, the result is identical to the one with large space vectors only (shown in Fig. 7.4). Thus the simulation results shown in Figs. 7.12a-c are for input reference voltage ranging from 95% down to 61.8% of the maximum achievable value. The values of the RMS fundamental voltage and low-order harmonic components are listed in Table 7.5.

Table 7.5. RMS of fundamental and low-order harmonic components of output phase voltages.

$\lvert \underline{v}_s^* \rvert$ (p.u.)	Fundamental (50 Hz)		3rd harmonic (150 Hz, p.u.)	7th harmonic (350 Hz, p.u.)
	Theoretical RMS (p.u.)	Simulation RMS (p.u.)		
95% of Max	0.413	0.413	0.06 (14.51%)	0.017(4.11%)
90% of Max	0.39	0.39	0.018 (4.6%)	0
80% of Max	0.348	0.348	0.062 (17.8%)	0.017 (4.8%)
70% of Max	0.304	0.303	0.15 (48.54%)	0.025 (8.22%)
61.8% of Max	0.268	0.268	0.204 (76.12%)	0.04 (14.9%)

The results in Table 7.5 show that the method is effective and produces close to sinusoidal waveform as the reference input voltage increases towards the maximum achievable value. This is due to the fact that the ratio of time of application of large to medium space vector increases with increase in the input reference voltage and thus x-y components cancel out with increasing ratio of large to medium voltage space vector. Thus this method can be used for higher values of reference input voltage value as it smoothly transits from four active (large and medium) vector application to two active (large) vector application with increase in the input reference voltage.

7.2.3.3 Modulation with pre-defined trajectory of zero space vector application time

In order to utilise the large and medium space vectors throughout the range of input reference voltage vector, another scheme is developed. It is based on the pre-defined zero space vector application time. The zero space vector trajectory is modified in such a way that it yields a positive time of application for zero space vector for reference input vector varying from zero to the maximum achievable value. The time of application of zero space vector is guaranteed to be positive through out the range of input reference if it is made positive at $\alpha = \pi/10$ (middle of a sector).

The time of application for zero space vector at $\alpha = \pi/10$, denoted with t_{oo} is shown in Fig. 7.13 for three different situations, as function of the input reference voltage: firstly, when only large vectors are used (t_{ool}), secondly when only medium vectors are used (t_{oom}), and thirdly, the modified trajectory when both large and medium vectors are used (t_{oo}). In Fig.

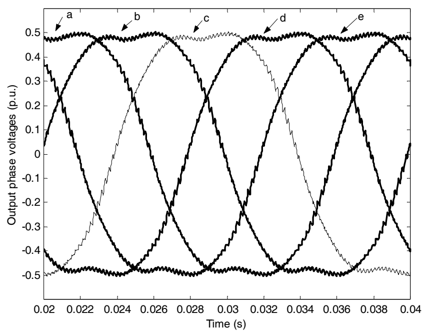

a.

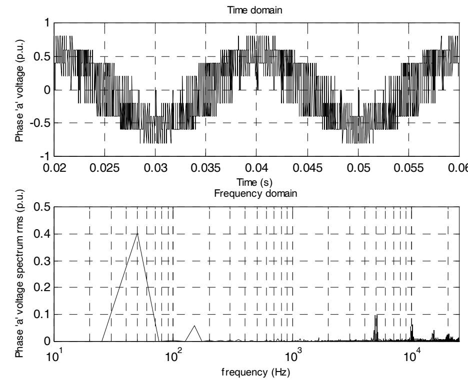

c.

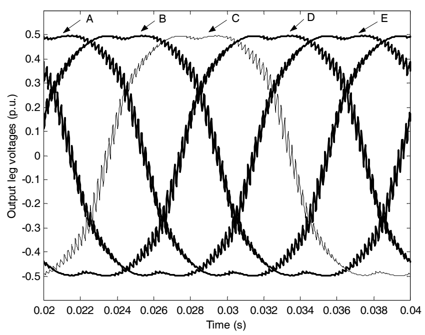

b.

Fig. 7.12a. Output of VSI for input reference equal to 95% of the maximum achievable: a. phase voltages, b. leg voltages, c. harmonic spectrum.

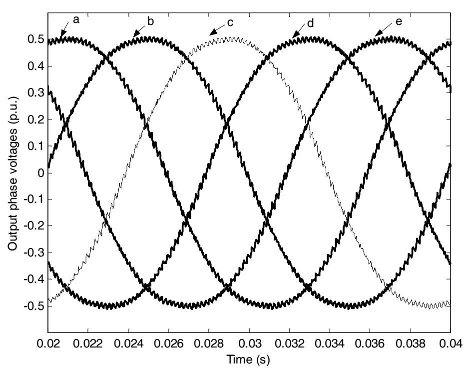

a.

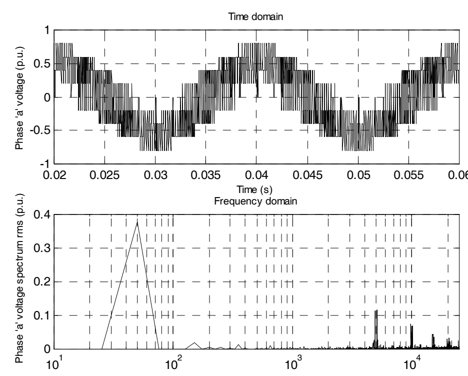

c.

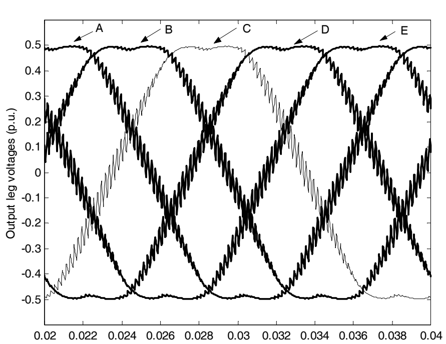

b.

Fig. 7.12b. Output of VSI for input reference equal to 90% of the maximum achievable: a. phase voltages, b. leg voltages, c. harmonic spectrum.

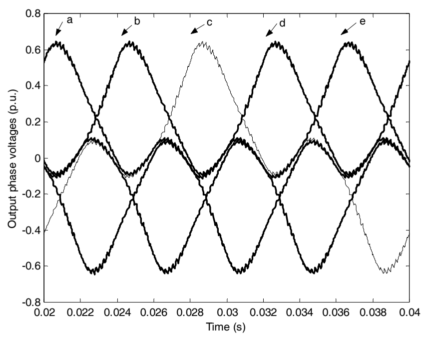

a.

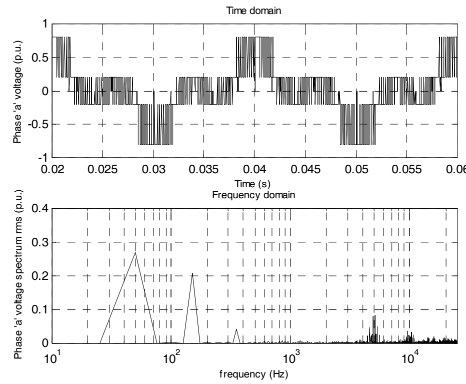

c.

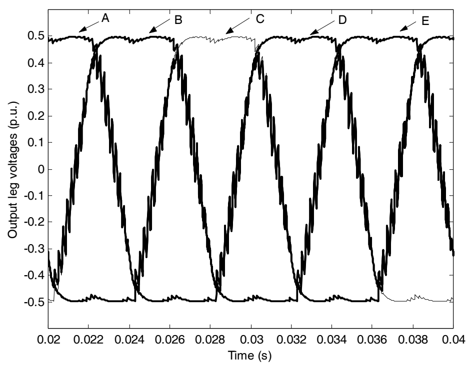

b.

Fig. 7.12c. Output of VSI for input reference equal to 61.8% of the maximum achievable: a. phase voltages, b. leg voltages, c. harmonic spectrum.

7.13, V_{ml} and V_{mm} represent the maximum achievable output voltage with large space vectors and medium space vectors, respectively. The expressions for time of application of zero space vector, if only large vectors and if only medium vectors are used are:

$$t_{ool} = t_s - \frac{\left|\underline{v}_s^*\right|}{\left|\underline{v}_l\right|\cos\left(\pi/10\right)} t_s$$

$$t_{oom} = t_s - \frac{\left|\underline{v}_s^*\right|}{\left|\underline{v}_m\right|\cos\left(\pi/10\right)} t_s \qquad (7.23)$$

These equations represent straight lines, varying linearly with the length of the input reference vector. The aim is now to apply both the large and medium vectors and thus the curve defining the time of application of zero space vector should lie between these two curves. The curve should pass through the two end-points and should be tangent to the lower curve for zero reference input voltage in order to apply predominantly medium vectors when the reference vector is small. The expression for the modified curve is assumed as

$$t_{oo} = a\left|\underline{v}_s^*\right|^2 + b\left|\underline{v}_s^*\right| + c \qquad (7.24)$$

To determine the constants, the boundary conditions are specified as: at $\left|\underline{v}_s^*\right| = 0$, $t_{oo} = t_s$; at $\left|\underline{v}_s^*\right| = V_{ml}$, $t_{oo} = 0$; further, the slope of the curve at $\left|\underline{v}_s^*\right| = 0$ should be equal to the slope of line t_{oom}. The slope at this point is found as $slope = -\dfrac{t_s}{\left|\underline{v}_m\right|\cos\left(\pi/10\right)}$. Thus the constants are determined as:

$$a = -\frac{b}{V_{ml}} - \frac{t_s}{V_{ml}^2}$$

$$b = -\frac{t_S}{\left|\underline{v}_m\right|\cos\left(\pi/10\right)} = -\frac{t_s}{V_{mm}}$$

$$c = t_s \tag{7.25}$$

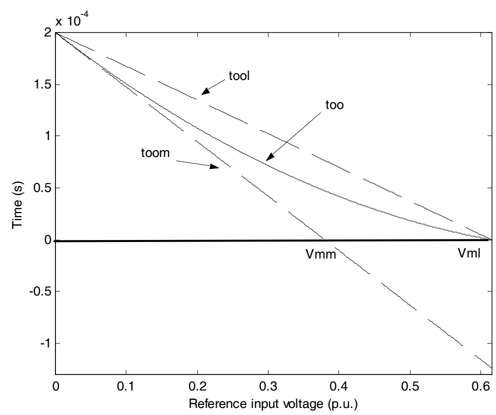

Fig. 7.13. Variation of zero times at $\alpha = \pi/10$ for different SVPWM schemes, as function of the reference input voltage (switching frequency = 5 kHz).

In order to determine the expression for time of application of zero space vector at an arbitrary angle α, the relationship is found as follows. In general, $t_o = t_s - t_a - t_b$, where for sector I

$$t_a = \frac{\left|v_s^*\right|\sin\left(\pi/5-\alpha\right)}{\left|\underline{v}\right|\sin\left(\pi/5\right)}t_s\,, \qquad t_b = \frac{\left|v_s^*\right|\sin\left(\alpha\right)}{\left|\underline{v}\right|\sin\left(\pi/5\right)}t_s \tag{7.26a}$$

Hence

$$t_o = t_s - \frac{\left|\underline{v}_s^*\right|\left(\sin\left(\pi/5-\alpha\right)+\sin\left(\alpha\right)\right)}{\left|\underline{v}\right|\sin\left(\pi/5\right)}t_s \tag{7.26b}$$

where $\left|\underline{v}\right|$ represents $\left|\underline{v}_l\right|$ or $\left|\underline{v}_m\right|$ depending on whether (7.26) is used to determine the time of application of large or medium space vector, respectively.

Further, $(t_o)_{\alpha=\pi/10} = t_{oo} = t_s - \dfrac{\left|v_s^*\right|}{\left|\underline{v}\right|\cos(\pi/10)} t_s$ and therefore,

$$t_s \left|\underline{v}_s^*\right| / \left|\underline{v}\right| = (t_s - t_{oo})\cos(\pi/10) \tag{7.27}$$

Substituting (7.27) in (7.26) one finds:

$$t_o = t_s - (t_s - t_{oo})\cos(\pi/10 - \alpha) \tag{7.28}$$

The equation (7.28) is used to calculate the time of application of zero space vector and t_{oo} used here is the one of equation (7.24).

The times of application of active space vectors need to be modified as well. The parabolic curve is again assumed for large active state vector. Fig. 7.14 shows the variation of application times of zero and active state vectors at $\alpha = \pi/10$. The expression for time of application of larger active space vectors is found as

$$t_{ol} = t_s \left(\frac{\left|v_s^*\right|}{V_{ml}} \right)^2 \tag{7.29}$$

and the times of application of medium active space vectors are then

$$t_{om} = t_s - t_{oo} - t_{ol} \tag{7.30}$$

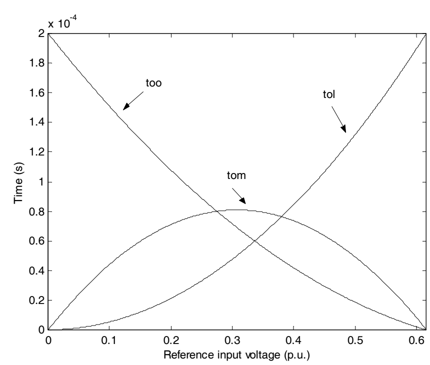

Fig. 7.14. Variation of active state and zero state vector application times at $\alpha = \pi/10$ as function of the reference input voltage (switching frequency = 5 kHz).

Expressions for time of application of neighbouring space vectors at arbitrary angle α are further obtained as follows. In general, $t_{al} = \dfrac{\left|\underline{v}_s^*\right|\sin(\pi/5-\alpha)}{\left|\underline{v}_l\right|\sin(\pi/5)} t_s$ and $t_{bl} = \dfrac{\left|v_s^*\right|\sin(\alpha)}{\left|\underline{v}_l\right|\sin(\pi/5)} t_s$.

Therefore

$$t_{al} + t_{bl} = \frac{\left|\underline{v}_s^*\right| t_s \left(\sin(\pi/5-\alpha) + \sin(\alpha)\right)}{2\left|\underline{v}_l\right|\cos(\pi/10)\sin(\pi/10)} \tag{7.31}$$

At $\alpha = \pi/10$, $t_{oa} = t_{ob} = \dfrac{\left|\underline{v}_s^*\right|}{2\left|\underline{v}_l\right|\cos\left(\pi/10\right)}t_s$ and thus $t_{oa} + t_{ob} = t_{ol} = \dfrac{\left|\underline{v}_s^*\right|}{\left|\underline{v}_l\right|\cos\left(\pi/10\right)}t_s$. Hence from (7.31) one obtains,

$$t_{al} + t_{bl} = \frac{\sin\left(\pi/5-\alpha\right)}{2\sin\left(\pi/10\right)}t_{ol} + \frac{\sin\left(\alpha\right)}{2\sin\left(\pi/10\right)}t_{ol} \qquad (7.32)$$

The first term in (7.32) is the time of application of 'a' large active space vector and the second term corresponds to the time of application of 'b' large active space vector. Similarly, for medium space vectors, the expression is found as

$$t_{am} + t_{bm} = \frac{\sin\left(\pi/5-\alpha\right)}{2\sin\left(\pi/10\right)}t_{om} + \frac{\sin\left(\alpha\right)}{2\sin\left(\pi/10\right)}t_{om} \qquad (7.33)$$

The first term in (7.33) is the time of application of 'a' medium active space vector and the second term corresponds to the time of application of 'b' medium active space vector.

To confirm that the output phase voltage magnitude is equal to the reference input phase voltage, the volt-second principle is verified using (7.8).

Simulation is done for input reference phase voltage magnitude values from maxmium achievable down to 10% of this value and the resulting plots are shown in Figs. 7.15a-d. Figs. 7.15a-d depict the filtered ouput phase voltages and leg voltages in addition to the harmonic spectrum of phase voltages. The filter time constant used for the first case is 0.4 ms, while it is 0.8 ms for other cases.

Table 7.6. RMS of fundamental and low-order harmonic components of output phase voltages.

$\left\|\underline{v}_s^*\right\|$ (p.u.)	Fundamental (50 Hz)		3rd harmonic (150 Hz, p.u.)	7th harmonic (350 Hz, p.u.)
	Theoretical RMS (p.u.)	Simulation RMS (p.u.)		
0.6155 (Max)	0.435	0.435	0.128 (29.42%)	0.022 (5.05%)
90% of Max	0.39	0.39	0.07 (17.9%)	0.008 (2.04%)
80% of Max	0.348	0.348	0.028 (8.2%)	0.0129 (3.7%)
70% of Max	0.304	0.303	0.0	0.0
61.8% of Max	0.268	0.266	0.024 (8.18%)	0.0
50% of Max	0.217	0.216	0.058 (26.85%)	0.0058 (2.68%)
38.2% of Max	0.166	0.166	0.057 (34.33%)	0.015 (9.03%)
30% of Max	0.13	0.129	0.056 (42.3%)	0.015 (11.53%)
20% of Max	0.087	0.085	0.045 (51.7%)	0.0155 (17.8%)
10% of Max	0.0435	0.043	0.0278 (63.9%)	0.0036 (8.27%)

Table 7.6 shows harmonic spectrum. The third and the seventh harmonic components vary as percentages of the fundamental. This is due to the fact that the ratio of time of application of large and medium space vectors and thus the x-y component magnitudes vary leading to a variable amount of harmonic components in the output.

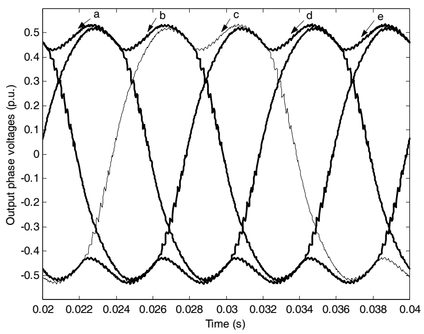

a.

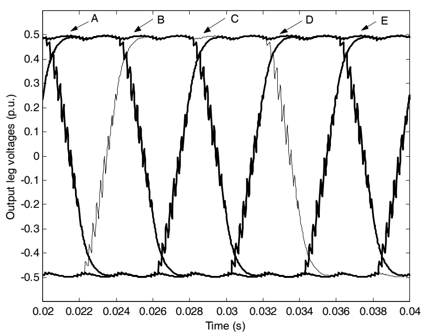

b.

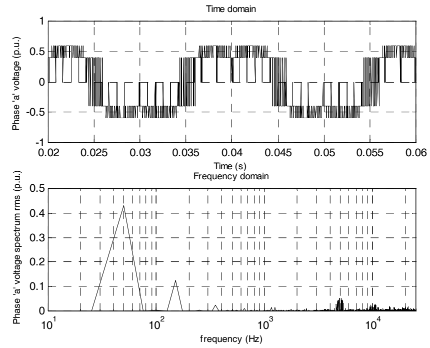

c.

Fig. 7.15a. Output of VSI for input reference voltage equal to the maximum achievable: a. phase voltages, b. leg voltages, c. harmonic spectrum.

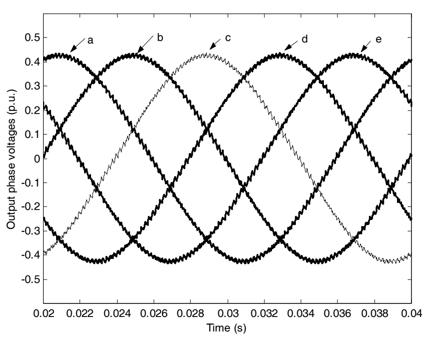

a.

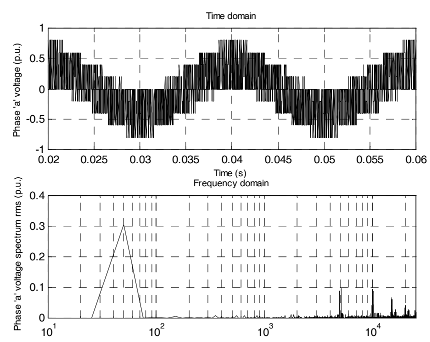

c.

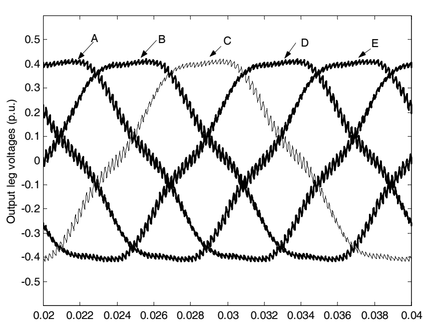

b.

Fig. 7.15b. Output of VSI for input reference voltage equal to the 70% of the maximum achievable: a. phase voltages, b. leg voltages, c. harmonic spectrum.

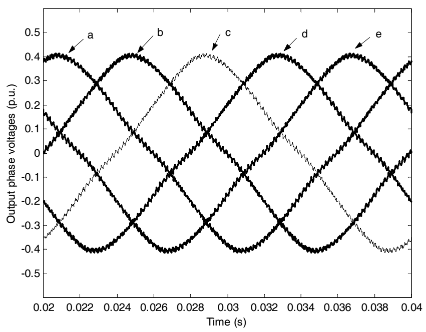

a.

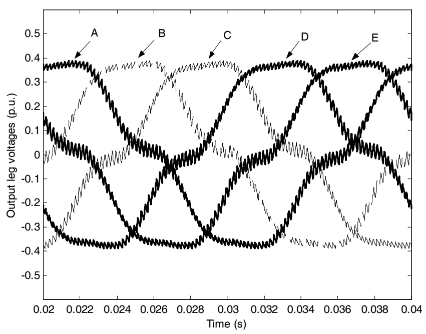

b.

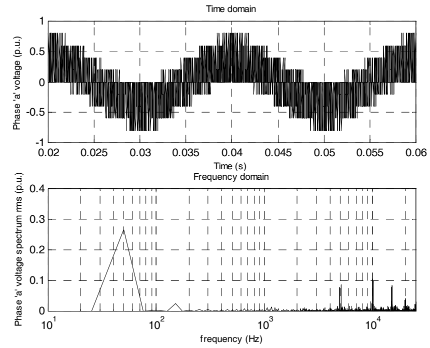

c.

Fig. 7.15c. Output of VSI for input reference voltage equal to 61.8% of the maximum achievable: a. phase voltages, b. leg voltages, c. harmonic spectrum.

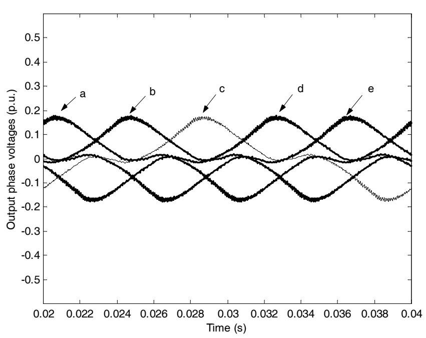

a.

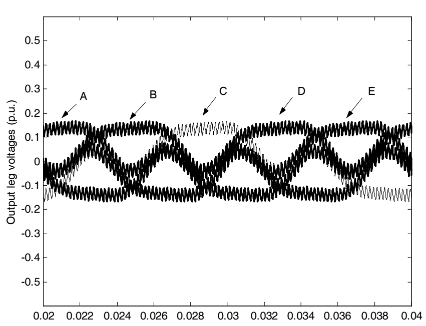

b.

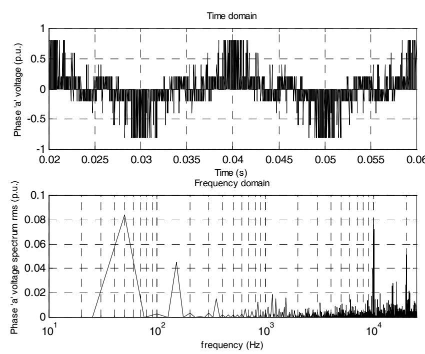

c.

Fig. 7.15d. Output of VSI for input reference voltage equal to 20% of the maximum achievable: a. phase voltages, b. leg voltages, c. harmonic spectrum.

7.2.3.4 SVPWM scheme of de Silva et al (2004)

The scheme developed by de Silva et al (2004) utilises four active space vectors, two from outer and two from middle decagons and two zero space vectors to implement SVPWM, similar to other methods of this section. The principle of this technique is to produce voltage in the $\alpha-\beta$ plane while simultaneously eliminating the voltage in the x-y plane. It is evident from Fig. 7.1 that for each sector the large and the medium space vectors of $\alpha-\beta$ plane fall diagonally opposite to each other in x-y plane. The lengths of these diagonally opposite space vectors in x-y plane are in proportion to the lengths of large and medium space vectors. Thus the ratio of times of application of large and medium active space vectors is kept equal to the ratio of lengths, i.e. $t_l / t_m = |\underline{v}_l| / |\underline{v}_m| = \tau$, where $\tau = 1.618$. This ensures the cancellation of undesirable x-y space vector components and achieves sinusoidal output phase voltages. The times of application of active space vectors are found using the volt-second principle of (7.8) and are given by

$$t_{al} = \frac{|\underline{v}_s^*| \sin(k\pi/5 - \alpha)}{|\underline{v}_m| \sin(\pi/5)} \left[\frac{\tau}{1+\tau^2}\right] t_s \tag{7.34}$$

$$t_{bl} = \frac{|\underline{v}_s^*| \sin(\alpha - (k-1)\pi/5)}{|\underline{v}_m| \sin(\pi/5)} \left[\frac{\tau}{1+\tau^2}\right] t_s \tag{7.35}$$

$$t_{am} = \frac{|\underline{v}_s^*| \sin(k\pi/5 - \alpha)}{|\underline{v}_m| \sin(\pi/5)} \left[\frac{1}{1+\tau^2}\right] t_s \tag{7.36}$$

$$t_{bm} = \frac{|\underline{v}_s^*| \sin(\alpha - (k-1)\pi/5)}{|\underline{v}_m| \sin(\pi/5)} \left[\frac{1}{1+\tau^2}\right] t_s \tag{7.37}$$

The time of application of zero space vectors remains to be given with (7.7). The switching pattern for this scheme is the same as in Fig. 7.9. This scheme can be used until the input reference reaches 0.5257 (p.u.) peak (85.41% of the maximum achievable with large vectors only). Further increase in input reference voltage leads to time of application of zero space vector becoming negative, which is meaningless.

Simulation is done for this technique to determine the behaviour of the space vector modulator. The resulting plot is shown in Fig. 7.16 for input reference equal to the maximum achievable.

Fig. 7.16 shows sinusoidal output phase voltages with fundamental output equal to the input reference. This is because of the fact that the undesirable x-y space vector components are eliminated completely due to the proper sub-division of the time of application of large and medium space vectors. It should be noted that properties of this SVPWM schemes are identical to the scheme of sub-section 7.2.3.1, developed as part of research in this thesis, although the approach to get the necessary application times for various space vectors is quite different.

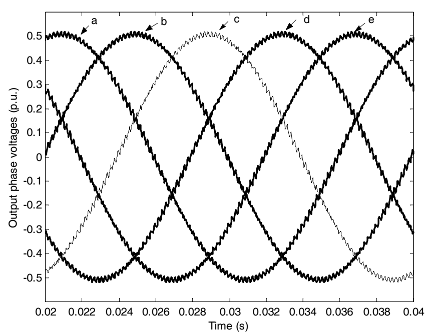

a.

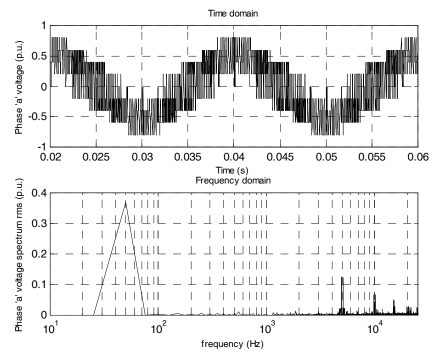

c.

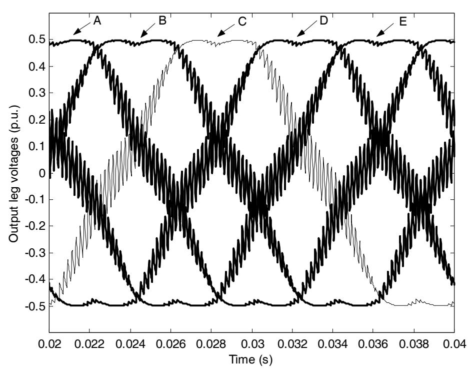

b.

Fig. 7.16. Output of VSI for input reference equal to the maximum achievable: a. phase voltages, b. leg voltages, c. harmonic spectrum.

7.2.3.5 Comparison of SVPWM schemes and a proposal for combined SVPWM scheme for entire operating region

A comparative performance evaluation of the different SVPWM schemes, detailed in 7.2.1-7.2.3.4, is performed and presented here. The following figures of merit are used to compare the performance of the different SVPWM modulators: the quality of the output inverter voltage and the range of applicability. One of the important factors to compare the effectiveness of the PWM process is the total harmonic distortion (THD) of the output waveform, which provides a handy reference for comparison [Holmes and Lipo (2003)]. The THD of the output voltages is therefore evaluated here for the purposes of comparison. There are few definitions of THD in practice [Holmes and Lipo (2003)].

The expression used here to evaluate THD of the output voltage waveform is

$$THD = \sqrt{\sum_{n=3,5,7,....}^{r} \left(\frac{V_{n,RMS}}{V_{1,RMS}} \right)^2} \tag{7.38}$$

where $V_{n,RMS}$ is the RMS value of the n^{th} harmonic component, $V_{1,RMS}$ is the RMS of the fundamental and r is the order of the harmonics used for calculation. Two THDs have been evaluated, one using $r = 80$ (up to 4 kHz) to obtain the effect of low-order harmonics only and another using $r = 500$ (up to 25 kHz) to observe the effect of both low-order and switching harmonics on the overall quality of the output voltage waveforms.

Fig. 7.17 and Fig. 7.18a-d comprehensively show the relative merits and demerits of the different SVPWM schemes. Fig. 7.17 depicts the circular locus of maximum achievable output voltage from different space vector modulators. It is evident from Fig. 7.17 that only the schemes discussed in 7.2.1 and 7.2.3.3 can be used for the complete range of the input reference. The scheme outlined in 7.2.3.2 is applicable from 0.268 (p.u.) RMS up to 0.435 (p.u.) RMS (maximum achievable). The scheme suggested by de Silva et al (7.2.3.4) and the one detailed in 7.2.3.1 can be used from zero to 0.371 (p.u.) RMS (85.41% of the maximum achievable). Fig 7.18 is produced by finding the best fit for the simulation results, reported in the previous sections. The scheme of 7.2.2, which utilises only medium space vectors, is the worst and is therefore not included in Fig. 7.18.

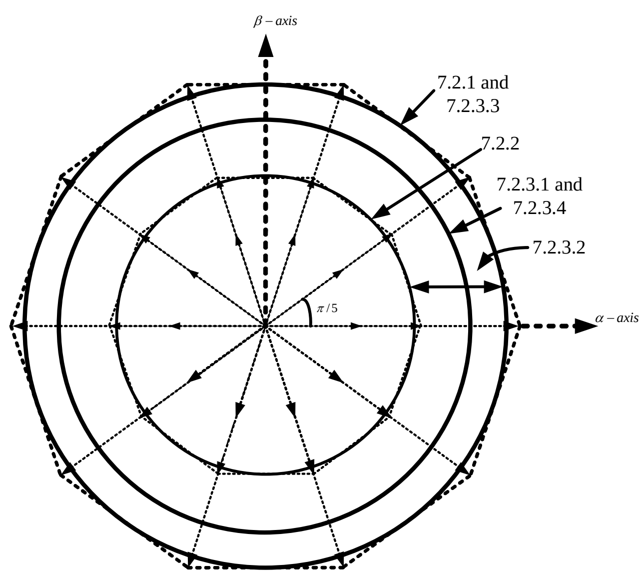

Fig. 7.17. The locus of the maximum achievable output voltage from different space vector modulators.

Fig. 7.18a and Fig. 7.18b depict the percentage of the 3rd harmonic component and percentage of the 7th harmonic component in the output voltage waveform, resepectively. It is observed that the scheme of 7.2.1, which utlises only large space vectors, gives consistent harmonic components for the complete input reference voltage range. The 3rd harmonic content is nearly 30% of the fundamental output while the 7th harmonic component is seen to be around 5% of the fundamenatl output. For schemes of 7.2.3.2 and 7.2.3.3 both the 3rd and the 7th harmonic components are variable and decrease with increase in the input reference voltage, reach a minimum value and then again increase. By comparing the trace of the 3rd and the 7th harmonic content for the scheme of 7.2.3.2 with that of 7.2.1, it is seen that both the 3rd and the 7th harmonic contents are less in scheme of 7.2.3.2 for input voltage reference above 80% of the maximum achievable. A similar comparision between schemes of 7.2.3.3 and 7.2.1 reveals that the 3rd and the 7th harmonic content is better in 7.2.3.3 for input voltage reference above approximately 50% of the maximum. It is furhter to be noted that the 3rd and 7th harmonic contents of schemes 7.2.3.2 and 7.2.3.3 are equal to 7.2.1 for 100% of the maximum achievable. It is so because of the fact that both the schemes of 7.2.3.2 and 7.2.3.3 become identical to 7.2.1 for input reference equal to the maximum acheivable. The 3rd and 7th harmonic content for schemes of 7.2.3.1 and 7.2.3.4 are zero for the entire range of their operation.

Figs. 7.18c–d show the THD of the output voltage waveforms produced by different space vector modulators, caused by low-order and by low-order and switching harmonics, resepectively. The THD is seen to be very high for small values of the input reference voltage, for all the schemes. The THD introduced in the output voltage waveform by schemes of 7.2.3.2 and 7.2.3.3 is seen to be smaller as compared to the one of 7.2.1 for input reference voltages above approximately 80% and 50%, resepectively. It is further seen that the THDs produced by the schemes of 7.2.3.1 and 7.2.3.4 are equal and the smallest compared to other schemes. Fig. 7.18d also shows similar trends but here it is difficult to distinguish between different traces as they are very close one to the other.

Based on the comparison of performance of different types of the space vector modulators, it is observed that the schemes discussed in 7.2.1 and 7.2.3.3 can be used for the complete range of the input voltage reference. However, the scheme outlined in 7.2.1 does not provide satisfactory output voltage quality in terms of its harmonic contents. To obtain sinusoidal output voltage, one can consider using the technique disscused in 7.2.3.1 or 7.2.3.4 for input reference voltage ranging from 0% to 85.41% of the maximum achievable. Both

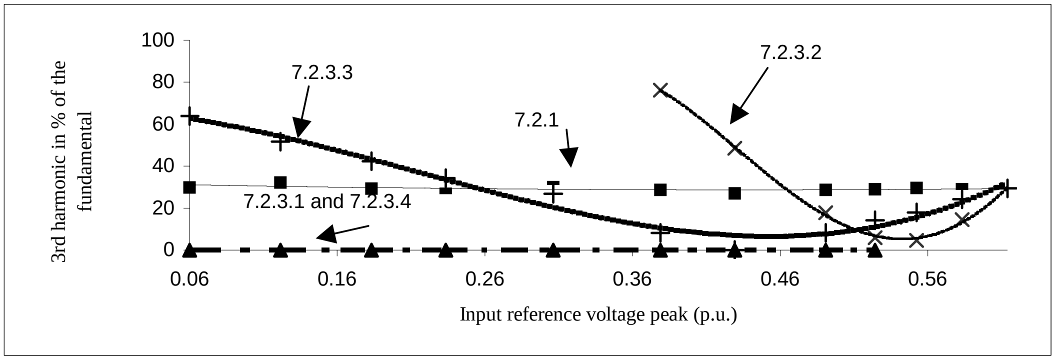

a.

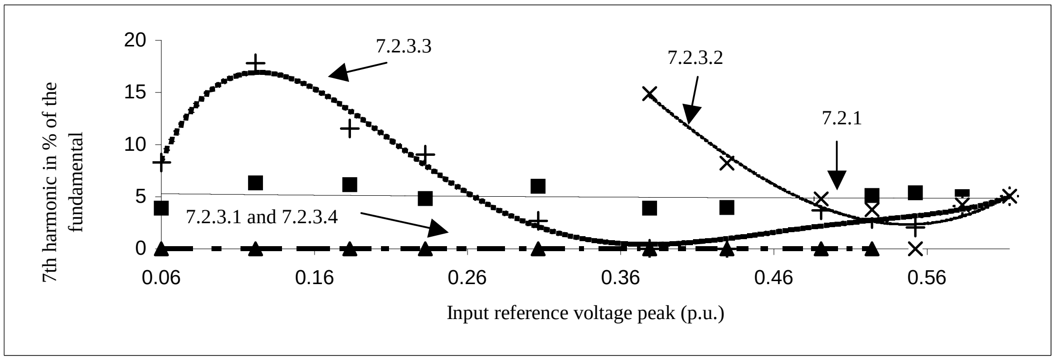

b.

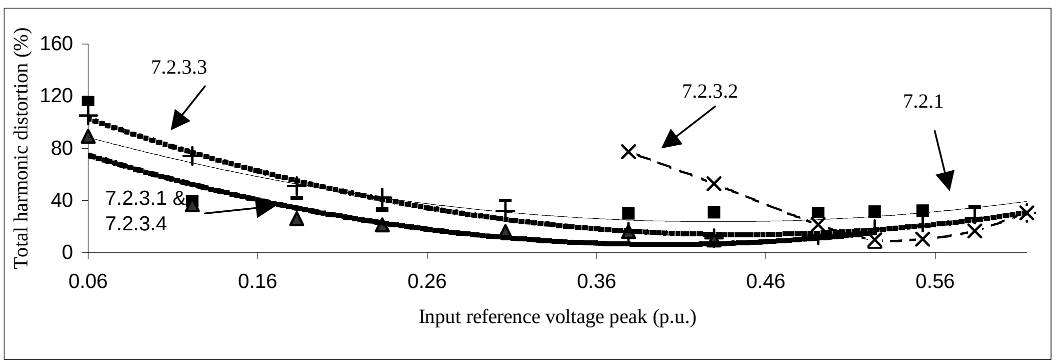

c.

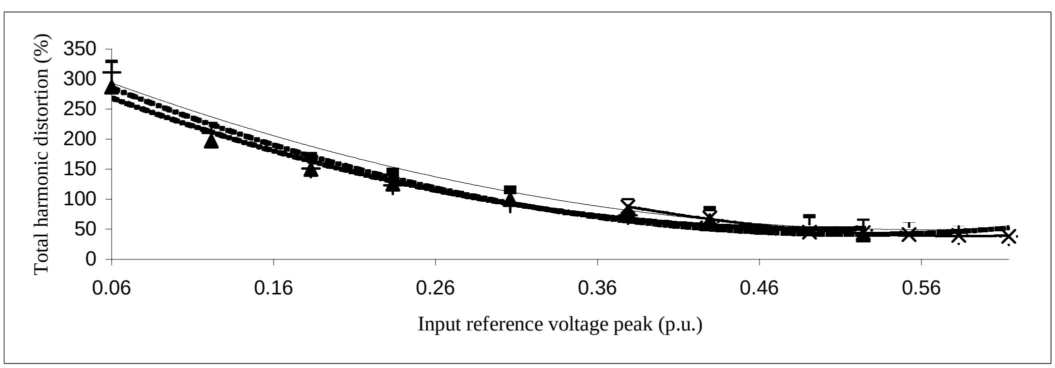

d.

Fig. 7.18. Performance of different space vector modulators from 7.2.1-7.2.3.4: a. 3rd harmonic content in the output voltages, b. 7th harmonic content in the output voltages, c. THD caused by low-order harmonic, d. THD caused by low-order and switching harmonics.

methods provide identical output voltage quality, as is evident from Fig. 7.18c. For input reference voltage greater than 85.41%, there are three possible schemes (7.2.1., 7.2.3.2 and 7.2.3.3). To further compare these three schemes, Figs. 7.19a-c illustrate their performance from 85.41% to 100% of the maximum acheivable output. It is to be noted here that for this comparison the THD which takes into account the switching harmonics is not considered. It is clearly seen from Figs. 7.19a-c that the method developed in 7.2.3.2 offers better performance, when compared to methods of 7.2.1 and 7.2.3.3, in terms of the output waveform quality. Thus it can be concluded from this disscussion that for input reference voltage above 85.41%, one should utilise the scheme of 7.2.3.2 to encompass the complete range from 0% to 100% of the maximum achievable output voltage.

7.3 SPACE VECTOR MODULATION SCHEME FOR TWO FIVE-PHASE SERIES-CONNECTED MACHINES

This section develops a space vector PWM technique for a five-phase VSI used to feed two five-phase machines connected in series with phase transposition, in order to provide decoupled control of the machines. The control of two five-phase machines connected in series and fed from a single five-phase inverter, using hysteresis and ramp-comparison current control schemes in stationary reference frame, has been explored in Chapter 4. The aim of this section is to develop an appropriate SVPWM scheme for a five-phase VSI which is applicable in conjunction with current control in the rotating reference frame.

The principle of control decoupling of two five-phase machines connected in series lies in the fact that the $\alpha-\beta$ voltage/current components of one machine become the x-y voltage/current components of the other machine and vice-versa. Thus the inverter feeding two-motor drive configuration needs to provide both $\alpha-\beta$ and x-y components of voltages/currents for two machines. The requirement on the space vector modulator is to keep the average volt-seconds of $\alpha-\beta$ and x-y reference voltage space vectors such as to satisfy the flux/torque control requirements of the two machines. The approach towards realising this requirement, adopted here, is the simplest possible. Consider the inverter switching period t_s. In the first switching period space vector modulator will apply $\alpha-\beta$ voltage reference by selecting a set of appropriate vectors. The set will be such that no x-y harmonics are generated. In the second switching period the space vector modulator will apply x-y voltage reference, by selecting a set of vectors that produce only x-y voltage components, but not the $\alpha-\beta$ components. This means that the effective rate of application of the two references

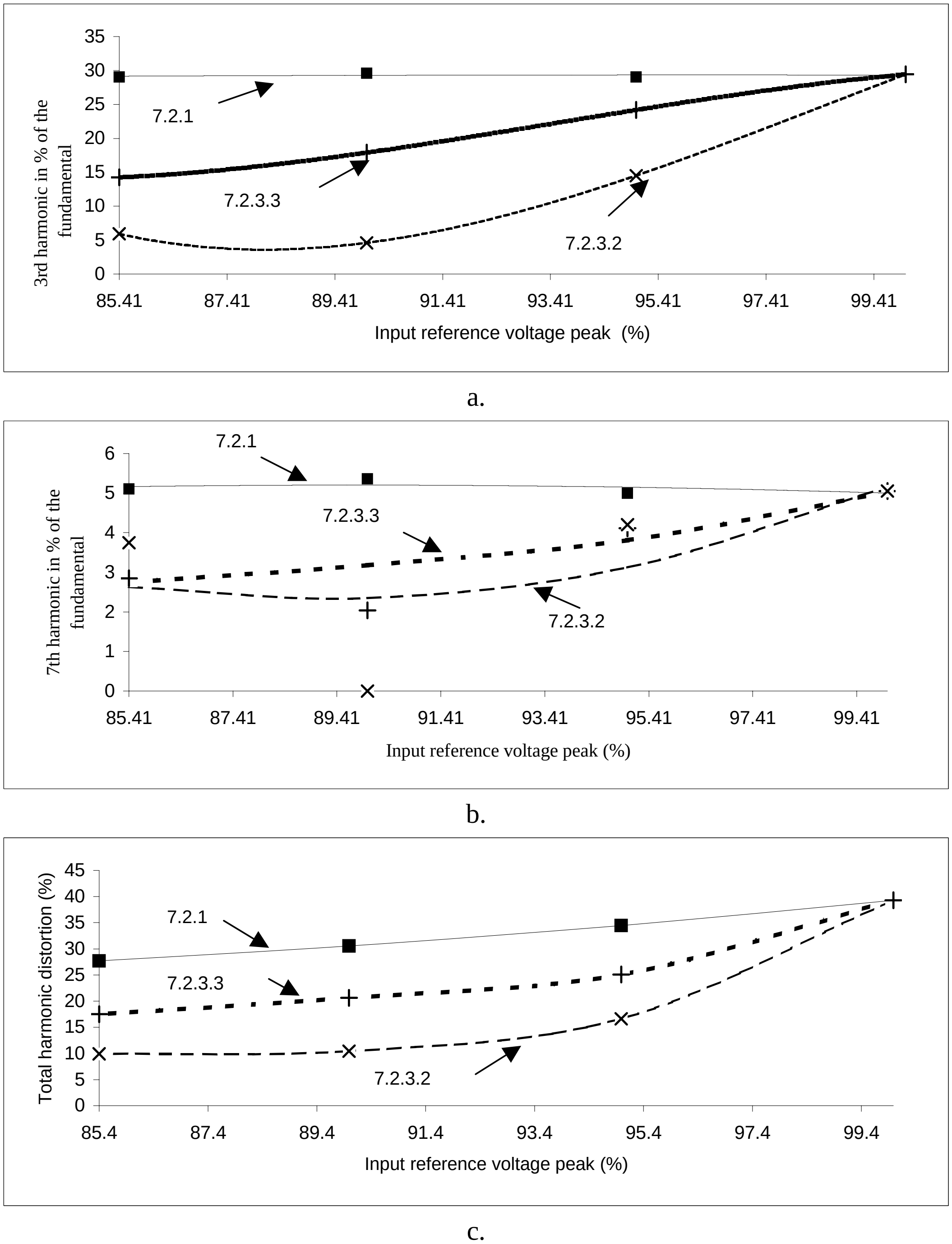

Fig. 7.19. Performance of space vector modulators for input reference above 85.41%: a. 3rd harmonic content in the output voltages, b. 7th harmonic content in the output voltages, c. THD caused by low-order harmonics.

($\alpha-\beta$ and x-y) is halved, since each is applied only in every second switching period. This automatically corresponds to one half of the available dc voltage being used for creation of any of the two references. The effective rate of application of the two references is in this way halved, compared to the inverter switching frequency. To further illustrate the concept, a block diagram of the space vector modulation is shown in Fig. 7.20.

Hence, the switching scheme used in the SVPWM is such that the five-phase inverter generates $\alpha-\beta$ axis voltages in the first cycle of the PWM, while simultaneously eliminating the x-y axis components, to control the first machine. In the second cycle it generates x-y axis voltages and simultaneously eliminates the $\alpha-\beta$ axis voltages to control the second machine. In essence, there are therefore two space vector modulators, $\alpha-\beta$ and x-y modulator. The $\alpha-\beta$ modulator imposes $\alpha-\beta$ axis voltage in the first cycle and the x-y modulator imposes the x-y axis voltage in the next cycle. The $\alpha-\beta$ modulator is identical to the one discussed in section 7.2.3.1. The x-y modulator is developed in this section.

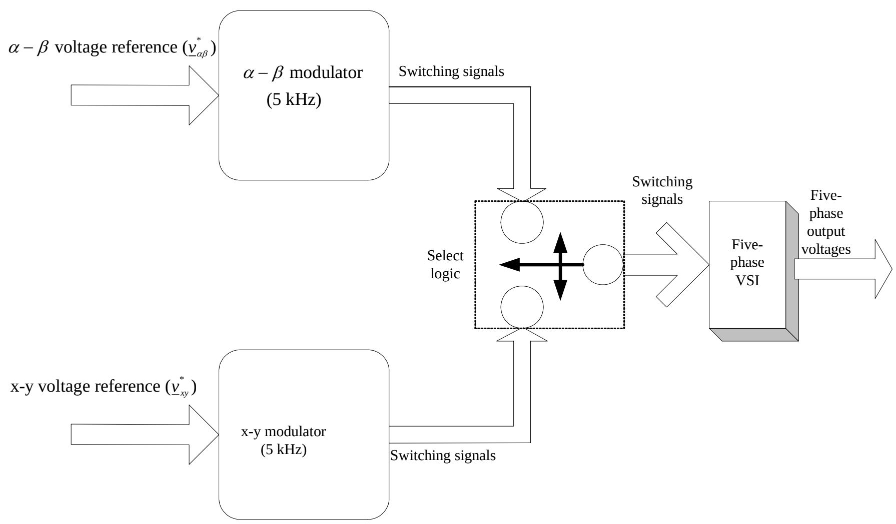

Fig. 7.20. Block diagram showing the principle of space vector modulation for five-phase series-connected two-motor drive configuration.

The principle of x-y reference generation is the same as that of $\alpha-\beta$ reference generation. It is evident from Fig. 7.1 that, for each sector, the large and the medium space vectors of the x-y plane fall diagonally opposite to each other in corresponding $\alpha-\beta$ plane. The lengths of these diagonally opposite space vectors in the $\alpha-\beta$ plane are in proportion to the lengths of large and medium space vectors. Thus to eliminate these $\alpha-\beta$ components from x-y modulator, a similar approach as that of $\alpha-\beta$ modulation is used. The switching pattern and the space vector sequence for ten sectors are shown in Fig. 7.21.

The simulation is done to evaluate the performance of the proposed space vector modulation. The simulation conditions of both $\alpha-\beta$ modulator and x-y modulator are kept identical. As the inverter has to feed two machines connected in series, the dc link voltage is

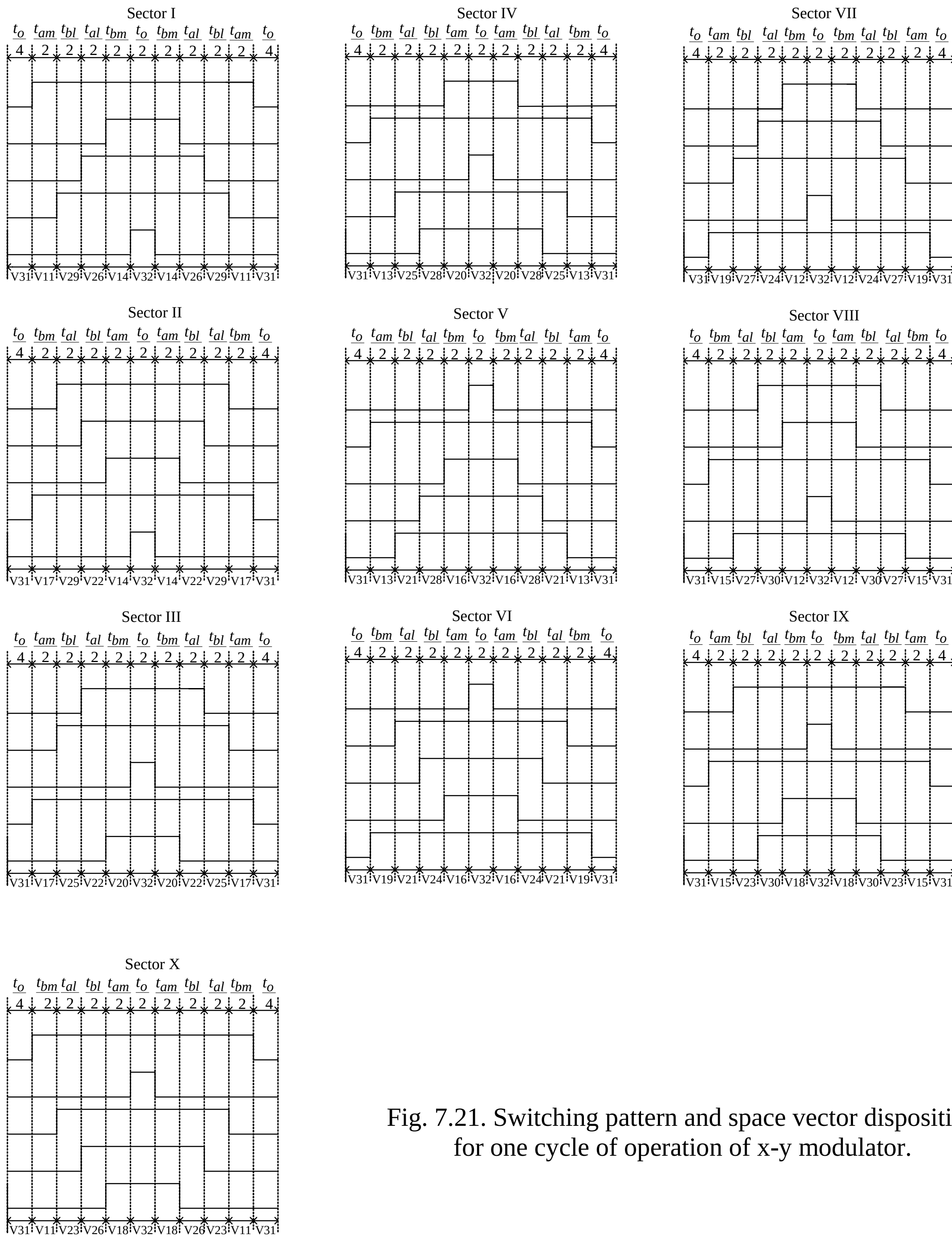

Fig. 7.21. Switching pattern and space vector disposition for one cycle of operation of x-y modulator.

arbitrarily set to 2 per unit and the switching frequency of both modulators is kept at 5 kHz. Since $V_{DC} = 2$ p.u., the output phase voltage from VSI for each machine is limited to $0.525V_{DC}$ (peak) or $0.371V_{DC}$ (RMS), as seen in section 7.2.3.1. Since $\alpha - \beta$ modulator imposes $\alpha-\beta$ axis voltages in the first cycle of the PWM and the x-y modulator produces x-y axis voltage in the second cycle, the effective frequency of the reference application becomes 2.5 kHZ. The frequencies of the input references are taken as 50 Hz and 25 Hz for the $\alpha-\beta$ modulator and the x-y modulator, respectively, and the magnitudes are 0.525 (p.u.) peak or 0.371 (p.u.) RMS. An analog first order filter is used to filter the high frequency components from the output voltage waveforms. The filtered output phase voltages, leg voltages and harmonic spectra are shown in Fig. 7.22.

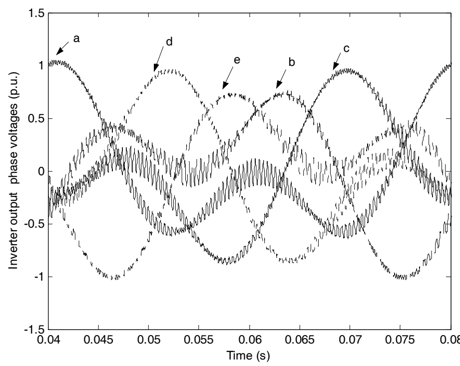

a.

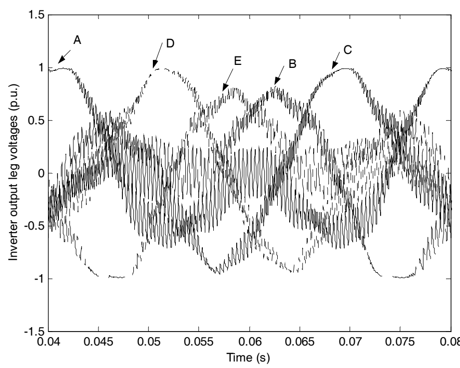

b.

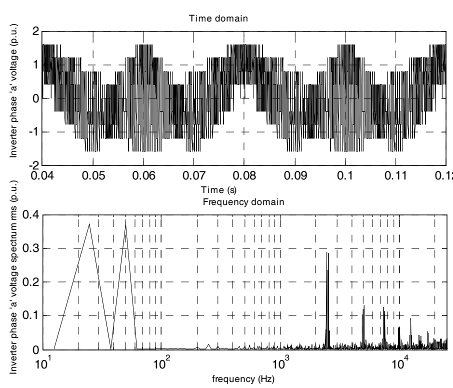

c.

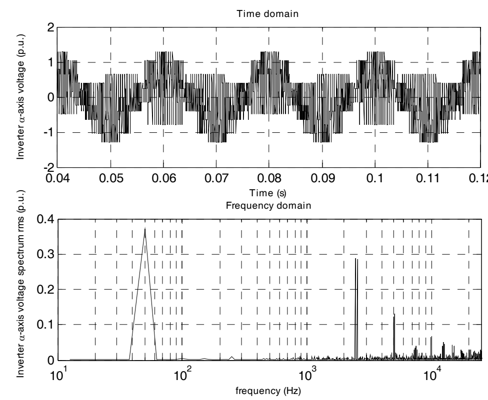

d.

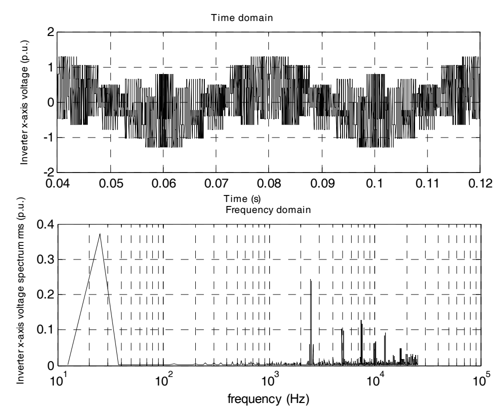

e.

Fig. 7.22. Output from VSI for input reference voltage of 0.525 (p.u.) peak: a. output phase voltages, b. output leg voltages, c. inverter phase ‘a’ voltage and its harmonic spectrum, d. inverter output α -axis voltage and its harmonic spectrum, e. inverter output x-axis voltage and its harmonic spectrum.

It is observed from the inverter phase 'a' voltage spectrum that it contains two fundamental frequency components, corresponding to 50 Hz and 25 Hz. The switching harmonics are appearing at multiples of 2.5 kHz, as expected. The fundamental voltage component of 50 Hz controls the first machine and the 25 Hz voltage fundamental component controls the second machine. The 50 Hz fundamental is thus seen in the α-axis voltage harmonic spectrum, while 25 Hz fundamental appears in the x-axis harmonic spectrum. It is further to be noted that the output phase voltages do not contain any undesirable low-order harmonic components.

7.4 SUMMARY

This chapter is devoted to the space vector modulation techniques for five-phase voltage source inverters. It initially elaborates the existing technique of using only two active space vectors from outer decagon to synthesise the input reference voltage. The method of using two active space vectors from middle decagon is also examined and it is found that both of these techniques generate undesirable large 3^{rd} and 7^{th} harmonic components in the output voltages. The percentage of these harmonic components is found to be significantly higher for method using two medium active space vectors only. This finding is also confirmed using the analytical expressions for average leg voltages for both cases.

Three techniques which utilise both large and medium active space vectors are developed and analysed next. The technique which divides the time of application of large and medium active space vectors in proportion to their length is found to provide sinusoidal output voltages. But the limitation of this method is that it can be employed for up to 85.41% of the maximum achievable fundamental voltage. The method proposed by de Silva et al (2004) is also investigated and is found to suffer from the same drawback while providing the same characteristics. Another method, devised using both large and medium space vectors, which drives the VSI along the maximum possible output by forcing the zero space vector time to remain zero in the middle of each sector is also investigated. This method generates output voltage with variable 3^{rd} and 7^{th} harmonic contents. It also suffers from the limitation of not being operational for the complete range of the input reference voltage. Another novel technique is thus formulated, which can be used for the complete range of the input reference voltage. This method relies on the pre-defined zero space vector application time trajectory. The method is found to generate output voltage with variable 3^{rd} and 7^{th} harmonic contents. It is thus concluded that only a combined scheme can yield the voltage closest to the sinusoidal output, while simultenously being operational for all references up to the maxmium acheivable. The scheme of 7.2.3.1 (or 7.2.3.4) combined with the one elaborated in 7.2.3.2 (or 7.2.3.3) is proposed for practical applications, since it produces the output voltage with acceptable harmonic content and enables full utilisation of the dc bus.

Finally, a SVPWM scheme, suitable for application in conjunction with series-connected five-phase two-motor drive, is proposed. It combines two SVPWM modulators, which are used in a sequential manner to generate $\alpha - \beta$ and x-y inverter voltage references. Generation of any unwanted low-order harmonics is avoided in this way, so that the output inverter voltages contain only two fundamental components at two required frequencies (plus, of course high frequency harmonics related to the switching frequency). The proposed SVPWM scheme for a series-connected two-motor drive is applicable in conjunction with current control in the rotating reference frame.

Chapter 8

SPACE VECTOR MODULATION SCHEMES FOR SIX-PHASE VOLTAGE SOURCE INVERTER

8.1 INTRODUCTION

It has been shown in section 2.3.1 that existing six-phase motor drives invariably utilise a quasi six-phase machine. This is the reason why most of the work related to SVPWM has been done for a quasi six-phase VSI. This chapter is devoted to the space vector modulation techniques for a six-phase VSI which can be used to feed a true six-phase machine.

Gopakumar et al (1993) have developed a SVPWM technique for six-phase inverter feeding a quasi six-phase induction motor, having two sets of three-phase windings with 30º spatial phase displacements. Two three-phase inverters are used to feed two sets of three-phase windings with dc link voltage of $V_{DC}/2\cos\left(15^0\right)$ adjusted in such a way so as to produce the same amount of air gap flux as that of an equivalent three-phase machine. The total number of distinct non-zero space vectors with this inverter configuration is 60, lying on four distinct 12-sided concentric polygons. Only outer polygon, containing the largest length vectors, is used to implement the SVPWM and three vectors are used per switching cycle, similar to three-phase inverters. In comparison to three-phase VSI, which gives maximum fundamental peak output voltage of $0.577V_{DC}$, this method yields fundamental peak voltage equal to $0.643V_{DC}$.

For a similar quasi six-phase induction machine, Zhao and Lipo (1995) have proposed SVPWM that eliminates harmonic components of the order 6*k*±1 (*k*=1,3,5..), developed by using space vector decomposition technique. The harmonics of order 6*k*±1 (*k*=1,3,5..) do not contribute to the torque production but cause the output voltage and subsequently current distortion. It is therefore desirable to eliminate these harmonics. The total number of possible space vectors is again 64 in this configuration. These are transformed into three orthogonal pairs of axes, namely $\alpha-\beta$, x-y and 0+-0-. The stator windings of each of two three-phase sets are connected to a separate neutral point, thus forming a double neutral topology. All the components in 0+-0- plane are thus nullified because of the double neutral point connection. The aim of the SVPWM here is to maximise $\alpha - \beta$ components and simultaneously minimise the x-y components. The value of average volt-second of $\alpha - \beta$ voltage space vectors is kept such as to satisfy the torque control requirement of the machine and the average volt-second of x-y voltage space vectors is kept at zero. Again, only the largest length vectors of the outer polygon are utilised in implementing the SVPWM. However, to synthesise the reference vector, four neighbouring active space vectors and zero space vectors are used, in contrast to the conventional method of using only two active neighbouring vectors and two zero state vectors. The required harmonic components are eliminated at the cost of high switching frequency of the inverter and complex DSP implementation.

In order to simplify the DSP implementation, Hadiouche et al (2003) have proposed SVPWM based on the same space vector decomposition technique but most of the calculations are done off-line in advance. Mohapatra et al (2002) have also used the same concept of space vector decomposition as that of Zhao and Lipo (1995) to eliminate harmonics of the order $6k \pm 1$ (k=1,3,5..) for a quasi six-phase open-end winding configuration of an induction machine. Two sets of three-phase windings are fed from two ends using two two-level VSIs. The dc link voltages of two of VSIs are isolated from each other (in order to limit the triplen harmonics) and the ratio of their magnitudes is 1:0.366.

SVPWM for six-phase VSI, feeding a symmetrical true six-phase induction machine, has hardly been investigated, the exception being Correa et al (2003a) and (2003b). The major aim of the developed schemes in Correa et al (2003a) is to eliminate the common-mode voltage. A number of strategies based on mean common-mode voltage elimination and instantaneous common-mode voltage elimination have been investigated. For instantaneous common-mode voltage elimination, 60° sector configuration has been chosen which encompasses 20 space vectors with null common-mode voltage. Three different schemes utilising only two and four active vectors in each 60° sector have been developed. The scheme which utilises four active vectors (one large and three short) in first PWM period followed by another set of four active vectors (one large and three short) from the same sector in the second PWM period, yields better performance in terms of lower THD. The other two methods which utilise zero common-mode voltage vectors from large active vectors set only and short active vectors set only, produce similar results with the difference that the scheme with short vectors is operational for smaller range. Two different schemes have been suggested considering 30° sectors. One of these methods utilises five zero common-mode active vectors and the second method also utilises five active vectors but two out of five are zero common voltage vectors. The first method yields better performance.

Two additional PWM schemes have been reported in Correa et al (2003b). Every 60° sector is viewed as consisting of four small equilateral triangles. The vectors used to synthesise input reference belong to the small triangular area in which input reference is available. One of the schemes utilises four active vectors with zero common-mode voltage while other method uses five active vectors with all non-zero common-mode voltage in each small triangular area. A comparison of different schemes has been presented and it is shown that the triangular based pattern yields better THD performance.

Yu et al (2003) have developed a SVPWM scheme for a quasi twelve-phase VSI. The quasi twelve-phase VSI is realized by using four three-phase VSIs with 15º phase shift between two subsequent three-phase VSI outputs. There are $2^{12} = 4096$ space vectors, out of which 4080 are the active state vectors and 16 are zero state vectors. To synthesise the reference vector only the 24 outer largest active state vectors and zero states are used. Once more, the two neighbouring active and zero state vectors are used in each sector to implement the SVPWM. This scheme greatly simplifies the control algorithm and provides very good performance.

The SVPWM schemes presented in this chapter are based on the principle of the first method reported in Correa et al (2003a) and (2003b). The method, chosen to be elaborated here is based on the most natural choice of vectors (none on, one on, two on, three on, four on, five on and six on from upper leg of VSI) to implement SVPWM. The aim of this chapter is simply to analyse the principle of space vector modulation for six-phase VSI and thus the simplest method is adopted. One additional method is proposed in this chapter to further extend the range of operation of the existing SVPWM method. In addition, analytical expressions of average leg voltages are derived for every scheme presented in the chapter. Further, an analytical expression is derived and presented in the chapter to determine the range of operation of different SVPWM schemes. Finally, a SVPWM scheme is developed for a six-phase inverter feeding series connection of a six-phase and a three-phase machine.

8.2 SPACE VECTOR MODULATION SCHEMES

It has been shown in section 5.2 that the total number of space vectors available in a symmetrical six-phase VSI with single neutral point is 64. Out of these 64 space vectors, 54 are active and ten are zero space vectors. These 64 space vectors in phase variable form are transformed into three orthogonal sub-spaces composed of $\alpha-\beta$, x-y and 0+-0- pairs of axes using power variant form of the transformation in the stationary reference frame, for the reason described in section 7.2. The scaling factor in transformation expression is 2/6 rather than $\sqrt{2/6}$. Hence the space vectors representing inverter output phase voltages in different sub-spaces are obtained by using $(\alpha = 2\pi/6)$,

$$
\begin{aligned}
\underline{v}_{\alpha\beta}^{INV} &= 2/6\left(v_a + \underline{a}v_b + \underline{a}^2 v_c + \underline{a}^3 v_d + \underline{a}^4 v_e + \underline{a}^5 v_f\right) \\
\underline{v}_{xy}^{INV} &= 2/6\left(v_a + \underline{a}^2 v_b + \underline{a}^4 v_c + v_d + \underline{a}^2 v_e + \underline{a}^4 v_f\right) \qquad (8.1) \\
\underline{v}_{0_+0_-}^{INV} &= 2/6(1/2)\left(v_a \pm v_b + v_c \pm v_d + v_e \pm v_f\right)
\end{aligned}
$$

The 64 space vectors in transformed domains, calculated using (8.1) and phase-to-neutral voltages in Tables 5.2, 5.12, 5.15 and 5.18, are given in Fig. 8.1. The lengths of the outer large space vectors are $\left|\underline{v}_l\right| = 2/3V_{DC}$, the inner short space vectors are $\left|\underline{v}_{sh}\right| = 1/3V_{DC}$ and the medium space vectors are $\left|\underline{v}_m\right| = 1/\sqrt{3}V_{DC}$. The $\alpha-\beta$ or x-y planes can be visualised as being composed of three different hexagons, which are formed by the outer space vector set, the medium space vector set and the short space vector set. It is observed from Fig. 8.1 that six outer large space vector set of the $\alpha-\beta$ plane map into the origin of the x-y plane. These space vectors correspond to three adjacent switches being 'on' from upper (lower) set and three adjacent switches being 'off' from upper (lower) set or vice-versa (section 5.2). The other zero space vectors in the x-y plane are number 7, 8, 15 and 22. These four also form the zero space vectors in the $\alpha-\beta$ plane. The space vectors 15 and 22 correspond to the upper switches of phases *a*, *c*, *e* being 'on' and lower switches from phases *b*, *d*, *f* being 'on' and vice-versa, respectively. Vectors 7 and 8 are the result of all the switches from lower set being 'on' (upper set being 'off', as the switching of each leg is complimentary) and all the switches from upper set being 'on' (lower set being 'off'), respectively. Thus the total number of zero space vectors remains ten in x-y plane, similar to $\alpha-\beta$ plane. The six remaining zero space vectors in the $\alpha-\beta$ plane form the six outer large length space vectors set in the x-y plane. These six space vectors, numbered as 41, 42, 43, 56, 57 and 58, correspond to four switches being 'on' from upper (lower) and two switches being 'off' from upper (lower) set or vice-versa. The medium space vectors of x-y plane are obtained by mapping the short space vectors 9-14 and 16-21 from the $\alpha-\beta$ plane. These vectors results when three switches are 'on' from upper (lower) and three 'off' from upper (lower), or vice-versa, group. The remaining space vectors resulting with three switches 'on', three 'off', four switches 'on', two 'off' and five switches 'on', one off from $\alpha-\beta$ plane map into the innermost region of the x-y plane, forming the set of short space vectors.

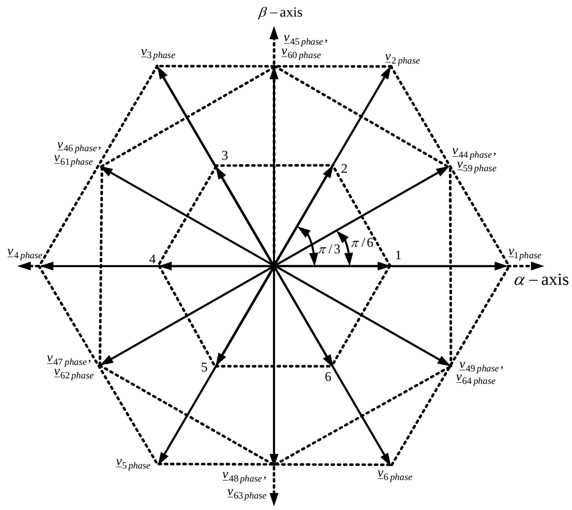

a.

1 = vectors 9,16,23,29,35,50;

2 = vectors 10,17,24,30,36,51;

3 = vectors 11,18,25,31,37,52;

4 = vectors 12,19,26,32,38,53;

5 = vectors 13,20,27,33,39,54;

6 = vectors 14,21,28,34,40,55;

Zero vectors (not shown):

7,8,15,22,41,42,43,56,67,58.

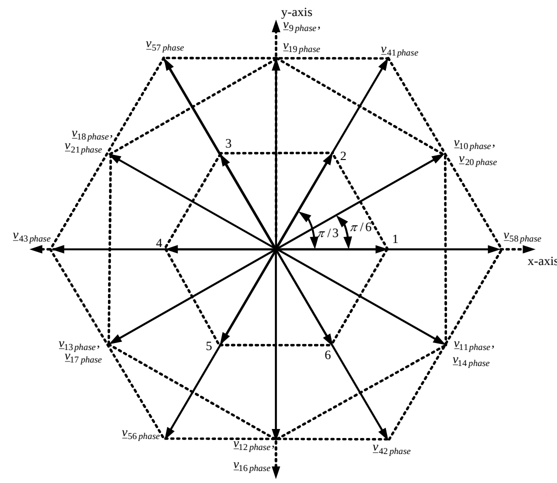

b.

1 = vectors 29,32,35,38,45,48;

2 = vectors 25,28,52,55,59,62;

3 = vectors 30,33,36,39,46,49;

4 = vectors 23,26,50,53,60,63;

5 = vectors 31,34,37,40,44, 47;

6 = vectors 24,27,51,54,61,64;

Zero vectors (not shown):

1,2,3,4,5,6,7,8,15,22.

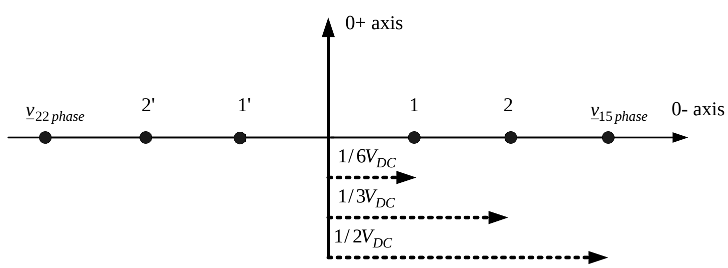

c.

1 = vectors 2,4,6,9,11,13,16,17,20,23,25,27,29,31,33;

2 = vectors 36,38,40,51,53,55;

1' = vectors 1,3,5,10,12,14,17,19,21,24,26,28,30,32,34;

2' = vectors 35,37,39,50,52,54;

Zero vectors (not shown): 7-8, 41-49,56-64.

Fig. 8.1. Six-phase voltage space vectors in: a. $\alpha-\beta$ plane, b. x-y plane and c. 0+-0- plane.

The zero-sequence space vectors are examined next. Out of the two zero-sequence components, 0+ is non-existent, however, the second component 0- is present. It is seen from Fig. 8.1c that these vectors are on the same straight line with different magnitudes. The space vectors on the locations denoted by primed numbers in Fig. 8.1c have the same magnitudes as those on un-primed number locations, but the polarity is opposite.

There are in total 12 sectors in the $\alpha-\beta$ plane, each spanning 30º. Four different symmetrical SVPWM schemes are presented in this chapter. These schemes use the concept developed in Correa et al (2003a) and (2003b). The first method utilises three neighbouring active space vectors (two medium and one large) and the zero space vectors. The second method utilises four active space vectors, two medium and two short ones and the zero space vectors. The third and the fourth methods utilise five active space vectors and the zero space vectors. These two schemes are mutually different because of different times of application of large and short vectors. However, the first and the second method can be considered as the special cases of the third method. The modulation schemes presented in this chapter have different range of applicability with different harmonic contents. The performance of the discussed schemes has been investigated in terms of total harmonic distortion of output voltages similar to Correa et al (2003ba) and (2003b), however, the expression used for calculation of THD is different. The expression used here to determine THD is the same as the one used in section 7.2.3.5 to keep consistency. In addition to THD this chapter also investigates the performance in terms of low-order harmonic content in phase voltages.

It is to be noted from Fig. 8.1 that each 30° sector in the $\alpha-\beta$ and the x-y plane is bounded by one large, two medium and six short space vectors. There could be numerous schemes to synthesise the reference voltage using the combination of available active and zero space vectors, as suggested in Correa et al (2003a) and (2003b). However, to keep low distortion in the output voltages it is mandatory to eliminate x-y components. Thus the reference voltage needs to contain only $\alpha-\beta$ components. With this consideration, the volt-second principle can be written as

$$\underline{v}_s^* t_s = \underline{v}_l t_l + \underline{v}_m t_m + \underline{v}_{sh} t_{sh} + \underline{v}_o t_o \tag{8.2}$$

where t_l, t_m and t_{sh} represent time of application of large, medium and short space vectors, respectively. Splitting (8.2) into real and imaginary parts with $\underline{v}_s^* = v_\alpha^* + jv_\beta^*$ and using the condition $\underline{v}_{sh} = (1/2)\underline{v}_l$ and $\underline{v}_o = 0$, one can obtain the expressions for time of application of different space vectors, as shown in Correa et al (2003a) and (2003b), as

$$\frac{t_{sh}}{2}+t_l=\frac{v_{m\beta}v_\alpha^*-v_{m\alpha}v_\beta^*}{v_{l\alpha}v_{m\beta}-v_{l\beta}v_{m\alpha}}t_s \tag{8.3a}$$

$$t_m=\frac{v_{l\alpha}v_\beta^*-v_{l\beta}v_\alpha^*}{v_{l\alpha}v_{m\beta}-v_{l\beta}v_{m\alpha}}t_s \tag{8.3b}$$

where

$$\underline{v}_m=v_{m\alpha}+jv_{m\beta}$$

$$\underline{v}_l=v_{l\alpha}+jv_{l\beta} \tag{8.3c}$$

The time of application of zero space vector is then given as

$$t_o=t_s-t_l-t_m-t_{sh} \tag{8.3d}$$

The proportion of sub-division of time of application of large and short space vectors can be used as a control variable to modify the PWM pattern as suggested in Correa et al (2003a) and (2003b). This control variable, which is used as a degree of freedom, is defined in Correa et al (2003a) and (2003b) as

$$\frac{t_l}{t_{sh}/2+t_l}=\rho \tag{8.4}$$

where $0\le\rho\le1$. Using (8.4), (8.3a) can be re-formulated into

$$t_l=\rho\frac{v_{m\beta}v_\alpha^*-v_{m\alpha}v_\beta^*}{v_{l\alpha}v_{m\beta}-v_{l\beta}v_{m\alpha}}t_s \tag{8.5a}$$

$$t_{sh}=2(1-\rho)\frac{v_{m\beta}v_\alpha^*-v_{m\alpha}v_\beta^*}{v_{l\alpha}v_{m\beta}-v_{l\beta}v_{m\alpha}}t_s \tag{8.5b}$$

There could be many possible values of the control variable ρ. The schemes presented in the following sections are the result of various choices of the control variable ρ.

There is a greater degree of freedom in a six-phase VSI, compared to a five-phase VSI, in choosing the space vectors to synthesise the reference space vector. However, there are only eighteen distinct active space vectors and the rest are redundant vectors. The choice of space vectors to implement SVPWM is done in accordance with the first method proposed in Correa et al (2003a) and (2003b). The sequence of vectors applied during one half PWM period is the result of no switches on, one switch on, two switches on, three switches on, four switches on, five switches on, and then six switches on, from upper set. The second half of the PWM period is the mirror image of the first half period. The position of zero space vector in a PWM period ensures the symmetrical SVPWM.

The switching pattern thus generated for all twelve sectors is shown in Fig. 8.2. The voltages of six inverter legs take values of $-1/2V_{DC}$ and $1/2V_{DC}$ and the six traces illustrate, from top to bottom, leg A, B, C, D, E and F, respectively.

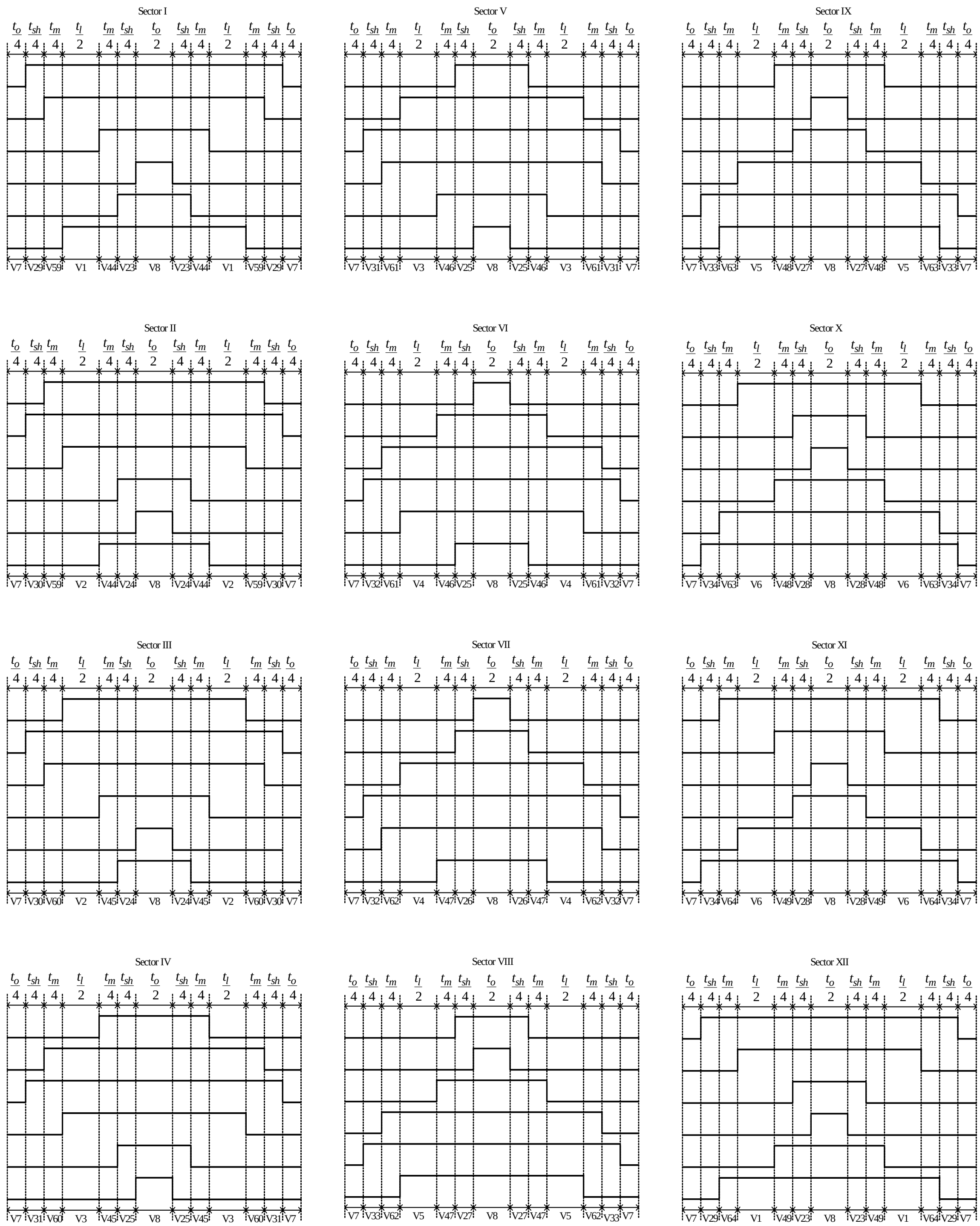

Fig. 8.2. Switching pattern and space vector disposition for one cycle of operation.

8.2.1 Application of large and medium space vectors (four vector values per switching period)

This scheme is similar to the one developed in Correa et al (2003b) as case 1 and is based on the utilisation of one large space vector, two medium space vectors and two zero space vectors in one PWM period. The control variable is chosen equal to one $(\rho = 1)$. The time of application of large space vectors becomes from (8.5a) for $\rho = 1$

$$t_l = \frac{v_{m\beta} v_\alpha^* - v_{m\alpha} v_\beta^*}{v_{l\alpha} v_{m\beta} - v_{l\beta} v_{m\alpha}} t_s \tag{8.6}$$

while time of application of medium space vector remains to be given with (8.3b). The time of application of zero space vector is given with (8.3d) where $t_{sh} = 0$. The range of application of this space vector modulator can be found by determining the range of the input reference voltage for which the time of application of zero space vectors remains positive. The expression for time of application of zero space vectors is found, by substituting (8.5a), (8.5b) and (8.3b) in (8.3d), as

$$t_o = t_s \left[1 - \frac{v_\beta^* \left(v_{l\alpha} - (2-\rho) v_{m\alpha} \right) - v_\alpha^* \left(v_{l\beta} - (2-\rho) v_{m\beta} \right)}{v_{l\alpha} v_{m\beta} - v_{l\beta} v_{m\alpha}} \right] \tag{8.7}$$

Hence for $t_o \geq 0$

$$\frac{v_\beta^* \left(v_{l\alpha} - (2-\rho) v_{m\alpha} \right) - v_\alpha^* \left(v_{l\beta} - (2-\rho) v_{m\beta} \right)}{v_{l\alpha} v_{m\beta} - v_{l\beta} v_{m\alpha}} \leq 1 \tag{8.8}$$

From (8.8) the range of the input reference for which the time of application of zero space vectors remains positive is found as $0 \leq \left| \underline{v}_s^* \right| \leq 1/\sqrt{3} V_{DC}$ for $\rho = 1$. Further, it is observed that the time of application of zero space vector is minimum at $\alpha = \pi/6$ in each sector, where angle α is measured from the starting point of every sector in anti-clockwise direction. The time of application of zero space vector is zero for the limiting condition of $\left| \underline{v}_s^* \right| = 1/\sqrt{3} V_{DC}$, consequently the locus of the output voltage is a circle with radius equal to $1/\sqrt{3} V_{DC}$. It is to be noted here that this value of input reference is also equal to the length of the medium vector. Hence the maximum achievable fundamental peak voltage from VSI using this space vector modulation is $V_{\max} = 1/\sqrt{3} V_{DC}$. The modified switching pattern can be obtained from Fig. 8.2 by substituting $t_{sh} = 0$ (i.e. $\rho = 1$).

The simulation is done for different peak values of the six-phase sinusoidal reference input ranging from maximum possible magnitude down to 10% of this value in 10% steps. Additionally, simulation is also done for 86.602%, and 57.735% of the maximum achievable output. These two percentage values correspond to the maximum possible output when large, medium and short vectors are applied together (section 8.2.3) and when only short and medium vectors are applied together (section 8.2.2), respectively. The dc link voltage is set to one per unit and the switching frequency is 5 kHz. An analog first order filter with time constants of 0.8 ms is used to filter the high frequency components from the output phase voltages and the leg voltages. The resulting filtered phase and leg voltages, which correspond to the maximum input reference voltage, are depicted in Fig. 8.3 along with the harmonic spectrum of the phase ‘a’ voltage. The frequency of the reference input is kept at 50 Hz. The nature of the output from VSI using this space vector modulation scheme remains the same for the complete range of the input reference, except for a corresponding reduction in the magnitudes, and thus only one plot is shown here. The harmonic analysis of output phase voltages is done for all the cases ranging from maximum achievable down to 10% of this value. In addition to the harmonic analysis, two different total harmonic distortion factors are also evaluated (up to the 80^{th} harmonic and the 500^{th} harmonic) for the reasons discussed in section 7.2.3.5. The defining expression used to evaluate the total harmonic distortion is given with equation (7.38). The RMS values of the fundamental output voltage, low-order harmonic components and THDs are listed in Table 8.1.

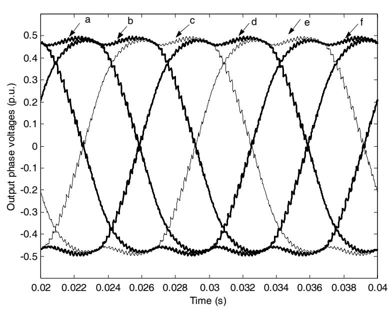

a.

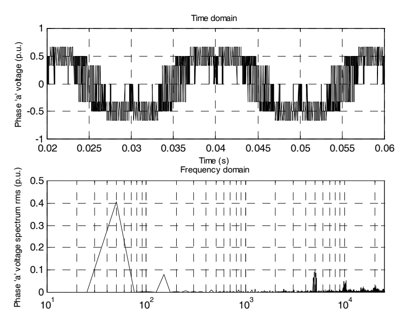

c.

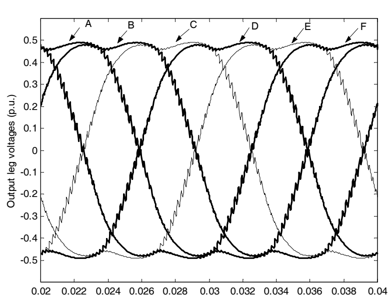

b.

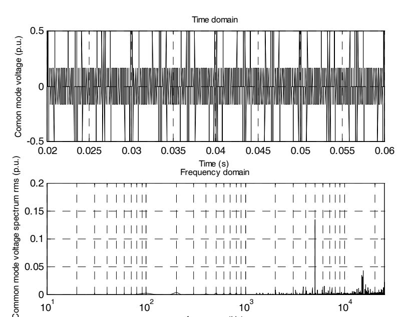

d.

Fig. 8.3. Output of VSI for input reference equal to the maximum achievable ($1/\sqrt{3}$ p.u.): a. phase voltages, b. leg voltages, c. phase ‘a’ voltage and its harmonic spectrum, d. common-mode voltage and its harmonic spectrum.

It is observed from Fig. 8.3a and Fig. 8.3b that the phase voltages and the leg voltages are identical. This is because of the fact that the common-mode voltage does not exist, as is evident from Fig. 8.3d. The expression used to determine the common-mode voltage is given with (5.4).

It is to be noted from Table 8.1 that the phase voltages contain a significant amount of the third harmonic component and this remains more or less constant throughout the range of the input (around 20% of the fundamental).

Table 8.1. RMS of fundamental and low-order harmonic components, and THDs of output phase voltages.

$\left\lvert \underline{v}_s^* \right\rvert$ (p.u.)	Fundamental (50 Hz) Simulation RMS value (p.u.)	3rd harmonic (150 Hz, p.u.)	THD1 (up to 4 kHz, p.u.)	THD2 (up to 25 kHz, p.u.)
$1/\sqrt{3}$ (Max)	0.408	0.081 (19.9%)	0.2158	0.4168
86.602% of Max	0.353	0.072 (20.39%)	0.2235	0.4839
80% of Max	0.326	0.07 (21.47%)	0.2371	0.6853
70% of Max	0.285	0.06 (21.05%)	0.2611	0.8341
57.735% of Max	0.235	0.049 (20.85%)	0.2699	0.9467
50% of Max	0.204	0.042 (20.58%)	0.2971	1.1577
40% of Max	0.163	0.031 (19.02%)	0.3584	1.3806
30% of Max	0.122	0.026 (21.31%)	0.3997	1.7236
20% of Max	0.081	0.018 (22.22%)	0.4376	2.1951
10% of Max	0.04	$7.8x10^{-3}$ (19.5%)	1.0894	3.1885

This third harmonic component in the output phase voltage is generated due to the zero-sequence component of the large space vectors. For instance, in sector 1 the active vectors used are 59, 1 and 44. The zero-sequence component due to vectors 59 and 44 is zero while it is $-1/6V_{DC}$ for vector 1, as is evident from Fig. 8.1c. This causes the 3rd harmonic in the phase voltages. In sector I the x-y components of vector 1 are zero, while they are diagonally opposite to each other, with equal length, for vectors 44 and 59. Thus they cancel each other and the same applies to the other eleven sectors. Thus the x-y components are completely eliminated from the phase voltages and the harmonic components of the order 5,7 etc. therefore do not exist (i.e. $6k\pm1$ where k=1,3,5…). The THDs are seen to increase with the reduction in the input reference voltage. They have the highest values at 10% of the reference which is because of the fact that the lengths of the space vectors used to synthesise the input reference are very large compared to the required output vector length.

The analytical expressions for the leg voltages, averaged over one switching cycle and referenced to the mid-point of the dc bus of the six-phase VSI, can be deduced from the switching pattern of Fig. 8.2. For sector 1, one has

$$V_A = \frac{V_{DC}}{2t_s}\left(-t_o/4 + t_m/4 + t_l/2 + t_m/4 + t_o/2 + t_m/4 + t_l/2 + t_m/4 - t_o/4\right)$$
$$V_B = \frac{V_{DC}}{2t_s}\left(-t_o/4 + t_m/4 + t_l/2 + t_m/4 + t_o/2 + t_m/4 + t_l/2 + t_m/4 - t_o/4\right)$$
$$V_C = \frac{V_{DC}}{2t_s}\left(-t_o/4 - t_m/4 - t_l/2 + t_m/4 + t_o/2 + t_m/4 - t_l/2 - t_m/4 - t_o/4\right)$$
$$V_D = \frac{V_{DC}}{2t_s}\left(-t_o/4 - t_m/4 - t_l/2 - t_m/4 + t_o/2 - t_m/4 - t_l/2 - t_m/4 - t_o/4\right)$$
$$V_E = \frac{V_{DC}}{2t_s}\left(-t_o/4 - t_m/4 - t_l/2 - t_m/4 + t_o/2 - t_m/4 - t_l/2 - t_m/4 - t_o/4\right)$$
$$V_F = \frac{V_{DC}}{2t_s}\left(-t_o/4 - t_m/4 + t_l/2 + t_m/4 + t_o/2 + t_m/4 + t_l/2 - t_m/4 - t_o/4\right) \quad (8.9)$$

Substituting the expressions for times of application for different space vectors from (8.3b) and (8.6), the average leg voltages are found and the expressions are given in Table 8.2.

The expressions for average leg voltages in eleven other sectors are obtained in a similar fashion. The expressions for sectors VII to XII are identical to those of sectors I to VI in the same order, but with opposite polarity, and are thus not given in Table 8.2. It is further to be noted from Table 8.2 that the expressions for legs D, E and F are the same as those for legs A, B and C with reverse polarity, which is expected since in six-phase system these two three-phase sets are in phase opposition one to the other.

The plot of average leg voltages obtained using analytical expressions of Table 8.2 for maximum achievable reference input voltage is shown in Fig. 8.4a. Average leg voltages obtained using simulation are shown in Fig. 8.4b.

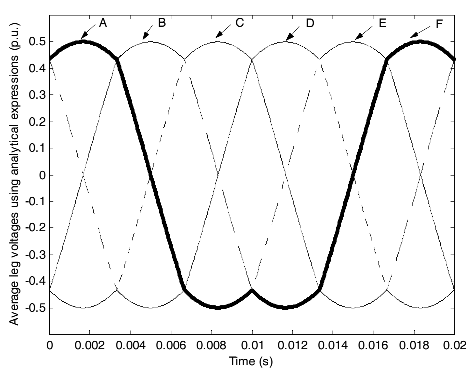

a.

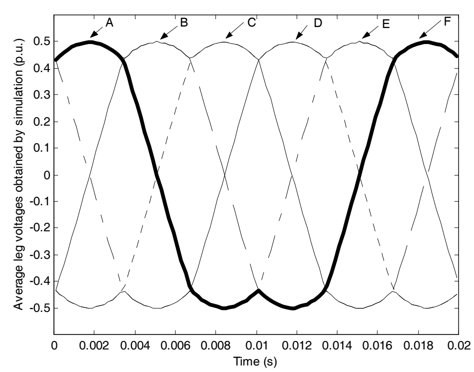

b.

Fig. 8.4. Average leg voltages obtained: a. using analytical expressions of Table 8.2, b. using simulation.

Fig. 8.4b was produced by following the same procedure as the one detailed in sections 7.2.1-7.2.3.1. By comparing Fig. 8.4a and Fig. 8.4b it can be concluded that the two are identical and thus this validates the analytical expressions of Table 8.2.

Table 8.2. Analytical expressions for average leg voltages when only large and medium vectors are used.

Sector I	Sector II	Sector III
$V_A = \frac{V_{DC}}{2}\left[\frac{v_\alpha^*\left(v_{m\beta}-v_{l\beta}\right)+v_\beta^*\left(v_{l\alpha}-v_{m\alpha}\right)}{v_{l\alpha}v_{m\beta}-v_{l\beta}v_{m\alpha}}\right]$ $V_B = \frac{V_{DC}}{2}\left[\frac{v_\alpha^*\left(v_{m\beta}-v_{l\beta}\right)+v_\beta^*\left(v_{l\alpha}-v_{m\alpha}\right)}{v_{l\alpha}v_{m\beta}-v_{l\beta}v_{m\alpha}}\right]$ $V_C = -\frac{V_{DC}}{2}\left[\frac{v_\alpha^* v_{m\beta}-v_\beta^* v_{m\alpha}}{v_{l\alpha}v_{m\beta}-v_{l\beta}v_{m\alpha}}\right]$ $V_D = -\frac{V_{DC}}{2}\left[\frac{v_\alpha^*\left(v_{m\beta}-v_{l\beta}\right)+v_\beta^*\left(v_{l\alpha}-v_{m\alpha}\right)}{v_{l\alpha}v_{m\beta}-v_{l\beta}v_{m\alpha}}\right]$ $V_E = -\frac{V_{DC}}{2}\left[\frac{v_\alpha^*\left(v_{m\beta}-v_{l\beta}\right)+v_\beta^*\left(v_{l\alpha}-v_{m\alpha}\right)}{v_{l\alpha}v_{m\beta}-v_{l\beta}v_{m\alpha}}\right]$ $V_F = \frac{V_{DC}}{2}\left[\frac{v_\alpha^* v_{m\beta}-v_\beta^* v_{m\alpha}}{v_{l\alpha}v_{m\beta}-v_{l\beta}v_{m\alpha}}\right]$	$V_A = \frac{V_{DC}}{2}\left[\frac{v_\alpha^*\left(v_{m\beta}-v_{l\beta}\right)+v_\beta^*\left(v_{l\alpha}-v_{m\alpha}\right)}{v_{l\alpha}v_{m\beta}-v_{l\beta}v_{m\alpha}}\right]$ $V_B = \frac{V_{DC}}{2}\left[\frac{v_\alpha^*\left(v_{m\beta}-v_{l\beta}\right)+v_\beta^*\left(v_{l\alpha}-v_{m\alpha}\right)}{v_{l\alpha}v_{m\beta}-v_{l\beta}v_{m\alpha}}\right]$ $V_C = \frac{V_{DC}}{2}\left[\frac{v_\alpha^* v_{m\beta}-v_\beta^* v_{m\alpha}}{v_{l\alpha}v_{m\beta}-v_{l\beta}v_{m\alpha}}\right]$ $V_D = -\frac{V_{DC}}{2}\left[\frac{v_\alpha^*\left(v_{m\beta}-v_{l\beta}\right)+v_\beta^*\left(v_{l\alpha}-v_{m\alpha}\right)}{v_{l\alpha}v_{m\beta}-v_{l\beta}v_{m\alpha}}\right]$ $V_E = -\frac{V_{DC}}{2}\left[\frac{v_\alpha^*\left(v_{m\beta}-v_{l\beta}\right)+v_\beta^*\left(v_{l\alpha}-v_{m\alpha}\right)}{v_{l\alpha}v_{m\beta}-v_{l\beta}v_{m\alpha}}\right]$ $V_F = -\frac{V_{DC}}{2}\left[\frac{v_\alpha^* v_{m\beta}-v_\beta^* v_{m\alpha}}{v_{l\alpha}v_{m\beta}-v_{l\beta}v_{m\alpha}}\right]$	$V_A = \frac{V_{DC}}{2}\left[\frac{v_\alpha^* v_{m\beta}-v_\beta^* v_{m\alpha}}{v_{l\alpha}v_{m\beta}-v_{l\beta}v_{m\alpha}}\right]$ $V_B = \frac{V_{DC}}{2}\left[\frac{v_\alpha^*\left(v_{m\beta}-v_{l\beta}\right)+v_\beta^*\left(v_{l\alpha}-v_{m\alpha}\right)}{v_{l\alpha}v_{m\beta}-v_{l\beta}v_{m\alpha}}\right]$ $V_C = \frac{V_{DC}}{2}\left[\frac{v_\alpha^*\left(v_{m\beta}-v_{l\beta}\right)+v_\beta^*\left(v_{l\alpha}-v_{m\alpha}\right)}{v_{l\alpha}v_{m\beta}-v_{l\beta}v_{m\alpha}}\right]$ $V_D = -\frac{V_{DC}}{2}\left[\frac{v_\alpha^* v_{m\beta}-v_\beta^* v_{m\alpha}}{v_{l\alpha}v_{m\beta}-v_{l\beta}v_{m\alpha}}\right]$ $V_E = -\frac{V_{DC}}{2}\left[\frac{v_\alpha^*\left(v_{m\beta}-v_{l\beta}\right)+v_\beta^*\left(v_{l\alpha}-v_{m\alpha}\right)}{v_{l\alpha}v_{m\beta}-v_{l\beta}v_{m\alpha}}\right]$ $V_F = -\frac{V_{DC}}{2}\left[\frac{v_\alpha^*\left(v_{m\beta}-v_{l\beta}\right)+v_\beta^*\left(v_{l\alpha}-v_{m\alpha}\right)}{v_{l\alpha}v_{m\beta}-v_{l\beta}v_{m\alpha}}\right]$
Sector IV	**Sector V**	**Sector VI**
$V_A = -\frac{V_{DC}}{2}\left[\frac{v_\alpha^* v_{m\beta}-v_\beta^* v_{m\alpha}}{v_{l\alpha}v_{m\beta}-v_{l\beta}v_{m\alpha}}\right]$ $V_B = \frac{V_{DC}}{2}\left[\frac{v_\alpha^*\left(v_{m\beta}-v_{l\beta}\right)+v_\beta^*\left(v_{l\alpha}-v_{m\alpha}\right)}{v_{l\alpha}v_{m\beta}-v_{l\beta}v_{m\alpha}}\right]$ $V_C = \frac{V_{DC}}{2}\left[\frac{v_\alpha^*\left(v_{m\beta}-v_{l\beta}\right)+v_\beta^*\left(v_{l\alpha}-v_{m\alpha}\right)}{v_{l\alpha}v_{m\beta}-v_{l\beta}v_{m\alpha}}\right]$ $V_D = \frac{V_{DC}}{2}\left[\frac{v_\alpha^* v_{m\beta}-v_\beta^* v_{m\alpha}}{v_{l\alpha}v_{m\beta}-v_{l\beta}v_{m\alpha}}\right]$ $V_E = -\frac{V_{DC}}{2}\left[\frac{v_\alpha^*\left(v_{m\beta}-v_{l\beta}\right)+v_\beta^*\left(v_{l\alpha}-v_{m\alpha}\right)}{v_{l\alpha}v_{m\beta}-v_{l\beta}v_{m\alpha}}\right]$ $V_F = -\frac{V_{DC}}{2}\left[\frac{v_\alpha^*\left(v_{m\beta}-v_{l\beta}\right)+v_\beta^*\left(v_{l\alpha}-v_{m\alpha}\right)}{v_{l\alpha}v_{m\beta}-v_{l\beta}v_{m\alpha}}\right]$	$V_A = -\frac{V_{DC}}{2}\left[\frac{v_\alpha^*\left(v_{m\beta}-v_{l\beta}\right)+v_\beta^*\left(v_{l\alpha}-v_{m\alpha}\right)}{v_{l\alpha}v_{m\beta}-v_{l\beta}v_{m\alpha}}\right]$ $V_B = \frac{V_{DC}}{2}\left[\frac{v_\alpha^* v_{m\beta}-v_\beta^* v_{m\alpha}}{v_{l\alpha}v_{m\beta}-v_{l\beta}v_{m\alpha}}\right]$ $V_C = \frac{V_{DC}}{2}\left[\frac{v_\alpha^*\left(v_{m\beta}-v_{l\beta}\right)+v_\beta^*\left(v_{l\alpha}-v_{m\alpha}\right)}{v_{l\alpha}v_{m\beta}-v_{l\beta}v_{m\alpha}}\right]$ $V_D = \frac{V_{DC}}{2}\left[\frac{v_\alpha^*\left(v_{m\beta}-v_{l\beta}\right)+v_\beta^*\left(v_{l\alpha}-v_{m\alpha}\right)}{v_{l\alpha}v_{m\beta}-v_{l\beta}v_{m\alpha}}\right]$ $V_E = -\frac{V_{DC}}{2}\left[\frac{v_\alpha^* v_{m\beta}-v_\beta^* v_{m\alpha}}{v_{l\alpha}v_{m\beta}-v_{l\beta}v_{m\alpha}}\right]$ $V_F = -\frac{V_{DC}}{2}\left[\frac{v_\alpha^*\left(v_{m\beta}-v_{l\beta}\right)+v_\beta^*\left(v_{l\alpha}-v_{m\alpha}\right)}{v_{l\alpha}v_{m\beta}-v_{l\beta}v_{m\alpha}}\right]$	$V_A = -\frac{V_{DC}}{2}\left[\frac{v_\alpha^*\left(v_{m\beta}-v_{l\beta}\right)+v_\beta^*\left(v_{l\alpha}-v_{m\alpha}\right)}{v_{l\alpha}v_{m\beta}-v_{l\beta}v_{m\alpha}}\right]$ $V_B = -\frac{V_{DC}}{2}\left[\frac{v_\alpha^* v_{m\beta}-v_\beta^* v_{m\alpha}}{v_{l\alpha}v_{m\beta}-v_{l\beta}v_{m\alpha}}\right]$ $V_C = \frac{V_{DC}}{2}\left[\frac{v_\alpha^*\left(v_{m\beta}-v_{l\beta}\right)+v_\beta^*\left(v_{l\alpha}-v_{m\alpha}\right)}{v_{l\alpha}v_{m\beta}-v_{l\beta}v_{m\alpha}}\right]$ $V_D = \frac{V_{DC}}{2}\left[\frac{v_\alpha^*\left(v_{m\beta}-v_{l\beta}\right)+v_\beta^*\left(v_{l\alpha}-v_{m\alpha}\right)}{v_{l\alpha}v_{m\beta}-v_{l\beta}v_{m\alpha}}\right]$ $V_E = \frac{V_{DC}}{2}\left[\frac{v_\alpha^* v_{m\beta}-v_\beta^* v_{m\alpha}}{v_{l\alpha}v_{m\beta}-v_{l\beta}v_{m\alpha}}\right]$ $V_F = -\frac{V_{DC}}{2}\left[\frac{v_\alpha^*\left(v_{m\beta}-v_{l\beta}\right)+v_\beta^*\left(v_{l\alpha}-v_{m\alpha}\right)}{v_{l\alpha}v_{m\beta}-v_{l\beta}v_{m\alpha}}\right]$

8.2.2 Application of medium and short space vectors (five vector values per switching period)

This scheme is based on the utilisation of two medium space vectors (of identical position), two short space vectors (of the same position) and two zero space vectors in one

PWM period. For instance, in sector 1 the vectors used are 29, 59, 44 and 23. The sequence of vectors used in each sector is as shown in Fig. 8.2. This scheme is also suggested in Correa et al (2003b) but the results are not shown and thus this method is elaborated further in the present section. The control variable is chosen equal to zero $(\rho = 0)$ which causes the large vector application time to become zero. The time of application of short space vectors from (8.5b) with $\rho = 0$ becomes

$$t_{sh} = 2\frac{v_{m\beta}v_{\alpha}^{*} - v_{m\alpha}v_{\beta}^{*}}{v_{l\alpha}v_{m\beta} - v_{l\beta}v_{m\alpha}}t_{s} \tag{8.10}$$

while time of application of medium space vectors remains to be given with (8.2b). The time of application of zero space vectors is given with (8.3d) where $t_l = 0$. The maximum achievable fundamental peak voltage from VSI using this space vector modulation technique is determined by following the same approach as that of section 8.2.1. The time of application of zero space vectors remains positive for the input reference range equal to $0 \le \left|\underline{v}_s^*\right| \le 1/3V_{DC}$. The time of application of zero space vectors is found to be minimum at $\alpha = 0$ (i.e. at the starting point of every sector) and the limiting condition is $\left|\underline{v}_s^*\right| = 1/3V_{DC}$. It is seen from Fig. 8.1a that every sector starts with short vector in anti-clockwise direction and thus the output circular locus must have largest radius equal to the length of the short vector. Hence the maximum achievable fundamental peak voltage from VSI using this type of space vector modulation is $V_{\max} = 1/3V_{DC}$, which is 57.735% of the maximum achievable with the method analysed in 8.2.1. The switching pattern for this method can be obtained from Fig. 8.2 with $t_l = 0$.

The simulation is done for different peak values of the six-phase sinusoidal reference input ranging from maximum possible magnitude down to 10% of this value in 10% steps. The simulation conditions are identical to those in section 8.2.1. The resulting filtered output phase and output leg voltages, which correspond to the maximum input reference voltage are depicted in Fig. 8.5 along with the harmonic spectrum of the phase ‘a’ voltage. The nature of the output from VSI using this space vector modulation approach remains the same for the complete range of the input reference except for a corresponding reduction in the magnitude, and thus only one plot is shown. The harmonic analysis of phase voltages is done for all the cases ranging from maximum achievable down to 10% of this value. In addition to the harmonic analysis, two different total harmonic distortions are also evaluated, similar to section 8.2.1. The RMS values of the fundamental output voltages, low-order harmonic components and THDs are listed in Table 8.3. It is evident from Fig. 8.5d that the common-mode voltage is again completely eliminated.

It is seen from Table 8.3 that the phase voltages contain a significant amount of the third harmonic component and this remains more or less constant throughout the range of the input (around 40% of the fundamental). This third harmonic component in the phase voltage

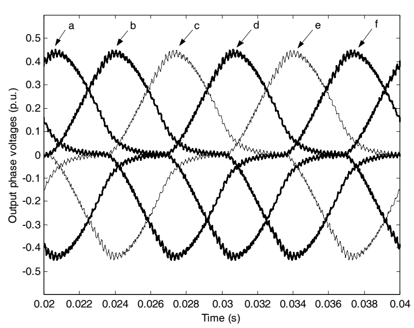

a.

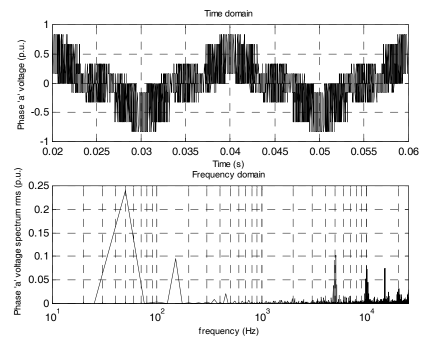

c.

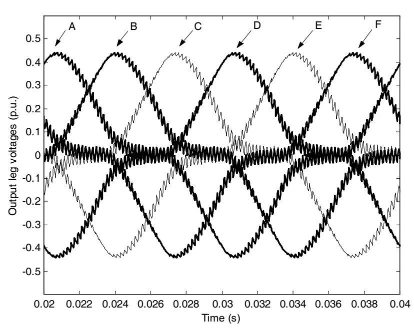

b.

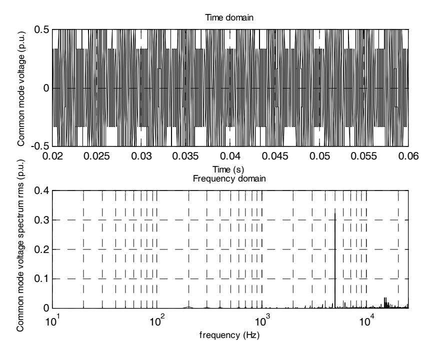

d.

Fig. 8.5. Output of VSI for input reference equal to the maximum achievable ($1/3$ p.u.): a. phase voltages, b. leg voltages, c. phase 'a' voltage and its harmonic spectrum, d. common-mode voltage and its harmonic spectrum.

Table 8.3. RMS of the fundamental and low-order harmonic components, and THDs of output phase voltages.

$\left\lvert \underline{v}_s^* \right\rvert$ (p.u.)	Fundamental (50 Hz) Simulation RMS value (p.u.)	3rd harmonic (150 Hz, p.u.)	THD1 (up to 4 kHz, p.u.)	THD2 (up to 25 kHz, p.u.)
57.735% of Max	0.235	0.095 (40.42%)	0.4237	0.7157
50% of Max	0.204	0.081 (39.7%)	0.4315	0.8395
40% of Max	0.163	0.065 (39.87%)	0.4455	1.0395
30% of Max	0.122	0.049 (40.16%)	0.493	1.3072
20% of Max	0.081	0.034 (41.97%)	0.5788	1.5667
10% of Max	0.04	0.0148 (37%)	0.9661	2.1813

is generated due to the presence of the zero-sequence components of the short space vectors. For instance, in sector 1, the active vectors used are 29, 59, 44 and 23. The zero-sequence component due to 59 and 44 is zero, while it has magnitude of $1/6V_{DC}$ for vectors 29 and 23, as is evident from Fig. 8.1c. The sum of these two zero-sequence components is equal to $1/3V_{DC}$, which is double the magnitude compared to the zero-sequence caused by the large vector 1. Thus the 3rd harmonic component observed in this case is twice as much as the one of section 8.2.1, where the 3rd harmonic component was the consequence of the large vectors only. The x-y components are non-existent again because they lie diagonally opposite to each other and are of equal length. For instance in sector I the x-y components of vectors 29 and 23 are diagonally opposite to each other, similar to vectors 44 and 59, and thus they cancel each other. The THDs follow the same trend as in section 8.2.1 but the values are higher. This is the consequence of an increased harmonic content in the output phase voltages, when compared to the output of the modulation in section 8.2.1.

The analytical expressions for the leg voltages, averaged over one switching cycle, can again be deduced from the switching pattern (Fig. 8.2). For sector 1, one has

$$\begin{aligned}
V_A &= \frac{V_{DC}}{2t_s}\left(-t_o/4+t_{sh}/4+t_m/4+t_m/4+t_{sh}/4+t_o/2+t_{sh}/4+t_m/4+t_m/4+t_{sh}/4-t_o/4\right)\\
V_B &= \frac{V_{DC}}{2t_s}\left(-t_o/4-t_{sh}/4+t_m/4+t_m/4+t_{sh}/4+t_o/2+t_{sh}/4+t_m/4+t_m/4-t_{sh}/4-t_o/4\right)\\
V_C &= \frac{V_{DC}}{2t_s}\left(-t_o/4-t_{sh}/4-t_m/4+t_m/4+t_{sh}/4+t_o/2+t_{sh}/4+t_m/4-t_m/4-t_{sh}/4-t_o/4\right)\\
V_D &= \frac{V_{DC}}{2t_s}\left(-t_o/4-t_{sh}/4-t_m/4-t_m/4-t_{sh}/4+t_o/2-t_{sh}/4-t_m/4-t_m/4-t_{sh}/4-t_o/4\right)\\
V_E &= \frac{V_{DC}}{2t_s}\left(-t_o/4-t_{sh}/4-t_m/4-t_m/4+t_{sh}/4+t_o/2+t_{sh}/4-t_m/4-t_m/4-t_{sh}/4-t_o/4\right)\\
V_F &= \frac{V_{DC}}{2t_s}\left(-t_o/4-t_{sh}/4-t_m/4+t_m/4+t_{sh}/4+t_o/2+t_{sh}/4+t_m/4-t_m/4-t_{sh}/4-t_o/4\right)
\end{aligned} \tag{8.11}$$

Substituting the expressions for times of application of different space vectors from (8.3b) and (8.10), the average leg voltages are found and are given in Table 8.4. The expressions for average leg voltages in eleven other sectors are obtained in a similar fashion.

A similar conclusion can be dawn from the analytical expressions for the average leg voltages as in section 8.2.1. The plot of average leg voltages, obtained using analytical expressions of Table 8.4 for maximum achievable reference input voltage, is shown in Fig. 8.6a.

Average leg voltages of the six-phase VSI, obtained using simulation, when short and medium vector are used, are shown in Fig. 8.6b. Once again the same procedure is adopted here as in section 8.2.1 to produce Fig. 8.6b. By comparing Fig.8.6a and Fig. 8.6b it can be concluded that the two are identical and thus this validates the expressions of Table 8.4.

Table 8.4. Analytical expressions for average leg voltages when short and medium vectors are used only.

Sector I	Sector II	Sector III
$V_A=\frac{V_{DC}}{2}\left[\frac{v_\alpha^*(2v_{m\beta}-v_{l\beta})+v_\beta^*(v_{l\alpha}-2v_{m\alpha})}{v_{l\alpha}v_{m\beta}-v_{l\beta}v_{m\alpha}}\right]$ $V_B=\frac{V_{DC}}{2}\left[\frac{v_\beta^*v_{l\alpha}+v_\alpha^*v_{l\beta}}{v_{l\alpha}v_{m\beta}-v_{l\beta}v_{m\alpha}}\right]$ $V_C=0$ $V_D=-\frac{V_{DC}}{2}\left[\frac{v_\alpha^*(2v_{m\beta}-v_{l\beta})+v_\beta^*(v_{l\alpha}-2v_{m\alpha})}{v_{l\alpha}v_{m\beta}-v_{l\beta}v_{m\alpha}}\right]$ $V_E=-\frac{V_{DC}}{2}\left[\frac{v_\beta^*v_{l\alpha}+v_\alpha^*v_{l\beta}}{v_{l\alpha}v_{m\beta}-v_{l\beta}v_{m\alpha}}\right]$ $V_F=0$	$V_A=\frac{V_{DC}}{2}\left[\frac{v_\beta^*v_{l\alpha}+v_\alpha^*v_{l\beta}}{v_{l\alpha}v_{m\beta}-v_{l\beta}v_{m\alpha}}\right]$ $V_B=\frac{V_{DC}}{2}\left[\frac{v_\alpha^*(2v_{m\beta}-v_{l\beta})+v_\beta^*(v_{l\alpha}-2v_{m\alpha})}{v_{l\alpha}v_{m\beta}-v_{l\beta}v_{m\alpha}}\right]$ $V_C=0$ $V_D=-\frac{V_{DC}}{2}\left[\frac{v_\beta^*v_{l\alpha}+v_\alpha^*v_{l\beta}}{v_{l\alpha}v_{m\beta}-v_{l\beta}v_{m\alpha}}\right]$ $V_E=-\frac{V_{DC}}{2}\left[\frac{v_\alpha^*(2v_{m\beta}-v_{l\beta})+v_\beta^*(v_{l\alpha}-2v_{m\alpha})}{v_{l\alpha}v_{m\beta}-v_{l\beta}v_{m\alpha}}\right]$ $V_F=0$	$V_A=0$ $V_B=\frac{V_{DC}}{2}\left[\frac{v_\alpha^*(2v_{m\beta}-v_{l\beta})+v_\beta^*(v_{l\alpha}-2v_{m\alpha})}{v_{l\alpha}v_{m\beta}-v_{l\beta}v_{m\alpha}}\right]$ $V_C=\frac{V_{DC}}{2}\left[\frac{v_\beta^*v_{l\alpha}+v_\alpha^*v_{l\beta}}{v_{l\alpha}v_{m\beta}-v_{l\beta}v_{m\alpha}}\right]$ $V_D=0$ $V_E=-\frac{V_{DC}}{2}\left[\frac{v_\alpha^*(2v_{m\beta}-v_{l\beta})+v_\beta^*(v_{l\alpha}-2v_{m\alpha})}{v_{l\alpha}v_{m\beta}-v_{l\beta}v_{m\alpha}}\right]$ $V_F=-\frac{V_{DC}}{2}\left[\frac{v_\beta^*v_{l\alpha}+v_\alpha^*v_{l\beta}}{v_{l\alpha}v_{m\beta}-v_{l\beta}v_{m\alpha}}\right]$
Sector IV	**Sector V**	**Sector VI**
$V_A=0$ $V_B=\frac{V_{DC}}{2}\left[\frac{v_\beta^*v_{l\alpha}+v_\alpha^*v_{l\beta}}{v_{l\alpha}v_{m\beta}-v_{l\beta}v_{m\alpha}}\right]$ $V_C=\frac{V_{DC}}{2}\left[\frac{v_\alpha^*(2v_{m\beta}-v_{l\beta})+v_\beta^*(v_{l\alpha}-2v_{m\alpha})}{v_{l\alpha}v_{m\beta}-v_{l\beta}v_{m\alpha}}\right]$ $V_D=0$ $V_E=-\frac{V_{DC}}{2}\left[\frac{v_\beta^*v_{l\alpha}+v_\alpha^*v_{l\beta}}{v_{l\alpha}v_{m\beta}-v_{l\beta}v_{m\alpha}}\right]$ $V_F=-\frac{V_{DC}}{2}\left[\frac{v_\alpha^*(2v_{m\beta}-v_{l\beta})+v_\beta^*(v_{l\alpha}-2v_{m\alpha})}{v_{l\alpha}v_{m\beta}-v_{l\beta}v_{m\alpha}}\right]$	$V_A=-\frac{V_{DC}}{2}\left[\frac{v_\beta^*v_{l\alpha}+v_\alpha^*v_{l\beta}}{v_{l\alpha}v_{m\beta}-v_{l\beta}v_{m\alpha}}\right]$ $V_B=0$ $V_C=\frac{V_{DC}}{2}\left[\frac{v_\alpha^*(2v_{m\beta}-v_{l\beta})+v_\beta^*(v_{l\alpha}-2v_{m\alpha})}{v_{l\alpha}v_{m\beta}-v_{l\beta}v_{m\alpha}}\right]$ $V_D=\frac{V_{DC}}{2}\left[\frac{v_\beta^*v_{l\alpha}+v_\alpha^*v_{l\beta}}{v_{l\alpha}v_{m\beta}-v_{l\beta}v_{m\alpha}}\right]$ $V_E=0$ $V_F=-\frac{V_{DC}}{2}\left[\frac{v_\alpha^*(2v_{m\beta}-v_{l\beta})+v_\beta^*(v_{l\alpha}-2v_{m\alpha})}{v_{l\alpha}v_{m\beta}-v_{l\beta}v_{m\alpha}}\right]$	$V_A=-\frac{V_{DC}}{2}\left[\frac{v_\alpha^*(2v_{m\beta}-v_{l\beta})+v_\beta^*(v_{l\alpha}-2v_{m\alpha})}{v_{l\alpha}v_{m\beta}-v_{l\beta}v_{m\alpha}}\right]$ $V_B=0$ $V_C=\frac{V_{DC}}{2}\left[\frac{v_\beta^*v_{l\alpha}+v_\alpha^*v_{l\beta}}{v_{l\alpha}v_{m\beta}-v_{l\beta}v_{m\alpha}}\right]$ $V_D=\frac{V_{DC}}{2}\left[\frac{v_\alpha^*(2v_{m\beta}-v_{l\beta})+v_\beta^*(v_{l\alpha}-2v_{m\alpha})}{v_{l\alpha}v_{m\beta}-v_{l\beta}v_{m\alpha}}\right]$ $V_E=0$ $V_F=-\frac{V_{DC}}{2}\left[\frac{v_\beta^*v_{l\alpha}+v_\alpha^*v_{l\beta}}{v_{l\alpha}v_{m\beta}-v_{l\beta}v_{m\alpha}}\right]$

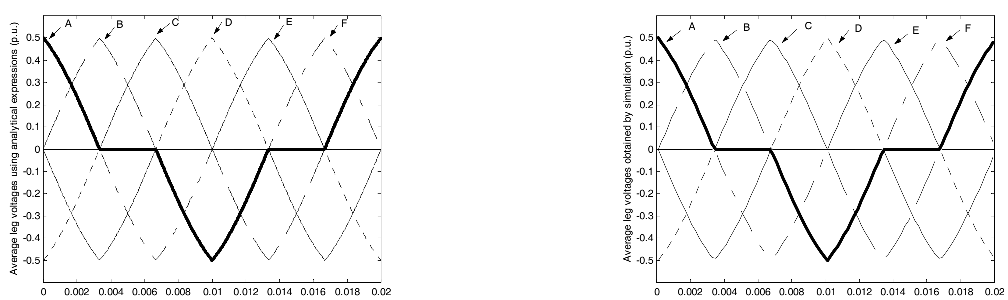

a. b.

Fig. 8.6. Average leg voltages (short and medium space vectors applied) obtained: a. using analytical expressions of Table 8.4, b. using simulation.

8.2.3 Application of large, medium and short space vectors (six vector values per switching period, equal time of application of short and large vectors)

This scheme is based on the utilisation of one large, two medium, two short and two zero space vectors in one PWM period. This scheme has been suggested in Correa et al (2003b) and is elaborated in this section. The control variable ρ is chosen as $\rho = 2/3$, so that the times of application of large and short space vectors are equal and are given with

$$t_l = t_{sh} = \frac{2}{3}\left(\frac{v_{m\beta}v_\alpha^* - v_{m\alpha}v_\beta^*}{v_{l\alpha}v_{m\beta} - v_{l\beta}v_{m\alpha}}\right)t_s \tag{8.12}$$

while application time of medium space vectors is still given with (8.3b). The time of application of zero space vector is given with (8.3d). The range of operation of this space vector modulator is once again determined by using the criterion that time of application of zero space vectors must be positive. This range is found as $0 \le \left|\underline{v}_s^*\right| \le 1/2V_{DC}$. The angle at which the application time of zero space vectors is zero is found to be at $\alpha = 0$, similar to section 8.2.2. The largest radius of the circular locus is at the limiting condition and is equal to $\left|\underline{v}_s^*\right| = 1/2V_{DC}$. Hence the maximum achievable fundamental peak voltage output from VSI utilising this space vector modulation scheme is $V_{\max} = 1/2V_{DC}$, which is 86.602% of the maximum achievable with the method discussed in section 8.2.1. The switching pattern for this method can be obtained from Fig. 8.2 with $t_l = t_{sh}$.

The simulation is done for different peak values of the six-phase sinusoidal reference input ranging from maximum possible magnitude down to 10% of this value in 10% steps. The simulation conditions are identical to those in sections 8.2.1 and 8.2.2. The resulting filtered phase and leg voltages, which correspond to the maximum input reference voltage, are depicted in Fig. 8.7 along with the harmonic spectrum of the phase ‘a’ voltage and the common-mode voltage. The nature of the output from the VSI using this space vector modulation method remains again the same for the complete range of the input reference, so that only one plot is shown. It can also be seen from Fig. 8.7d that the common-mode voltage is once more eliminated and this is the reason why both the leg and the phase voltages are identical. The harmonic analysis of output phase voltages is done again for all the references ranging from the maximum achievable down to 10% and two THDs are also evaluated. The RMS values of the fundamental output voltages and THDs are listed in Table 8.5.

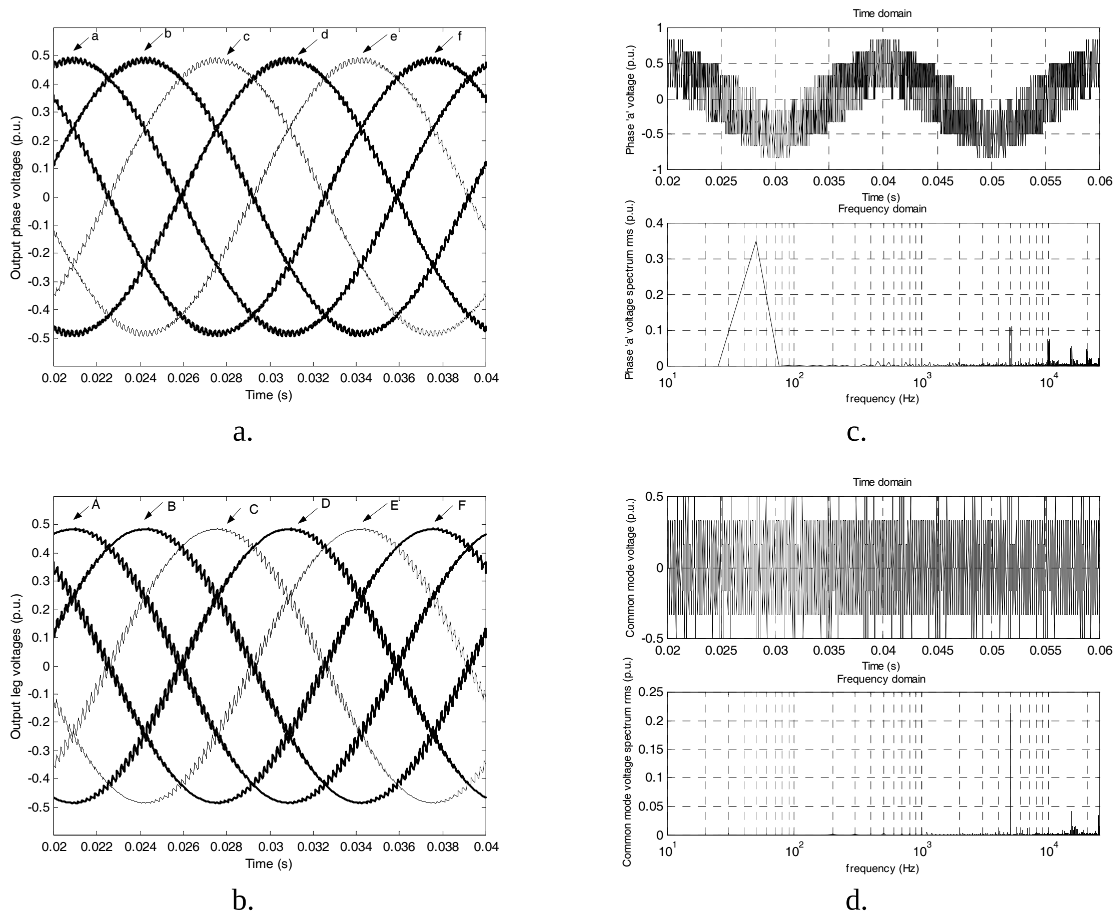

Fig. 8.7. Output of VSI for input reference equal to the maximum achievable ($1/2$ p.u.): a. phase voltages, b. leg voltages, c. phase ‘a’ voltage and its harmonic spectrum, d. common-mode voltage and its harmonic spectrum.

Table 8.5. RMS of fundamental component and THDs of output phase voltages.

$\left\|\underline{v}_s^*\right\|$ (p.u.)	Fundamental (50 Hz) Simulation RMS value (p.u.)	THD1 (up to 4 kHz, p.u.)	THD2 (up to 25 kHz, p.u.)
86.602% of (Max)	0.353	0.1113	0.4549
80% of Max	0.326	0.1295	0.5133
70% of Max	0.286	0.1311	0.5901
57.735% of Max	0.235	0.159	0.8423
50% of Max	0.204	0.2377	1.1794
40% of Max	0.163	0.3395	1.3455
30% of Max	0.122	0.3526	1.2636
20% of Max	0.081	0.3827	1.4171
10% of Max	0.04	0.4833	1.6398

The output from this space vector modulator does not contain any undesirable low-order harmonics and is in essence sinusoidal. This is a consequence of the cancellation of x-y and zero-sequence components. The elimination of these undesirable harmonics is the result of a proper choice of space vectors and their application time in each sector. For instance, in sector I, the active space vectors used are 29, 59, 1, 44 and 23. The only additional space vector in this scheme, compared to section 8.2.2, is the vector 1. It has already been explained that space vectors are in such a position in x-y plane that x-y components are cancelled. The x-y components due to the additional space vector number 1 are zero. The zero-sequence components are eliminated due to the equal time of application of large and short space vectors, thus leading to sinusoidal output (except for the PWM ripple). The THDs follow the same pattern as in sections 8.2.1 and 8.2.2. The magnitude of THDs is the smallest when compared to the values in sections 8.2.1 and 8.2.2, which is due to clean output voltage waveform.

The analytical expressions for the leg voltages, averaged over one switching cycle, are deduced once more from the switching pattern (Fig. 8.2). For sector 1, one has

$$V_A = \frac{V_{DC}}{2t_s}\left(-t_o/4+t_{sh}/4+t_m/4+t_l/2+t_m/4+t_{sh}/4+t_o/2+t_{sh}/4+t_m/4+t_l/2+t_m/4+t_{sh}/4-t_o/4\right)$$

$$V_B = \frac{V_{DC}}{2t_s}\left(-t_o/4-t_{sh}/4+t_m/4+t_l/2+t_m/4+t_{sh}/4+t_o/2+t_{sh}/4+t_m/4+t_l/2+t_m/4-t_{sh}/4-t_o/4\right)$$

$$V_C = \frac{V_{DC}}{2t_s}\left(-t_o/4-t_{sh}/4-t_m/4-t_l/2+t_m/4+t_{sh}/4+t_o/2+t_{sh}/4+t_m/4-t_l/2-t_m/4-t_{sh}/4-t_o/4\right)$$

$$V_D = \frac{V_{DC}}{2t_s}\left(-t_o/4-t_{sh}/4-t_m/4-t_l/2-t_m/4-t_{sh}/4+t_o/2-t_{sh}/4-t_m/4-t_l/2-t_m/4-t_{sh}/4-t_o/4\right)$$

$$V_E = \frac{V_{DC}}{2t_s}\left(-t_o/4-t_{sh}/4-t_m/4-t_l/2-t_m/4+t_{sh}/4+t_o/2+t_{sh}/4-t_m/4-t_l/2-t_m/4-t_{sh}/4-t_o/4\right)$$

$$V_F = \frac{V_{DC}}{2t_s}\left(-t_o/4-t_{sh}/4-t_m/4+t_l/2+t_m/4+t_{sh}/4+t_o/2+t_{sh}/4+t_m/4+t_l/2-t_m/4-t_{sh}/4-t_o/4\right) \tag{8.13}$$

By substituting the expressions for times of application for different space vectors from (8.3b) and (8.12), the average leg voltages are found and are given in Table 8.6. The expressions for average leg voltages in eleven other sectors are obtained in a similar fashion.

A similar conclusion can be drawn from the analytical expressions for the average leg voltages as that of sections 8.2.1 and 8.2.2. The plot of average leg voltages is shown in Fig. 8.8a. Average leg voltages, obtained using simulation, when small, medium and large vector are used, are shown in Fig. 8.8b. By comparing Fig.8.8a and Fig. 8.8b it can be concluded that the two are identical and thus expressions of Table 8.6 are validated.

Table 8.6. Analytical expressions for average leg voltages when short, medium and large vectors are used.

Sector I	Sector II	Sector III
$V_A=\frac{V_{DC}}{2}\left[\frac{v_\alpha^*(4v_{m\beta}-3v_{l\beta})+v_\beta^*(3v_{l\alpha}-4v_{m\alpha})}{3(v_{l\alpha}v_{m\beta}-v_{l\beta}v_{m\alpha})}\right]$ $V_B=\frac{V_{DC}}{2}\left[\frac{v_\alpha^*(2v_{m\beta}-3v_{l\beta})+v_\beta^*(3v_{l\alpha}-2v_{m\alpha})}{3(v_{l\alpha}v_{m\beta}-v_{l\beta}v_{m\alpha})}\right]$ $V_C=-\frac{V_{DC}}{2}\left[\frac{2}{3}\frac{v_\alpha^*v_{m\beta}-v_\beta^*v_{m\alpha}}{v_{l\alpha}v_{m\beta}-v_{l\beta}v_{m\alpha}}\right]$ $V_D=-\frac{V_{DC}}{2}\left[\frac{v_\alpha^*(4v_{m\beta}-3v_{l\beta})+v_\beta^*(3v_{l\alpha}-4v_{m\alpha})}{3(v_{l\alpha}v_{m\beta}-v_{l\beta}v_{m\alpha})}\right]$ $V_E=-\frac{V_{DC}}{2}\left[\frac{v_\alpha^*(2v_{m\beta}-3v_{l\beta})+v_\beta^*(3v_{l\alpha}-2v_{m\alpha})}{3(v_{l\alpha}v_{m\beta}-v_{l\beta}v_{m\alpha})}\right]$ $V_F=\frac{V_{DC}}{2}\left[\frac{2}{3}\frac{v_\alpha^*v_{m\beta}-v_\beta^*v_{m\alpha}}{v_{l\alpha}v_{m\beta}-v_{l\beta}v_{m\alpha}}\right]$	$V_A=\frac{V_{DC}}{2}\left[\frac{v_\alpha^*(2v_{m\beta}-3v_{l\beta})+v_\beta^*(3v_{l\alpha}-2v_{m\alpha})}{3(v_{l\alpha}v_{m\beta}-v_{l\beta}v_{m\alpha})}\right]$ $V_B=\frac{V_{DC}}{2}\left[\frac{v_\alpha^*(4v_{m\beta}-3v_{l\beta})+v_\beta^*(3v_{l\alpha}-4v_{m\alpha})}{3(v_{l\alpha}v_{m\beta}-v_{l\beta}v_{m\alpha})}\right]$ $V_C=\frac{V_{DC}}{2}\left[\frac{2}{3}\frac{v_\alpha^*v_{m\beta}-v_\beta^*v_{m\alpha}}{v_{l\alpha}v_{m\beta}-v_{l\beta}v_{m\alpha}}\right]$ $V_D=-\frac{V_{DC}}{2}\left[\frac{v_\alpha^*(2v_{m\beta}-3v_{l\beta})+v_\beta^*(3v_{l\alpha}-2v_{m\alpha})}{3(v_{l\alpha}v_{m\beta}-v_{l\beta}v_{m\alpha})}\right]$ $V_E=-\frac{V_{DC}}{2}\left[\frac{v_\alpha^*(4v_{m\beta}-3v_{l\beta})+v_\beta^*(3v_{l\alpha}-4v_{m\alpha})}{3(v_{l\alpha}v_{m\beta}-v_{l\beta}v_{m\alpha})}\right]$ $V_F=-\frac{V_{DC}}{2}\left[\frac{2}{3}\frac{v_\alpha^*v_{m\beta}-v_\beta^*v_{m\alpha}}{v_{l\alpha}v_{m\beta}-v_{l\beta}v_{m\alpha}}\right]$	$V_A=\frac{V_{DC}}{2}\left[\frac{2}{3}\frac{v_\alpha^*v_{m\beta}-v_\beta^*v_{m\alpha}}{v_{l\alpha}v_{m\beta}-v_{l\beta}v_{m\alpha}}\right]$ $V_B=\frac{V_{DC}}{2}\left[\frac{v_\alpha^*(4v_{m\beta}-3v_{l\beta})+v_\beta^*(3v_{l\alpha}-4v_{m\alpha})}{3(v_{l\alpha}v_{m\beta}-v_{l\beta}v_{m\alpha})}\right]$ $V_C=\frac{V_{DC}}{2}\left[\frac{v_\alpha^*(2v_{m\beta}-3v_{l\beta})+v_\beta^*(3v_{l\alpha}-2v_{m\alpha})}{3(v_{l\alpha}v_{m\beta}-v_{l\beta}v_{m\alpha})}\right]$ $V_D=-\frac{V_{DC}}{2}\left[\frac{2}{3}\frac{v_\alpha^*v_{m\beta}-v_\beta^*v_{m\alpha}}{v_{l\alpha}v_{m\beta}-v_{l\beta}v_{m\alpha}}\right]$ $V_E=-\frac{V_{DC}}{2}\left[\frac{v_\alpha^*(4v_{m\beta}-3v_{l\beta})+v_\beta^*(3v_{l\alpha}-4v_{m\alpha})}{3(v_{l\alpha}v_{m\beta}-v_{l\beta}v_{m\alpha})}\right]$ $V_F=-\frac{V_{DC}}{2}\left[\frac{v_\alpha^*(2v_{m\beta}-3v_{l\beta})+v_\beta^*(3v_{l\alpha}-2v_{m\alpha})}{3(v_{l\alpha}v_{m\beta}-v_{l\beta}v_{m\alpha})}\right]$
Sector IV	**Sector V**	**Sector VI**
$V_A=-\frac{V_{DC}}{2}\left[\frac{2}{3}\frac{v_\alpha^*v_{m\beta}-v_\beta^*v_{m\alpha}}{v_{l\alpha}v_{m\beta}-v_{l\beta}v_{m\alpha}}\right]$ $V_B=\frac{V_{DC}}{2}\left[\frac{v_\alpha^*(2v_{m\beta}-3v_{l\beta})+v_\beta^*(3v_{l\alpha}-2v_{m\alpha})}{3(v_{l\alpha}v_{m\beta}-v_{l\beta}v_{m\alpha})}\right]$ $V_C=-\frac{V_{DC}}{2}\left[\frac{v_\alpha^*(4v_{m\beta}-3v_{l\beta})+v_\beta^*(3v_{l\alpha}-4v_{m\alpha})}{3(v_{l\alpha}v_{m\beta}-v_{l\beta}v_{m\alpha})}\right]$ $V_D=\frac{V_{DC}}{2}\left[\frac{2}{3}\frac{v_\alpha^*v_{m\beta}-v_\beta^*v_{m\alpha}}{v_{l\alpha}v_{m\beta}-v_{l\beta}v_{m\alpha}}\right]$ $V_E=-\frac{V_{DC}}{2}\left[\frac{v_\alpha^*(2v_{m\beta}-3v_{l\beta})+v_\beta^*(3v_{l\alpha}-2v_{m\alpha})}{3(v_{l\alpha}v_{m\beta}-v_{l\beta}v_{m\alpha})}\right]$ $V_F=-\frac{V_{DC}}{2}\left[\frac{v_\alpha^*(4v_{m\beta}-3v_{l\beta})+v_\beta^*(3v_{l\alpha}-4v_{m\alpha})}{3(v_{l\alpha}v_{m\beta}-v_{l\beta}v_{m\alpha})}\right]$	$V_A=-\frac{V_{DC}}{2}\left[\frac{v_\alpha^*(2v_{m\beta}-3v_{l\beta})+v_\beta^*(3v_{l\alpha}-2v_{m\alpha})}{3(v_{l\alpha}v_{m\beta}-v_{l\beta}v_{m\alpha})}\right]$ $V_B=\frac{V_{DC}}{2}\left[\frac{2}{3}\frac{v_\alpha^*v_{m\beta}-v_\beta^*v_{m\alpha}}{v_{l\alpha}v_{m\beta}-v_{l\beta}v_{m\alpha}}\right]$ $V_C=\frac{V_{DC}}{2}\left[\frac{v_\alpha^*(4v_{m\beta}-3v_{l\beta})+v_\beta^*(3v_{l\alpha}-4v_{m\alpha})}{3(v_{l\alpha}v_{m\beta}-v_{l\beta}v_{m\alpha})}\right]$ $V_D=\frac{V_{DC}}{2}\left[\frac{v_\alpha^*(2v_{m\beta}-3v_{l\beta})+v_\beta^*(3v_{l\alpha}-2v_{m\alpha})}{3(v_{l\alpha}v_{m\beta}-v_{l\beta}v_{m\alpha})}\right]$ $V_E=-\frac{V_{DC}}{2}\left[\frac{2}{3}\frac{v_\alpha^*v_{m\beta}-v_\beta^*v_{m\alpha}}{v_{l\alpha}v_{m\beta}-v_{l\beta}v_{m\alpha}}\right]$ $V_F=-\frac{V_{DC}}{2}\left[\frac{v_\alpha^*(4v_{m\beta}-3v_{l\beta})+v_\beta^*(3v_{l\alpha}-4v_{m\alpha})}{3(v_{l\alpha}v_{m\beta}-v_{l\beta}v_{m\alpha})}\right]$	$V_A=-\frac{V_{DC}}{2}\left[\frac{v_\alpha^*(4v_{m\beta}-3v_{l\beta})+v_\beta^*(3v_{l\alpha}-4v_{m\alpha})}{3(v_{l\alpha}v_{m\beta}-v_{l\beta}v_{m\alpha})}\right]$ $V_B=-\frac{V_{DC}}{2}\left[\frac{2}{3}\frac{v_\alpha^*v_{m\beta}-v_\beta^*v_{m\alpha}}{v_{l\alpha}v_{m\beta}-v_{l\beta}v_{m\alpha}}\right]$ $V_C=\frac{V_{DC}}{2}\left[\frac{v_\alpha^*(2v_{m\beta}-3v_{l\beta})+v_\beta^*(3v_{l\alpha}-2v_{m\alpha})}{3(v_{l\alpha}v_{m\beta}-v_{l\beta}v_{m\alpha})}\right]$ $V_D=\frac{V_{DC}}{2}\left[\frac{v_\alpha^*(4v_{m\beta}-3v_{l\beta})+v_\beta^*(3v_{l\alpha}-4v_{m\alpha})}{3(v_{l\alpha}v_{m\beta}-v_{l\beta}v_{m\alpha})}\right]$ $V_E=\frac{V_{DC}}{2}\left[\frac{2}{3}\frac{v_\alpha^*v_{m\beta}-v_\beta^*v_{m\alpha}}{v_{l\alpha}v_{m\beta}-v_{l\beta}v_{m\alpha}}\right]$ $V_F=-\frac{V_{DC}}{2}\left[\frac{v_\alpha^*(2v_{m\beta}-3v_{l\beta})+v_\beta^*(3v_{l\alpha}-2v_{m\alpha})}{3(v_{l\alpha}v_{m\beta}-v_{l\beta}v_{m\alpha})}\right]$

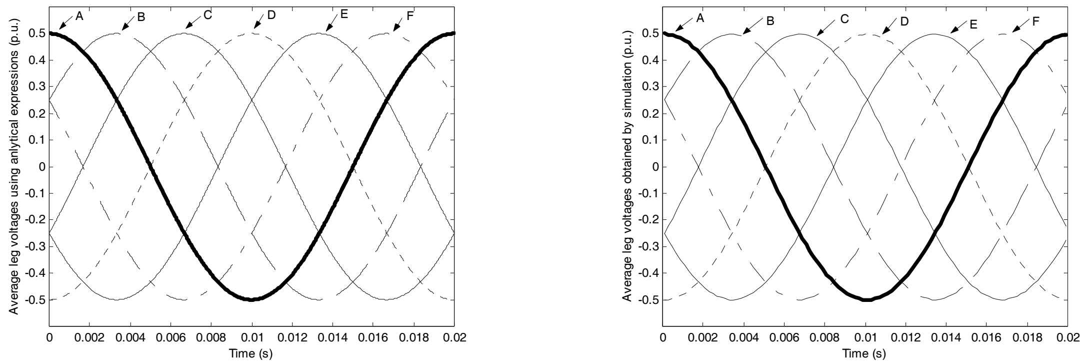

a. b.

Fig. 8.8. Average leg voltages (short and medium space vectors applied) obtained: a. using analytical expressions of Table 8.6, b. using simulation.

8.2.4 Application of large, medium and short space vectors (six vector values per switching period, variable time of application of short and large vectors)

The scheme developed in this section is a novel technique for extending the range of operation of the existing SVPWM method discussed in section 8.2.3. This method is devised to be operational for input reference ranging from $1/2V_{DC} \le \left|\underline{v}_s^*\right| \le 1/\sqrt{3}V_{DC}$. The motive behind this is to develop a method, which may be used for the input reference above $1/2V_{DC}$ (above which SVPWM of section 8.2.3 is not operational) to obtain output close to sinusoidal. It is very much obvious from section 7.2.1 that, to extract the maximum possible output voltage from the inverter one ultimately has to revert to the use of only the largest vectors. In other words, one has to reduce the time of application of the short vectors linearly until they are dropped completely for the maximum possible input reference. Thus the principle of this method is to reduce the time of application of short vectors with increasing input reference until the application time reaches zero for input reference equal to the maximum possible. The idea is more clearly seen from Fig. 8.9, which depicts the variation of the control variable ρ for the input reference voltage between $1/2V_{DC} \le \left|\underline{v}_s^*\right| \le 1/\sqrt{3}V_{DC}$. The control variable ρ is linearly increased from 2/3 at $\left|\underline{v}_s^*\right| = 1/2V_{DC}$ to one at $\left|\underline{v}_s^*\right| = 1/\sqrt{3}V_{DC}$ so that the time of application of short vectors becomes zero at this point. The expression of ρ is obtained from Fig. 8.9 as,

$$\rho = -\frac{2}{3-2\sqrt{3}}\left|\underline{v}_s^*\right| + \frac{3\sqrt{3}-4}{3\sqrt{3}-6} \qquad (8.14)$$

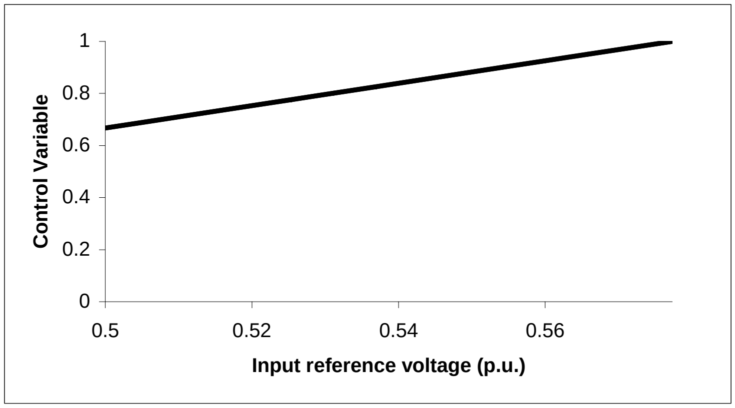

Fig. 8.9. The variation of control variable with input reference voltage.

Thus this scheme is based on the utilisation of one large, two medium, two short and two zero space vectors with variable time of application of the large and short space vectors. The times of application of large and short space vectors are given with (8.5a) and (8.5b), respectively but the control variable is now given with (8.14). The times of application of the medium and zero space vectors are still given with (8.3b) and (8.3d), respectively.

A simulation is done again for different peak values of the six-phase sinusoidal reference input, ranging from 86.602% to 100% of the maximum achievable, with two intermediate input reference values of 95% and 90%. The resulting filtered phase voltages, filtered leg voltages and harmonic spectrum of phase 'a' voltage are shown in Figs. 8.10a-b for 95% and 90% of the maximum achievable. The simulation results at 86.602% and 100% of the maximum achievable are identical to those of Fig. 8.7 and Fig. 8.3, respectively, and are thus not shown. The RMS values of the fundamental output voltage and low-order harmonic components, obtained using FFT, are listed in Table 8.7.

Table 8.7. RMS of fundamental and low-order harmonic components, and THDs of output phase voltages.

$\left\lvert \underline{v}_s^* \right\rvert$ (p.u.)	Fundamental (50 Hz) Simulation RMS value (p.u.)	3rd harmonic (150 Hz, p.u.)	THD1 (up to 4 kHz, p.u.)	THD2 (up to 25 kHz, p.u.)
$1/\sqrt{3}$ (Max)	0.408	0.081 (19.9%)	0.2158	0.4168
95% of Max	0.388	0.055 (14.3%)	0.1724	0.381
90% of Max	0.367	0.023 (6.26%)	0.1205	0.4259
86.602% of Max	0.353	0	0.1113	0.4549

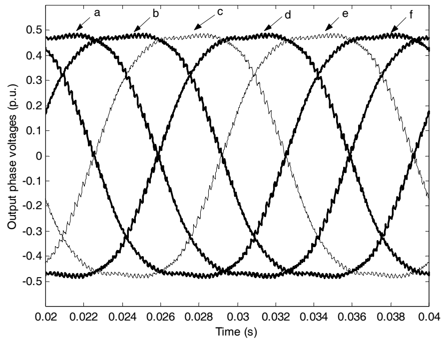

a.

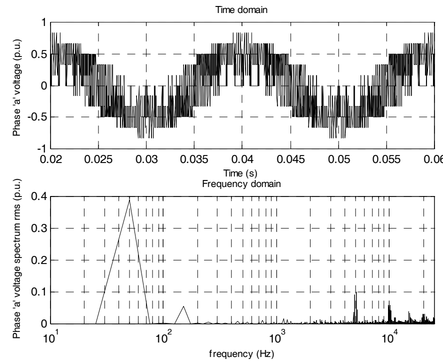

c.

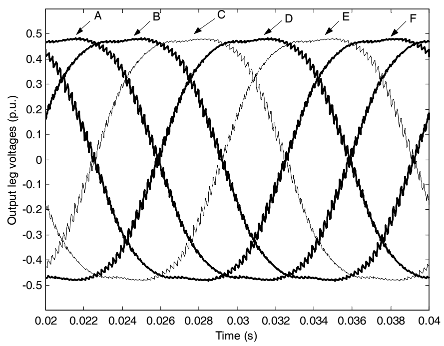

b.

Fig. 8.10a. Output of VSI for input reference equal to 95% of the maximum achievable ($1/\sqrt{3}$ p.u.): a. phase voltages, b. leg voltages, c. phase ‘a’ voltage and its harmonic spectrum.

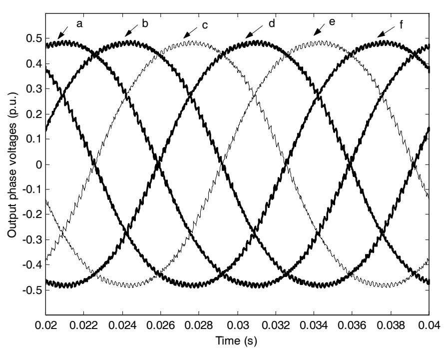

a.

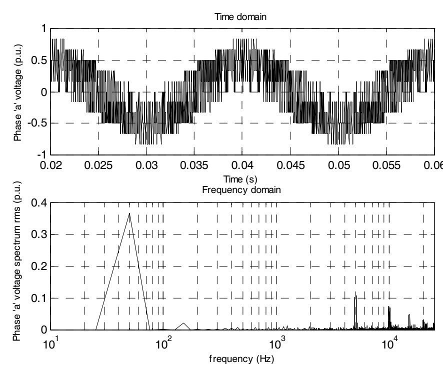

c.

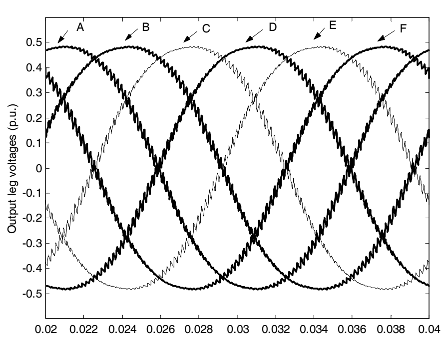

b.

Fig. 8.10b. Output of VSI for input reference equal to 90% of the maximum achievable ($1/\sqrt{3}$ p.u.): a. phase voltages, b. leg voltages, c. phase ‘a’ voltage and its harmonic spectrum.

It is seen from Table 8.7 that, with the increase in the input reference above 86.602% of the maximum achievable, the 3rd harmonic component is introduced in the output voltage waveforms and it increases further with the increase in the input reference magnitude. As the reference increases the control variable increases leading to increase in the time of application of the large vectors and a simultaneous decrease in the time of application of the short vectors. This results in the introduction of the zero-sequence component due to the large vector, leading to the 3rd harmonic component (and the 9th etc) in the phase voltages.

8.3 COMPARISON OF SVPWM SCHEMES

This section presents a detailed comparison of different schemes analysed in the sections 8.2.1-8.2.4. The same comparison criteria are chosen as in section 7.2.3.5. The four methods discussed are applicable to different ranges of input reference voltage. To have a quick comparison of the range of operation, Fig. 8.11 shows the circular locus of maximum achievable output phase voltages from VSI utilising different space vector modulation schemes.

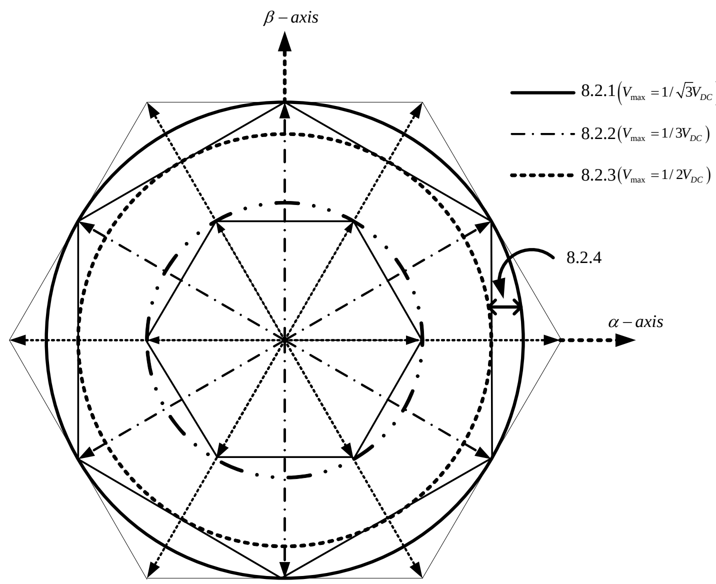

Fig. 8.11. Circular locus, corresponding to the largest radii (i.e. reference voltages) achievable with different types of SVPWM.

Fig. 8.11 clearly shows that the scheme of section 8.2.1 can be used for the largest range while scheme of 8.2.4 can be used for the smallest range of the input voltage reference. It is worth emphasising here that the range of operation of a space vector modulator depends mainly upon the length of the space vectors used in the synthesis. The larger the length, the larger will be the range. The same conclusion has also been drawn in section 7.2.3.5 in conjunction with the five-phase SVPWM. Once again it has been proved that, to obtain maximum possible output from VSI using SVPWM, one has to revert to the maximum available length vectors only.

Figs. 8.12a-c compare the performance of different space vector modulators. These curves are the best fits of discrete results given in previous sections. Fig. 8.12a depicts the percentage of the 3rd harmonic component in the phase voltages with respect to the input reference voltage. It is observed that the 3rd harmonic in the phase voltages from VSI with space vector modulation of sections 8.2.1 and 8.2.2 is substantial and is more or less constant. Further, the 3rd harmonic with the space vector modulation of section 8.2.2 is twice that of scheme of section 8.2.1. The reason for this has already been explained in section 8.2.2. The method developed in section 8.2.4 produces a variable 3rd harmonic content, with the highest amount when the voltage reference equals the maximum achievable voltage. The output from the VSI with the space vector modulation of section 8.2.3 is free from the 3rd harmonic, but this method is applicable only up to 86.602% of the maximum achievable output. However, for sinusoidal phase voltage, this scheme can be utilised. Operating region can be extended up to the maximum achievable output by using the SVPWM of section 8.2.4, where the 3rd harmonic re-appears, for references above 86.602%

Figs. 8.12b-c show the plots of total harmonic distortions in output phase voltages. It is evident from Figs. 8.12b-c that the THD increases with the reduction in the input reference voltage. This is because the lengths of the space vectors used for synthesis become very large, compared to the length of the reference. The THD in Fig. 8.12b is seen to be the smallest for the space vector modulation of section 8.2.3 and is the largest for the space vector modulation of section 8.2.2. This is expected since the space vector modulation of section 8.2.2 produces a significant amount of triplen harmonic components. THDs in Fig. 8.12c, showing the combined effect of low-order and switching harmonics, follow the same trend as in Fig.8.12b.

Based on the above observations it can be concluded that none of the methods can be used for the complete range of the input reference while giving near sinusoidal output and thus a combined scheme may be utilised. This is similar to the space vector PWM for a five-phase VSI (Chapter 7). For input references up to 86.602% of the maximum, method given in section 8.2.3 can be used and for input references above this value the scheme of 8.2.4 may be utilised effectively.

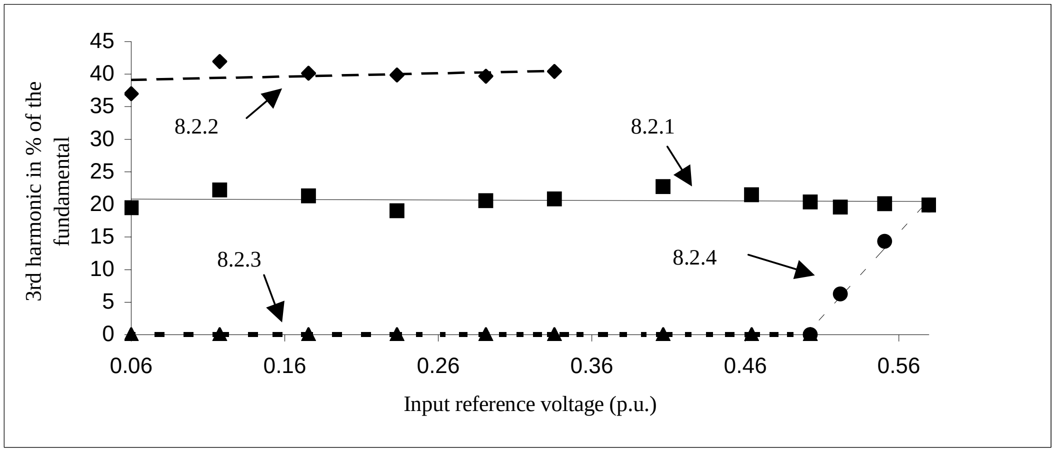

a.

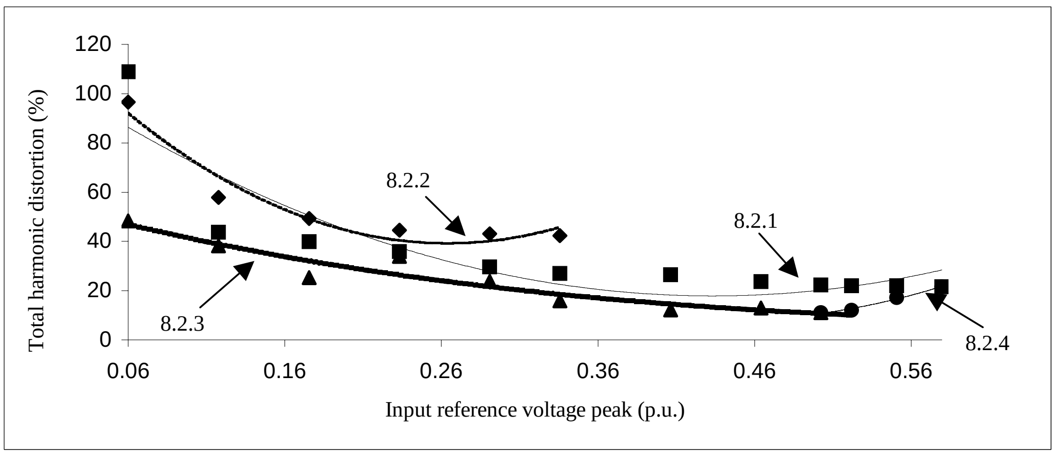

b.

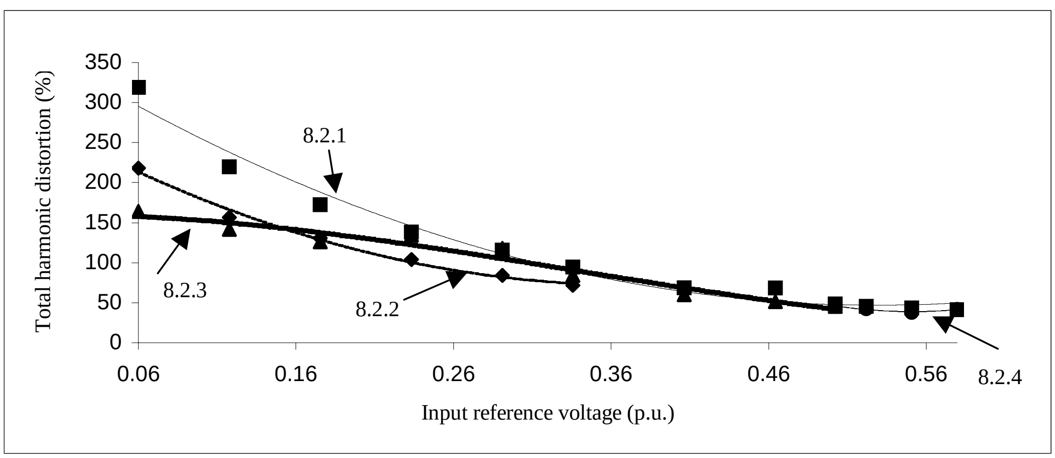

c.

Fig. 8.12. Performance of different space vector modulators from section 8.2.1-8.2.4: a. 3rd harmonic content in the output voltages, b. THD caused by low-order harmonics, c. THD caused by low-order and switching harmonics.

8.4 SPACE VECTOR MODULATION SCHEME FOR A SERIES-CONNECTED TWO-MOTOR DRIVE

This section develops a space vector PWM technique for a six-phase VSI used to feed a six-phase and a three-phase machine connected in series with phase transposition, in order to provide decoupled control of the machines. The control of this two-motor drive configuration fed from a single six-phase inverter, using hysteresis and ramp-comparison current control schemes in stationary reference frame, has been explored in chapter 6. The aim of this section is to develop an appropriate SVPWM scheme for a six-phase VSI which is applicable in conjunction with current control in the rotating reference frame.

The principle of control decoupling of a six-phase and a three-phase machine connected in series lies in the fact that the $\alpha-\beta$ voltage/current components of the six-phase VSI control the six-phase machine and the x-y voltage/current components of the six-phase VSI control the three-phase machine. The x-y voltage/current components of the six-phase VSI appear as $\alpha-\beta$ components for the three-phase machine. Thus the inverter feeding two-motor drive configuration needs to provide six-phase supply for the six-phase machine and three-phase supply for the three-phase machine. The requirement on the space vector modulator is to keep the average volt-seconds of $\alpha-\beta$ and x-y reference voltage space vectors such as to satisfy the flux/torque control requirements of the two machines. The approach towards realising this requirement, adopted here, is the simplest possible and is similar to the one discussed and applied in section 7.3. The effective rate of application of the two references ($\alpha-\beta$ and x-y) is halved similar to section 7.3 and the references are applied in an alternating manner.

Hence, the switching scheme used in the SVPWM is such that the six-phase inverter generates $\alpha-\beta$ axis voltages in the first cycle of the PWM, while simultaneously eliminating the x-y axis components, to control the first machine (six-phase). In the second cycle it generates x-y axis voltages and simultaneously eliminates the $\alpha-\beta$ axis voltages to control the second machine (three-phase). In essence, there are therefore two space vector modulators, $\alpha-\beta$ and x-y modulator. The $\alpha-\beta$ modulator imposes $\alpha-\beta$ axis voltage in the first cycle and the x-y modulator imposes the x-y axis voltage in the next cycle. The $\alpha-\beta$ modulator is identical to the one discussed in section 8.2.3. The x-y modulator is developed in this section.

The requirement of x-y reference modulation is to produce a three-phase supply with only x-y voltage/current components. Thus the space vectors chosen here are such as to generate two identical sets of three-phase voltages. The space vectors chosen comprise six large length vector set, numbered 41, 42, 43, 56, 57 and 58, from the x-y plane. These space vectors in corresponding $\alpha-\beta$ plane are null vectors thus ensuring zero $\alpha-\beta$ voltage components. The times of application of two neighbouring active vectors, shown in Fig. 8.13, are determined using the equal volt-seconds principle as

$$t_{al} = \frac{v_\alpha^* v_{bl\beta} - v_\beta^* v_{bl\alpha}}{v_{al\alpha} v_{bl\beta} - v_{al\beta} v_{bl\alpha}} t_s \tag{8.15}$$

$$t_{bl} = \frac{v_\beta^* v_{al\alpha} - v_\alpha^* v_{al\beta}}{v_{al\alpha} v_{bl\beta} - v_{al\beta} v_{bl\alpha}} t_s \tag{8.16}$$

The time of application of zero space vectors is given as

$$t_o = t_s - t_{al} - t_{bl} \tag{8.17}$$

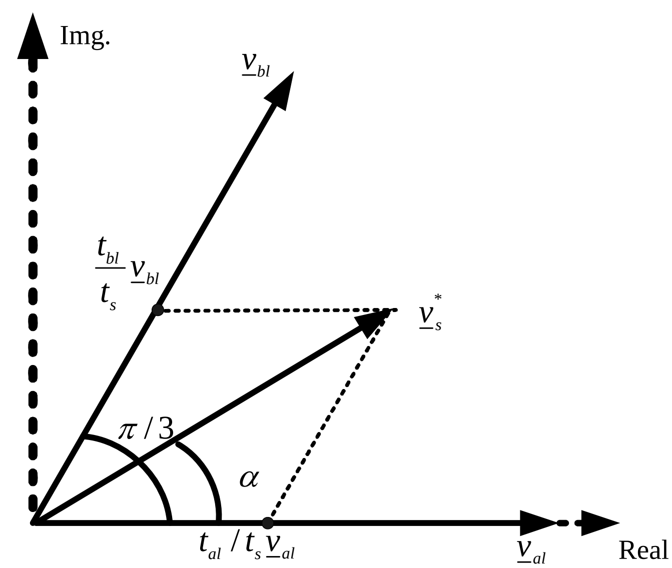

Fig. 8.13. Principle of space vector time calculation for x-y modulator for a six-phase VSI.

The maximum achievable output phase voltage from VSI with this modulator is $1/\sqrt{3}V_{DC}$ (peak). The switching pattern and the space vector sequence for six sectors are shown in Fig. 8.14.

The simulation is done to evaluate the performance of the proposed space vector modulation. The simulation conditions of both $\alpha-\beta$ modulator and x-y modulator are kept identical. As the inverter has to feed two machines connected in series, the dc link voltage is again arbitrarily set to 2 per unit and the switching frequency of both modulators is kept at 5 kHz. The output phase voltage from VSI for the six-phase machine is limited to

$0.5V_{DC}$ (peak) or $0.353V_{DC}$ (RMS), as seen in section 8.2.3, while the maximum value for the three-phase machine is $1/\sqrt{3}V_{DC}$. Since $\alpha-\beta$ modulator imposes $\alpha-\beta$ axis voltages in the first cycle of the PWM and the x-y modulator produces x-y axis voltage in the second cycle, the effective frequency of the reference application becomes 2.5 kHz. The frequencies of the input references are once more 50 Hz and 25 Hz for the $\alpha-\beta$ modulator and the x-y modulator, respectively, and the magnitudes are 0.5 (p.u.) peak or 0.353 (p.u.) RMS (which is for the three-phase modulation less than the maximum achievable value). An analog first order filter is used to filter the high frequency components from the output voltage waveforms. The filtered output phase voltages, leg voltages and harmonic spectra are shown in Fig. 8.15.

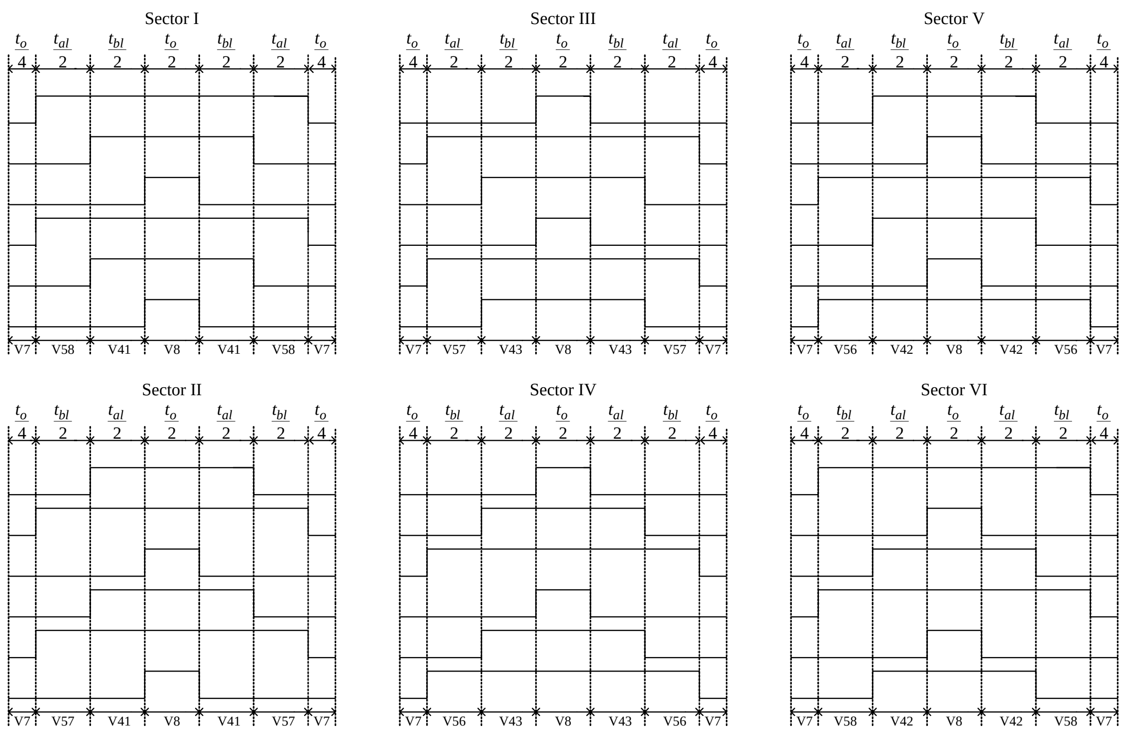

Fig. 8.14. Switching pattern and space vector disposition for one cycle of operation of x-y modulator.

It is observed from the inverter phase ‘a’ voltage spectrum that it contains two fundamental frequency components, corresponding to 50 Hz and 25 Hz. The switching harmonics are appearing around multiples of 2.5 kHz, as expected. The fundamental voltage component of 50 Hz controls the first machine (six-phase) and the 25 Hz voltage fundamental component controls the second machine (three-phase). The 50 Hz fundamental is thus seen in the α -axis

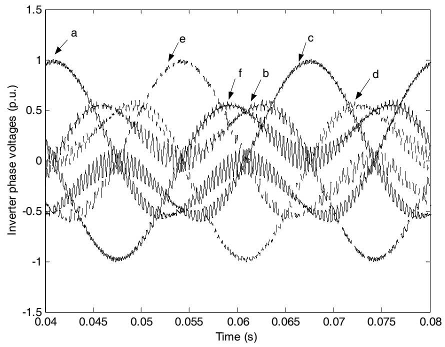

a.

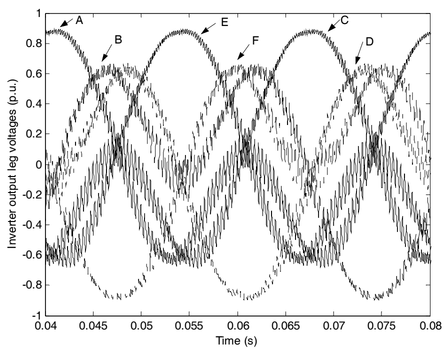

b.

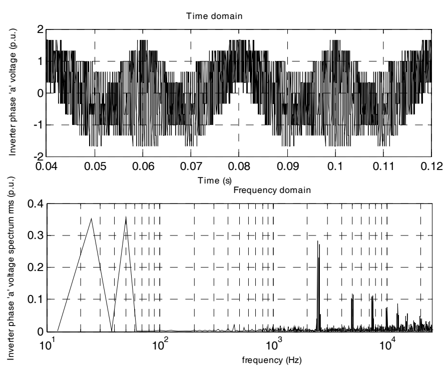

c.

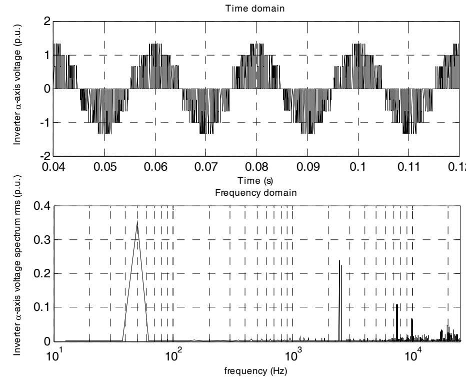

d.

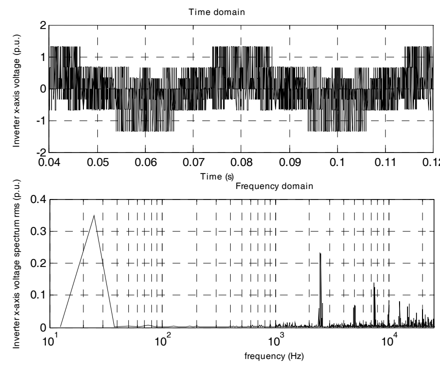

e.

Fig. 8.15. Output from VSI for input reference voltage of 0.5 p.u. peak: a. output phase voltages, b. output leg voltages, c. inverter phase 'a' voltage and its harmonic spectrum, d. inverter output α -axis voltage and its harmonic spectrum, e. inverter output x-axis voltage and its harmonic spectrum.

voltage harmonic spectrum, while 25 Hz fundamental appears in the x-axis harmonic spectrum. It is further to be noted that the output phase voltages do not contain any undesirable low-order harmonic components.

8.5 SUMMARY

This chapter is devoted to the space vector modulation techniques for a six-phase VSI. The original idea is taken from Correa et al (2003a) and (2003b). The SVPWM analysed in this chapter is based on the powerfull technique of space vector decomposition. The original six-dimensional space vectors of six-phase VSI are transformed into three two-dimensional orthogonal planes, namely $\alpha-\beta$, x-y and 0+-0- using transformation matrix. Based on the space vector dispositions, a method of using only medium and large space vectors is firstly investigated. This method is shown to generate a significant amount of the 3rd harmonic component but it is operational for the complete range of the input reference. Another approach based on using space vectors from medium and short sets is investigated next. This method produces the worst results since the magnitude of the 3rd harmonic is doubled and the range of operation is the smallest. Another method is then analysed which has been reported in Correa et al (2003a) and Correa et al (2003b) and is based on the use of space vectors from the large, medium and short vector sets to generate sinusoidal phase voltages. This yields clean phase voltages but is operational only up to 86.602% of the maximum achievable output. The fourth SVPWM technique extends the operating region for input reference from 86.602% up to 100% of the maximum achievable at the cost of re-introduction of triplen harmonics. A comprehensive comparison of different space vector modulators is also given in this chapter and finally a combined scheme is suggested to cover the entire range of the input reference variation.

Finally, a SVPWM scheme, suitable for application in conjunction with series-connected six-phase two-motor drive, is proposed. It combines two SVPWM modulators, which are used in a sequential manner to generate $\alpha-\beta$ (six-phase voltages) and x-y (two identical three-phase voltage sets) inverter voltage references. Generation of any unwanted low order harmonics is avoided in this way, so that the output inverter voltages contain only two fundamental components at two required frequencies (plus, of course high frequency harmonics related to the switching frequency). The proposed SVPWM scheme for a series-connected two-motor drive is applicable in conjunction with current control in the rotating reference frame.

Chapter 9

EXPERIMENTAL INVESTIGATION

9.1 INTRODUCTION

This chapter is devoted to the experimental proof of decoupled dynamic control of two five-phase series-connected machines, supplied from one five-phase VSI and controlled using indirect rotor flux oriented control scheme. The chapter at first describes the experimental rig. This is followed by detailed presentation of experimental results. The variable frequency supply for five-phase machine drive is obtained from two commercially available three-phase inverters, which are configured as a five-phase current controlled VSI. This is a part of the four three-phase inverter assembly capable of supplying three- to twelve-phase configurations. It can control up to five series-connected multi-phase machines, provided that at least one of the machines operates in sensor-less speed mode, or up to four machines in full sensored mode.

The dynamic performance of a single five-phase induction machine and a single five-phase synchronous reluctance machine under indirect vector control condition is investigated first. Acceleration, deceleration and reversing transients are studied for a wide range of speeds. The induction motor drive behaviour for step loading and unloading is also examined.

The second stage of experimental testing is related to five-phase series-connected two-motor drive configurations. Two five-phase series-connected induction machines are tested first for the same acceleration, deceleration and reversing transients. The performance for step loading and unloading is also investigated. One of the induction machines is held at constant speed while transients are initiated for the other induction machine. This enables a direct comparison of single-motor and two-motor drive behaviour.

Next, two different types of five-phase machines (an induction and a synchronous reluctance) are connected in series and supplied from one five-phase VSI to prove the control decoupling among these machines. The transients investigated are once more acceleration, deceleration, reversing and loading/unloading. The induction machine is allowed to run at a constant speed and transients of the synchronous reluctance machine are recorded, and vice-versa.

Finally, steady state current and voltage measurement results are reported for single-motor and two-motor drive systems. Some of the results presented in this chapter can be found in Iqbal et al (2005).

9.2 DESCRIPTION OF THE EXPERIMENTAL RIG

A multi-phase inverter, multi-phase motors and a drive control system constitute the main components of the experimental rig used in this work. The five-phase VSI is constructed using two three-phase commercially available industrial, MOOG DS2000, drives as shown schematically in Fig. 9.1. Each drive is rated at 14/42 A/A (continuous RMS/transient peak). The two drives are part of the twelve-phase rig, constructed by using four three-phase inverters and shown in Fig. 9.2 [Jones (2005)]. The right-hand half of the complete power electronic system of Fig. 9.2 is used in the work presented in this chapter. The three-phase drives are powered from the common three-phase mains 415 V, 50 Hz supply. Each drive comprises a 6-pack IGBT bridge (three-phase inverter), dynamic brake and a three-phase uncontrolled bridge rectifier with the dc link circuit. The power connections of the dc-bus ('+AT' for the positive rail and '-AT' for negative rail) are connected so that the dc links of the inverters are in parallel. This results in an inverter with a total of 12 IGBT power switches and six output phases. However, in this work only five out of the total of six phases are utilised and hence one of the phases is kept floating. The first (left-hand side) three-phase inverter supplies phases A, C and E, while the second inverter (right most) supplies phases B and D. Each DS2000 drive has an internal dynamic braking circuit with IGBT and associated control, along with an external braking resistor, which allows the excessive dc voltage to be suppressed during the braking period. The power circuit topology of the five-phase inverter is shown in Fig. 9.3.

The purpose of the five-phase inverter is to control the phase currents and it behaves as a current source. The current controlled VSI operates at 10 kHz switching frequency. Each of the five-phase inverter phases has a Hall-effect current sensor (LEM) for measuring the output phase current. For this purpose, an additional LEM sensor has been added to one of the DS2000 (the first one, which is supplying three phases) since a standard DS2000 drive is aimed for a three-phase servomotor drive and is therefore equipped with only two current sensors. Hence all the five-phase currents are measured and made controllable. The measured inverter currents are sampled in such a way as to filter out the PWM current ripple. A total of 2^n equidistant samples of the current are taken and averaged in each switching period. Current signals, which are now ripple-free, are further used for current control. Each DS2000 has its own DSP (Texas instruments TMS320F240). The purpose of the DSP is to read the analogue signals representing the current references, to read the current feedback from LEM sensors, to perform the function of digital phase current control and to produce necessary PWM pattern. Additionally, the DSP does the auxiliary functions such as the conditioning of the encoder pulses, communication, parameter settings, offset calibration etc. The DSP performs current control in the stationary reference frame using digital form of the ramp-comparison PWM, with the PI current controller in the most basic form. The structure of the current controller is shown in Fig. 9.4. If the current control is performed in the manner shown in Fig. 9.4, the phase current error cannot be driven to zero [Jones (2005)]. The main control code, which performs indirect rotor flux oriented vector control, closed loop speed control and current mixing algorithm, is written in C programming language and runs on a PC under DOS platform. It is necessary to provide the C-code with the motor shaft positions and measured phase current values for subsequent post-processing of results. C-code sends the current references to the DS2000 drives in analogue form. For this purpose a dedicated interface board, plugged into the LPT1 port, is used to interface the PC with the drives. The board is based on Xilinx Spartan-family FPGA (field programmable gate array) device

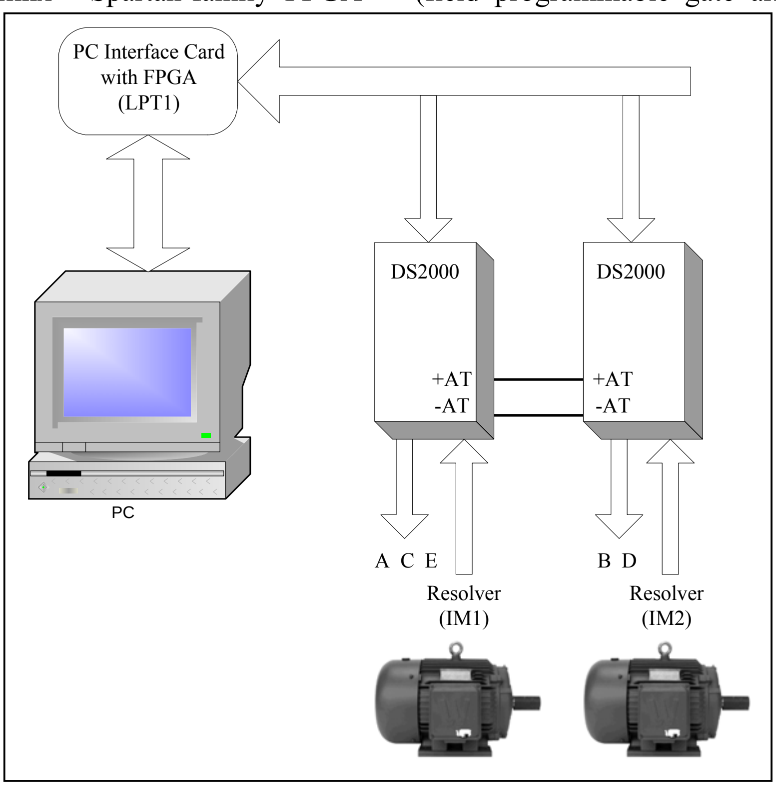

Fig. 9.1. Block schematic of the five-phase experimental rig.

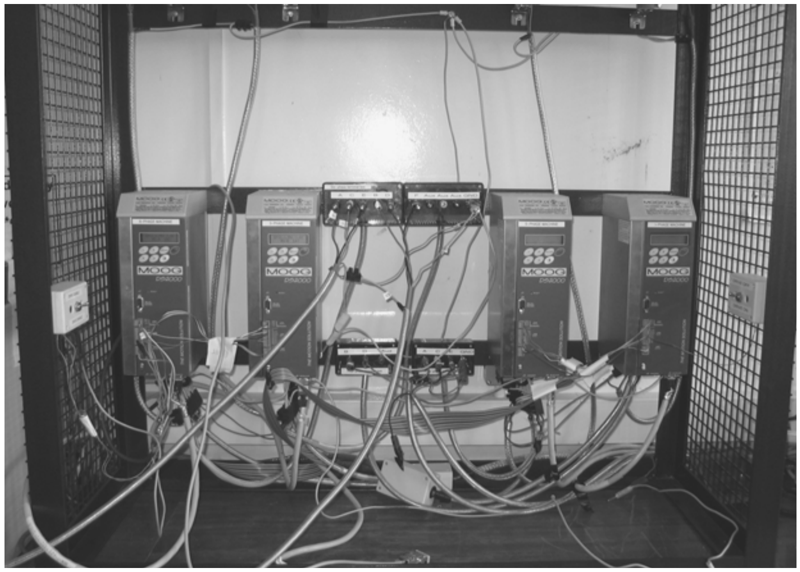

Fig. 9.2. Experimental 12-phase rig, capable of driving up to four series-connected motors in sensored mode (up to five, if at least one motor operates in speed sensorless mode).

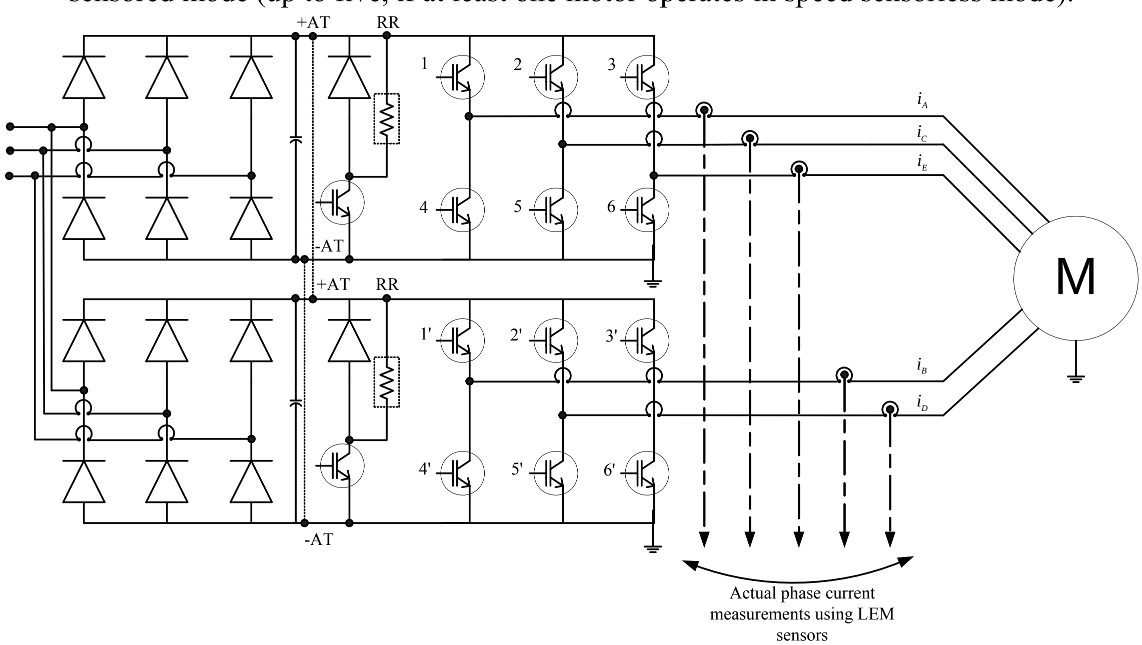

Fig. 9.3. Power circuit topology for a five-phase motor drive.

and is programmed using VHDL (very high speed integrated circuit hardware description language) in the Xilinx foundation 3.1 design tool. The LPT1 board has three MAX525 ICs, each of them being a quadruple 12-bit D/A converter connected to the FPGA over a bus, and MAX1202 A/D converter with 8 channels of 12-bit resolution. The A/D converter also communicates to the FPGA chip through the same bus. In addition the LPT1 board has IC 65LBC173 that serves as an interface between FPGA and encoder pulses. The board communicates with the PC through the parallel port and over a flat cable with DS2000. The

LPT1 board delivers to the C-code the shaft positions values, and the C-code sends to the drives the current references in an analogue form, over D/A converters. Measured phase currents are passed to the PC as well, for storage purposes. The LPT1 board generates an interrupt every 220μs for the PC. Within the interrupt, the communication routine is activated and all the necessary data are exchanged with the real world. Main control part of the software is executed each 220μs and it follows after the communication part.

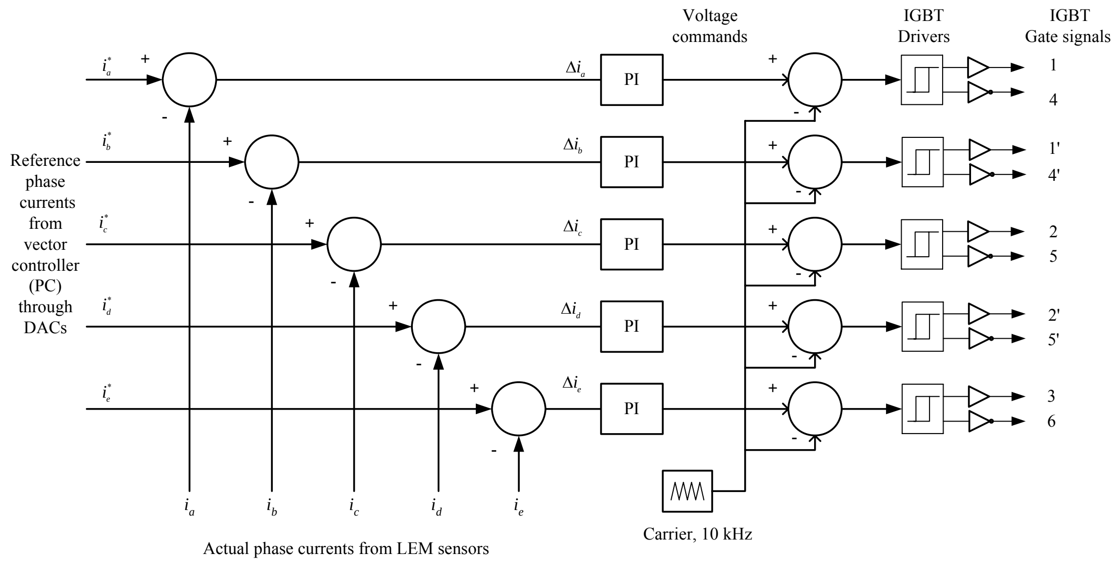

Fig. 9.4. Current controller structure for five-phase inverter.

Each motor is equipped with a shaft position sensor (resolver). The resolver signals are sent to the DS2000 drives, where the DSPs perform the necessary signal processing. At the output of each DS2000 drive, simulated encoder pulses are generated. These signals are sent to the LPT1 interface board, where the FPGA circuit counts the encoder pulses and generates the motor shaft position in a digital form. The PC reads the shaft position and provides the necessary control actions. The LPT1 board uses four channels of A/D converter for data acquisition. Each 220μs four analogue current inputs are sampled. These A/D inputs are used to record the measured inverter phase currents namely A, B, D and E (A and E from the inverter supplying three phases and B and D from inverter supplying two phases) and to send them to the PC through the parallel port, where they are stored along with the rotor speeds, q-axis current references and d-q transformation angles (for two induction motor drive case).

At the end of each experimental run the data stored on the PC is processed using a Matlab m-file. This allows plotting of inverter current references, motor current references, actual inverter currents (phases A, B, D, E), q-axis current references and motor speeds. The whole experimental set up is shown in Fig. 9.5.

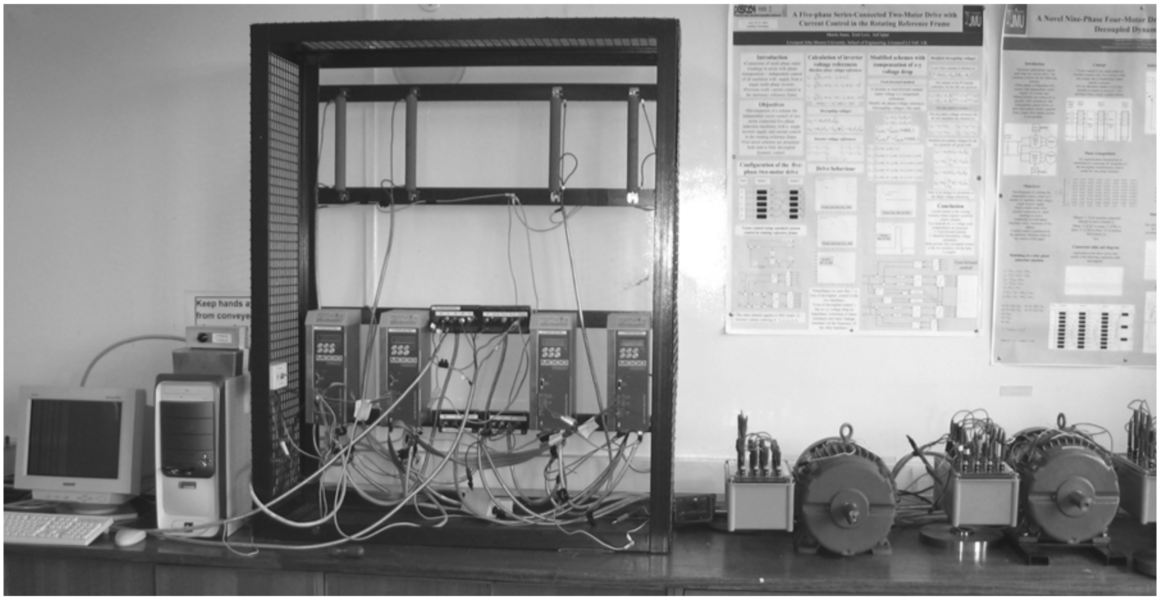

Fig. 9.5. Experimental rig for five-phase single-motor and two-motor drive.

9.3 DETAILS OF THE MOTORS USED IN THE EXPERIMENTS

Three motors are used in this experimental rig. Two of them are identical five-phase induction motors while one is a five-phase synchronous reluctance motor. The two five-phase induction motors are obtained by designing new stator laminations and a five-phase stator winding for an existing three-phase squirrel cage type induction machine. The rotor was kept the same. The original three-phase induction motor was 7.5 HP, 460 V and 60 Hz. For the five-phase machines the number of stator slots is 40 and the rotor has 28 unskewed slots. There are 10 separate coils (with both coil ends available) in the stator winding where two coils belong to one phase. Thus the motor windings are open ended. Two coils of each phase are connected in parallel to form one phase winding. The two five-phase induction motors are shown in Fig. 9.6. The five-phase synchronous reluctance motor is also obtained from the same three-phase induction motor. The stator with 40 slots is wound to accommodate five-phase winding and is the same as for five-phase induction machines. The rotor is obtained from the original three-phase induction motor squirrel cage rotor by cutting out the slot depth at four 45° mechanical spans, thus forming a salient four-pole rotor structure. Fig. 9.7 depicts the five-phase synchronous reluctance motor.

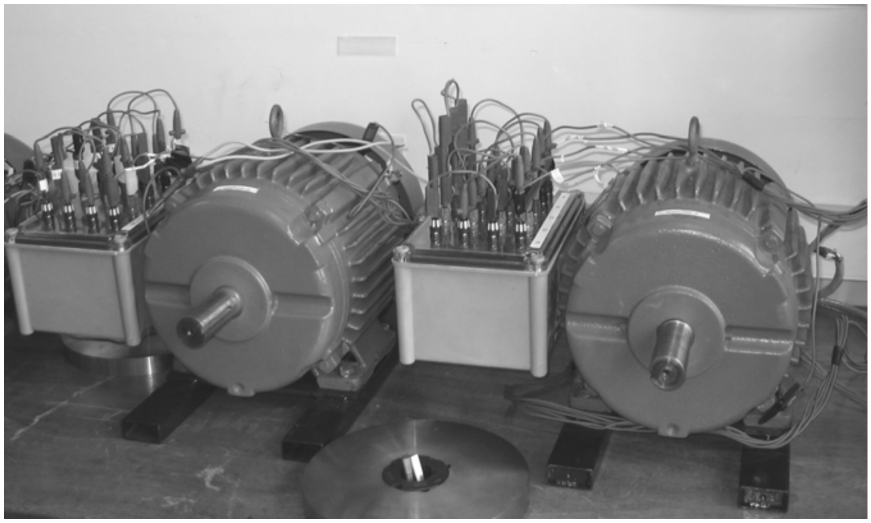

Fig. 9.6. Two five-phase induction motors used in the experimentation.

Fig. 9.7. Five-phase synchronous reluctance motor used in the experimentation.

A permanent magnet dc machine is used as a dc generator for loading purposes. The rating of the dc machine is 180 V, 24.5 A, 3.7 kW and 1750 rpm. A variable resistor bank is used as a load for the dc generator. The loading arrangement is shown in Fig. 9.8. Load profile of the five-phase induction motor is examined for various setting of the resistor bank. Induction motor is coupled to the dc generator whose armature terminals are connected to the resistor bank. Armature voltage and current are measured for various loading and speed settings and output torque is calculated. The variation of torque with speed is shown in Fig.

9.9. Since the excitation of the dc generator is constant, torque is almost linearly proportional to the operating speed.

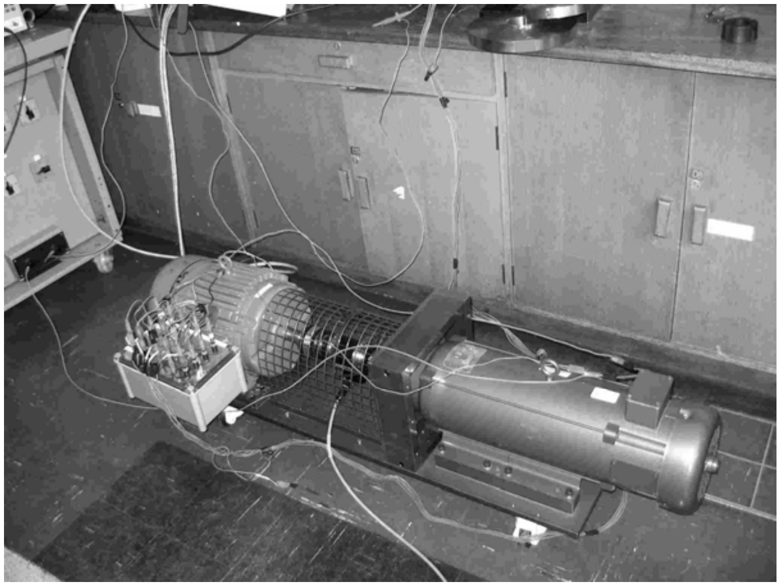

Fig. 9.8. Loading arrangement for five-phase motor.

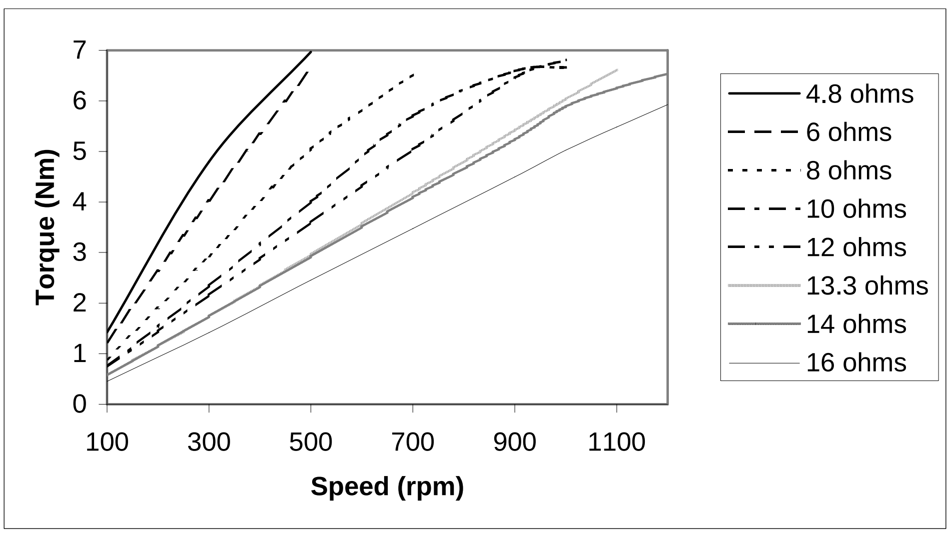

Fig. 9.9. Variation of torque with speed of the vector controlled induction motor drive for various loads on dc generator.

9.4 TRANSIENT PERFORMANCE OF THE FIVE-PHASE INDUCTION MOTOR

A series of experimental tests are performed in order to examine the dynamic performance of the five-phase induction motor operating under indirect rotor flux oriented control. Since the two five-phase induction motors used for series connection, elaborated in section 9.6, are identical, the results for one of them are presented in this section. The tests are performed with the stator windings of the two five-phase induction motors connected in series with appropriate phase transposition (Fig. 4.1). The current references for the idle motor are removed in the C-code. Thus the idle motor represents a static R-L load for the drive. This configuration ensures the same operating conditions for the current controllers as in the case when both motors are running (section 9.6). The drive is operated in the base speed region (constant flux) with constant stator d-axis current reference (2.5 A RMS). The q-axis current is limited to 5 A RMS. The five-phase induction motor is fitted with a resolver and operates in sensored speed mode. The speed commands are given to the motor through the keyboard of the PC. Indirect rotor field oriented control is executed, phase current references are generated and sent to the DSPs, which then perform necessary current control calculations and send switching signals to the inverter. The transient data are logged into the PC and are further processed using MATLAB code. The results of the experimental study are illustrated for all transients by displaying the speed response, stator q-axis current reference (peak value), and actual current and reference current for one inverter (stator) phase. A step speed command is initiated in all the cases. There is no inertia wheel fitted to the motor nor is the motor coupled to any other motor. It operates under no-load conditions.

Acceleration transients, starting from standstill, are shown in Figs. 9.10 a-d. The step speed command is 300 rpm, 500 rpm, 800 rpm and 1000 rpm, respectively and is applied at t = 0.22 s. The total duration of the transient, recorded here, is 1 s. Typical behaviour of a vector controlled induction motor is observed, with rapid stator q-axis current reference build up corresponding to almost instantaneous torque build up. Speed response is therefore the fastest possible for the given current limit. Stator phase current reference and measured current are in excellent agreement and closely correspond one to the other in final steady state.

The second test is a deceleration transients illustrated in Figs. 9.11 a-d. The motor is decelerated from 300 rpm, 500 rpm, 800 rpm and 1000 rpm, respectively, down to zero speed. The same quality of performance as for the acceleration transient is obtained.

Next, reversing performance of the drive is investigated. Transitions from 300 rpm to –300 rpm, 500 rpm to –500 rpm, 800 rpm to –800 rpm and 1000 to –1000 rpm are depicted in Figs. 9.12 a-d. Prolonged operation in the stator current limit results in all the cases, leading to rapid change of direction of rotation. Measured phase current and reference phase current are once more in excellent agreement. It is important to note that the actual current in all steady states at non-zero frequency contains essentially only the fundamental harmonic (PWM ripple is filtered out using FIR filters).

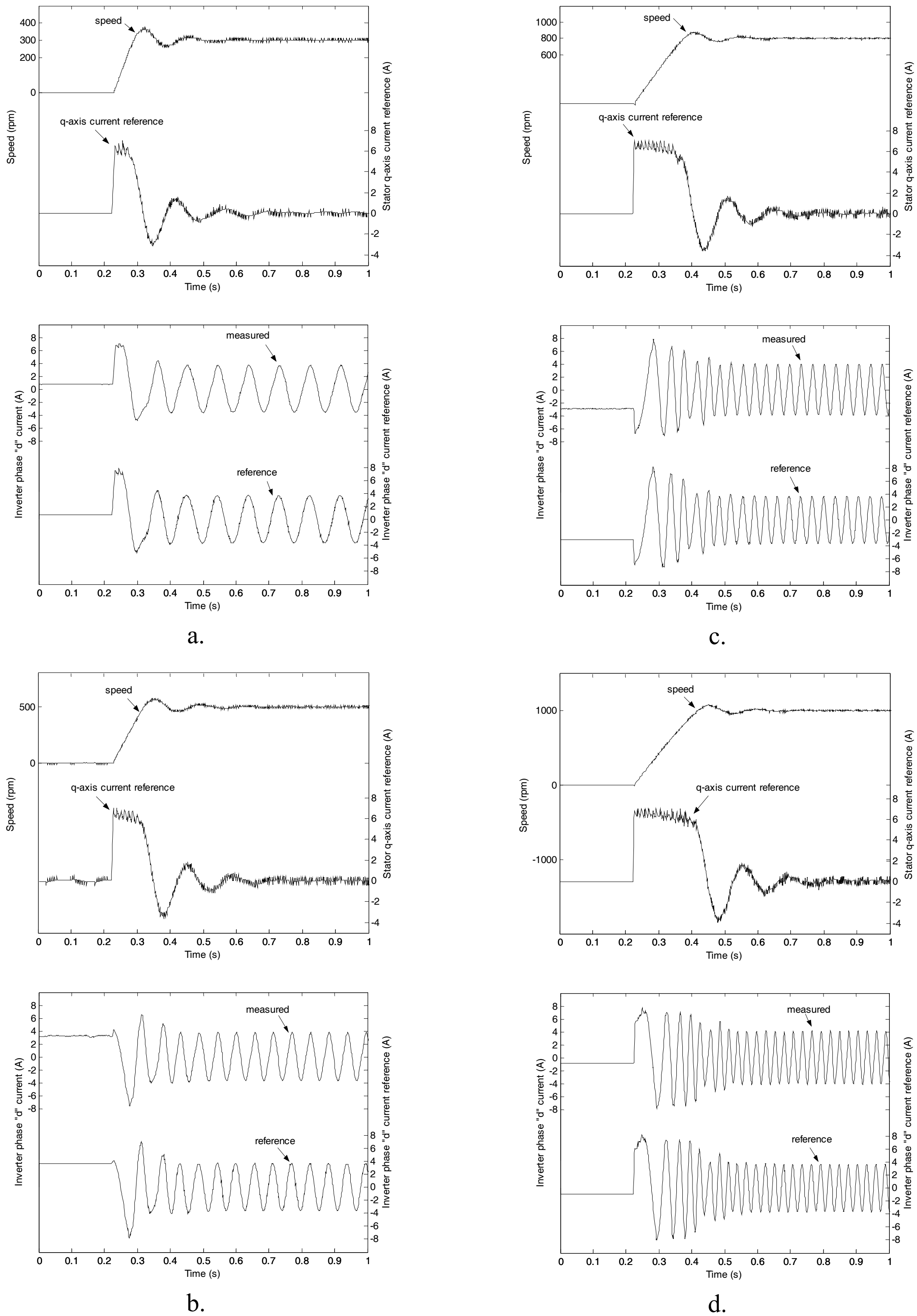

Fig. 9.10. Transient performance of the five-phase induction motor during acceleration: a. 0 to 300 rpm, b. 0 to 500 rpm, c. 0 to 800 rpm, d. 0 to 1000 rpm.

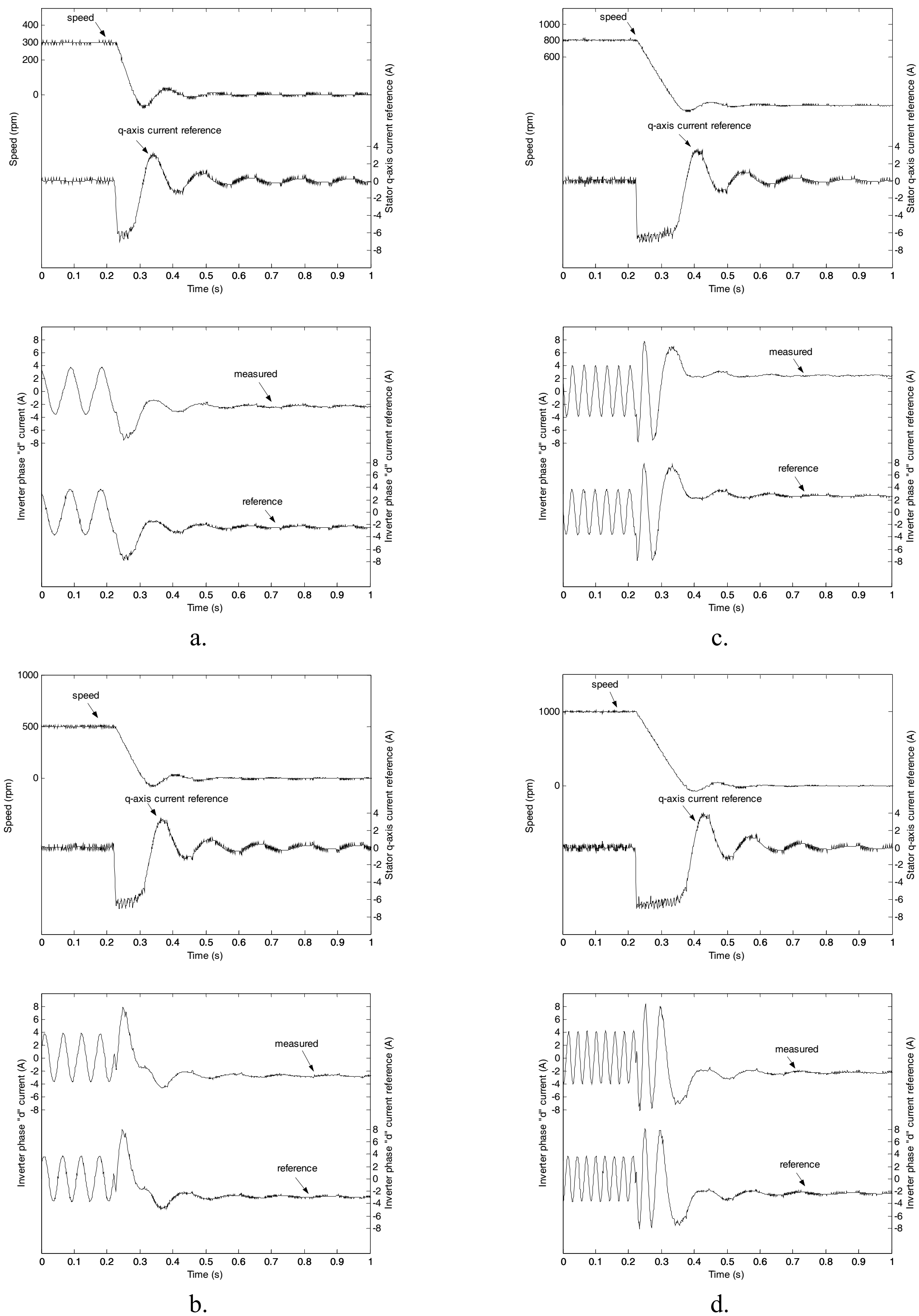

Fig. 9.11. Transient performance of the five-phase induction motor during deceleration: a. 300 to 0 rpm, b. 500 to 0 rpm, c. 800 to 0 rpm, d. 1000 to 0 rpm.

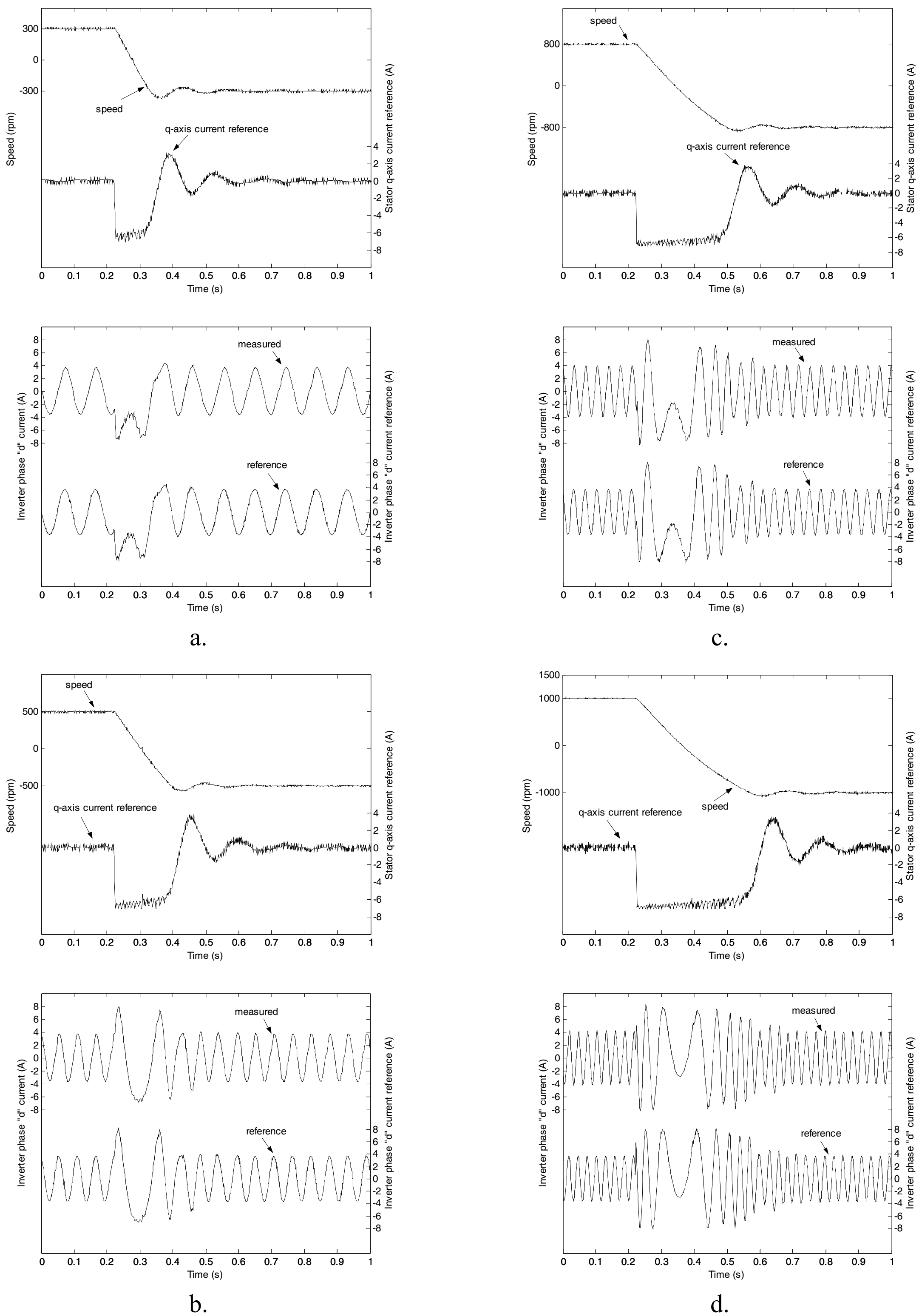

Fig. 9.12. Reversing transient of the five-phase induction motor: a. 300 to -300 rpm, b. 500 to -500 rpm, c. 800 to -800 rpm, d. 1000 to -1000 rpm.

Next, one induction motor is coupled to the dc generator and the drive performance during step loading and step unloading is examined. The results are illustrated in Fig. 9.13a and Fig. 9.13b, respectively. The induction motor is at first brought to 500 rpm under no-load condition. During steady state operation a step load is applied by switching the loading resistor 'on' (set to 12 Ω). Similarly, for step unloading, the motor is initially running loaded and the load is then removed. A poorly damped oscillation is observed in the q-axis current reference, especially for the unloading transient. This is believed to be due to speed controller setting which, is kept the same as for the other studied transients. The speed controller has been tuned to yield a good response to speed reference changes (Fig. 9.10 to Fig. 9.12) before its connection to the dc generator (i.e. with a considerable lower inertia than it is in the case of transients of Fig. 9.13).

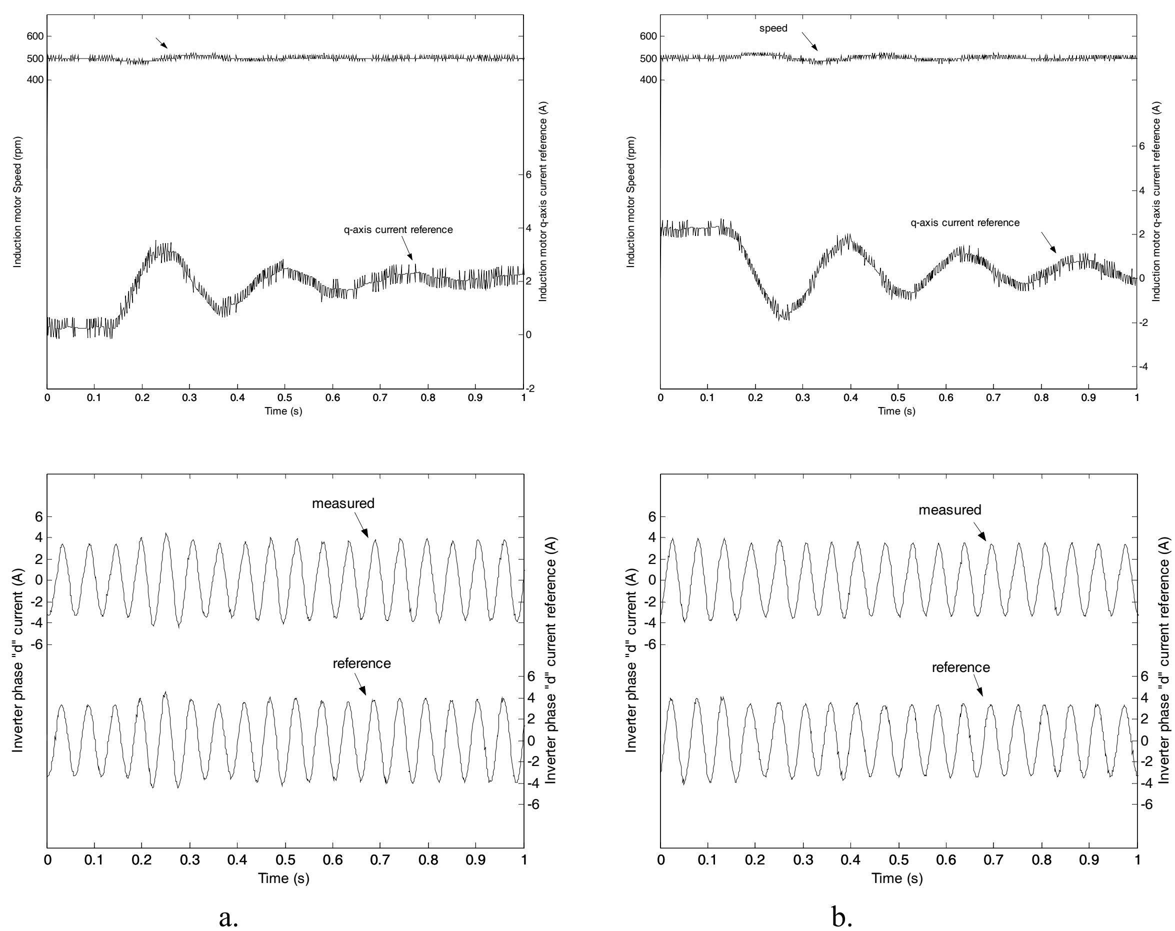

Fig. 9.13. Transient performance of the five-phase induction motor during: a. step loading at 500 rpm, b. step unloading at 500 rpm.

9.5 TRANSIENT PERFORMANCE OF THE FIVE-PHASE SYNCHRONOUS RELUCTANCE MOTOR

A series of experimental tests are performed in order to examine the dynamic performance of the five-phase synchronous reluctance motor operating under indirect rotor flux oriented control. The test conditions are the same as those of section 9.4. The drive is operated in the base speed region. One particular salient feature of the synchronous reluctance motor is the way in which the d-axis current reference is set. There are many different algorithms [Nasar et al (1993), Kazmierkowski et al (2002)], the simplest one being operation with constant stator d-axis current reference setting. Such an approach was initially adopted and tested. Setting of d-axis current reference to 2.5 A RMS was found to produce excellent dynamics but it simultaneously led to excessive stator q-axis current reference in steady state no-load operation. Reduction of d-axis current reference to 1 A RMS resulted in acceptable q-axis current steady state value but led to instability for large speed transients. The solution implemented in the rig is a simple algorithm, illustrated in Fig. 9.14. Stator d-axis current reference is fixed to 1 A RMS as long as q-axis current reference is below 1 A RMS. Similarly, if q-axis current reference exceeds 2.5 A RMS, d-axis current reference is fixed to 2.5 A RMS. In between, d-axis current reference is made equal to q-axis current reference. Thus the stator d-axis current reference value is a non-linear function of stator q-axis current reference value, Fig. 9.14. The q-axis current is limited to 5 A RMS. The vector control scheme of the five-phase synchronous reluctance motor is depicted in Fig. 9.15.

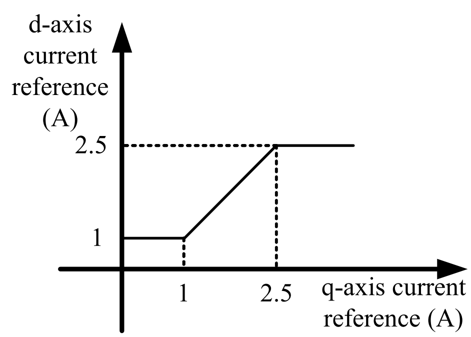

Fig. 9.14. Relationship between stator d-axis current reference and stator q-axis current reference (RMS values).

The five-phase synchronous reluctance motor is fitted with a resolver and it operates in sensored speed mode. The procedure of testing followed here is the same as the one explained in section 9.4. The results of the experimental study are illustrated once more for all transients by displaying the speed response, stator q-axis current reference (peak value), and actual current and reference current for one inverter (stator) phase. A step speed command is initiated in all the cases. There is no inertia wheel fitted on the motor and it is also not coupled to any other machine. Hence it operates under no-load condition.

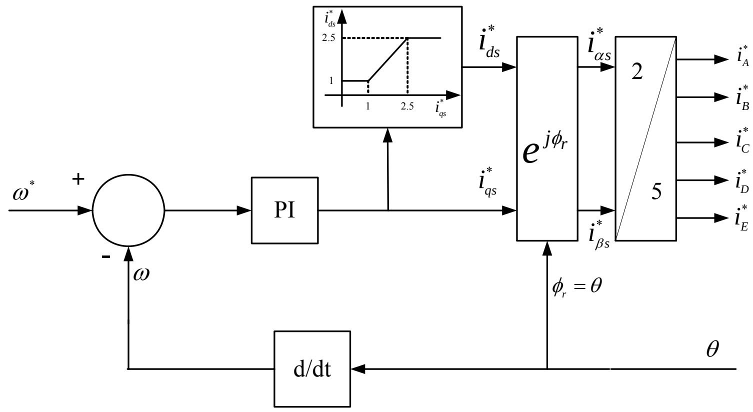

Fig. 9.15. Vector control scheme for the five-phase synchronous reluctance motor.

Acceleration transients, starting from standstill, are shown in Figs. 9.16 a-d. The step speed command is 300 rpm, 500 rpm, 600 rpm and 800 rpm, respectively, and is applied at t = 0.22 s. The total duration of transients, recorded here, is again 1 s. The nature of the dynamic response of the five-phase synchronous reluctance motor is similar to that of the five-phase induction motor, except for a higher ripple in the speed and stator q-axis current reference. The resulting higher ripple in the inverter (stator) phase current can also be observed. The origin of the ripple is two-fold. First of all, for all stator q-axis current references in between 1 A and 2.5 A RMS, stator d-axis current reference varies. Hence any change of q-axis current reference causes change in d-axis current reference. The second source of ripple is inherent to synchronous reluctance machines [Jovanovic (1996)] and is due to the slotting effect and saliency of the rotor structure. However, measured and reference inverter (stator) phase current are in good agreement. Another important observation from the q-axis current reference plot is that the synchronous reluctance motor draws a significant amount of q-axis current under steady state no-load condition. It is further seen that this value increases with the increase in the operating speed. This phenomenon is attributed to the structure of the five-phase reluctance motor under test. Under no-load operating condition, the motor has to generate sufficient electromagnetic torque to overcome the no-load losses of the machine, which are neglected in the vector controller development. This torque is proportional to the product of d-axis current, q-axis current and the difference between the d-axis and q-axis inductances ($T_e = k(L_d - L_q)i_{ds}i_{qs}$). Thus the amount of q-axis current drawn by the motor depends upon the saliency of the rotor and the operating speed, since both mechanical and iron losses increase with speed.

The second test is a deceleration transient, illustrated in Figs 9.17 a-d. The motor is decelerated from 300 rpm, 500 rpm, 600 rpm and 800 rpm, respectively, down to zero speed. The same quality of performance as for the acceleration transient is obtained. However, the q-axis current reference is now present in the beginning when the motor is running at certain speed before the transient. The q-axis current reference reaches zero after the transient is over, because the motor reaches stand-still condition.

Next, reversing performance of the drive is investigated. Transitions from 300 rpm to –300 rpm, 500 rpm to –500 rpm, 600 rpm to –600 rpm and 800 to –800 rpm are depicted in Figs. 9.18 a-d. Once again the same quality of performance as for acceleration and deceleration is observed. The change in the direction of rotation is also evident in the inverter (stator) phase current where the change in phase sequence is clearly seen. The q-axis current reference is once again seen to be present during the period of normal running at any non-zero speed.

9.6 DYNAMICS OF THE SERIES-CONNECTED FIVE-PHASE TWO-MOTOR DRIVE SYSTEM (TWO INDUCTION MOTORS)

This section present the experimental results for the five-phase two-motor drive with two induction motors. A number of tests are performed to validate experimentlly the existence of decoupled dynamic control in the five-phase series-connected two-motor drive, elaborated in section 4.2. The two identical five-phase induction motors, discussed in section 9.3, are connected in series according to Fig. 4.1. The first motor which is connected directly to the five-phase VSI is labelled as IM1 and the second motor which is connected to the first induction motor with appropriate phase transposition is called IM2. Both motors are equipped with resolvers and operate in sensored speed mode. The resolver of IM1 is connected to the left DS2000 (suplying three phases) and the resolver of IM2 is connected to the right DS2000 (suplying two phases). Operation in the base speed region only is considered and the stator d-axis current references of both motors are constant at all times and equal to 2.5 A (RMS). The q-axis current reference limit is set to 5 A (RMS) for both motors. Both motors are running under no-load conditions. The C-code, running on the PC, performs closed loop speed control and indirect rotor flux oriented control according to Fig. 3.10, in parallel for the two motors.

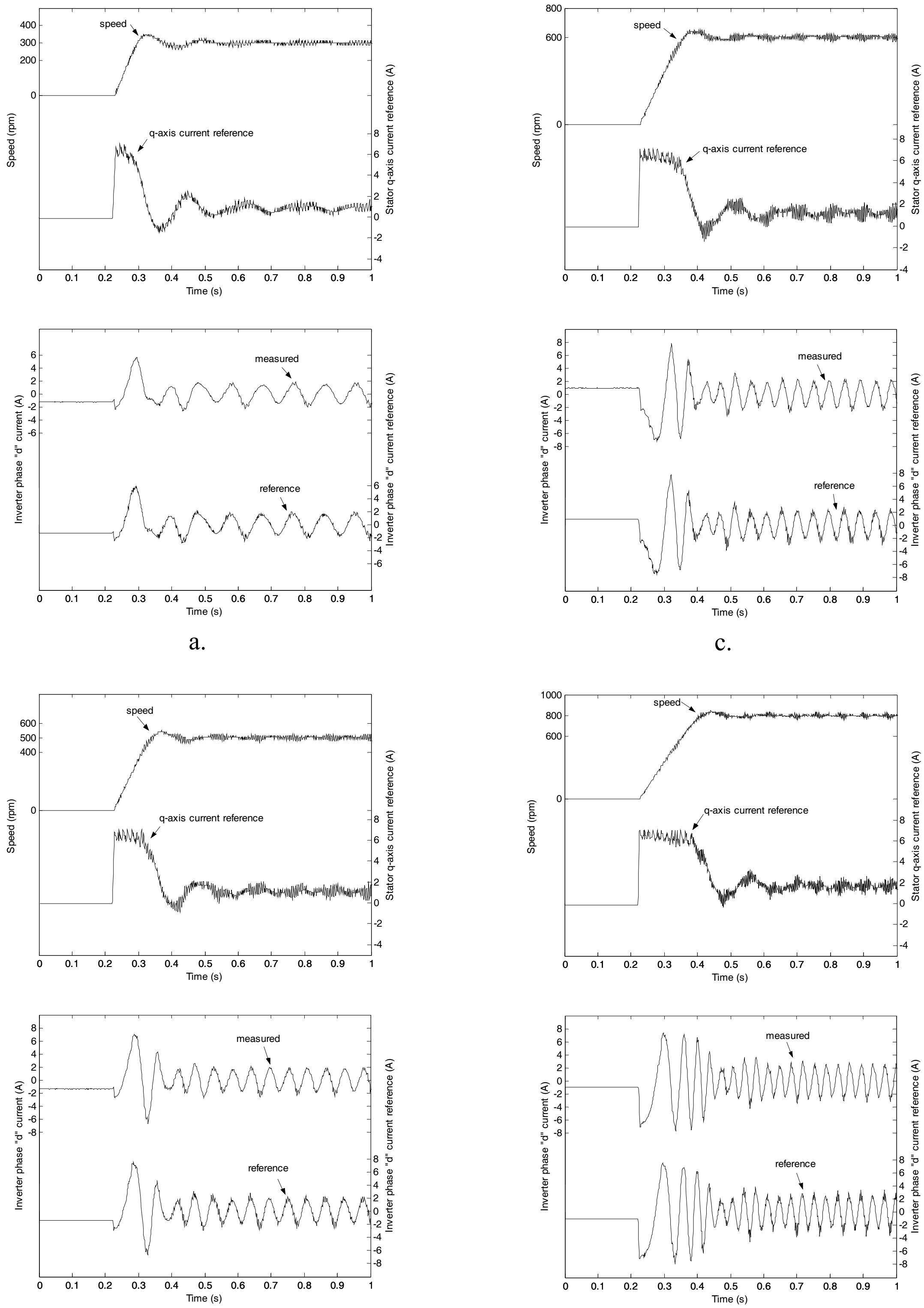

Fig. 9.16. Acceleration transients of the five-phase synchronous reluctance motor: a. 0 to 300 rpm, b. 0 to 500 rpm, c. 0 to 600 rpm, d. 0 to 800 rpm.

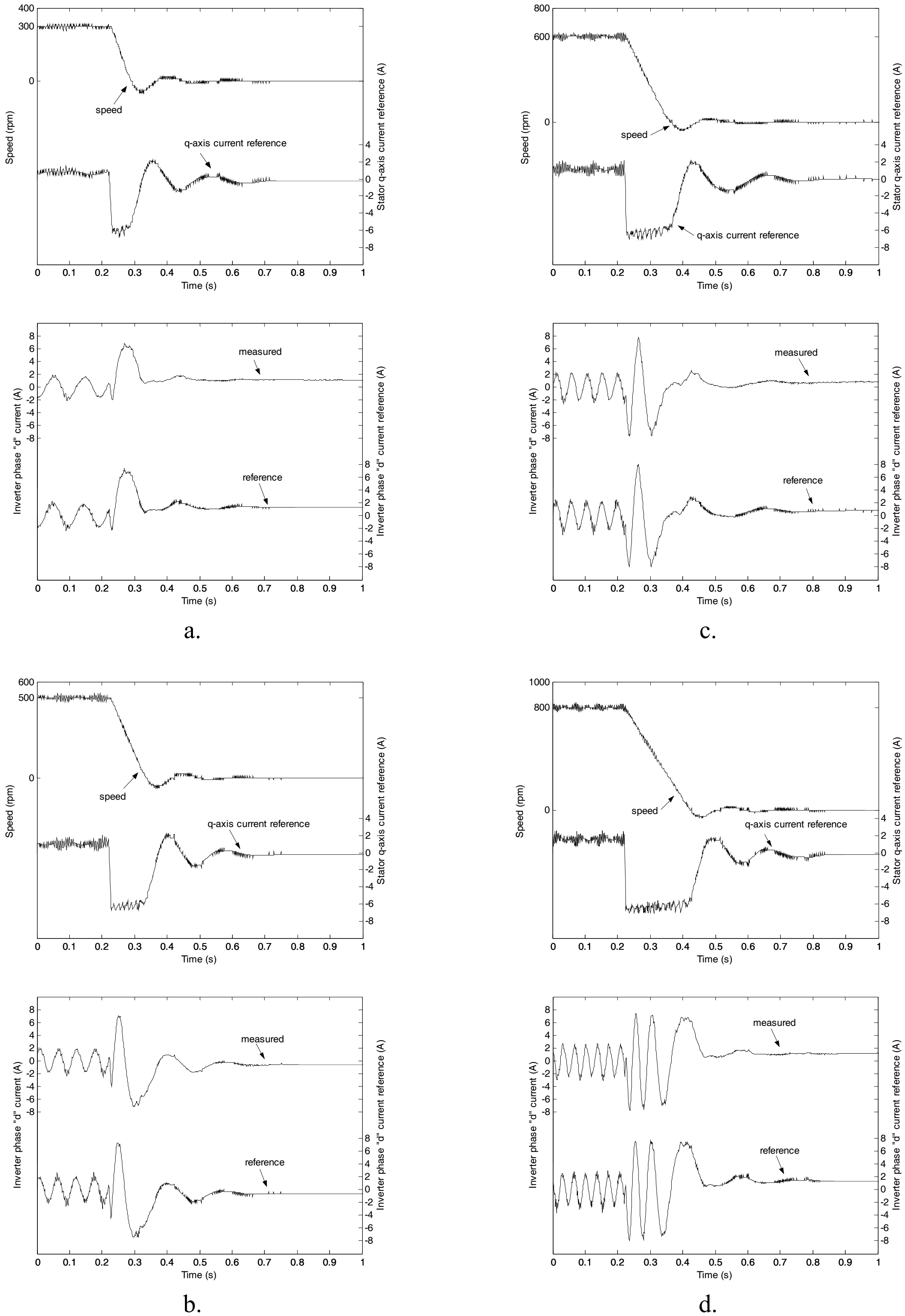

Fig. 9.17. Deceleration transients of the five-phase synchronous reluctance motor: a. 300 to 0 rpm, b. 500 to 0 rpm, c. 600 to 0 rpm, d. 800 to 0 rpm.

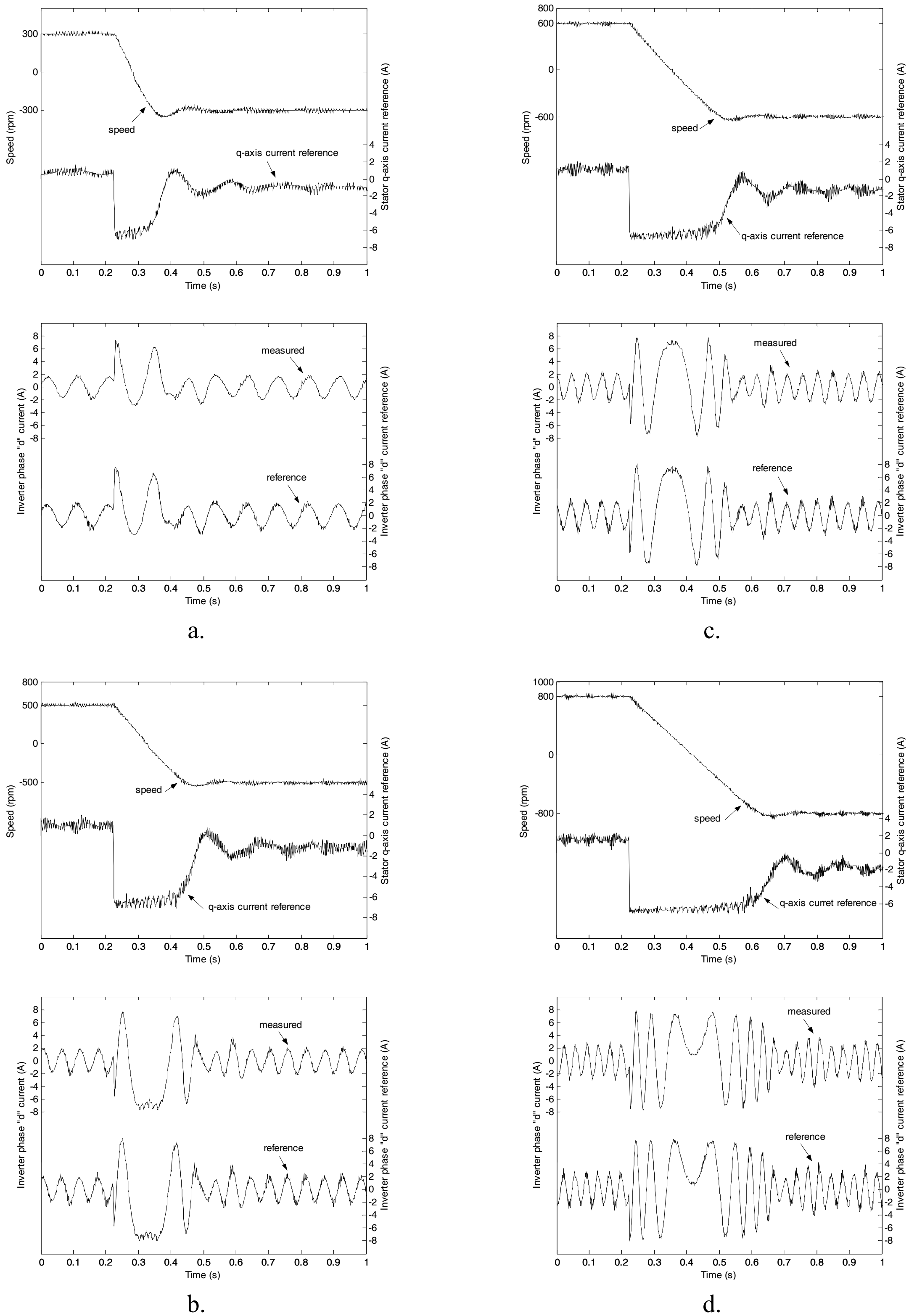

Fig. 9.18. Reversing transients of the five-phase synchronous reluctance motor: a. 300 to –300 rpm, b. 500 to –500 rpm, c. 600 to –600 rpm, d. 800 to –800 rpm.

Individual stator current references of the two motors are calculated according to (4.75) and (4.76) and summed according to (4.77) to form inverter phase current references.

The approach adopted in the experimental investigation is similar to the one used in Jones (2005). Both motors are excited and brought to a certain steady state operating speed. A step speed transient is then initiated for one of the two motors, while the speed reference of the other remains constant. If the control is truly decoupled, operating speed of the motor running at constant speed should not change when a transient is initiated for the other motor. However, due to the fast action of the speed controller, some small variation of the speed could be unobservable. The ultimate proof of the truly decoupled control is therefore the absence of variation in the stator q-axis current command of the motor running at constant speed, since this indicates absence of any speed error at the input of the speed controller. In addition the phase current of the motor running at constant speed should remain undisturbed during the transient of the other motor. Experimentally obtained traces include in all cases speeds, stator q-axis current references (peak values), stator phase current references (one phase only) for both motors, and the measured and reference current for one inverter phase. The transients examined in the experiments are acceleration, deceleration and reversal all under no-load condition, and step loading/unloading. The IM1 is coupled to the dc generator only for step loading/unloading transients. Since the two motors are identical, the transient results for only one motor are presented. The plots are shown in Figs. 9.19-9.22.

In the acceleration transient test, IM2 is held at constant speed of 500 rpm (16.67 Hz) and IM1 is initially at stand-still. A step speed command is then applied to IM1 at t = 0.33 s in all cases. The total duration of the transient recorded here is 0.9 s. The step speed commands are 300 rpm and 800 rpm. The resulting plots are shown in Figs. 9.19 a-b. It is evident from speed plots that initiation of the acceleration transient for IM1 does not affect the operational speed of IM2 in any way and it stays at 500 rpm. Stator q-axis current reference of IM2 shows no observable changes during the acceleration of IM1 indicating a practically perfect dynamic decoupling between the two series-connected five-phase induction motors. The inverter phase 'd' reference and actual currents are in very good agreement. In final steady state inverter current is a complex function, containing two sinusoidal components at two different frequencies corresponding to the operating speeds of IM1 and IM2. Further evidence of undisturbed operation of IM2 is the phase current reference trace of IM2 which does not exhibit any change during acceleration of IM1. The quality of current control is excellent, as evidenced by the comparison of the measured and reference currents for inverter phase 'd'.

The inverter phase current is seen to have initially a dc offset (while IM1 is at standstill), due to the magnetising current of IM1.

Comparison of the results for the five-phase single-motor drive, shown in Fig. 9.10, and five-phase two-motor drive, shown in Fig. 9.19, shows that the speed response of IM1, as well as the stator q-axis current reference, are practically identical regardless of whether IM2 is operational or not. The duration and nature of both speed and stator q-axis current reference transients are the same in Fig. 9.10 and Fig. 9.19.

The second transient, illustrated in Figs. 9.20 a-b, is deceleration from 300 to 0 rpm and 800 to 0 rpm. Once again IM2 is held at 500 rpm and transient is initiated for IM1. The decoupled dynamic control of the two motors is again evident during deceleration transient. Further, by comparing Fig. 9.11 and Fig. 9.20 it can be concluded that the dynamic performance of IM1 in single-motor drive mode and two-motor drive mode is identical. Thus the series connection of two motors has no impact on the behaviour of individual motors.

The reversing transients of IM1 are presented for 300 to -300 rpm and 800 to -800 rpm in Figs. 9.21 a-b with IM2 running again at 500 rpm. The undisturbed operation of IM2 is once again evident from speed traces, which remain unaffected during the transients of IM1. A negligibly small disturbance in the q-axis current of the constant speed machine (IM2) is seen for speed reversal from 300 to –300 rpm. There is no noticeable change in the phase current reference of IM2 during the transient of IM1 due to no-load operation. Comparison of Fig. 9.12 and Fig. 9.21 shows identical behaviour of IM1 when used either as a single-motor drive or within the two-motor drive system. The results of Figs. 9.19-9.21 provide proof of decoupled control of two series-connected five-phase induction motors supplied from a single five-phase voltage source inverter and controlled using indirect rotor flux oriented vector control scheme.

Finally, step loading and unloading transients of IM1 are examined and are illustrated in Fig. 9.22 a and 9.22 b, respectively. The speed controller setting is kept the same as for other studied transients although the total drive inertia is now significantly higher than in previous transients, due to the coupling with the dc generator. IM1 is accelerated to 500 rpm from standstill and IM2 is accelerated to 300 rpm from standstill, without load. After attaining steady state condition, a step load is applied to IM1 while IM2 is still running under no-load condition. Damped oscillation is observed in the q-axis current reference of IM1. No disturbance is seen in either the q-axis current reference or speed of IM2. The phase current reference of IM2 is also constant and unaffected by loading or unloading of IM1. This indicates dynamic decoupling between IM1 and IM2 for step loading and step unloading

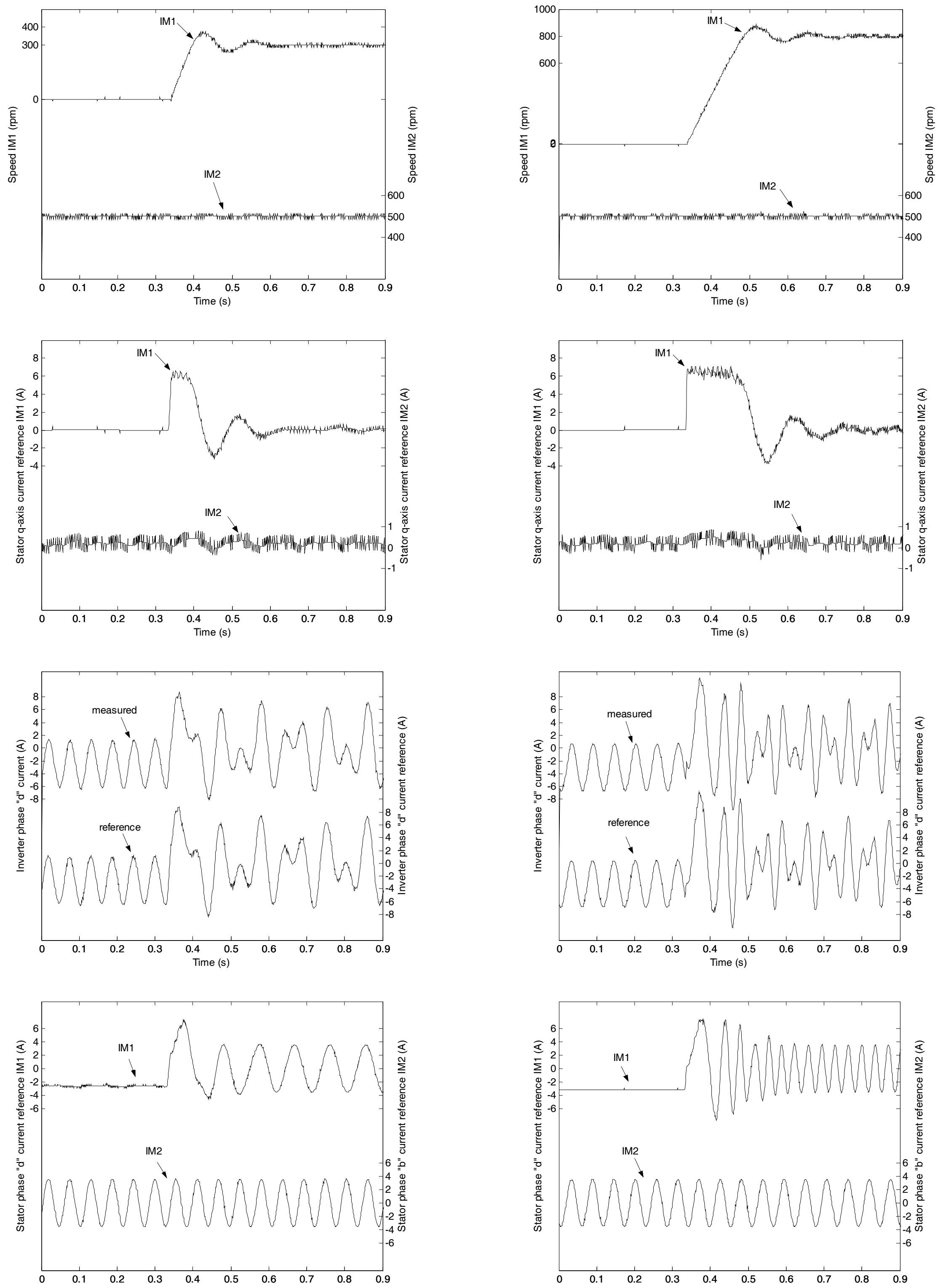

a. b.

Fig. 9.19. Acceleration transient of the five-phase two-motor drive (two induction motors): a. 0 to 300 rpm, b. 0 to 800 rpm.

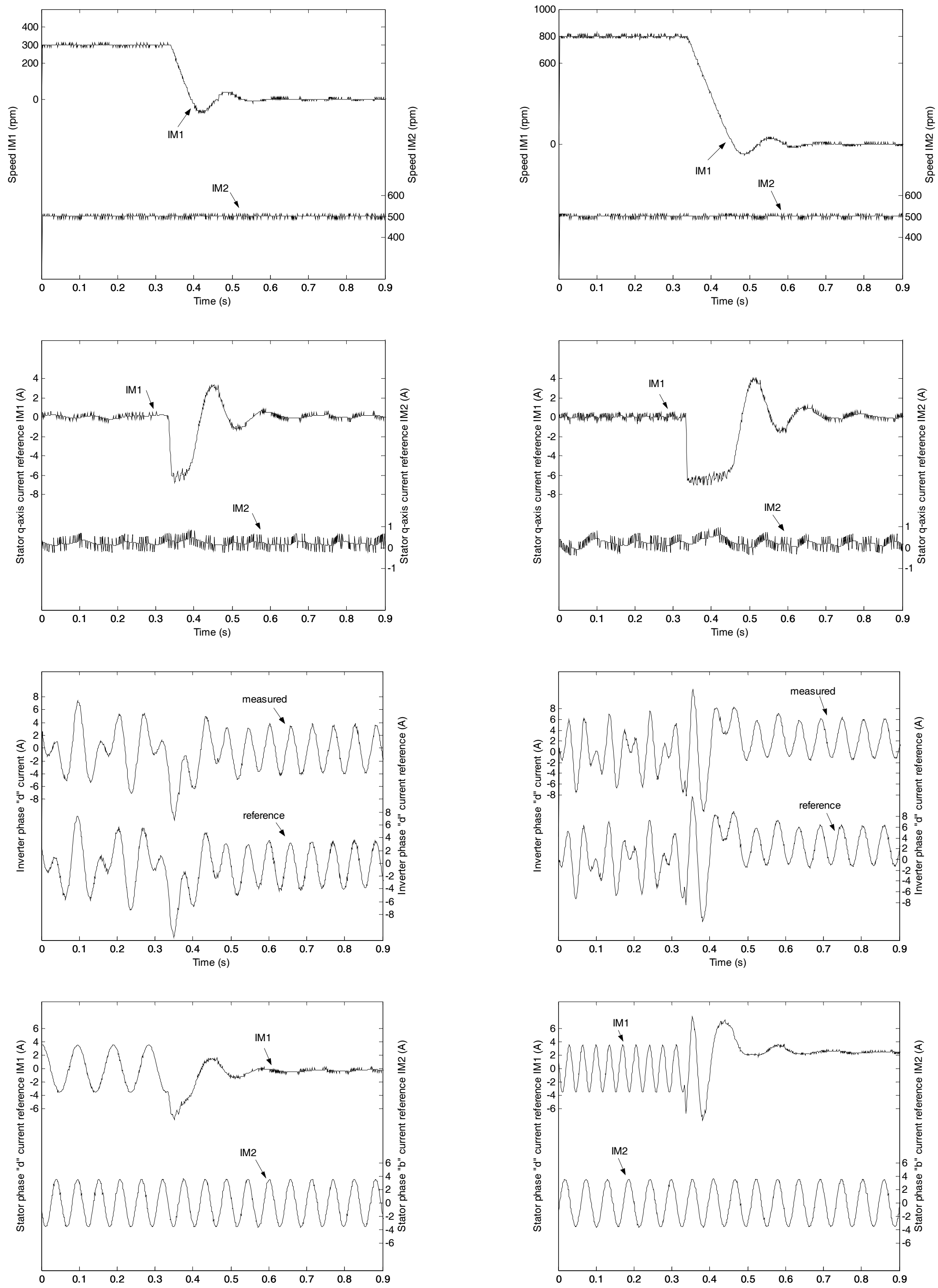

a. b.

Fig. 9.20. Deceleration transients of the five-phase two-motor drive (two induction motors): a. 300 to 0 rpm, b. 800 to 0 rpm.

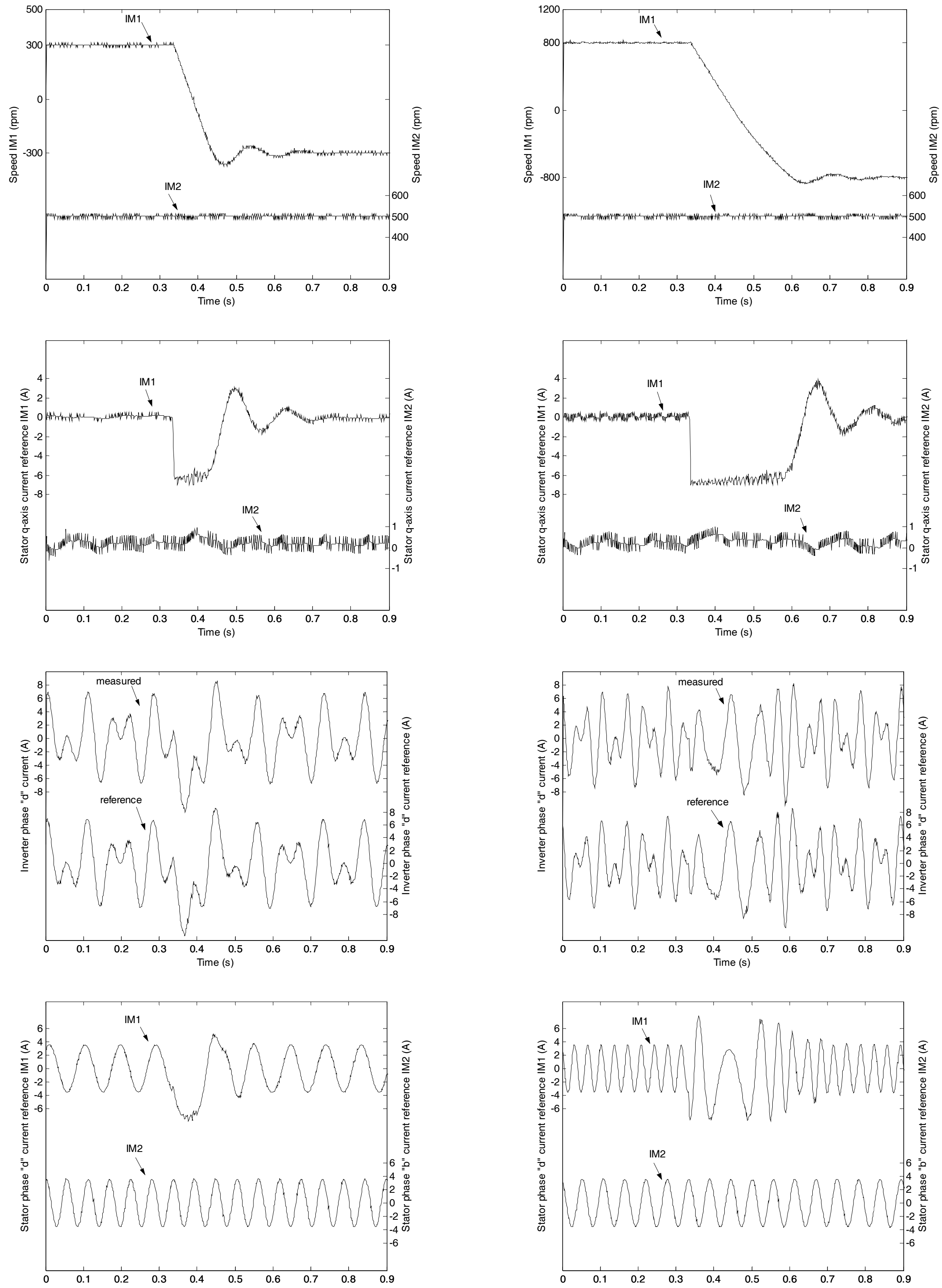

a. b.

Fig. 9.21. Reversing transients of the five-phase two-motor drive (two induction motors): a. 300 to -300 rpm, b. 800 to –800 rpm.

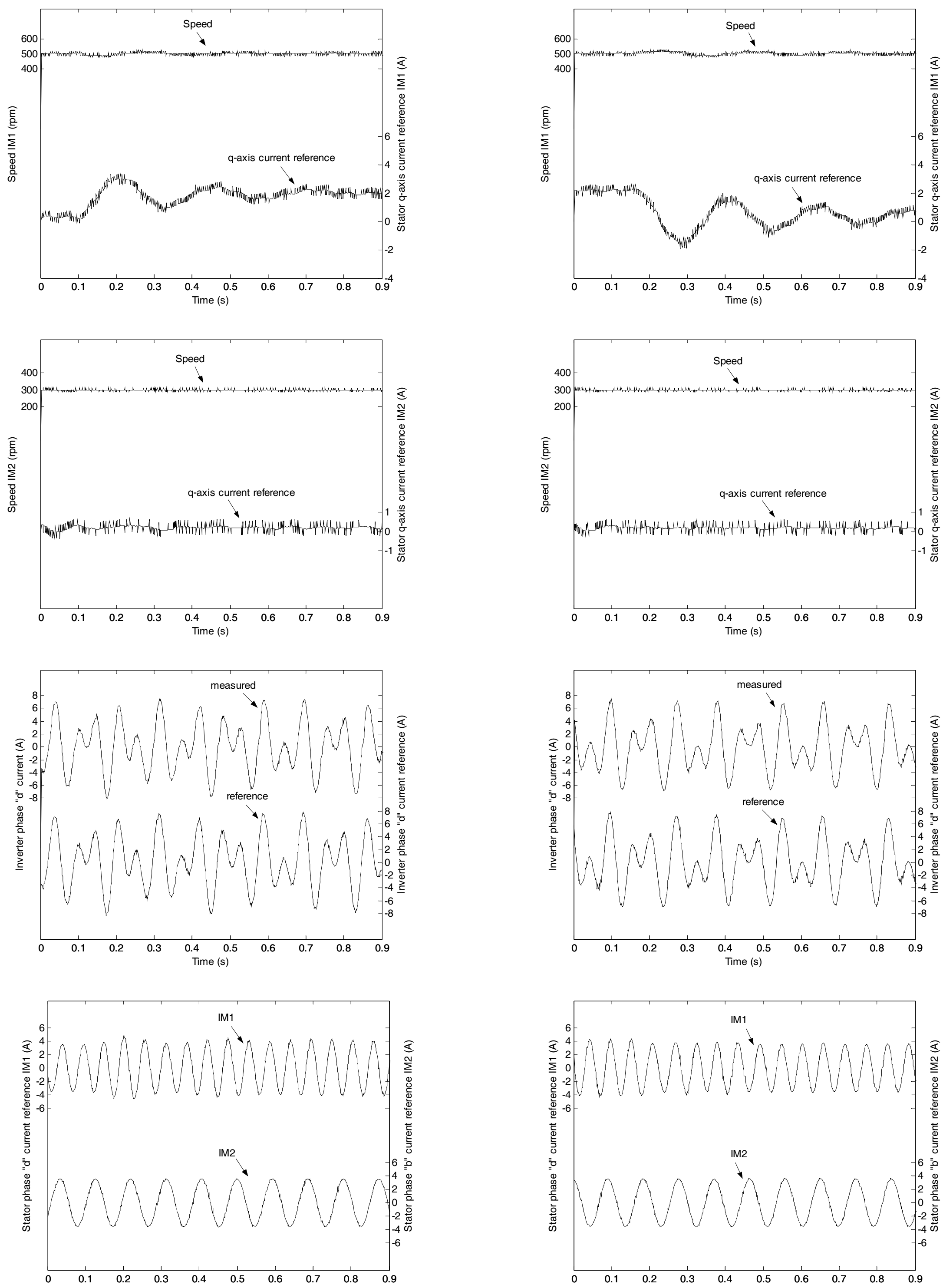

a. b.

Fig. 9.22. Loading/unloading transients of the five-phase two-motor drive (two induction motors): a. step loading, IM1 at 500 rpm and IM2 at 300 rpm, b. step unloading, IM1 at 500 rpm and IM2 at 300 rpm.

transients. Further, comparing Fig. 9.22 with Fig. 9.13, nothing changes due to the series connection of two induction machines.

9.7 DYNAMICS OF THE SERIES-CONNECTED FIVE-PHASE TWO-MOTOR DRIVE SYSTEM (INDUCTION MOTOR AND SYNCHRONOUS RELUCTANCE MOTOR)

The concept of the series-connected five-phase two-motor drive supplied from a single five-phase inverter, developed in section 4.2, is not constrained to any particular type of ac machines. The possibility of using different types of ac machines with sinusoidal flux distribution in the multi-phase multi-motor drive has been discussed in Jones (2005) and experimental verification has been provided for a permanent magnet synchronous machine connected in series with an induction machine within the six-phase two-motor drive. This is further elaborated experimentally in this section for the five-phase two-motor drive. The five-phase synchronous reluctance motor (section 9.3), which has been tested as a single-motor drive in section 9.5, is connected in series with the five-phase induction motor (section 9.3). The synchronous reluctance machine is directly connected to the five-phase VSI and induction machine is connected to the synchronous reluctance machine with appropriate phase transposition. The synchronous reluctance motor resolver is connected to the left DS2000 (suplying three phases) and induction machine resolver is connected to the right DS2000. The five-phase induction motor used in this experiment is the one which has been tested in single-motor drive and two-motor drive modes, with the results illustrated in sections 9.4 and 9.6.

Various experimental tests are again performed in order to prove the existence of decoupled dynamic control among the two different types of five-phase machines. The vector control schemes used are those shown in Fig. 3.10 and Fig. 9.15 for the induction motor and for the synchronous reluctance motor, respectively. The approach adopted in the experimental investigation is the same as described in section 9.6. Both machines are initially brought to a certain steady state operating speed. A speed transient is then initiated for one of the two machines, while the speed reference of the other machine remains constant. Both machines are running under no-load operating conditions. Step loading and unloading of the induction machine is also examined with synchronous reluctance machine running under no-load condition. The results of experiments include in all cases speed, stator q-axis current references and measured and reference current for one inverter phase. Due to somewhat different structure of the C-code used in this case individual phase current references for the two machines are not available for display purposes.

9.7.1 Five-phase induction motor transients

This section describes the results for five-phase induction motor transients when synchronous reluctance machine runs at constant speed. Acceleration, deceleration, reversing and loading/unloading transients of the induction motor are illustrated in Figs. 9.23-9.26.

Acceleration transients are investigated first. The synchronous reluctance motor is running at constant speed of 400 rpm and induction motor is accelerated from 0 to 300 rpm and from 0 to 800 rpm. The results are illustrated in Figs. 9.23 a-b. The decoupling of control is evident from the speed plots and also from stator q-axis current reference plots. The speed

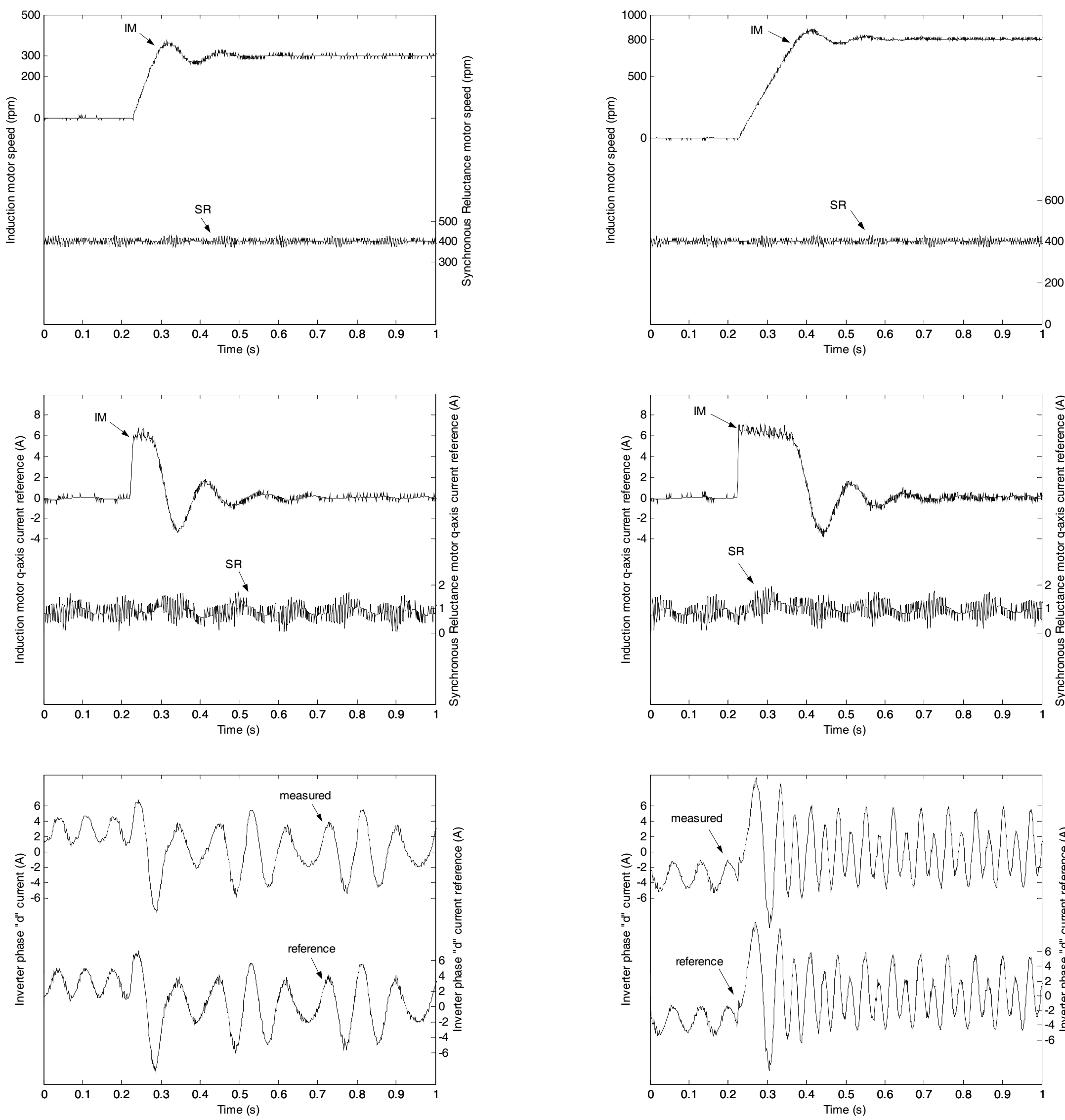

a. b.

Fig. 9.23. Acceleration transient of the five-phase induction motor (synchronous reluctance motor at constant 400 rpm speed): a. 0 to 300 rpm, b. 0 to 800 rpm.

and stator q-axis current reference of synchronous reluctance motor do not show any noticeable change during the acceleration of induction motor. By comparing Fig. 9.23 and Fig. 9.10 it can be seen that the dynamic behaviour of the induction motor is not affected by series connection. The measured and reference inverter phase 'd' current are in very good agreement.

Deceleration transient of the induction motor is investigated next. The synchronous reluctance motor is again held at 400 rpm and induction motor is decelerated from 300 to 0 rpm and 800 to 0 rpm. The resulting plots are shown in Figs. 9.24 a-b. The same conclusion as that for acceleration transient applies here as well.

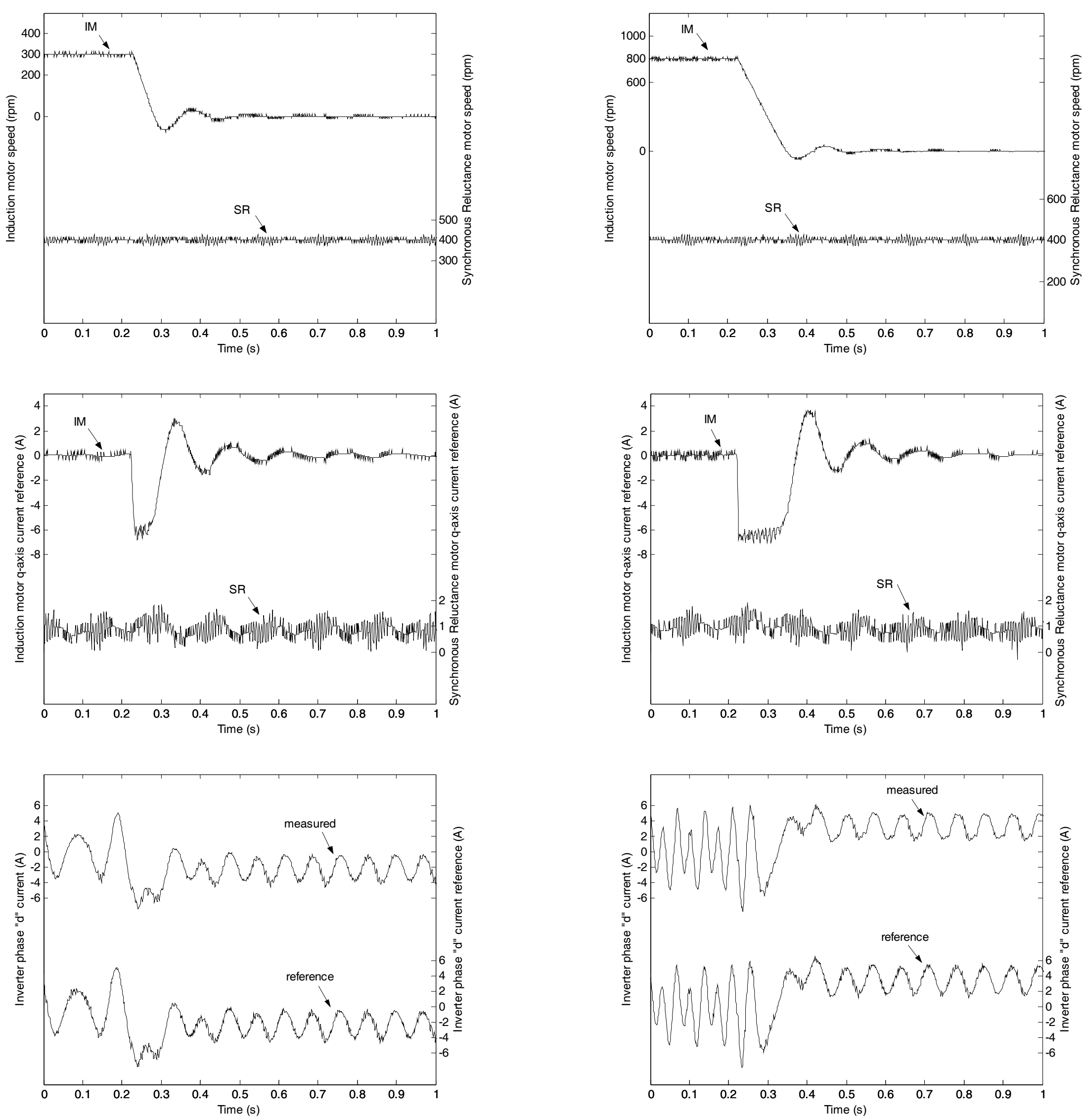

a. b.

Fig. 9.24. Deceleration transients of the five-phase induction motor (synchronous reluctance motor at constant 400 rpm speed): a. 300 to 0 rpm, b. 800 to 0 rpm.

Next, reversing transients are studied. The synchronous reluctance motor speed is at first set to 400 rpm and induction motor reversal is done from 300 to –300 rpm. In the second test synchronous reluctance machine runs at constant speed of 500 rpm while induction machine reverses from 800 to –800 rpm. The plots are shown in Figs. 9.25 a-b. Some rather small variation in q-axis current of synchronous reluctance machine is observable for speed reversal of induction motor from 300 to –300 rpm. Nevertheless, almost fully decoupled dynamic control is achieved.

Finally, step loading and step unloading transient is investigated for induction machine, while keeping synchronous reluctance machine at constant speed (300 rpm).

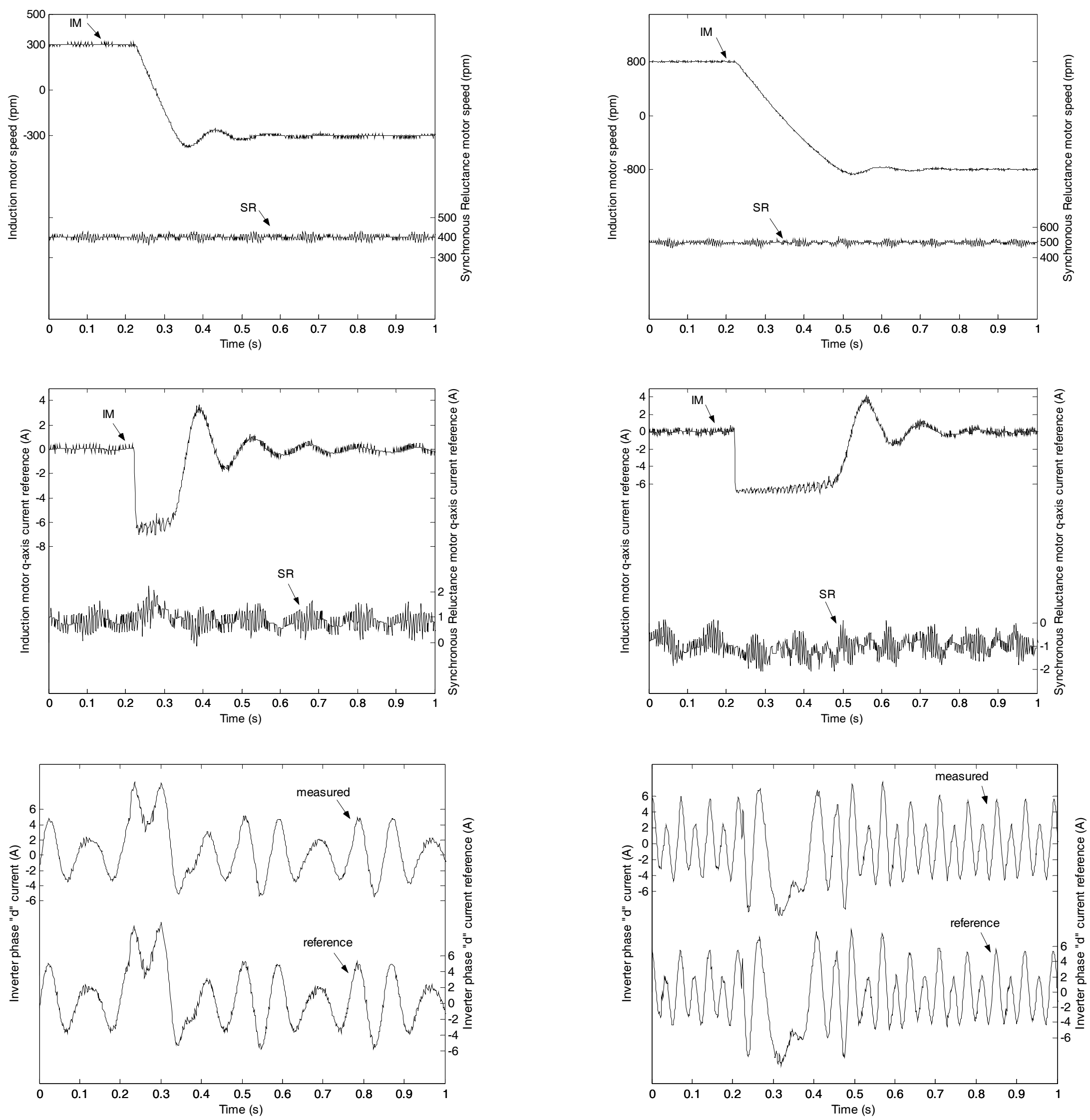

a. b.

Fig. 9.25. Reversing transients of the five-phase induction motor (synchronous reluctance motor at constant speed): a. 300 to –300 rpm, b. 800 to –800 rpm.

Induction motor is accelerated to 500 rpm and synchronous reluctance motor is accelerated to 300 rpm. A step load (12 Ω) is applied to the induction motor and the transients are recorded. The response is illustrated in Fig. 9.26a. Similarly, step unloading is done for induction machine and the response is shown in Fig. 9.26b. The q-axis current reference of induction machine shows damped oscillation. There is no appreciable change in the q-axis current reference of synchronous reluctance machine, which indicates good control decoupling between the two machines during loading and unloading transients. By comparing Fig. 9.13 with Fig. 9.26, it can be concluded that the series connection does not affect the drive behaviour.

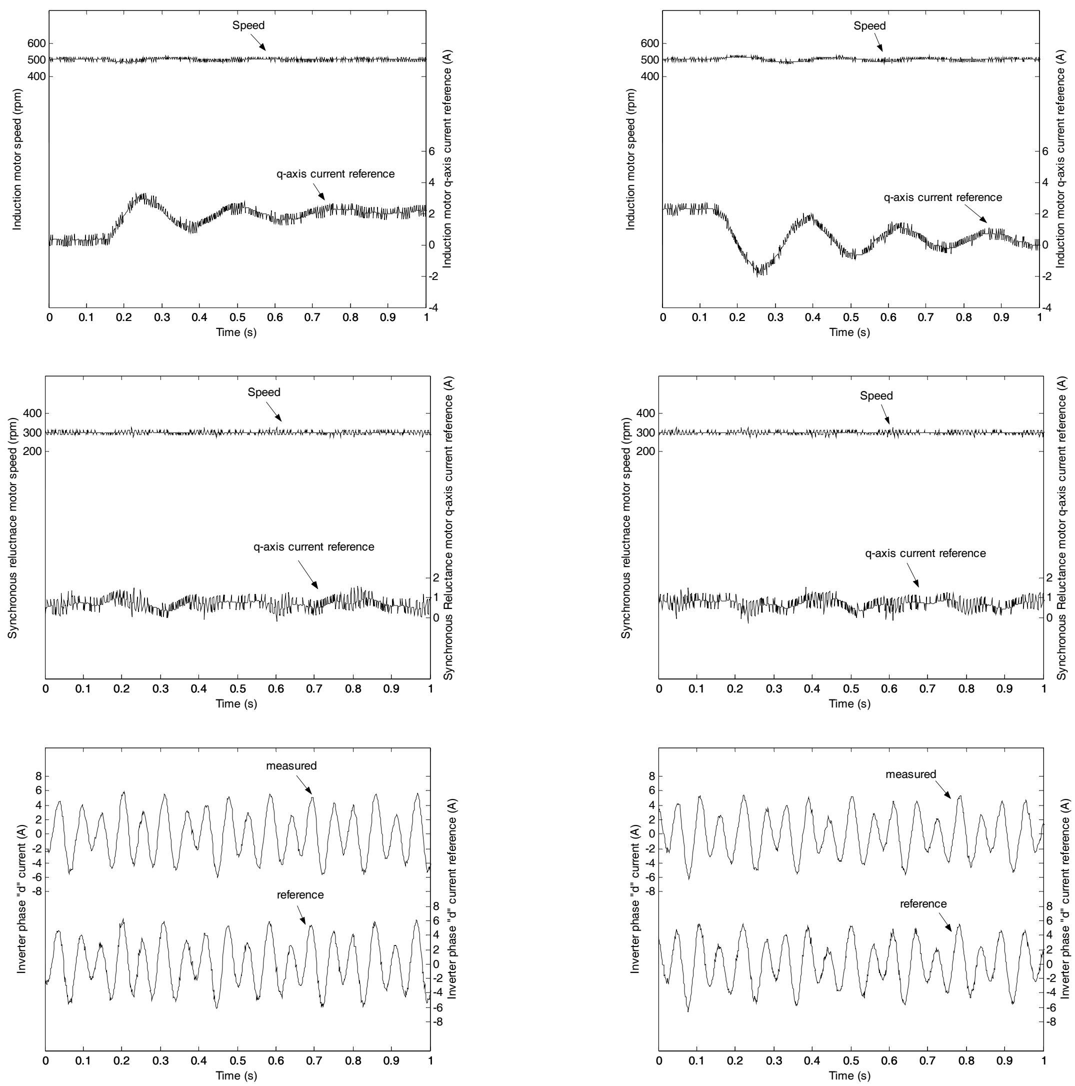

a. b.

Fig. 9.26. Loading/unloading transients of the five-phase induction motor at 500 rpm (synchronous reluctance motor at constant speed of 300 rpm): a. step loading, b. step unloading.

9.7.2 Five-phase synchronous reluctance motor transients

This section presents the transients of the five-phase synchronous reluctance motor. The five-phase induction motor runs at constant speed and the acceleration, deceleration and reversal transients are initiated for synchronous reluctance motor. The approach adopted is the same as the one used in section 9.7.1. The plots are given in Figs. 9.27-29.

Synchronous reluctance motor accelerations from 0 to 300 rpm and from 0 to 800 rpm, while induction motor runs at constant speed of 600 rpm and 500 rpm, repectively, are recorded. The plots are shown in Figs. 9.27 a-b. Almost perfect control decoupling between two series-connected machines can be observed, with a negligebly small variation in q-axis

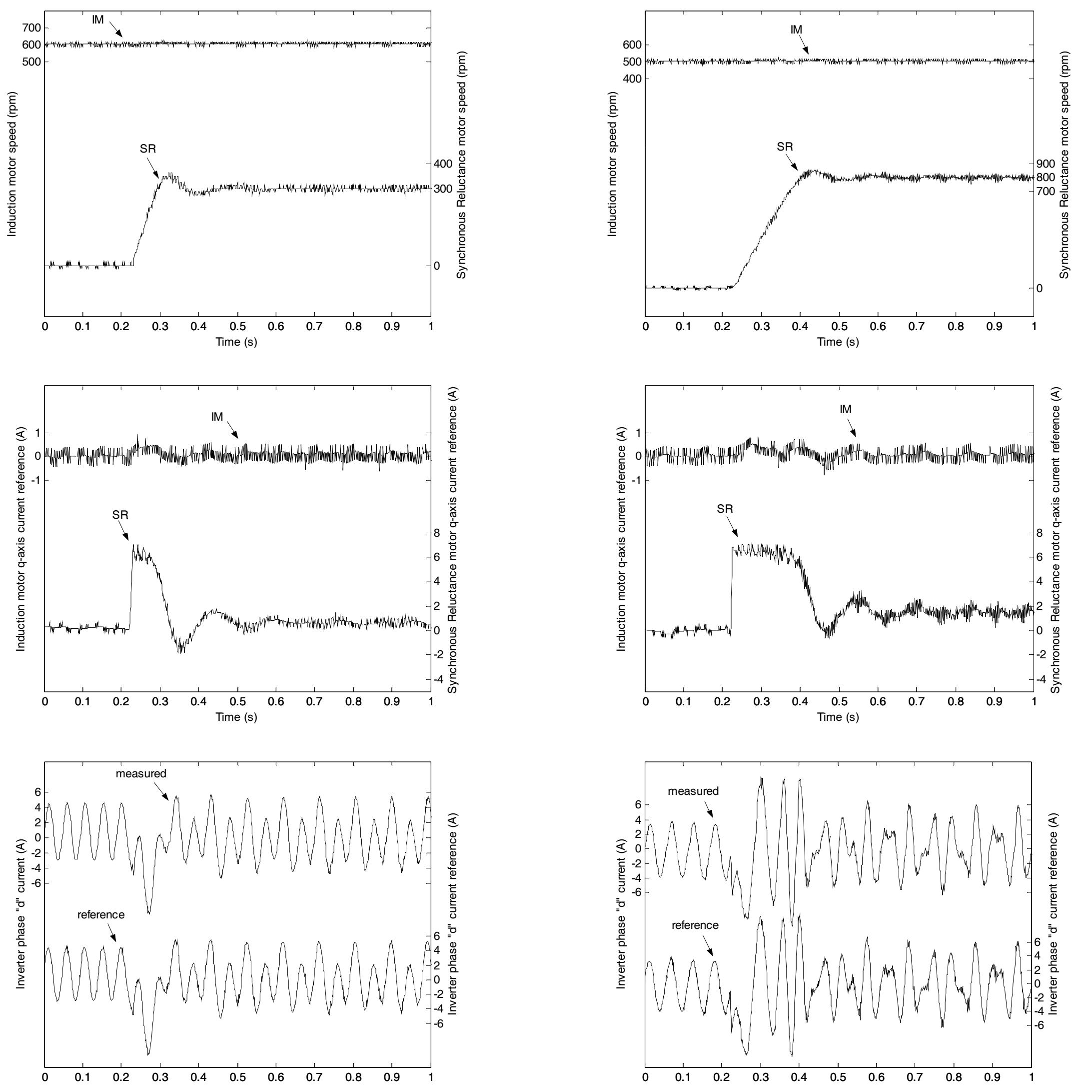

a. b.

Fig. 9.27. Acceleration transients of the synchronous reluctance motor (induction motor at constant speed): a. 0 to 300 rpm, b. 0 to 800 rpm.

current of the induction machine. Further comparison of Fig. 9.27 with Fig. 9.16 shows practically identical response of the synchronous reluctance motor in the two-motor and the single-motor drive mode. Thus the series connection has a negligible impact on the dynamic behaviour of the synchronous reluctance motor.

The deceleration transients of synchronous reluctance motor from 300 to 0 rpm and 800 to 0 rpm are illustrated in Figs. 9.28 a-b. The induction motor runs at 600 rpm and at 500 rpm, respectively. The same quality of performance is observable in deceleration transients as seen during acceleration transients. Only a very small variation in the q-axis current of induction machine is observed during the synchronous reluctance motor transient.

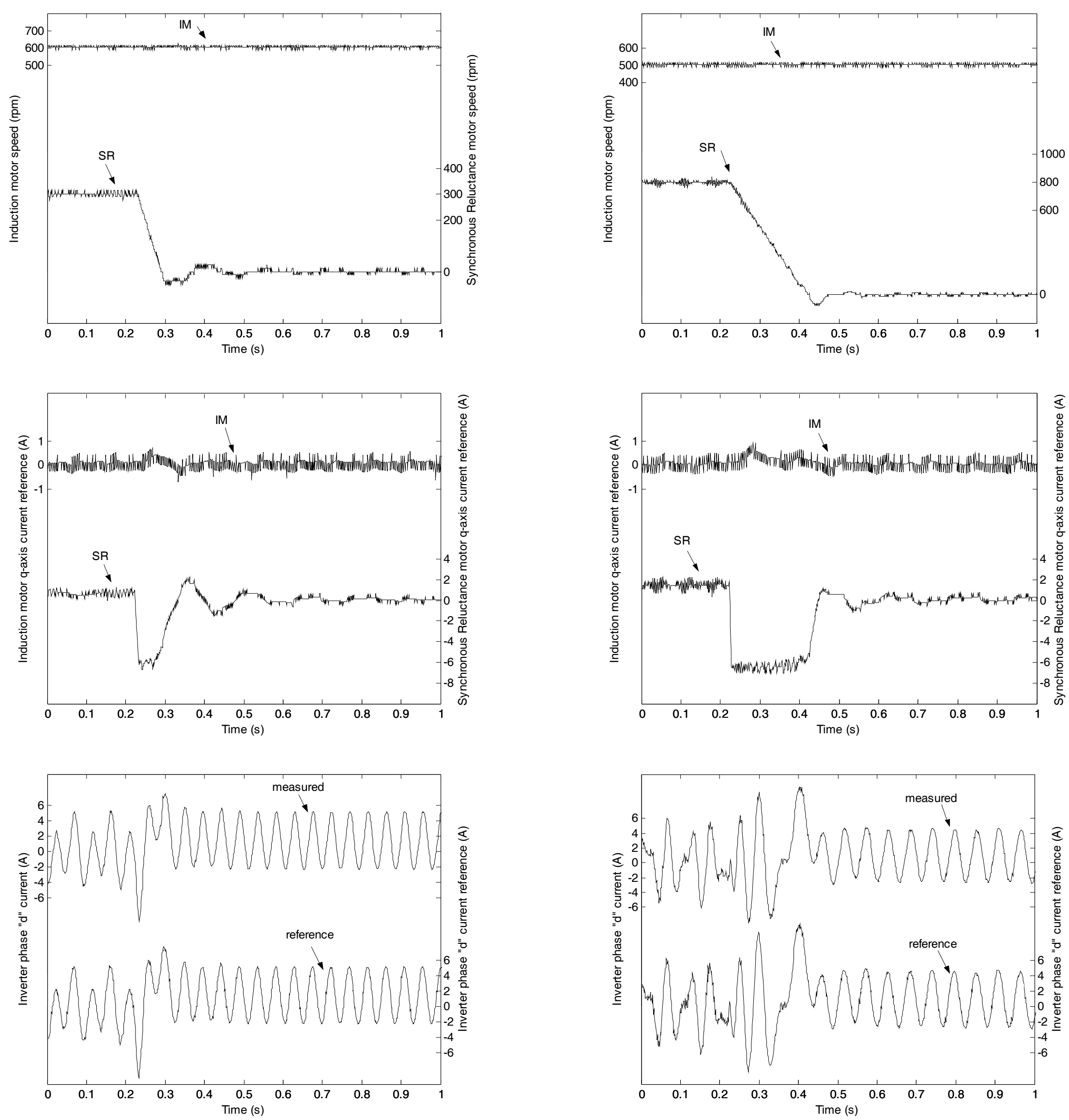

a. b.

Fig. 9.28. Deceleration transients of the synchronous reluctance motor (induction motor at constant speed): a. 300 to 0 rpm, b. 800 to 0 rpm.

The synchronous reluctance motor speed reversals are investigated for 300 to –300 rpm and 800 to –800 rpm. The results are shown in Figs. 9.29 a-b. The induction motor runs at 400 rpm and at 600 rpm, respectively, for these two transients. Once again, an excellent dynamic decoupling of control of the induction motor and the synchronous reluctance motor is evident. A negligibly small disturbance in the q-axis current of the induction machine is once more observed.

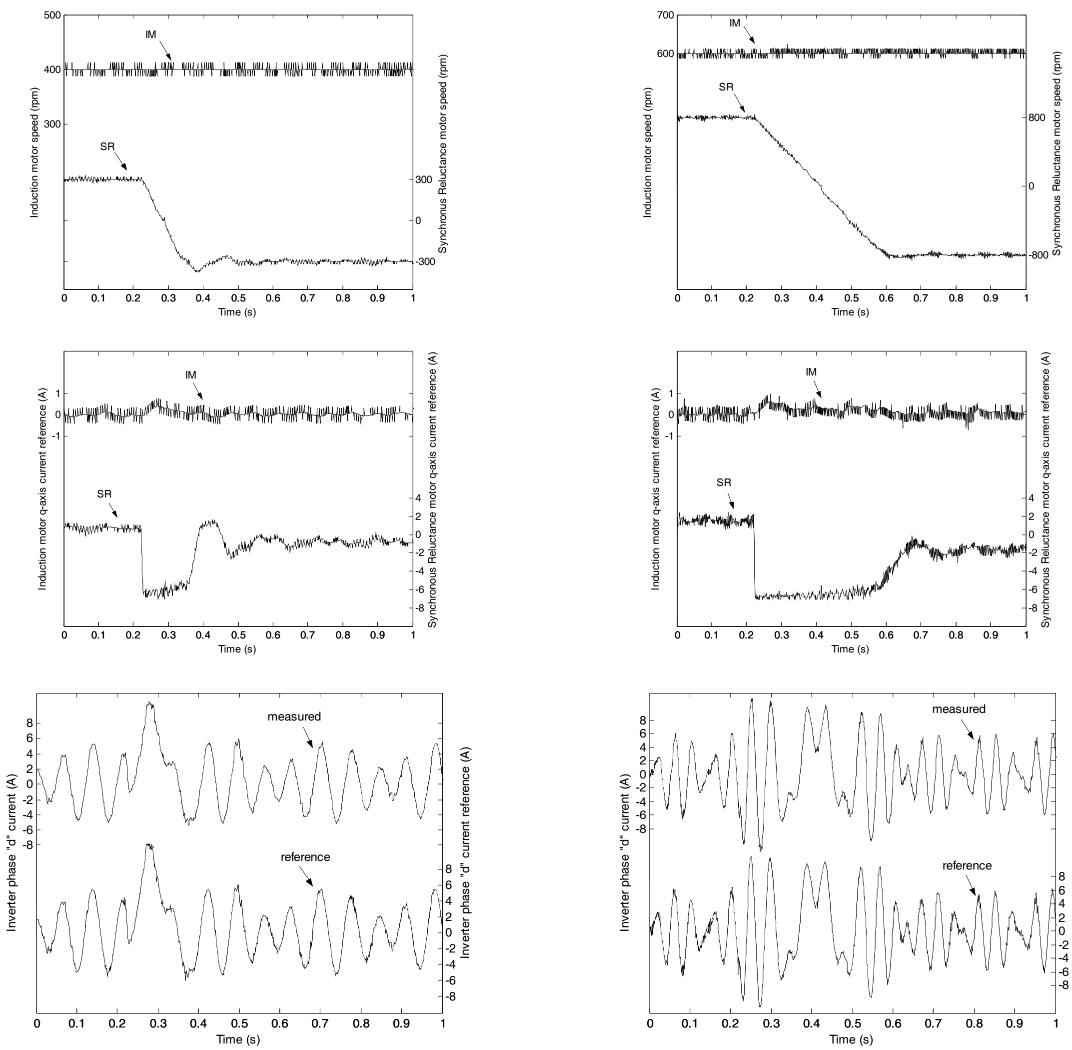

a. b.

Fig. 9.29. Reversing transients of the synchronous reluctance motor (induction motor at constant speed): a. 300 to –300 rpm, b. 800 to –800 rpm.

9.8 EXPERIMENTAL INVESTIGATION OF STEADY STATE OPERATION

The steady state behaviour of the five-phase single-motor (sections 9.4 and 9.5) and two-motor drives (sections 9.6 and 9.7) is elaborated in this section. Stator currents are measured for all the four configurations under no-load steady state conditions. The resulting current waveforms and corresponding spectra are presented. The line voltages are also recorded for the single-motor and two-motor drives under no-load steady state conditions. The resulting time domain and the corresponding frequency domain waveforms are presented. Operating conditions are chosen to match some of the cases described in dynamic analysis.

The equipment used for steady state current measurement comprises TEKTRONICS AM6203 Hall-effect current probe, TEKTRONICS AM503 amplifier and HEWLETT-PACKARD HP3566SA dynamic signal analyser. The range of current that can be measured using this probe is from 0 to 20 A with frequency from dc to 20 MHz. The amplifier is connected to the HP dynamic signal analyser to which it provides analogue signals up to ± 50 mV. The current waveform and the corresponding frequency spectrum are recorded using the HP dynamic signal analyser. The data stored using the scope is further processed in a PC using Matlab code to reconstruct the current waveforms and their spectra.

The line voltage measurement is done using a potential divider with an attenuation factor of 53. A low pass filter (simple R-C network) with cut-off frequency of 500 Hz is used to eliminate the high frequency PWM ripple. The voltage is recorded in differential mode by connecting two oscilloscope probes to two attenuated and filtered phase voltage signals. The two voltage signals are recorded using HP dynamic signal analyser. The recorded data are further processed in a PC using Matlab code to reconstruct the time-domain and frequency-domain waveforms.

9.8.1 Steady state performance of the single-motor drive system

This section illustrates the steady state performance of the five-phase single-motor drive. At first the results for the five-phase induction motor are presented. This is followed by the presentation of the five-phase synchronous reluctance motor results. The machines run under no-load condition.

The speeds considered for the single induction motor drive are 500 rpm (16.67 Hz) and 800 rpm (26.67 Hz). The time domain current waveforms and the corresponding spectra for low frequency range are shown in Figs. 9.30 a-b. The low-order current harmonics in the spectra are negligible. This confirms the good performance of the adopted current control scheme. The magnitude of the fundamental stator current (in essence the d-axis current) is in excellent agreement with the commanded value at 500 rpm (2.5 A, RMS). However, the small discrepancy between the actual and the commanded current appears at higher frequency (800 rpm). This is an inherent feature of the ramp-comparison current control and it has been discussed in more detail in conjunction with six-phase two-motor drive in Jones (2005).

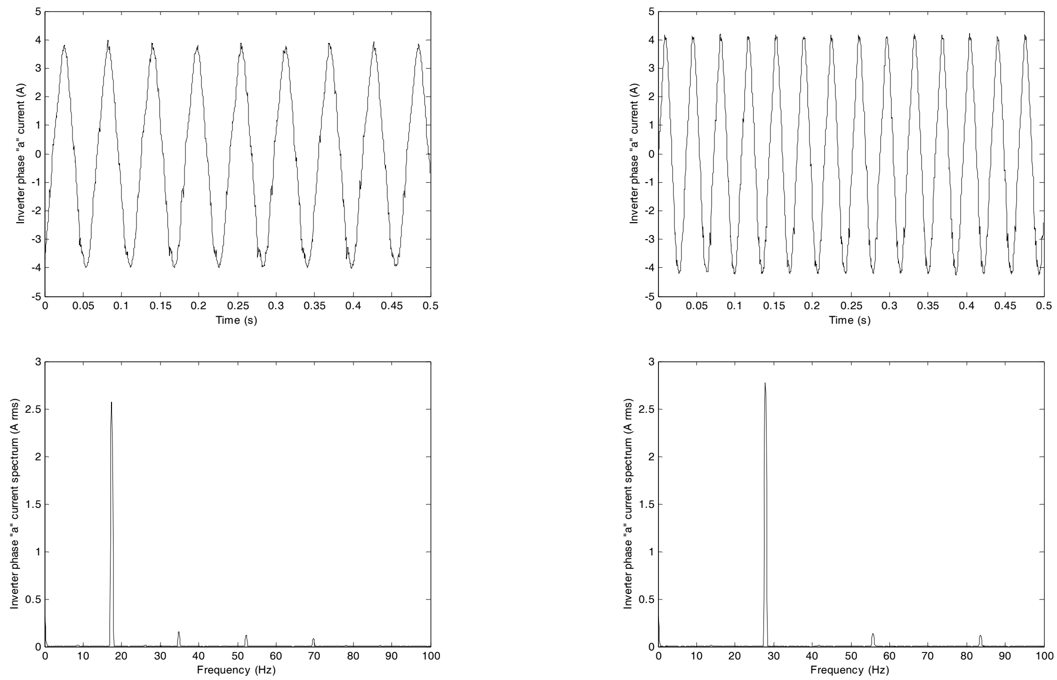

a. b.

Fig. 9.30. Steady state operation of the five-phase induction motor, phase current and its spectrum: a. 500 rpm (16.67 Hz), b. 800 rpm (26.67 Hz).

Line voltages and their corresponding low frequency spectra are recorded for the same operating speeds across phases ‘a-c’. The resulting waveforms are shown in Figs. 9.31 a-b. For voltage measurement, the second machine is removed from the circuit and the current controller gains are halved. This is done in order to eliminate the x-y voltage drops on the second machine. In five-phase system there are two possible line voltages (Chapter 3) called adjacent (72°, phase displacement) and non-adjacent (144°, phase displacement). Both line voltages are measured here. The ratio of the magnitude of non-adjacent to adjacent voltage is 1.618 (Chapter 3). The ratio is found to be 1.603 for 500 rpm and 1.633 for 800 rpm which is close to the theoretical value. The low-order harmonics are almost completely eliminated from the voltage waveforms due to the adopted current control scheme.

Next, the operation of the five-phase synchronous reluctance motor is investigated for steady state no-load conditions. The speed considered for this configuration is 800 rpm (26.67 Hz). The resulting time-domain waveform and the corresponding low frequency spectrum for phase current is illustrated in Fig. 9.32. Some low-order harmonic are observed in the phase current spectrum. This is believed to be the consequence of saliency and slotting effects, which are inherent to the synchronous reluctance motor. However, a more detailed investigation of this phenomenon has not been undertaken.

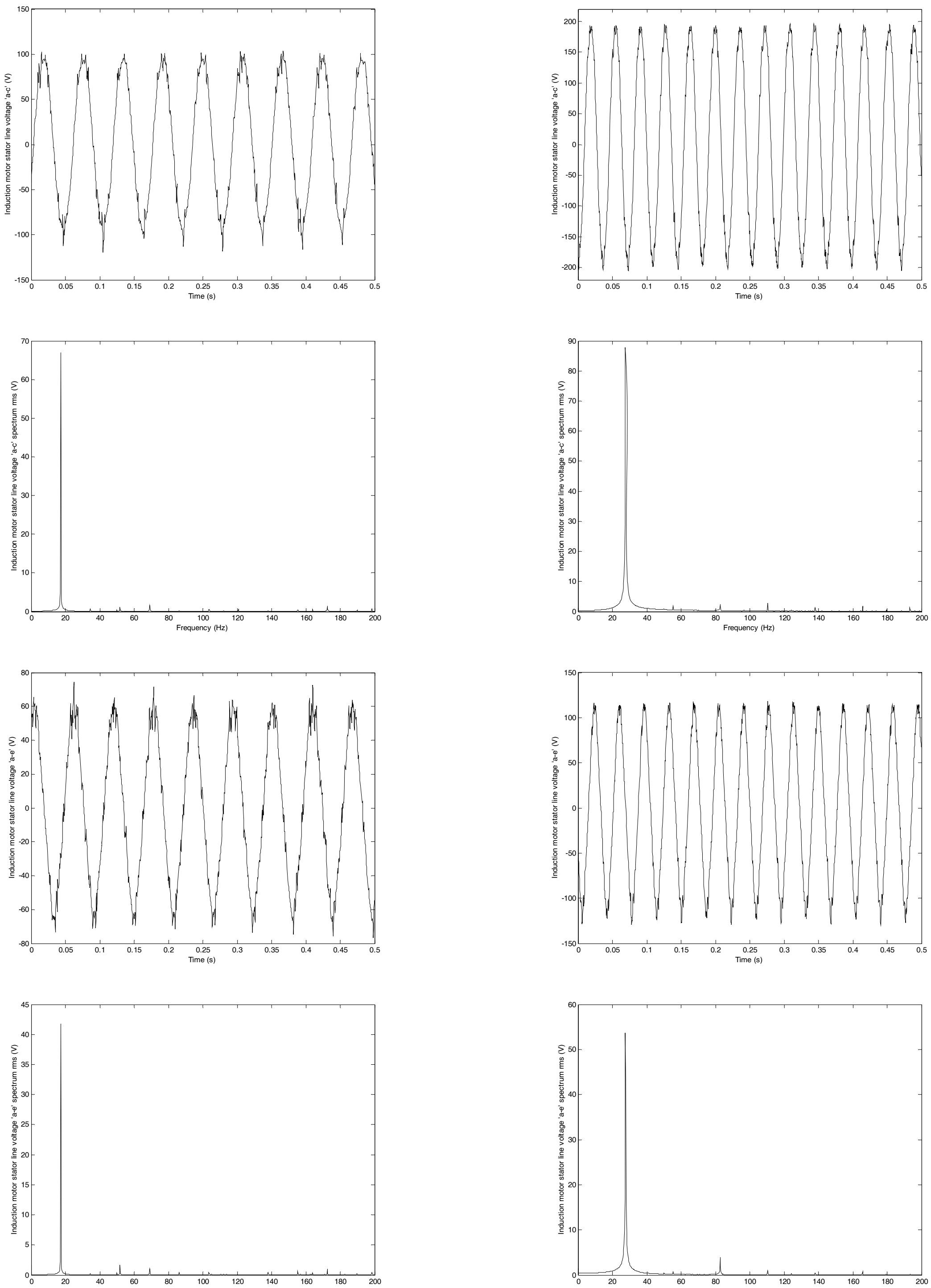

a. b.

Fig. 9.31. Steady state performance of the five-phase induction motor, line voltages and their spectra: a. 500 rpm (16.67 Hz), b. 800 rpm (26.67 Hz). Non-adjacent line-to-line voltages in the upper part and adjacent lint-to-line voltages in the lower part of the figure.

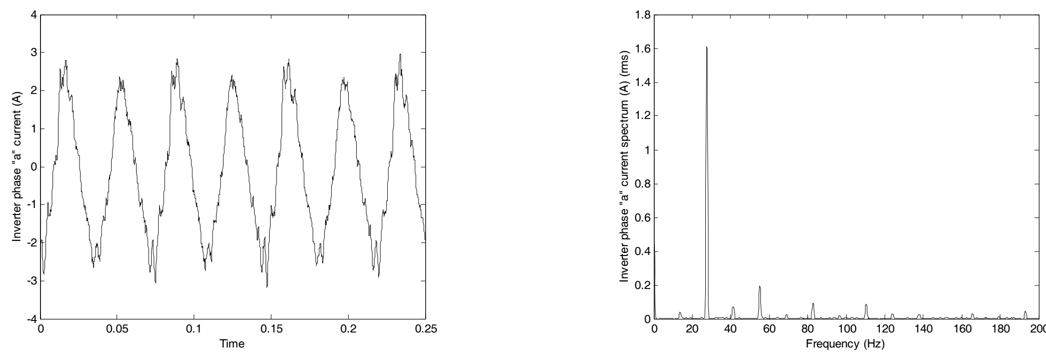

Fig. 9.32. Steady state operation of the five-phase synchronous reluctance motor, phase current and its spectrum at 800 rpm (26.67 Hz).

The line voltages are also recorded for the same operating speeds of the synchronous reluctance motor. The line voltage is measured after removing the second machine from the circuit and reducing the current controller gains to half the original value. Both the adjacent and non-adjacent line voltages are recorded and ratio of their magnitude is found to be 1.6385. The time-domain waveforms and corresponding spectra are presented in Fig. 9.33. Once more, low-order harmonics are seen in the spectra. The low-order harmonics are more prominent in the adjacent line voltage spectra.

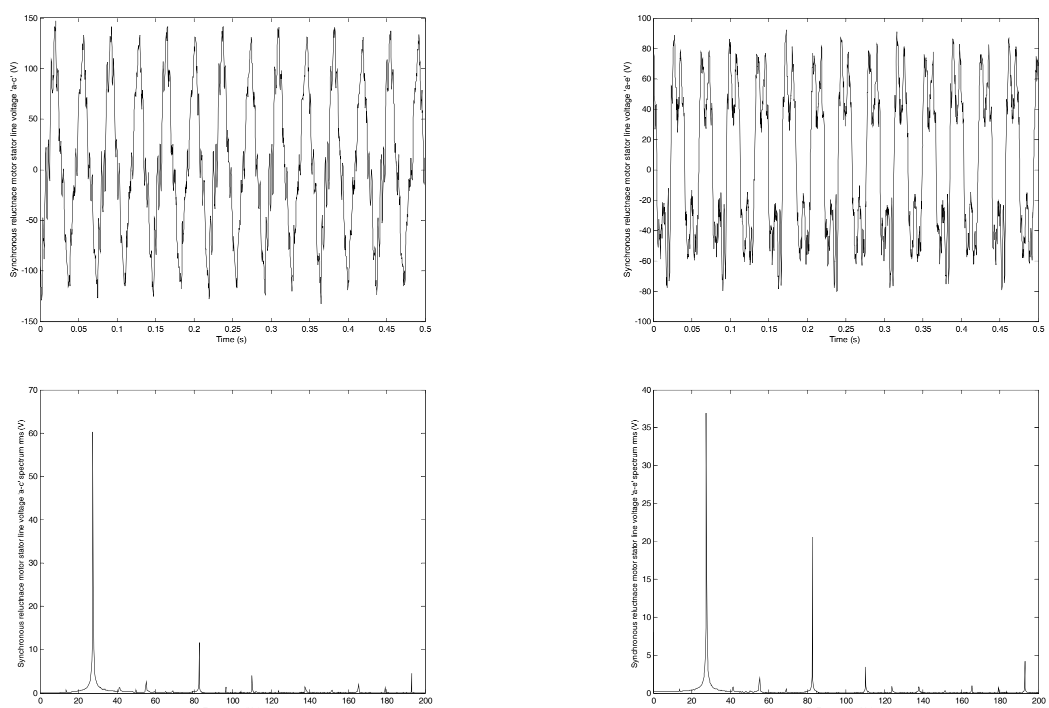

Fig. 9.33. Steady state operation of the five-phase synchronous reluctance motor, line voltages and their spectra (non-adjacent left and adjacent right) for 800 rpm (26.67 Hz).

9.8.2 Steady state performance of the two-motor drive system

This section examines the steady state operation of the five-phase two-motor drive systems (section 9.6 and section 9.7). At first the results are given for the two series-connected induction machines. The results are presented next for the two-motor drive consisting of the induction machine and the synchronous reluctance machine.

The phase current measurement is done using the same method as described in section 9.8. The inverter phase 'a' current is measured at the point of connection of the inverter with the induction machine. Thus the measured current is the sum of phase 'a' current of IM1 and phase 'a' current of IM2. The operating speeds of IM1 and IM2 are 800 rpm (26.67 Hz) and 500 rpm (16.67 Hz), respectively. The time-domain and frequency-domain plots for inverter phase 'a' current are illustrated in Fig. 9.34. The inverter phase current is essentially a sum of two sinusoidal components at two frequencies corresponding to the operating speeds of two machines, as seen in the spectrum. The current component at 16.67 Hz closely corresponds to the stator d-axis current setting (2.5 A, RMS), while at 26.67 Hz it is slightly higher than the commanded value. These current RMS values are consistent with the single-motor drive case (Fig. 9.30). The magnitude of the low-order harmonic components in the current spectrum is very small. Thus the quality of the current control is very good.

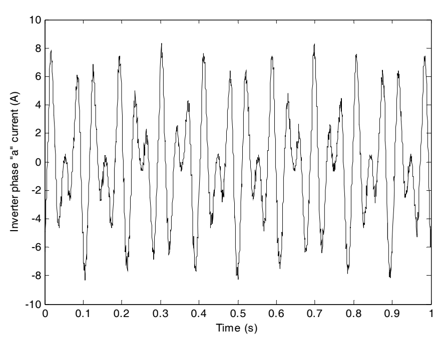

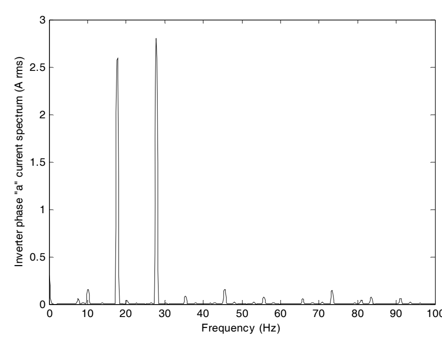

Fig. 9.34. Steady state operation of the two-motor drive (two induction motors), inverter phase current and its spectrum (IM1 at 800 rpm and IM2 at 500 rpm).

The line voltage measurement is undertaken at the point of connection of the inverter with induction machine IM1 across phase 'a' and phase 'c' and across phase 'a' and 'b'. The line voltage is also measured across the phases 'a-c' and 'a-e' of IM2. The resulting time-domain and frequency-domain plots are shown for inverter voltage and stator voltage of IM2 in Fig. 9.35a and Fig. 9.35b, respectively. Two voltage components are expected corresponding to the operating frequencies of the two machines. Since IM1 is connected directly to the inverter and IM2 is connected to IM1, line voltage a-c on inverter side refers to the non-adjacent line voltage for IM1 and adjacent voltage for IM2 and vice versa for the line voltage measured across ‘a-c’ on IM2 side. The line voltage measured across ‘a-b’ corresponds to the adjacent voltage for IM1 and non-adjacent voltage for IM2. The voltage across ‘a-e’ on IM2 side corresponds to the adjacent for IM2 and non-adjacent for IM1. The inverter line voltage across ‘a-c’ corresponding to the operating frequency of IM1 (26.67 Hz) is expected to be higher than in the single-motor drive case due to the additional x-y voltage component of IM2. The result obtained here (91.3 V) is 3.98% higher than the single-motor drive case (87.8 V). Similarly, the line voltage corresponding to the operating frequency of IM2 is expected to be higher than the single-motor drive case again due to additional x-y voltage drop of IM1. The value recorded here (45.5 V) is 8.85% higher than in the single-motor drive case (41.8 V). The inverter line voltage across ‘a-b’ corresponding to the operating frequency of IM1 (62.5 V) is 16.6% higher than in the single-motor drive case (53.6 V). The line voltage corresponding to the operating frequency of IM2 (69.36 V) is 3.52% higher than its single-motor drive counterpart (67 V).

Consider next the line voltages measured on the IM2 end. The voltages corresponding to the operating frequency of IM1 (around 26.67 Hz) are only the x-y voltage drops on IM2. The voltages at the operating frequency of IM2 closely match with the values of the single-motor drive case, as can be seen by comparing the results in Fig. 9.31a with those of Fig. 9.35b.

The measurements are undertaken next for two-motor drive system consisting of the five-phase synchronous reluctance machine and the five-phase induction machine. The inverter is directly connected to the synchronous reluctance motor and the induction motor is connected to the synchronous reluctance motor. The inverter phase ‘a’ current is measured at the point of connection of the inverter with the synchronous reluctance motor. Thus the measured current is the sum of phase ‘a’ current of the synchronous reluctance motor and phase ‘a’ current of the induction motor. The operating speeds of synchronous reluctance motor and induction motor are 800 rpm (26.67 Hz) and 500 rpm (16.67 Hz), respectively. The time-domain and frequency-domain plots for inverter phase ‘a’ current are illustrated in Fig. 9.36. The inverter phase current is essentially a sum of two sinusoidal components at two frequencies corresponding to the operating speeds of two machines as seen in the spectrum. The synchronous reluctance motor related current component at 26.67 Hz is slightly higher compared to the corresponding single-motor drive case (Fig. 9.32). The increase in the current is believed to be the consequence of the higher losses in the synchronous reluctance motor

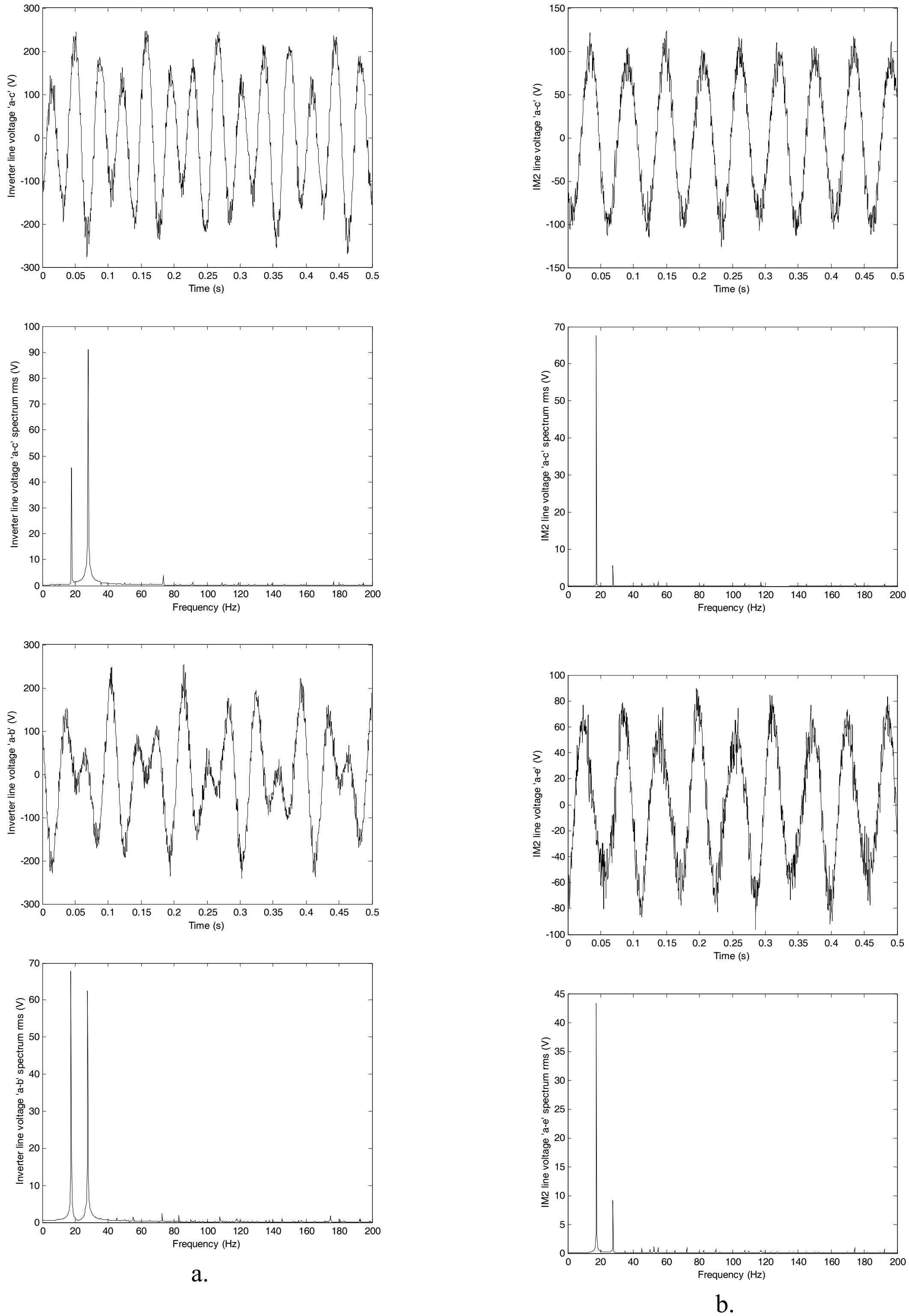

Fig. 9.35. Steady state operation of two-motor drive (two induction motors), line voltages and their spectra (IM1 at 800 rpm and IM2 at 500 rpm): a. Inverter line voltages, b. IM2 stator line voltages.

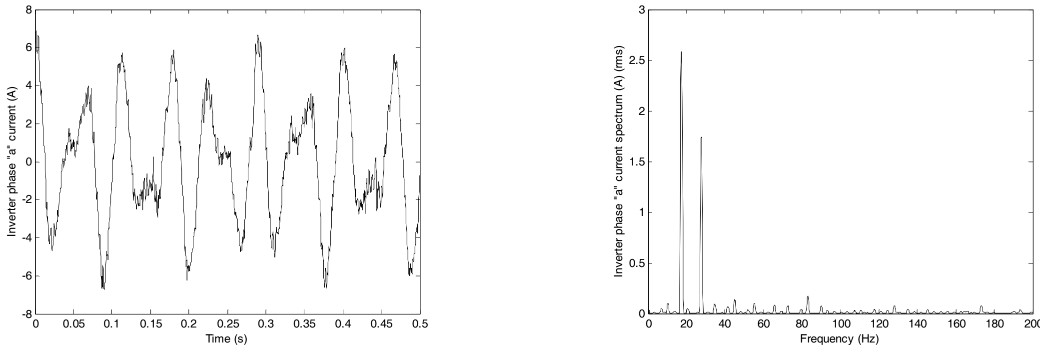

Fig. 9.36. Steady state operation of two-motor drive (synchronous reluctance motor and induction motor), phase current and its spectrum (SR at 800 rpm and IM at 500 rpm).

due to series connection. The current spectrum at 16.67 Hz closely corresponds to the stator d-axis current setting for the induction motor (2.5 A, RMS). The magnitude of low-order harmonic components in the current spectrum is very small. Thus it follows that the quality of the current control method is very good.

The line voltage measurement is undertaken at the point of connection of inverter with synchronous reluctance motor across phase ‘a’ and phase ‘c’ and across phases ‘a-b’. The line voltage is also measured across the phases ‘a-c’ and phases ‘a-e’ of induction motor. The resulting time-domain and frequency-domain plots are shown for inverter voltages and stator line voltages of IM in Fig. 9.37a and Fig. 9.37b, respectively. Since synchronous reluctance motor is connected directly to the inverter and induction motor is connected to synchronous reluctance motor, line voltage a-c on inverter side refers to the non-adjacent line voltage for synchronous reluctance motor and adjacent voltage for induction motor and vice versa for the line voltage measured across a-c on induction motor side. The line voltage measured across ‘a-b’ of inverter corresponds to the adjacent line voltage for synchronous reluctance motor and non-adjacent for IM. The line voltage measured across ‘a-e’ of IM corresponds to the adjacent line voltage for synchronous reluctance motor and non-adjacent for IM. The inverter line voltage corresponding to the operating frequency of synchronous reluctance motor (26.67 Hz) is expected to be higher than in the single-motor drive case due to the additional x-y voltage component of induction motor and higher current. The result obtained here (67.69 V) is 12.25% higher than in the single-motor drive case (60.3 V). A third harmonic component of voltage is observed corresponding to the operational speed of synchronous reluctance motor. It is negligibly small in the ‘a-c’ line-to-line voltage and just above 5 V in ‘a-e’ line-to-line voltage. The voltage component at 16.67 Hz is in essence identical in both line-to-line voltages as it was in Fig. 9.35 (two induction motors in series). Since the running speed of IM is 500 rpm in both cases, this confirms repeatability of the tests. The voltage corresponding to the operating frequency of IM (43.18 V) is 3.3% higher than in the single-motor drive case (41.8 V) due to the extra x-y voltage drop on synchronous reluctance motor. The inverter voltage across phases ‘a-b’ also contains two voltage components. The voltage corresponding to the operating frequency of synchronous reluctance motor (40.6 V) is 10.32% higher than in the single-motor drive case (36.8 V). The voltage corresponding to the operating frequency of IM (68.13 V) is 1.68% higher than in the single-motor drive case (67 V). A third harmonic component is again observed corresponding to the synchronous reluctance motor operating speed.

Consider next the voltages measured on the induction motor side. The voltage component corresponding to the operating frequency of the synchronous reluctance motor is the x-y voltage drop. This component should not exist and its appearance requires a further investigation, which is beyond the scope of this thesis. The voltage values corresponding to the operating frequency of IM closely correspond to the values obtained in the single-motor drive case (Fig. 9.31).

9.9 SUMMARY

This chapter has detailed the experimental investigation related to five-phase single-motor and five-phase series-connected two-motor drives. The experimental rig is described first. The five-phase variable voltage and variable frequency supply is obtained from two commercial MOOG DS2000 three-phase VSIs. The five-phase supply is used to run one five-phase machine and two five-phase machines connected in series.

Experiments are conducted at first on the single five-phase induction motor drive under indirect vector control conditions. The transients examined are acceleration, deceleration, reversing and disturbance rejection. Full decoupling of flux and torque control is achieved, thus validating the simulation results of Chapter 3. Further, a five-phase synchronous reluctance machine is tested for the same transients and once again very good response is observed. Experiments are further performed on the five-phase two-motor drive with two identical induction machines. The transients are initiated for one of the two induction machines while the other machine is operated at a constant speed. The results obtained show an excellent dynamic decoupling between the two machines under test. The results are also compared with the single-motor drive and it is concluded that nothing changes in the behaviour of the machine undergoing transients, regardless of whether it is a single-

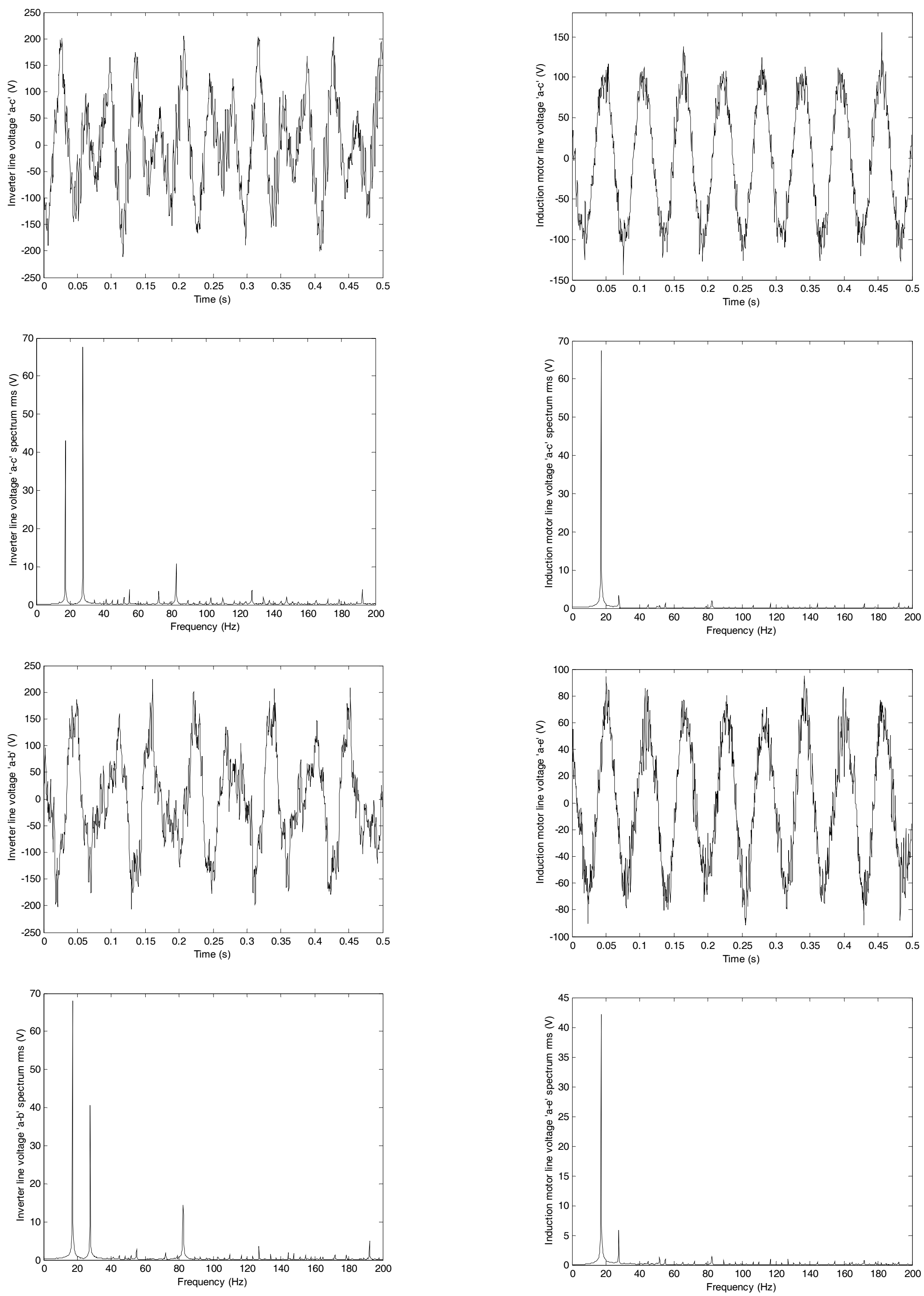

a. b.

Fig. 9.37. Steady state operation of two-motor drive (synchronous reluctance motor and induction motor), line voltages and their spectra (SR at 800 rpm and IM at 500 rpm): a. Inverter line voltages, b. IM stator line voltages.

motor or a two-motor drive. Thus the theoretical foundations, laid down in Chapter 4, are confirmed experimentally.

The concept of multi-phase multi-motor drive is independent of the type of ac machines under consideration. This is further confirmed by using one five-phase induction machine in series with a five-phase synchronous reluctance machines. The transient behaviour obtained for this configuration validates this statement.

Steady state behaviour of the single-motor and two-motor drive is also analysed. The current and voltage spectra are examined for all four cases studied previously in transient operation. In two-motor drive system, the current and voltage spectra show two fundamental components at the operating frequencies of the two machines, which is in full agreement with the presented theory.

Chapter 10

CONCLUSION

10.1 SUMMARY AND CONCLUSIONS

This thesis deals with various aspects of the five-phase two-motor and six-phase two-motor series-connected drive systems, fed using a single current-controlled pulse width modulated voltage source inverter. Modelling and control of a five-phase induction machine is considered first. It can be seen from the developed model that only two stator current components are responsible for torque and rotor flux production while other components are non flux/torque producing. These additional degrees of freedom are further utilized to connect in series the other machine in such a way that the flux/torque producing current components of one machine become non flux/torque producing currents for the other machine and vice versa. This is enabled by an appropriate phase transposition of the phases of the stator windings. The vector control then enables independent flux and torque control of each machine in two-motor drive system, as well as an independent control of two machines with respect to each other.

The major advantages of the proposed scheme are the reduction in the number of inverter legs, when compared to an equivalent two-motor three-phase drive system, and easiness of implementation of the whole control algorithm in a single DSP. The reduction in the number of inverter leg implies smaller number of electronic components, which translates into higher reliability. Use of a single DSP means simple and cheaper control. Another advantage of the developed scheme is the possibility for direct utilisation of the braking energy by the motoring machine in the multi-motor drive group. Thus the braking energy needs not to flow back to the inverter. Hence the proposed multi-phase multi-motor drive system provides full regenerative braking as long as the total braking energy is smaller than the motoring energy.

The major shortcoming of the five-phase two-motor drive system is the increase in the stator winding losses due to flow of flux/torque producing current of both machines through stator windings of both machines. As x-y components of current do not flow in the rotor the rotor copper losses are not affected. The higher losses mean lower efficiency of individual machines and will lead to reduction of efficiency of the overall drive system, compared to an equivalent three-phase drive system. This drawback is significant in the five-phase two-motor drive system since both machines are affected.

This shortcoming of the five-phase two-motor drive prevents its application in general-purpose drives. However, one potential application area for this drive configuration has been identified, where it may offer considerable saving in the installed inverter power when compared to the standard solution with two three-phase motors and two three-phase VSIs. The area includes processes where the two motors are required to operate in the constant power mode, with opposing requirements on rotational speeds and torques. Such a situation arises in winders. In winder applications one machine typically operates at low speed (low voltage) with high torque (high current) while the other machine operates at high speed (high voltage) with low torque (low current). Thus the situation may be such that the total stator copper losses remain less than or equal to the rated value, hence avoiding the need for de-rating of the machines. The total losses compared to the conventional three-phase two-motor drive, would still be higher. However, the rating of the five-phase VSI may be kept approximately equal to the rating of just one three-phase VSI, thus enabling saving in the installed power.

A complete mathematical model of the five-phase voltage source inverter has been developed for operation in ten-step and PWM modes. The model is developed on the basis of space vector representation and the results obtained are verified using the available literature on modelling of five-phase inverters. Current control schemes for three-phase inverters are reviewed and speed and current controllers are designed for the single five-phase motor drive. The current control is exercised upon the phase currents of the drive. Performance of a vector controlled single five-phase induction motor drive, obtainable with hysteresis current control and ramp-comparison control methods, is evaluated and illustrated for a number of operating conditions on the basis of simulation results. Full decoupling of rotor flux control and torque control was realised by both current control techniques under the condition of a sufficient voltage reserve. Dynamics, achievable with a five-phase vector controlled induction machine, are identical to those obtainable with a three-phase induction machine. Steady state analysis of stator voltages and currents under no-load conditions is performed as well.

A novel mathematical model for two-motor five-phase series-connected drive is developed in Chapter 4. The model is at first constructed in phase variable form. Clark’s transformation in power invariant form is then applied to develop a set of decoupled equations. Application of appropriate rotational transformations leads to corresponding models in stationary and arbitrary reference frames. Vector control scheme is developed next for the two-motor drive system. The simulation is done for various transients using a single current-controlled PWM voltage source inverter with hysteresis and ramp-comparison current control in stationary reference frame. Simulations were performed using both phase variable model and the novel d-q model in stationary reference frame, in order to validate the modelling procedure. Both models are found to yield the same simulation results. A completely independent control of two machines is observed from the simulation results. Finally, steady state analysis of inverter and stator voltages and inverter current is performed using harmonic spectrum analysis and the results obtained are found to be in full agreement with the theoretical predictions.

The second structure, analysed in the thesis, is the two-motor six-phase drive, supplied from a symmetrical six-phase VSI and consisting of a symmetrical six-phase machine and a three-phase machine, connected in series. In contrast to the two-motor five-phase drive, this configuration does not offer the advantage of a reduced number of inverter legs, when compared to an equivalent two-motor three-phase drive. The advantages related to the use of a single DSP for two-motor drive control and to direct utilisation of braking energy remain to be valid. On the other hand, the shortcoming related to an increase in the stator winding losses is here much less pronounced, since only six-phase machine is affected by connection to the three-phase machine. This is so since only the flux/torque producing currents of the three-phase machine flow through the six-phase machine. Provided that the three-phase machine is of a small power rating and that the six-phase machine is a high power machine, deterioration in efficiency of the six-phase machine will be negligible. It is therefore believed that this drive structure holds good prospect for industrial applications where a six-phase high-power machine is used anyway. In such a case a three-phase machine can be added to the existing drive at practically no extra cost and it can be used to perform an auxiliary function requiring small power rating.

A complete mathematical model of the six-phase voltage source inverter is developed for operation in 180° conduction mode, leading to square wave output, and in PWM mode. The model is developed on the basis of space vector representation. In PWM mode, 64 space vectors are available out of which 54 are active while 10 are zero vectors. A brief summary of the mathematical model of a true six-phase (60° spatial phase displacement) induction machine is presented in phase variable form. These equations are then transformed into an arbitrary rotating reference frame. The model once more shows that only two components (d-q) generate flux/torque, while the other set of orthogonal components, designated as x-y, are non flux/torque producing and merely produce current distortion. Another set of non flux/torque components are positive and negative zero-sequence components. It is further seen in the simulation results that the positive zero-sequence component is completely eliminated while negative zero-sequence component may be present because of the true six-phase configuration. Performance of a vector controlled single six-phase induction motor drive and single three-phase induction motor drive, obtainable with hysteresis current control and ramp-comparison control methods, is evaluated and illustrated for a number of operating conditions on the basis of simulation results. Full decoupling of rotor flux control and torque control was realised by both current control techniques under the condition of a sufficient voltage reserve. In essence, dynamics, achievable with a six-phase vector controlled induction machine, are identical to those obtainable with a three-phase induction machine. Steady state analysis of stator voltages and currents under no-load conditions is finally performed.

A novel mathematical model for two-motor six-phase series-connected drive is developed in Chapter 6. A three-phase induction machine is connected in series with a true six-phase induction machine with an appropriate phase transposition in order to enable fully decoupled control of two machines. The series-connected machines are fed using a single six-phase current controlled PWM voltage source inverter. The model of the series-connected six-phase drive system is at first constructed in phase variable state space form. Clark's transformation in power invariant form is then applied to develop a set of decoupled equations. Application of appropriate rotational transformations leads to corresponding models in stationary and arbitrary reference frames. The model of the whole assembly is also developed in specific rotor flux oriented reference frames. The developed model clearly shows the coupling of the rotor of the six-phase machine with the d-q inverter currents and the rotor of the three-phase machine with x-y inverter currents. This dependence enables the torque and flux control of the six-phase machine with inverter d-q currents and the flux and torque control of the three-phase machine with inverter x-y currents. A vector control scheme is utilised to control the machines independently. The simulation is done for various transients using a single current-controlled PWM voltage source inverter with hysteresis and ramp-comparison current control in stationary reference frame. Simulations were performed using both phase variable model and the novel d-q model in the stationary reference frame, in order to validate the modelling procedure. Both models are found to yield the same simulation results. A completely independent control of two machines is observed from the simulation results. Finally steady state analysis of inverter and stator voltages and inverter current is performed using harmonic spectrum analysis and the results obtained are found to be in full agreement with the theoretical predictions.

Space vector PWM is one of the most popular choices to implement current control of a VSI in rotational reference frame because of easier digital implementation and better dc bus utilisation. SVPWM for five-phase VSI is investigated in Chapter 7. At first the space vectors of a five-phase VSI, found in Chapter 3, are further mapped into x-y plane. It is seen that the large space vectors of $\alpha-\beta$ plane map into small space vectors, the medium space vectors remain in their positions while the short space vectors map into the large space vectors. The two zero vectors in $\alpha-\beta$ plane also map as zero vectors in x-y plane. It is further noted from this mapping that the x-y components appear as third harmonic. The existing technique of utilising only large space vectors to synthesise the input reference is analysed in detail. The method is found to yield a significant amount of low-order harmonics especially the 3^{rd} and the 7^{th}, in output phase voltages. A possible extension of this method is to use only medium space vectors. The simulation is carried out for this scheme and it shows poor output phase voltage quality with very large amount of low-order harmonics. This is because the medium space vectors in x-y plane are of equal magnitude as $\alpha-\beta$ space vectors, causing production of large amount of low-order harmonics. To provide sinusoidal phase voltages using SVPWM the x-y components have to be eliminated completely and this is possible by utilising both large and medium space vectors with appropriate ratio of time of application of these vectors. Thus the scheme is developed using this concept and the simulation shows sinusoidal output phase voltages. However, this scheme is found to be applicable only up to 85.41% of the maximum achievable fundamental using only large space vectors. To further extend the range of application of SVPWM, two more methods are proposed. One of the methods drives the VSI along the maximum available output voltage and the second method uses a pre-defined zero vector application time. Both of these methods are applicable for input reference over 85.41% of the maximum achievable fundamental and up to the maximum achievable $\left(0.6155V_{DC}\right)$. It is found that both of these methods yield near sinusoidal phase voltages with small low-order harmonic contents. A detailed comparison of existing and newly developed schemes is also given and a combined method is suggested to cover the entire range of operation. Analytical expressions for leg voltages are derived for existing and developed schemes and are verified using simulation results. Further, SVPWM scheme is developed for a five-phase VSI feeding two five-phase machine connected in series. The aim of the scheme is to yield output voltage with two sinusoidal components at desired operating frequencies of the two machines. $\alpha-\beta$ and x-y references are applied sequentially to control two machines independently. The simulation results validate the theoretical findings.

SVPWM for six-phase VSI is analysed in Chapter 8. The space vector model of the six-phase VSI, developed in Chapter 5 is further mapped into x-y plane. It is seen that six large space vectors in $\alpha-\beta$ plane map into the origin of x-y plane. Out of the total of ten zero vectors in $\alpha-\beta$ plane, six zero space vectors form the large vector set in x-y plane and the remaining four zero vectors map into the origin of the x-y plane. The number of zero vectors remains ten in x-y plane and there are 54 active vectors in both $\alpha-\beta$ and x-y plane. The basic principle of SVPWM is taken from Correa et al (2003a) and (2003b). The first method uses vectors from large and middle sets. The simulation results show a considerable amount of low-order harmonic content (3^{rd}) in the output phase voltages, which remains more or less constant (approximately 20%) throughout. The low-order harmonic content in the output phase voltages is due to the presence of zero-sequence components of large vectors. The second method uses short and medium set of space vectors and yields approximately 40% of the 3^{rd} harmonic in output phase voltages, due to the presence of zero-sequence components of short vectors. The operational range of this method is smaller than for the first method. Another analysed method utilises space vectors from large, medium and short vector sets and the times of application of short and large vectors are the same. This technique yields sinusoidal output phase voltages due to complete elimination of zero-sequence and x-y components. However, the range of operation of this method is still smaller than for the first method. To cover the entire range, a fourth method is suggested which utilises again all the available vectors but the times of application of short and large vectors are variable (in contrast to the third method where they are equal). This scheme yields variable low-order harmonics in the output phase voltages. Analytical expressions for leg voltages for every scheme are determined and are validated using simulation results. In addition to the low-order harmonic content, total harmonic distortion in the output phase voltages is found for all the discussed schemes. A detailed comparison of the existing and newly developed schemes is presented. Further, a SVPWM scheme is developed for a six-phase VSI feeding a series-connected six-phase and a three-phase machine. The goal of this SVPWM scheme is again to provide output voltages containing only two fundamental components at desired operating frequencies of the two machines. $\alpha-\beta$ and x-y modulators are developed, which apply $\alpha-\beta$ and x-y references, respectively, in an alternating manner. The viability of the proposed scheme is proved by simulation.

The ultimate proof of the existence of means for decoupled control of two series-connected machines is provided experimentally for the two-motor five-phase drive. At first, dynamic and steady state performance of a single five-phase induction motor and a single five-phase synchronous reluctance motor under vector control is investigated for no-load and loaded conditions (base speed region). Typical vector control behaviour of the drive is achieved. Dynamic and steady state performance of five-phase two-motor drive comprising two five-phase induction machines are examined for no-load and loaded conditions. The experimental results fully confirm the existence of full control decoupling between the two machines. Finally, application of two five-phase ac machines of different type in a multi-motor drive group is examined. The five-phase two-motor drive configuration consisting of a five-phase induction motor and a five-phase synchronous reluctance motor is considered. Once more the experimental results fully verify that the control of the two series-connected machines is truly decoupled.

By comparing the work described in this thesis with the research objectives listed in section 1.4 it can be concluded that all the set goals have been achieved successfully.

10.2 FUTURE WORK

This project explores the feasibility of independent control of five-phase and six-phase two-motor drive systems, fed from a single five-phase and single six-phase current regulated PWM voltage source inverter, respectively. Since both drive structures are novel, it is believed that there is plenty of scope for further research. Some possible directions are the following:

- Investigation of the feasibility of using parallel connection of multi-phase machines, with supply coming again from one VSI. The analogy between series and parallel circuits implies that such drive systems should be possible.
- Experimental implementation and testing of the SVPWM schemes developed in this thesis.
- Development of different SVPWM schemes for two-motor five-phase and six-phase drives, using the concept of multi-dimensional space (five-dimensional and six-dimensional, respectively), with the idea of maximising the dc bus utilisation for two-motor drives.
- A detailed investigation of applicability of five-phase two-motor drives in winders.

- An evaluation of the overall efficiency of the proposed drive systems for specific applications.
- Detailed study of the rating of the power switches for five-phase and six-phase VSIs aimed at supplying two series-connected machines.
- The multi-phase machine do not have perfect sinusoidal spatial distribution of windings, which leads to production of unwanted spatial air-gap harmonics and to the cross coupling between the two machines within the multi-motor drive group. This aspect should be addressed in order to arrive at appropriate machine designs for two-motor drive applications.
- Investigation into fault tolerant properties of two-motor drive systems.
- The thesis has developed dynamic models for the two two-motor drive structures. A further work is required to derive from these models corresponding steady state models and equivalent circuit representations.

`

Chapter 11

REFERENCES

Andriux, C. and Lajoie-Mazenc, M., (1985), Analysis of different current control systems for inverter-fed synchronous machine, *Proc. European Power Electronics and Applications Conf. EPE*, Brussels, Belgium, pp. 2.159-2.165.

Baiju, M.R., Mohapatra, K.K., Somasekhar, V.T., Gopakumar, K. and Umanand, L., (2003), A five-level inverter voltage space phasor generation for an open-end winding induction motor drive, *Proc. IEEE Applied Power Electronics Conf. APEC,* Miami Beach, Florida, pp. 826-832.

Benkhoris, M.F., Tali-Maamar, N. and Terrien, F., (2002), Decoupled control of double star synchronous motor supplied by PWM inverter: Simulation and experimental results, *Proc. Int. Conf. on Electrical Machines ICEM,* Bruges, Belgium, CD-ROM Paper 632.

Bojoi, R., Lazaari, M., Profumo, F. and Tenconi, A., (2002a), Digital field oriented control for dual three-phase induction motor drives, *Proc. IEEE Ind. Appl. Soc. Annual Meeting IAS,* Pittsburgh, Pennsylvania, CD-ROM Paper 22P1.

Bojoi, R., Tenconi, F., Profumo, F., Griva, G. and Martinello, D., (2002b), Complete analysis and comparative study of digital modulation techniques for dual three-phase AC motor drives, *Proc. IEEE Power Elec. Spec. Conf. PESC,* Cairns, Australia, CD-ROM Paper 10159.

Bojoi, R., Caponet, M.C., Grieco, G., Lazzari, M., Tenconi, A. and Profumo, F., (2002c), Computation and measurements of the DC link current in six-phase voltage source PWM inverters for AC motor drives, *Proc. Power Conversion Conf. PCC,* Osaka, Japan, pp. 953-958.

Bolognani, S. and Zigliotto, M., (2002), A space vector approach to the analysis and design of three-phase current controllers, *Proc. IEEE Int. Symp. on Industrial Electronics ISIE,* L'Aquila, Italy, pp. 645-650.

Bose, B.K., (1990), An adaptive hysteresis-band current control technique for voltage fed PWM inverter for machine drive system, *IEEE Trans. on Industry Applications,* vol. 37, no. 5, pp. 402-408.

Bose, B.K., (1996), *Power electronics and variable frequency drives,* IEEE Press, New York, USA.

Brabandere, K. De, Keybus, J. Van den, Bolsens, B., Driesen, J. and Belmans, R., (2002), Sampled-data dual-band hysteresis current control of three-phase voltage-source inverters, *Proc. Int. Conf. on Electrical Machines ICEM,* Bruges, Belgium, CD-ROM Paper 386.

Brod, D.M. and Novotony, D.W., (1985), Current control of VSI-PWM inverters, *IEEE Trans. on Industry Applications*, vol. IA-21, no. 4, pp. 562-570.

Calfo, R.M., Fulmer, J.A. and Tessaro, J.E., (2002), Generators for use in electric marine ship propulsion systems, *Proc. IEEE Power Eng. Soc. Summer Meeting,* Chicago, Illinois, pp. 254-259.

Correa, M.B.R., Jacobina, C.B., Silva da, C.R., Lima A.M.N. and Silva da, E.R.C., (2003a), Six-phase AC drive system with reduced common-mode voltage, *Proc. International Electrical Machine and Drives Conf. IEMDC,* Madison, WI, USA, pp. 1852-1858.

Correa, M.B.R., Jacobina, C.B., Silva da, C.R., Lima A.M.N. and Silva da, E.R.C., (2003b), Vector modulation for six-phase voltage source Inverters, *Proc. European Power Electronics and Applications Conf. EPE,* Toulouse, France, CD-ROM Paper 1084.

Doncker, de R.W., (2003), Twenty years of digital processing in power electronics and drives, *Proc. IEEE Ind. Elec. Soc. Annual Meeting, IECON*, Roanoke, Virginia, CD-ROM Paper 1166.

Ede, J.D., Atallah, K., Wang, J.B. and Howe, D., (2002), Modular fault-tolerant permanent magnet brushless machines, *Proc. IEE Power Electronics, Machines and Drives Conf. PEMD,* Bath, UK, pp. 415-420.

Ertugrul, N., Soong, W., Dostal, G. and Saxon, D., (2002), Fault tolerant motor drive system with redundancy for critical applications, *Proc. IEEE Power Elec. Spec. Conf. PESC,* Cairns, Australia, CD-ROM Paper 10499.

Figueroa, J., Cros, J. and Viarouge, P., (2002), Current control strategies for seven phase brushless DC motors, *Proc. Int. Conf. on Electrical Machines ICEM,* Bruges, Belgium, CD-ROM Paper 560.

Franceschetti, N.N. and Simoes, M.G., (2001), A new approach for analysis, modeling and simulation of brushless multiphase machines, *Proc. IEEE Ind. Elec. Soc. Annual Meeting IECON,* Denver, Colorado, pp. 1423-1427.

Francois, B. and Bouscayrol, A., (1999), Control of two induction motors fed by a five-phase voltage source inverter, *Proc. Electrimacs,* Lisbon, Portugal, pp. III.313-III.318.

Gataric, S., (2000), A polyphase Cartesian vector approach to control of polyphase ac machines, *Proc. of IEEE Ind. Appl. Soc. Annual Meeting IAS*, Rome, Italy, CD-ROM Paper 38_02.

Gio, E., Piovan, R. and Malesani, L., (1988), Evaluation of current control methods for voltage source inverter, *Proc. Int. Conf. on Electrical Machines ICEM,* Pisa, Italy, pp. 345-350.

Gopakumar, K., Ranganathan, V.T. and Bhat, S.R., (1993), Split-phase induction motor operation from PWM voltage source inverter, *IEEE Trans. on Industry Applications,* vol. 29, no. 5, pp. 927-932.

Green, S., Atkinson, A.G., Mecrow, B.C. and King, A., (2003), Sensorless operation of a fault tolerant PM drive, *IEE Proc. – Electr. Power Appl.*, vol. 150, no. 2, pp. 117-125.

Hadiouche, D., Razik, H. and Rezzoug, A., (2000), Modelling of a double-star induction motor with an arbitrary phase shift angle between its three phase windings, *9th Int. Conf. on Power Electronics and Motion Control PEMC*, Kosice, Slovakia, pp. 5.125-5.130.

Hadiouche, D., Razik, H. and Rezzoug, A., (2002), Design of novel winding configurations for VSI fed dual-stator induction machines, *Proc. Electrimacs*, Montreal, Canada, CD-ROM Paper 263.

Hadiouche, D., Baghli, L. and Rezzoug, A., (2003), Space vector PWM techniques for dual three-phase ac machine: Analysis, performance evaluation and DSP implemenatation, *Proc. IEEE Ind. Appl. Soc. Annual Meeting IAS*, Salt Lake City, Utah, USA, CD-ROM Paper 18_02.

Holmes, G.D. and Lipo, T.A., (2003), *Pulse Width Modulation for Power Converters-Principles and Practice*, IEEE Press Series on Power Engineering, John Wiley and Sons, Piscataway, NJ, USA.

Iqbal, A., Vukosavic, S.N. and Levi, E., (2003), Vector control of a five-phase induction motor drive, *Proc. Int. Universities Power Eng. Conf. UPEC*, Thessaloniki, Greece, pp. 57-60.

Iqbal, A. and Levi, E., (2004), Modelling of a six-phase series connected two-motor drive system, *Proc. 16th International Conference on Electrical Machines ICEM*, Krakow, Poland, CD ROM Paper 98.

Iqbal, A., Vukosavic, S.N., Levi, E., Jones, M. and Toliyat, H.A, (2005), Dynamics of a series-connected two-motor five-phase drive system with a single-inverter supply, *Proc. IEEE Industry Applications Society Annual Meeting IAS*, Hong Kong.

Iqbal, A. and Levi, E., (2005a), Space vector modulation schemes for a five-phase voltage source inverter, *11th European Conf. on Power Electronics and Applications EPE*, Dresden, Germany.

Iqbal, A. and Levi, E., (2006), Space vector PWM techniques for sinusoidal output voltage generation with a five-phase voltage source inverter, *Electric Power Components and Systems*, vol. 34, no. 2.

Jacobina, C.B., Azevedo, C.C. de, Silva, C.R. da, Lima, A.M.N. and Silva, E.R.C. da, (2002), On-line estimation of the stator resistance of a six-phase induction machine, *Proc. IEEE Ind. Appl. Soc. Annual Meeting IAS*, Pittsburgh, Pennsylvania, CD-ROM Paper 20P4.

Jiang, S.Z., Chau, K.T. and Chan, C.C., (2003), Spectral analysis of a new six-phase pole-changing induction motor drive for electric vehicles, *IEEE Trans. on Industrial Electronics*, vol. 50, no. 1, pp. 123-131.

Jones, M., (2002), A novel concept of a multi-phase, multi-motor vector controlled drive system, *MPhil/PhD Transfer Report*, Liverpool John Moores University, Liverpool, UK.

Jones, M., Levi, E., Vukosavic, S.N. and Toliyat, H.A., (2003a), Independent vector control of a seven-phase three-motor drive system supplied from a single voltage source inverter, *Proc. IEEE Power Elec. Spec. Conf. PESC,* Acapulco, Mexico, pp. 1865-1870.

Jones, M., Levi, E., Vukosavic, S.N. and Toliyat, H.A., (2003b), A novel nine-phase four-motor drive system with completely decoupled dynamic control, *Proc. IEEE Ind. Elec. Soc. Annual Meeting IECON*, Roanoke, Virginia, pp. 637-642.

Jones, M., Vukosavic, S.N., Levi, E. and Iqbal, A., (2004), A novel six-phase series connected two-motor drive with decoupled dynamic control, *IEEE Industry Applications Society Annual Meeting IAS*, Seattle, WA, USA, pp. 639-646.

Jones, M., (2005), A novel concept of a multi-phase, multi-motor vector controlled drive system, *PhD Thesis*, Liverpool John Moores University, Liverpool, UK.

Jovanovic, M.G., (1996), Sensorless control of synchronous reluctance machines, *PhD Thesis,* The university of Newcastle, Newcastle, Australia.

Kalantari, A., Mirsalim, M. and Rastegar, H., (2002), Adjustable speed drive based on fuzzy logic for a dual three-phase induction machine, *Proc. Electrimacs,* Montreal, Canada, CD-ROM Paper 124.

Kawai, H., Kouno, Y. and Matsuse, K., (2002), Characteristics of speed sensorless vector controlled dual induction motor drive connected in parallel fed by a single inverter, *Proc. IEEE Ind. Appl. Soc. Annual Meeting IAS,* Pittsburgh, Pennsylvania, CD-ROM Paper 22P3.

Kazmierkowski, M.P., Krishnan, R. and Blaabjerg, F., (2002), *Control in power electronics-selected problems*, Academic Press, California, USA.

Kelly, J.W., Strangas, E.G. and Miller, J.M., (2001), Multi-phase inverter analysis, *Proc. IEEE Int. Electric Machines and Drives Conf. IEMDC,* Cambridge, Massachusetts, pp. 147-155.

Kelly, J.W, Strangas, E.G. and Miller, J.M., (2003), Multi-phase space vector pulse width modulation, *IEEE Trans. on Energy Conversion,* vol. 18, no. 2, pp. 259-264.

Klingshirn, E.A., (1983), High phase order induction motors - Part I - Description and theoretical considerations, *IEEE Trans. on Power Apparatus and Systems,* vol. PAS-102, no. 1, pp. 47-53.

Krause, P.C., Wasynczuk, O. and Sudhoff, S.D., (2002), *Analysis of electric machinery and drive systems,* IEEE Press Series on Power Engineering, John Wiley and Sons, Piscataway, NJ, USA.

Kuono, Y., Kawai, H., Yokomizo, S. and Matsuse, K., (2001a), A speed sensorless vector control method of parallel connected dual induction motor fed by a single inverter, *Proc. IEEE Ind. Appl. Soc. Annual Meeting IAS*, Chicago, Illinois, CD-ROM Paper 29_04.

Kuono, Y., Kawai, H., Yokomizo, S. and Matsuse, K., (2001b), Speed sensorless vector control of parallel connected dual induction motor, *Proc. European Power Electronics and Applications Conf. EPE*, Graz, Austria, CD-ROM Paper 00566.

Levi, E., Iqbal, A., Vukosavic, S.N. and Vasic, V., (2003a), Vector-controlled multi-phase multi-motor drive systems with a single inverter supply, *Proc. XIIth Int. Symp. on Power Electronics Ee2003* (Invited paper), Novi Sad, Serbia and Montenegro, CD-ROM Paper IP2-1.

Levi, E., Iqbal, A., Vukosavic, S.N. and Toliyat, H.A., (2003b), Modelling and control of a five-phase series-connected two-motor drive, *Proc. IEEE Industrial Electronics Society Annual Meeting IECON*, Roanoke, Virginia, pp. 208-213.

Levi, E., Jones, M. and Vukosavic, S.N., (2003c), Even-phase multi-motor vector controlled drive with single inverter supply and series connection of stator windings, *IEE Proc. – Electr. Power Appl.*, vol. 150, no. 4, pp. 580-590.

Levi, E., Jones, M., Vukosavic, S.N. and Toliyat, H.A., (2003d), A five-phase two-machine vector controlled induction motor drive supplied from a single inverter, *Proc.10th European Power Electronics and Applications Conf. EPE*, Toulouse, France, CD ROM Paper 0001.

Levi, E., Iqbal, A., Vukosavic, S.N. and Vasic, V., (2003e), Vector-controlled multi-phase multi-motor drive systems with a single inverter supply, *Electronics*, vol. 7, no. 2, pp. 9-20.

Lyra, R.O.C. and Lipo. T.A., (2002), Six-phase induction machine with third harmonic current injection, *Proc. Electrimacs*, Montreal, Canada, CD-ROM Paper 304.

Martin, J.P., Semail, E., Pierfederici, S., Bouscayrol, A., Meibody-Tabar, F. and Davat, B., (2002), Space vector control of 5-phase PMSM supplied by 5 H-bridge VSIs, *Proc. Electrimacs*, Montreal, Canada, CD-ROM Paper 170.

Matsumoto, Y., Ozaki, S. and Kawamura, A., (2001), A novel vector control of single-inverter multiple-induction motors drives for Shinkansen traction system, *Proc. IEEE Applied Power Elec. Conf. APEC*, Anaheim, California, USA, pp. 608-614.

Matsuse, K., Kouno, Y., Kawai, H. and Yokomizo, S., (2002), A speed sensorless vector control method of parallel-connected dual induction motor fed by a single inverter, *IEEE Trans. on Industry Applications*, vol. 38, no. 6, pp. 1566-1571.

McCleer, P.J., Bailey, J.M. and Lawler, J.S., (1991), Five phase trapezoidal back emf PM synchronous machines and drives, *Proc. European Power Elec. and Appl. Conf. EPE*, Florence, Italy, pp. 4.128-4.133.

Mecrow, B.C., Jack, A.G., Atkinson, D.J., Green, S. and Atkinson, G.J., (2003), Testing of four-phase, fault-tolerant drives for aircraft fuel pumps, *Seminar on Electrical Drive Systems for the More Electric Aircraft – U.K. Magnetics Society*, Bristol, UK, ISSN 1740-2239.

Merabtene, M. and Benkhoris, M.F., (2002), Modelling of a double star synchronous machine fed by PWM inverters under fault condition, *Proc. Int. Conf. on Electrical Machines ICEM*, Bruges, Belgium, CD-ROM Paper 456.

Miller, J., Ostovic, V., Stefanovic, V. and Kelly, J., (2001a), An integrated automotive starter-generator with pole-phase modulation, *Proc. XIth Int. Symp. on Power Electronics Ee2001*, Novi Sad, Serbia and Montenegro, pp. 3-10.

Miller, J.M., Stefanovic, V., Ostovic, V. and Kelly, J., (2001b), Design considerations for an automotive integrated starter-generator with pole-phase modulation, *Proc. IEEE Ind. Appl. Soc. Annual Meeting IAS,* Chicago, Illinois, CD-ROM Paper 56_06.

Miller, J.M. and Stefanovic, V., (2002), Prognosis for integrated starter alternator systems in automotive applications, *Proc. Power Electronics and Motion Control Conf. PEMC,* Cavtat, Croatia, CD-ROM Paper T5-001.

Mohapatra, K.K., Somasekhar, V.T. and Gopakumar, K., (2002), A harmonic elimination scheme for an open-end winding induction motor drive fed from two inverters using asymmetrical dc link voltages, *EPE Journal*, vol. 12, no. 4, 2002, pp. 28-36.

Mohapatra, K.K., Gopakumar, K., Somasekhar, V.T. and Umanand, L., (2002a), A novel modulation scheme for a six phase induction motor with open-end windings, *Proc. IEEE Ind. Elec. Soc. Annual Meeting IECON,* Seville, Spain, pp. 810-815.

Nasar, S.A., Boldea, I. and Unnewehr, L.E., (1993), *Permanent magnet, reluctance and self-synchronous motors,* CRC press, Florida, USA.

Neascu, D.O., (2001), Space vector modulation – An introduction, *Proc. IEEE Ind. Elec. Soc. Annual Meeting IECON,* Denver, Colorado, pp. 1583-1592.

Novotony, D. and Lipo, T.A., (2000), *Vector control and dynamics of ac drives,* Clarendon Press, Oxford, UK.

Pavithran, K.N., Parimelalagan, R. and Krishnamurthy, M.R., (1988), Studies on inverter-fed five-phase induction motor drive, *IEEE Trans. on Power Electronics,* vol. 3, no. 2, pp. 224-235.

Pereira, L.A. and Canalli, V.M., (2002), Five-phase permanent magnet synchronous machine operating as generator – Design, parameter determination by FEM and performance, *Proc. IEEE Ind. Appl. Soc. Annual Meeting IAS,* Pittsburgh, Pennsylvania, CD-ROM Paper 10P5.

Pienkowski, K., (2002), Analysis of squirrel cage induction motor with dual stator winding, *Proc. Int. Conf. on Electrical Machines ICEM*, Bruges, Belgium, CD-ROM Paper 518.

Rattei, F., (2001), Design of a permanent magnet polyphase machine for a hybrid vehicle, *Proc. Electromotion Conf.,* Bologna, Italy, pp. 99-101.

Robert-Dehault, E., Benkhoris, M.F. and Semail, E., (2002), Study of a 5-phases synchronous machine fed by PWM inverters under fault conditions, *Proc. Int. Conf. on Electrical Machines ICEM,* Bruges, Belgium, CD-ROM Paper 446.

Ryu, H. M., Kim, J. H. and Sul, S.K., (2004), Analysis of multi-phase space vector pulse width modulation based on multiple d-q spaces concept, *Proc. Int. Conf. on Power Electronics and Motion Control IPEMC,* Xian, China, CD-ROM Paper 2183.pdf.

Shi, R., Toliyat, H.A. and El-Antably, A., (2001), Field oriented control of five-phase synchronous reluctance motor drive with flexible 3rd harmonic current injection for high specific torque, *IEEE Ind. Appl. Soc. Annual Meeting IAS,* Chicago, CD-ROM Paper 50_05.

Shi, R. and Toliyat, H.A., (2002), Vector control of five-phase synchronous reluctance motor with space vector pulse width modulation (SVPWM) for minimum switching losses, *Proc. IEEE Applied Power Elec. Conf. APEC,* Dallas, Texas, pp. 57-63.

Shireen, W., Arefeen, M.S. and Figoli, D., (2003), Controlling multiple motors utilizing a single DSP controller, *IEEE Trans. on Power Electronics,* vol. 18, no. 1, pp. 124-130.

Shivakumar, E.G., Gopakumar, K., Sinha, S.K., Pittet, A. and Ranganathan, V.T., (2001), Space vector PWM control of dual inverter fed open-end winding induction motor drive, *Proc. IEEE Power Electronics Spec. Conf. PESC,* Vancouver, Canada, CD-ROM Paper S12P5.

Shivakumar, E.G., Gopakumar, K., Sinha, S.K., Pittet, A. and Ranganathan, V.T., (2002), Space vector PWM control of dual inverter fed open-end winding induction motor drive, *EPE Journal,* vol. 12, no. 1, pp. 9-18.

Silva, de, P.S.N., Fletcher, J.E. and Williams, B.W., (2004), Development of space vector Modulation strategies for five-phase voltage source inverters, *Proc. IEE Power Electronics, Machines and Drives Conf. PEMD,* Edinburgh, UK, pp. 650-655.

Simoes, M.G. and Vieira, P., (2002), A high-torque low-speed multi-phase brushless machine – A perspective application for electric vehicles, *IEEE Trans. on Industrial Electronics,* vol. 49, no. 5, pp. 1154-1164.

Simoes, M.G., Franceschetti, N.N. and Vieira, P., (2001), Design and evaluation of a polyphase brushless DC-machine direct drive system, *Proc. IEEE Ind. Appl. Soc. Annual Meeting IAS,* Chicago, Illinois, CD-ROM Paper 19_07.

Singh, G.K., Pant, V. and Singh, Y.P., (2003), Voltage source inverter driven multi-phase induction machine, *Journal of Computer and Electrical Engineering,* pp. 814-834.

Somasekhar, V.T., Gopakumar, K., Pittet, A. and Ranganathan, V.T., (2002a), PWM inverter switching strategy for a dual two-level inverter fed open-end winding induction motor drive with a switched neutral, *IEE Proc. – Electr. Power Appl.,* vol. 149, no. 2, pp. 152-160.

Somasekhar, V.T., Gopakumar, K., Shivakumar, E.G. and Pittet, A., (2002b), A multi-level voltage space phasor generation for an open-end winding induction motor drive using a dual-inverter scheme with asymmetrical dc link voltages, *EPE Journal,* vol. 12, no. 3, pp. 21-29.

Sokola, M., Knezevic, M. and Levi, E., (1992), A comparative study of current control techniques for permanent magnet synchronous motor drives, *Proc. 21st Int. Conf. on Intelligent Motion PCIM,* Nürnberg, Germany, pp. 58-69.

Takami, H. and Matsumoto, H., (1993), Optimal pulse patterns of a nine-phase voltage source PWM inverter for use with a triple three-phase wound AC motor, *Electrical Engineering in Japan*, vol. 113, no. 6, pp. 102-113.

Telford, D., Dunnigan, M.W. and Williams, B.W., (2003), Adaptive high bandwidth current control for induction machines, *IEEE Trans. on Power Electronics,* vol. 18, no. 2, pp. 527-538.

Toliyat, H.A., (1998), Analysis and simulation of five-phase variable-speed induction motor drives under asymmetrical connections, *IEEE Trans. on Power Electronics,* vol. 13, no. 4, pp. 748-756.

Toliyat, H.A. and Qahtany, N.H., (2002), Finite element analysis of a concentrated winding multi-phase induction machine, *Proc. Int. Conf. on Electrical Machines ICEM,* Bruges, Belgium, CD-ROM Paper 501.

Toliyat, H.A., Rahmian, M.M. and Lipo, T.A., (1993), Analysis and modeling of five phase converters for adjustable speed drive applications, *Proc. 5th European Conference on Power Electronics and Applications EPE,* Brighton, UK, IEE Conf. Pub. No. 377, pp. 194-199.

Toliyat, H.A., Shi, R. and Xu, H., (2000), DSP-based vector control of five-phase synchronous reluctance motor, *IEEE Industry Applications Society Annual Meeting IAS,* Rome, Italy, CD-ROM Paper 40_05.

Toliyat, H.A. and Xu, H., (2000), DSP-based direct torque control (DTC) for five-phase induction machines, *Proc. Int. Power Elec. Conf. IPEC,* Tokyo, Japan, pp. 1195-1199.

Wang, F., (2002), Sine-triangle versus space-vector modulation for three-level PWM voltage-source inverters, *IEEE Trans. on Industry Applications,* vol. 38, no. 2, pp. 500-506.

Ward, E.E. and Härer, H., (1969), Preliminary investigation of an invertor-fed 5-phase induction motor, *Proc. IEE,* vol. 116, no. 6, pp. 980-984.

Weiming, M., Xusheng, W., Junzhong, S. and Qing, Y., (2002), Mathematical models and parameters of a 3&12-phase generator, *Proc. Int. Conf. on Electrical Machines ICEM,* Bruges, Belgium, CD-ROM Paper 256.

White, D.C. and Woodson, H.H., (1959), *Electromechanical energy conversion,* John Wiley and Sons, New York.

Xu, H., Toliyat, H.A. and Petersen, L.J., (2002a), Five-phase induction motor drives with DSP-based control system, *IEEE Trans. on Power Electronics,* vol. 17, no. 4, pp. 524-533.

Xu, H., Toliyat, H.A. and Petersen, L.J., (2002b), Resilient current control of five-phase induction motor under asymmetrical fault conditions, *Proc. IEEE Applied Power Elec. Conf. APEC,* Dallas, Texas, pp. 64-71.

Yu, F., Zhang, X., Li, H. and Ye, Z., (2003), The space vector PWM control research of a multi-phase permanent magnet synchronous motor for electrical propulsion, *Proc.*

International Conf. on Electrical Machines and Systems, ICEMS, Beijing, China, pp. 604-606.

Zhou, K. and Wang, D., (2002), Relationship between space-vector modulation and three-phase carrier-based PWM: A comprehensive analysis, *IEEE Trans. on Industrial Electronics*, vol. 49, no. 1, pp. 186-196.

Zhao, Y. and Lipo, A., (1995), Space vector PWM control of dual three-phase induction machine using vector space decomposition, *IEEE Trans. on Industry Applications*, vol. 31, no. 5, pp. 1100-1109.

APPENDIX A

MOTOR DATA

The basis for all the simulations is a four-pole, 50 Hz three-phase induction machine, with magnetising inductance of 0.42 H and rated torque of 5 Nm. Due to the lack of data for multi-phase machines, it is assumed that per-phase parameters and ratings of the multi-phase induction machines are the same as for the three-phase machine. Rated rotor flux (RMS) for this benchmark three-phase machine is equal to 0.5683 Wb [Jones (2005)]. Due to the use of power invariant transformation the following values of rotor flux and rated torque are used for simulation:

Five-phase machine:

$$\psi_r^* = \sqrt{5}\psi_{rn} = 1.2707 \text{ Wb}$$

$$T_{en} = 5(5/3) = 8.33 \text{ Nm}$$

Six-phase machine:

$$\psi_r^* = \sqrt{6}\Psi_{rn} = 1.392 \text{ Wb}$$

$$T_{en} = 6(5/3) = 10 \text{ Nm}$$

Per-phase stator leakage inductance (L_{ls}) = Rotor leakage inductance (L_{lr}) =0.04 H; Per-phase stator resistance (R_s)=10 Ω; Per-phase rotor resistance (R_r) = 6.3 Ω; Mutual inductance (M) in the phase variable model is $0.42/\left(\frac{5}{2}\right) = 0.168$ H for five-phase machine and $0.42/\left(\frac{6}{2}\right) = 0.14$ H for six-phase machine. Rated phase voltage and current (RMS) are 220 V and 2.1 A, respectively.

APPENDIX B

FIVE-PHASE INDUCTION MOTOR STATOR WINDING

The five-phase induction motors used in the experimental investigation in chapter 9 have 4-poles and 40 slots. This means that there are 20 slots per pole-pair. Further this gives 4 slots per phase per pole, or 2 slots per phase per pole. Thus the slot angle is 18 degrees. The winding used is single layer, full pitch (coil span is 10 slots), lap type and integral slot. The complete winding layout is shown in the Fig. B1.

In Fig. B1, red shows phase A, blue shows phase B, yellow shows phase C, green shows phase D and phase E is shown by black. One group of coil is formed by series connection of two individual coils. Each phase winding is comprised of two groups. Thus four terminals of each phase winding are available: two input terminals and two output terminals. In Fig. B1, the index 1 and 2 indicates the coil numbers while prime quantities referred to the second coil group. The phase shift between two groups of same phase winding is zero degree (displaced by 20 slots) so they can be connected either in series or in parallel. In the experimental investigation these coils are connected in parallel as shown in Fig. B2.

Deleted: 1. INTRODUCTION
Deleted: Chapter 1
Deleted: INTRODUCTION¶
Deleted: 1.1 PRELIMINARY ... [1]
Deleted: is currently under
Deleted: investigated
Deleted: ion
Deleted: in
Deleted: another
Deleted: PhD research project [J ... [2]
Deleted: 2
Deleted: 2) and Jones (2004)]. T ... [3]
Deleted: 2
Deleted: 4) considers this conce ... [4]
Deleted: The c
Deleted: Current control algorit ... [5]
Deleted:
Deleted: space vector PWM for ... [6]
Deleted: and
Deleted: current control in rotati ... [7]
Deleted: with
Deleted: sinusoidal PWM
Deleted: space vector PWM. On ... [8]
Deleted: The drive systems cons ... [9]
Deleted:
Deleted: The first group encon ... [10]
Deleted: project
Deleted: will examine applica ... [11]
Deleted: both
Deleted: . The existing SVPW ... [12]
Deleted: .
Deleted: and reported here. Fe ... [13]
Deleted: as well as current con ... [14]
Deleted: for both two-motor fi ... [15]
Deleted: This report contains o ... [16]
Deleted: 1.3 MAIN FEATUR ... [17]
Deleted:
Deleted: stator windings. How ... [18]
Deleted: ¶
Deleted: 1.4 RESEARCH ... [19]
Deleted: *To investigate*
Deleted: *the possibility of appl* ... [20]
Deleted: *on the multi-phase eq* ... [21]
Deleted: .¶
Deleted: *To evaluate the perfo* ... [22]
Deleted: <sp>*To participate in* ... [23]
Deleted: This report summaris ... [24]
Deleted: This thesis is organise ... [25]
Deleted: The original research ... [26]
Deleted: ¶
Deleted:
Deleted: Chapter 4 is dedicated ... [27]
Deleted: 5
Deleted: , while Chapter
Deleted: 6
... [28]

Deleted: 1. INTRODUCTION

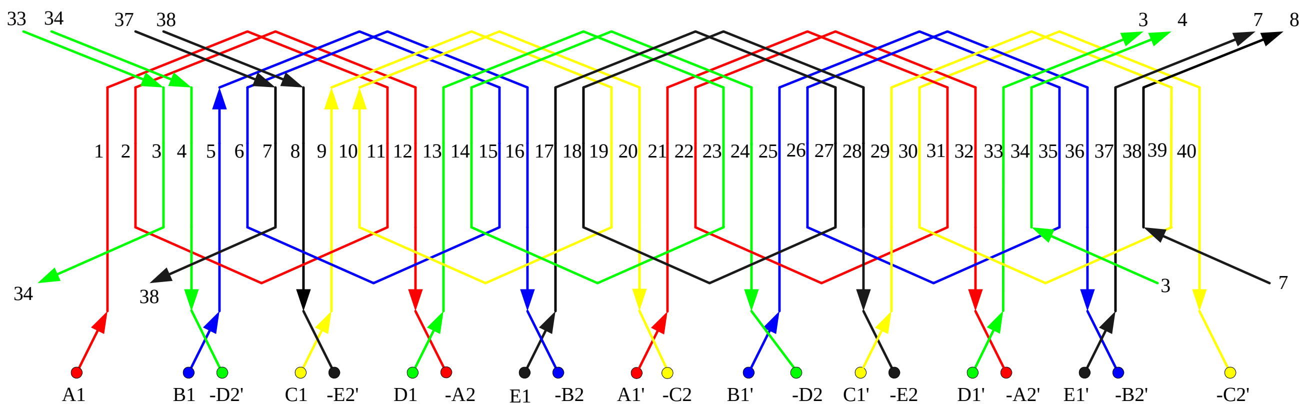

Fig. B1. Stator winding layout of five-phase induction motor.

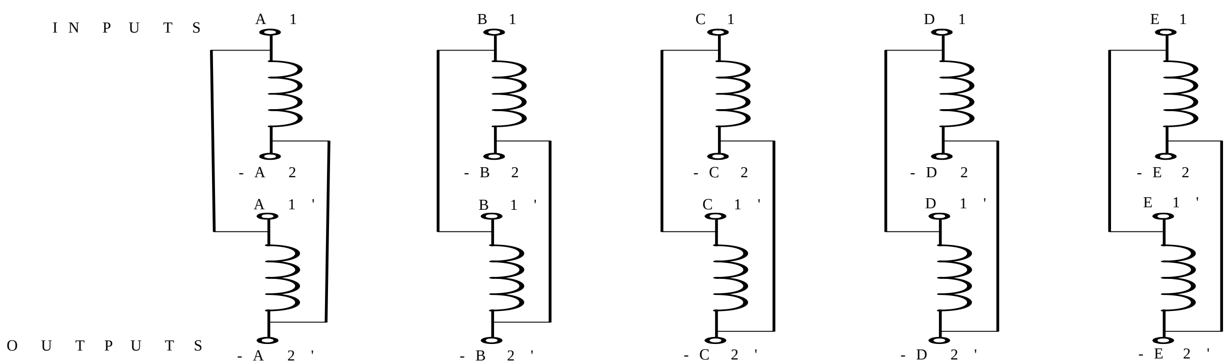

Fig. B2. Stator winding coils arrangement of five-phase induction motor.

Page 319: [1] Deleted	School of Engineering	4/6/2005 12:06:00 PM

1.1 PRELIMINARY CONSIDERATIONS

Numerous industrial applications such as textile industry, paper mills, robotics, railway traction and electric vehicles require more than one electric drive. Multi-machine drives are available in two configurations. The first one comprises *n* three-phase machines fed by *n* three-phase inverters, while the second one is the system with *n* three-phase motors fed from a single voltage source inverters (VSI) [Kuono et al (2001a, 2001b), Matsumoto et al (2001)]. In the first method the power electronics include *n* voltage source inverters (VSIs), that are fed from a single common dc link. This allows the speed of each motor to be controlled independently using its own VSI with an appropriate control algorithm. The second method uses one inverter to feed parallel-connected three-phase motors. In this structure motors, that have to be identical and loaded with the same load torque, will run at exactly the same angular speed. These are the major disadvantages of this system. However, the approach is useful in traction applications such as locomotives, buses and electric vehicles, where it is currently considered as a potentially viable solution. A method that enables independent control of at least two machines, of the same or different types and ratings, while using only one VSI does not exist at present. The proposed research will attempt to change this situation by utilizing drives with a phase number greater than the traditional three phases.

The research to be undertaken is intended to further advance the concept that has been

Page 319: [2] Deleted	School of Engineering	4/6/2005 12:06:00 PM

PhD research project [Jones (200

Page 319: [3] Deleted	School of Engineering	2/9/2005 10:12:00 AM

2) and Jones (2004)]. The research of Jones (200

Page 319: [4] Deleted	School of Engineering	2/9/2005 10:12:00 AM

4) considers this concept on a conceptual level for an arbitrary number of phases using an appropriate series connection of stator windings of multi-phase machines. All the

simulation studies are done under the assumption of idealised sinusoidal supply conditions, assuming ideal current control in the stationary reference frame for the series-connected system. This project, in contrast, deals with a detailed analysis of modelling and control aspects for two specific drive configurations: five-phase two-motor drive (two five-phase machines connected in series) and six-phase two-motor drive (a six-phase machine connected in series with a three-phase machine). In both cases the drives are fed using realistic supply, a current controlled PWM voltage source inverter. One especially important aspect of this project, not covered in Jones (2002) and Jones (2004) in any depth, is the modelling and control of five-phase and six-phase voltage source inverters. The research at first develops appropriate mathematical models for multi-phase inverters along with PWM strategies and current control schemes as applicable to the case of single multi-phase motor drives and also series-connected stator windings of multi-phase machines. The emphasis has been put on specific case of five-phase and six-phase VSI.

Page 319: [5] Deleted	School of Engineering	4/6/2005 12:06:00 PM

Current control algorithms to be used are hysteresis and ramp-comparison methods in stationary reference frame. The appropriate

Page 319: [6] Deleted	School of Engineering	4/6/2005 12:06:00 PM

space vector PWM for multi-phase VSIs has to be developed to be used in conjunction with

Page 319: [7] Deleted	School of Engineering	4/6/2005 12:06:00 PM

current control in rotating reference frame.

Page 319: [8] Deleted	Atif Iqbal	12/3/2004 10:54:00 AM

space vector PWM. On the basis of preliminary studies, it appears that current control in rotating reference frame will require a substantial modification when compared to the existing vector control scheme for three-phase machines.

The drive systems consisting of induction machines will be investigated.

1.2 STRUCTURE OF THE ANALYSED MULTI-MOTOR DRIVE SYSTEMS

In conventional electric drives, three-phase machines are used because of the economic factor as three-phase power supply is readily available. However, a variable speed drive application invariably requires a power electronic converter to supply an electric machine. In ac machine (induction machines, permanent magnet synchronous machines, synchronous reluctance machines) drive applications, inverters are the best choice. If power inverters are used to supply the machines then any number of phases can be used just by adding additional legs. The advantages of using multi-phase machines over three-phase counterpart are discussed in Levi et al (2003 c), Jones et al (2003 a) and Jones et al (2003 b).

This project deals with two specific series-connected two-motor drives. The first one comprises two five-phase machines connected in series with an appropriate phase transposition supplied from a single five-phase VSI. The second one consists of a six-phase machine connected in series to a three-phase machine with supply coming from a six-phase VSI. The basic idea behind the concept was explored by Jones (2002) and Jones (2004). It was concluded that, regardless of the number of phases, only two stator currents are required for decoupled dynamic flux and torque control (vector control) of an *n*-phase ac machine. This means that the remaining currents can be used to control the other machines, provided that the stator windings of all the machines are connected in series. However, in order to enable decoupling of flux/torque control of one machine from all the other machines in a group, it is necessary that flux/torque producing currents of one machine do not produce a rotating field in all the other machines. This requires introduction of an appropriate phase transposition in series connection of stator windings. Thus by series connection of the motor with an appropriate phase transposition and using vector control principle it is possible to control independently all the machines in the group.

Current controlled PWM inverter is the most frequent choice in vector controlled ac drives as decoupled flux and torque control by instantaneous stator current space vector amplitude and position control is achieved relatively easily. One can use either a current regulated voltage source inverter or a current source inverter (CSI). In CSIs a large inductor is used at the dc side, thus limiting the available rate of change of current. It is for this reason that a standard solution for vector controlled drives utilises current regulated voltage source inverter. All the current control techniques for voltage source inverters essentially belong to one of the two major groups.

Page 319: [10] Deleted **School of Engineering** **4/6/2005 12:06:00 PM**

The first group encompasses the current control methods that operate in the stationary reference frame while the second group includes current control techniques with current controllers operating in the rotational frame of reference. This thesis

Page 319: [11] Deleted **School of Engineering** **4/6/2005 12:06:00 PM**

will examine applicability and features of two current control techniques in the stationary reference frame, namely hysteresis PWM and ramp-comparison PWMsingle five-phase, single six-phase,

Page 319: [12] Deleted **School of Engineering** **4/6/2005 12:06:00 PM**

. The existing SVPWM technique for five-phase and six-phase VSIs will be analysed

Page 319: [13] Deleted **School of Engineering** **4/6/2005 12:06:00 PM**

and reported here. Few novel SVPWM techniques will be developed and will be compared with the existing methods and the detail comparison will be presented. An experimental investigation for indirect rotor field oriented control of single five-phase motor drive will be done. The decoupled and independent control of two-motor five-phase drives fed using single five-phase inverter will be examined experimentally. Both five-phase machines will be of induction type in two-motor five-phase drive. The ramp-comparison current control technique in stationary reference frame will be utilised throughout the experimental investigation to control the five-phase VSI. The feasibility of connecting permanent magnet synchronous reluctance machine in series with induction machine and their independent control will be explored experimentally.

Page 319: [14] Deleted **Atif Iqbal** **12/4/2004 8:46:00 AM**

as well as current control in rotational reference frame using ramp-comparison PWM and space vector PWM

Page 319: [15] Deleted **School of Engineering** **12/2/2004 1:20:00 PM**

for both two-motor five-phase and six-phase drives.

Page 319: [16] Deleted **Atif Iqbal** **12/4/2004 8:57:00 AM**

This report contains only the results and discussion related to current control in the stationary reference frame using hysteresis and ramp-comparison PWM for single five-phase and two-motor five-phase drives. The work will be extended further to current control in rotational reference frame for five-phase two-motor drive and current control in stationary and rotational reference frame for six-phase two-motor drive and results will be reported in the PhD thesis.

Page 319: [17] Deleted **School of Engineering** **4/6/2005 12:06:00 PM**

1.3 MAIN FEATURES OF THE INVESTIGATED DRIVE CONFIGURATIONS

The main objective of the research is to obtain completely independent control of all the machines within a multi-motor system, while feeding the whole assembly from a single multi-phase inverter, using vector control techniques. The work undertaken here discusses five-phase two-motor drives and six-phase two-motor drives. The scheme of the five-phase two-motor drive offers three main advantages. The first one is the saving in the number of inverter legs from six to five compared to an equivalent three-phase two-motor drive system. This smaller number of legs leads to the use of smaller number of semiconductor power switches and associated control circuit components, which ultimately enhances the reliability of the overall system. The second advantage is the easiness of the vector control algorithm implementation for the whole system within a single low cost Digital Signal Processor (DSP). The new class of DSPs integrate all the important power electronics peripherals in addition to traditional mathematical functions. The integration of power electronics functions simplifies the overall system implementation, lowers overall part count and reduces the board size. A detail review of the development of DSPs and their real time processing capabilities from 1980 onward has been summarised by Doncker (2003). The use of a single DSP controller TMS320F240 is demonstrated by Shireen et al (2003) in controlling two inverters which supply independently two three-phase induction motors in HVAC application. The third advantage is related to the possibility of direct regenerative braking of the system. As long as the braking energy of the decelerating machine is smaller than the motoring energy required by the other machine, braking energy will be supplied directly to the machine that is motoring. This means that the braking energy does not circulate through the inverter and moreover, full regenerative braking takes place since the energy is used by the other machine in the group. As far as the six-phase two-motor drive is concerned, only the second and the third of the described three advantages remain to hold true. The first one does not exist, since the supply comes from a six-phase inverter. However, since multi-phase machines are in general used for high power applications, the six-phase two-motor drive system offers the possibility of adding to the existing high-power six-phase drive an additional low-power low-voltage three-phase drive at no extra cost.

The major disadvantage of the proposed two-motor drives is the increase in stator copper losses due to flow of the non-flux/torque producing currents through

Page 319: [18] Deleted **School of Engineering** **4/6/2005 12:06:00 PM**

stator windings. However, the rotor copper loss are not affected. This increase in the losses will reduce the overall efficiency of the drive system when compared to an equivalent three-phase counterpart. This shortcoming will be more pronounced in the five-phase two-motor drive since both machines affect each other in this sense. In the six-phase two-motor drive configuration three-phase machine does not carry the current of the six-phase machine and thus the copper losses will remain the same in the three-phase machine. The six-phase machine still carries the current of the three-phase machine and the copper losses in the six-phase machine will be increased. However, if the three-phase machine is of low power rating while the six-phase machine is of high power rating, this increase in losses of the six-phase machine will be very small, leading to an insignificant reduction in efficiency.

Page 319: [19] Deleted School of Engineering 4/6/2005 12:06:00 PM

1.4 RESEARCH OBJECTIVES

The principal objectives of the proposed project are:

To carry out a comprehensive investigation of the modelling procedure for five-phase and six-phase two-motor series-connected drive systems, which will result in phase variable and d-q variable models of the complete two-motor drive systems.

To examine and model the operation of five-phase and six-phase voltage source inverters in 180° conduction mode and PWM mode.

To investigate current control methods for five-phase and six-phase inverters and to develop appropriate strategies for current control in the stationary reference frame, in conjunction with vector control of the two motors.

To evaluate the performance of the series-connected five-phase and six-phase two-motor drives by performing detailed simulation studies.

To develop space vector pulse width modulation (SVPWM) techniques for five-phase and six-phase VSIs for use in single five-phase and single six-phase motor drive and to compare the developed schemes with the existing methods.

To develop an appropriate SVPWM technique for five-phase and six-phase VSIs for

Page 319: [20] Deleted School of Engineering 4/6/2005 12:06:00 PM

the possibility of application of current control in the rotating reference frame in conjunction with series-connected five-phase and six-phase two-motor drives. The emphasis will be placed to provide sinusoidal output phase voltage from the VSIs to feed two-motor drive configuration

Page 319: [21] Deleted Atif Iqbal 12/3/2004 11:16:00 AM

on the multi-phase equivalents of sinusoidal PWM and voltage space vector PWM for three-phase drives

Page 319: [22] Deleted Atif Iqbal 12/3/2004 11:12:00 AM

To evaluate the performance of the series-connected five-phase and six-phase two-motor drives by performing detailed simulation studies.

To investigate the possibilities of using machine parallel connection instead of the series connection, within multi-phase multi-motor drive systems.

Page 319: [23] Deleted **School of Engineering** **4/6/2005 12:06:00 PM**

To participate in the realization of an experimental rig that will incorporate multi-machine drive system[1] *and to verify some of the theoretical investigations experimentally.*

Atif Iqbal **12/4/2004 9:17:00 AM**

;o far.

Page 319: [25] Deleted **School of Engineering** **4/6/2005 12:06:00 PM**

This thesis is organised in thirteen different chapters. Chapter 1 gives brief introduction to the research to be undertaken highlighting its main features in addition to the advantages and disadvantages of the proposed system. A brief overall structure of the system to be investigated has been presented in this chapter. The research objectives has been set and presented in chapter 1.

Chapter 2 presents a literature survey in the areas of multi-phase and multi-phase drives with an emphasis on references published since Jones (2002). The modern developments in the areas of the proposed research work have been studied and are summarised in this chapter. The potential application field of the multi-phase machine drives are considered as ship propulsion, more electric aircraft and safety critical application areas. The research carried out in these areas are reviewed and presented in this chapter. The present development in quasi six-phase and five-phase machine drives are also analysed in this chapter. The other relevant aspect related to the proposed research is the development in the control of multi-phase VSIs, are studied and outlined in this chapter. Further, the research focussing on the reduced inverter switch rating and switch count have been surveyed in this chapter.

---

[1] Experimental rig will be realized within the EPSRC project GR/R64452/01, on which a post-doctoral research associate is working. The work on this project includes myself and another PhD student, Mr. M. Jones.

Chapter 3 is devoted to the modelling and analysis of single five-phase induction motor drive and it constitutes the basis for the discussion of the modelling and control of the series-connected five-phase two-motor drive system in Chapter 4. A detail model of five-phase VSI for 180° conduction and PWM modes, based on space vector representation is discussed in this chapter. The model of five-phase induction machine in phase variable form and in arbitrary common reference machine is further elaborated in this chapter. The basic design of the vector controller is presented which is then used in dynamic simulation of drives system further on in this chapter and subsequent chapter in conjunction with five-phase two-motor drives system. A brief review of different current control schemes utilised in three-phase VSI is also presented. The design of analogue form of speed controller is also reported. The procedure of current and speed controller parameter tuning in their discrete form is outlined in the chapter. The same speed and current controller are used in single five-phase, single six-phase and five-phase and six-phase two-motor drives in subsequent chapters. A detailed dynamic simulation results for single five-phase induction motor drive is presented and analysed. The harmonic spectrum analysis is done for single five-phase induction motor drive which is of paramount importance in five-phase two-motor drive which is discussed in chapter 4.

Page 319: [26] Deleted **Atif Iqbal** **12/4/2004 1:40:00 PM**

The original research results are reported in section 3.7 of Chapter 3 and throughout Chapter 4.

Page 319: [27] Deleted **School of Engineering** **4/6/2005 12:06:00 PM**

Chapter 4 is dedicated to the modelling and control of five-phase two-motor drives system. The major aim of this chapter is to investigate the possibility of independent control of two five-phase induction machines connected in series and fed using a single five-phase VSI. A novel mathematical model in state space form is developed for the assembly of two five-phase induction machine connected in series. The model is first developed in the phase variable form which is then transformed using decoupling transformation matrix in its power invariant form to obtain set of decoupled equations. These set of decoupled equations are then transformed into stationary common reference frame which is then further transformed into arbitrary and to rotor flux oriented reference frames. The principle of vector control of series connected five-phase two-motor drive is discussed in this chapter. The simulation results of dynamic behaviour of indirect rotor field oriented controlled five-phase two-motor drive system is given in this chapter. Two different current control scheme in stationary reference frame namely hysteresis and ramp-comparison is utilised to control the current regulated PWM VSI feeding the whole drive assembly. To elaborate further the concept of decoupled control of five-phase two-motor drive system, harmonic analysis is done using Fast Fourier Transform.

The foundation of six-phase two-motor drive is laid down in chapter 5 by looking into a six-phase and a three-phase induction motor drive individually. Since the intention is to use a true six-phase induction machine (60° spatial phase displacement) a six-phase VSI model is developed to provide the required supply voltage. The model of six-phase VSI is developed at first in 180° conduction mode and then in PWM mode. The mathematical model development is done using space vector representation. A number of interesting feature of six-phase VSI is highlighted. The model of true six-phase induction motor is briefly discussed. The principle of indirect rotor field oriented control for six-phase and three-phase induction motor drive is investigated. The dynamic performance of a true six-phase and a three-phase induction machine is evaluated individually by simulation. The harmonic analysis of both six-phase and three-phase induction machine drive is also done and reported in this chapter.

Chapter 6 discusses the independent and decoupled control of six-phase two-motor drive system fed using a six-phase current regulated PWM VSI. The six-phase two-motor drive assembly consist of a true six-phase and a three-phase induction machine with appropriate phase transposition. A novel state space mathematical model of six-phase two-motor drive system is developed in phase variable form which is then transformed to obtain decoupled set of equations. These decoupled set of equations are further transformed to stationary, arbitrary and rotor field oriented frame of references. The developed set of equations is then used to simulate the drive system in Matlab/simulink platform to evaluate its performance and results are reported in chapter 6. The current regulation method used to control the six-phase VSI feeding two-motor drives are hysteresis and ramp-comparison methods in stationary reference frame. To further explain the concept of decoupled control of the six-phase two-motor drive, harmonic analysis is done and presented in this chapter.

Chapter 7 discusses the space vector PWM (SVPWM) implementation for five-phase VSI. The intention is to use the space vector decomposition technique and thus the mapping of the space vectors associated with five-phase VSI is done in x-y plane. The review of the literature concerning the SVPWM is given at first in this chapter. The existing technique which utilises only two outer large space vectors to synthesise the input reference is analysed and reported. The same concept is extended and two medium vectors are used to implement SVPWM and the results are reported in this chapter. Few more schemes are investigated aiming at production of sinusoidal output voltages. The feasibility of each method is validated by simulation throughout the chapter. A detailed comparison of performance of developed and existing schemes is also given. Further, a SVPWM scheme is developed to provide sinusoidal output to be utilised in decoupled control of five-phase two-motor drives fed using a single five-phase VSI. The viability of the proposed scheme is proved by simulation results.

The emphasis of Chapter 8 is to investigate into the principle of SVPWM for six-phase VSI. The literature related to SVPWM of even phase number VSI is reviewed and presented in this chapter. Some of the existing techniques exploiting the basic principle of SVPWM is further analysed in this chapter. One novel scheme is suggested to extend the range of application of the existing method and the results are presented in the chapter. A detailed comparison of performance of developed and existing schemes is also eloborated. A SVPWM scheme is developed focussing on production of sinusoidal output for use in decoupled control of six-phase two-motor drives. The simulation results are presented throughout to support the theoretical findings.

Chapter 9 discusses the results of experimental investigation. Some of the theoretical findings of the preceding chapters are implemented practically. The detail of the experimental rig is reported. Indirect rotor field oriented control of a five-phase induction motor drive is investigated using DSP based control system. The two-motor five-phase drive with decoupled control of each induction motor fed using a single five-phase VSI is implemented and the results are presented. The feasibility of using different types of ac machines in five-phase two-motor drive system is validated by using one five-phase induction motor and one permanent magnet synchronous reluctance motor. The independent control of these two type of machines are successfully implemented using a single DSP based control system with indirect rotor flux oriented control and the dynamic performance is presented. To further elaborate the concept of decoupled control of two five-phase machines, steady state no-load performance is carried out and the results are reported in this chapter. The load test is also performed on five-phase induction motor where the load used is a dc generator and the dynamic and steady state performance is investigated. To investigate the load torque profile a torque transducer is installed on the five-phase motor drive and the resulting performance is presented.

Conclusions are given in Chapter 10

Page 319: [28] Deleted **School of Engineering** **2/9/2005 1:14:00 PM**

11 summarises further work. Finally, references and drive data are listed in Chapter 12

APPENDIX B

PUBLICATIONS FROM THE THESIS

B1. Refereed Journal Papers

Levi, E., Iqbal, A., Vukosavic, S.N. and Vasic, V., (2003), Vector-controlled multi-phase multi-motor drive systems with a single inverter supply, *Electronics*, vol. 7, no. 2, pp. 9-20.

Jones, M., Vukosavic, S.N., Levi, E. and Iqbal, A., (2005), A six-phase series-connected two-motor drive with decoupled dynamic control, *IEEE Trans. on Industry Applications*, vol. 41, no. 4, pp. 1056-1066.

Jones, M., Levi, E. and Iqbal, A., (2005), Vector control of a five-phase series-connected two-motor drive using synchronous current controllers, *Electric Power Components and Systems*, vol. 33, no. 4, pp. 411-430.

Iqbal, A. and Levi, E., (2006), Space vector PWM techniques for sinusoidal output voltage generation with a five-phase voltage source inverter, *Electric Power Components and Systems*, vol. 34, no. 2 (accepted for publication).

B2. Refereed Conference Papers

Levi, A., Iqbal, A., Vukosavic, S.N. and Toliyat, H.A., (2003), Modeling and control of a five-phase series-connected two-motor drive, *IEEE Ind. Elec. Soc. Annual Meeting IECON*, Roanoke, Virginia, pp. 208-213.

Jones, M., Vukosavic, S.N., Levi, E. and Iqbal, A., (2004), A novel six-phase series-connected two-motor drive with decoupled dynamic control, *IEEE Industry Applications Society Annual Meeting IAS*, Seattle, WA, pp. 639-646.

Iqbal, A. and Levi, E., (2004), Modelling of a six-phase series-connected two-motor drive system, *International Conf. on Electrical Machines ICEM*, Krakow, Poland, CD-ROM Paper 98.

Jones, M., Levi, E. and Iqbal, A., (2004), A five-phase series-connected two-motor drive with current control in the rotating reference frame, *IEEE Power Electronics Specialists Conf. PESC*, Aachen, Germany, pp. 3278-3284.

Iqbal, A., Vukosavic, S.N., Levi, E., Jones, M. and Toliyat, H.A., (2005), Dynamics of a series-connected two-motor five-phase drive system with a single-inverter supply, *IEEE Industry Applications Society Annual Meeting IAS*, Hong Kong (accepted for publication).

Iqbal, A. and Levi, E., (2005), Space vector modulation schemes for a five-phase voltage source inverter, *11th European Conf. on Power Electronics and Applications EPE*, Dresden, Germany (accepted for publication).

Levi, E., Iqbal, A., Jones, M and Vukosavic, S.N., (2005), Experimental testing of series-connected vector controlled multi-phase multi-motor drives, *XIIIth Int. Symposium*

on Power Electronics Ee2005, Novi Sad, Serbia and Montenegro (accepted for publication).

B3. Invited Conference Keynote Paper

Levi, E., Iqbal, A., Vukosavic, S.N. and Vasic, V., (2003), Vector-controlled multi-phase multi-motor drive systems with a single inverter supply, *XIIth Int. Symposium on Power Electronics Ee2003,* Novi Sad, Serbia and Montenegro, CD-ROM Paper IP2-1.

B4. Full Conference Paper

Iqbal, A., Vukosavic, S.N. and Levi, E., (2003), Vector control of a five-phase induction motor drive, *38th Int. Universities Power Engineering Conf. UPEC,* Thessaloniki, Greece, pp. 57-60.

.